ADVANCED PLANETARY PROBE

FINAL TECHNICAL REPORT

TO THE JET PROPULSION LABORATORY

VOLUME 2
SPIN-STABILIZED SPACECRAFT FOR THE BASIC MISSION

TRW SYSTEMS

Rq/41128

4547-6005-R0000

ADVANCED PLANETARY PROBE STUDY

FINAL TECHNICAL REPORT

27 July 1966

Prepared for the Jet Propulsion Laboratory
under Contract 951311

Volume 2

Spin-Stabilized Spacecraft for the Basic Mission

This work was performed for the Jet Propulsion Laboratory, California Institute of Technology, sponsored by the National Aeronautics and Space Administration under Contract NAS7-100.

TRW SYSTEMS
1 Space Park
Redondo Beach, California

CONTENTS

CONTENTS (Continued)

CONTENTS (Continued)

CONTENTS (Continued)

CONTENTS (Continued)

CONTENTS (Continued)

CONTENTS (Continued)

ILLUSTRATIONS

ILLUSTRATIONS (Continued)

ILLUSTRATIONS (Continued)

ILLUSTRATIONS (Continued)

ILLUSTRATIONS (Continued)

ILLUSTRATIONS (Continued)

ILLUSTRATIONS (Continued)

ILLUSTRATIONS (Continued)

ILLUSTRATIONS (Continued)

ILLUSTRATIONS (Continued)

TABLES

TABLES (Continued)

TABLES (Continued)

1. INTRODUCTION AND CONCLUSIONS

The major conclusions of this part of the study of the Advanced Planetary Probe is that a 50-pound science payload, performing a valuable Jupiter flyby mission, can be delivered and accommodated by the 500-pound, spin-stabilized spacecraft shown in Figure 1-1, launched by an Atlas/Centaur/TE-364-3, which can deliver nearly 600 pounds to Jupiter. This is true not only for 1972, but, with slight variations, for the entire period 1970 to 1980. The studies show that this spacecraft can approach within 1.5 radii of Jupiter's surface and that the probability of mission success is quite high. The spinning spacecraft provides a scan mode for plasma probe, the solar cosmic ray counter, infrared radiometer, the auroral detector, and the TV.

This spacecraft can provide relatively high bit rates, keeping the required ground station time low and permitting effective backup modes in the event of system degradation. In general this system can get by with weekly DSIF contacts or, if data loss is allowed, monthly or longer periods between contact are reasonable after the initial part of the mission. The spacecraft design is related to that of Pioneer 6 and uses a similar system approach and subsystem technologies. Pioneer 6, however, has a 20 percent payload factor and this spacecraft has only a 10 percent factor. The complexity of this mission, requiring RTG power units with their relatively low efficiency, and a propulsion system, not necessary on Pioneer 6, a large antenna system weighing about 70 pounds, and 30 pounds of micrometeoroid protection, explains the decrease in payload efficiency.

The spacecraft antenna has been made as large as the booster fairing allows, 16 feet in diameter when deployed, folded during launch as shown in Figure 1-2. The antenna design is based on the well-tested Sunflower concept. The three RTG units and the magnetometer are also stowed during launch and deployed on booms after separation from the last stage of the booster. The spin rate is reduced from 60 to 7 rpm by means of two monopropellant 1-pound thrusters; the final rate of 5 rpm is achieved when these booms are deployed.

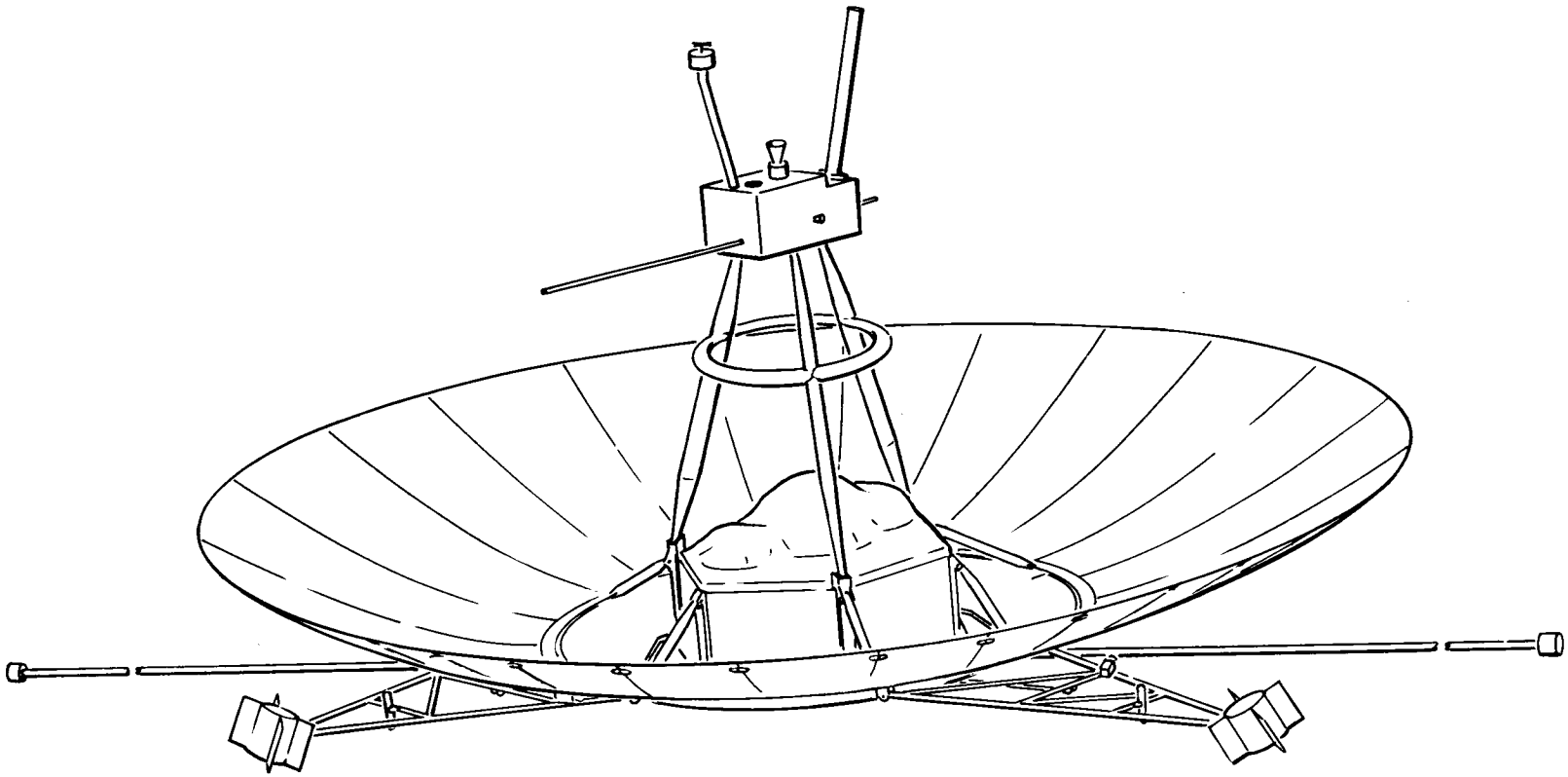

Figure 1-1. Jupiter Flyby Spin-Stabilized Spacecraft, 50-Pound Payload

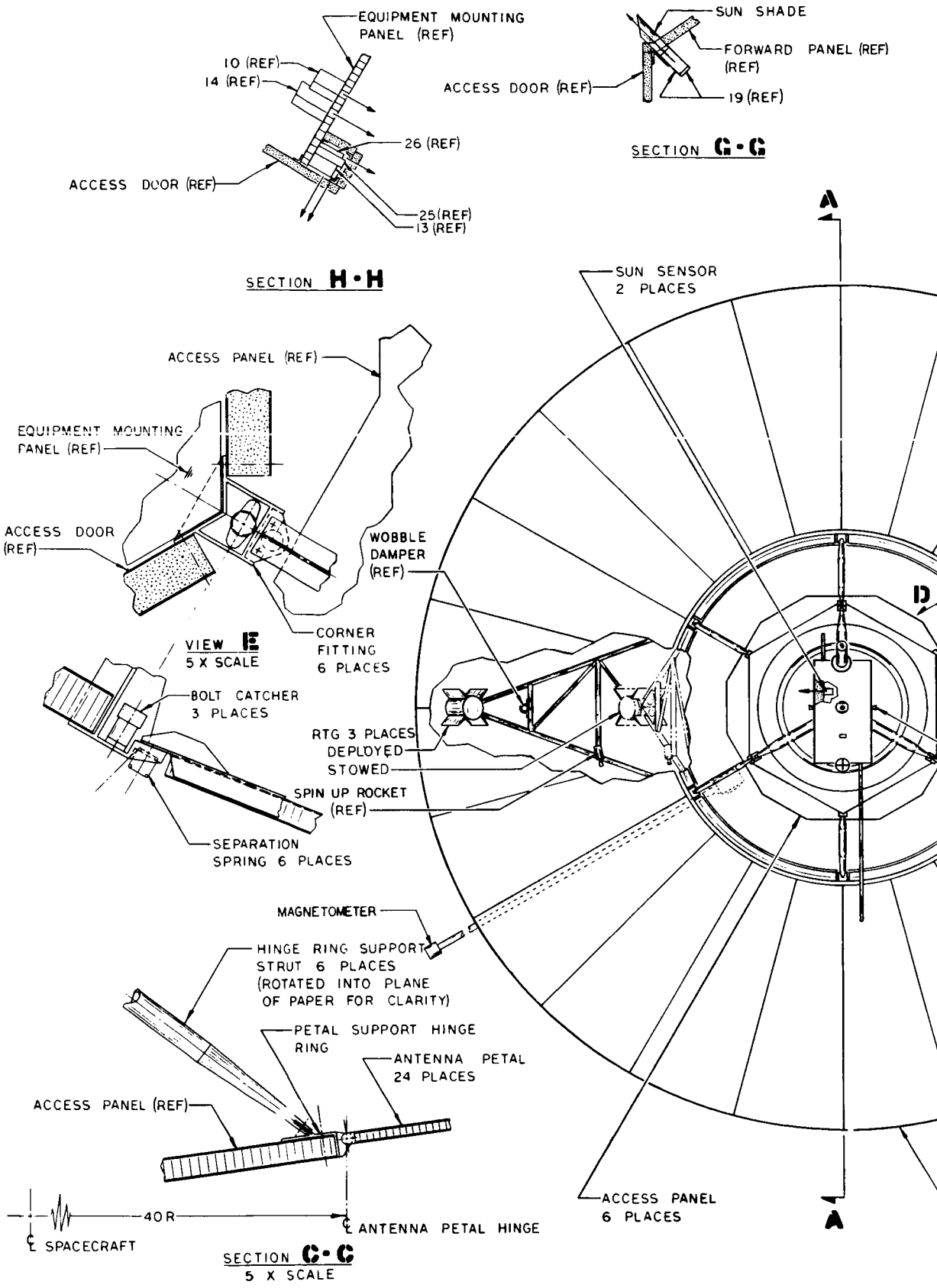
EQUIPMENT MOUNTING PANEL (REF)
10 (REF)
14 (REF)
26 (REF)
ACCESS DOOR (REF)
25 (REF)
13 (REF)
SECTION H-H
SUN SHADE
FORWARD PANEL (REF)
(REF)
ACCESS DOOR (REF)
19 (REF)
SECTION G-G
A
SUN SENSOR
2 PLACES
ACCESS PANEL (REF)
EQUIPMENT MOUNTING
PANEL (REF)
ACCESS DOOR
(REF)
WOBBLE
DAMPER
(REF)
CORNER
FITTING
6 PLACES
VIEW E
5 X SCALE
BOLT CATCHER
3 PLACES
RTG 3 PLACES
DEPLOYED
STOWED
SPIN UP ROCKET
(REF)
SEPARATION
SPRING 6 PLACES
D
MAGNETOMETER
HINGE RING SUPPORT
STRUT 6 PLACES
(ROTATED INTO PLANE
OF PAPER FOR CLARITY)
PETAL SUPPORT HINGE
RING
ANTENNA PETAL
24 PLACES
ACCESS PANEL (REF)
40R
℄ SPACECRAFT
℄ ANTENNA PETAL HINGE
SECTION C-C
5 X SCALE
ACCESS PANEL
6 PLACES
A

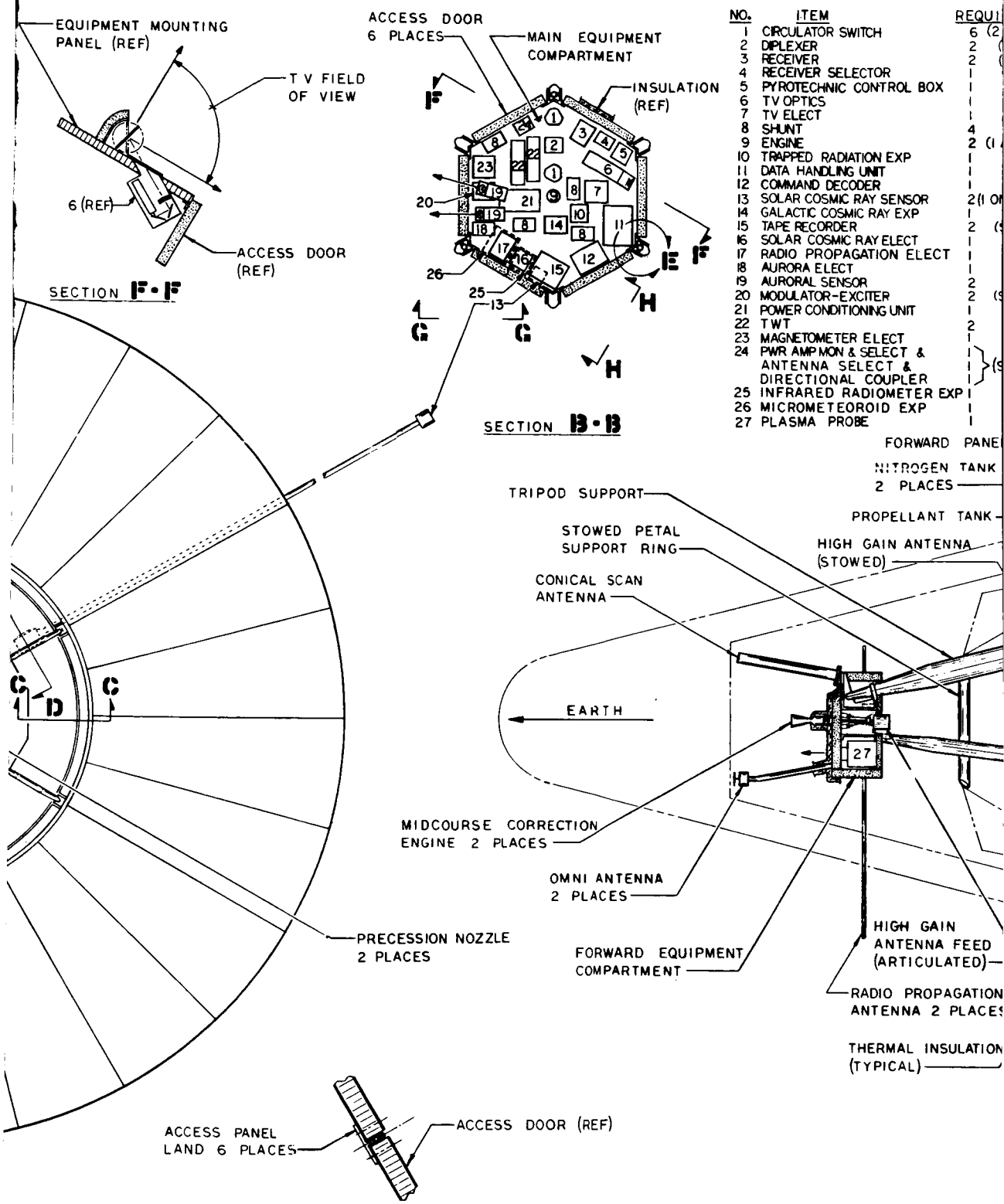

NO.	ITEM	REQUI
1	CIRCULATOR SWITCH	6 (2
2	DIPLEXER	2 (
3	RECEIVER	2 (
4	RECEIVER SELECTOR	1
5	PYROTECHNIC CONTROL BOX	1
6	TV OPTICS	1
7	TV ELECT	1
8	SHUNT	4
9	ENGINE	2 (1
10	TRAPPED RADIATION EXP	1
11	DATA HANDLING UNIT	1
12	COMMAND DECODER	1
13	SOLAR COSMIC RAY SENSOR	2 (1 O
14	GALACTIC COSMIC RAY EXP	1
15	TAPE RECORDER	2 (9
16	SOLAR COSMIC RAY ELECT	1
17	RADIO PROPAGATION ELECT	1
18	AURORA ELECT	1
19	AURORAL SENSOR	2
20	MODULATOR-EXCITER	2 (9
21	POWER CONDITIONING UNIT	1
22	TWT	2
23	MAGNETOMETER ELECT	1
24	PWR AMP MON & SELECT & ANTENNA SELECT & DIRECTIONAL COUPLER	1 (9
25	INFRARED RADIOMETER EXP	1
26	MICROMETEOROID EXP	1
27	PLASMA PROBE	1

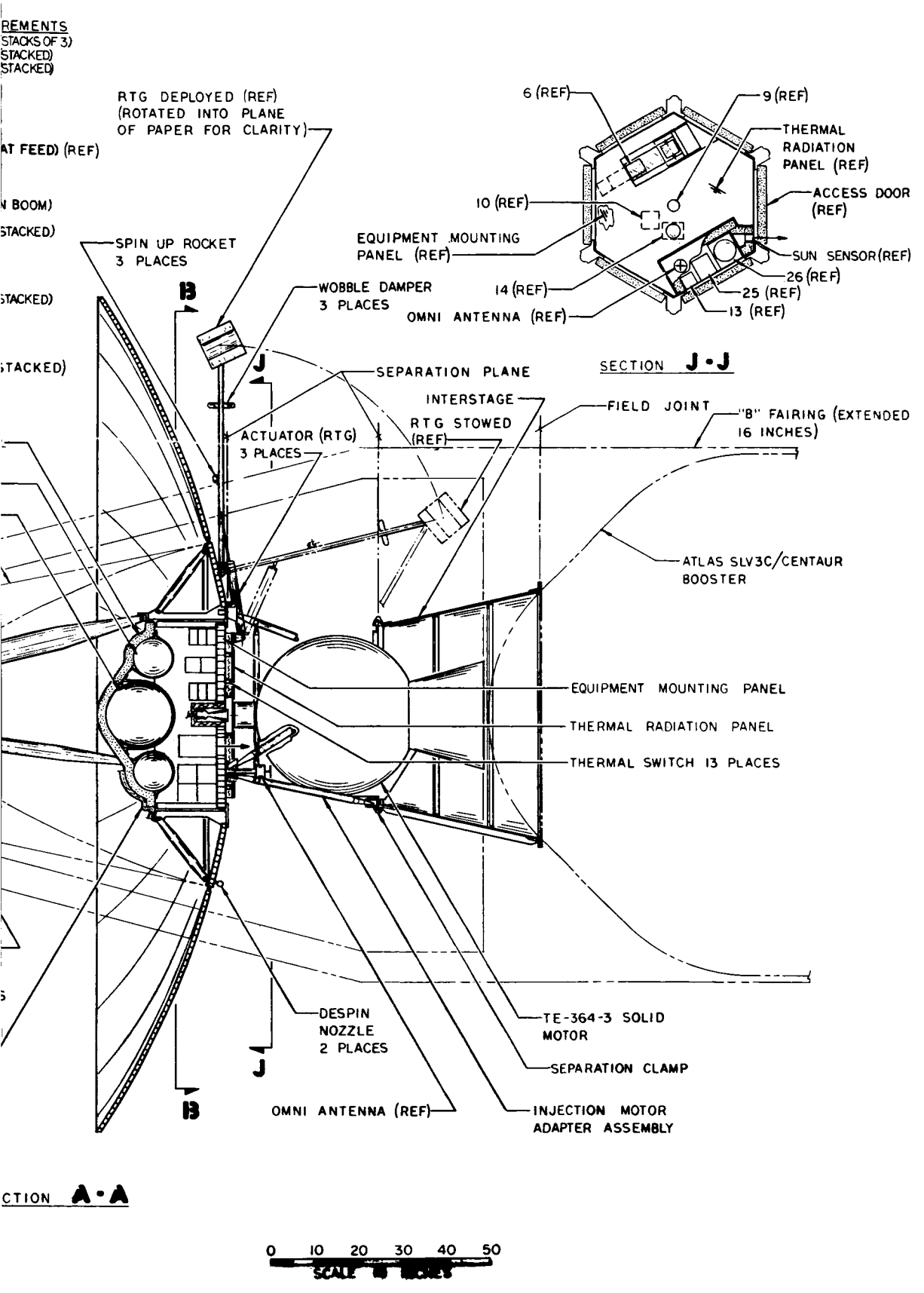

Figure 1-2. Advanced Planetary Probe Inboard Profile

The fixed antenna is directed toward the earth by torquing the entire spacecraft. Two low-gain antennas, one covering the forward hemisphere and one the aft, are used for initial acquisition. Commands to the spacecraft through these antennas are possible out to 10 AU. Normally, however, the probe will be commanded early in the flight to precess automatically to an orientation in which acquisition will be possible through the 25-degree beamwidth of the helix antenna. After acquisition, the earth pointing accuracy of the spacecraft can be kept within 0.5 degree by conical scan of the ground-transmitted signal. To facilitate the conical scan system the feed of the 16-foot antenna is offset on command from the ground. A simplified block diagram of the spacecraft is shown in Figure 1-3.

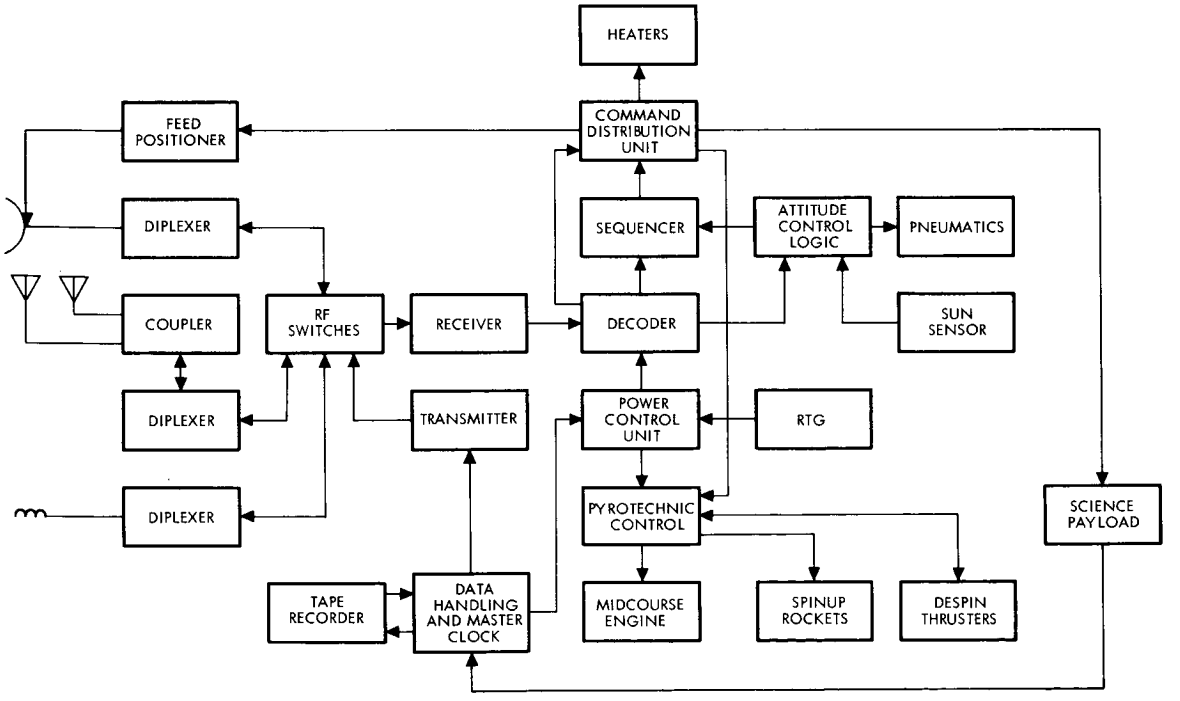

Figure 1-3. Simplified Block Diagram of 500-Pound, Spin-Stabilized Jupiter Flyby Spacecraft

With a 10-watt traveling wave tube amplifier, telemetry to the earth can probably be maintained at 700 bits/sec from the vicinity of Jupiter; information rates from 1400 to 8 bits/sec are selectable on command. A tape recorder is incorporated to permit telemetry acquisition by the spacecraft during planetary encounter at a rate faster than 700 bits/sec.

There are special problems in the Jupiter mission such as the effects of the asteroid belt and the radiation belt around Jupiter upon the spacecraft, but these questions are precisely what the mission is intended to answer. A conservative approach to these hazards has been adopted in the design study. There are also some problem areas in spacecraft design but these do not appear to be insurmountable, requiring only thorough engineering rather than advances in the state of the art. There are three such problems whose solutions have not been demonstrated in prior spacecraft: the deployable antenna, thermal design, and the low frequency conical scan used for attitude control. It is believed that adequate justification of the feasibility of the solution to these problems has been presented. There is one major problem involved in the basic concept of all the spacecraft concepts studied, that is, the cost and availability of the Pu 238 for the RTG's. Although a significant problem, it is clearly not one of feasibility. The mission analyzed appears, therefore, to be entirely feasible.

The estimated cost of the spacecraft, while substantial, is relatively modest compared with the scope of the mission and with other methods of its achievement. The overall estimated cost of the program appears to be appropriate to the type and significance of the scientific data to be gathered. The 42-month schedule given, which allows 13 months for Phases B and C, appears reasonable and does not demand an accelerated effort in any areas; the schedule does, however, assume that the RTG and isotope fuel development will begin with the Phase B effort for the spacecraft. It has also been recommended that deployable antenna work begin in Phase C to provide additional assurance that no unknowns remain relating to spin deployment or the extreme temperature ranges.

This spacecraft is directly suitable for flyby missions to Saturn, Uranus, and Neptune if the launch vehicle is the Titan IIICx/Centaur/TE-364-3. Some evolutionary improvement in reliability would be desirable for the Uranus and Neptune missions but, with this launch vehicle, the Saturn mission takes only a little longer than the Jupiter mission with the least expensive booster. Minor changes in the science instruments, together with data management changes associated with lower data rate, would be appropriate. Use of a lower spin rate beyond Jupiter would allow

the TV experiment to be unchanged except for an increase in exposure time (see Volume 3).

The approach of this volume in presenting and evaluating these conclusions is first in Section 2 to discuss in some detail the functional requirements placed on a precursor flyby mission to Jupiter. The effects of making use of a spin-stabilized spacecraft on the attainment of these functional requirements are then reviewed in Section 3 both from the point of view of the mission and the spacecraft. Sections 4 through 7 view the 1972 Jupiter flyby using a spin-stabilized spacecraft carrying 50 pounds of science payload from its system aspects. Preliminary designs of each of the spacecraft subsystems are presented in Section 8. The volume concludes with analyses of the reliability of the design, a feasible schedule for its implementation, its costs, and the cost effectiveness factors considered in the study.

Appendixes to these discussions are collected in Volume 4 of this report, except for Appendix J, which is separately bound because of its classification.

2. FUNCTIONAL REQUIREMENTS

This section reviews the functional requirements to be met by the spacecraft system for it to satisfactorily meet the objectives of the 1972 Jupiter flyby mission, with the 50-pound science payload. Although these requirements are intended to be generally applicable, those pertinent to spin-stabilized spacecraft design are emphasized. However, where specific interpretation of the requirements is necessary in the light of spacecraft design constraints—RTG power, large body-fixed antenna, earth orientation, and spin stabilization—this is deferred to Section 3.

Much of this section is applicable to other portions of the report (Volume 3) in which progressive variations from the basic mission are studied. For example, the material of Section 2.1, describing the characteristics of available launch vehicle systems, is applicable to all subsequent sections of the report.

2.1 LAUNCH VEHICLES

The characteristics of launch vehicle systems which influence the conduct of missions and impose design constraints on the spacecraft system are summarized. Eight launch vehicle systems were considered as candidates for the missions in this study. These include six configurations identified for use in the study by a JPL memorandum "Launch Vehicle Future Missions Study Guideline," by W. A. Ogram, Nov. 1, 1965:

A Saturn V/Centaur
B Saturn V
C Saturn IB/Centaur/HEKS
D Titan IIICx/Centaur
E Atlas SLV3x/Centaur/HEKS
F Atlas SLV3x/Centaur

(HEKS represents the proposed High Energy Kick Stage, with 7000 pounds thrust.) In addition, two combinations were generated by the incorporation of the TE-364-3 solid rocket motor into the injection sequence as a final stage:

D1 Titan IIICx/Centaur/TE-364-3
F1 Atlas SLV3x/Centaur/TE-364-3

As will be shown later, the addition of these two combinations provides a performance capability for certain combinations of spacecraft weight and mission C_3 requirements which could be provided only by more costly vehicles from the group A to F.

2.1.1 Weight Versus Injection Energy

Performance data for the eight launch vehicles have been generated, based on data supplied in the JPL memorandum. The results are plotted in Figure 2-1. The injection energy parameter employed as the abscissa is C_3, the square of the geocentric asymptotic departure velocity. (The Atlas SLV3x/Centaur cannot achieve C_3 of 60 km^2/sec^2, and does not appear in the figure.)

The net payload provided in this figure includes the payload adapter weight. For the vehicles using the TE-364-3, two adapters are required: an adapter between the Centaur and the spacecraft TE-364-3 combination and an adapter between the TE-364-3 and the spacecraft. Only the weight of the second adapter is included in the net payload. A weight of 67 pounds was utilized for the Centaur/TE-364-3 adapter and it was assumed that this weight was jettisoned prior to ignition of the TE-364-3 motor. The payload tradeoff factors with respect to the Centaur/TE-364-3 adapter weight are:

$$\frac{\partial W_{pl}}{\partial W_{adapter}} = -0.18 \text{ lb/lb}$$

for the Atlas configuration and:

$$\frac{\partial W_{pl}}{\partial W_{adapter}} = -0.4 \text{ lb/lb}$$

for the Titan III configuration.

The vehicle nose fairing need not be deducted from the net injected payload of Figure 2-1, since it has been accounted for in deriving the curves. This accounting was based on the estimated nose fairing weights, reduced by a factor of 10 consistent with fairing separation at 350,000 feet altitude.

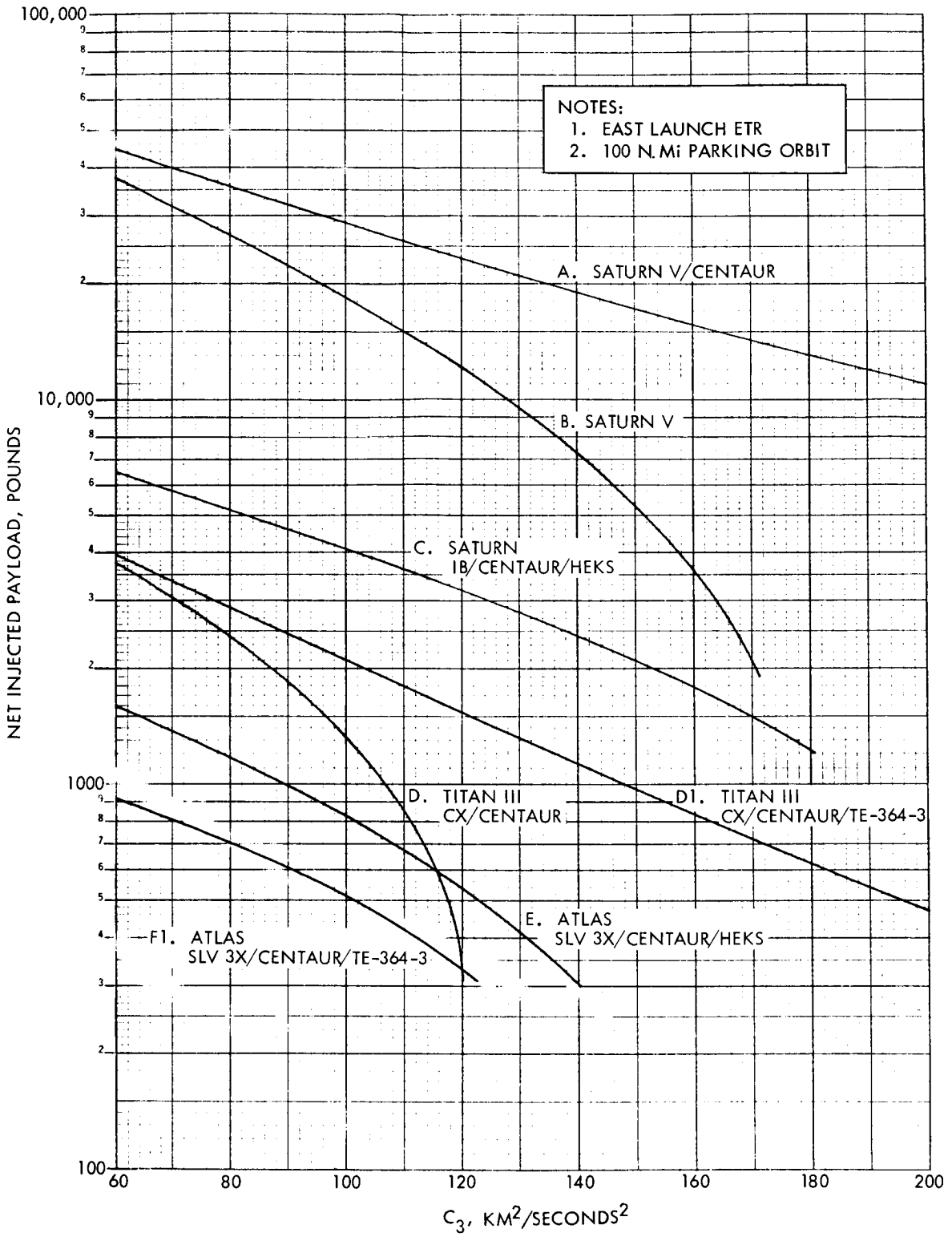

Figure 2-1. Launch Vehicle Performance Capability

As noted, the Atlas SLV3x/Centaur is unsuitable for missions to Jupiter and beyond, because it cannot generate adequate injection energy. The Titan IIICx/Centaur, while adequate for missions requiring 80 to 110 km^2/sec^2 injection energy, falls off in capacity at higher energies. The addition of a solid motor stage provides the capabilities indicated for vehicles F1 and D1 in Figure 2-1. The motor chosen for this added stage, Thiokol's TE-364-3, is a version of the Surveyor main retrorocket, which has been thoroughly tested and verified for reliability, impulse accuracy, and thrust alignment The "-3" version employs the identical rocket casing and nozzle as the Surveyor rocket; by reducing the size of the internal void space, the propellant weight is maximized. Performance data for the TE-364-3 are:

Propellant weight, lb	1440
Burnout weight, lb	134
Total weight, lb	1574
Specific impulse, sec	288.5

The feasibility of incorporating this rocket into the injection sequence has been validated by the development of the Burner II launch vehicle stage by Boeing. From this development, versions are available in which the third-stage attitude is controlled during solid rocket firing either by spin or 3-axis stabilization.

As an alternate to the use of the Burner II stage, in this study we have treated the TE-364-3 functionally as part of the launch vehicle, but physically as integrated into the spacecraft system. The spacecraft system provides for stabilization during solid rocket firing and for separation of the spent motor after burnout.

2.1.2 Limitations on Launch Vehicle Capability

For the configurations being considered, a restart of either the Centaur or the S-IVB will be required to establish the transfer orbit. Both of these stages have restart capability; however the use of cryogenic propellants in these stages will require that the coast time be kept to a minimum to reduce boiloff. The coast time for the Centaur is currently limited to 25 minutes for the Surveyor mission. Either an increase in

this allowable coast time or a limitation on the spectrum of acceptable transfer orbits would be required by the Advanced Planetary Probe missions. The S-IVB can restart after coasting for a full revolution and therefore should present no problem in this regard. For the high energy missions being considered, restart of the HEKS and TE-364 motor would not be required for injection into the transfer orbit since these stages would be utilized only in this phase.

The permitted range of launch azimuths from ETR has been 90 to 114 degrees for the Mariner IV earth-Mars mission. It has been proposed as 71 to 108 degrees for Voyager 1971. Such limitations restrict the selection of the transfer orbit in conjunction with the coast time limitations just discussed. Detailed analyses of these limitations would have to be conducted separately for each mission and each launch opportunity. Such an analysis for 1972 earth-Jupiter missions is given in Section 2. 2. If it is required to increase the range of allowable launch azimuths, detailed range safety analysis would be required.

The performance data presented in Figure 2-1 are based on the utilization of a 90-degree launch azimuth. The effect of other launch azimuths on performance is given in Figure 2-2 in terms of ΔC_3 as a function of launch azimuth and C_3.

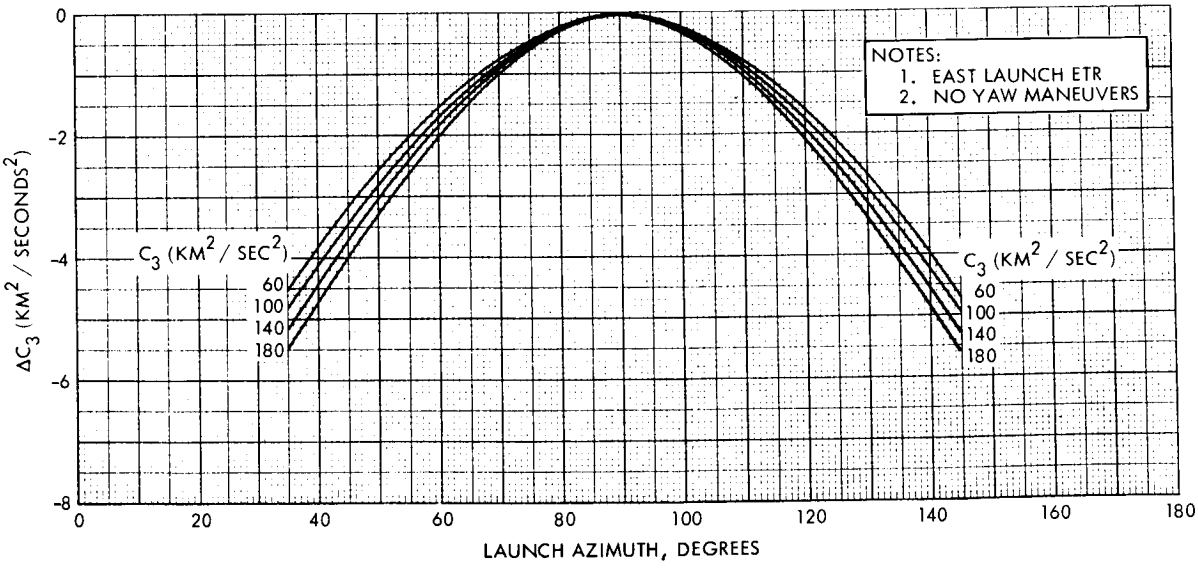

Figure 2-2. C_3 Correction for Launch Azimuth

2.1.3 Injection Accuracy

The injection accuracy of any of the launch vehicle combinations is largely a function of the accuracy of the last stage operation; where the final stage is a liquid (SIVB, Centaur, or HEKS) closed-loop control largely compensates for the inaccuracies of previous stages, and where the final stage is a solid (TE-364-3) operated open loop, it is inherently less accurate than the preceding liquid stages.

Because the High Energy Kick Stage is not yet in the development phase, and the Saturn V appears oversize for the first generation spacecraft concepts of this study, we examine the Centaur injection accuracy, and take it to be representative of launch vehicles with liquid final stages.

An early estimate* of the Atlas/Centaur injection accuracy produced a "figure of merit" of 10 m/sec. A more recent analysis** determines the 3σ injection accuracy for the Surveyor mission to be approximately 5 m/sec in velocity and 0.09 degree in flight path angle for an Atlas/Centaur configuration utilizing two burns of the Centaur stage and a coast time of 1500 seconds. The two estimates differ in the degree of refinement. Also, the second applies to dispersions at the moment of injection, while the first is stated in terms of velocity deviations after the influence of the earth's gravitation has effectively ceased. Even though the two estimates are not directly comparable, an approximate transformation indicates that the first is somewhat more pessimistic than the second. For purposes of this study either estimate is considered applicable to launch vehicles A through F.

For vehicles D1 and F1 the Centaur estimate is employed, but the injection error is substantially influenced by the solid motor operation. The TE-364 itself is estimated to have a 3σ impulse error of 1 percent.*** However, the solid motor operation introduces additional errors which are associated with the Centaur attitude error at separation, the tipoff, spinup,

---

*"Mariner Mars 1969 Orbiter Technical Feasibility Study," JPL Engineering Planning Document 250, 16 Nov. 1964, p. 8-110.

**"Centaur Guidance System Bimonthly Report, AC-8 Accuracy Analysis," General Dynamics, 1 Jan 1966, GD/C-BTD 64-013-10.

***"Spherical Rocket Motors," Thiokol Chemical Corporation, Elkton Division, EB7-64, January 1965.

and mass unbalance errors of the spacecraft (if spin-stabilized), and thrust alignment of the solid motor. Since these effects depend largely on the spacecraft design, they are not considered to constitute functional requirements on the spacecraft. Their consideration is deferred to Section 7.4, where other elements of spacecraft trajectory accuracy analysis are taken up in greater detail, for vehicle F1, the Atlas/Centaur/TE-364-3.

It is noted that vehicle D1 will have a smaller injection error from the solid rocket than will F1, because the heavier payload carried by D1, the Titan IIICx/Centaur/TE-364-3, receives a smaller ΔV from the solid stage.

2.1.4 Longitudinal Accelerations

The maximum longitudinal accelerations imposed on the payload by the various launch vehicle configurations are listed in Table 2-1.

Table 2-1. Maximum Longitudinal Acceleration

	Launch Vehicle	~ g
A	Saturn V/Centaur	4.35
B	Saturn V	4.35
C	Saturn IB/Centaur/HEKS	4.0
D1	Titan IIICx/Centaur/TE-364	4.07
E	Atlas SLV3x/Centaur/HEKS	6.0
F1	Atlas SLV3x/Centaur/TE-364	13.45

For configurations A, B, C, and E the maximum acceleration is obtained during the operation of the first stage. Configurations D1 and F1, however, encounter maximum acceleration at the termination of the TE-364 solid motor burning phase. The acceleration in the latter case is highly dependent on payload weight. The payload at $C_3 = 100$ $(km/sec)^2$ was used in determining the peak acceleration for these two configuration. For reduced payloads corresponding to higher values of C_3, the peak acceleration will be higher than the above values. This increase is most pronounced for D1 and F1.

2.1.5 Launch Vehicle Dynamic Environments

The dynamic environments for the launch vehicles presently considered are given below. These vehicles are Atlas SLV3x/Centaur with or without upper stage, Titan IIICx/Centaur with or without upper stage, and Saturn IB/Centaur/HEKS.

2.1.5.1 Atlas/Centaur

The data* is preliminary, intended for use in feasibility or preliminary calculations.

A requirement to design a rigid payload structure is given. A recommended lowest cantilever frequency is 20 cps.

The payload's structure and small components (up to approximately 50 pounds) should be designed to withstand the following sinusoidal and random vibrations without adverse effects.

a) Sinusoidal

0.25 inch single amp (O-P) 5 to 13 cps

3.15 g (rms) 13 to 500 cps

4.5 g (rms) 500 to 2000 cps

b) Random Vibration

0.0013 g^2/cps at 50 cps increasing 6 db per octave to 0.225 g^2/cps at 600 cps. Constant at 0.225 g^2/cps from 600 to 1100 cps. Decreasing at 12 db/octave to 0.0205 g^2/cps at 2000 cps.

Sweep rate 2 minutes per octave, duration 17.3 minutes in each of three mutually perpendicular axes.

Payload Weight, lb	100	200	400	1000	2000	5000
Permissible load factor, g	10	7.5	5.4	3.2	2.5	1.8

The only significant shock in the Centaur environment is caused by the separation of insulation panels on Centaur and the nose fairing jettison or spacecraft separation. This may be represented by a sinusoidal shock for one-half wavelength in which maximum shock amplitude is 1000 g and the duration 0.0004 second. The shock is applied along any axis.

*Centaur Capability Handbook," GD/A Project Centaur, GD/A-BTD 64-119-1.

Equipment, while operating, will undergo a maximum, broadband, random incidence, sound pressure field with an overall sound pressure level of 141 decibels. (The detailed levels are given in Volume 2 (p 364) of TRW's Phase IA Study Report on Voyager.)

2.1.5.2 Titan IIICx/Centaur/Upper Stage.

Data* applies to Titan IIIC with transtage. However, test levels are not expected to deviate with use of Centaur as opposed to the transtage.

The vibration environment described is applicable for periods of approximately 10 seconds during launch and 40 seconds during the transonic and maximum dynamic pressure regions of flight. During the remaining portions of powered flight, the overall rms vibration levels will be less than half the values described.

For payload weights less than 2000 pounds:

Flat 22 to 180 cps at 0.065 g^2/cps
Rolloff at 3 db/oct below 22 cps
Flat 550 to 1000 cps at 0.2 g^2/cps
Rolloff at 3 db/oct below 550 cps
Rolloff at 6 db/oct above 1000 cps
Overall 15.8 g rms

(1) Reduce spectra by 3 db for total weights of 2000 to 10,000 pounds, overall 11.3 g rms.

(2) Reduce spectra by 6 db for total weight of 10,000 to 20,000 pounds, overall 7.9 g rms.

Transient accelerations at shroud and spacecraft separation are to be considered. Shock input can be represented by a sinusoidal shock for one-half wavelength which maximum shock amplitude will be 850 g's and the duration 0.00035 second.

The maximum noise levels for test is 150 db qualification level (includes 5 db margin for test), 1 minute for test. This covers both the launch and the transonic and maximum dynamic pressure flight conditions.

*Interface Specification, Standard Space Launching System to Spacecraft Environmental, Standard Interface Capabilities and Requirements, Specification IFS-T111-20004.

2.1.5.3 Saturn IB/Centaur

a) Low Frequency Vibration. The low frequency flight vibration, covering all events from liftoff to spacecraft injection, is estimated to be a sinusoidal input as follows:

Lateral	0.6 g rms	5 to 200 cps
Axial	1.2 g rms	5 to 200 cps

b) Random Vibration. The liftoff and transonic vibration environment, with the exception of low frequency, is assumed to be the following omnidirectional input to the spacecraft separation plane: power spectral density peaks of 0.07 g^2 cps ranging from 100 to 1500 cps with a 6 db/octave rolloff in the envelope defining peaks below and above these frequencies. Maximum total time is 60 seconds. Random vibration at other mission times is predicted to be insignificant by comparison.

Depending on the launch vehicle characteristics, shock response during events other than separation is predicted to be insignificant. The shock response to shroud and spacecraft separation may be approximated by an input consisting of a 200-g terminal peak sawtooth of 0.7 to 1.0 millisecond rise time.

The maximum acoustic field, for either liftoff or transonic, is assumed to be a reverberant field as follows: overall sound pressure level is approximately 142 db total duration about 2 minutes.

2.1.6 Dynamic Envelopes and Mechanical Interfaces

The Saturn class of launch vehicle (A, B, C) carries a nose fairing with a nominal diameter of 20 feet. For the other launch vehicles, the shroud diameter is 10 feet. Sketches of the dynamic payload envelopes within these fairings are given in Figure 2-3. Sketches of the mechanical interface between the spacecraft and launch vehicle are shown as follows:

Figure 2-4	A. Saturn V/Centaur
Figure 2-5	B. Saturn V
Figure 2-6	C. Saturn IB/Centaur/HEKS
Figure 2-7	D, F. Titan IIICx/Centaur and Atlas SLV3x/Centaur (also applicable to D1, F1)
Figure 2-8	E. Atlas SLV3x/Centaur/HEKS

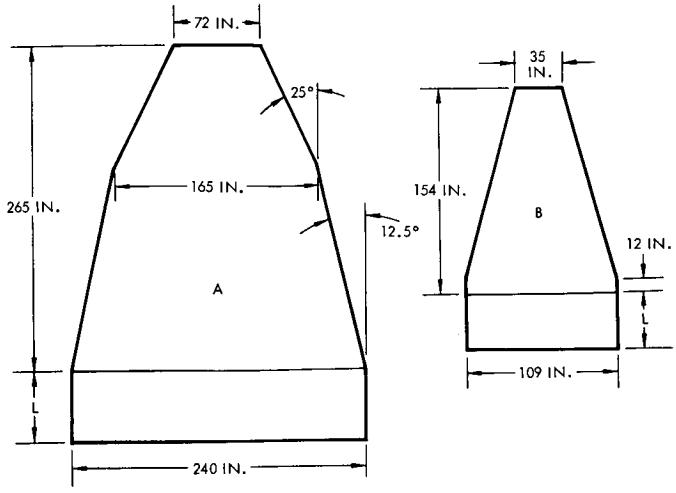

VEHICLE	FAIRING	MAXIMUM CYLINDRICAL SECTION LENGTH (L) (FT)	REMARKS
A	A	5	NO HAMMERHEAD POSSIBLE
B	A	35	
C	A	0	
D	B	10	HAMMERHEAD POSSIBLE; MAY BE PREFERRED. DETAILED INFORMATION NOT AVAILABLE. CONSIDER 2 FT ADDITIONAL DIAMETER MAXIMUM
E	B	5	
F	B	10	

Figure 2-3. Dynamic Payload Envelopes for Launch Vehicles

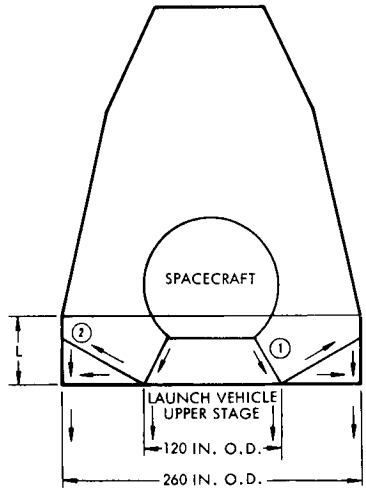

① PAYLOAD ADAPTER SHOULD BE DESIGNED TO TRANSFER LOAD IN A UNIFORMLY DISTRIBUTED PATH TO THE LAUNCH VEHICLE (L.V.) UPPER STAGE CIRCUMFERENCE

②a. PROVISION SHOULD BE MADE TO TRANSMIT ENTIRE PAYLOAD WEIGHT FROM CIRCUMFERENCE OF UPPER STAGE UNIFORMLY INTO THE FAIRING CIRCUMFERENCE WITHIN THE LENGTH (L) SHOWN DURING TIME WHEN L.V. IS UNPRESSURIZED

b. LOAD SHOULD BE UNIFORMLY DISTRIBUTED OVER THE L.V. UPPER STAGE AND THE FAIRING DURING BOOST PHASE OF TRAJECTORY. LOAD SHOULD BE SHARED APPROXIMATELY EQUALLY BETWEEN THE FAIRING AND THE L.V. UPPER STAGE.

c. LOAD SHOULD BE TRANSMITTED ENTIRELY THROUGH THE L.V. UPPER STAGE FOLLOWING FAIRING JETTISON.

Figure 2-4. Mechanical Interface, Vehicle A, Saturn V/Centaur

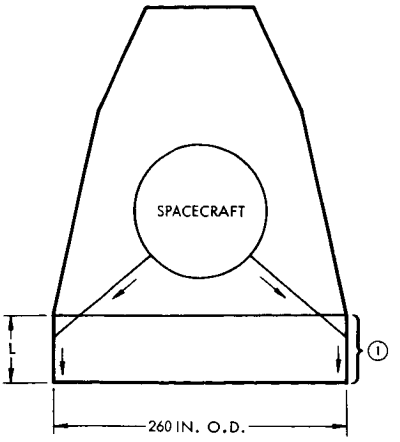

① PAYLOAD ADAPTER SHOULD BE DESIGNED TO TRANSFER LOAD OVER A UNIFORMLY DISTRIBUTED PATH TO THE FAIRING CIRCUMFERENCE GENERALLY WITHIN THE LENGTH (L) AS SHOWN.

Figure 2-5. Mechanical Interface, Vehicle B, Saturn V

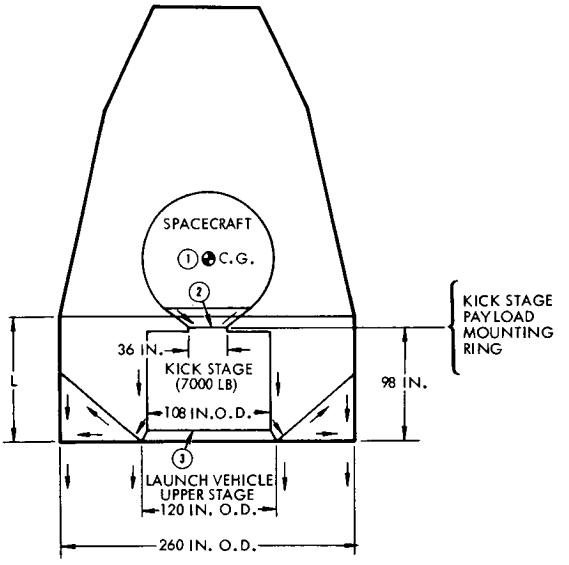

① C.G. OF SPACECRAFT SHOULD NOT BE HIGHER THAN 60 INCHES ABOVE THE ASSUMED 36 INCH O.D. KICK STAGE PAYLOAD MOUNTING RING.

② PAYLOAD ADAPTER SHOULD BE DESIGNED TO TRANSFER LOAD OVER A UNIFORMLY DISTRIBUTED PATH TO THE KICK STAGE MOUNTING RING CIRCUMFERENCE

③ A. PROVISION SHOULD BE MADE TO TRANSMIT ENTIRE PAYLOAD AND ASSUMED KICK STAGE WEIGHT OF 7400 LBS THROUGH THE KICK STAGE ADAPTER UNIFORMLY DISTRIBUTED INTO THE LAUNCH VEHICLE (L.V.) UPPER STAGE CIRCUMFERENCE

B. PROVISION SHOULD ALSO BE MADE TO TRANSMIT ENTIRE LOAD OF PAYLOAD, KICK STAGE AND BOTH ADAPTERS FORM THE CIRCUMFERENCE OF L.V. UPPER STAGE UNIFORMLY INTO THE FAIRING CIRCUMFERENCE WITHIN THE LENGTH (L) SHOWN, DURING TIME WHEN L.V. UPPER STAGE IS UNPRESSURIZED.

C. LOAD SHOULD BE UNIFORMLY DISTRIBUTED OVER THE L.V. UPPER STAGE AND THE FAIRING DURING BOOST PHASE OF THE TRAJECTORY.

D. LOAD SHOULD BE TRANSMITTED ENTIRELY THROUGH THE L.V. UPPER STAGE FOLLOWING FAIRING JETTISON.

Figure 2-6. Mechanical Interface, Vehicle C, Saturn IB/Centaur/HEKS

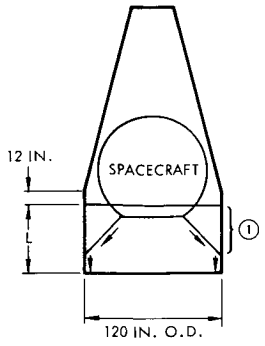

① PAYLOAD ADAPTER SHOULD BE DESIGNED TO TRANSFER LOAD OVER A UNIFORMLY DISTRIBUTED PATH TO THE FAIRING CIRCUMFERENCE GENERALLY WITHIN THE LENGTH (L) SHOWN

Figure 2-7. Mechanical Interface, Vehicles D and F, Titan IIICx/Centaur and Atlas SLV3x/ Centaur

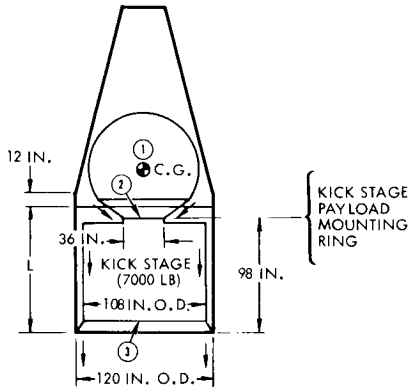

① C.G. OF SPACECRAFT SHOULD NOT BE HIGHER THAN 60 INCHES ABOVE THE ASSUMED 36 INCH O.D. KICK STAGE PAYLOAD MOUNTING RING

② PAYLOAD ADAPTER SHOULD BE DESIGNED TO TRANSFER LOAD OVER A UNIFORMLY DISTRIBUTED PATH TO THE KICK STAGE MOUNTING RING CIRCUMFERENCE

③ PROVISION SHOULD BE MADE TO TRANSMIT ENTIRE PAYLOAD AND ASSUMED KICK STAGE WEIGHT OF 7400 LBS THROUGH THE KICK STAGE ADAPTER UNIFORMLY DISTRIBUTED INTO THE LAUNCH VEHICLE (L.V.) UPPER STAGE CIRCUMFERENCE

Figure 2-8. Mechanical Interface, Vehicle E, Atlas SLV3x/Centaur/HEKS

These sketches were all taken from the JPL memorandum of November 1, 1965.

We have assumed that a satisfactory alternate to the mechanical interface shown in Figure 2-7 is that employed by the Surveyor, in which spacecraft loads are introduced into the Centaur stage in the forward conical section (at a radius of 30 inches), rather than at the fairing circumference.

2.2 TRAJECTORIES

This section serves to identify the constraints which limit the choice of interplanetary trajectories for earth-Jupiter flyby missions with launch dates in the 1972 opportunity, to describe the resulting class of suitable trajectories, to examine the characteristics of sample trajectories of the class, and to review the requirements for trajectory accuracy. Launch dates of the 1972 opportunity occur in February and March.

Volume 2 is devoted to a spin-stabilized spacecraft for a Jupiter flyby mission, satisfying the mission requirements of this opportunity. This concentration on the 1972 opportunity is in accordance with the priorities and emphasis indicated by JPL personnel to be desirable in this study. Volume 3 discusses, among other things, the extension to other launch years in the period 1970 to 1980; it serves to make other results applicable to missions in years other than 1972 by accounting for the variations in the important trajectory characteristics over the decade.

Launch date from the earth and arrival date at Jupiter are chosen as the two coordinates which specify a single interplanetary trajectory. When these two dates are given, the trajectory is unique, and all of its characteristics, including the geometry of departure and arrival asymptotes, are determinable. Graphical descriptions of the interplanetary trajectories, therefore, will be illustrated as plots against these two variables and the delineation of the launch period by the imposition of various constraints will be described in the same framework.

This uniqueness of the trajectory applies only to the interplanetary, or heliocentric portion, however, and the specific launch and encounter geometries are subject to the choice of additional variables. In particular, the time of day of launch completes the specification of the geocentric portion of the trajectory (assuming that injection altitude and flight path angle are established to optimize launch vehicle performance, and are essentially invariant). Encounter geometry is described by the vector $\overline{B}$, which gives the distance and direction from Jupiter to the approach asymptote, and thus fixes the altitude and location of the point of closest approach.

The general characteristics of the 1972 launch opportunity (before the imposition of constraints) are shown in Figures 2-9 through 2-14.

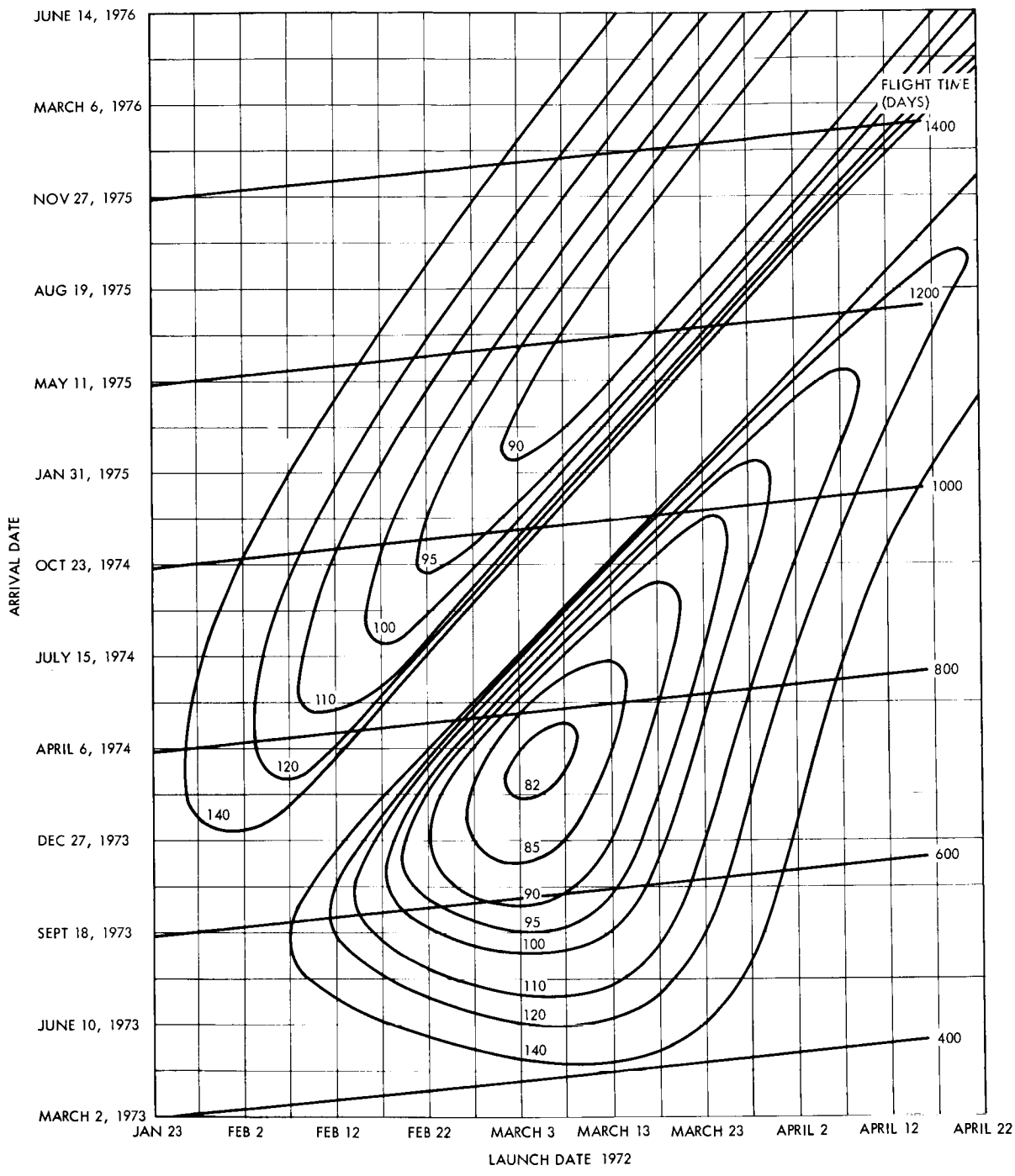

Figure 2-9. Earth-Jupiter 1972 Trajectories

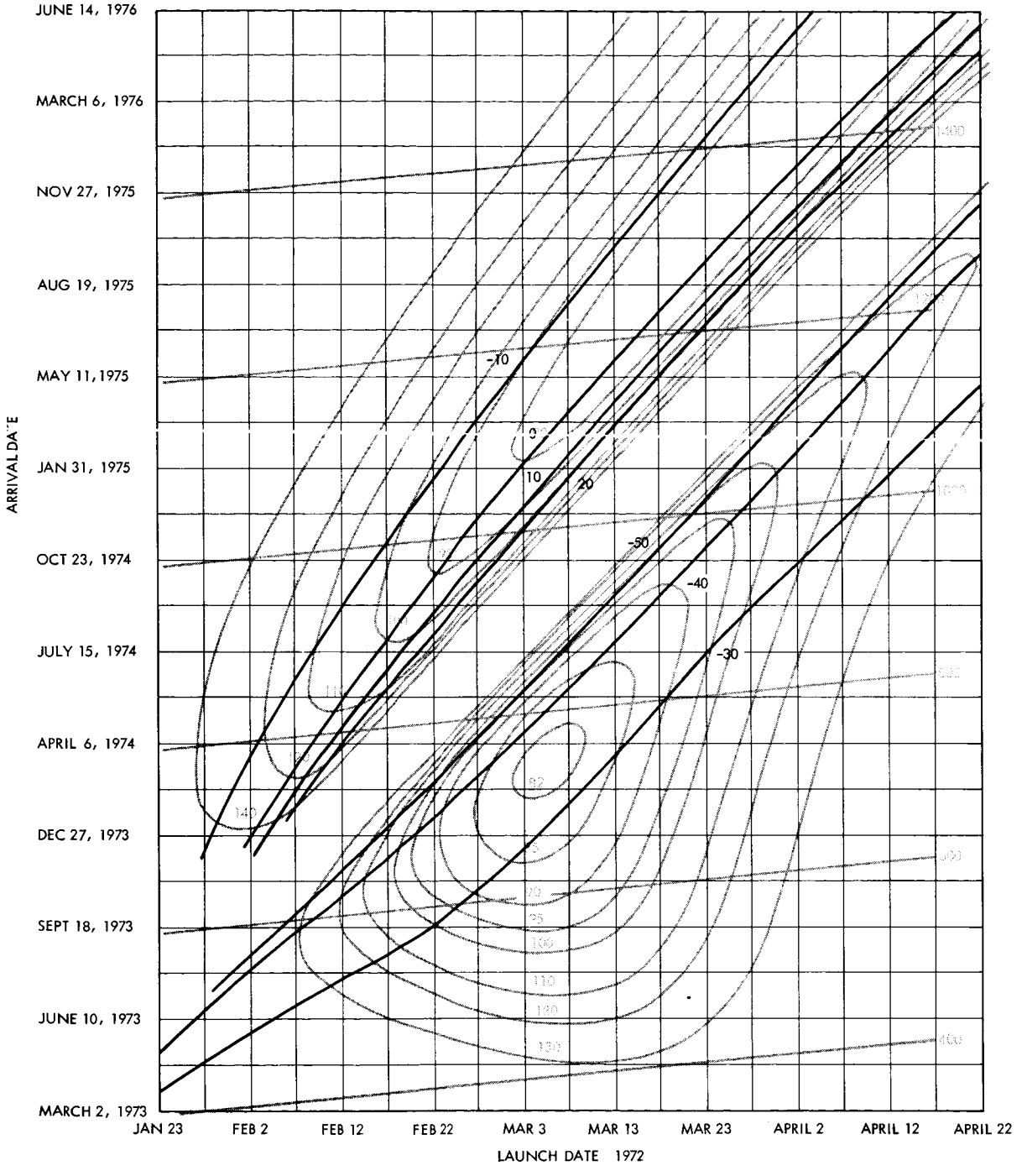

Figure 2-10. Earth-Jupiter 1972 Trajectories, DLA, Declination of Geocentric Departure Asymptote

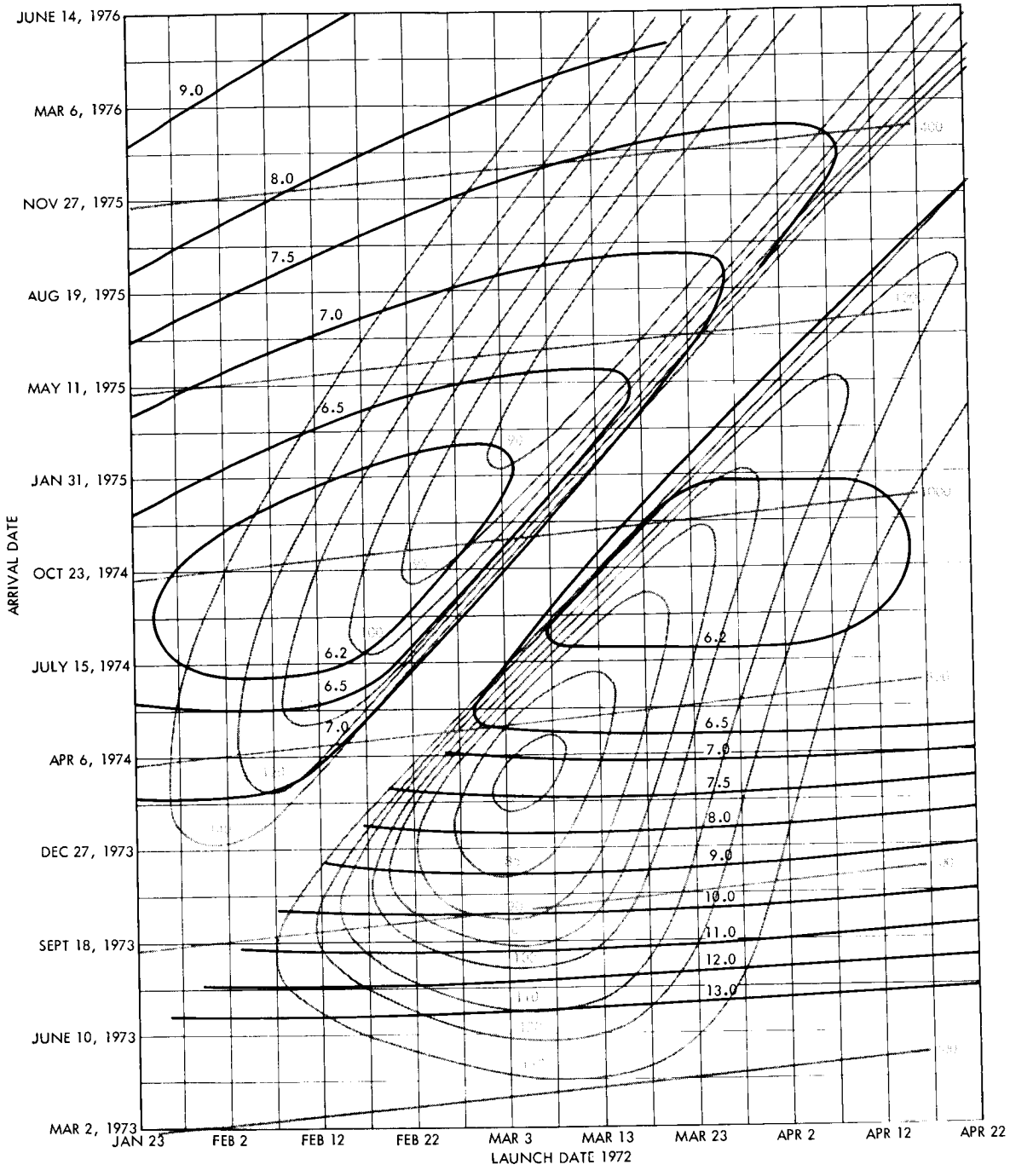

Figure 2-11. Earth-Jupiter 1972 Trajectories, V_{HP}, Planetocentric Asymptote Approach Velocity at Jupiter

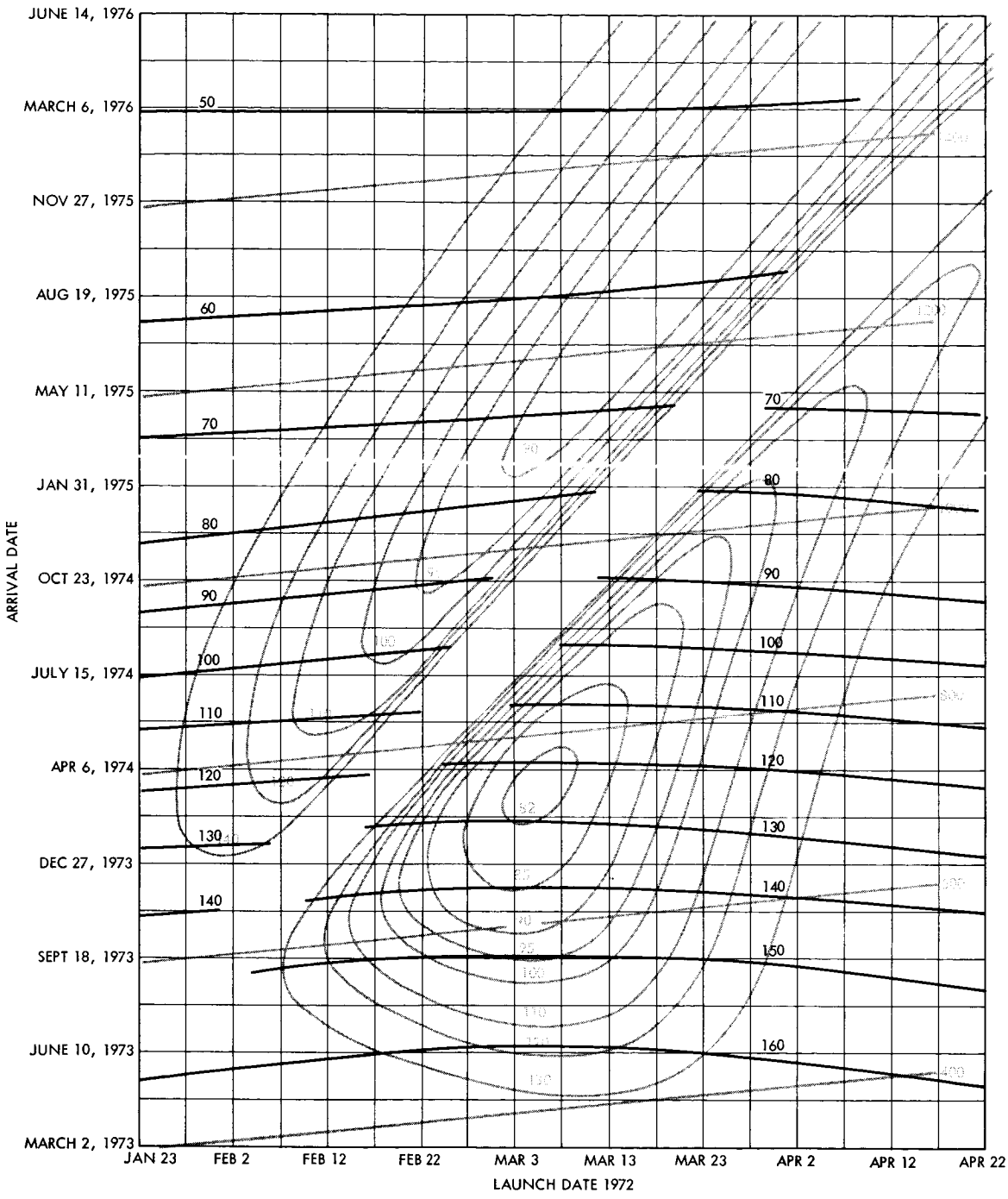

Figure 2-12. Earth-Jupiter 1972 Trajectories, ZAP, Angle Between Planetocentric Approach Asymptote and Jupiter-Sun Vector

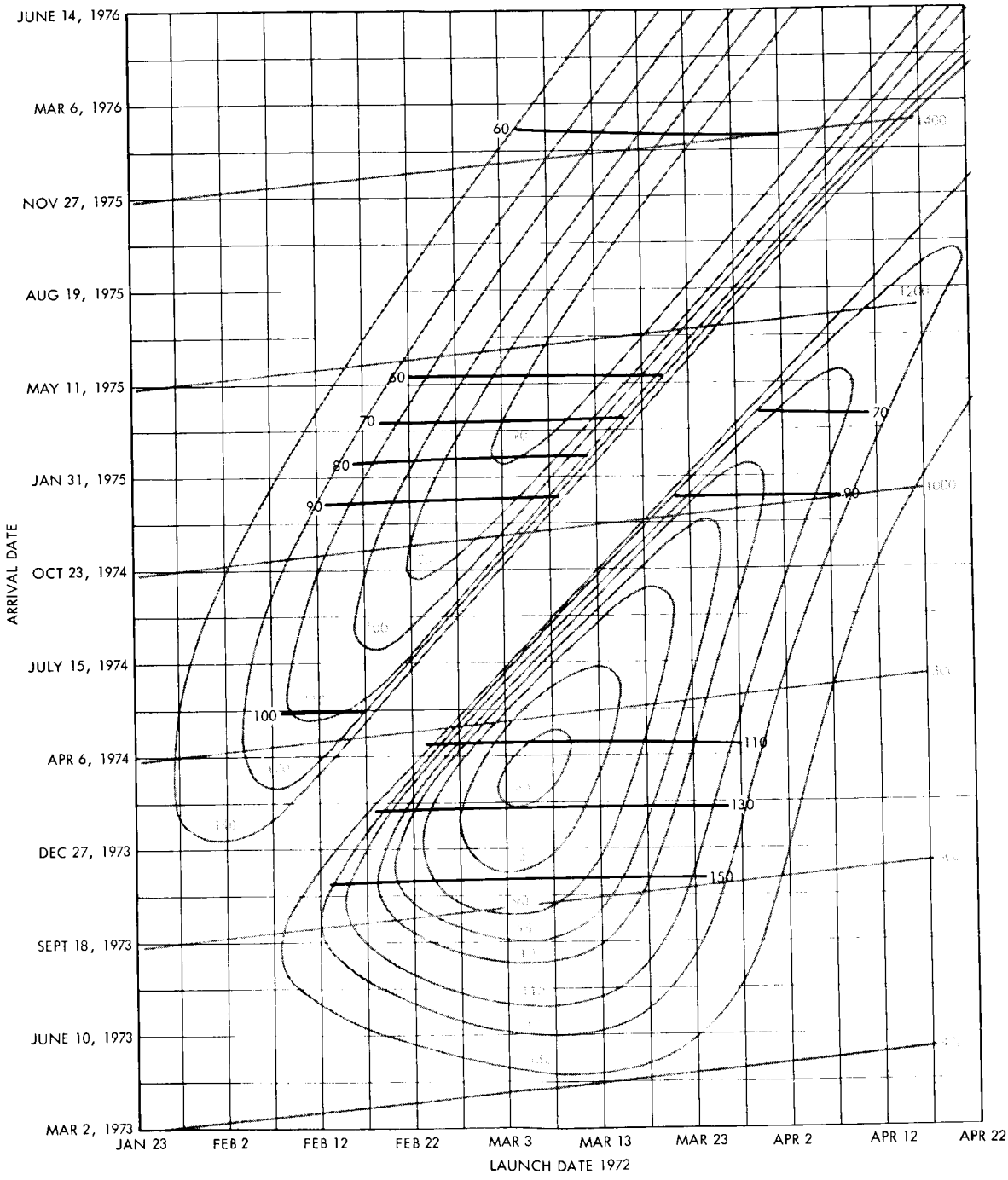

Figure 2-13. Earth-Jupiter 1972 Trajectories, ZAE, Angle Between Planetocentric Approach Asymptote and Jupiter-Earth Vector

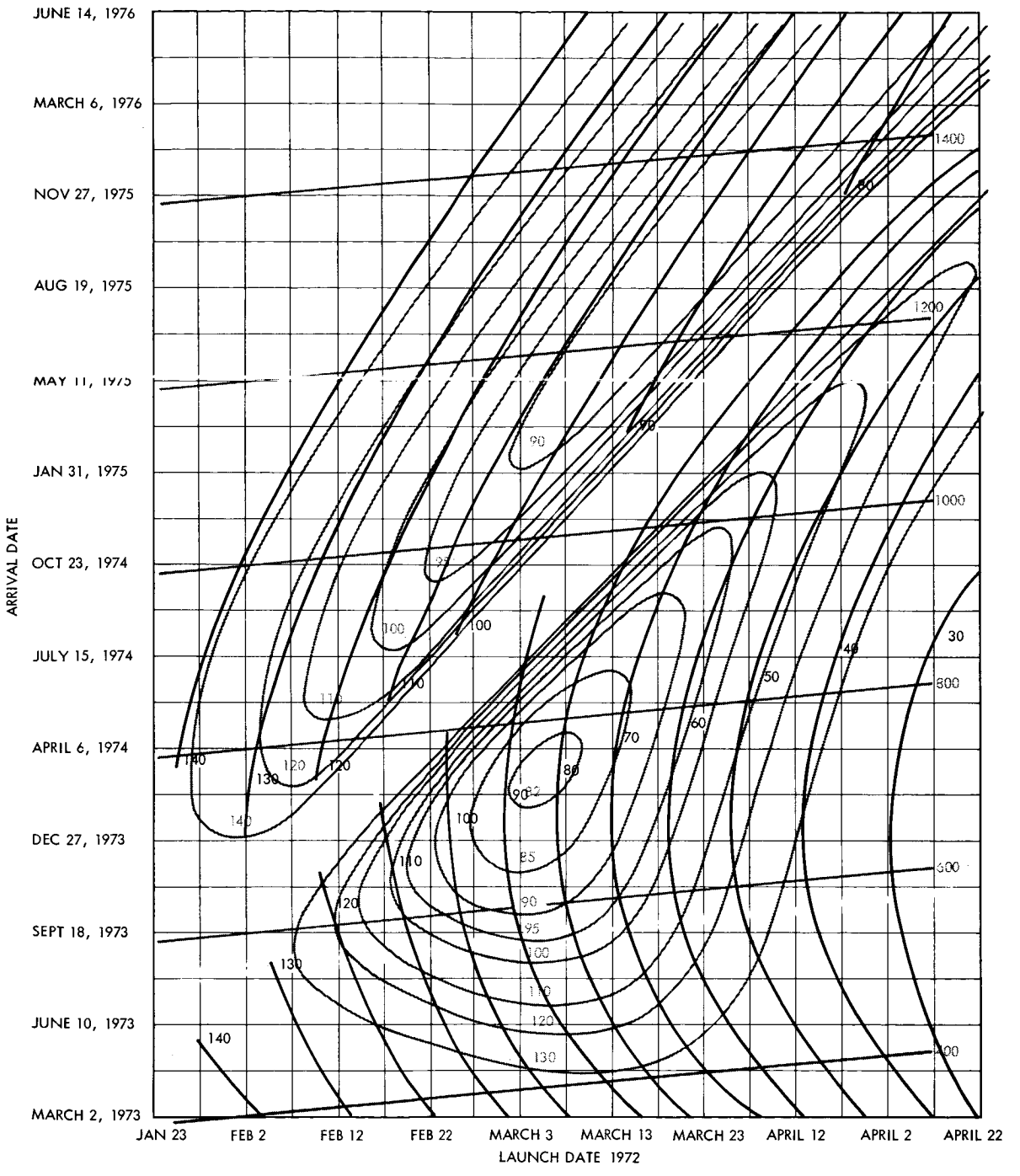

Figure 2-14. Earth-Jupiter 1972 Trajectories, ZAL, Angle Between Geocentric Departure Asymptote and the Sun-Earth Vector

Figure 2-9 gives, by contours of constant C_3, the injection energies required for earth-Jupiter trajectories of this opportunity.* (This figure also serves as a base, or background, for the presentation of other quantities in Figures 2-10 through 2-14.) The separation of the opportunity into Type I trajectories (those describing a central angle about the sun between launch and arrival which is less than 180 degrees) in the lower right-hand portion of the figure and Type II trajectories (greater than 180 degrees) in the upper left is evident. Also, the time of flight between the earth and Jupiter is indicated by sloping lines and the Jupiter-earth distance at the arrival date is indicated by a scale on the right side of the figure.

Figure 2-10 shows contours of constant DLA (declination of the outgoing geocentric launch asymptote) in the same coordinates, with the C_3 contours in the background. The DLA angle indicates approximately the latitude of the point on earth which is under the spacecraft in the initial portion of its heliocentric trajectory. The ability to achieve the appropriate value of the DLA angle by the launch and injection processes is chiefly a function of the launch site latitude and the permitted range of launch azimuths.

Figure 2-11 shows contours of constant values of V_{HP}, the planetocentric asymptotic approach velocity at Jupiter. This curve indicates that trajectories leading to minimum approach velocities at Jupiter have flight times greater than those for minimum C_3 (Type I) trajectories, but less than minimum energy Type II trajectories.

Figure 2-12 and 2-13 illustrate the variation of the ZAP and ZAE angles over the launch opportunity. These are the angles between the incoming planetocentric asymptote at Jupiter and the Jupiter-sun, and Jupiter-earth vectors, respectively. It is seen that these angles depend almost exclusively on arrival date, as they exhibit negligible variation with launch date. Because the earth, as seen from Jupiter, is always within 12 degrees of the sun, ZAE never varies from ZAP by more than 12 degrees.

*C_3 = the square of the geocentric asymptotic departure velocity, in km^2/sec^2.

Figure 2-14 illustrates the angle ZAL. This angle, descriptive of the geometry of departure from earth, is measured from the outgoing geocentric asymptote to the sun-earth vector. The principal variations of ZAL are with launch date rather than arrival date; for early launch dates, the low values of ZAL indicate that the interplanetary trajectory is initially directed inward from the earth's orbit, while for late launches the initial direction is outward.

The data provided in Figures 2-9 through 2-14 permit the delineation of the launch period, as it is circumscribed by the imposition of various constraints.* These constraints are considered in the following paragraphs.

2.2.1 Declination of Launch Asymptote

In the process of launching and injecting the spacecraft into an interplanetary trajectory from the earth, the declination of the launch asymptote (DLA) cannot exceed the inclination of the geocentric orbit to the earth's equator, unless plane-change maneuvers, which exert a very costly penalty on launch vehicle performance, are programmed. This maximum inclination of the initial orbit, in turn, is limited by the latitude of the launch site and the allowable limits of launch azimuth. The following relation applies:

$$\cos i_{max} = \sin Az_{ext} \cos lat$$

where

i_{max} = maximum inclination of the initial geocentric orbit

Az_{ext} = extreme limit of the launch azimuth, i.e., the azimuth limit farthest from 90 degrees

lat = latitude of the launch site

*In this section the term "launch period" is employed loosely as that space in the arrival date-launch date coordinate system in which trajectories are permitted during an earth-Jupiter opportunity, after the imposition of various constraints. It is defined more precisely as the number of days from the earliest possible launch date to the latest possible launch date within this period. The term "launch window" describes the time in hours during which a launch is possible on a particular day.

In order to achieve a particular value of DLA from a geocentric departure orbit of given inclination, it is necessary to make use of a coasting or parking orbit, essentially a low altitude, circular orbit, and a second firing of the launch vehicle at the appropriate time. If the launch vehicle is capable of sustaining a coasting phase, lasting through one revolution about the earth—i.e., 90 minutes or more—then any value of DLA whose magnitude is less than or equal to the inclination of the coast orbit can be achieved. This capability is decreased slightly if it is required that the launch be conducted at any time within a specific launch window. In this case the maximum achievable DLA is given by the following relation:

$$\tan \left|DLA\right|_m = \tan \left|DLA\right|_{m,o} \cos \frac{1}{2} LW$$

where

$\left|DLA\right|_m$ = maximum magnitude of DLA which can be achieved over a launch window LW

$\left|DLA\right|_{m,o}$ = maximum magnitude of DLA which can be achieved without a minimum launch window constraint, i.e., i_{max}

LW = launch window duration $\times \frac{360 \text{ degrees}}{24 \text{ hours}}$

Table 2-2 indicates the limits in achievable DLA arising from sample launch azimuth limits, and modified by the imposition of launch windows of zero, one, and two hours. (Note that two different classes of launch azimuth limits are identified in the table. The geographical azimuths, which are referred to a rotating earth's coordinate system, are those in which range safety constraints are usually stated. The inertial azimuths, with respect to a stationary frame of reference, are those which apply in the above equations. The two differ only slightly, as can be seen in the table.) For launch azimuth ranges lying between particular limits, Figure 2-15 shows graphically the ranges of DLA available, provided the launch vehicle has the 90 minute coast capability.

A number of the launch vehicles considered in this study are programmed so that the Centaur stage must be shut off at the start of the parking orbit, and must be reignited at the end of the parking orbit to

Table 2-2. Launch Asymptote Declination Limits Due to Launch Azimuth Limits

No parking orbit coast time limits
Launch site latitude = 28.3 degrees
Selected launch azimuth limits
Selected minimum daily launch window

Launch azimuth limit farthest from 90 degrees					
Geographical					
North, deg	35	60	66	70	90
South, deg	145	120	114	110	
Inertial					
North, deg	37.5	61.5	67.2	71.0	90
South, deg	142.5	118.5	112.8	109.0	
DLA limits					
No minimum launch window, deg	±57.6	±39.4	±35.7	±33.6	±28.3
One hour minimum launch window, deg	±57.4	±39.1	±35.5	±33.4	±28.1
Two hour minimum launch window, deg	±56.8	±38.4	±34.8	±32.8	±27.5

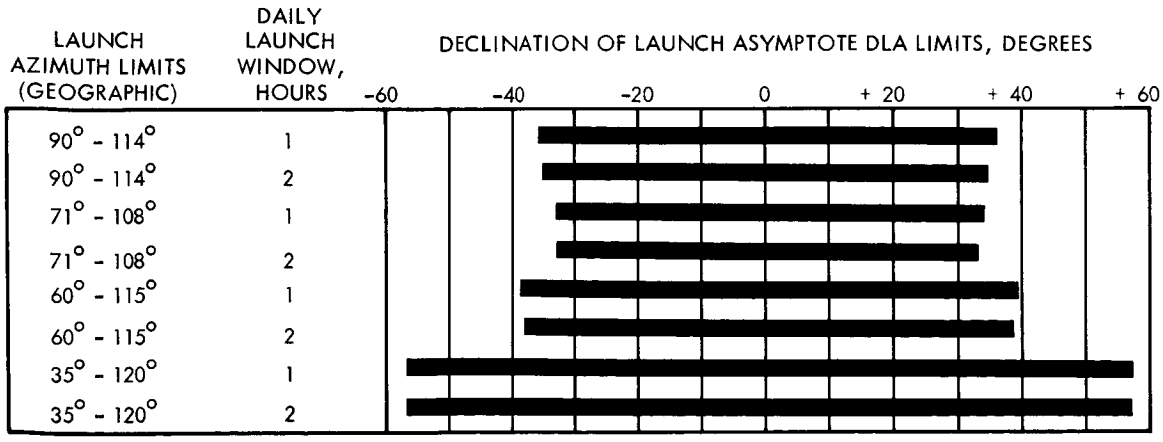

Figure 2-15. Launch Azimuth Declination Limits: No Limitation on Parking Orbit Coast Time

complete the injection. The present specifications for development of the Centaur provide for a coast period capability between 2 and 25 minutes, substantially less than the 90 minutes required for a complete orbit. Therefore, it is appropriate to consider these shorter coast times, and to examine the consequent imposition of further limitations on the achievable range of DLA angles. These further limitations depend also on the geocentric angle traversed during launch vehicle firing phases, the true anomaly of the injection point on the departure hyperbola, and the geocentric injection energy C_3. These latter quantities are interdependent. The resulting limitations on the DLA angle are somewhat complex. Computations of the range of DLA achievable have been made for a coast time constrained to lie between 2 and 25 minutes, and with various combinations of the other significant variables. The results are presented in Figure 2-16.

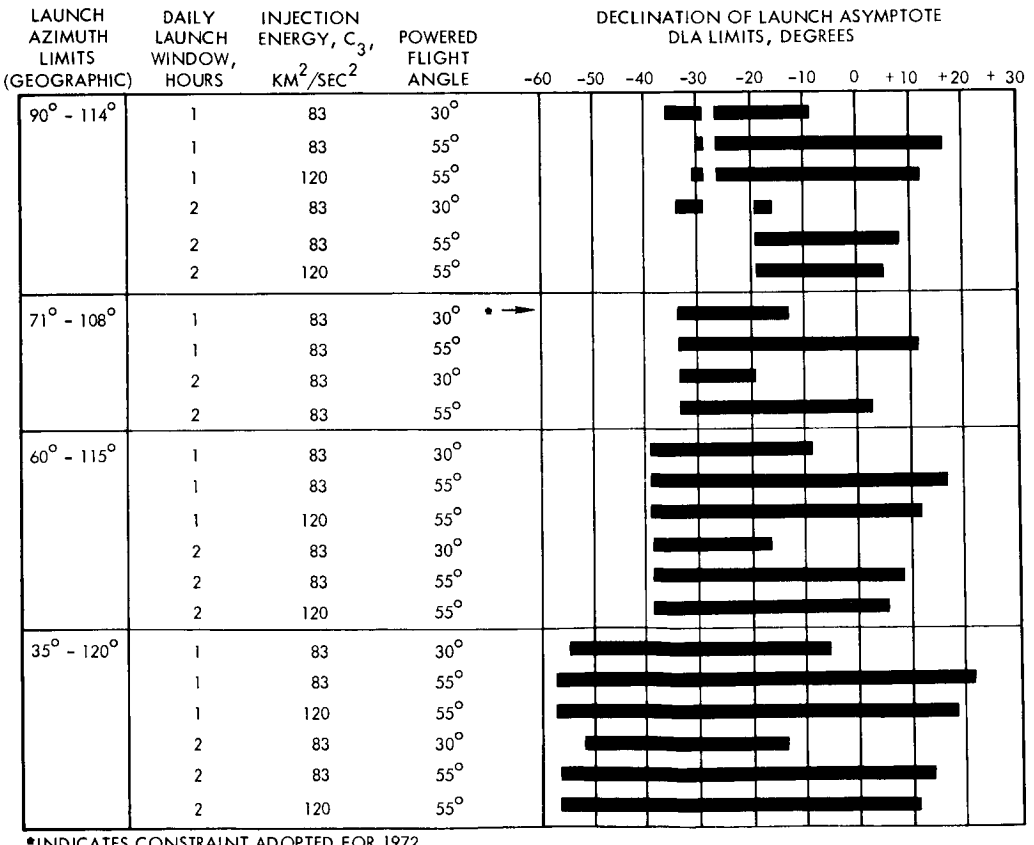

Figure 2-16. Launch Azimuth Declination Limits: Parking Orbit Coast Time Between 2 and 25 Minutes

As a basis for selecting a permitted range of the DLA angle as a constraint on the launch period, the following discussion pertains to the variables which influence it.

In the Phase 1A study of the Voyager spacecraft, the ground rules required that the launch vehicle be capable of operating with a one-hour daily launch window; however, it was proposed that a two-hour launch window be available for the spacecraft. In comparison, the Advanced Planetary Probe for a 1972 Jupiter flyby mission is a simpler concept (it does not include separate orbiter and lander vehicles, only one spacecraft is proposed on a single launch vehicle, and rigid sterilization requirements are not foreseen) and the requirement of a launch window longer than one hour does not seem warranted. Therefore, a daily launch window of one hour was used in determining the limits on the DLA angle. (Actually, a selection of two hours would not impose an appreciable penalty.)

The powered flight angle, or geocentric angle traversed during launch vehicle firing before and after the coast phase, is likely to vary from 30 degrees for Atlas or Titan launch vehicles with Centaur and TE-364 upper stages, injecting at low values of C_3, about 80 km^2/sec^2, to 55 degrees at the other extreme, Saturn V class launch vehicles injecting at higher values of C_3. The effect of variations in the powered flight angle is not very great. Calculations were made employing both 30 and 55 degrees.

The injection energy corresponding to the interplanetary trajectory influences the range of DLA angles because it determines the geocentric angle from perigee to asymptote of the departure hyperbola. However, this angle varies only 5 degrees if C_3 is varied from 83 to 120 km^2/sec^2, and therefore has only a slight influence. Values of C_3 of 83 and 120 km^2/sec^2 were employed in the sample case.

The true anomaly of the departure hyperbola at the point of injection is taken as 15 degrees.

For the cases illustrated in Figure 2-16, the coast time corresponding to present Centaur specifications was employed (2 to 25 minutes).

The examples of Figure 2-16 employ launch azimuth limits corresponding to the following examples:

• 90 to 114 degrees	Constraint applicable for the launch of Mariner IV to Mars, 1964
• 71 to 108 degrees	Preliminary selection for Voyager Mars 1971 (Task A)
• 60 to 115 degrees	Selection for Voyager Mars 1971 (Task B)
• 35 to 120 degrees	Indicated possible requirements for Voyager Mars 1973, 1975, etc. (Task B)

The general characteristics of the 1972 and subsequent Jupiter opportunities are similar to the characteristics of the 1971 and subsequent Mars opportunities. In each case, Type I trajectories require substantial negative DLA angles in the indicated year, while Type II trajectories are associated with DLA angles around zero or slightly negative. In each case, the next opportunity (Jupiter 1973, Mars 1973) has an even more negative DLA requirement for Type I trajectories. For still later opportunities, the DLA requirement becomes less extreme, and then reverses to northerly declinations.

For these reasons, the major restrictions outlined for the Voyager program of Mars exploration appear to be directly applicable to the Advanced Planetary Probe study. These restrictions are:

- A launch azimuth range of 90 to 114 degrees is unduly restrictive when applied to a launch vehicle with a 25 minute coast limit.
- A launch azimuth range of 70 to 108 degrees is satisfactory for Jupiter 1972, despite a parking orbit coast time limit of 25 minutes. (These limits, plus values of C_3 of 83 km^2/sec^2 and powered flight angle of 30 degrees lead to the following range of launch azimuth declinations:

$$-33.5 \text{ degrees} \leq \text{DLA} \leq -12 \text{ degrees.})$$

- For later missions (Jupiter 1975 through 1982) in which positive DLA angles are required for Type I trajectories, the imposition of a 25 minute coast time limit is prohibitive.

- In addition to the required increase in coast time capability, increasing the launch azimuth range to 60 to 115 degrees will ease launch vehicle performance requirements in those years when the greatest values of |DLA| are required. These years are 1972, 1973, 1977, 1978, and 1979. From this point of view, 1973 and 1978 are most critical.

As a result of these major restrictions, the following restrictions on DLA are used for the Jupiter flyby missions:

$$-33.5 \text{ degrees} \leq \text{DLA} \leq -12 \text{ degrees}.$$

Although not influencing the 1972 opportunity, limitations on the DLA angle also exist which are imposed by radio tracking considerations. Basically, these limitations are that if |DLA| is too great (over 40 degrees) the services of tracking stations in either the northern or southern hemisphere are lost during the initial phases of the interplanetary period. If |DLA| is too small (e.g., less than 5 degrees) a reduction in the sensitivity of the orbit determination process is possible. Figure 2-10 indicates that these two limitations have no effect on Type I trajectories to Jupiter in 1972.

Further discussion of DLA requirements in the years after 1972 is given in Volume 3.

2.2.2 Approach Asymptotic Velocity

The approach velocity (V_{HP}) at Jupiter has little influence on a flyby mission, because the planetary escape velocity at points within several radii of the surface is very large compared to practical asymptotic approach velocities, and the actual spacecraft velocity when close to Jupiter is dominated by the former effect. Escape velocities range from 60 km/sec at Jupiter's surface to 30 km/sec at a distance of 4 radii from the center of the planet, while V_{HP} ranges from 6 to 12 km/sec for the earth-Jupiter trajectories which are most attractive. As the spacecraft velocity is derived from these two by a root-sum-square process, the approach velocity has very little influence on the spacecraft velocity as it passes the planet.

As a result, it is not felt that V_{HP} considerations impose any constraint on a flyby mission to Jupiter, although it will be seen that this quantity does have a substantial effect on an orbiter mission; this will be considered in Section 6, Volume 3.

2.2.3 ZAP Angle

The ZAP angle describes the relation of the approach asymptote at Jupiter to the Jupiter-sun direction. The principal effects of variations of this angle on a Jupiter flyby mission are considered.

One effect is the illumination of the planetary disc and its phase as seen from the approaching spacecraft. This could affect the nature of visual observations of the planet. For large ZAP angles, the approaching spacecraft would view almost a "full" Jupiter, while for a ZAP angle of 90 degrees or less, a "half" Jupiter or less would be visible during approach. Although the bending of the trajectory by Jupiter's gravitational field permits the spacecraft's instruments to view the planet from a large range of directions (typically 270 degrees or more) and therefore experience widely varying phases during a single trajectory, the possibility of taking an extended series of observations while at a substantial distance from the planet under optimum lighting conditions would impose limits on the ZAP angle. For trajectories or similar experiments requiring solar illumination, it appears that ZAP angles less than 90 degrees would reduce the illuminated portion of the planet to an unduly small fraction. Therefore, ZAP angles of greater than 90 degrees are considered appropriate. This may be considered a weak constraint since the decrease in experiment effectiveness is gradual as the ZAP angle decreases.

The possibility of the spacecraft being eclipsed from the sun by Jupiter is not very sensitive to the ZAP angle; eclipse can be achieved by encounters from almost any interplanetary trajectory. In addition, the possibility of eclipse is not important for the spin-stabilized spacecraft design, although the attitude control of the 3-axis spacecraft (Volume 3) makes use of the sun as an optical reference.

The ZAP angle, in combination with the approach velocity V_{HP}, exerts a major effect on the trajectory of the spacecraft subsequent to

Jupiter encounter. Table 2-3 shows the general characteristics of these trajectories, for eastward and westward equatorial passages and polar passages, and indicates how they vary with ZAP angle. Although the scientific objectives associated with the period starting several weeks after Jupiter encounter are considered to be of secondary importance to the mission, the most attractive post-encounter objectives are those associated with a heliocentric trajectory continuing outward, essentially in the plane of the ecliptic. In this regard, Table 2-3 indicates that these objectives may be met over the entire range of ZAP angles associated with different values of the flight time by an eastward equatorial passage over Jupiter. For such a passage the post-encounter trajectory is approximately tangential to Jupiter's orbit for large ZAP angles (150 degrees), and more outward for smaller ZAP angles. The heliocentric velocity ranges from about 1.3 times the velocity required to escape from the solar system for a 150-degree ZAP angle to 0.9 times solar escape velocity at a ZAP angle of 60 degrees. These variations show that the trajectory after encounter is not extremely dependent on ZAP angle, although a ZAP angle range of 90 to 150 degrees appears to promote the most desirable characteristics. A specific constraint on the launch period does not seem warranted by these considerations.

2.2.4 ZAE Angle

ZAE angle describes the relation of the approach asymptote at Jupiter to the Jupiter-earth direction. As the spacecraft is stabilized about a spin axis pointing towards the earth, the angle ZAE is equal to the cone angle of an instrument mounted on the spacecraft which can view Jupiter as the spacecraft approaches the planet. In this case, cone angle is the direction measured in spacecraft coordinates away from the spin axis, with zero degrees indicating the direction towards the earth, in the cruise attitude.

From Figure 2-13 it can be seen that the ZAE angle is essentially a function of arrival date, with large values, of the order of 150 degrees, associated with early arrivals in the launch opportunity, and values as low as 60 degrees for late arrival dates. For encounters in which the spacecraft passes eastward in the equatorial plane and fairly close to

Table 2-3. General Characteristics of Trajectory Subsequent to Jupiter Encounter

Launch Energy Required (C_3) (km^2/sec^2)	Flight Time (days)	V_{HP} (km/sec)	ZAP (deg)	Jupiter Encounter Characteristic		
				Eastward (Equatorial)	Westward (Equatorial)	Polar
				Characteristics of Heliocentric Trajectory after Jupiter Encounter*		
100 (Type I)	550	11	150	In ecliptic, approximately tangential to Jupiter's orbit, velocity 1.3 times solar escape velocity	In ecliptic, returning inward to perihelion as close as 0.6 AU	Inclined up to 43 degrees to ecliptic
82 (minimum, Type I)	750	7	120	In ecliptic, tangential or outward from Jupiter's orbit, velocity 1.1 times solar escape velocity	In ecliptic, inward to perihelion 0.9 to 4 AU, depending on closeness of approach to Jupiter	Inclined up to 31 degrees to ecliptic
95 (Type I or II)	950	6	90	In ecliptic, outward from tangential, velocity up to 0.95 times solar escape velocity	In ecliptic, inward from tangential, velocity up to 0.95 times solar escape	Inclined up to 27 degrees to ecliptic
90 (Type II)	1250	7	60	In ecliptic, outward from tangential, velocity up to 0.9 times solar escape velocity	In ecliptic, tangential or inward from Jupiter's orbit, velocity up to 1.05 times solar escape velocity	Inclined up to 31 degrees to ecliptic

*All heliocentric orbits subsequent to encounter are posigrade

Jupiter, the high ZAE angle associated with early arrival dates mean that Jupiter would appear at a high cone angle during approach to the planet, and would be at a moderate cone angle after encounter when the spacecraft is departing from the planet. For late arrival dates, Jupiter would appear at a low cone angle during approach, and would be at a very low cone angle when the spacecraft departs from the planet. These cone angles do not have critical ramifications with regard to the placing of instruments and their use during the mission, but in some instances they have minor effects. For example, in the television experiment, the amount of picture smear generated in a given exposure time is proportional to the spin rate and the sine of the cone angle of Jupiter. For this purpose it is least desirable to have cone angles of Jupiter close to 90 degrees at the time that photographs of greatest angular resolution are to be taken.

The cone angle requirements for instruments which make observations in the region of Jupiter's terminator are not dependent on the ZAE angle alone, but are related to the difference, ZAE - ZAP. This difference is restricted to the interval ±12 degrees, so that this variation has minor importance for observations of the terminator.

The angle ZAE also affects the characteristics of occultation of the earth by the planet Jupiter. The possibility of the occurrence of an earth occultation is not particularly sensitive to ZAE; it is achievable for almost any direction of approach to Jupiter by the spacecraft. However, the timing and duration of the occultation is sensitive to the angle ZAE. For high values of ZAE associated with early arrival dates, the occultation period begins soon after periapsis passage, and is of relatively short duration (again assuming an eastward passage). For the low values of ZAE associated with late arrival dates, the occultation starts later, measured from periapsis passage, and has a longer duration. To avoid having the occultation experiment occur simultaneously with other observations which must be made at the closest approach to Jupiter, high ZAE angles are undesirable. Conversely, it is not desirable for the occultation period to be too long or to occur too far from the planet, and therefore very low ZAE angles are not desired either. It would appear that the earth occultation experiment is compatible with a wide range of

ZAE angles—60 to 150 degrees—with preference for a range between 80 and 140 degrees. However, this is not considered to represent a strong constraint.

2.2.5 Arrival Date

The arrival date influences the desirability of the mission in several ways. Some geometrical characteristics of the approach of the spacecraft to Jupiter are essentially functions of the arrival date. In particular, the ZAP and ZAE angles vary only slightly with launch date, and to the extent that they constrain the mission, indicate the value of one arrival date in comparison with another.

A second implication of arrival date choice is that the duration of the mission, or at least the interplanetary portion, is essentially fixed by the arrival date. Launch dates for a particular earth to Jupiter opportunity are within a relatively short interval (40 to 50 days), while feasible arrival dates can take place over a period of three years or more. It is very desirable, apart from considerations of planetary geometry and launch vehicle requirements, to keep flight time as short as possible. The principal reason is to maximize the probability of a successful mission, recognizing that the probability of component failures increases with mission time. A second advantage of choosing short duration missions is that the cycle from early missions, making the first measurements of scientific data at the target planet, to later launches, in which the spacecraft and experiment design are influenced by these early results, is reduced, resulting in compression of the entire planetary exploration program. A third advantage is that the cost of conducting operations in support of the spacecraft is diminished. These reasons all favor shorter flight times and therefore earlier arrival dates. They are all relatively continuous functions, and therefore are not characterized by a strong constraint indicating that arrivals after some particular date were unacceptable.

A third consideration involving the arrival date has to do with the geometrical relation of the sun, earth, and Jupiter at the time of encounter. One characteristic is the communication distance between the two planets. This distance varies between a minimum of approximately

4 AU and a maximum of about 6 AU during the 400-day synodic period. To maximize the communications capability at encounter, it is desirable to schedule the arrival date at a time when this distance is minimum. However, it is an unfortunate characteristic of most earth-Jupiter opportunities that those Type I trajectories characterized by the lowest injection energy requirements at earth correspond to encounters at a time when the interplanetary distance is maximum. In 1972, for example, the minimum-energy Type I trajectory has a communication range at encounter of 5.8 AU.

Figure 2-17(A) illustrates the variation of injection energy at earth (C_3) and the earth-Jupiter distance as a function of the arrival date

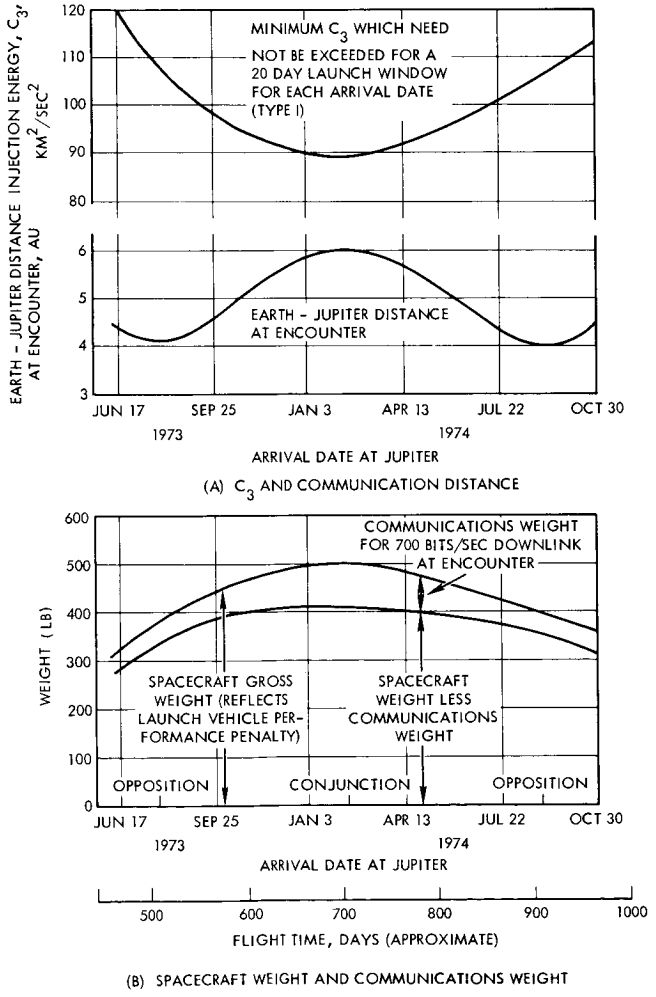

Figure 2-17. Influence of Communication Distance and C_3 Requirement on Selection of Arrival Date

at Jupiter, for launches in the 1972 opportunity. For the class of spin-stabilized spacecraft described in this volume, an analysis was made to determine whether the communications advantage in choosing arrival dates with shorter interplanetary distances would offset the disadvantage incurred by necessitating launches at higher injection energy. The method of approach was to assume that a vehicle of 500 pounds could be launched with a C_3 of 89 km^2/sec^2 (the minimum injection energy for a 20-day launch period for 1972) and would be capable of transmitting 700 bits/sec over the 6 AU communication distance. To achieve this bit rate, the incremental spacecraft weight devoted to communications is about 90 pounds, 30 pounds for power generation and conditioning equipment for a transmitter capable of radiating 10 watts and 60 pounds for the structural weight of a 16-foot antenna. For different arrival dates, degradation of the launch vehicle capability was assumed to follow the equation:

$$LW = LW_o \, e^{-0.0138 \, \Delta C_3}$$

where

LW = the weight which may be launched at injection energy, C_3
LW_o = the weight launched at C_3 = 89 km^2/sec^2, i.e., 500 lb
ΔC_3 = the increment of C_3 over 89, in km^2/sec^2

This decrease in performance as C_3 is increased is representative of the launch vehicles available in this study. In addition, the spacecraft weight devoted to communication is assumed to vary according to

$$W_C = \frac{BR \cdot D^2}{280}$$

where

W_C = spacecraft weight devoted to communications, lb
BR = encounter transmission data rate capability, bit/sec, taken to be 700 bits/sec in this analysis
D = earth-Jupiter distance at encounter, AU

This expression for W_C is based on the assumption that the power-gain product of the spacecraft is changed by varying spacecraft weights for communications power and for antenna structure in equal proportions.

Under these conditions, variation of the arrival date from the minimum energy point is accompanied by a reduction in spacecraft weight which must be devoted to communications, but an even greater reduction in the spacecraft weight which can be placed on an earth-Jupiter trajectory by the launch vehicle. This effect is illustrated in Figure 2-17(B). The conclusion is, therefore, that trajectories for spacecraft of the design outlined in this volume are more appropriately selected on the basis of injection energy requirements than interplanetary communication requirements. (A similar analysis for Type II trajectories does not produce the same results because the variation of C_3 with arrival date is much more gradual. However, because 1972 Type II trajectories have minimum C_3 requirements, somewhat higher than Type I trajectories, the optimum Type I arrival date is also the optimum arrival date for the opportunity, from considerations of injection energy and communication distance.) The constraint imposed by injection energy requirements will be discussed in a subsequent paragraph.

Another consequence of the solar and planetary geometry at the time of encounter is the possibility of communications interference arising from thermal noise emitted by the sun. If the arrival date corresponds to either a conjunction or an opposition of the planet Jupiter (as viewed from the earth) then the spacecraft receiving antenna, in addition to accepting signals from ground transmitters on the earth, will receive noise radiated from the sun. For arrival dates at conjunction only, there is an additional solar noise interference with the downlink transmission. The latter effect occurs for a shorter period of time than the former, but is more critical. The shorter duration is due to the narrower beamwidth of the ground antenna than that of the spacecraft antenna, 210 and 85-foot ground antennas having beamwidths 1/13 and 1/5 as great as that of the 16-foot spacecraft dish. The consequent disparity in antenna gains and the much higher power which is transmitted from the earth make the downlink interference problem the more critical one. Arrival at Jupiter in a brief interval encompassing the date of conjunction, therefore, is considered undesirable.

Taking twice the 0.36-degree beamwidth of the (85 foot) ground receiving antenna, adding the 0.54-degree diameter of the sun at 1AU,

and dividing by the 0.81-degree daily change in the Jupiter-earth-sun angle, gives 1.6 days as the period in which part of the sun's disc can be within the main lobe of a Jupiter-directed antenna. Because it is undesirable for encounter data to be subjected to solar noise within ±10 days of the closest passage, a prescribed period of ±11 days of conjunction is adopted. For the 1972 mission, the following arrival dates are prohibited.

February 1, 1974 to February 23, 1974
March 10, 1975 to April 1, 1975
April 18, 1976 to May 10, 1976

Thus, while launch injection energy characteristics favor Type I trajectories with arrival dates in a broad period encompassing Jupiter conjunction (even though these correspond to maximum communications distances), arrival during a short interval centered at conjunction should be avoided.

2.2.6 ZAL Angle

ZAL is the angle between the outgoing geocentric asymptote of the spacecraft and the sun-earth vector. The mission objectives do not directly impose any constraints on this angle. However, two elements of the spin-stabilized spacecraft design presented in this section are sensitive to the ZAL angle.

For the initial open-loop orientation of the spacecraft from its injected orientation to the earth-tracking attitude to be maintained during the cruise mode (or more likely, to an attitude which will be earth-pointing several days after injection) the control of the direction of precession of the axis depends on the sun sensors for establishing a roll attitude reference at the appropriate instant of each spin cycle. However, if the spin axis is close to the direction toward or away from the sun, the accuracy of this roll attitude establishment is diminished. Accuracy is degraded within 20 degrees of the solar direction, and within 10 degrees the sensor may cease to provide adequate signals. An analysis was made to indicate any combinations of earth-Jupiter trajectories and launch azimuths which should be excluded to avoid the possibility that, in the injected attitude,

the spin axis can lie within 20 degrees of the sun line or anti-sun line—a possibility which would delay the accomplishment of the initial orientation maneuver.

The results of the analysis are illustrated in Figure 2-18. Three curves are plotted as a function of C_3. One indicates the minimum permitted value of ZAL if injection attitudes in which the spin axis is within 20 degrees of the sun line are to be prohibited. The other two curves represent the minimum achievable value of ZAL, for given values of C_3,

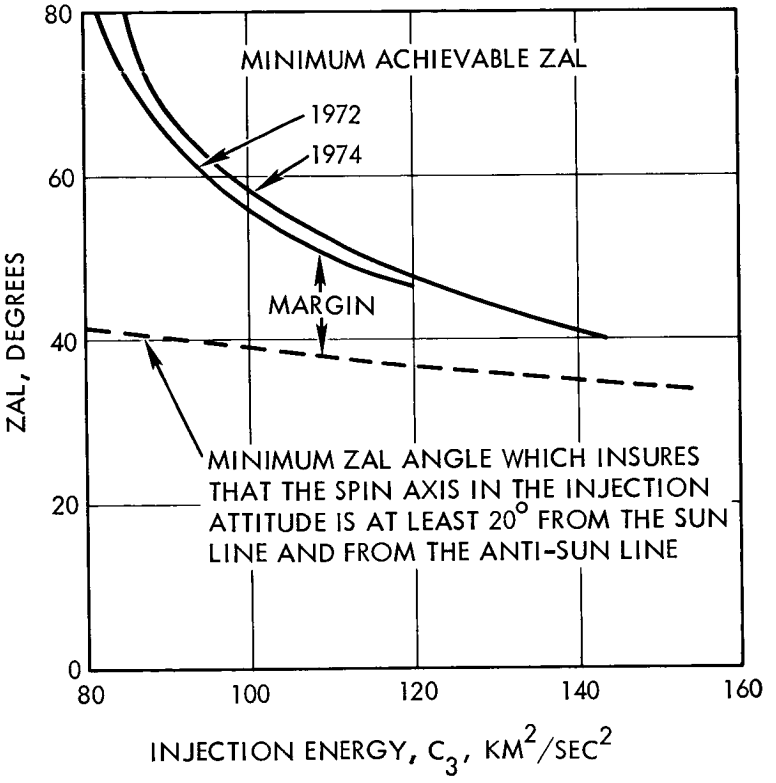

Figure 2-18. Injection Orientation Margin Beyond a 20-Degree Angle Between Spin Axis and Sun Line

for trajectories in the 1972 and 1974 opportunities. The conclusion is that undesirable injection attitudes cannot be achieved for any reasonable launch in 1972 or 1974; the margin of safety is over 5 degrees for C_3 = 140 km^2/sec^2, over 10 degrees for C_3 = 120 km^2/sec^2, and greater for lower energy launches. This margin should be adequate to cover displacements from the theoretical injection attitude caused by tipoff errors, spin and despin errors, solid engine firing errors, etc.

A second facet of the spin-stabilized spacecraft design which makes it sensitive to the ZAL angle is the possibility that the rear surface of the equipment compartment—the active temperature control radiating surface—will be subjected to incident solar radiation during the early phases of the mission. There is no concern if the ZAL angle is less than 90 degrees, because the sun always appears on the forward hemisphere of an earth-oriented spacecraft. However, for ZAL angles greater than 90 degrees, the sun would appear in the rear hemisphere, and therefore would illuminate the aft thermal control surface. For angles just slightly over 90 degrees, the incidence is near grazing, and the amount of solar radiation is slight. For this section, a limitation of 100 degrees for the ZAL angle has been adopted. This limitation is greater than the 90 degrees geometrical boundary between solar incidence and no incidence, for the following reasons:

a) The thermal control design presented in Section 5 limits the area of active thermal radiation surface to a minimum value. Thus, when the spacecraft is 1 AU from the sun, the internal temperature of the equipment compartment approaches the upper end of the thermal control range (85°F) even if no sunlight impinges on the control area. In this design, there is adequate margin so that compartment temperatures are above the minimum limit of 40°F, even at remote distances in the solar system where solar radiation on the spacecraft has negligible effect. Therefore, it would be a minor alteration of the design to increase the active surface area. This would not compromise thermal behavior at great distances from the sun, and would provide enough margin at 1 AU from the sun so that a small amount of incident sunlight on the active surface could be transmitted.

b) Another minor alteration in design would be the addition of a cylindrical section below the perimeter of the equipment compartment to shade the active thermal radiating surface from the sun for sun-probe-earth angles up to approximately 100 degrees.

c) On the other hand, it is not necessary for the initial attitude to which the spacecraft is oriented after injection to be earth-pointing. As low gain antennas are adequate for the first week of the mission, communications performance does not require immediate earth-pointing. In fact, it is desirable not to orient immediately to an earth-pointing attitude, but to orient to an attitude which will be earth-pointing several days later,

because initially the spacecraft earth line rotates rapidly due to near-earth variations in geometry, and because there is little point in having the spacecraft track the earth until it is far enough that its high gain antenna beam illuminates the entire earth, rather than just a portion of the disc. With these considerations in mind, it is feasible to extend the period in which the spacecraft does not point at the earth. In particular, because the sun-probe-earth angle is initially equal to ZAL, but decreases at about 1.2 to 1.5 degrees per day, delaying earth acquisition for a week will reduce the maximum sun-probe-earth angle to a value 8 to 10 degrees less than the value of ZAL.

d) This delay in establishing an earth-pointing attitude should not be indefinite, however. It is necessary to achieve it before the midcourse correction is made, so that an accurate base is established for conducting open-loop precessing maneuvers necessary for the propulsive maneuver. The midcourse maneuver probably will be conducted between 5 and 20 days after launch. Even if it were conducted early enough so that the earth-pointing attitude produces a sun-probe-earth angle of slightly over 90 degrees, it may not be necessary to remain in this attitude long enough for transient temperature changes to be unacceptable.

As a result of these considerations, the limit of 100 degrees for the ZAL angle was adopted, without verification by further detailed analysis. It appears that by either effecting simple changes in the spacecraft design, or delaying the adoption of an earth-pointing attitude in the interplanetary trajectory, there will be no difficulty in accommodating ZAL angles up to 100 degrees.

2.2.7 Launch Period

A minimum launch period of 20 days has been arbitrarily adopted as a constraint. This is considered adequate for the launch of one spacecraft or of two spacecraft from separate launch vehicles. It is recognized that 20 days would impose tight scheduling if the two launches were to be conducted from the same pad. The consequence of this selection is that for any opportunity, there will be a minimum C_3 requirement of the launch vehicle-spacecraft combination. This requirement will be identified for the 1972 opportunity in the next section.

We have defined a 20 day launch period to be one in which the separation between the earliest and latest launch dates is 20 days, without

requiring that the same arrival date at Jupiter be achievable for launch dates over the entire period. As a result of the definition of the 20 day launch period which permits a variable arrival data, the required C_3 is not as great as it would be if the definition implied a constant arrival date for the entire 20 day period. This effect is illustrated in Figure 2-19, and the magnitude of the effect, as a function of launch period duration, is shown in Figure 2-20.

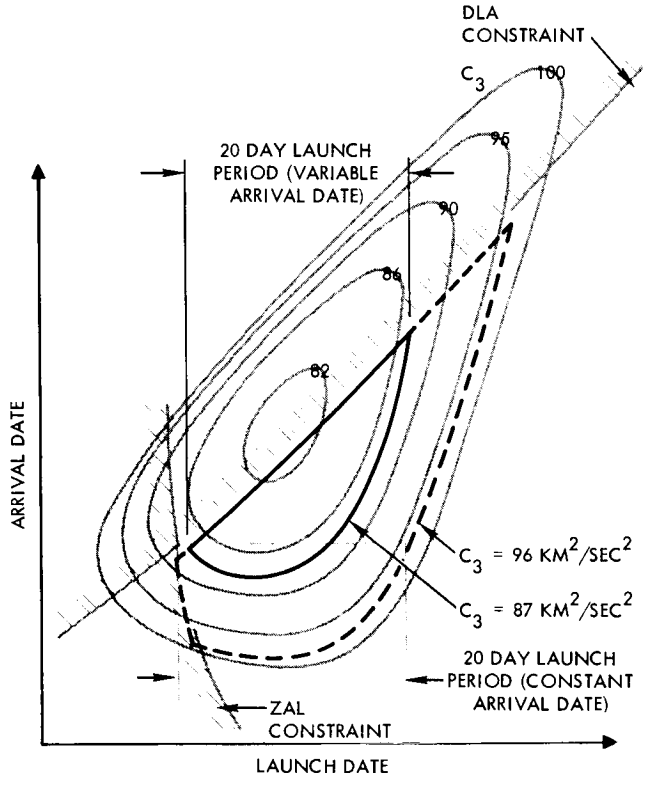

Figure 2-19. Comparison of C3 to Provide 20-Day Launch Periods with Variable or Constant Arrival Date

It is recognized that to be consistent with the variable arrival date approach, the spacecraft design must be capable of performing its mission over a wide range of possible trajectories. This range encompasses arrival dates which may differ by 200 days, as they correspond to trajectories with the earliest and latest launch dates. Thus the spacecraft, while probably launched on a 650-day trajectory, would have to be capable of performing its mission if launched at the end of the launch period on a

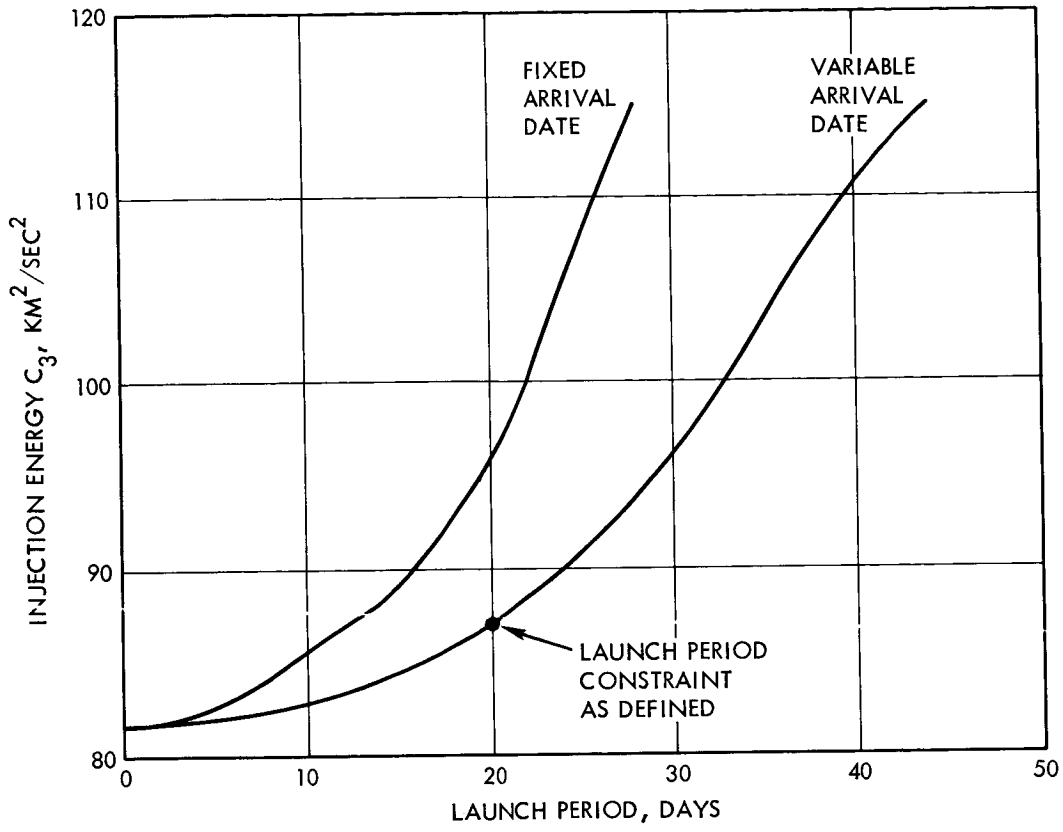

Figure 2-20. C_3 Versus Launch Period, 1972 Earth-Jupiter Trajectories

830-day trajectory. Similarly, for example, it must be possible to accommodate to a different approach geometry (lower ZAP angle) characteristic of a later arrival, and the capability to do this by adjusting the mounting of appropriate sensors late in the checkout sequence must be provided.

Although this required spacecraft design versatility appears as a penalty, a reduction in required C_3 is effected (as indicated in Figure 2-20). For a 20 day window this reduction is from 96 to 87 km^2/sec^2. For the Atlas/Centaur/TE-364 launch vehicle, this corresponds to a significant increase in payload capability of over 80 pounds.

By imposing the constraints discussed in the preceding sections, it is possible to delineate the available launch period by plotting the constraints against the two variables—launch date and arrival date. This is shown in Figure 2-21 for 1972 earth-Jupiter trajectories. Each constraint is represented by a line, with shading on the prohibited side of the line. The constraints indicated in Figure 2-21 are summarized as follows:

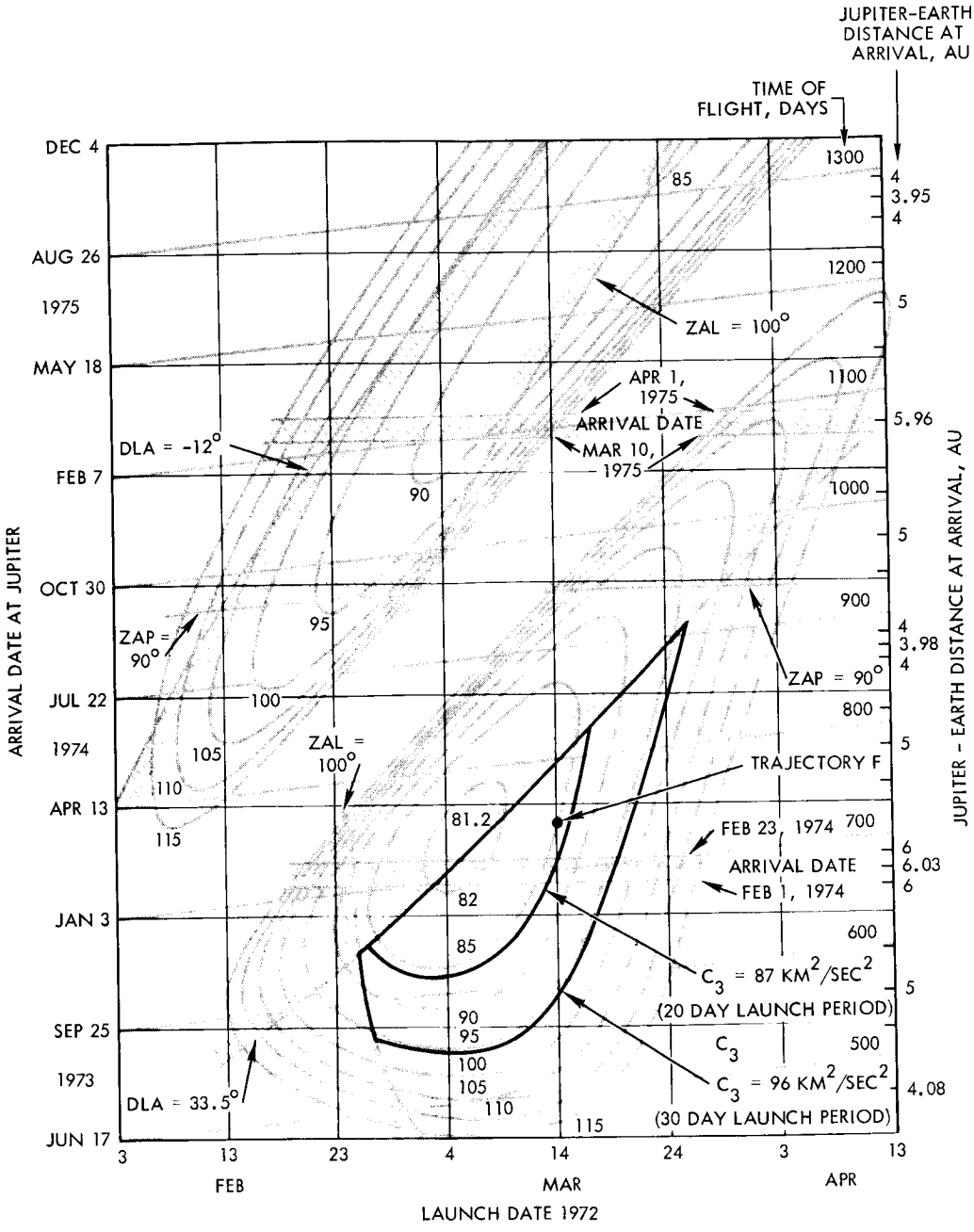

Figure 2-21. Delineation of the 1972 Launch Period

a) The DLA angle is constrained to the following limits:

$$-33.5° \leq \text{DLA} \leq -12°$$

These correspond to a launch azimuth range of 70 to 108 degrees, a parking orbit coast time which is greater than 2 minutes and less than 25 minutes, a powered flight angle of 30 degrees, an injection true anomaly of 15 degrees, and a daily launch window of one hour.

b) To favor the television experiment during the approach to Jupiter, ZAP angle is limited to be no less than 90 degrees.

c) Arrival dates during the periods February 1, 1974 to February 23, 1974 and March 10, 1975 to April 1, 1975 are excluded, in order to avoid communications interference associated with earth-Jupiter conjunction.

d) For reasons associated with the spacecraft design, the ZAL angle is limited to be no greater than 100 degrees.

e) A minimum launch period of 20 days (which may correspond to a variable arrival date) is required.

Several observations may be made by examination of Figure 2-21. The entire region of Type II trajectories appears unsatisfactory. Those Type II trajectories which would seem to be most desirable because of iow injection energy requirements and moderate ilight time are prohibited by three different constraints:

- DLA is greater than -12 degrees
- ZAL is greater than 100 degrees
- ZAP is less than 90 degrees

If Type II trajectories were to be considered, these constraints would have to be removed. Removal of the first requires coast times of over 25 minutes in parking orbit. The second devolves from the spacecraft thermal control design, and could be relaxed without extensive change. The third constraint favors a single experiment, television, by constraining the phase of Jupiter's illuminated portion during the approach of the spacecraft. For the constraints as described, however, Type II trajectories are effectively ruled out, and attention will be centered on Type I trajectories.

In the region of Type I trajectories, the constraints on DLA and ZAL tend to limit trajectories available at low values and intermediate values of C_3, respectively, although they do not limit the duration of the launch period appreciably for a given value of C_3. The ZAP constraint does not become effective until launch windows of over 30 days and C_3's of over 100 km^2/sec^2 are utilized. Figure 2-20, which indicates the C_3 requirements associated with launch periods (those corresponding to both variable arrival date and fixed arrival date), was determined by reference to Figure 2-21.

Characteristics of 1972 earth-Jupiter trajectories for the 20- and 30-day launch periods delineated in Figure 2-21 are summarized in Table 2-4. For each parameter listed, the extreme values encompassed by the launch period are given. The trajectories vary not only in launch date but also over a range of arrival dates.

For the 20-day launch period, the communications distance between Jupiter and the earth at encounter can vary between 4.7 and 6.0 AU. This range of distances includes the maximum ranges associated with arrival dates relatively close to earth-Jupiter conjunction. The consequent communications penalty is more than offset by the reduced injection energy requirements for these trajectories, as discussed in Section 2.2.5.

For launch periods up to 30 days in duration, the inclination of the heliocentric orbit plane of the spacecraft to the ecliptic is 1.2 to 3.3 degrees. The possible advantage in selecting trajectories which are highly inclined to the plane of the ecliptic in order to avoid the regions of the asteroid belt in which the meteoroid density is greatest is described in Section 2.2.8. However, it is not possible to achieve such trajectories within the constraints which have been outlined here. Type I trajectories of the 1972 opportunity which exhibit substantial inclinations are those which have late arrival dates for a given launch date, i.e., those lying close to the boundary between Type I and Type II trajectories. For a given launch date, the inclination is increased by delaying the arrival date. As a result, the C_3 requirement is increased, and the declination of the launch asymptote becomes progressively more negative. These effects are shown in Figure 2-22 for three sample launch dates. Because of the negative values of DLA required to provide a significant inclination of the spacecraft orbit plane, these trajectories can be considered only if the launch azimuth constraint is relaxed to enable the attainment of these launch asymptotes. Specifically, launches to the northeast (azimuths of the order of 35 degrees) would have to be employed.

2.2.8 Sample Trajectory

A sample earth-to-Jupiter trajectory has been generated for the 1972 opportunity. It is designated "Trajectory F" and is indicated on Figure 2-21. The characteristics of the heliocentric portion of this trajectory are indicated in Table 2-5.

Table 2-4. Characteristics of 1972 Earth-Jupiter Trajectories

The 20- and 30-day launch periods are those indicated in Figure 2-21. The extreme range of characteristics is derived from variations of both launch date and arrival dates. Extremes of different characteristics are not necessarily achievable simultaneously.

	Launch Periods (Variable Arrival Date)	
	20 Days	30 Days
Launch date	Feb. 26, 1972 to Mar. 17, 1972	Feb. 25, 1972 to Mar. 26, 1972
C_3, km^2/sec^2	81.4 to 87	81.4 to 96
Arrival date	Nov. 9, 1973 to June 22, 1974	Sept. 1, 1973 to Sept. 22, 1974
Flight time, days	616 to 827	544 to 910
DLA, deg	-33.5 to -28	-33.5 to -25.5
V_{HP}, km/sec	6.4 to 9.4	6.2 to 11.3
ZAP, deg	108 to 142	95 to 150
ZAE, deg	98 to 153	96 to 157
ZAL, deg	68 to 98	59 to 100
Jupiter-earth distance at encounter, AU	4.7 to 6.0	4.0 to 6.0
Inclination of spacecraft orbit plane to ecliptic, deg	1.6 to 3.1	1.2 to 3.3

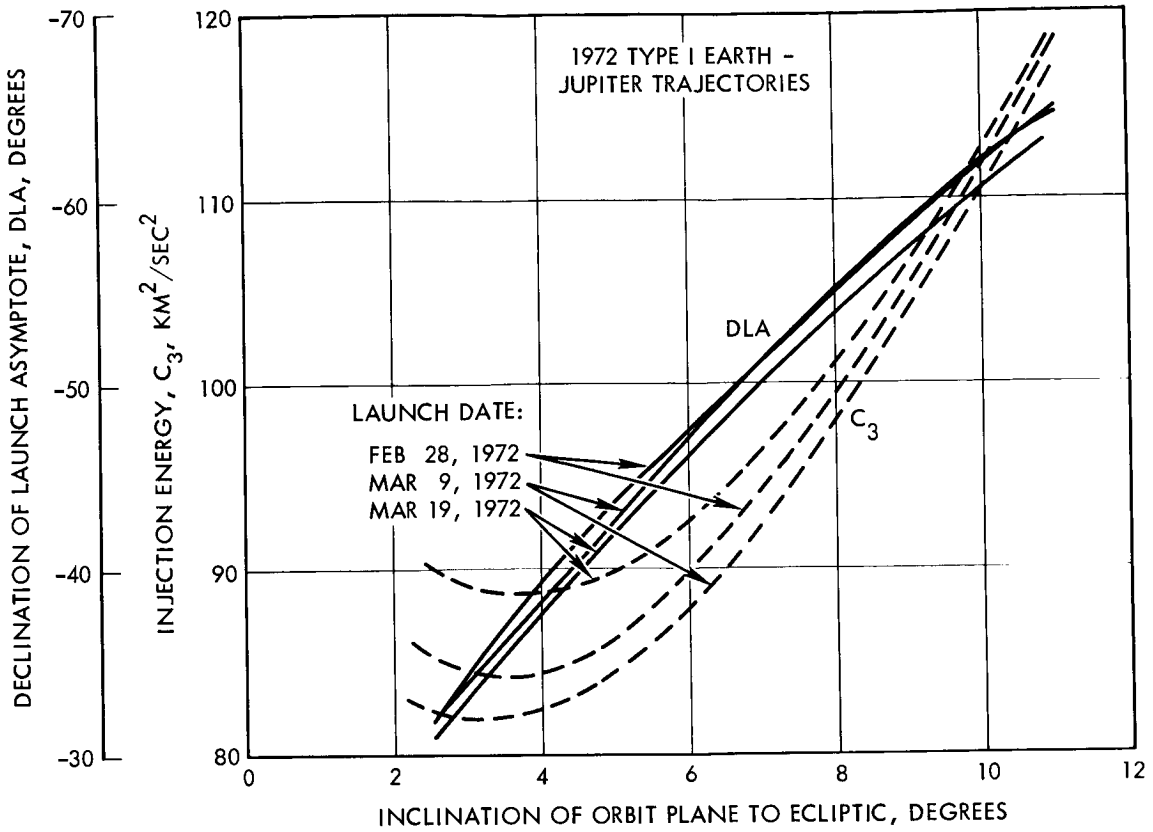

Figure 2-22. Requirements on C_3 and DLA to Attain Transfer Orbits of High Inclination

The launch date is March 14, 1972, and flight time is 742 days. The variation of geometrical quantities during the interplanetary phase is indicated in Figures 2-23 through 2-26.

The sun-spacecraft-earth angle has significance in its effect in the transfer of attitude reference from earth to sun for the performance of maneuvers, and from sun to earth to restore the cruise orientation. The earth-spacecraft-Jupiter angle determines the body angles for Jupiter-directed, spacecraft-mounted instruments during interplanetary cruise. The sun-earth-spacecraft angle is correlated with the time of day on earth when the spacecraft passes the meridian of any ground station; it also indicates the occurrence of spacecraft-earth conjunction at 308 and 702 days after launch.

The orientation of the earth-spacecraft line and its variation during interplanetary cruise indicate steering requirements for the spacecraft to maintain an earth-pointing attitude.

Table 2-5. Characteristics of Trajectory F, 1972 Earth-Jupiter

Launch date	March 14, 1972
C_3, km^2/sec^2	86
Arrival date	March 26, 1974
Flight time, days	742
DLA, deg	-30.2
V_{HP}, km/sec	7.00
ZAP, deg	122
ZAE, deg	116
ZAL, deg	70
Jupiter-earth distance at encounter, AU	5.83
Inclination of spacecraft orbit plane to ecliptic, deg	2.30

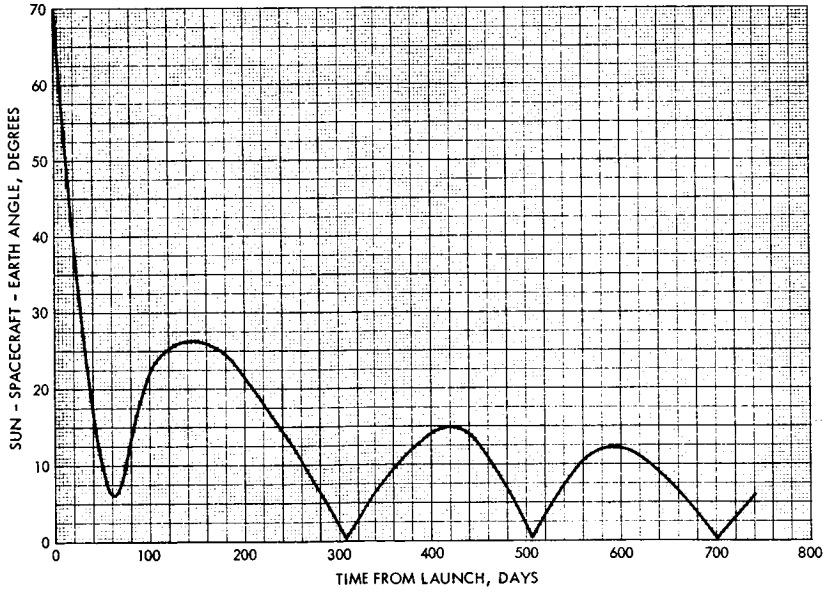

Figure 2-23. Sun-Spacecraft-Earth Angle for Trajectory F

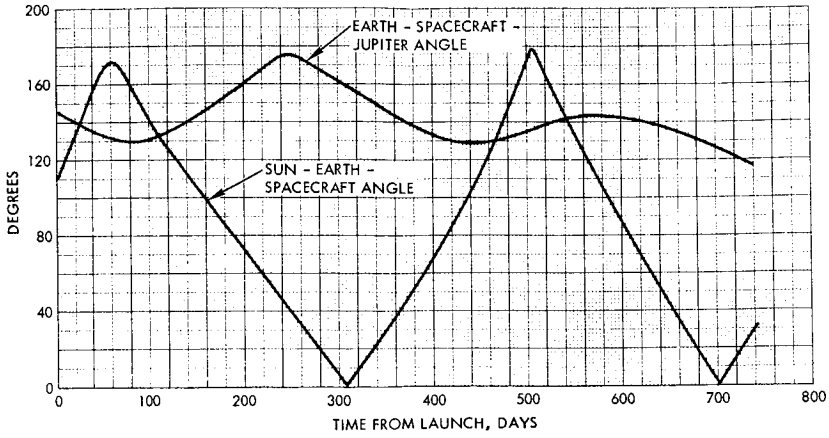

Figure 2-24. Earth-Spacecraft-Jupiter and Sun-Earth-Spacecraft Angles for Trajectory F

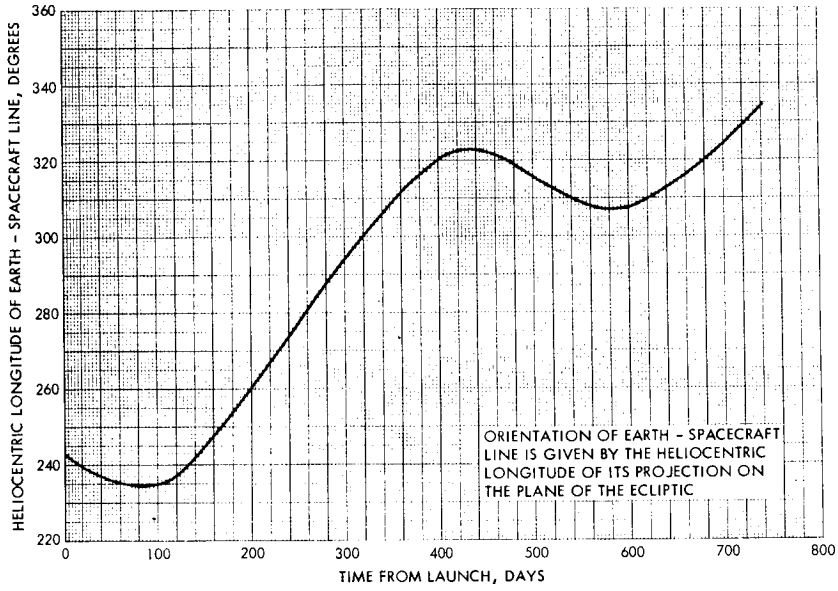

Figure 2-25. Orientation of Earth-Spacecraft Line For Trajectory F

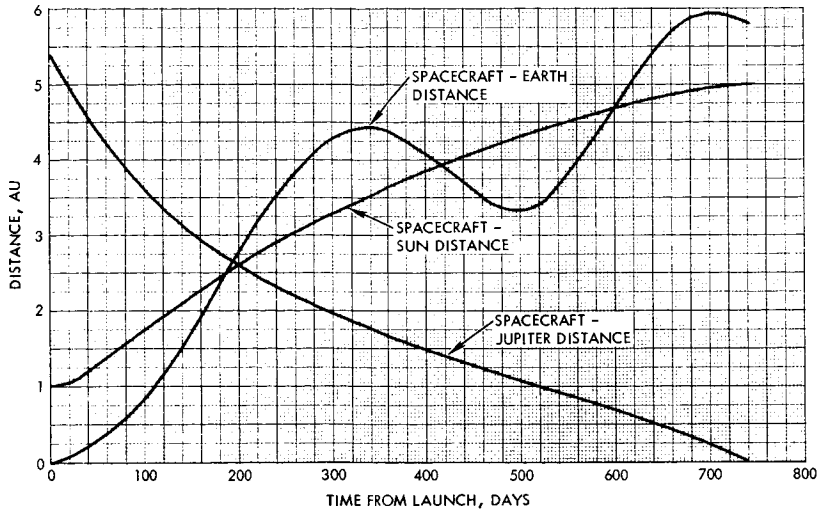

Figure 2-26. Distances from Spacecraft to Earth, Sun, and Jupiter for Trajectory F

The distances plotted in Figure 2-26 affect communications characteristics (spacecraft-earth distance), solar radiation, and wind intensities (spacecraft-sun distance).

2.2.9 Encounter Geometry

The geometrical characteristics of the spacecraft trajectory in the near vicinity of Jupiter are determined by 1) the large gravitational influence of the planet, 2) the choice of interplanetary trajectory, and 3) the choice of $\overline{B}$. While the first influence is not subject to our control, the other two are. To the extent that the desired near-Jupiter characteristics should influence the choice of interplanetary trajectory (launch date and arrival date), these influences have been examined in Sections 2.2.1 through 2.2.8. To the extent that these characteristics depend on the choice of $\overline{B}$, they are considered here.

The influence of the choice of interplanetary trajectory on the encounter geometry may be ascribed to the orientation of the planetocentric approach asymptote and the asymptotic approach velocity. For the 20-day launch period of the 1972 earth-Jupiter opportunity (which is identified in Figure 2-21), these quantities experience the following ranges:

ZAP,	angle between approach asymptote and Jupiter's orbit plane	108 to 142 deg
GAP,	angle between approach asymptote and Jupiter's orbit plane	+2.0 to +4.5 deg

VHP, asymptotic approach velocity 6.4 to 9.4 km/sec

Sample interplanetary trajectory F has these values: ZAP = 122 degrees, GAP = +3.2 degrees, V_{HP} = 7.0 km/sec; thus, it is near the middle of the indicated ranges and serves as a satisfactory sample for the purpose of examining encounter geometry.

For a given interplanetary trajectory, the choice of the impact parameter vector $\overline{B}$ specifies in which direction from Jupiter and what distance the approach asymptote lies. $\overline{B}$ is commonly expressed in components $\overline{B} \cdot \overline{R}$ and $\overline{B} \cdot \overline{T}$, where $\overline{R}$, $\overline{S}$, $\overline{T}$ are a right-hand set of mutually orthogonal unit vectors aligned as follows: $\overline{S}$ is parallel to the planetocentric approach asymptote, $\overline{T}$ is parallel to the plane of the ecliptic and positive eastward, and $\overline{R}$ completes the set and has a positive southerly component. The magnitude B determines the distance of closest approach to Jupiter, and the angle

$$\theta = \tan^{-1} \frac{\overline{B} \cdot \overline{R}}{\overline{B} \cdot \overline{T}}$$

specifies the orientation of the Jupiter-centered orbit plane as a rotation about the $\overline{S}$ axis. These definitions are illustrated in Figure 2-27.

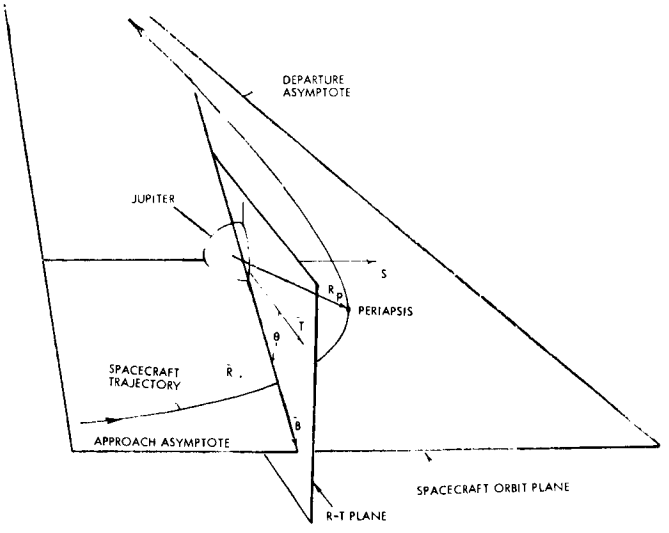

Figure 2-27. Encounter Geometry

It is worth observing here that a number of possible reference planes at Jupiter are within a few degrees of being parallel with each other. These are the planes of Jupiter's equator, Jupiter's orbit, and the earth's orbit (ecliptic). The closeness of these planes to coincidence is shown in Figure 2-28 by the orientation of their perpendiculars, or north poles.

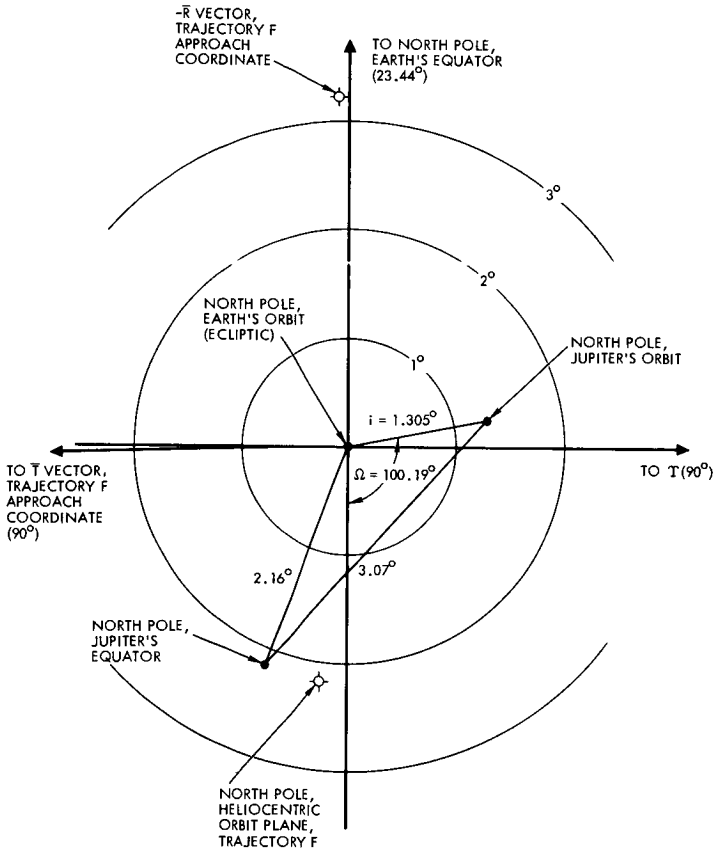

Figure 2-28. Proximity of Reference Planes at Jupiter

The significance of this near coincidence is that we may speak broadly of equatorial and polar passages of Jupiter by the spacecraft, knowing that the terms apply approximately to any of the three reference planes. Figure 2-28 also indicates the alignment of the 1972 Trajectory F, both heliocentric (by the north pole of its heliocentric orbit plane) and planetocentric (by locating the approach $\overline{R}$ vector). These two directions are also clustered within 3 to 5 degrees of the poles of the three reference planes noted. This proximity indicates that the flyby orbit inclination may be chosen over a wide range: only indications between ±5 degrees (with respect to Jupiter's equator) are excluded.

The effects of Jupiter's gravitational field are to increase the spacecraft velocity to a maximum, at the point of closest approach to the planet, and to focus and bend the trajectory. The closer the distance from Jupiter at periapsis, the greater these effects are. Figure 2-29 indicates how

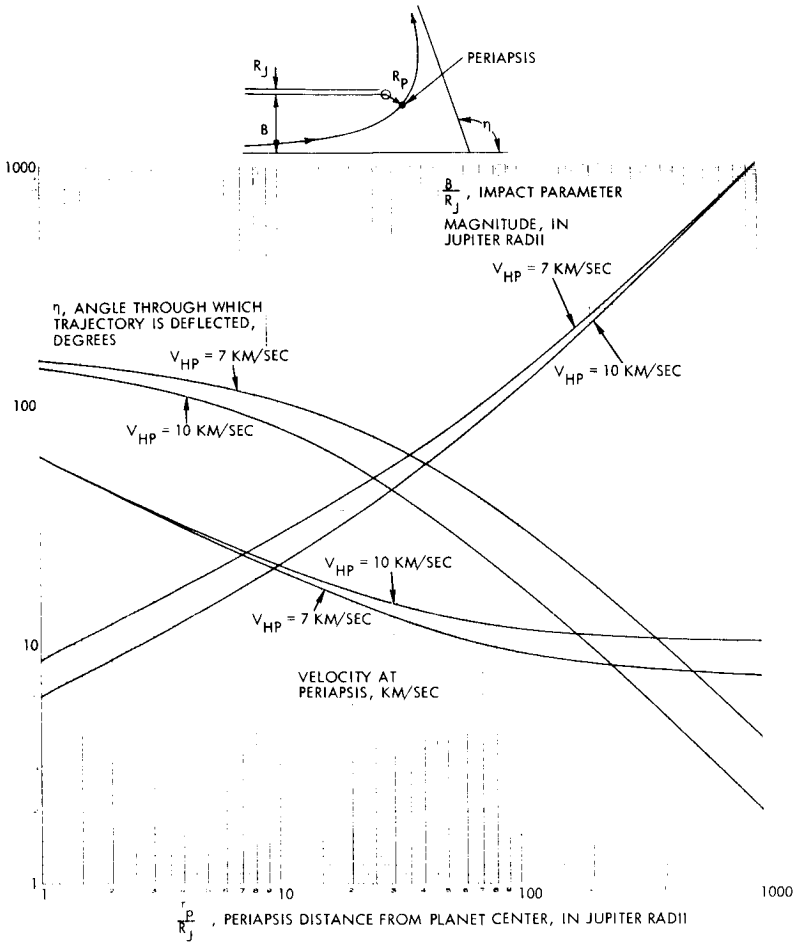

Figure 2-29. Jupiter Gravitational Effects Versus Periapsis Distance

some of these quantities vary with R_P, the distance from the planet center at periapsis, for two different values of the asymptotic approach velocity. All quantities in the figure are expressed in planet-centered coordinates.

2.2.9.1 Mission Objectives

The influence of the mission objectives on the selection of the near-Jupiter trajectory may be divided into several classes, as follows:

Class of Objective	Nature of Influence on Near-Jupiter Trajectory
Interplanetary particles and fields	No influence
Planetary particles and fields	Importance is attached to where the spacecraft trajectory lies
Planetary surface (atmosphere) observations	Importance is attached to what aspect of the planetary surface can be seen from the spacecraft trajectory
Mission objectives for the period subsequent to encounter (secondary interplanetary objectives)	Affects encounter geometry according to its influence on the heliocentric trajectory of the spacecraft after encounter

For the planetary particles and fields objectives, it is necessary for the spacecraft to fly through the environments which are to be measured. Measurements associated with the magnetosphere boundary are made far enough from Jupiter (50 to 150 radii) that planetary encounter geometry does not significantly affect the region where the approaching spacecraft penetrates the boundary. However, the encounter geometry has a large effect on the location of the region where the spacecraft departs from the magnetosphere after encounter. It would seem appropriate for the departing spacecraft to measure a portion of the boundary where the spacecraft-Jupiter-sun angle differs substantially from its value at the approach penetration. Thus, the deflection of the trajectory should be such that the departing ZAP angle differs from the arrival ZAP angle.

For particle and field measurements within the magnetosphere, measurements 3 radii or less from the planetary center are desired, to observe the expected peak-trapped particle intensity. Although the equivalent dipole strength and orientation of the magnetic field may be deduced from measurements along a trajectory which approaches to only 10 R_J, a close trajectory is desirable to determine possible deviations from the dipole model. Measurement of the dust cloud surrounding Jupiter does not require a particularly close approach. In summary, planetary particles and fields measurements are most significant if made from a trajectory for which $R_P = 3R_J$ or less.

The inclination of the hyperbolic orbit plane is also a matter to be considered. If the magnetic field of Jupiter and the consequent trapped radiation were known to be symmetric, with respect to both the polar axis and the equatorial plane, then a passage in the equatorial plane would give the most unambiguous data to indicate intensity versus altitude. However, it is suspected that neither of these two symmetries is present. It is not clear, then, whether the best strategy is to pass in the equatorial plane, and determine the best-fit symmetric model of the radiation patterns, or to incline the trajectory to deliberately seek out the asymmetric components of the patterns. It might be noted that the magnetic field measurements, consisting of all components of the vector field, permit asymmetric components to be inferred from a trajectory in or out of the equatorial plane.

The experiments involved in observations of Jupiter's surface (actually the atmosphere) are the television and occultation experiments, the infrared radiometer, and the auroral detector. For a given television experiment, surface resolution improves as the altitude of the camera decreases, until it is limited by smear due to relative motion. However, surface resolution does not assume the importance in photography of Jupiter that it does in lunar and Martian missions. Resolution is valuable to a point, in aiding in the interpretation of Jovian cloud formations, but equally significant is the ability to observe temporal changes in the cloud patterns over an extended period. For this reason, it is felt that good viewing conditions for 100 hours previous to encounter (during approach) or after encounter (during departure) have a significance to the television experiment which is equal to or greater than either a close periapsis passage or favorable lighting conditions at periapsis. Also, it is probably desirable for initial flyby missions to favor observation of regions of low and intermediate latitudes, as the most prominent and interesting surface features—the Great Red Spot and dark bands— are located in these regions. This would lead to a preference for trajectories remaining close to the equatorial plane while passing Jupiter.

Figure 2-30 shows the range of encounter geometries possible for equatorial passages. Eastward and westward passages are shown for relatively early and late arrival dates, and for periapsis distances 1.5

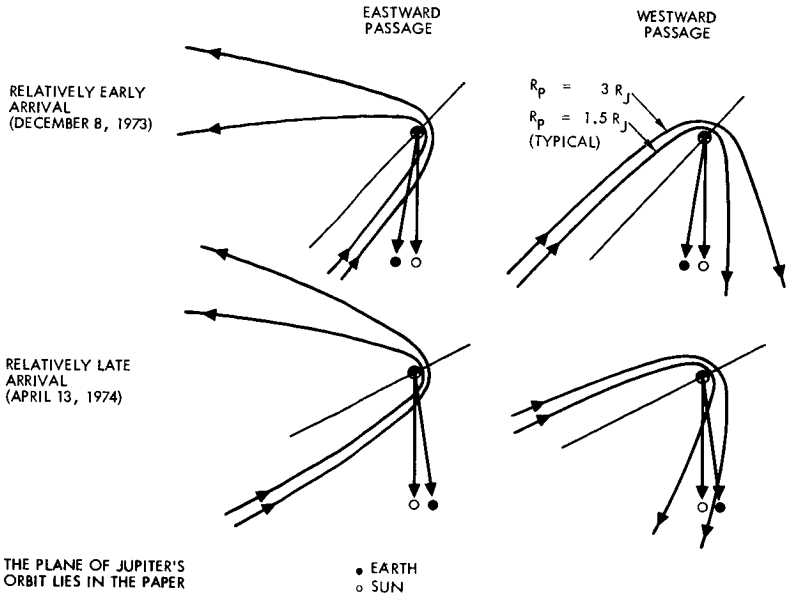

Figure 2-30. Possible Encounter Geometries, Equatorial Passages

and 3 radii from the planet center. The directions to the sun and earth are shown. The following observations may be made.

- In all cases, periapsis occurs over the dark side of the planet, although it is much closer to the terminator in eastward passages than in westward.
- The viewing conditions during approach are somewhat better for eastward than for westward passages, and somewhat better for early than for late arrival dates. As the spacecraft gets closer to the planet, the phase improves (increases) for eastward passages, but it worsens for westward passages.
- The viewing conditions after periapsis, when the spacecraft is receding from the planet, are excellent for westward passages, with almost the entire sunlit hemispheres visible; however, conditions are poor after eastward passages, as the phase is only half or less.
- For R_P between 1.5 and 3 R_J the above observations are independent of the actual value of R_P.

These observations do not lead to a clear superiority (with respect to the television experiment) of one type of equatorial passage over the others. The westward passages may have the better viewing conditions from 20 to 100 radii away, but eastward passages are superior within 20 radii, and

have the additional advantages that the television experiment need not wait until after occultation and periapsis passage, and that the orbit is posigrade, minimizing relative angular motion between spacecraft and planet.

A prerequisite for the occultation experiment is, of course, that the spacecraft follow a trajectory so that Jupiter is interposed between the spacecraft and the earth. The nature of the boundary between occulting and nonocculting trajectories, as projected onto the R-T plane (that is, as it pertains to the spacecraft approach trajectory preceding the influence of Jupiter's gravitation), is indicated in Figure 2-31 for earth-Jupiter Trajectory F, 1972. A second consideration is that the occultation should not take place at too great a distance from the planet, because the density of the atmospheric layer from which the refracted and dispersed waves will exceed communication system threshold sensitivity decreases as the spacecraft distance from the planet increases. Also plotted on Figure 2-31 is the eclipse boundary—the boundary between trajectories which

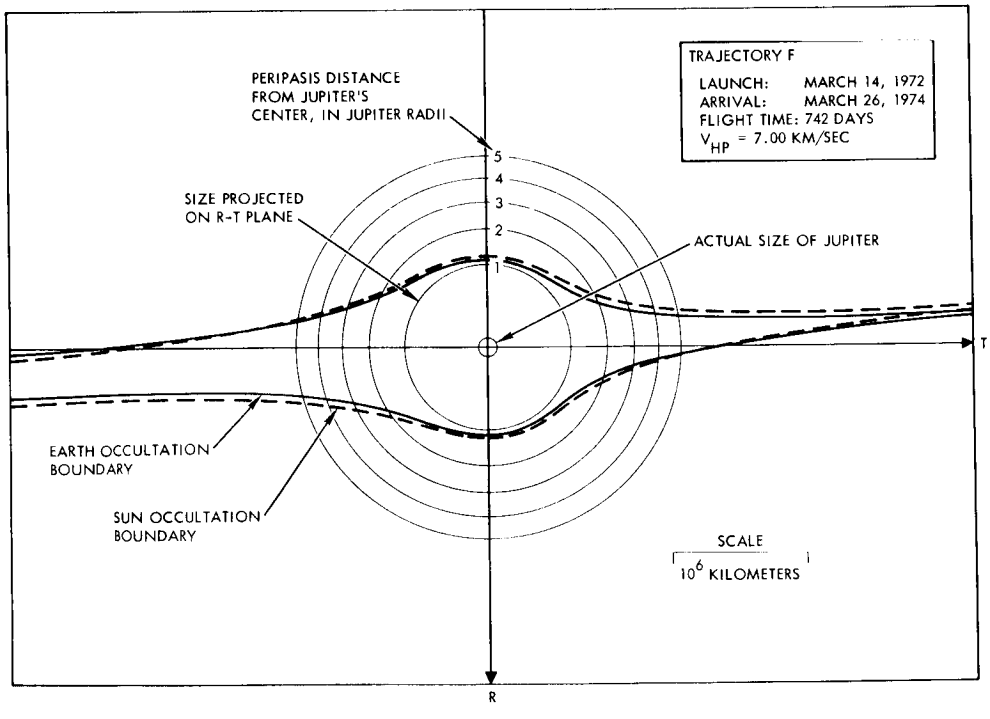

Figure 2-31. Occultation Boundaries

subject the spacecraft to an eclipse from the sun and those which do not. A spherical Jupiter was assumed in generating these boundaries. The figure indicates the following:

- Ruling out near-grazing trajectories for reasons of guidance accuracy limitations, trajectories which provide for occultation from the earth should be chosen to have low or moderate inclination. Actually θ, the angle of rotation of $\bar{B}$ from $\bar{T}$ axis, should be within approximately ±30 degrees.

- No aiming points close to the planet will lead to an earth occultation without also entailing eclipse from the sun. Only trajectories leading to periapsis distances of greater than 6 R_J can provide occultation without eclipse, and only if guidance errors are restricted to extremely small values.

The infrared radiometer is a scanning instrument designed to measure radiation from selected regions of the planetary disc. With a 2-degree field of view, the principal requirements on trajectory are that the use of this instrument from large distances leads to poor resolution, and its use from points very close to the planet restricts the area which may be seen—that is, within the visible horizon—to a limited portion of the total planet. Furthermore, this instrument is designed to observe both the sunlit and the darkened sides of the planet; therefore, if the mechanization is restricted to a single scanning degree of freedom (provided by the spinning of the spin-stabilized spacecraft, or a single gimballed platform of a 3-axis stabilized spacecraft), the observations must be made from a particular segment of the trajectory, preferably that encompassing the plane of the terminator. For the reasons noted above, it is most desirable for the spacecraft distance from the planet's center at this segment of the trajectory to be in the range 1.5 to 5 R_J.

The fourth instrument for surface observation is the auroral detector, intended to pick up visible and ultraviolet radiation emanating from the auroral zones (latitudes 50 to 70 degrees) on the dark side of the planet. It is evident that if the spacecraft is in an equatorial passage, this instrument can be used only if the distance is great enough that these latitudes can be seen. If the spacecraft is 2 R_J from the planet's center, the horizon is at 60 degrees; if at 3 R_J, 70 degrees. However, it should not be too far from the planet for the same reason which applies to the infrared radiometer—the surface resolution resulting from the 2 degree field of view will be inadequate to confirm the auroral phenomena by latitude. For inclined orbits leading to observations made when the spacecarft is over points of higher latitude, the path may be closer to the

surface, and still provide coverage of the desired regions. On the other hand, the auroral detector is used only on the dark side of the planet, and, unlike the infrared radiometer, it may be oriented in a way that its observations are performed from the optimum portion of the trajectory. In particular, where the scan is provided by the spin-stabilized spacecraft, the detector may be mounted so as to sweep out a cone whose axis is directed toward the earth. This mechanization can provide two periods of observations, corresponding to the entry into and exit from the cone by Jupiter. For an eastward passage, these would lead to a first period of observations from distances close to the periapsis distance, and a second period from greater distances, perhaps 5 to 10 radii from the planet. Because of this flexibility in mounting and employing the auroral detector, it is not felt that a strong constraint is imposed on the choice of near-Jupiter trajectories.

It has been indicated (JPL Report 32-849, et al) that spacecraft passing close to the planet Jupiter can make use of the gravitational energy added to or subtracted from the orbital energy expressed in heliocentric coordinates, to achieve a number of missions subsequent to encounter. Among these missions are those leading to the far reaches of the solar system—exploration of the outer planets and interplanetary space beyond Jupiter, even to the extent of achieving trajectories which escape from the solar system—those in which heliocentric energy is decreased and the spacecraft returns to the earth or even substantially closer to the sun, and those employing orbits highly inclined to the ecliptic. Not all of these options are possible from the earth-Jupiter trajectories associated with the relatively low launch energies of the 20- or 30-day launch periods. Some of the options which are available include trajectories which lead to trans-Jupiter regions of the solar system, achievable by eastward equatorial passages, trajectories which return closer to the sun (perihelion distances 4 to 0.6 AU) achieveable by westward equatorial passages, and 20- to 40-degree inclinations of subsequent heliocentric orbits to the ecliptic, achievable by polar passages.

It is felt that many of these options are logically candidates for the post-encounter trajectories to be produced in a program of Jupiter flyby missions. However, it is most consistent with the initial complement of

instruments and mission objectives for a Jupiter flyby mission that the initial effort be directed towards the first class of options, that of exploring interplanetary space in the plane of the ecliptic beyond Jupiter, to the extent that spacecraft lifetime permits. Therefore, for the purpose of this section, it is concluded that the secondary mission objectives associated with the interplanetary segment of the trajectory subsequent to encounter are best achieved by eastward equatorial passages.

2.2.9.2 Spacecraft Design Constraints

The purpose of this section is to examine any influences which characteristics of the spacecraft system design would logically impose on the choice of Jupiter trajectory.

The near-Jupiter trapped radiation environment is discussed in Section 2.4. It is concluded that, for a flyby mission, the exposure of the spacecraft to the estimated intensity of Jupiter's radiation belts will not significantly degrade operational reliability, particularly if a parts selection program excludes the use of the most sensitive components. Of course, it is necessary to penetrate this environment in order to determine its intensity accurately; the possibility of an adverse effect on spacecraft operation is related principally to the uncertainty of the present estimates of the radiation intensity. For an orbiter mission, the prognosis is less clear. The flyby mission should serve in the engineering role of accurately ascertaining the medium to which the orbiter will later be subjected.

The Jovian magnetic field may be as high as 50 gauss at the surface. This would lead to intensities of 15, 6, and 2 gauss at 1.5, 2, and 3 radii from the planet center, respectively. In Section 2.4, it is indicated that magnetic shielding may be necessary to keep certain instruments operating in such environments. It is not felt that trajectory constraints should be applied to avoid penetrating regions of high magnetic field intensity.

The accuracy with which the spacecraft trajectory can be controlled to conform to the intended trajectory places a limit on the choice of the intended trajectory. For example, if it is desired to achieve a 99 percent probability of undergoing occultation, then the intended trajectory must be

sufficiently far inside the occultation boundary to allow for expected dispersions. Section 7.4 examines this subject in detail; only broad conclusions are reviewed here. Accuracies achievable lead to dispersions in the R-T plane such that trajectories will conform to intended aiming points within 99 percent ellipses with major axes no greater than 50,000 kilometers. In Figure 2-31, it can be seen that the aiming area prescribed by occultation requirement and the avoidance of impacting trajectories is not greatly reduced by the imposition of 50,000-kilometer border to accommodate guidance inaccuracies.

The question of whether a planetary quarantine is to be observed in the case of Jupiter, similar to that which has been formulated for the Voyager program of exploration of Mars, might be raised. Without going into the many ramifications of such a question, we can look at one aspect of it: the requirement that the probability that the spacecraft would impact the planet be restricted to a very small value, of the order of 10^{-4}. For a flyby mission, the conformance to this sort of a requirement involves, in addition to guidance accuracy considerations, considerations of reliability of the midcourse correction maneuvers and the processes by which the spacecraft is injected onto an interplanetary path by the launch vehicle. However, to the extent that they influence the choice of trajectories and aiming point, the results are more simply stated. Instead of requiring that the aiming point be buffered from a graze trajectory by a 99 percent ellipse, the requirement is simply raised to a 99.99 percent ellipse, or whatever is necessary. In the present instance this could have the effect of imposing a border of, say, 150,000 kilometers instead of 50,000 kilometers. With or without the application of a stringent planetary quarantine policy, it appears that the guidance accuracy is adequate to permit nominal trajectories to be selected which approach Jupiter as close as altitudes of 0.5 R_J.

2.2.9.3 Sample Encounter Trajectories

As a result of the considerations reviewed above, sample encounter trajectories have been generated and plotted for eastward equatorial passages following interplanetary Trajectory F, described in Section 2.2.8. (As mentioned above, the planet-centered trajectory is not exactly in the

plane of the equator, but can be within about 5 degrees of the equatorial plane.) Values of R_P, the periapsis distance from the planet's center, of 1.5 and 3 R_J, are used. Figure 2-32 shows the path within 100 R_J of Jupiter, with R_P equal to 1.5 R_J. Figure 2-33 shows the same trajectory at an enlarged scale, within 6 R_J of the planet. Figure 2-34 plots the spacecraft's distance from Jupiter's center and the cone angle of the

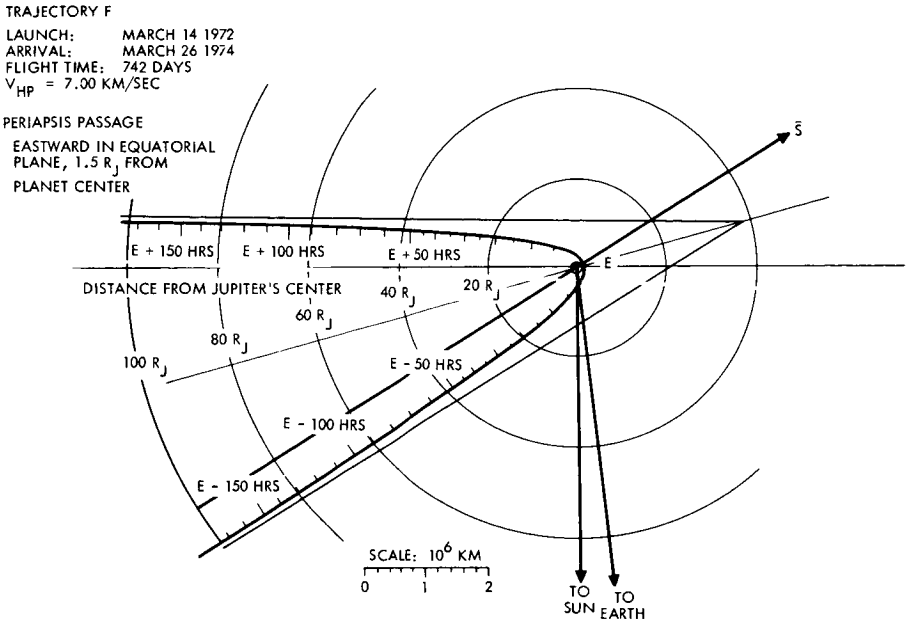

Figure 2-32. Encounter Geometry at Jupiter, R_P = 1.5 R_J

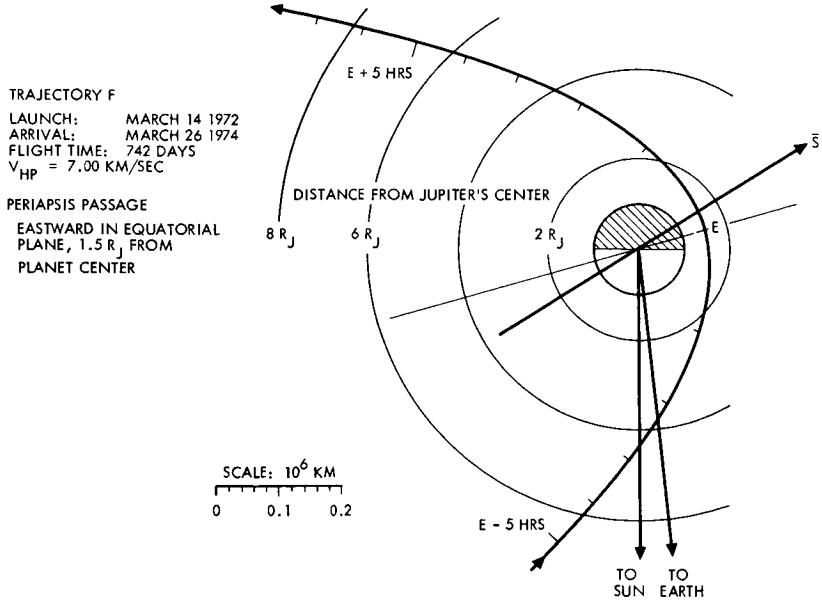

Figure 2-33. Encounter Geometry at Jupiter, R_P = 1.5 R_J, Enlarged Scale

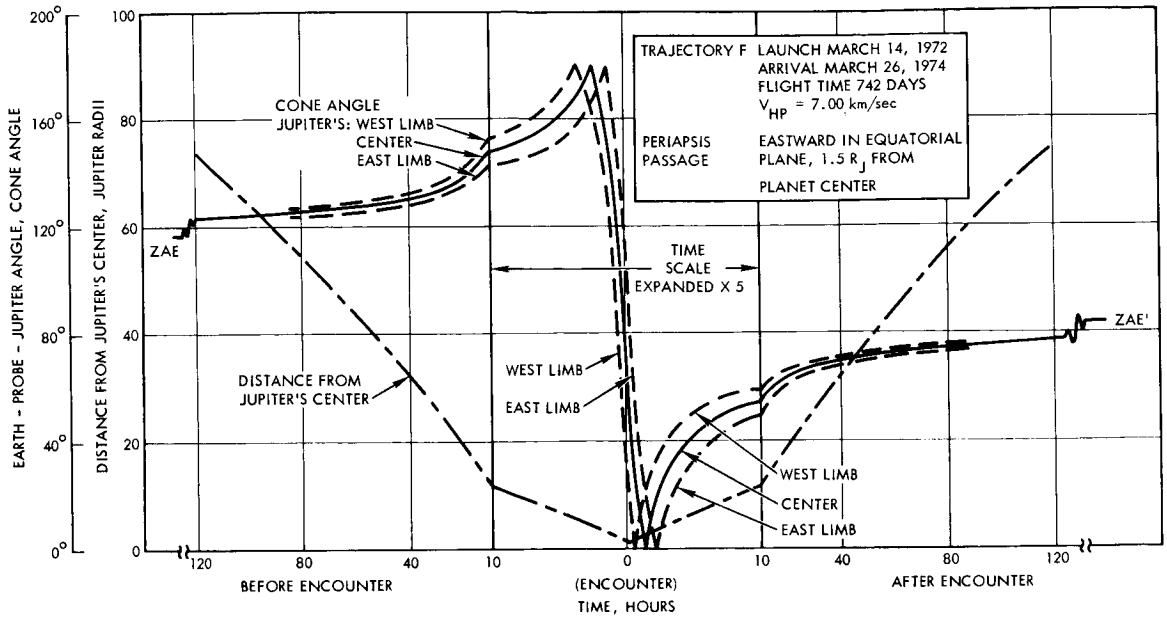

Figure 2-34. Cone Angle and Distance from Jupiter Versus Time from Encounter, $R_P = 1.5\ R_J$

planet as seen from the spacecraft as functions of time before and after encounter. It should be pointed out that cone angle, when used with reference to an earth-pointing spacecraft, refers to the angle measured at the spacecraft between the earth and the object. For a spin-stabilized, earth-oriented spacecraft, this cone angle, then, specifically describes the spin-swept cone which intercepts the object. In Figure 2-34 the cone angle of the center of Jupiter is plotted, and in addition the cone angle of the east and west limbs are plotted, indicating the apparent size of the planet at any time.

These three figures are repeated in Figures 2-35 to 2-37 for a periapsis distance of 3 R_J from the center of the planet.

2.2.10 Trajectory Accuracy

The requirements for trajectory accuracy to be attained by the spacecraft system result from the scientific objectives of the mission. Several of these objectives which are associated with the encounter phase of the mission have the most stringent accuracy requirements. The influence of these experiments on the choice of the nominal trajectory at encounter has been reviewed in Section 2.2.9. The general conclusion of that section was that for an initial Jupiter flyby mission it was reasonable to adopt as a nominal trajectory one which remains close to the equatorial

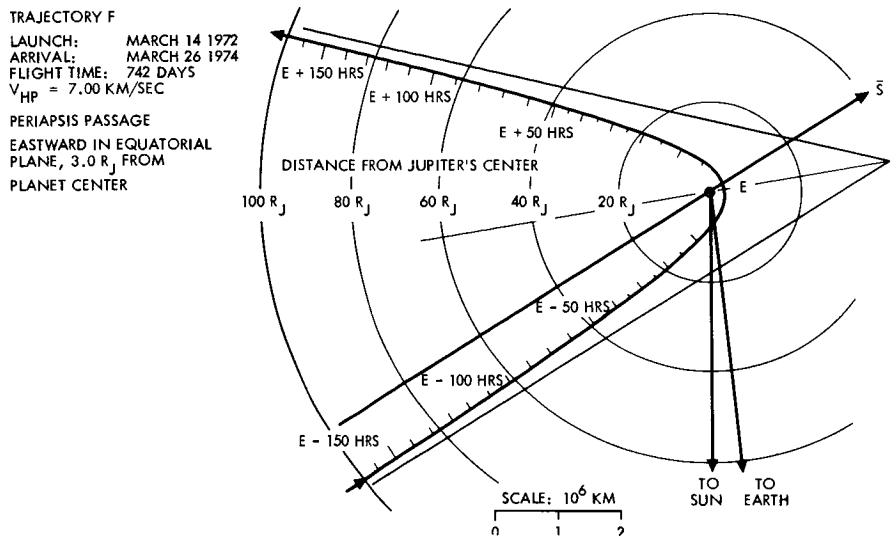

Figure 2-35. Encounter Geometry at Jupiter, R_P = 3 R

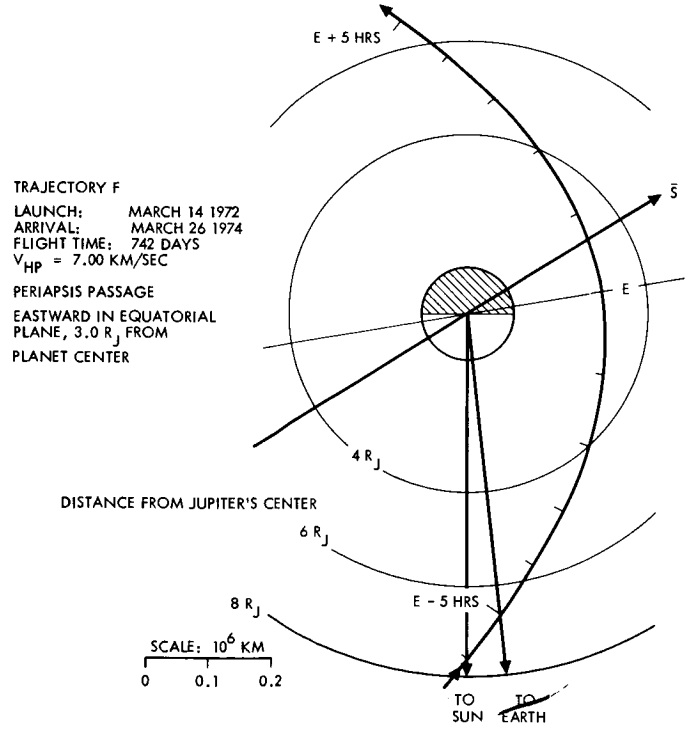

Figure 2-36. Encounter Geometry at Jupiter, R_P = 3 R_J

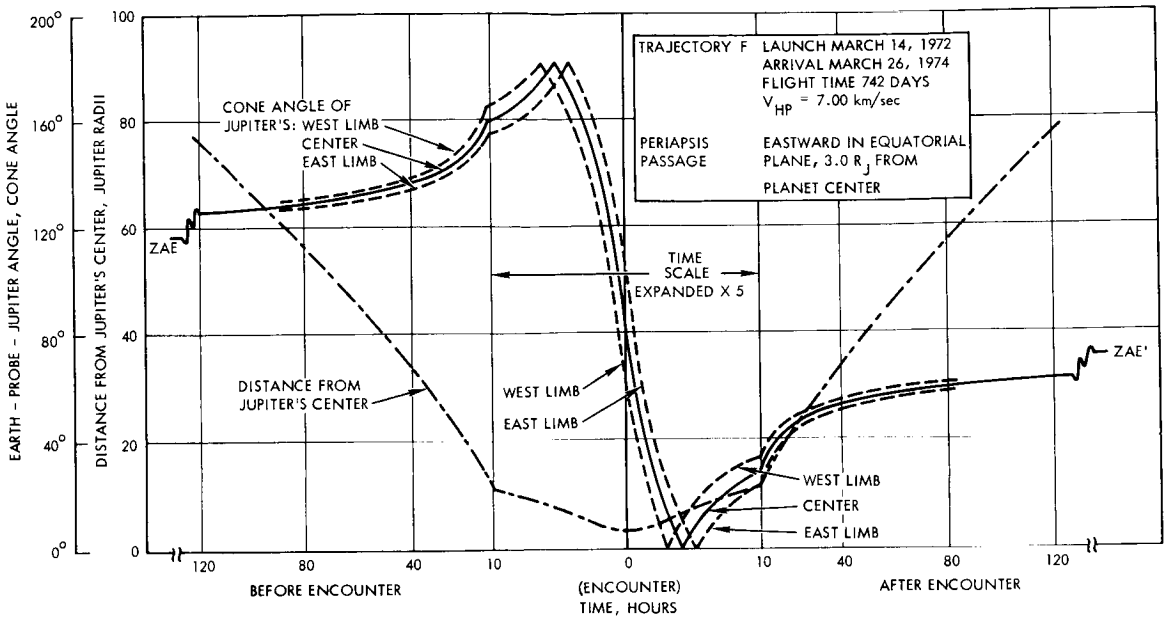

Figure 2-37. Cone Angle and Distance from Jupiter Versus Time from Encounter, $R_P = 3\ R_J$

plane of Jupiter, and, at periapsis is between 1.5 and 3 Jupiter radii from the planet center. Reference to Figure 2-31 shows that such a targeting lies well within the earth occultation boundary.

For such a trajectory, the purpose of accuracy requirements are the following.

- To ensure that there is a negligible probability that the spacecraft will impact the planet
- To ensure a high probability that the trajectory will lie within the occultation boundary
- To ensure that, for all Jupiter-oriented experiments in general, any preset mounting and pointing angles will lead to satisfactory data, trajectory dispersions notwithstanding.

A point worth observing is the focusing effect of Jupiter's gravitational influence. This is evident in comparing periapsis distance with the magnitude of the B vector in Figures 2-29 and 2-31. For R_P in the range proposed, dispersions in B are divided by a factor of 2.6 to 3.6 to obtain the resulting dispersions in R_P. A similar focusing takes place in the direction perpendicular to the plane of the planetocentric orbit. Dispersions in that direction in the R-T plane are reduced by factors of 7 to

13 to determine the out-of-plane dispersion at the time of periapsis passage. The result of this focusing effect is that permitted dispersions expressed in the R-T plane can be substantially larger than the actual trajectory dispersions measured at the point of closest approach to the planet.

Based on the above considerations, it is a reasonable requirement on trajectory accuracy that 99 percent of the trajectories lie within a circle of radius 70,000 km of the intended trajectory, expressed in the R-T plane.

The ability to control the time of arrival at Jupiter is not as clearly a necessity of the mission as control of the miss distance. It might be stated, for purpose of ensuring Goldstone visibility at encounter, that the desired accuracy of the time of arrival be within ±2 hours for 99 percent of the trajectories. However, acceptable missions can exceed this limit.

(Accuracies are stated as "99 percent of trajectories" in recognition of the non-gaussian distribution resulting from the nature of midcourse corrections. Using percentage avoids possible misinterpretation of terms such as 1σ or 3σ, where percentages usually associated with normal distributions may not apply.

The requirements stated above apply to the accuracy with which the trajectory can be controlled. It is anticipated that the accuracy with which they can be determined, benefiting from extended radio tracking after performance of the midcourse trajectory correction maneuver(s), will be greatly superior to the numbers given above. However, the orbit determination accuracies are not considered to be a requirement on the spacecraft system design, so they are not stated or estimated in this section.

2.3 INTERPLANETARY ENVIRONMENT

In this section, possible effects on the spacecraft of the solar wind, cosmic rays, and micrometeoroids are considered.

2.3.1 Solar Wind

Bombardment by solar wind during the long interplanetary cruise portion of the mission does not appear to result in any significant sputtering effects on the spacecraft. KenKnight and Wehner* have studied the effects of sputtering dry Kev energy H^+, H_2^+, and H_3^+ ions on various metals. Significant measurements of H^+ were not possible because the target weight actually increased during the experiment because of the large sticking probability of these ions. The yields for H_2^+ and H_3^+ were in the order of 10^{-2} atom/incident ion. For a vehicle exposed to the solar wind near earth, this would correspond to a loss of $\sim 10^{13}$ atoms/cm^2 year, a totally unimportant effect.

Sputtering yields by He^{++}, about 10 percent abundant in the solar wind, has not been determined in laboratory experiments. Sputtering yields depend on the target crystal configuration and angle of incidence. However, taking the largest yield** for Kev argon ions (A^+) as 10 atoms/incident ion, we obtain for a conservative upper limit to He^{++} effects, an upper mass loss estimate of $\sim 10^{15}$ atoms/cm^2 year, again totally unimportant.

2.3.2 Cosmic Rays

For the steady state (nonflare) cosmic ray radiation dose, we use an estimate of ~ 3 rad/cm^2 year. This can be enhanced by flare occurrence by a factor of about 50 using maximum proton fluxes of 10^3 particles/cm^2 sec ster > 80 Mev which have been observed in the earth's environment,*** a duration of about 10 hours, and an occurrence rate of 10 large (Class 3) flares per year (solar maximum). Fluxes should decrease as the spacecraft moves away from the sun, so that this estimate represents an upper limit. This dose rate is large but appears to be sufficiently less than the damage limit of 10^5 rad.

---

*C.E. KenKnight and G.K. Wehner, "Sputtering of Metals by Hydrogen Ions," J. Appl. Phys., 35, (1964) 322.

**G.D. Magnuson and C.E. Carlston, "Sputtering Yields of Single Crystals Bombarded by 1-10 Kev Argon Ions," J. Appl. Phys., 34, (1963) 3267.

***E.P. Ney and W.A. Stein, "Solar Protons, Alpha Particles and Heavy Nuclei in November 1960," J. Geophys. Res., 67, (1962) 2087.

2.3.3 Interplanetary Meteoroids

The parameters describing the meteoroid environment are the flux, the number of particles per unit area per unit time of mass m or greater, and the particle velocity and direction. These parameters and their possible variations are covered in the following sections.

2.3.3.1 The Meteoroid Flux

The meteoroid flux varies over interplanetary distances. For spacecraft trajectories for a Jupiter flyby mission, four regions of space can be distinguished, each presumed to have distinct characteristics: near-earth, near interplanetary (1 to 2 AU), the asteroid region (2 to 4 AU), and far interplanetary (4 to 5.2 AU). The upper boundary on the meteoroid flux for these regions is given in the following sections. A plot of the flux levels is given in Figure 2-38, the curve designations matching those used for the equations of the text. The uncertainty in the meteoroid flux is discussed at the end of the section.

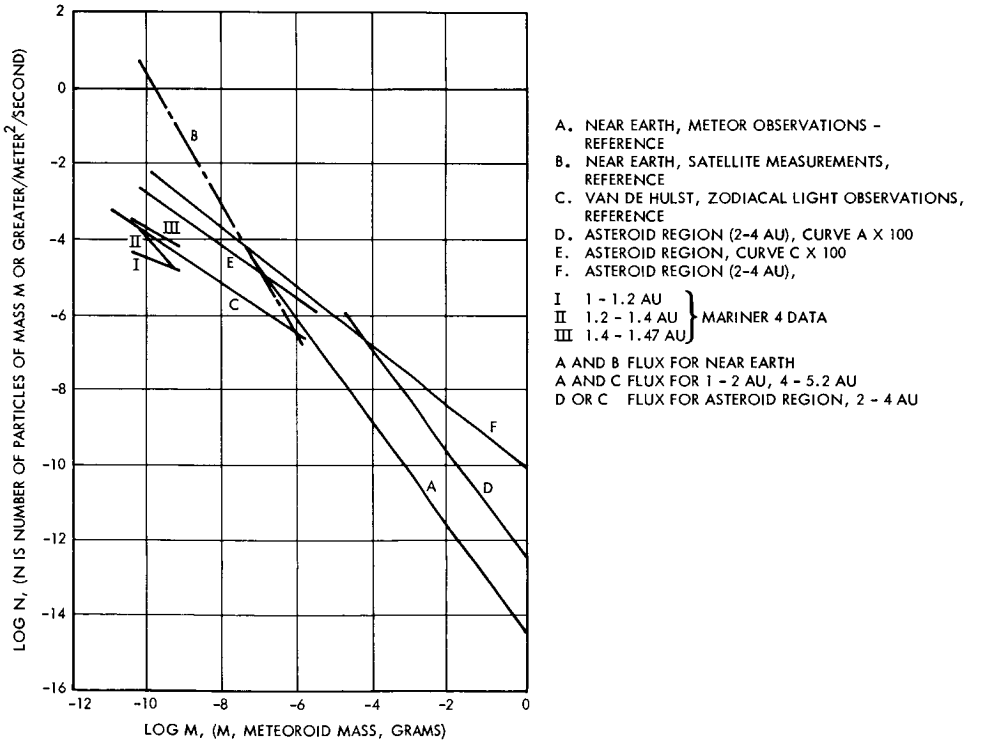

Figure 2-38. Micrometeoroid Flux

The flux near the earth is considered to commence at 4000 miles geocentric radius and extend to 65 earth radii. The flux for this region is expressed by two equations covering two ranges of particle mass:

For particles with $M > 10^{-5}$ gm

$$\log N = -1.34 \log M - 14.18$$

This flux is based on meteor observations and has been modified from its original form, known as Whipple 63*, to remove the effect of earth shielding.

For particles with $10^{-10} < M < 10^{-6}$ gm

$$\log N = -1.7 \log M - 16.87$$

This flux is based on satellite measurements,** and has been modified to remove the effect of earth shielding assuming the average orbital altitude of 2500 miles for the measuring satellites.

When this flux is pertinent to the spacecraft design, the earth shielding is accounted for by a shielding factor which is applied either to the flux or the vehicle area.

At 1 AU, but away from the earth, the flux for the small particle sizes is reduced for the interplanetary regions from the level near the earth. Evidence of a so-called dust cloud around the earth has been best shown by the Mariner 4 data.*** This data showed a reduction of 10^4 to 10^5 in the mass range 4×10^{-11} to 6×10^{-10} gm, compared to earth satellite data. Beard**** predicted a reduction of 10^4 in dust particles. Both the Mariner 4 data and Beard's conclusion fall below the flux proposed by van de Hulst, which is recommended***** as applicable to "deep space" (5×10^4 to 2×10^5 km) for the small particle range.

---

*F. L. Whipple, "On Meteoroids and Penetration," J. Geophys Res., 68 (Sept 1, 1963)

**M. Dubin and C. W. McCraken, "Measurements of Distribution of Interplanetary Dust," NASA RP-103

***W. G. Fawcett et al, "Scientific Exploration with Mariner 4," Astro and Aero, Oct 1965, pp 23, 28.

****D. B. Beard, "Interplanetary Dust Distribution," Astrophys. J., 129 (March 1959)

*****P. B. Burbank et al. "A Meteoroid Environment for Near Earth Circular and Near Lunar Operations," NASA ND 2747.

Whipple (op. cit.) sees no basis for there being a great terrestrial concentration of the larger particles ($m > 10^{-5}$ gm). Consequently, for the smaller particles, the flux at 1 AU is assumed covered by van de Hulst's equation,

$$\log N = -0.65 \log M - 10.44$$

assumed to apply for $M < 10^{-6}$ gm. For the larger particles, $M > 10^{-5}$ gm, the near-earth flux is used.

For the interplanetary flux from 1 out to 2 AU, various investigators have proposed reduced flux levels. Whipple believes the variation in the meteoroid flux will be at least an inverse law of the solar distance. Beard, based on scattered light observations, concluded that for small dust particles the distribution varies inversely with the solar distance to the V power, where V is possibly less than, but probably equal to, 1.5 for small elongations. For large elongations, the observations of zodiacal light favor V = 1.5.

The Mariner 4 data, for the mass range 4×10^{-4} to 5×10^{-10} gm, disagrees with the above conclusions. The preliminary data shows, once past the earth's dust cloud, the flux increased by 4 to 6 times going from 1.0 to 1.2 AU to 1.4 to 1.47 AU (Figure 2-38). The meteoroid model used for the Voyager studies shows the flux levels out to 1.56 AU. At this distance, the flux is 2.5 times that at 1 AU.

Whipple estimates that the incidence of larger particles (> 0.1 gm) will remain equal to that observed at earth for decreasing solar distance at least to the orbit of Venus, and should increase as the asteroid belt is approached, up to a value possibly 10 times greater at the orbit of Mars.

Based on the difference between predictions and the Mariner 4 results, the flux is not assumed to decrease with increasing solar distance. The flux model then is taken as identical to that for 1 AU (away from earth).

Various authors predict an increased flux level in the asteroid region. Volkoff* concludes the cumulative particle concentration in this

*J.J. Volkoff, "Protection Requirements for the Resistance of Meteoroid Penetration Damage of Interplanetary Spacecraft Systems," JPL TR 32-410, July 1, 1964.

region is 20 or 30 times that of other interplanetary space. For his flux model, then, the particle concentration "shall be conservatively assumed to be 100 times that of interplanetary space concentration." However, his interplanetary space concentration is low, i.e., the flux at 1 AU was 10^{-3} times the near-earth flux and the flux is then taken as distributed inversely with the solar distance to the 1.5 power. This means that at 3 AU the flux is

$$100 \frac{(10^{-3})}{(3^{1.5})} = 1.92 \times 10^{-2}$$

times the near-earth flux. The 10^{-3} reduction applies only to dust particles and no evidence is available that the reduction applies to the mass range above 10^{-5} gm. The flux being distributed inversely with the distance from the sun to the 1.5 power is also incorrect for small particles, based on the Mariner results. Consequently, the factor of 100 is retained, but it is applied to the assumed interplanetary flux given in the previous three equations. The resulting flux is then given by

$$\text{for } M > 10^{-5} \text{ grams, } \log N = -1.34 \log -12.18$$

$$\text{for } M < 10^{-6} \text{ grams, } \log N = -0.65 \log M - 8.44$$

Marshall* extrapolates the data from asteroid observations to the mass range of interest to provide a flux for this region. His results contain substantial scatter and consequently "the flux used to calculate the shielding for the spacecraft was a compromise but was heavily in favor of the upper limit." This flux is also considered applicable to the asteroid region; however, for this study, this region is assumed to extend from 2 to 4 AU compared to the 1.5 to 5.2 AU used by Marshall. This change was based on data on observed asteroids. The Marshall flux is given by

$$\log N = -0.77 \log M - 10$$

*R. Marshall, "Shielding of Jupiter Flyby Spacecraft from Meteoroids," JPL Memo 2947-49, 1 March 1966

The uncertainty in the meteoroid flux is best described by discussing what would be a lower boundary on the meteoroid flux levels. Based partially on Mariner 4 data, Whipple's prediction, and all other estimates, a plausible estimate of the lower bound can be made. This lower bound on the meteoroid environment would be that given by reducing curves B and C (Figure 2-38) by 1 order of magnitude and Curve A by 1 order of magnitude at m = 10^{-5} gm and two orders at m = 0.1 gm. This boundary is applicable to all mission phases. In the asteroid region, this is a substantial change, ranging from 2.5 orders of magnitude in the mass range 10^{-10} gm to 10^{-6} gm to 7 orders at m = 0.1 gm.

The critical flux level is that between 2 and 4 AU, i.e., the asteroid belt region. In Section 4.10, to calculate the micrometeoroid protection required, the flux recommended by Marshall's curve F was used, since it is a conservative estimate and insures conservative engineering design. Marshall's flux can be defined by the number of particles per square meter per second = 10^{-10} $m^{-0.77}$ when m is particle mass in grams.

2.3.3.2 Meteoroid Velocity and Direction

Except for the particles associated with "meteoroid streams" encountered by the earth in its orbit around the sun, the velocity magnitudes and directions for meteoroids are not known accurately. It is believed that although interplanetary meteoroids have the greatest probability of following direct (posigrade) circular orbits around the sun, as do the planets, the deviation from such a model is great. Meteoroids with both retrograde orbits and highly elliptical orbits exist as shown by meteoroid stream trajectory data.

Investigators have concluded that the origin of interplanetary meteoroids is predominantly from two sources, the asteroids and the comets. The interstellar contribution to the interplanetary debris environment is negligible. Consequently, the velocity extremes of meteoroids can be stated. The maximum possible velocity of a meteoroid is the local escape velocity from the central attracting body. The relative velocity between the meteoroid and the spacecraft is of primary concern. The minimum relative velocity is zero, since it is possible that both the spacecraft and the meteoroid are on essentially the same trajectory. The maximum possible relative velocity occurs between a meteoroid at escape velocity

impacting from a direction opposite to the spacecraft velocity. Table 2-6 summarizes the spacecraft velocity, the circular orbit velocity, and escape velocity for various points of a typical, 650-day mission, trajectory. The maximum relative velocity between the meteoroid and the spacecraft is also listed.

Table 2-6. Spacecraft and Meteoroid Velocities

Distance from Sun	V, Spacecraft (km/sec)	V, Circular Orbit (km/sec)	V, Escape (km/sec)	Maximum Relative Velocity (km/sec)
1.0	39	30	42.1	81
2.0	25.5	21.2	30	55.5
3.0	18.3	17.3	24.4	42.7
4.0	14	15	21.1	35.1
5.1	9	13.3	18.7	21.0

The distribution of the directions of the relative meteoroid velocities is unknown. However, the maximum relative velocities are attained only when the meteoroid is travelling in a direction opposite to the spacecraft. Consequently the surfaces subjected to the maximum relative velocities are those facing the direction in which the spacecraft is travelling around the sun.

For the analysis of the effects of the meteoroid environment, the velocity direction will be random when the flux is described by all equations except that of Marshall. However, Marshall's was derived from extrapolation of asteroid observations. Therefore, it is assumed these particles will have asteroid type orbits, i.e., all direct (posigrade) and close to circular. Figure 2-39 shows the relative velocity and direction between the spacecraft and the meteoroids.

2.3.3.3 Meteoroid Density

Meteoroid density is one of the most difficult parameters to determine since it is not directly measurable. Satellite measurements with piezoelectric or microphone pickups are momentum sensitive and do not yield mass, much less density measurements. Consequently, much of the

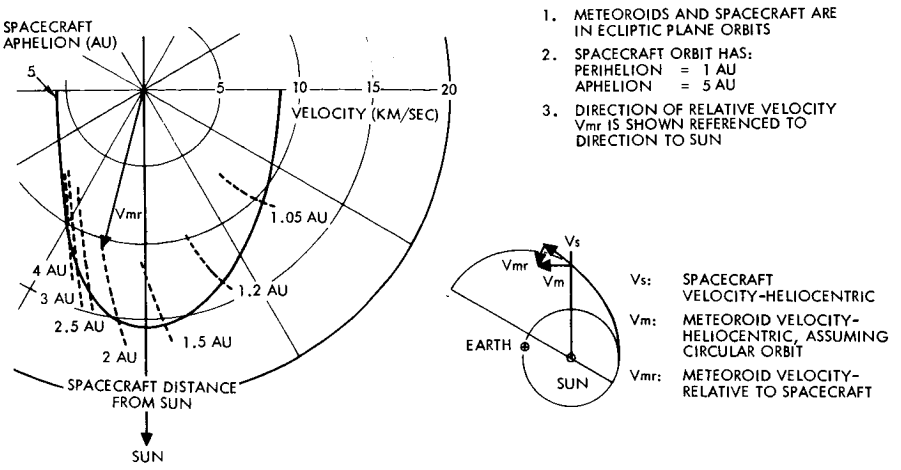

Figure 2-39. Velocity of Meteoroids in Circular Orbits Relative to a Spacecraft

literature is inconclusive. In general, most weight is given to values determined by Whipple, who adopted a value of 0.44 gm/cm^3. This value is based on a review of photographic meteor data. However, Whipple also comments that the results due to Cook, et al, available just before publication of his paper would lead to a mean meteoroid density of 0.25 gm/cm^3. For the environment upper boundary, the 0.44 gm/cm^3 value is to be used for all missions except the asteroid region. This is consistent with the meteoroid flux used for both the near-earth region and "deep space."

Volkoff, based on an assumed percentage distribution of asteroidal and cometary matter in the asteroid region, obtained a mean density for this region of 0.75 gm/cm^3.

For the particles entering the earth's atmosphere, it can be concluded that the variation of meteoroid density from the mean density is at least 1 order of magnitude and may possibly range from 0.01 to 8 gm/cm^3. Such a variation would be applicable to the interplanetary matter.

2.4 ENVIRONMENT NEAR JUPITER

2.4.1 Magnetic Field

If the Jovian surface magnetic field is as large as 50 gauss and is dipolar and the dipole is centered, then the field at 3 R_J will be about 0.5 gauss. This field intensity is sufficiently high to perturb (usually decrease) the gain of those detectors which employ secondary emission multiplication or those in which electron trajectories are specified. These

instruments include the television, proton particle detector, and the auroral photometers and spectrometer detector. Therefore, magnetic shielding must be employed over the sensitive regions of these instruments.

2.4.2 Trapped Radiation

The trapped particle belts at Jupiter may impose a serious radiation damage problem particularly for an orbiter mission. Present observations yield no data with respect to energetic proton fluxes, energies, or spatial distribution. However, since the range of 10 Mev protons is only ~ 0.17 gm/cm^2 Al or 6.3×10^{-2} cm thickness Al, we assume that protons will be effectively shielded by container walls and spacecraft structure.

In the case of electrons, the problem is more severe. The radio noise observations indicate a flux of $\sim$ 10 Mev electrons, a factor of 10^3 greater than those in the terrestrial belts. For the purpose of these estimates, a flux of 10^6 electrons/cm^2 sec at 10 Mev is assumed. The range of 10 Mev electrons in Al is $\sim$ 1.8 cm; therefore, shielding effects associated with the containers can be neglected. For high energy electrons > 2 Mev, the energy loss in aluminum is about constant, equal to $\sim$ 2 Mev/gm. At 10 Mev approximately 16 percent of the energy loss appears as X-rays; these X-rays will not be considered in evaluation of radiation loss.

The total energy dissipation is therefore 2.7 ergs/gm/sec or 2.7×10^{-2} rad/sec. This corresponds to $\sim 10^2$ rad/hr or approximately twice the radiation dose expected from the RTG power sources during the transit to Jupiter.

Damage to most normal components is expected to occur at integrated doses of $\sim 10^5$ rad. Thus a total of 10 hours in the high energy electron region appears to be a reasonably safe operating range. If the spacecraft velocity is 50 km/sec at 3 R_J, then the time required for transit of a distance corresponding to 1 R_J is 1400 seconds, with a dose of some 50 rad. Clearly, care must be taken to select sensitive components to minimize the effects of the irradiation.

For the currently estimated belts with a toroidal configuration of 3 R_J major radius and 1 R_J minor radius, the belts do not appear to represent a large problem. However, the extent of the high energy electron

may be greater than defined by the radio noise data. Probably electrons with energy < 2 Mev will be adequately shielded by walls since the range at 2 Mev is only 2 mm Al. If the maximum electron energies are spatially distributed as B/B_{3R_J}, then the maximum energy at 5 R_J will be ~ 2 Mev. The time spent in the high intensity region will therefore be significantly increased.

It is possible that specific shielding may be required for the television experiment since fluorescence induced by electron bombardment may decrease the effective photographic SNR. Since the detector is small, this shielding will not significantly increase the weight of the experiment. Photomultipliers will also be perturbed and may require some shielding. Increased glass thickness (2 cm) in the sensitive regions should be adequate for this purpose.

2.4.3 Radio Noise Environment

When the spacecraft is in the vicinity of Jupiter, the DSIF antenna may be pointed directly at Jupiter for a short period of time. Again, when the probe gets behind Jupiter, the planet may be in the spacecraft antenna beam. Since the sun and Jupiter radiate a considerable amount of noise around 2300 Mc, this noise will increase the antenna noise temperature and degrade the system performance. When the probe is near Jupiter and the spacecraft antenna is pointed at the planet, the noise spectral density will increase by a maximum 1.8 db above the nominal -164.4 dbm/Hz level, that is a reduction of 1.5 in bit rate.

The noise spectral density of the ground system with the 210-foot antenna will increase by 1.7 db/Hz due to Jupiter noise. The noise temperature of the 85-foot antenna, because of its wide beamwidth will not be affected by the radiation from Jupiter. The problem of the contribution of Jupiter and the sun to the system noise temperature is analyzed in Appendix G.

2.5 SCIENCE PAYLOAD

The functional requirements placed by the science payload on the spacecraft and the mission stem from two general sources: the specific allotments of weight, power, and volume needed by the experiments and

the general objectives of the experiments that call for maximizing telemetry bit rate and shaping the trajectory and spacecraft look angles to increase the value of the measurements. All of these factors are reviewed in this section.

2.5.1 Look Angles and Scan Requirements

For the interplanetary particle and field measurements, some instruments (plasma and solar cosmic ray detectors) require a scan in most of the ecliptic plane including the sun and, together with the galactic cosmic ray detector, require a scan out of the plane of the ecliptic.

With the mission requiring an earth-oriented antenna fixed to the body of the spacecraft, the spacecraft-sun angle changes rapidly during the early part of the mission, but as the spacecraft moves further away from the sun, this angle narrows, being within ±10 degrees in the vicinity of Jupiter. The problem then is most acute from launch to about 3 AU, and the pointing directions and scanning angles of some sun-pointing instruments must be positioned and sized accordingly.

A second problem arises from the fact that the spacecraft spin axis is in the plane of the ecliptic, unlike Pioneer 6, which spins perpendicular to the ecliptic plane. An instrument, therefore, with a given look angle, samples a cone which includes the plane of the ecliptic, unlike Pioneer 6 in which the angle between the look angle and the plane of the ecliptic is defined by construction. The instrument we have selected will scan through the desired regions of space; however, because the sun angle varies over the mission, and the angle to the plane of the ecliptic is not defined, the interpretation of the data on the ground could become more complex than is true with Pioneer 6.

To provide the desired coverage, we have employed two solar cosmic ray detectors, and the method for defining the sun angle is by means of sun sensors. The angle to the plane of the ecliptic can be defined reasonably well by the plasma probe data, since it is expected that in the undisturbed regions at least, the solar wind will be peaked in the ecliptic plane. If a disturbed region is encountered the plasma flux will become isotropic and the identification of the angle from these measurements is no longer possible. However, a knowledge of this angle does not appear to be important in the event that a disturbed region is encountered.

The look angles required during a planetary encounter are defined in Section 6 of Volume 1.

2.5.2 Data Handling and Storage

With two exceptions, all experiments pass data to the spacecraft data handling unit in digital form, for the necessary processing prior to storage or transmission to earth. The exceptions are the radio propagation experiment and the TV camera. These are both analog.

A 6- or 8-bit digital word is suitable to cover the dynamic ranges of the experiments and is also consistent with the encoding accuracy limitations of the onboard spacecraft converter. The experiment diagnostic information will, in the majority of cases, be analog, 0 to 5 volts in amplitude and will be subcommutated with the main frame readout.

2.5.3 Data Transmission

A data transmission capability averaging approximately 100 bits/sec is required for the scientific payload during the interplanetary flight, from launch to 100 planet radii from Jupiter. This modest requirement places no burden on the spacecraft design which has been sized to accommodate the larger bit-rate capability needed when the planetary optical experiments come into use.

During the planetary encounter storage is required for 1.2×10^8 bits, largely imposed by the TV experiment. A transmission rate of 700 bits/sec at Jupiter allows pictures to be taken and transmitted once an hour for seven days before encounter while still transmitting all other scientific data. Pictures taken every 5 minutes for 5 hours before passing the illuminated portion of Jupiter will be stored.

2.5.4 Command Requirements

A total of 31 commands are required by the science payload and are listed below. The necessary calibrate signal to all experiments will be provided from the spacecraft sequencer.

Cosmic Ray

Solar	Power On, Power Off, calibrate override
Galactic	Power On, Power Off, calibrate override

Solar Plasma	Power On, Power Off, mode change
Radio Propagation	Power On, Power Off
Micrometeoroid	Power On, Power Off
Magnetometer	Power On, Power Off, mode change 1, mode change 2
Trapped Radiation	
Electrons	Power On, Power Off
Protons	Power On, Power Off
Auroral	Power On, Power Off
TV	Power On, Power Off, acquisition mode, override mode
Infrared Radiometer	Power On, Power Off, mode change 1, mode change 2

2.5.5 Spacecraft Magnetic and Nuclear Radiation Environment

2.5.5.1 Magnetic Constraints

Local measurements of the interplanetary magnetic field impose stringent requirements upon the magnetic configuration of the spacecraft. At the large distances from the sun in these missions, the interplanetary field will very likely be less than 1 γ. The magnetic constraints therefore are more severe than for Pioneer 6.

In general, spacecraft magnetic fields arise from electrical currents and the magnetization of components and materials. For this particular series of spacecraft, an additional large contribution to the spacecraft magnetic field may arise from the use of magnetic components in the RTG power sources. The spacecraft magnetic fields are subject to change because of changes in operating conditions, temperature changes, vibration, etc. Thus, attempts to cancel these fields with applied fields is usually unsatisfactory. The approach adopted for Pioneer 6 was to limit the maximum magnetic field of the magnetized operating spacecraft to a value, at the magnetometer, comparable to the expected interplanetary field. In fact, limits of 0.1 γ were attained. Since this measured field represented the maximum possible value, lower values were expected in reality.

The degree of magnetic cleanliness required for the spacecraft represents a compromise between remote location of the magnetometer and the removal of the spacecraft fields. It appears for these deep-space missions that a maximum spacecraft field of 0.1 γ at the magnetometer will suffice.

2.5.5.2 Nuclear Radiation Environment

The use of an RTG power source results in the presence of a neutron and γ-ray source on the spacecraft. Thus a problem in spacecraft design is the prevention of radiation damage to components during a long-lived mission from this source and the avoidance of masking effects on radiation-sensitive experiments.

The sensitive scientific experiments are the single particle detectors including the plasma probe, G-M trapped radiation detectors, and the cosmic-ray detectors; the Zn-S trapped proton detectors are relatively insensitive to γ-ray or neutron irradiation and need not be considered further. In the case of the G-M tubes and plasma probe experiments, the background counting rate will correspond to cosmic-ray background (2 events/cm^2/sec) and a comparable counting rate due to the RTG power sources is entirely acceptable. Since both these experiments detect γ rays through essentially photoelectron emission from metallic surfaces, we have conservatively adopted an efficiency of 1 percent over the complete RTG γ-ray spectrum; the efficiency for neutron detection should at best be comparable. With this efficiency an incident γ-ray and neutron flux of about 200/cm^2/sec will equal the cosmic ray background rate. A flux from the RTG an order of magnitude larger would still not compromise these experiments.

The cosmic-ray experiments are more seriously affected since their spurious counting rates must be small compared to the cosmic ray rates. However, both types of instruments employ coincidence techniques; the spurious counting rates due to the RTG's should not produce real but rather accidental coincidences. An improvement in the coincidence time from 10^{-5} to 10^{-6} second will decrease the spurious effects markedly. Secondly, the Cerenkov counter is insensitive to γ rays and neutrons; the solid state dE/dx counters are inefficient. Lastly, the CsI crystals detect

rather large energy losses and can be biased so that the detection threshold is > 1 Mev.

It is difficult to estimate the response of these instruments quantitatively. However, with some modification these instruments should operate satisfactorily with an incident neutron and γ-ray flux of some 200 to $1000/cm^2/sec$.

2.5.6 Weight

The total weight of the science payload is estimated at 57.5 pounds. The individual experiment weights are as follows:

Experiment	Sensor Weight (lb)	Electronics Weight (lb)
Cosmic ray		
Solar	3.0	3.0
Galactic	*	6.0
Solar plasma	*	5.5
Radio propagation	1.5	5.0
Micrometeoroid	*	4.0
Magnetometer	1.5	4.0
Trapped Radiation		
Electrons	*	3.0
Protons	*	3.0
Auroral	2.0	3.0
TV	*	10.0
Infrared radiometer	*	3.0
Radio occultation	-	-
Total	8.0	49.5

*Experiment sensor combined with the experiment electronics package.

2.5.7 Power Requirements

The maximum electrical power requirements of the experiment payload are estimated as follows (in watts):

Interplanetary		Planetary	
Cosmic ray		Micrometeoroid	1.0
Solar	2.0	Magnetometer	4.0
Galactic	2.0	Trapped radiation	
Solar plasma	1.5	Electron	1.0
Radio propagation	1.5	Proton	
Micrometeoroid	1.0	Auroral	2.0
Magnetometer	4.0	TV	10.0
		Infrared radiometer	3.0
Total	12.0	Total	22.0

These requirements include conversion losses but do not include the power required for telemetry data storage or processing.

2.5.8 Temperature Control

The temperature extremes within which the science payload sensors and electronics are known to operate satisfactorily are as follows, in degrees Farenheit:

Experiment	Sensor	Electronics
Cosmic ray		
Solar	-4 to 104	-4 to 167
Galactic	-30 to 100	-4 to 167
Solar plasma	-	5 to 122
Radio propagation	to 200	5 to 120
Micrometeoroid	-	-40 to 140
Magnetometer	to 200	-40 to 140
Trapped radiation	-	-40 to 140
Auroral	-30 to 100	-30 to 140
Television	-270 to 212	-30 to 140
IR radiometer	-	-30 to 140

These are generally conservative values. It is possible that detailed study and test will extend the lower limits given, keeping in mind, however, that the lowest temperature an appendage can be expected to survive is about -250°F.

Changes in the configuration of the experiment, i.e., the combination of sensor and electronics, can be made to minimize heat leaks and optimize the effects of thermal coupling.

However, remote placing of sensors, while satisfying the thermal requirements, often imposes other limitations in the form of extra cabling to the sensor for signal conditioning, prior to being handled by the now remote data handling section of the experiment. Weight is usually increased when an experiment is separated.

2.6 MISSION DURATION

From Section 2.2 it is seen that the extremes for flight times to Jupiter corresponding to a 30-day launch period in 1972 are 544 to 910 days. The primary objectives of the mission are achieved during the period starting at the launch date and ending approximately 15 days after the arrival date. (At this time the spacecraft will have departed from the near-planet environment, construed to be the estimated maximum size of the Jovian magnetosphere.) Secondary objectives may continue almost indefinitely after departure from Jupiter. The attitude control gas supply has been sized on the basis of a one-year life after encounter with the planet Jupiter, assuming worst case gas usage prior to encounter; but if nominal gas usage is experienced, the supply will last for about 10 years after encounter.

2.7 RELIABILITY

To embark upon the design of a spacecraft system to perform a specific mission, such as a 1972 Jupiter flyby mission, it is necessary to have as a ground rule for that design a target probability of mission success. However, it is not felt appropriate to place such a requirement on this conceptual design and feasibility study, because such a requirement must take into account certain factors that are outside the scope of this study.

First, it is not meaningful to propose a required probability of success for a single spacecraft on a single mission without realistically accounting for the actual number of spacecraft intended to be launched on the same or similar missions, or without establishing the role of the single mission in an overall program which may consist of a number of missions, to the same planet and to other target planets.

Second, when a desired or target probability of mission success is stated for a particular mission, it is necessary to allocate target probabilities of success to each of the major systems involved in the mission: the launch vehicle system, launch and spacecraft operations, and the spacecraft system. In addition, because the science payload bears a different relationship to the accomplishment of the mission objectives from that of the spacecraft, and because it is commonly developed separately, it is desirable to state the target probability of success of the science payload separately from the rest of the spacecraft.

Section 9 discusses the reliability of the spacecraft but in view of the general goals of maximizing the likelihood of individual mission success rather than the achievement of a specific reliability goal.

2.8 SCHEDULE REQUIREMENTS

The critical dates for earth-to-Jupiter flyby missions during the 1972 launch opportunity are abstracted from the material of Section 2.2. Although we have proposed that the mission be conducted on the basis of a 20-day launch period, the schedule requirements stated here are derived from a 30-day launch period, in order to encompass dates which would provide somewhat greater flexibility. Launch dates lie in the range February 25, 1972 to March 26, 1972. The arrival dates at Jupiter lie in the range September 1, 1973, to September 22, 1974.

2.9 GROWTH CAPABILITY

One of the objectives of this study is that the spacecraft system designs proposed for flyby missions have a growth capability which makes them applicable to more advanced missions with a maximum applicability of the basic design concepts. The extended missions which are logically the goal of the 1972 Jupiter flyby designs include flyby missions to Jupiter in later years, flyby missions to planets beyond Jupiter, orbiter missions

to Jupiter and the outer planets, and the delivery of entry capsules to Jupiter and the outer planets. In addition (and possibly correlated with the mission extensions just identified), it is desirable to be able to accommodate science payloads which vary in the nature of the scientific instruments as well as in the total weight devoted to scientific instruments.

The organization of this report devotes Volume 2 to a specific mission, the accommodation of a 50-pound science payload on a 1972 Jupiter flyby mission with a spin-stabilized spacecraft. Extended missions are examined in Volume 3. However, it is not the intention that the design presented in this volume be limited in its growth capability. Therefore, even though other sections of the report examine the extended missions, it is a requirement of the spacecraft described in this section that the design concepts utilized be applicable to the extended missions.

3. EFFECTS OF SPIN STABILIZATION

There are three basic constraints imposed in this study on the spacecraft: (1) the use of RTG power, (2) the use of a large body-fixed antenna, and (3) continuous earth pointing. This section describes the effects of spin stabilization upon them.

The use of spin stabilization imposes the following important requirements. The ratio of moments of inertia must be suitable to maintain spin stabilization, which means basically that the mass must be arranged in a disk-like configuration. Further, the principal inertia axis and hence the spin axis must be carefully controlled to match the mechanical axes and, even more important, the high-gain antenna electrical axis. The second is that there are limits to the differences in the principal transverse moments of inertia which arise from the requirement for torquing the spacecraft open-loop to a desired direction. Large differences will lead to wobble during an open-loop maneuver and result in increased maneuver angle errors. The third requirement, related to the second, is that flexible appendages cannot safely be used (without detailed analysis and test) before an open-loop maneuver is completed since the whipping motion of the flexible appendage during precession will add to the error in the open-loop pointing maneuver. The fourth requirement, affecting torquing requirements and the frequency of attitude updating by the ground station, is the appropriate spin rate, as discussed in Section 4.5. Since the spacecraft is constantly earth pointing, the gas torquing requirement is established by the angular motion of the earth, precession due to disturbing torques, and the spin rate, and these in turn determine the intervals between which ground station control of the attitude of the spacecraft will be needed. The principal external torque on the system is solar pressure, which for the configuration studied is kept below that required for earth tracking, except for a short period near 50 days from launch, by using a spin rate of 5 rpm.

3.1 RTG's

The RTG's weigh about 22 pounds. Each must be deployed to achieve the proper ratio of moments of inertia since the launch vehicle

fairing envelope does not allow them to be body-fixed and in a disk-like configuration. Although the deployment introduces a complexity, the deployment occurs but once early in the mission with high reliability.

3.2 BODY-FIXED ANTENNA

The second basic ground rule of the study is the use of a large body-mounted antenna. The design study has a 16-foot parabola with a beamwidth of 1.9 degrees to assure maximum bit rate. It is desired to point the antenna so that antenna gain is never more than 1 db off. This requires that the angle between the boresight axis and the earth line not exceed 0.5 degree. To this end three critical spacecraft requirements must be satisfied. First, the mechanical alignment between the spacecraft spin axis and the axis of symmetry of the antenna must be carefully controlled, by careful design, antenna pattern measurements, and careful evaluation of perturbations such as those caused by thermal variations. The second requirement is to measure and control the boresight error, that is the error between the electrical axis and the mechanical axis on the antenna. Lastly, the means of pointing the spin axis at the earth must be capable of the required accuracy.

3.3 EARTH POINTING

Spin stabilization coupled with the constraint that the large antenna must always be pointed toward the earth imposes the following requirements:

- An earth detection reference system must be used. A conical scan tracking system using the DSIF signal appears to be the logical choice since spin provides the scan and the stability needed between attitude updatings. Acquisition requires a fairly broad antenna while accurate earth pointing at long ranges demands the use of a narrower beam antenna.

- A torquing system must be used to drive the system toward the earth.

- For stability and economy in the torquing system, a dead zone in the reference system must be provided.

- For economy of DSIF operations, the torquing requirements to keep the spacecraft pointing to the earth must dominate over disturbance torques, which in turn establish the spin rate.

3.4 OPEN-LOOP MANEUVERS

With respect to midcourse corrections for the Jupiter flyby mission, several possibilities were considered:

1) An injection attitude correction followed by an earth-line correction using axial engines

2) One or two earth-line corrections (two engines)

3) Pulsed lateral corrections, fired normal to the spin axis at the appropriate time in the spin cycle

4) Combination of (3) with an additional axial correction

5) Open-loop precession to a desired attitude for an axial midcourse correction. Open-loop precession techniques, in any of four directions related to the sun, have been developed for Pioneer

   a) One engine

   b) An engine at each end of the spacecraft

Options 1) and 2) use an inordinate amount of fuel. Options 3) and 4) involve a significant propulsion system complication, are of doubtful accuracy, and involve a slight increase in fuel over Option 5).

Option 5) in general represents minimum weight and complexity since an open loop attitude maneuver is already required for initial acquisition. The crucial question for selection of this option is attitude accuracy after reorientation. This favors Option 5)b which demands a smaller reorientation, with consequently greater accuracy and also satisfies the desire to reduce the time during which the aft of the spacecraft, with its thermal radiating plate, is exposed to the sun. Section 4.3 evaluates the accuracy for choice of this option.

4. SPACECRAFT SYSTEM CONCEPT

Generating a system concept which satisfies the requirements and constraints developed in Section 2, and meeting the spin stabilization requirements summarized in Section 3 is relatively straightforward.

The first step was to determine the overall spacecraft weight necessary to support a 50-pound payload. Although a 50-pound payload was a ground rule, this weight is compatible with present planetary and interplanetary spacecraft: both Mariner and Pioneer 6 carry about 40 pounds of experiments. The initial weight estimate was between 400 and 500 pounds.

For comparison, Pioneer 6 weighs 140 pounds and carries 35 pounds of experiments. Like the Advanced Planetary Probe it is spin-stabilized; however, it uses solar cells for power supply and has a fan beam antenna rather than a parabola. The solar cells on Pioneer 6 provide about 4.5 watts per pound. Power requirements of Pioneer 6 are about 60 watts, for the Advanced Planetary Probe about 90 watts at about 1.2 watts/pound. Thus, the Advanced Planetary Probe power generation equipment should weigh about 4.5 times the present Pioneer system, i.e., about 77 pounds. The fan beam antenna on Pioneer weighs less than 3 pounds, while the parabola on the Advanced Planetary Probe weighs about 60 pounds. The Advanced Planetary Probe requires three items not included in Pioneer 6: 35 pounds for a propulsion system, 31 pounds for micrometeoroid protection, and 16 pounds for data storage. Adding the total additional weight of 302 pounds (including 15 pounds for experiments) to the Pioneer 6 weight of 138 pounds gives a spacecraft weight of 437 pounds. Allowing for the facts that the spacecraft structure is larger and that a number of other minor changes are made, a total spacecraft weight of approximately 500 pounds appears a reasonable estimate.

In addition, we can compare this system with Mariner 4, which weighed 570 pounds and carried about 40 pounds of experiments. With respect to power generation equipment the systems are comparable, since the array on Mariner weighed 79 pounds. However, Mariner 4 carried 66 pounds of batteries, a 7-pound planetary scan platform, and

a 12-pound data automation system; guidance and control weighed 63 pounds as compared with an Advanced Planetary Probe control system weight of 29 pounds. When this difference in weight of 119 pounds is subtracted from 570 pounds, the weight of a comparable spacecraft would be 451 pounds, to which must be added about 50 pounds for the 16-foot parabola, giving the resultant weight of about 500 pounds for the spin-stabilized Advanced Planetary Probe. Thus, the weight of the Advanced Planetary Probe appears reasonable from both of these points of view. Section 6 gives comparative weight statements for Mariner 4, Pioneer 6, and the Advanced Planetary Probe.

The ground rules of the study tend to define the spacecraft configuration. The large body-mounted antenna produces a spacecraft configuration which looks like a large parabola mounted to a small central box. The requirement for spin stabilization requires that the spacecraft mass be distributed as a disk. The use of RTG power with the requirement for spin stabilization and minimization of experiment interference requires that the RTG's be deployed out from the spacecraft approximately in the plane of the mass disk. The selection of the Atlas/Centaur/TE-364 booster with limited extension of the Surveyor fairing requires that the RTG's and the antenna must be deployed after the fairing has been jettisoned. The particular science payload selected means that experiment windows observing specific areas of the sky must be provided and that experiment isolation (e.g., for the magnetometer) must also be provided.

A critical element in the system concept is the use of Pu 238 as the fuel for the RTG's. Presently this fuel is scarce and expensive. Estimates of future availability and cost are doubtful. For these reasons we have made every effor to minimize the total amount of fuel required. Thus, for example, rather than optimize the weight allocated to the antenna and to the transmitter and power subsystems, we have decided to put as much weight in the antenna as is feasible. The antenna, therefore, has been made a s large as the booster configuration allows. For this configuration, it is 16 feet in diameter. In addition, to demonstrate feasibility rather than to optimize the design, we have selected a deployable antenna configuration which has already been designed and tested.

Similarly, we have selected TWT's for the power amplifier since they have demonstrated exceptionally good lifetime characteristics in Mariner 4, Pioneer 6, Syncom, Telstar, and other space applications, rather than selecting more reliable solid-state transmitters which have not yet been developed.

To assure reliability and simplicity we have used existing propulsion techniques and hardware based on Mariner 4 and Intelsat III monopropellant technology. We have selected two engines at opposite ends of the spacecraft with spin stabilization for system simplicity and reliability. In additon, this arrangement permits a final midcourse maneuver late in the flight without changing the body attitude from that providing the communication capability.

The use of the large body-mounted antenna pointing toward earth means that the spin axis must point toward the earth. For the acquisition step we have used the sun sensor and cold gas technology already developed for Pioneer 6 and Syncom. For the fine earth-pointing mode we have exploited the simplest, most reliable techniques available, conical scan of the signal transmitter from earth, while simultaneously providing backup modes at somewhat reduced data rates.

A high data rate system was made an objective, first to satisfy all scientific requirements and, second, to simplify ground station operations and to minimize ground station on-time. The tradeoffs between science objectives, data rate requirements, RTG fuel cost and schedule problems, a deployable antenna structure, reliability, etc., led to the system described in Section 7.

The major design objective of the thermal control subsystem was reliability, and therefore the design objective was to use the passive, insulated box concept. To permit isolation of the box from the external radiant surfaces when the spacecraft is far from the sun, thermal switches were selected to radiate heat near the earth's orbit. This selection provides a greater margin for heat leaks than could be provided by the use of louvers.

Spin stabilization coupled with booster fairing constraints made it desirable to deploy the RTG's, which in turn reduced the effects of the

RTG's on experiments. Wherever possible, science sensors were separated from the electronics to minimize heater requirements and heat leaks from the spacecraft compartment. The spin rate selected for the spacecraft was developed as a result of a tradeoff between the science sensors and spin stabilization requirements.

Finally, one of the key system considerations was micrometeoroid protection since the spacecraft must pass through the asteroid belt. Engineering estimates of a particle mass flux were made and protection provided to give a 0.9 probability of avoiding a catastrophic impact.

4.1 ANTENNA CONFIGURATION

A major feature of the spacecraft design is the use of a large, 16-foot diameter, deployable antenna. Since the feasibility of the spacecraft concept hinges on the feasibility of such an antenna, a conservative approach was used. The antenna concept selected was chosen because it had been designed, fabricated, and subjected to the critical tests of deployment and vibration in a larger size (32.2-foot diameter) as a solar collector for the Sunflower project for NASA, Figures 4-1 and 4-2. The resulting antenna system, while it is probably not the lightest concept, has the least development risk, and flight hardware can be obtained in the shortest time.

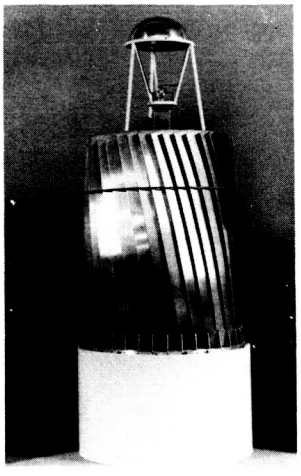

Figure 4-1. Solar Collector, Stowed

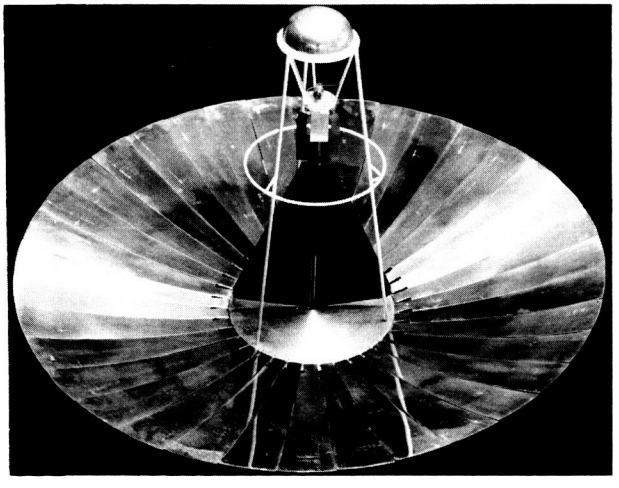

Figure 4-2. Solar Collector, Deployed

Reliable petal deployment is the most critical area. The Sunflower collector was deployment tested with a restraining harness to simulate the zero-g condition. With the 16-foot design, deployment should be less of a problem, since the petals are only a third the weight of a Sunflower petal. For deployment, the hinge moment is a critical parameter. For the 16-foot structure, hinge length on each petal is reduced only slightly but the moment arm to the petal c.g. and the petal weights are substantially less. For the same acceleration at the petal c.g. at the end of the deployment motion, the hinge moment per unit.

In this section, the important differences between the antenna required and the Sunflower collector are described and the design, fabrication, testing, and status of the Sunflower collector are summarized. Table 4-1 compares the major features of the Sunflower collector and the required antenna.

Since the antenna is deployed on a spin-stabilized spacecraft, the problem is generally that of deployment of appendages with a spinning spacecraft. Pioneer 6 deployes four booms, 5 feet long with 1-pound tip masses. The booms are 0.75-inch diameter tubes. The deployment starts at 120 rpm and terminates at approximately 60 rpm.

Based on the substantial analysis and testing with Pioneer, backed up by a successful flight, the general conclusion regarding such deployment is that if dampers are used the motion control available is large and a symmetrical deployment can be accomplished. The damper force time history can be guided by analysis and design. However, the requirement for a damper system, with the antenna design selected, has not been demonstrated. The antenna deployment will be initiated at a slow spin rate, just above the final spacecraft spin rate of 5 rpm. The two experiment booms are the last items deployed leading to dish deployment initiation at 7.5 rpm. The upper bound on the energy to be absorbed during deployment of the dish for this initiation rate in a zero-g environment is 5.4 ft-lb. In computing this energy no reduction was made to account for hinge friction, damping, wobble, or friction between the individual petals during deployment. An estimate was made of the

Table 4-1. Comparison of Sunflower Collector and Antenna

	Sunflower Collector	APP Antenna
Outside diameter, ft	32.2	16.0
Inner diameter of petals, ft	9.2	7.67
Number of petals	30.0	24.0
Approximate petal length, ft	12.0	5.0
Petal width at hinge line, in	11.6	10.4
Area of one petal, in^2	3740.0	1096.0
Distance from hinge line to petal c.g., in	85.0	35.0
Radial distance to petal c.g. from centerline of spacecraft	138.0	75.0
Maximum longitudinal acceleration (stowed condition), g	10.0	5.85
Maximum lateral acceleration (stowed condition), g	3.0	1.5
Maximum acceleration in any direction with reflector deployed, g	1.0	small compared to 1.0
Spin rate, rpm	1.68 about any axis	6.0 about spacecraft spin axis

energy that can be absorbed by the petals. Based on a maximum stress in the facings of 10,000 psi the total energy that can be absorbed is 8 ft-lb. Based on these values, dampers at the hinge points to control the deployment would not be required.

The approach would be to design for 1 g testing. The observed 1-g deployment of the antenna can verify the deployment analysis in general and will aid the design of the dampers. These will be designed with the flexibility to control with a 1-g or zero-g deployment without resetting. Designing for 1 g testing will not change the antenna weight except that allowance for dampers at the hinges would be included.

Spacecraft spin will not adversely affect the deployed antenna, since the Sunflower specification called for a rotational velocity capability of 10 deg/sec about any axis (1.67 rpm). For the same centrifugal acceleration force at the petal c.g., the antenna spin rate required is 3 rpm and for the same force per unit length of hinge line the spin rate would be 9.2 rpm. At the time of antenna deployment, the spin rate will be down to 6 rpm. Consequently, the spacecraft spin rate should not affect the design.

Vibration testing of the spacecraft with the antenna stowed is a critical design requirement. The Sunflower collector was successfully vibration tested with sinusoidal and random vibrations. The reduced size of this antenna compared to the Sunflower, particularly the reduction in petal length and weight, but with little reduction in the length at the hinge line and no reduction in the honeycomb construction, indicates that the antenna has a substantial increase in stiffness and strength to sustain the vibration environment.

4.1.1 Sunflower Design

The Sunflower collector stowage arrangement is based on a "flower-petal" or petaline concept for folding segments of the paraboloid. This concept was adopted because of the inherent kinematic simplicity and because it is well suited to the Centaur nose cone envelope. The number of sectors was minimized to 30 by scalloping the tips to clear the coned portion of the envelope. Each sector is hinged at a center structural support ring. In the stowed position, Figure 4-1, the sectors are folded against an upper structural support ring, and bands around the outside restrain the bundle during launch. A torsion spring at each sector hinge is fully torqued in the stowed position. At the time of deployment, the restraining bands are released and the springs actuate the

deployment. When the open position is reached, the spring is in the free position and locking devices along the sectors connect adjacent sectors into a structure of revolution.

4.1.1.1 Sectors

Each sector is contructed of aluminum honeycomb sandwich material which is adhesive bonded. Edge close-outs for the sectors consist of 3-mil aluminum Z-sections lap-joint bonded to the skins. Components such as hinges and locks are attached to the sector by threaded fasteners. For these attachments, metal inserts are bonded into the honeycomb core during fabrication of the sector. Potting-in of adjacent cell areas around the insert provides a reliable shear tie to the skins.

4.1.1.2 Hinge-Torsion Spring

The hinge and torsion bar hardware is shown in Figures 4-3 and 4-4. The torsion spring is a rectangular spring-metal torsion bar which runs through the hollow hinge pin. Connections on each end fix the bar to the sector and mounting ring. A rectangular cross section torsion bar was used to obtain the proper relationship between required angle of twist, torque, and stress.

The hinge itself is made of cast aluminum alloy and has integral torsion bar end connections and a mounting pad for attachment to a damping device linkage. As shown in Figure 4-4, the hinge assembly is edge-mounted to the honeycomb sector by threaded fasteners. The hinge attaches to the center structural ring also using threaded fasteners.

The torsion bar-hinge arrangement is designed so that the torsion bar can be torqued or released with a hand tool when the sector is in the stowed position, thus eliminating the necessity of deploying the collector to load the actuating springs.

4.1.1.3 Lock

Two basic approaches to a locking device were investigated during the design: 1) a combination shock absorber-lock, and 2) detent lock-continuous viscous damping. If the deployment design is such that the actuating spring energy is absorbed only by the sliding friction between

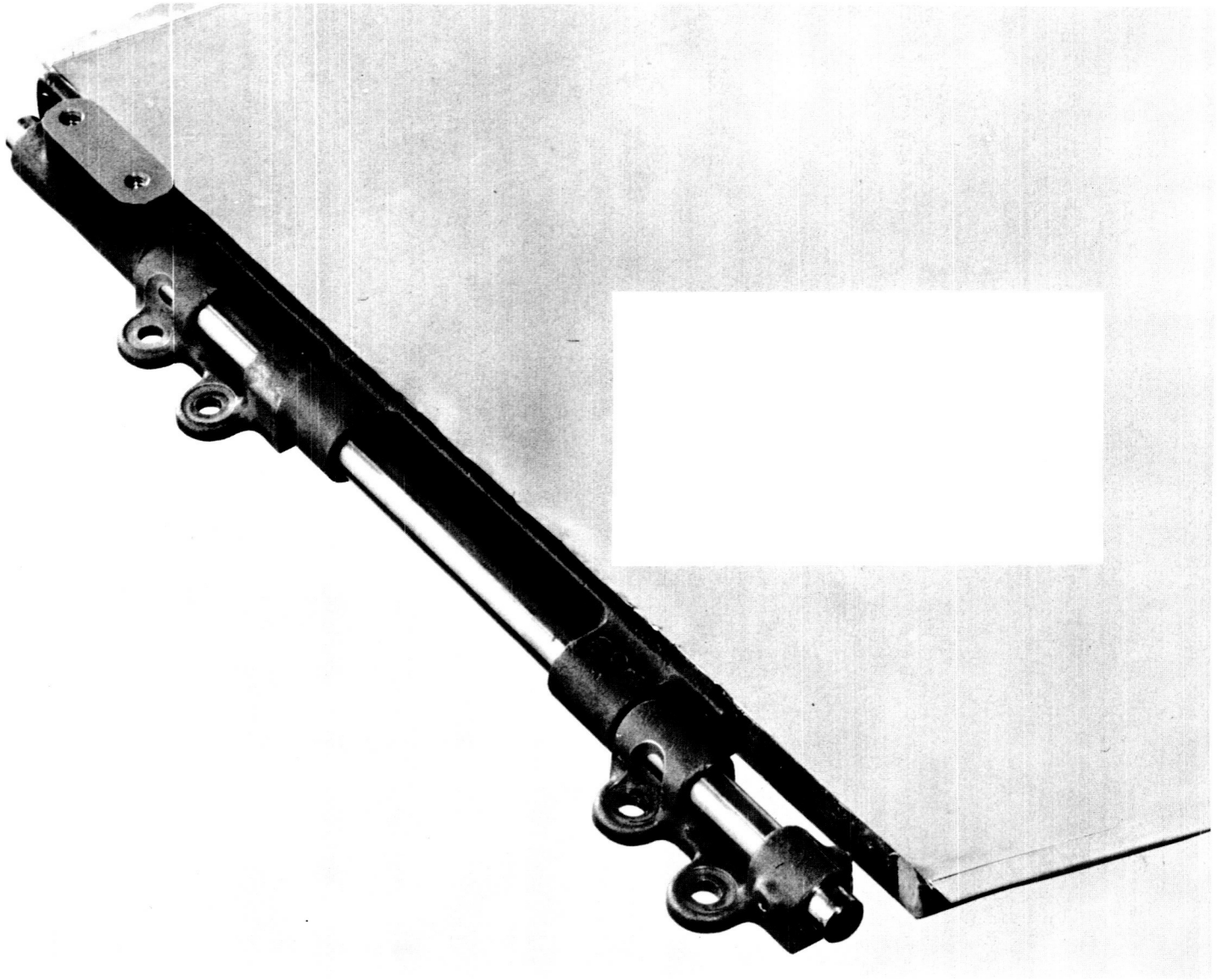

Figure 4-3. Hinge and Torsion Bar, Assembled

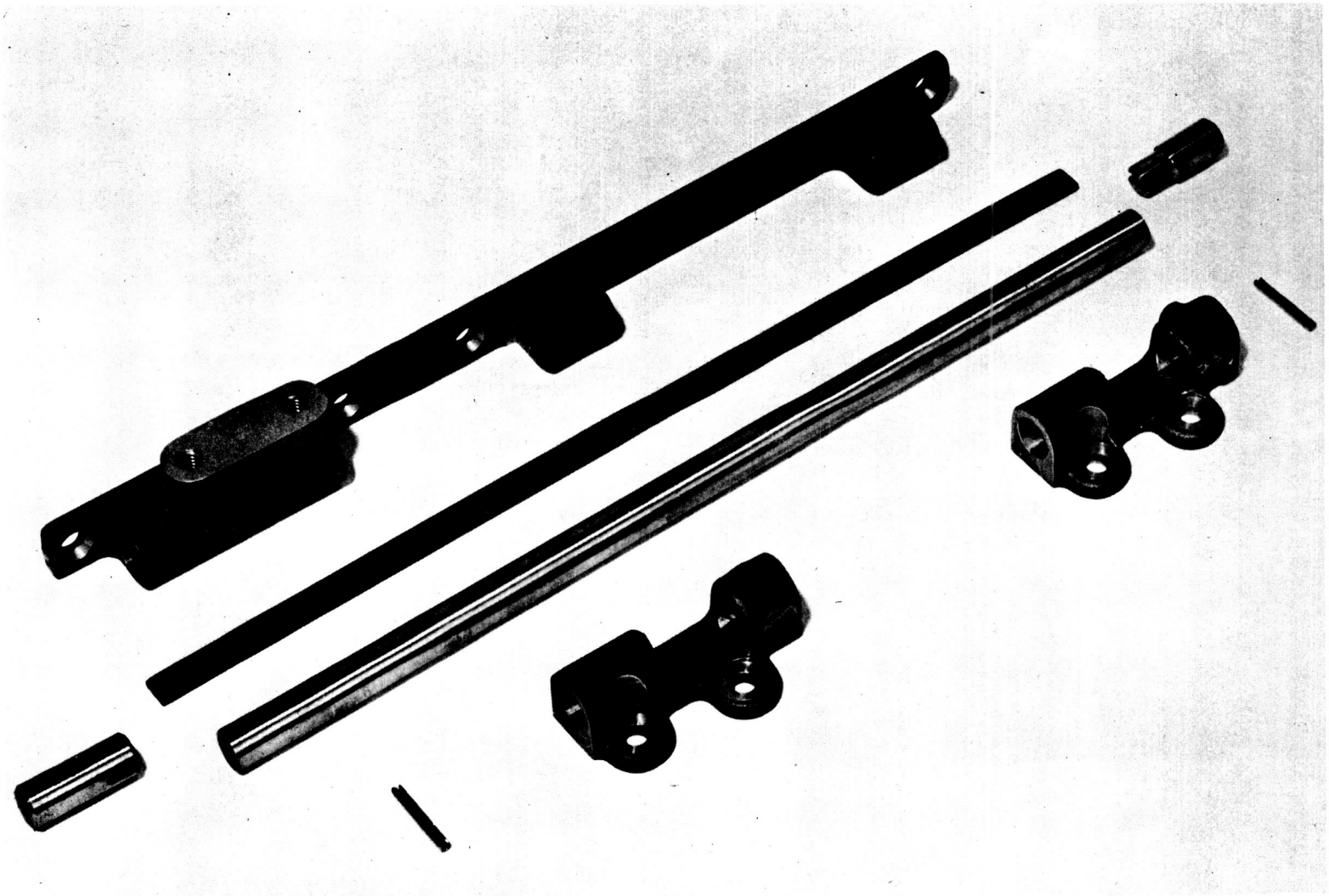

Figure 4-4. Hinge and Torsion Bar, Disassembled

sectors, then the kinetic energy remaining in the system must be absorbed by the lock. On the other hand, if a viscous device is used in conjunction with the spring actuator, torque is absorbed continuously by the damper, thus requiring only a detenting lock in the open positions.

The second type of lock design involves the separation of the dashpot portion of the device from the detent portion. The detents remain at the tips of the petals, but the dashpots are at the pivot points of the petals. In this way, two advantages are realized.

- Fewer dashpots are used, each acting on a set of three petals.
- Petal kinetic energy is controlled over the entire deployment sequence.

The second deployment system was selected for the preprotype design. Typical lock hardware is shown in Figure 4-5. Figure 4-6 shows the detail of the detent lock design. A damper, such as the one shown in Figure 4-7, was sized for the critical estimates of intersector friction.

4.1.1.4 Vibration Isolation

In the stowed position, the sectors are supported at the hinges by the lower mounting ring, the upper stacking ring, and by intermediate bands. Based on the results of preliminary low level vibration testing of the collector and simulated system structural response, military standard isolators were modified for mounting the upper stacking ring. The ring was also structurally damped by viscoelastic damping tape. In the deployed position, the collector is supported only at the mounting ring. Low level testing of the ring alone was again used as an isolation design basis. Large transmissibilities were observed. Since the deployed orbital transfer vibration specifications are quite severe (the same as those generated by the launch engines), isolators were selected for vibration isolation with the mounting ring supporting the 1 g weight of the collector. This will be the weight experienced by the collector due to acceleration during orbital transfer.

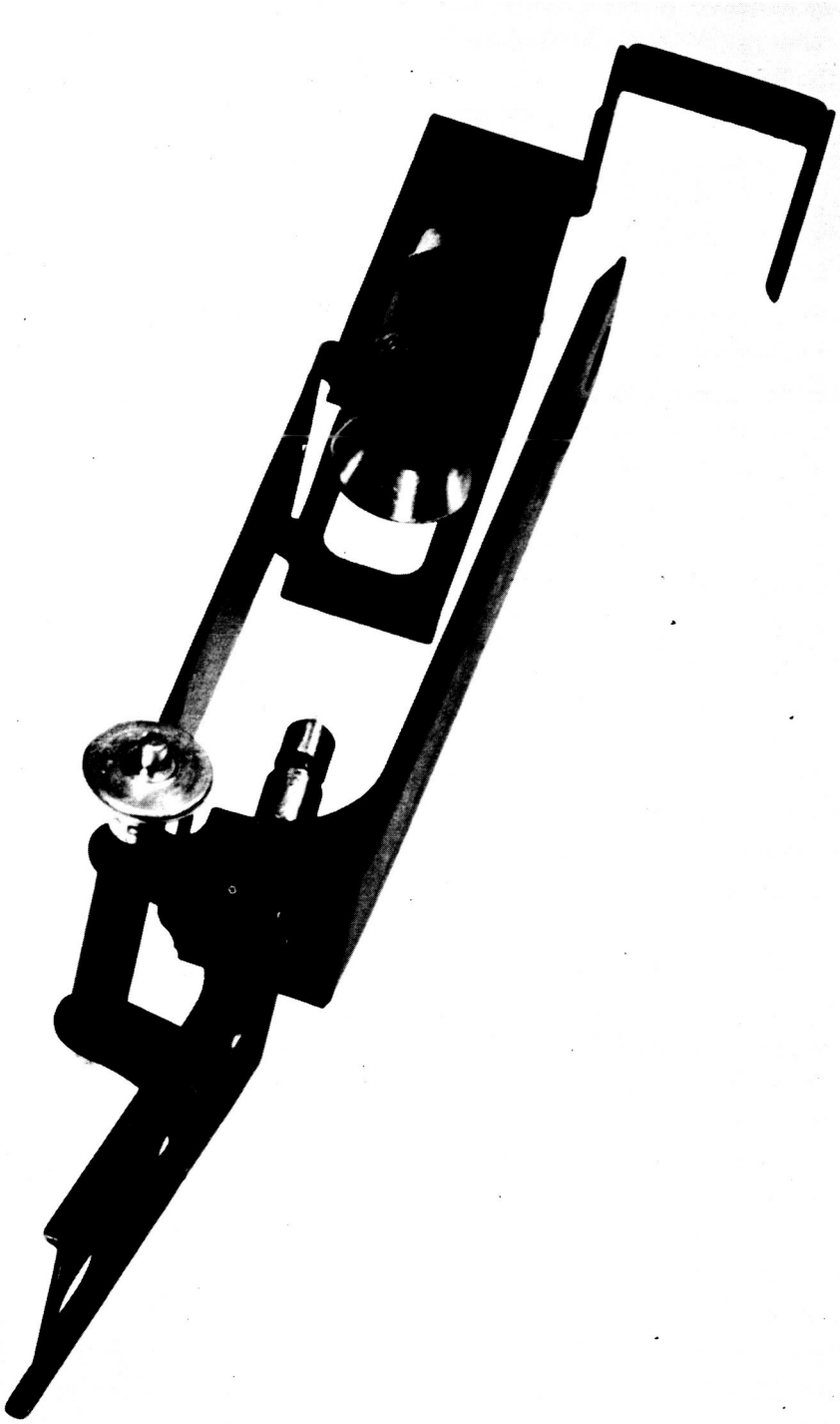

Figure 4-5. Lock Hardware

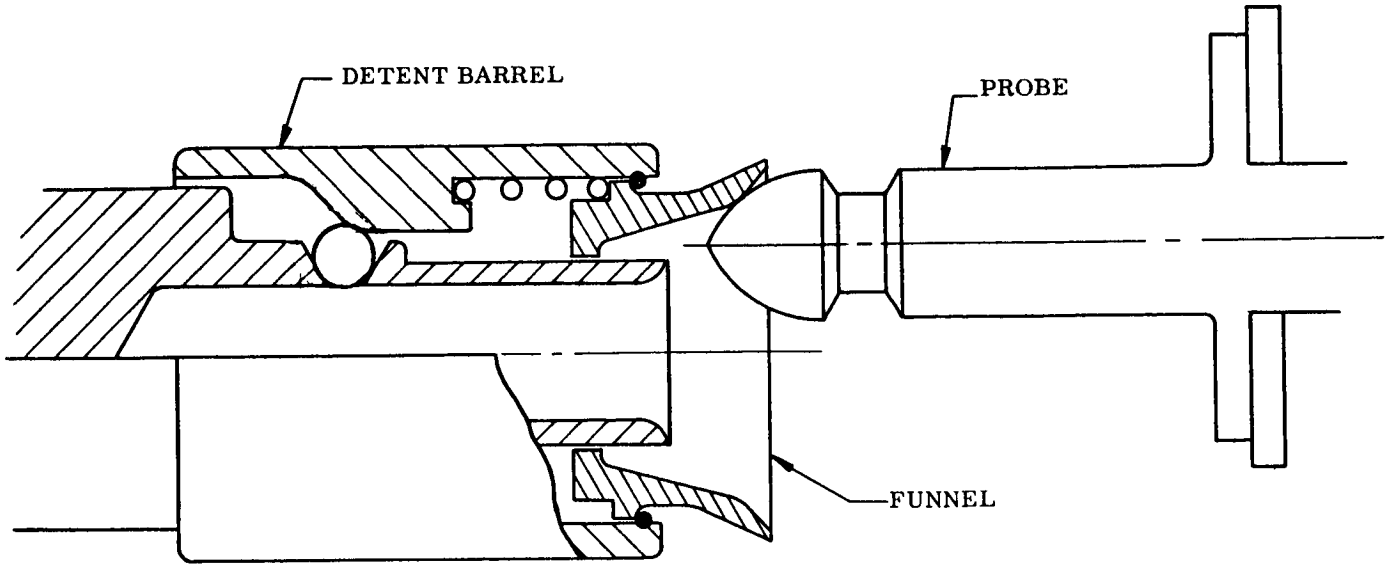

(a) INITIAL ENGAGEMENT

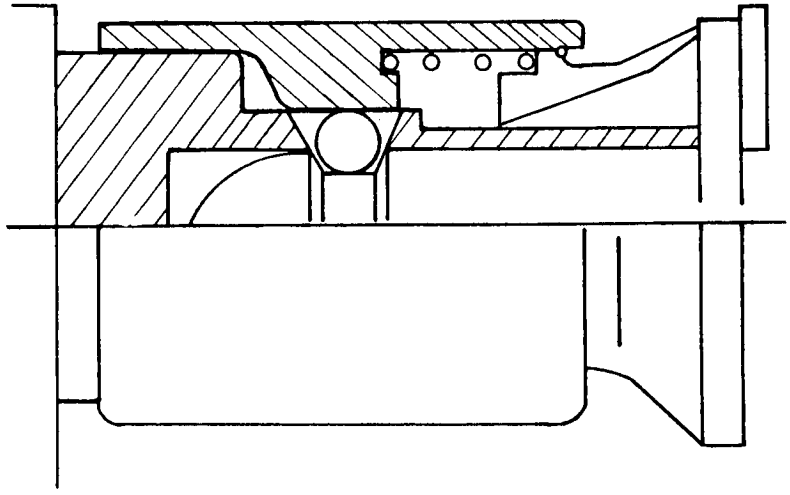

(b) LOCKED POSITION

Figure 4-6. Detent Lock Design

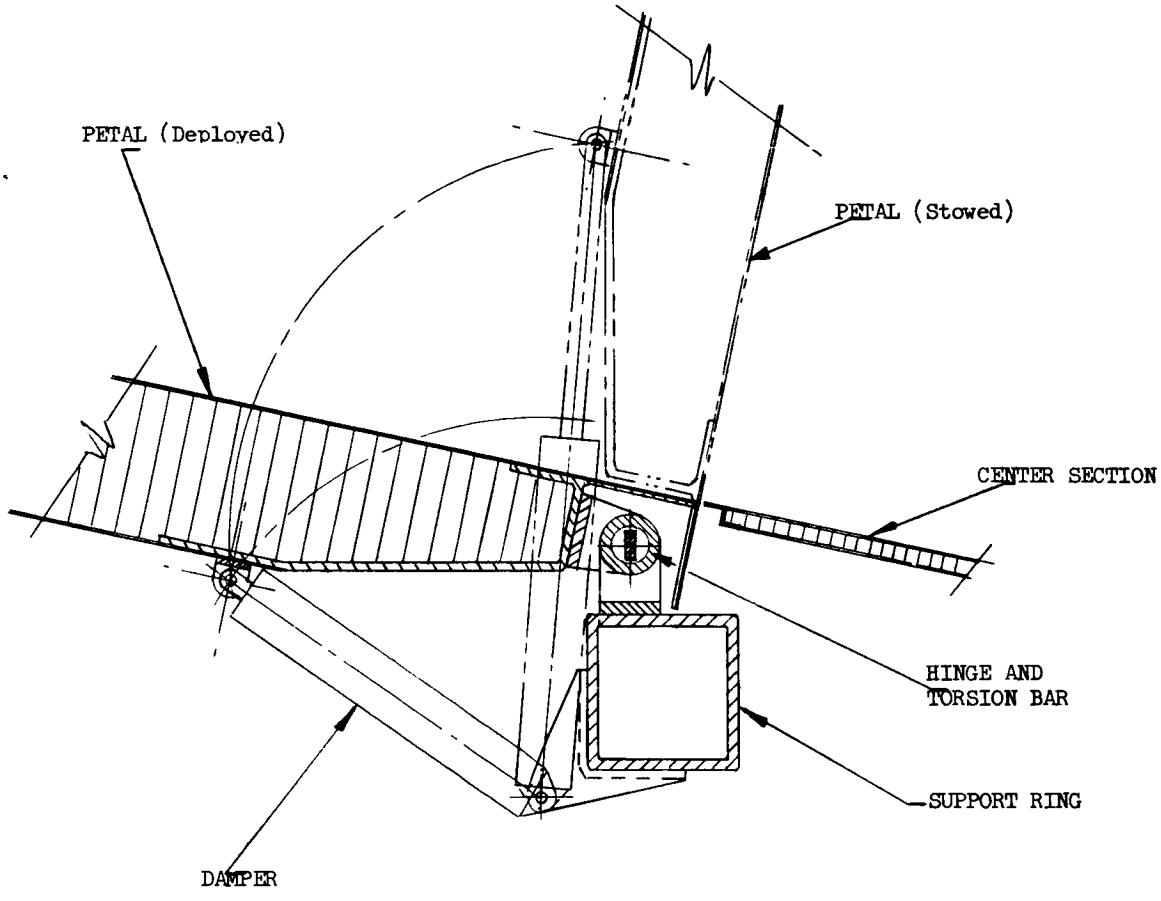

Figure 4-7. Viscous Damper

4.1.2 Collector Fabrication

Sectors were fabricated as individual parts on a single tool, using vacuum bagging and electrical resistance heat curing. The surface of the layup tool is made of reinforced epoxy and has a floating mounting attachment to the metal support frame to allow differential thermal expansion. The male tool was replicated from the master female pattern. The master pattern was generated by sweeping out the paraboloidal shape using a master template pivoted at the optic axis. Progressively finer sweeps were made using a quick drying plaster compound. The male tool surface was layed-up directly on the master pattern in successive laminates of epoxy and reinforcing glass cloth. Electrical resistance heater blankets were imbedded in the layup for later use in curing the honeycomb sectors. Also imbedded were vacuum lines and ports. Attachment lugs were bonded directly into the epoxy tool back surface, the prefabricated metal frame was attached after curing, and the completed female tool was lifted from the master pattern.

The tool design is such that the tool surface is supported by closely spaced adjustable attachments. By a combination of adjustment and barbering of the surface, the tool shape can be corrected or modified as determined by the inspection of fabricated honeycomb sectors.

a) Composite material heat transfer tests. These tests were conducted on six honeycomb constructions to determine necessary parameters for conducting the heat balance calculations for the collector.

b) Thermal conductivity tests were conducted on six adhesive systems for the honeycomb construction to guide the selection of the adhesive used.

c) Composite material thermal distortion tests. Specimens were subjected to heating on one surface. Temperature gradients and displacements were measured to enable theoretical correlation and determine the pertinent parameters for thermoelastic analysis of the collector.

d) Composite mechanical testing. Specimens were tested to determine the strength and stiffness parameters for the honeycomb to aid in structural analysis.

4 .4 Geometric and Surface Tests

Procedures have been established for measuring the geometric quality of the collector. Individual contributions due to fabrication effects of springback, overall waviness, and honeycomb construction effects at doublers and fastener points were measured. Following the environmental testing phases, the effects on the collector geometry from the 1-g load in the deployed condition and the vibration testing, both in the stowed and deployed condition, were determined. Figures 4-8 and 4-9 show the combined surface deviation for the complete collector.

Visual inspections of the collector were also made before and after testing to observe any deviations or structural damage which might not be apparent from optical inspections. Damage was observed in the form of skin peels where the adhesive bond to the core had failed. Only 0.3 percent of the collector surface areas showed this type of damage, of which less than half was on the optical face. The majority of the observed damange is due to increases in skin peel in areas which were originally peeled, indicating the need for rigid fabrication process control to eliminate weak or completely unbonded areas.

In general, no structural damage was observed during environmental testing. The deviations which were encountered can be eliminated by adequate process and quality control.

4.1.4 Environmental Testing

Environmental testing of the full size preprototype collector consisted of the following tests:

- One-g orbital transfer acceleration loading in the axial direction
- Deployment dynamic loadings
- Launch vibration spectrum in the stowed position
- Orbital transfer vibration spectrum in the deployed position

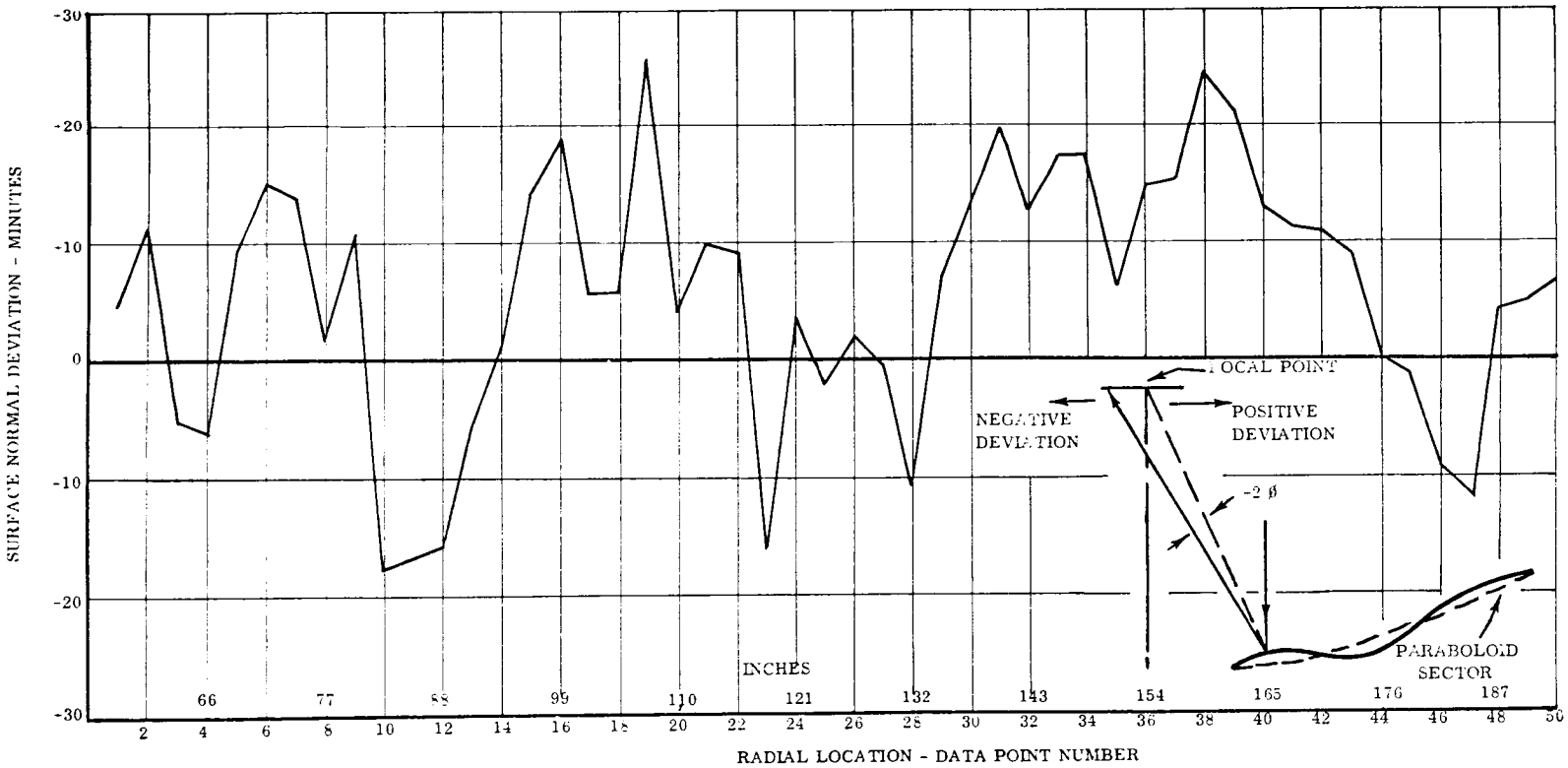

Figure 4-8. Surface Deviations of Collector 1

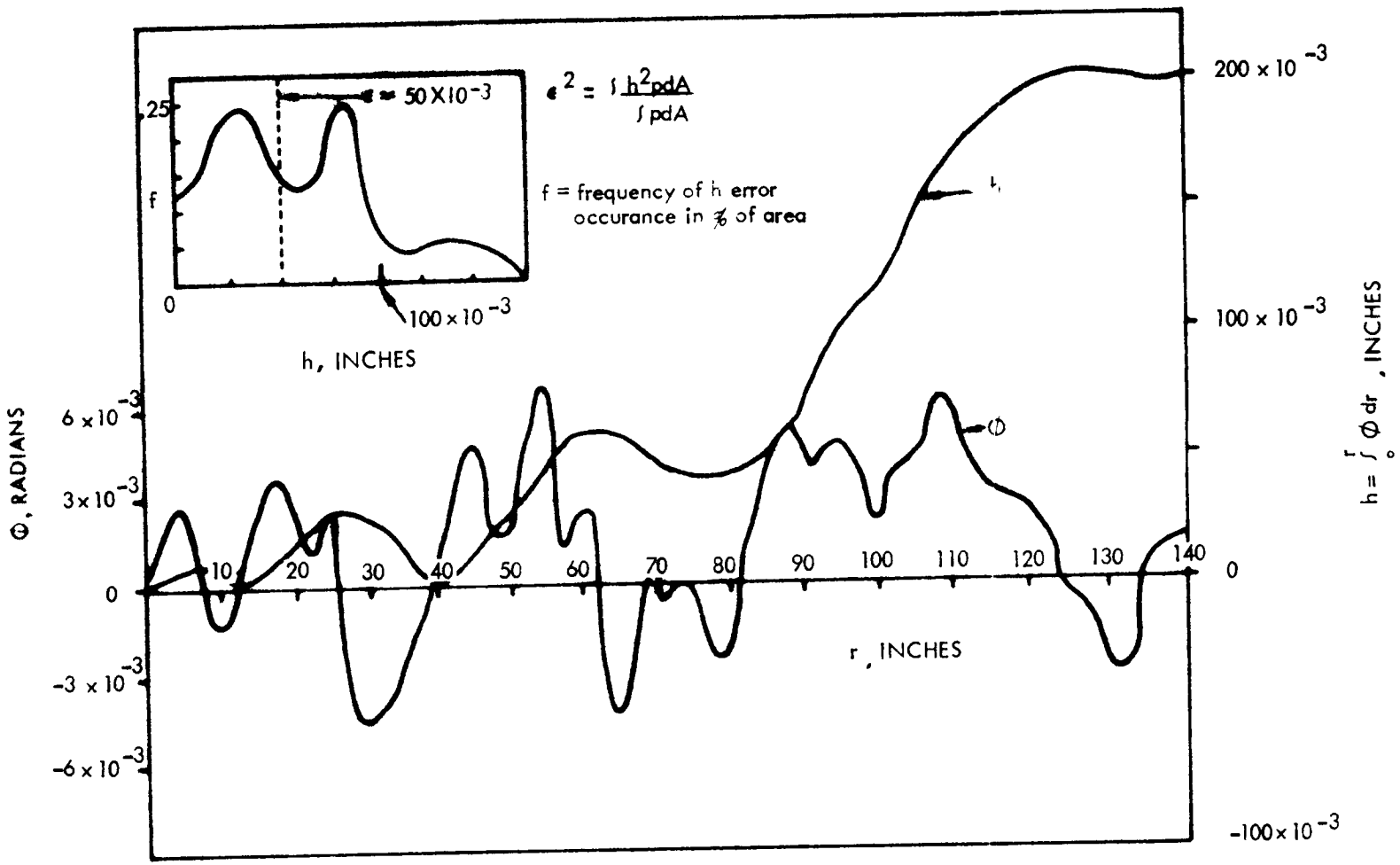

Figure 4-9. Surface Deviations of Collector 2

The objectives of environmental testing were to obtain developmental information concerning loads, stress conditions, modes of deflection, and general structural integrity characteristics which would aid in efficient and reliable prototype design. Also to be determined was the relationship of the structure and locks to geometric shape and optical performance. The tests were planned, therefore, to separate the various environmental and performance conditions so that the individual effects could best be determined. For this reason, comparison optical inspections follow each test phase to determine any geometric or optical deviations. The collector is not externally supported and is in its dead weight position during inspection.

4.1.4.1 Dead Weight Structural Testing

To simulate the 1-g orbital transfer acceleration loadings on the deployed collector, the auxiliary support stands used for initial assembly were removed, thereby loading the collector by its own weight. Surface strain data is obtained at various locations on the collector from which the typical stresses were calculated. Deflection data was also obtained. Stress levels are appreciably reduced from a maximum of 3209 psi to below 500 psi with the addition of the intermediate locks, due to the reduction of the bending in the long or radial direction of the sectors. The maximum deflections are also reduced, from 4.5 inches with rim locks only, to 1.7 inches with prototype rim locks and rigid intermediate locks, and to 1.0 inch with rigid rim and intermediate locks.

4.1.4.2 Collector Deployment Testing

Orbital deployment is actuated by torsion bar springs at the hinges of each sector. To simulate the zero gravity deployment dynamics in the laboratory, a deployment simulation harness was designed, consisting of continuous elastic cords around the collector bundle at the lock locations which, when they expand during deployment, counteract the dead weight torque of the sectors, thereby simulating only the net effect of the actuating springs. During harness calibrations, the net static torque was measured for various deployment positions. The net energy input to the sectors simulates quite closely the energy input during an orbital deployment.

The same strain gage arrangement used in the 1-g dead weight testing was used to record surface strains during deployment. An accelerometer which is sensitive to angular position with respect to the vertical was used to record displacement versus time. In addition, motion pictures were taken to record dynamics and symmetry characteristics of the deployment. A microtimer is positioned in the picture to provide an accurate time reference. After final calibration of the deployment harness, the collector bundle is manually opened approximately seven degrees to position the center of gravity of the sector over the vertical. A tethering cord is automatically released to initiate the deployment and data is recorded during the entire sequence.

Some nonsymmetry in the deployment action was observed. In general, the deployment nonsymmetry is within 2 degrees of travel for sectors which are directly opposite. This is approximately a 4.5-inch displacement at the rim, which would be 0.3 inch per sector for the 15 sectors between the diagonally opposite measured positions. This is within lock piloting funnel capabilities.

Stress levels during deployment, calculated from measured strain values, ranged from 200 psi tension to 200 psi compression during most of the deployment sequence. Momentary peak values of 750 psi compression were measured at the time of lock engagement. Observation of the locks after deployment revealed that the collector locks had not fully detented. It was found that the piloting length of the probe in the detent was too long for the relative motion required near the detenting position. Binding occurred in the lock, which stopped the deployment motion before final detenting. Dry film lubricant was applied to the probes during the second deployment test; however, the final detenting was still prevented by the binding condition. All but one lock engaged (but did not detent) and this lock would also have engaged if a slightly larger funnel, such as the one shown in Figure 4-6, were used.

General conclusions drawn from the deployment testing are:

a) Measured high levels of intersector friction indicate that viscous dampers at the hinge are not required. Simple detent locks have been shown to adequately absorb the stopping loads.

b) The kinematics of the locking action must be studied more closely to insure a nonbinding condition.

c) Deployment symmetry was observed to be satisfactory.

4.1.4.3 Collector Vibration Testing

Vibration testing of the preprototype collector was conducted in both the stowed and deployed configurations. The stowed vibration test setup is shown in Figure 4-1. The collector and quadrupod structure are mounted on an adapter fixture to the C-210 vibration exciter. To best simulate the launch environment, the lower mounting ring is hard mounted to the fixture to simulate the bottomed-out condition of the mounting ring isolators under the 10-g launch acceleration loading.

Tests were conducted at a frequency sweep rate of 1.4 octaves per minute in progressively higher g-level surveys. Accelerometer data at various locations was recorded and motion pictures were taken at times of resonance. Input vibration control of the exciter was based upon the highest of four control accelerometers located on the fixture mounting pads.

The vehicle vibration inputs to the mounting points of the Sunflower system can be amplified or damped by the response characteristics of the quadrupod and structural mounting rings. The transmissive characteristics of the mounting structure and rings were measured to determine the input to the sectors. The stacking ring, which is vibration isolated and structurally damped, was found to have a much lower transmissive characteristic.

The honeycomb sectors mid-span response was measured, and showed vibration to be highly damped in the axial direction. In the lateral direction the vibration was not as highly damped, and in some cases amplification occurred. In general, the honeycomb sectors response followed the response of the quadrupod and support rings with isolation and damping over the full frequency spectrum.

The deployed vibration test setup is shown in Figure 4-2. The collector was opened and locked while in place on the exciter fixture.

The auxiliary support stands used for support during opening and lock assembly were pulled back during vibration testing so that the deployed collector was supported at the center mounting ring only. This position combines the orbital transfer environments of 1-g acceleration and the vibration spectrum. Vibration isolators were added to the mounting ring at the mounting pad locations and tests similar to the stowed vibration test procedures were conducted.

Certain portions of the input spectrum were limited by resonances and control capabilities. From the measured response of the mounting ring, it can be seen that the isolators damped the vibration in the higher frequency range. However, at low frequencies the structural response of the ring produced generally high amplifications of the motion at mid-span. This displays the need for viscoelastic structural damping and additional supports in subsequent mounting ring designs.

Typical honeycomb sector response was measured. It was found that the honeycomb sandwich material and lock connections produced a general damping characteristic which improved at the collector rim.

The structural response of the honeycomb sectors was monitored by dynamic strain gage measurements at various locations. Typical cyclic stresses appeared at frequencies where apparent large amplitude sector flexure occured. The maximum cyclic stress was 1208 psi, with values at other positions in general much lower. This stresses were observed to cycle about the dead weight stress at the frequency of the base input vibration. The dead weight stress at the location of maximum cyclic stress was only 224 psi. It appears that the highest stresses occur at the low frequencies. For this reason, and since the low frequency vibration specification for the deployed orbital environment is not well defined, higher g-levels at low frequencies were not attempted. The two other areas where g-level inputs were reduced are 30 cps, due to the mounting ring flexural resonance, and approximately 150 cps due to power and control limitations of the C-210 excitor.

4.1.5 Conclusions

Although the preprototype collector was not intended as a high optical quality design, a standard surface deviation of less than 0.5

degree has been demonstrated in single panel performance tests. Based upon the knowledge obtained during the development program, a standard deviation of 1/4 degree including estimated environmental errors can be attained in a prototype design. The structural integrity of the adhesive-bonded aluminum honeycomb sandwich construction used in the Sunflower concentrator has been established as well as the operability of deployment concept in a full-size configuration. Fabrication techniques and tooling concepts have been evaluated and critical factors have been defined. Vacuum deposition processes have been established for the Sunflower collector as well as quality control requirements to obtain a mirror surface.

Although much detailed investigation remains before reliability can be verified, the development work performed during the Sunflower program demonstrates the feasibility of producing and utilizing large, light-weight, foldable solar concentrators for space power conversion systems.

4.2 MIDCOURSE GUIDANCE

The different launch vehicle guidance systems considered in this study vary in establishing an accurate interplanetary trajectory. For all of these vehicles, midcourse guidance must be performed in order to achieve optimal scientific investigation of the near-Jupiter space. The theoretical structure of midcourse guidance including quantitative results computed for a specific trajectory are reported in this section. Several guidance policies are evaluated, each consistent with a spin-stabilized spacecraft carrying a 50-pound science payload spacecraft.

4.2.1 Midcourse Guidance Techniques

Two different techniques of removing trajectory errors can be employed with this spacecraft configuration. Midcourse guidance may be performed by pointing the effective spacecraft motor thrust in a direction so that a single velocity increment removes the target errors. Arbitrary pointing, used with Ranger, Mariner, and Surveyor, allows a single correction to remove all target errors or to remove two components of miss at the target (critical plane correction) and not correct time-of-flight errors. This arbitrary pointing of the spacecraft is achieved by precessing the spin axis with gas jets.

Alternatively, velocity increments may be added while the spacecraft remains earth-pointing. This technique, motivated by the attitude control design, in general requires a separate correction for each target error component to be removed. However, by proper selection of the correction times, two or more target errors can sometimes be removed with a single correction.

It is possible to combine the techniques when multiple corrections are desirable. For example, a correction using arbitrary pointing is made early in flight, when the omni-antenna is adequate for downlink communications. Later, beyond the range of the omni-antenna, supplementary earth pointing corrections might be performed. Late corrections may be desirable to adjust the trajectory more accurately or to remove the accrued effects of perturbations such as uncertainties in solar pressure or micrometeoroid drag. Multiple corrections of course will complicate any orbit redetermination, which might interfere with celestial mechanics measurements.

4.2.2 Trajectory

The trajectory selected for this study represents a sample from the Jupiter 1972 launch opportunity. The selection was influenced by favorable characteristics for scientific experimentation and therefore is representative for midcourse guidance analysis. Detailed trajectory characteristics are as follows:

Launch date	March 14, 1972
Flight time	742 days
Trajectory type	I
Trajectory class	I
Injection energy	86.244389 $(km/sec)^2$
Heliocentric transfer angle	156.62839 degrees

Graphs of interplanetary geometric angles and distances for this trajectory are given in Section 2.2. In addition, Figure 4-10 shows the angular relationship between the critical plane normal and the sun line. Critical plane corrections are discussed later.

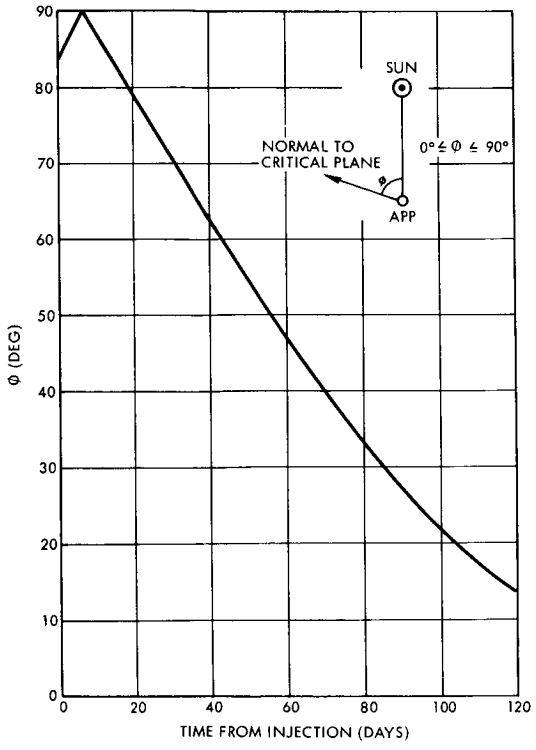

Figure 4-10. Orientation of Normal to Critical Plane

The hyperbolic, Jupiter-centered orbit of the encounter phase is determined by the parameters $B \cdot T$, $B \cdot R$, and time of flight t_f. These parameters are typically used for lunar and interplanetary missions.*

The numerical information was generated by the TRW Interplanetary Search Program (ISP) and the Matrix Abstraction Program (MAP). The ISP is designed for computing interplanetary free flight trajectories in the gravitational fields of the earth, moon, sun, Mars, Venus, and Jupiter. The gravitational forces from all of these bodies and solar light pressure force are included in the integration of the equations of motion. Integration is performed using a combination of the Cowell and Runge-Kutta method. This program is similar to the JPL trajectory program TRAJ.

*V. C. Clarke et al, "Design Parameters for Ballistic Interplanetary Trajectories, Part II, One-Way Transfers to Mercury and Jupiter," JPL TR 32-77, January 15, 1966.

MAP is an auxiliary program used to manipulate data in matrix form. Thus matrix multiplication and inversion, and the computation of eigenvalues and eigenvectors may be automatically performed.

4.2.3 Injection Errors

The launch vehicle configuration selected for study is the Atlas-Centaur with thrust augmentation provided by an additional spin-stabilized solid stage. The solid stage allows a larger payload to be injected and provides an extended launch window. The performance characteristics of this configuration are presented in Section 2.1.

The spin-stabilized solid stage introduces errors in addition to those from the Atlas-Centaur. The predominant source of these errors is the attitude uncertainty of the Centaur at Centaur-solid stage separation. Present state of the art indicates that this error may be as large as a degree or more. Error sources of several launch vehicle configurations are included in Section 7.4.

The Atlas-Centaur-solid stage configuration will introduce a 9.5 m/sec rms uncertainty in the injection velocity magnitude and 34.7 m/sec rms uncertainty in a circular region perpendicular to the direction of the injection velocity. The velocity injection errors ΔV_I are statistically represented by a covariance matrix Σ_I

$$\Sigma_I = E\left[\Delta V_I \, \Delta V_I^T\right]$$

where E indicates expected value. It is assumed for this study that each component of ΔV_I is normally distributed and that errors in position at injection have negligible effect on the miss at the target. For the trajectory described above,

$$\Sigma_I = \begin{bmatrix} 541.87 & -446.00 & -315.18 \\ -446.00 & 902.13 & -212.90 \\ -315.18 & -212.90 & 1052.2 \end{bmatrix} \times 10^{-6} \ (\text{km/sec})^2$$

in the geocentric equatorial coordinate system.

Because the injection errors are linearly related to the components of miss at the target $B \cdot T$ and $B \cdot R$, the uncorrected target miss is statistically represented as

$$\Sigma_T = C_I \Sigma_I C_I^T$$

where C is the matrix of partial derivatives of the target coordinates with respect to the components of velocity:

$$C = \begin{bmatrix} \frac{\partial (B \cdot T)}{\partial \dot{x}} & \frac{\partial (B \cdot T)}{\partial \dot{y}} & \frac{\partial (B \cdot T)}{\partial \dot{z}} \\ \\ \frac{\partial (B \cdot R)}{\partial \dot{x}} & \frac{\partial (B \cdot R)}{\partial \dot{y}} & \frac{\partial (B \cdot R)}{\partial \dot{z}} \end{bmatrix}$$

and the subscript I refers to the time of injection. Thus, Σ_T is the covariance matrix of the two dimensional normal distribution for the two components of miss at the target. Σ_T is a symmetrical matrix of the form

$$\Sigma_T = \begin{bmatrix} a & x \\ x & b \end{bmatrix}$$

Then

$$\Sigma_T^{-1} = \frac{1}{ab - x^2} \begin{bmatrix} b & -x \\ -x & a \end{bmatrix}$$

and the two dimensional probability density function is

$$p\left[(B \cdot T),\ (B \cdot R)\right] = \frac{1}{2\pi\,(ab - x^2)^{1/2}}$$

$$\exp\left\{ - \frac{1}{2(ab - x^2)} \left[b(B \cdot T)^2 - 2x(B \cdot T)(B \cdot R) + a(B \cdot R)^2 \right] \right\}$$

Contours of constant probability p are ellipses in the B·T, B·R plane and are described by

$$b(B\cdot T)^2 - 2x(B\cdot T)(B\cdot R) + a(B\cdot R)^2 = \text{constant}$$

The square roots of the eigenvalues of the matrix Σ_T are the size of the semimajor and semiminor axes of the ellipse which contains a certain probability. The numerical value of the probability is dependent upon the relative sizes of the eigenvalues. Standard tables* have been prepared which indicate the factor by which the square roots of the eigenvalues must be multiplied so that the resulting ellipse contains a certain percentage of possible situations.

The numerical value of Σ_T is

$$\Sigma_T = \begin{bmatrix} 90.811076 & 10.241762 \\ 10.241762 & 15.161822 \end{bmatrix} \times 10^{10} \text{ km}^2$$

The square roots of the eigenvalues of this matrix multiplied by an appropriate factor* indicate the size of the 99 percent probability miss ellipse at the target. The 99 percent semimajor and minor axes are 2,208,138 and 854,404 km respectively. This miss ellipse is illustrated in Figure 4-11.

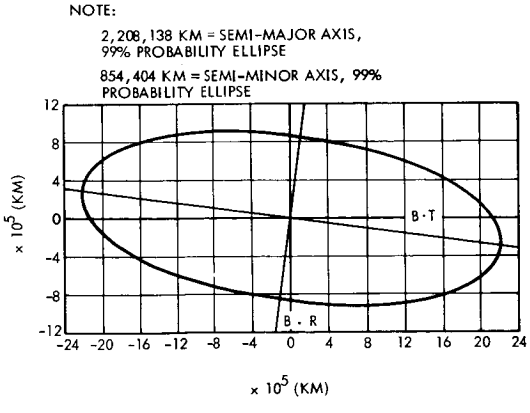

Figure 4-11. 99 Percent Probability Miss Ellipse

*H. Solomon, "Distribution of Quadratic Forms," Stanford University Technical Report 45, January 1960.

4.2.4 Arbitrary Pointing Midcourse Guidance

The mathematical technique of midcourse guidance where a velocity impulse may be imparted to the spacecraft in an arbitrary direction* has been exploited for use with previous lunar and interplanetary flights such as Ranger, Surveyor, and Mariner.

For control of B·T, B·R, and time of flight, t_f, the spin axis will be required to point in any direction in space. Constraints on the spin axis-sun line angle however preclude accurate spin axis pointing closer than 20 degrees from the sun line. Thus all arbitrary injection errors cannot be removed at any single correction time. Advantage may be taken of the change in trajectory geometry as a function of time however and a slight delay in a nominal correction time (several days) can allow all errors to be removed.

Critical plane corrections to control B·T and B·R only require that the spin axis be properly pointed in a plane. Figure 4-10 illustrates the angle between the critical plane normal and the sun line. Note that the critical plane normal and the spin axis is near 90 degrees early in flight. For injection errors in specific directions, this would require the spin axis to be pointed closer than 20 degrees to the sun line. The scheduling of a nominal correction for this trajectory would occur no earlier than about 30 days from injection if all pointing directions in the critical plane might be required. This constraint may be relaxed if a small probability of pointing near the sun line existed, made possible by a bias of the trajectory. It could be removed if, while B·T and B·R are corrected, the time of flight is permitted to be altered even though not corrected. The maximum fuel penalty entailed by this method of removing the constraint is a factor of $\sec 20^{\circ} - 1 = 0.064$.

The velocity requirements to remove target errors including time of flight deviations and the requirements to remove miss-only errors are presented in Figure 4-12. The numbers represent 99 percent velocity

---

* A. R. M. Noton et al, "Analysis of Radio Command Midcourse Guidance," JPL TR 32-28, September 8, 1960.

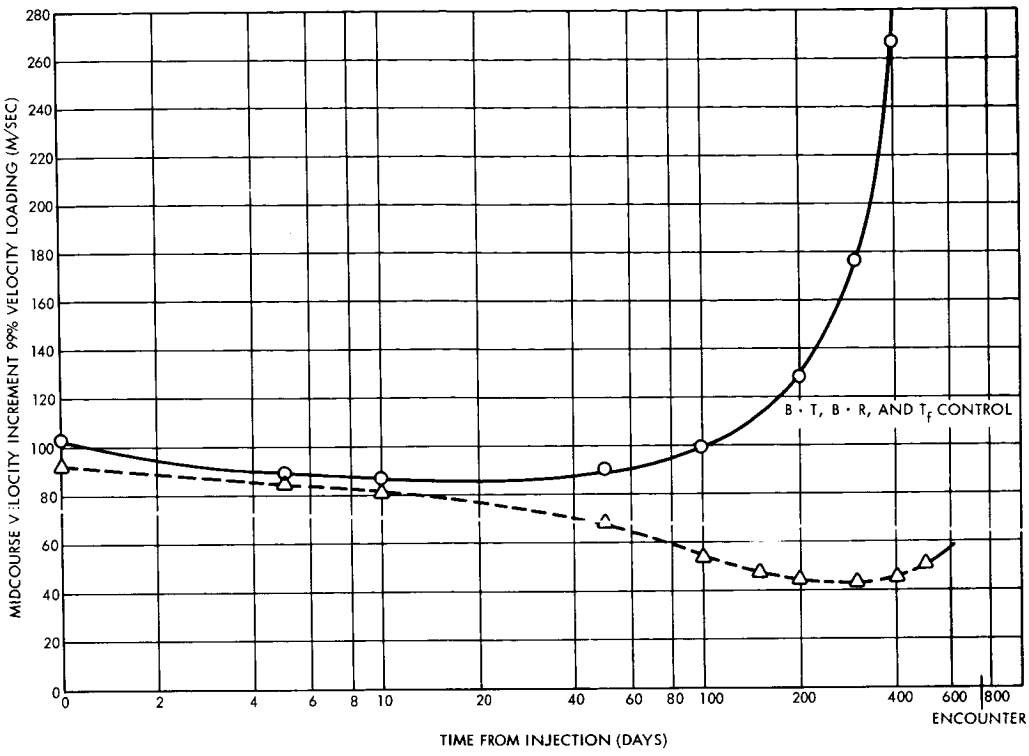

Figure 4-12. Midcourse Correction Requirement, 99 Percent Velocity Loading

loading, i.e., the velocity required to remove 99 percent of all possible injection errors. The least velocity requirement for control of all target errors is 85 m/sec and occurs 20 days after injection. The least velocity requirement for control of miss only is 43 m/sec and occurs 300 days after injection. In order to perform a correction early, for example at 10 days after injection, between 82 and 87 m/sec are required. The numbers were computed from

$$\Sigma_V = C\Sigma_T C^T$$

where C is evaluated at the time of the midcourse correction. For a critical plane correction 10 days past injection,

$$\Sigma_{V_{10}} = \begin{bmatrix} 1001.64 & -52.702607 & -98.524102 \\ & 73.535761 & 102.51410 \\ \text{Symmetric} & & 143.56311 \end{bmatrix} \times 10^{-6} \text{ (km/sec)}^2$$

4.2.5 Earth Pointing Midcourse Guidance

Analytic investigations are reported here for earth pointing midcourse guidance of the spacecraft for control of two position components at the target. For this analysis, it is assumed that two midcourse engines are used, aimed in opposite directions along the earth-oriented spin axis. This midcourse guidance technique takes advantage of the relative motion in target-centered coordinates of the midcourse correction sensitivities to provide control of B·T and B·R. The matrix of partial derivatives of B·T and B·R with respect to the components of a midcourse correction velocity at an arbitrary time i is

$$C_i = \begin{bmatrix} \frac{\partial(B\cdot T)}{\partial \dot{x}_i} & \frac{\partial(B\cdot T)}{\partial \dot{y}_i} & \frac{\partial(B\cdot T)}{\partial \dot{z}_i} \\ \frac{\partial(B\cdot R)}{\partial \dot{x}_i} & \frac{\partial(B\cdot R)}{\partial \dot{y}_i} & \frac{\partial(B\cdot R)}{\partial \dot{z}_i} \end{bmatrix}$$

Thus

$$\Delta M = \begin{bmatrix} \Delta B\cdot T \\ \Delta B\cdot T \end{bmatrix} = C_i \begin{bmatrix} \Delta\dot{x} \\ \Delta\dot{y} \\ \Delta\dot{z} \end{bmatrix}_i$$

where ΔM is the change in B·T and B·R effected by the midcourse correction, and $\left[\Delta\dot{x}\ \Delta\dot{y}\ \Delta\dot{z}\right]_i^T$ are the three components of the midcourse correction velocity increment. The velocity increment may be written

$$\begin{bmatrix} \Delta\dot{x} \\ \Delta\dot{y} \\ \Delta\dot{z} \end{bmatrix}_i = \Delta V \begin{bmatrix} \ell \\ m \\ n \end{bmatrix}_i$$

where ΔV is the velocity magnitude and $\left[\ell\ m\ n\right]_i^T$ are the direction cosines of the effective thrust direction. Therefore

$$\Delta M = C_i \begin{bmatrix} \ell \\ m \\ n \end{bmatrix}_i \Delta V = C_i' \Delta V$$

The 2 x 1 matrix C_i' is the midcourse correction sensitivity matrix at time i.

The guidance equation which relates the velocity increments for each of n correction maneuvers to the target errors to be eliminated is

$$\Delta M = - D \begin{bmatrix} \Delta V_1 \\ \Delta V_2 \\ \vdots \\ \Delta \overline{V}_i \\ \Delta \overline{V}_n \end{bmatrix} = - D\, \Delta \overline{V}$$

where ΔV_i are the correction velocity magnitudes, and

$$D = \left[C_1' \,\vdots\, C_2' \,\vdots\, C_3' \text{ --- } C_i' \text{ --- } C_n' \right]$$

Because the midcourse correction motors are mounted collinear with the spin axis and the spin axis is constrained to point continuously toward the earth, the matrices C_i' are not variable at a given time. Therefore, for three or more corrections, a unique combination of velocity increments which will remove an arbitrary target error does not exist. For two corrections however,

$$\Delta \overline{V} = - D^{-1} \Delta M$$

The velocity requirements for the sum of these two corrections are statistically represented by a covariance matrix Σ_V defined by

$$\Sigma_V = D^{-1} \Sigma_T D^{-T}$$

An illustration of the two correction maneuver scheme is presented in Figure 4-13. Because the midcourse correction sensitivites are generally not perpendicular to each other, the effects of two corrections at different times form a nonorthogonal basis in B·T, B·R space. The dashed lines in the figure indicate how an arbitrary target error is removed. The letters A and B in the figure denote the correction sensitivities for two different times.

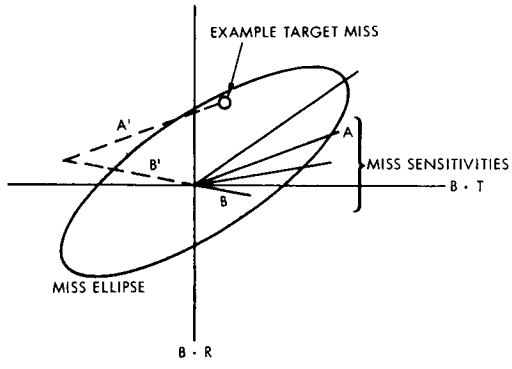

Figure 4-13. Elimination of Miss by Two Earth-Pointing Corrections

The midcourse correction sensitivities are shown as a function of time in Figure 4-14. Comparison of these sensitivities with the uncorrected miss ellipse drawn in Figure 4-11, shows that a major fraction of injection errors can be removed with only one correction, provided the correction can be performed late in flight. If corrections must be performed early, for example less than 100 days, a smaller fraction of the injection errors are removable with a single correction. Two corrections performed at any two distinct times can remove all errors. Other

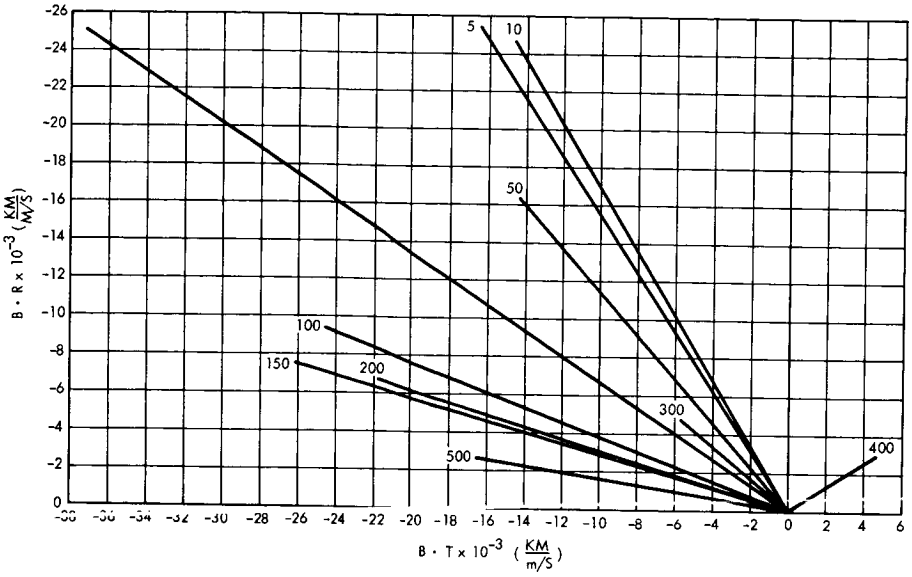

Figure 4-14. Earth-Pointing Midcourse Correction Sensitivities

methods, such as purposely aiming the trajectory at injection to miss the target (biasing), can be exploited to permit the removal of target errors with a single correction.

The relative rotation of the midcourse correction sensitivities plotted in Figure 4-14 exhibits an oscillatory motion. From injection to a time past 10 days, the sensitivities rotate clockwise and decrease in magnitude. From this time to a time near 150 days, the sensitivities rotate counterclockwise and increase slightly in magnitude. This process repeats again between 150 and 400 days and 400 days to a time not determined.

In order to provide insight into this phenomenon, the direction of the spacecraft-earth line, ΔE, is plotted as a function of time in Figure 4-15. The slope of this curve appears to be correlated with the characteristics of the midcourse correction sensitivities, indicating that the continual alignment of the spin axis with the earth line accounts for at least a portion of the change in the sensitivities. Earth pointing spacecraft offer a particular advantage when compared with a sun or inertial pointing spacecraft (not considered here) because of the rapid

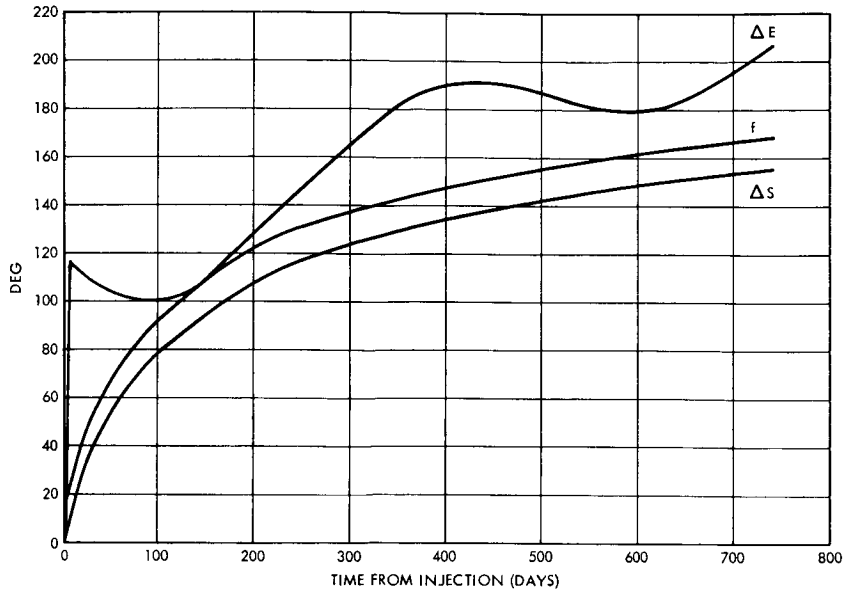

Figure 4-15. Earth and Sunline Motion

change of the sensitivities at times other than near injection. Figure 4-15 also shows the change in direction of the sun line, ΔS, and the true anomaly, f, on the sun-centered orbit.

The velocity requirements to remove target errors are 122.25 m/sec. It was assumed that two corrections would always be performed (even though both are not always required) at 10 and 100 days. This assumption causes the velocity estimate to be larger than it would be if midcourse time(s) were programmed after determination of the post-injection trajectory. The estimate represents 99 percent velocity loading. The covariance matrix Σ_V is

$$\Sigma_V = \begin{bmatrix} 509 & -763.5 \\ -763.5 & 2185.8 \end{bmatrix} \times 10^{-6} \text{ (km/sec)}^2$$

Because of the nonorthogonality of the correction sensitivities and the fact that the sensitivities lie in directions different from the major and minor axes of the miss ellipse, the target errors removable using this velocity estimate does not give a locus similar to the miss ellipse. This is also true of the locus of removable target errors for arbitrary pointing guidance. Thus, one technique may enable more control over a favored miss component, for example B·T.

Time of flight may be controlled by performing an additional correction or by selecting the two correction times after initial orbit determination, time of flight is incidentally controlled. A small increase in the correction velocity would be required.

Unlike arbitrary pointing midcourse guidance, earth pointing guidance has no limitations on the correction times caused from sun line geometry. In addition, the fixed attitude of the corrections causes very small pointing errors. An error analysis of this guidance technique is discussed in Section 7.4.

4.2.6 Location of Spacecraft Engines

Spin stabilization of the spacecraft suggests that midcourse correction engines be mounted axially along the spin vector or mounted perpendicular to the spin vector with the thrust direction pointed through the center of gravity. Axially-mounted engines allow control of the spacecraft to be maintained during continuous motor thrusting. Engines mounted on the equator of spin however require thrust pulsing in order to change the spacecraft velocity. Axial mounting is preferred because of the continuous engine operation and less stringent c.g. alignment requirements.

Engines may be mounted on one or both ends of the spacecraft, thrusting parallel to the spin axis. Engines mounted on both ends provide the following advantages.

- Two engines provide redundancy. Failure of one engine would not cause failure of the mission. For another example, failure of one of the omnidirectional antennas would restrict the pointing during midcourse thrusting to regions in which communications could be maintained. This restriction could be accommodated by the two-engine configuration. The other advantages below accrue, assuming no failures occur which preclude the use of either engine.

- The spin axis need not be precessed more than 90 degrees from the earth line to point in an arbitrary direction. Thus less attitude control gas is required and the pointing errors proportional to the precessed angle are small. In addition, temperature constraints are more easily satisfied because the aft end of the spacecraft need not be pointed very close to the sun.

- Two engines require less midcourse correction velocity requirement for the earth pointing guidance scheme.
- Growth to powered swingby and orbiter missions where thrusting in arbitrary directions in deep space might be required is more attractive.

4.2.7 Comparison of Midcourse Guidance Techniques

The characteristics of arbitrary pointing and earth pointing midcourse guidance presented in Table 4-2 are factors which affect the selection of a technique.

Table 4-2. Guidance Characteristics

	Midcourse Guidance Technique	
	Arbitrary Pointing	Earth Pointing
Minimum number of corrections	1	Generally 2 or more (possibly 1)
Fuel requirements 99% loading (m/sec)	82 at 10 days; 43 at 300 days (critical plane type correction)	122.25; corrections at 10 and 100 days (conservative estimate)
Semimajor and minor axes of post-correction 99% miss ellipse (km)	24,478 17,295	65,850 10,680
Tracking time constraints	Correction performed $\gtrsim$10 days	First correction $\gtrsim$10 days; second correction $\gtrsim$50 days later
Factors increasing reliability	Single motor burn	No spin axis precession
Attitude control gas requirements	Approximately 300 degree precession (max)	None
Sun line geometry constraints	Cannot point spin axis < 20 degrees from sun line	None
Launch window constraints	None	Possible in order to guarantee rotation of the correction sensitivities
Maximum correction time	200 days	None

Combination of the two techniques can provide attractive features. For example, earth-pointing trim corrections following an arbitrary pointing correction can result in a very accurate orbit or can remove long term effects on the trajectory such as uncertainties in solar pressure, forces on the spacecraft from the precession of the spin axis, and micrometeoroid drag. In addition, for a particular trajectory error, an optimal scheduling policy of midcourse corrections can enable the most efficient use of the spacecraft engine fuel. These aspects are not reported here.

4.2.8 Selection

For the spin-stabilized spacecraft for a Jupiter flyby mission, the selection of the midcourse guidance concept is indicated by the "tree" of Figure 4-16. This concept is necessarily closely associated with the method of attitude control for cruise and noncruise orientations.

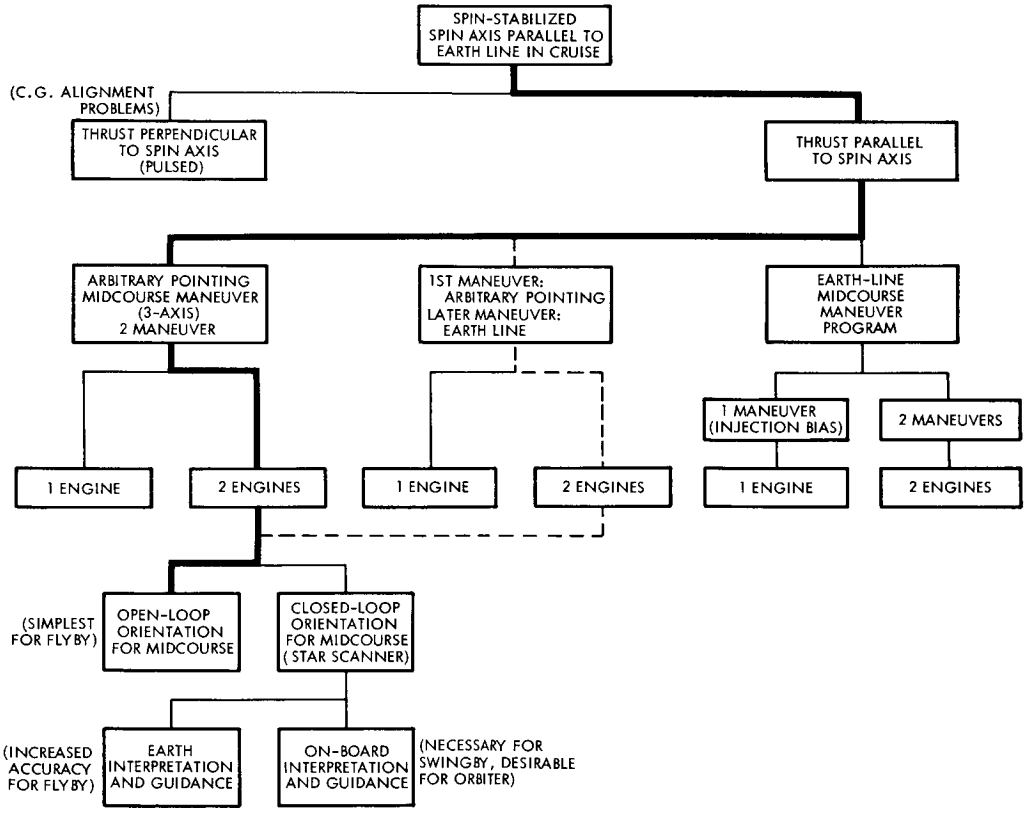

Figure 4-16. Midcourse Guidance Alternatives for Spin-Stabilized Spacecraft

The first choice indicated, thrust parallel to the spin axis, avoids stringent c.g. alignment problems and the accuracy decrease due to pulsed engine operation.

The second choice shows the preference for arbitrary pointing for the midcourse correction program (i.e., "3-axis pointing") over an earth-line maneuver. This choice is based on these disadvantages of the earth-line program, which are conclusions of the above analysis:

- Penalties in propellant weight required for removal of injection errors (particularly if injection is biased).
- Additional maneuver (required if injection is not biased).
- Reduced accuracy, with a one-maneuver program (or two-maneuver, unbiased-injection program), compared with a one-maneuver, arbitrary-pointing program.
- Possible constraints on the interplanetary trajectory selection, to assure adequate rotation of the sensitivity vector of earth-line maneuvers.

The choice of two engines, with opposite thrust directions parallel to the spin axis, follows the arguments of Section 4.2.6. Command capability and explosive valves are provided for two firings of each engine.

The selection and implementation of the arbitrary-pointing, one-maneuver program does not preclude the possibility of either of the following options, which may be embarked upon either before launch or after desirability is established during the flight:

a) The execution of a second arbitrary-pointing maneuver, to improve trajectory accuracy. This would be programmed long enough after the first maneuver to permit tracking to redetermine the orbit, but soon enough that low-gain antenna usage still provides satisfactory uplink and downlink capability. The time of the second maneuver should also avoid periods when the sun-spacecraft-earth angle is less than 20 degrees, to maintain high open-loop pointing accuracy.

b) The execution of a late earth-line maneuver, to improve trajectory accuracy and to compensate for unpredicted perturbations during the heliocentric portion of the trajectory. This usage of the earth-line maneuver capitalizes on some of the advantages of the earth-line correction: retention of high-gain antenna communications during the maneuver, independence of open-loop precession constraints and inaccuracies, and minimum sensitivity to long (1 hour) round trip communications delay times. Although Figure 4-14 indicates a late rotation of the sensitivity vector which would permit two maneuvers to remove any error, the primary advantage of this option lies in the ability to remove only the error components in the plane of the ecliptic. This objective can be achieved without compromising time-of-day-of-arrival objectives, by a single, late earth-line maneuver, if it is appropriately timed. This option is attractive, because it offers a minimum-risk means of compensating for the unpredictable portions of interplanetary trajectory perturbations, which tend to lie in the plane of the ecliptic, as discussed in Section 7.4.

The choice for open-loop orientation for arbitrary midcourse pointing (Figure 4-16) reflects the simplest implementation for the flyby mission. It also retains the potential of growth to the more accurate closed-loop orientation, possible with the addition of the star scanner sensor discussed in Section 4.7, to achieve greater accuracy for a flyby mission and necessary capability for swingby trajectories and orbiter missions.

The mode selected for midcourse guidance leads to a propellant requirement of less than 100 m/sec to remove injection errors of 99 percent of the launches. With a single correction it achieves a 99 percent error ellipse with a semimajor axis of about 30,000 km at the R-T plane (discussed in Section 7.4) compared with a requirement of 70,000 km.

4.3 OPEN-LOOP PRECESSION

Attitude control for the present mission consists of the two following basic modes:

- Precession to desired orientation, e.g. for initial acquisition and midcourse maneuver
- Antenna pointing to the earth during cruise mode

Orientation changes are required during the initial phases of the mission for a) preventing prolonged exposure of the aft of the spacecraft to the sun, b) acquiring the earth reference, and c) performing midcourse velocity corrections in the commanded directions. Therefore, the attitude control system must be capable of precessing the spacecraft to any desired orientation with sufficient accuracy. A spinning body can be precessed simply by a mass expulsion system producing torques about an axis orthogonal to the spin axis. Since these torques are body fixed, accurate synchronization with respect to a position reference is necessary to precess in any given direction. Therefore, precessing will not be continuous but discrete in time, over periodic angular increments keyed to the period of spin revolution.

Arbitrary orientations can be obtained by means of open- and closed-loop maneuvers. Open-loop maneuvers have the disadvantage of depending on the accuracies of the system components and parameters, but the simplicity of mechanization of this approach makes it attractive from the reliability standpoint. However, higher accuracies can be obtained by means of closed-loop maneuvers in which the attitude errors are determined by measurement, and control action takes place until these errors are reduced to an acceptably small value.

The sun can be used as a reference for open-loop precession and, depending on the relative positions of thrusters and sun sensors, motions in specified directions with respect to the sun can be obtained. These maneuvers can be performed by thrusting in the same direction once per spin revolution under sun sensor control. If a single thrusting axis is assumed, control can be based on four sun sensors of the Pioneer type, one for each direction of motion. Another alternative is the use of a single sun sensor in conjunction with a delay unit.

The final attitude after each precession maneuver can be estimated, if the initial orientation is known, by counting the number of precession steps and computing the precession per step on the basis of previous knowledge or actual measurement of the pertinent system parameters.

Closed-loop maneuvers require devices for the determination of attitude, a star scanner or a sun aspect indicator. The star scanner signals provide sufficient information for unique attitude determination when the observed stars are identified. The required computations can be performed on the earth; the identification process is greatly facilitated if the initial attitude is known and the orientation change can be estimated as discussed above. The process would consist then in a series of successive approximations to the desired attitude. Communication could be established by means of omnidirectional antennas. Attitude could be measured with an accuracy of the order of 0.05 degree.

The second alternative utilizes a sun aspect indicator which measures the angle between the spin axis and the sun line with an accuracy of the order of 1 degree. Therefore, precession on the sun plane can be measured directly. Rotation about the sun line can be determined by measuring phase displacement of a roll reference signal which could be generated by the same device. By observation of these signals on the ground over a sufficiently long interval an accuracy of the order of 1 percent or better could be obtained.

Open-loop precession has been selected for the APP baseline design because of its inherent simplicity and reliability. The concept has been proven successfully in the Pioneer spacecraft and can be adapted to the requirements of the present mission without significant increase in system complexity.

For improving the accuracy, it is desirable that the nutation or wobble generated by each precession step be reduced to the lowest possible level by active means. In particular, this will be desirable for midcourse maneuvers where there might not be enough time to wait until the wobble is sufficiently damped by passive methods.

The system proposed for the Advanced Planetary Probe is based on a two-pulse precession scheme. This method has the advantage of

reducing the wobble as well as changes in spin speed. A cold gas pneumatic system is used to develop torques about an axis perpendicular to the spin axis. Assuming impulsive torques, the first impulse of each pair will initiate a nutational motion which will be terminated by the second impulse when the spin axis completes a conical rotation of 180 degrees. Two nozzles are required because the spin rotation between pulses generally is not 360 degrees. The angle between these nozzles depends on the ratio of moments of inertia.

The first thrust pulse will be triggered by a timing device at appropriate time delays from a sun sensor pulse. In the analysis that will follow, an expression will be obtained for upper bound values of the wobble angle as a function of the number of thrust pulses. This residual wobble will be a consequence of uncertainties in the thrust levels, time lags in the control channels, nozzle and sensor misalignments, and initial wobble and timing errors due to uncertainties in the estimation of the actual ratio of moments of inertia.

4.3.1 Precession Dynamics

In the derivations made in this section the following approximations are assumed:

- The spacecraft is symmetric about the spin axis, which is the principal axis of maximum inertia.
- The only torques acting on the spacecraft are produced by the control system and can be considered to be impulse functions.
- Effects of misalignments and delays in the control system are negligible.

Let x, y, z be a set of orthogonal body-fixed axes, where z coincides with the spin axis. In the absence of external torques the Euler equations for the system reduce to

$$\omega_x + \lambda \omega_y \omega_z = 0$$

$$\omega_y - \lambda \omega_z \omega_x = 0$$

$$C \omega_z = 0$$

where ω_x, ω_y, and ω_z are components of the rotation vector $\bar{\omega}$ along the respective body axes, C is the symmetric moment of inertia, A is the transverse moment of inertia and λ is given by

$$\lambda = \frac{C - A}{A}$$

Integration gives

$$\omega_z = \omega_s = \text{const}$$

Using complex notation, the component of the rotation vector $\bar{\omega}$ on the plane x - y is

$$\omega_E = \omega_x + j\,\omega_y$$

where $j = \sqrt{-1}$

Multiplying the second Euler equation by j and adding to the first gives

$$\omega_E - j\,\omega_s\,\lambda\,\omega_E = 0$$

Integrating:

$$\omega_E(t) = K\,e^{j\omega_s\lambda t}$$

The constant of integration can be evaluated by considering conditions existing immediately after the application of an impulse. If this event occurs at the time $t = t_o$, the constant K is given by

$$K = \omega_E(t_o)\,e^{-j\omega_s\lambda t_o}$$

where $\omega_e(t_o)$ is the step change in angular velocity produced by a torque impulse at $t = t_o$. If $H_o = C\,\omega_s$ is the initial amplitude of the angular momentum and δH is the transversal component due to the applied impulse, the magnitude of the transversal component of rotation will be

$$\omega_E(t_o) = \frac{\delta H}{A}$$

Substitution yields

$$\omega_E(t) = \frac{\delta H}{A} e^{j\omega_s \lambda (t-t_o)}$$

Assuming $t_o = 0$, this equation reduces to

$$\omega_E(t) = \frac{\delta H}{A} e^{j\omega_s \lambda t}$$

If H is the amplitude of the angular momentum after the application of the first impulse, the angular velocity of nutation will be

$$\omega_N = \frac{H}{A} \cong \frac{H_o}{A}$$

The process is represented schematically in Figure 4-17. The time to complete 180 degrees of nutational motion will be

$$t_1 = \frac{\pi}{\omega_N} \cong \frac{A\pi}{C\omega_s}$$

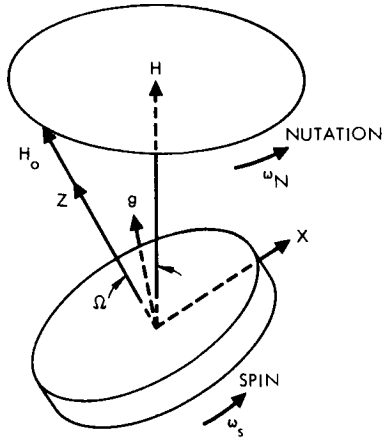

Figure 4-17. Nutational Motion Due to Impulsive Torquing

The spin rotation during this interval is

$$\alpha = \omega_s t_1 \cong \frac{A}{C}\pi$$

Another impulse will be applied at $t = t_1$ so that the resulting component of rotation is of equal amplitude and parallel to $\omega_E(o)$. This change in angular velocity will be given by

$$\Delta\omega = \frac{\delta H}{A} e^{-j\alpha} = \frac{\delta H}{A} e^{-j\frac{A}{C}\pi}$$

Consequently, the resultant transversal component at $t = t_1$ is

$$\frac{\delta H}{A} e^{j\lambda\omega_s t_1} + \Delta\omega = 0$$

which indicates the nutation is terminated with a resulting precession of the spin axis on the plane determined by the initial directions of H_o and δH. The precession angle is given by

$$\Delta\theta = 2 \tan^{-1} \frac{\delta H}{H_o} \cong 2\frac{\delta H}{H_o}$$

4.3.2 Residual Wobble

The object of the following analysis is to evaluate the residual wobble after a given number of precession steps have been completed. The following sources of error are considered:

- Time lags in the control hardware
- Valve and sensor mechanical misalignments
- Thrust variations
- Initial wobble
- Timing errors due to uncertainties in the ratio of moments of inertia.

The following assumptions are made:

- Control moments are impulsive
- The precession step is a small angle
- Control torque misalignments are not coupled into the spin axis

Locations of the gas jets with respect to the sensor axis are assumed to be as shown in Figure 4-18. Let

τ_1 = time lag in the control system for gas jet 1

τ_2 = time lag in the control system for gas jet 2

δH_1 = amplitude of the angular momentum increment produced by the nth thrust pulse of gas jet 1

δH_2 = same for gas jet 2

α_1 = misalignment angle of gas jet 1

α_2 = misalignment angle of gas jet 2

The actual firing axis shown in Figure 4-18 is the position in body coordinates of the line from the spacecraft to the reference body at the time the trigger signal for gas jet 2 is developed. The ideal firing axis is the position of this same line at the time the trigger signal for gas jet 2 should be developed.

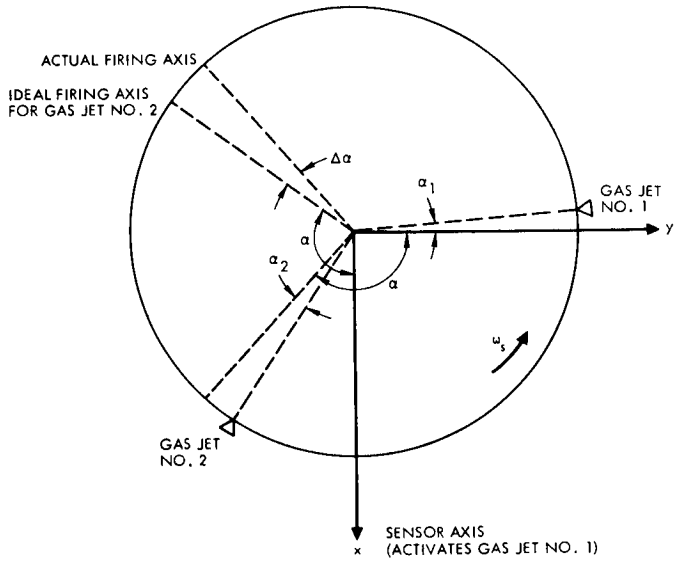

Figure 4-18. Gas Jet and Sensor Locations and Errors

The ideal firing axis and the sensor axis are displaced by an angle

$$\alpha = \frac{A_e}{C_e}\pi,$$

where A_e and C_e are the estimated moments of inertia. The nutation angle between thrust pulses is 180 degrees when the actual moment of inertia ratio is equal to the estimated one. Otherwise, this angle will be

$$\xi = \frac{C}{A}\alpha$$

where C/A is the actual moment of inertia ratio. Therefore, the error in nutation angle corresponding to an error $\Delta\alpha$ is

$$\Delta\xi = \frac{C}{A}\Delta\alpha$$

If a timing error Δt_1 is also included, $\Delta\alpha$ will be

$$\Delta\alpha = \left(\frac{A_e}{C_e} - \frac{A}{C}\right)\pi + \omega_s \Delta t_1$$

Consequently

$$\Delta\xi = \frac{\left(\frac{A_e}{C_e} - \frac{A}{C}\right)\pi}{\frac{A}{C}} + \frac{\omega_s C}{A}\Delta t_1$$

In the analysis that follows, the system behavior is investigated at discrete intervals. The transversal component of rotation is evaluated once every spin revolution at the instant when the sensor crosses the line from the spacecraft to the reference body. Therefore, the sampling per period is $T = 2\pi/\omega_s$ and the time variable is $t = nT$.

Let

$$\omega_E(nT) = \omega_n e^{j\gamma_n}; \quad n = 0, 1, 2, \ldots$$

be the value of ω_E at the nth sampling instant. The value of ω_E at the following sampling instant n + 1 is

$$\omega_{n+1} e^{j\gamma_{n+1}} = e^{j2\lambda\pi}\left[\omega_n e^{j\gamma_n} + \epsilon_1 + j\epsilon_2\right]$$

where

$$\epsilon_1 = \frac{\delta H_1 - \delta H_2}{A}$$

$$\epsilon_2 = \frac{\delta H_1}{A}(\alpha_1 - \lambda\omega_s\tau_1) + \frac{\delta H_2}{A}(\Delta\xi - \lambda\omega_s\tau_2 - \alpha_2)$$

The quantities ϵ_1 and ϵ_2 are assumed to remain constant during an n-pulse torquing process, and the following expression is obtained by induction

$$\omega_n e^{j\gamma_n} = \omega_o e^{j(2n\pi\lambda+\gamma_o)} + (\epsilon_1 + j\epsilon_2) \sum_{k=1}^{n} e^{j2\lambda k\pi}$$

where $\omega_o e^{j\gamma_o}$ is the initial value of transversal angular velocity. After a series of algebraic manipulations the following closed-form expression is obtained

$$\omega_n^2 = \omega_o^2 + \epsilon \frac{2\sin^2(n\lambda\pi)}{\sin^2(\lambda\pi)} + 2\omega_o\epsilon \frac{\sin(n\lambda\pi)}{\sin(\lambda\pi)} \cos[(n-1)\lambda\pi + \gamma_o - \phi]$$

in which ϵ and ϕ are defined by

$$\epsilon e^{j\phi} = \epsilon_1 + j\epsilon_2$$

The expression for ω_n^2 can be considered the result of applying the cosine law to the triangle shown in Figure 4-19, in which the angle α is given by

$$\alpha = (n-1)\lambda\pi + \gamma_o - \phi$$

When the initial wobble is negligible, the expression reduces to

$$\omega_n = \epsilon \frac{\sin(n\pi\lambda)}{\sin(\pi\lambda)}$$

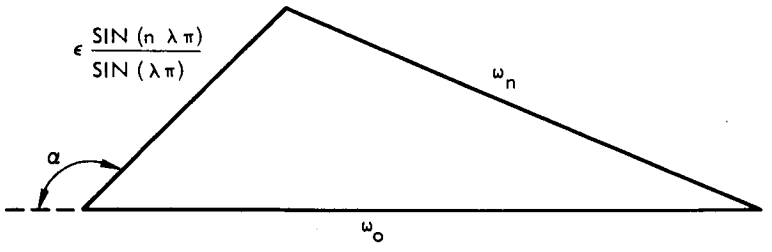

Figure 4-19. Triangle Relating Magnitudes of Transversal Rotational Components

The wobble angle after n precession steps is

$$\Omega_n = \tan^{-1} \frac{\delta H_n}{H_o} = \tan^{-1} \frac{A\omega_n}{C\omega_s}$$

For small angles the tangent can be approximated by the arc and if A/C is expressed in terms of λ,

$$\Omega_n \cong \frac{\epsilon}{(1+\lambda)\omega_s} \frac{\sin(n\lambda\pi)}{\sin(\lambda\pi)}$$

The wobble angle obtained will be an upper bound when the errors used to compute ϵ correspond to worst case conditions.

The wobble angle Ω_n is a periodic function of the number of precession steps. The number of steps per cycle is $N = 2/\lambda$. The discrete function

$$f(n, \lambda) = \frac{\sin(n\lambda\pi)}{\sin(\lambda\pi)}$$

is shown in Figure 4-20 for three values of λ.

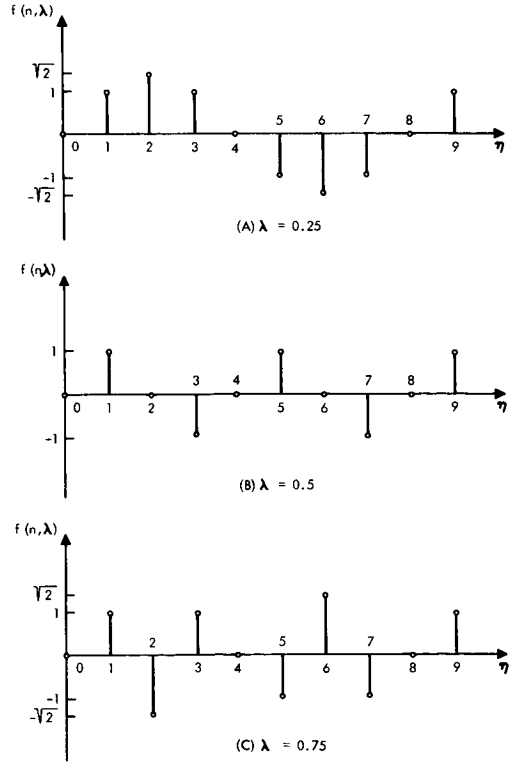

Figure 4-20. Discrete Function f(n, λ)

Therefore, when constant systematic errors are assumed, the upper bound of the wobble angle can be reduced substantially by proper choice of the firing sequence. For example, when $\lambda = 0.5$ the optimal control law would consist in precessing an even number of steps.

The following is a list of parameters used to compute worst case wobble angles for the Advanced Planetary Probe:

$$A = 170 \text{ slug ft}^2$$

$$C = 200 \text{ slug ft}^2$$

$$\omega_s = 5 \text{ rpm} = \frac{\pi}{6} \text{ rad/sec}$$

$$\Delta\theta = 0.2 \text{ degree; } 2 \text{ deg}$$

$$\text{Accuracy of 2 deg steps} = 2.5\%$$

$$\text{Accuracy of 0.2 deg steps} = 10\%$$

$$\alpha_1 = \alpha_2 = 0.5 \text{ deg}$$

$$\omega_s \Delta t_1 = 0.3 \text{ deg}$$

$$\frac{A_e}{C_e} - \frac{A}{C} = 0.03 \frac{A}{C}$$

$$\tau_1 = \tau_2 = 0.01 \text{ sec}$$

The corresponding results are given in Table 4-3. For a precession step size of 2 degrees the maximum contribution is from the error in the estimation of the actual moment of inertia ratio, as shown by the F_3 term. In the case of a 0.2 degree step size most of the wobble is due to the large difference in moment impulse as well as to the error in moment of inertia ratio.

Summarizing, an expression has been obtained for an upper bound of the wobble angle due to systematic errors. This upper bound is a periodic function of the number of precession steps. This result shows how the residual wobble can be minimized by proper choice of the control policy. Calculations made using APP parameters have shown the principal source of residual wobble is the error in the angular offset of the nozzles due to incorrect estimation of the actual ratio of moments of inertia.

Table 4-3. Worst Case Wobble Angles

Parameters	Precession Step Size	
	2 Degrees	0.2 Degree
δH	1.83 ft-lb-sec	0.183 ft-lb-sec
λ	0.1765	0.1765
$\Delta\xi$	0.10 rad	0.10 rad
F_1	9.15×10^{-2} ft-lb-sec	3.66×10^{-2} ft-lb-sec
F_2	1.42×10^{-2} ft-lb-sec	1.42×10^{-3} ft-lb-sec
F_3	0.168 ft-lb-sec	1.68×10^{-2} ft-lb-sec
ϵ	1.2×10^{-3} sec^{-1}	2.4×10^{-4} sec^{-1}
Ω	0.212 sin (31.8 n) deg	0.0424 sin (31.8 n) deg

4.3.3 Attitude Error Analysis

The attitude changes with respect to a known initial orientation which are produced by open-loop control can be estimated by counting the number of thrust pulses. Because of uncertainties in the thrust levels, misalignments, and timing errors, there will be errors in this estimation. The analysis that follows establishes quantitatively the effects of errors from all significant sources on the accuracy of the open-loop precession maneuvers. Cross-axis errors produced by wobble during thrusting are neglected. This assumption is justified by the results obtained in the preceding section, which shows the wobble can be reduced to very low magnitudes by proper choice of the control policy. In addition, if sufficient time is allowed between precessing steps, any residual wobble will be attenuated by the passive damper.

The open-loop precession system consists of the following devices:

- A pair of sun sensors to provide a roll reference with a field of view of ±85 degrees with respect to the equatorial plane of the spacecraft.
- A pneumatic torquing system to produce torques along two axes perpendicular to the spin axis of the spacecraft. The angle between the nozzles is selected to minimize the wobble resulting after each precession step.
- A digital electronic system to produce the required delays for precessing in the desired directions and to control the duration of the thrust pulses and the timing between pulses for wobble damping.

Two sun sensors are used, because the geometry of the spacecraft prevents obtaining the desired field of view with a single device. Since the accuracy of the null plane is degraded considerably for large angles away from the equatorial plane, the field of view for accurate use is nominally limited to ±70 degrees. At 70 degrees, the error is no greater than 0.92 degree.

The dynamics of the pneumatic precession system have been discussed in Section 4.3.1. Two step sizes will be provided because of the following reasons:

a) Long firing times are desirable to minimize the effects of uncertainties in the rise and decay times of the thrust pulses. A firing angle of 60 degrees has been chosen to obtain a pulse duration of 2 seconds with a nominal spin speed of 5 rpm.

b) Shorter pulses are required for attitude trimming because with a 60-degree firing angle the resulting precession per pair of pulses is of the order of 2 degrees. A firing angle of 6 degrees was chosen for these short pulses to give a precession of the order of 0.2 degree per pulse pair.

By proper selection of the angular delay between sun sensor and thrust pulses the following directions of precession are obtained:

- Towards the sun on the plane determined by the initial spin axis orientation and the sun

- Away from the sun on the same plane as above
- Clockwise about the sun line with constant aspect angle as seen from the spacecraft
- Same, but counterclockwise

Basically, the first two are similar except for a delay of 180 degrees. In the following analysis they are considered as a single mode, "motion in the sun plane." The second two cases are of the same nature and are discussed under the heading of "coning about the sun line."

4.3.3.1 Motion in the Sun Plane

The precession step size is given by

$$\Delta\theta = 2\frac{\delta H}{H_o}$$

where $H_o = C\omega_s$ is the spin angular momentum and δH is the angular momentum increment produced by each pulse of the sequence. If F is the thrust in pounds, ℓ is the moment arm and t_f is the pulse duration:

$$\delta H = F\ell t_f \eta$$

where η, the efficiency factor, is given by

$$\eta = \frac{\sin\frac{\beta}{2}}{\frac{\beta}{2}}$$

in which β is the firing angle. For a given spin speed, ω_s, the pulse duration and the firing angle are related by

$$\beta = \omega_s t_f$$

Substitution into the expression for $\Delta\theta$ yields

$$\Delta\theta = 4\frac{F\ell}{C\omega_s{}^2}\sin\frac{\beta}{2}$$

Assuming

$$\Delta\theta = 2 \text{ deg}$$

$$\ell = 8 \text{ ft}$$

$$C = 200 \text{ slug ft}^2$$

$$\omega_s = 5 \text{ rpm} = \frac{\pi}{6} \text{rad/sec}$$

$$\beta = 60 \text{ deg}$$

the thrust is F = 0.12 pound. With a firing angle of 6 degrees the precession step size becomes

$$\Delta\theta = 0.22 \text{ degree}$$

Errors in $\Delta\theta$ are caused by uncertainties in parameters. Let ϵ_F, ϵ_ℓ, ϵ_C, ϵ_{ω_s} and ϵ_β be the percent errors in $\Delta\theta$ due to uncertainties in F, ℓ, C, ω_s and β, respectively. By differentiation with respect to each parameter and division by the expression for $\Delta\theta$ the sensitivities are obtained as follows:

$$\epsilon_F = \frac{\Delta F}{F}$$

$$\epsilon_{\omega s} = -2\frac{\Delta\omega_s}{\omega_s}$$

$$\epsilon_\ell = \frac{\Delta\ell}{\ell}$$

$$\epsilon_C = \frac{\Delta C}{C}$$

$$\epsilon_\beta = \frac{\frac{\beta}{2}}{\tan\frac{\beta}{2}}\frac{\Delta\beta}{\beta}$$

As shown in Section 4.3.4, the thrust level can be predicted or measured with an error of 1 percent. Therefore, ϵ_F = 1 percent. If the longitudinal position of the spacecraft center of mass can be determined with a 3σ error of 0.1 inch and the assumed moment-arm length of 8 feet can be maintained within 0.1 inch (3σ), ϵ_ℓ is

$$\epsilon_{\ell} = \frac{\sqrt{2} \cdot 0.1 \text{ in.}}{8 \text{ ft} \times 12 \frac{\text{in.}}{\text{ft}}} = 0.15 \text{ percent}$$

The spin moment of inertia C can be estimated from measurements performed under simulated conditions on the ground and telemetered spacecraft temperatures and tank pressures. The 3σ error in the estimation of C is assumed to be $\epsilon_C = 1$ percent.

The open loop precession maneuver for the first midcourse correction is the most critical and this accuracy of 1 percent is assumed to apply to that one period shortly after launch. One percent accuracy could probably be obtained for more than one condition but would involve further testing under simulated conditions. The booms are not deployed until after the midcourse corrections have been completed so that it is feasible to make an inertia measurement in a vacuum test chamber with solar simulation. The effect of gravity (spacecraft up versus spacecraft down) can be evaluated without solar simulation.

The spin frequency can be measured accurately on the ground using the modulation of the downlink signal produced by a mechanical offset of the antenna feed. The resulting accuracy depends on the noise levels and the averaging intervals chosen. For the present analysis, $\Delta\omega_s / \omega_s$ is assumed to be 0.1 percent (3σ). Therefore, $| \epsilon_{\omega_s} | = 0.2$ percent.

Firing angle errors are originated by the digital logic and variable delays in the pneumatic system. By proper choice of the numbers of bits for the different registers, the trigger pulses can be generated with any practicable degree of accuracy. The only limitation to this accuracy is imposed by the resulting complexity. A 3σ error of 0.1 percent can be assumed for the logic without requiring excessive equipment. Typical values for uncertainties in rise times and delays in solenoid valves are of the order of 2 milliseconds. Assuming a spin rate of 5 rpm, these delays correspond to 0.060 degree. Consequently

$$\frac{\Delta\beta}{\beta} = \left(0.1^2 + 2\,\frac{0.060^2}{60^2}\right)^{1/2} = 0.1 \text{ percent}$$

$$\epsilon_{\beta} = \frac{30 \times 0.1}{57.3 \times 0.576} = 0.091 \text{ percent (for } \Delta\theta = 2 \text{ deg)}$$

$$\epsilon_\beta = \frac{3 \times 0.1}{57.3 \times 0.0524} = 0.1 \text{ percent (for } \Delta\theta = 0.2 \text{ deg)}$$

The total error for motions in the sun plane is given by

$$\epsilon = \left(\epsilon_F^2 + \epsilon_\ell^2 + \epsilon_{\omega_s}^2 + \epsilon_C^2 + \epsilon_\beta^2\right)^{1/2}$$

Substituting, the following results are obtained:

$$\epsilon = 1.44 \text{ percent for } \Delta\theta = 2 \text{ deg}$$

$$\epsilon = 1.44 \text{ percent for } \Delta\theta = 0.2 \text{ deg}$$

Cross-axis errors are due to the precession component which occurs about the axis orthogonal to both the desired precession axis and the spin axis. The result is a rotation of the spin axis about the sun line. These errors are the consequence of a displacement of the effective center of thrust due to the following reasons:

- Sun sensor mechanical misalignments with respect to the nozzles
- Uncertainties in the sun sensor null plane
- Time delay errors in the control system
- Uncertainties in the rise and decay characteristics of the pneumatic thrust

Based on previous experience with similar sensor arrangements, sun sensor mechanical misalignments are assumed to be of the order of 0.5 degree (3σ). Errors due to uncertainties in the sun sensor null plane are dependent on the angle ϕ between the sun line and the spin axis. The azimuth error for $\phi = 20$ degrees is 1.3 degrees (3σ) for the particular sun sensor proposed for the Advanced Planetary Probe. For other values of ϕ in the range of 5 deg $\leq \phi \leq$ 90 deg the azimuth error is given approximately by

$$\epsilon_a = 0.92 \frac{\sin 20 \text{ deg}}{\sin \phi} = \frac{0.314}{\sin \phi} \text{ degrees}$$

Values of ϵ_a for ϕ varying from 10 to 90 degrees are given in Table 4-4.

The control system logic is assumed to introduce a 3σ timing error of 0.1 percent. Opening and closing times for a typical solenoid valve are functions of the input voltage. For a regulation of ± 5 percent, an

Table 4-4. Azimuth Errors

ϕ	ϵ_a
degrees	degrees
10	1.80
20	0.92
30	0.63
40	0.49
50	0.410
60	0.363
70	0.334
80	0.318
90	0.314

uncertainty of 2 milliseconds is assumed. The equivalent angular error for a nominal spin speed of 5 rpm is 0.06 degree.

Different pressures and temperatures will cause uncertainties in the thrust rise and decay times, which are estimated to be of the order of 1 millisecond. The corresponding angular error for a nominal spin speed of 5 rpm is 0.03 degree.

Precessional motions can be analyzed approximately by assuming small angles and projecting the arcs described by a unit vector coinciding with the momentum vector on a plane perpendicular to the initial orientation of this unit vector. The geometry of the process is illustrated in Figure 4-21. Here the x-axis represents the desired direction of precession, F_1 is the desired direction for the thrust vector corresponding to the first pulse, F_1' is the actual direction of this vector due to an error ϵ_{CT1} in the center-of-thrust position. As a consequence of the torque produced by F_1', the angular momentum vector is precessed $\frac{\Delta\theta}{2}$ in the direction x'. The cross-axis precession due to the first pulse is

$$\epsilon_1 = \frac{\Delta\theta}{2} \sin \epsilon_{CT1} \cong \frac{\Delta\theta}{2} \epsilon_{CT1}$$

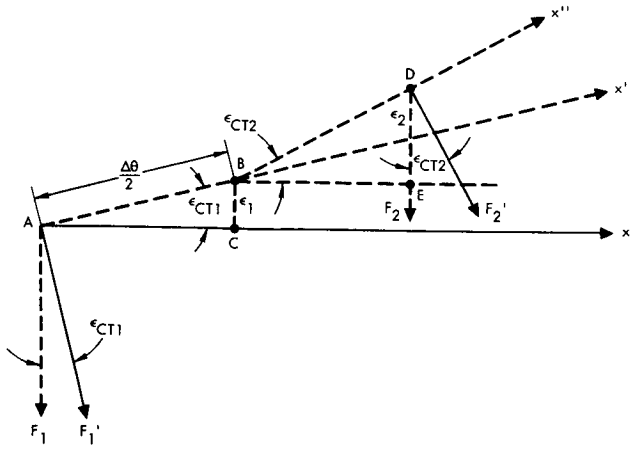

Figure 4-21. Cross Axis Precession

Of all the errors contributing to ϵ_{CT1} the most significant are the mechanical misalignment and the null plane uncertainties (of the sun sensor). Thus

$$\epsilon_{CT1} = \left[\left(\frac{0.5}{57.3} \right)^2 + \left(\frac{\epsilon_a}{57.3} \right)^2 \right]^{1/2} \text{rad} = \left(0.76 + \frac{0.3}{\sin^2 \phi} \right)^{1/2} 10^{-2} \text{ rad}$$

If the null plane error were zero the second pulse would be fired automatically by the logic system to give a thrust vector F_2 parallel to F_1. As a consequence of an error ϵ_{CT2} in the center of thrust the resulting precession of the angular momentum vector will be $\frac{\Delta\theta}{2}$ in the direction x'', perpendicular to F_2'. Consequently, the cross-axis precession due to the second pulse will be

$$\epsilon_2 = \frac{\Delta\theta}{2} \sin \epsilon_{CT2} \cong \frac{\Delta\theta}{2} \epsilon_{CT2}$$

The sources of error contributing to ϵ_{CT2} are the null plane uncertainty of the sun sensor and the mechanical misalignment of the sun sensor with respect to the second nozzle. Therefore

$$\epsilon_{CT2} = \left(0.76 + \frac{0.3}{\sin^2 \phi} \right)^{1/2} 10^{-2} \text{ rad}$$

The total cross-axis precession error will be

$$\epsilon_t = \left(\epsilon_1^2 + \epsilon_2^2 \right)^{1/2} = \frac{\Delta\theta}{2} \left(1.52 + \frac{0.6}{\sin^2 \phi} \right)^{1/2} 10^{-2}$$

Expressing this error in percent of the step size:

$$\frac{\epsilon_t}{\Delta\theta} = 1/2 \left(1.52 + \frac{0.6}{\sin^2 \phi} \right)^{1/2}$$

The corresponding values of $\epsilon_t/\Delta\theta$ as a function of ϕ are given in Table 4-5. Accumulation of errors due to cross-axis precession does not occur necessarily on a strictly additive basis since the trajectory described by the spin axis on the unit sphere centered on the spacecraft center of mass will be a pursuit curve (with systematic errors) aimed at the intersection of the sun line with this sphere.

Table 4-5. Cross-Axis Precession Errors

ϕ	$\frac{\epsilon_t}{\Delta\theta}$
degrees	%
10	2.32
20	1.29
30	0.98
40	0.86
50	0.795
60	0.765
70	0.74
80	0.73
90	0.725

4.3.3.2 Coning About the Sun Line

Coning about the sun line is accomplished by precession at 90 degrees with respect to the plane determined by the spin axis and the sun. The errors with which this precession is accomplished are equal to the values determined for precession in the sun plane, i.e., 1.44 percent on

the desired plane and as per Table 4-5 on the transverse plane. Cross axis precession will result in changes in the angle ϕ. In this case the error accumulation is additive.

4.3.4 Error Analysis of the Pneumatic System

The purpose of this analysis is to establish the feasibility of predicting and/or measuring with ± 1 percent accuracy the level of pneumatic thrust used in the open loop attitude control of the spacecraft for midcourse maneuver orientation. This result has been used in analysis of attitude errors in Section 4.3.2.

The thrust generated by an expansion nozzle is basically a function of the pressure directly upstream of the nozzle. The governing equation for thrust is

$$F = C_D C_F C_L p_1 A$$

where

F = generated thrust, lb

C_D = nozzle discharge coefficient, dimensionless

C_F = thrust coefficient, dimensionless

C_L = thrust correlation factor, dimensionless

p_1 = nozzle inlet pressure, psia

A = nozzle thrust area, in^2

Nozzle discharge coefficient is the familiar correction factor for orifices which arise due to the vena contracta effect. It is assumed that this factor remains essentially constant for the narrow range of flow rates which will be experienced. The thrust correction factor is basically a function of nozzle geometry and arises due to the departure from ideal of the gas expansion process. The basic equation for the thrust coefficient is:

$$C_F = \sqrt{\frac{2k^2}{k-1}\left[\frac{2}{k+1}\right]^{\frac{k+1}{k-1}}\left[1-\left(\frac{p_2}{p_1}\right)^{\frac{k-1}{k}}\right]} + \frac{p_2 - p_3}{p_1} \times \frac{A_2}{A}$$

where

k = ratio of gas specific heats, dimensionless

p_2 = pressure at the nozzle exit, psia

p_3 = ambient pressure, psia

A_2 = nozzle exit area, in^2

Over the inlet gas temperature range considered for this analysis, -20 to +90 °F, changes in k will have a negligible effect on C_F. Nozzle exit pressure will remain essentially constant since it is a function only of the expansion ratio, A_2/A, and the inlet pressure. Therefore, for all practical purposes, it can be assumed that thrust will be strictly a function of pressure directly upstream of the nozzle. Using a nozzle whose thrust is sufficiently accurately calibrated, it is thus possible to predict the thrust level if the nozzle inlet pressure is known.

Figure 4-22 is a schematic of the proposed pneumatic assembly. Nozzle pressure will be influenced by the following effects:

- The ability of the pressure regulator to maintain the required pressure.
- The pressure drop across the tubing leading from the regulator to the solenoid valve.
- The pressure drop across the solenoid valve.

Each of these effects will be discussed.

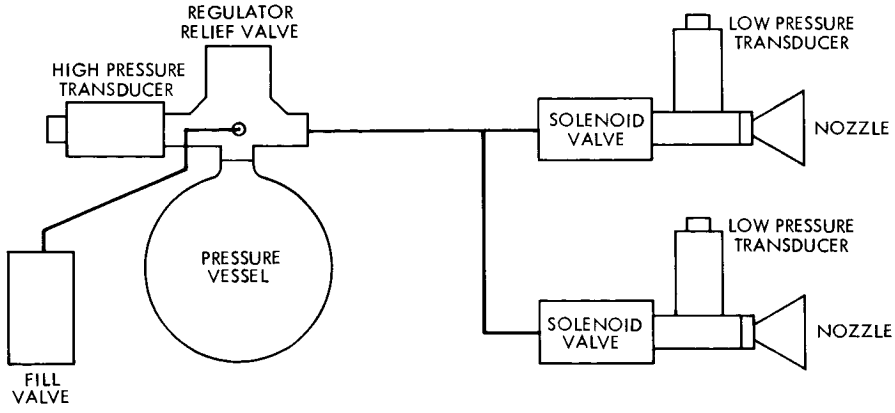

Figure 4-22. Pneumatic Assembly Schematic

4.3.4.1 Pressure Regulation

The ability of a regulator to maintain a desired pressure is affected by the inlet pressure range, the flow range, the temperature range, and the system dynamics. It will be assumed that system dynamics can be properly adjusted so that no perceptible oscillations in pressure occur in the steady state condition, that the pressure build-up and delay times are a small percentage of the total pulse duration, and that the time required to reach a stabilization pressure is repeatable and a small percentage of the total pulse duration. These assumptions are considered valid based upon the experience gained on previous programs.

As an example of the accuracy of regulation obtainable with an off-the-shelf unit, the regulation accuracy of a Pioneer regulator will be presented. This unit is identical with the OGO regulator which was developed with a relatively wide regulation band because of the noncritical nature of the thrust level on that program.

The following is a list of parameters pertinent to the midcourse orientation maneuver:

w_{tot} = total weight of stored gas, 6.0 lb

p_{max} = maximum storage pressure, 4000 psi

F = nozzle thrust, 0.12 lb

t_f = thrust pulse duration, 2.0 sec

ω_s = spacecraft spin speed, 5.0 rpm

n = maximum number of pulses required, 120 (one way)

k = ratio of specific heats; for nitrogen, $k = 1.40$

In addition, the temperature of the pneumatic assembly will be controlled within 30 to 90 °F under nonoperative conditions.

Assuming a specific impulse for nitrogen of 70 seconds, the flow rate is:

$$\dot{w} = \frac{F}{I_{sp}} = \frac{0.12}{70} = 0.00171 \text{ lb/sec}$$

For 120 pulses, the maximum weight of gas required for orientation is:

$$w_o = \dot{w}t_f n = (0.00171)(2.0)(120) = 0.410 \text{ lb}$$

This gas weight represents a change of storage pressure of the magnitude:

$$\Delta p = \frac{w_o}{w_{tot}} p_{max} = \frac{0.410}{6.0} \times 4000 = 273 \text{ psi}$$

Assuming adiabatic expansion of the stored gas during the orientation maneuver, the gas temperature, T, will change according to the following relationship:

$$T_2 = T_1 \left(\frac{p_2}{p_1}\right)^{\frac{k-1}{k}}$$

Taking a conservative approach, it is assumed that the temperature of the regulator and the pressure vessel will be the same as that of the gas. The minimum storage pressure at the time of the midcourse correction maneuver is assumed to be 3000 psi. The minimum temperature ratio will then be:

$$\frac{T_2}{T_1} = \left(\frac{2740}{3000}\right)^{0.286} = 0.9746$$

Assuming a maximum operating temperature of 90 °F, the maximum temperature drop is:

$$\Delta T = 550(1 - 0.9746) = 14 \text{ °F}$$

In summary:

- Operating temperature range of the regulator = 90 - 30 + 14 = 74 °F
- Variation in inlet pressure during the midcourse correction maneuver = 273 psi
- Gas flow rate = 0.00171 lb/sec

Figures 4-23 and 4-24 are plots of the regulation performance of the Pioneer regulator as a function of both inlet pressure and flow for temperatures of 0 and 110 °F. A flow of 0.0016 lb/sec shall be used for

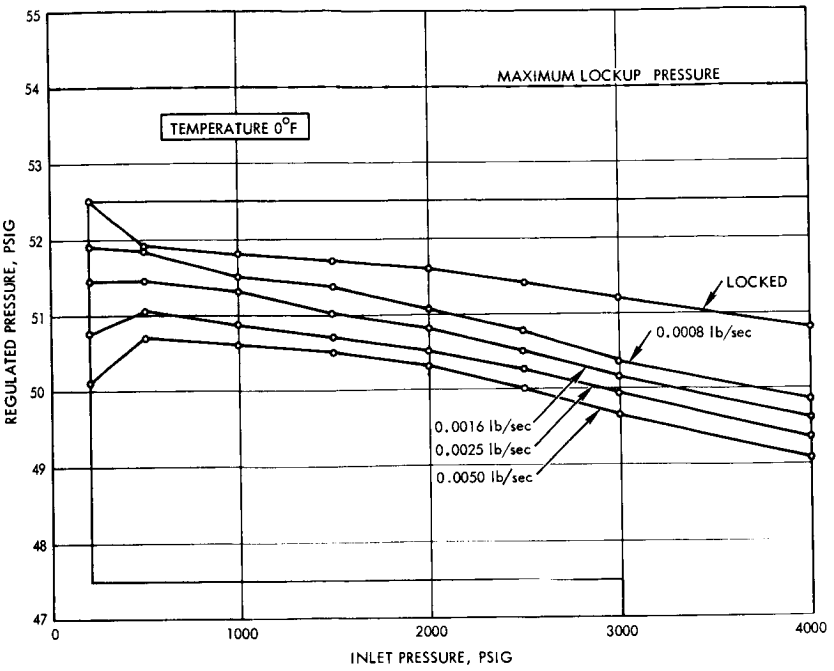

Figure 4-23. Characteristics of Pioneer Pressure Relief Valve

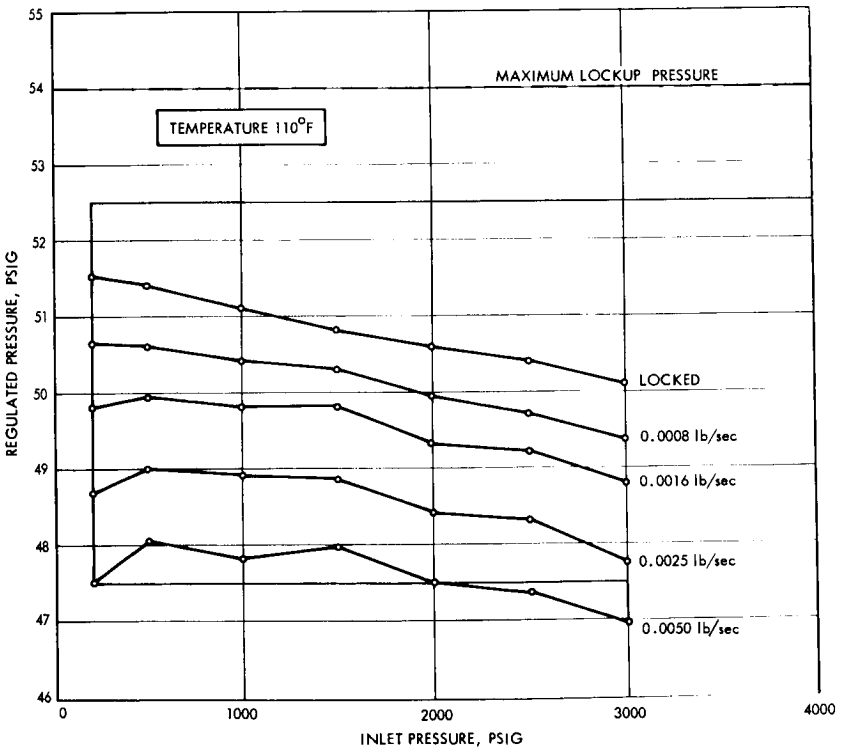

Figure 4-24. Characteristics of Pioneer Pressure Regulator-Relief Valve

the purposes of this example. The figures show that the regulation pressure changes by approximately 0.3 psi due to a change in inlet pressure from 3000 to 2700 psi corresponding to the change which would occur during the orientation maneuver. The regulation pressure changes by approximately 1.4 psi due to a 110 °F change in temperature within the 2700 to 3000 psi range of inlet pressures. The percentage of regulation is therefore:

$$\frac{0.3 + 1.4}{(2)\ (50.0)} \times 100 = \pm 1.7 \text{ percent}$$

This example shows that with an off-the-shelf unit not designed for this type of application, regulation pressure can be controlled to ± 1.7 percent.

Sterer Engineering, the vendor for this unit, was consulted with regard to the pressure regulation problem. Based upon their experience with other regulator designs requiring precise accuracy, they advised that a regulation accuracy of ± 0.50 percent could be attained with this style unit incorporating the following modifications:

a) Reduction in the size of the main seat. The regulator is not balanced against changes in inlet pressure; therefore, a reduction in the magnitude of the unbalance area will make the unit less sensitive to inlet pressure changes.

b) Redesign the reference spring using N_1 -Span C material in place of Inconel X. N_1 -Span C has a torsional modulus which is relatively insensitive to changes in temperature. The change in spring modulus is the basic source of pressure shift due to temperature change.

c) Increase the size of the sensing area. This change would provide higher driving forces with which to overcome friction and obtain higher gain.

4.3.4.2 Pressure Drop Across Low Pressure Tubing

Using 5/16 inch OD tubing, it can be shown that the pressure drop across a 3 foot length will be less than 0.10 psi. Assuming a variation in this drop of ± 10.0 percent due to changes in gas temperature, this amounts to a total variation at the nozzle of

$$\frac{0.01}{(2)\ (50)} \times 100 = \pm 0.01 \text{ percent}$$

4.3.4.3 Pressure Drop Across the Solenoid Valve

The solenoid valve is the major source of pressure drop in the system. The solenoid valve used on OGO has a drop of approximately 6.5 psi at 0.00171 lb/sec. It is recommended that this unit be modified to give the lowest practical pressure drop. The majority of the drop in the valve takes place across the seat and is analogous to orifice flow. For constant supply pressure, variations in orifice pressure drop are a function of temperature. Assuming a drop of 0.5 psi at 0 °F, a temperature of 100 °F will produce a drop of approximately 0.6 psi. This error is then

$$\frac{0.10}{(2)\ (50)} \times 100 = \pm 0.10 \text{ percent}$$

4.3.4.4 Calibration of Nozzle Thrust

A servoed force balance thrust measuring device was designed and built by TRW for the advanced Vela which can measure thrust levels of 0.10 pound magnitude within ± 0.50 percent accuracy. The major source of error in this device is instability or hunting about the null position. It is expected that with some development effort this uncertainty can be halved by eliminating the instability.

4.3.4.5 Summary

Regulator	± 0.50 percent
Line drop	± 0.01
Solenoid valve drop	± 0.10
Nozzle calibration	± 0.25
Sum total	± 0.86 percent

Thus it appears possible to meet the desired accuracy of ± 1.0 percent by proper design of the system within the present state of the art.

4. 4 EARTH POINTING

One of the basic objectives of the attitude control subsystem is to point the body-fixed paraboloidal antenna at the earth, maintaining the downlink gain within 1 db of the maximum or boresight gain. For a 16-foot paraboloid, this requirement is equivalent to a maximum pointing error on the order of 0. 5 degree. The logical choice to satisfy this requirement is a closed-loop precession control system using the earth as a reference body. Optical sensors are not adequate for this application because of the range of distances over which the system must operate. The only practical alternative available to provide antenna pointing with this degree of accuracy is the use of an RF angle tracking system. There are two techniques for angular error sensing which could be used in this particular application: simultaneous lobing and conical scanning. Conical scanning is preferred for the following reasons:

- The spacecraft spinning motion automatically provides conical scan of the antenna beam if the feed is fixed off-center.
- Only one receiver channel is required in the conical scan mode as compared to two channels for simultaneous lobing.
- Variations in individual receiver characteristics would cause an angular bias in the simultaneous lobing mode.
- Acquisition and fine pointing can be implemented in the conical scan mode by means of one or two antennas (high-gain paraboloid antenna and helix antenna). In the simultaneous lobing mode one more antenna (a second helix antenna) is needed to provide earth acquisition.

Three alternate ways of mechanizing the conical scan system were considered:

a) Use of a helix antenna with a 25 degree beamwidth for both earth acquisition and fine pointing

b) Use of two separate antennas for conical scanning exclusively: the helix for acquisition and a 4 foot paraboloid for fine pointing

c) Use of the high gain paraboloid antenna for fine pointing as well as telemetry and the helix antenna for acquisition

The first approach was analyzed in considerable detail because it appeared to be simpler. The basic problem encountered was the signal processing required to reduce the errors produced by thermal noise to a tolerable level. The mechanization of appropriate filtering devices is complicated by the low scan frequency, which is of the order of 1/12 cps. In addition, this frequency will vary during the mission and consequently the center frequency of the filter must be variable to accommodate these changes. Two types of mechanizations were considered: a phase-locked loop and a digital bandpass filter with variable center frequency. A detailed analysis of these two devices is given in Appendix C.

The second approach is characterized by the use of separate antennas for each function. This results in adequate performance without any sophisticated signal processing, but the weight penalty and the mechanical complexity involved make this approach less appealing.

Approach (c) has the advantage of not requiring an additional antenna for fine pointing. The paraboloid can be used for this purpose if the beam is offset with respect to the spin axis. This is not desirable from the communications viewpoint because of the resulting decrease in downlink gain. The problem can be avoided by mechanically offsetting the antenna feed from the centerline before the fine pointing control system starts to operate. After fine pointing corrections have been performed the feed is returned to the center line and communications can proceed without any loss of gain. Actually, adequate conical scan modulation could be achieved with very small beam offsets and a fixed feed. This appeared attractive until it was recognized that small boresight errors would drastically change the gain of the system, leading to great variability in the deadzone size. A deadzone near null is required to avoid wasting propellant due to noise.

The first approach was discarded because of the complexity of the signal processing required to remove noise. The second approach was eliminated because of its weight penalty and mechanical complexity. The third method was adopted because of the following reasons:

- Errors produced by noise are small as a result of the large antenna gain

- Because of the large gain, the operating range of the system can be extended beyond Jupiter distances without significant deterioration of performance.
- Very simple electronics are required to develop triggering signals for the attitude control system.
- No additional antennas are required for fine pointing.
- The system is insensitive to spin rate variations.

Mechanical feed displacement can be accomplished by means of a flexure joint and a two-position actuating system. A detailed description of the proposed assembly is given in Appendix D. A backup pyrotechnic device insures that in case of failure the conical scan mode can be selected.

In this section the implementation of the closed-loop earth-pointing system is discussed. Errors produced by receiver thermal noise are analyzed and improvements feasible by using different types of antennas or resorting to filtering are evaluated.

4. 4. 1 The Conical-Scan System

The conical-scan attitude control system is represented in Figure 4-25 in block diagram form. The conical-scan antenna rotates with constant angular velocity ω_s. The radiation pattern of this antenna is offset with respect to the spin axis of the spacecraft. The RF carrier from the earth, $e_c(t)$, is modulated in amplitude by the scan and the resulting modulated signal to the receiver is $e_R(t)$. The receiver is represented by a variable gain amplifier to take into consideration the AGC. To simplify the analysis, receiver noise is assumed to be generated at the input to the first amplifier stage. The modulation envelope is recovered in the synchronous demodulator, and after filtering this signal is used to develop trigger pulses for the pneumatic thrusting system. The final result will be a stepwise precession of the spin axis until the error is reduced to a value inside the specified deadzone region. The noise affects the accuracy of the determination of the desired direction of motion, and near null noise errors dictate the deadzone amplitude required to minimize gas waste.

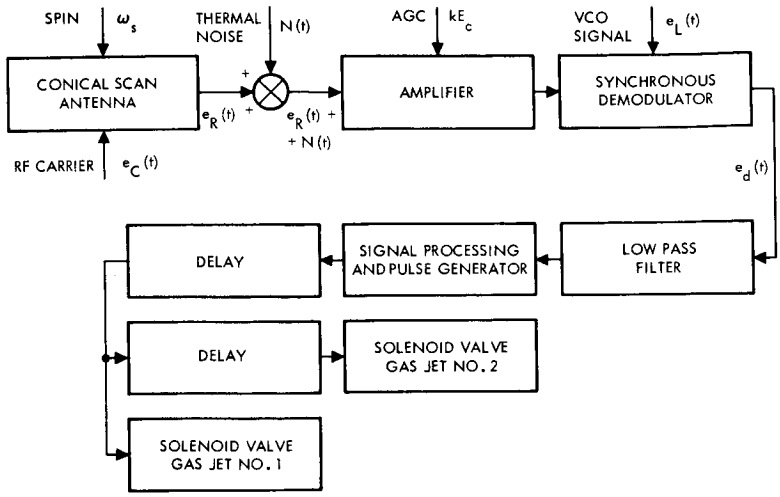

Figure 4-25. Block Diagram of the Conical Scan Attitude Control System

Assuming the spacecraft is a symmetric body rotating about the axis of maximum inertia (spin axis), the geometry of the conical-scan process is as shown in Figure 4-26. The z-axis coincides with the spin axis; the y-axis is orthogonal to it and is contained in the plane determined by the spin axis and a given inertial reference point. The antenna is assumed to have a circularly symmetric radiation pattern whose axis of symmetry is inclined α degrees with respect to the spin axis. The spacecraft-to-earth line is called the target axis, and the angle between it and the spin axis is the pointing error ϵ. The plane containing the spin and beam axes rotates with constant angular velocity ω_s, and the angle between this plane and the reference plane y-z is then $\phi = \omega_s t$.

Assuming the antenna pattern is gaussian for small pointing errors, if the received carrier amplitude is $\sqrt{2}\, E_c$ when the beam and target axes coincide, then with a pointing error ϵ the received signal will be

$$e_R(t) = \sqrt{2}\, E_c e^{-\nu^2(\alpha^2+\epsilon^2)} I_o(2\nu^2\alpha\epsilon) \cdot \left\{ 1 + \sum_{n=1}^{\infty} m_n(\epsilon) \cos\left[n(\omega_s t - \psi)\right] \right\} \cos \omega_c t$$

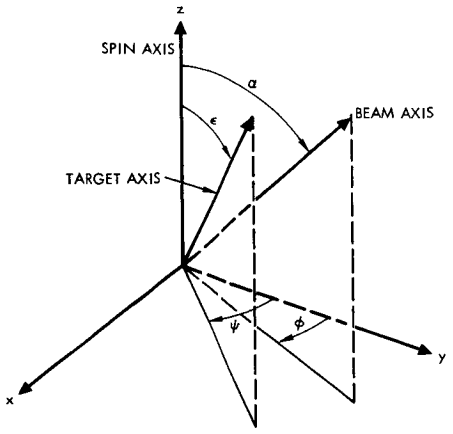

Figure 4-26. Geometry of the Conical Scan Process

in which:

$$\nu = \frac{70}{\text{BW [deg]}}$$

BW = half-power beamwidth

α = squint angle; usually, the optimum α is

$$\alpha \cong \frac{1}{2}\text{BW [rad]} = \frac{\text{BW [deg]}}{114.6}$$

Unless otherwise indicated, this value will be assumed in the following calculations

$m_n(\epsilon)$ = modulation index for the nth harmonic

$$= 2\,\frac{I_n(2\nu^2\alpha\epsilon)}{I_o(2\nu^2\alpha\epsilon)}$$

ω_c = carrier angular frequency

For small values of the pointing error ϵ, these equations reduce to

$$e_R(t) \cong \sqrt{2}\,E_c\,e^{-\nu^2\alpha^2}\left[1 + m_1(\epsilon)\cos(\omega_s t - \psi)\right]\cos\omega_c t$$

$$m_1(\epsilon) \cong 2\,I_1(2\nu^2\alpha\epsilon)$$

The receiver has a variable gain $A = A(E_c)$ due to AGC. The signal input to the synchronous demodulator will be $Ae_R(t)$. Consequently, the demodulator output signal will be

$$e_d(t) = 2AE_cE_L e^{-\nu^2\alpha^2}\left[1 + m_1(\epsilon)\cos(\omega_s t - \psi)\right]$$

where E_L is the RMS value of the VCO signal. In this analysis, the filter following the synchronous demodulator is assumed to have unity transmittance throughout the passband and zero transmittance elsewhere.

The conical-scan system signal, represented in Figure 4-27, may be assumed to be sinusoidal, i. e.

$$e_s = \sqrt{2}\,E_s \cos(\omega_s t - \psi)$$

where E_s is the RMS value of the AC component of the signal.

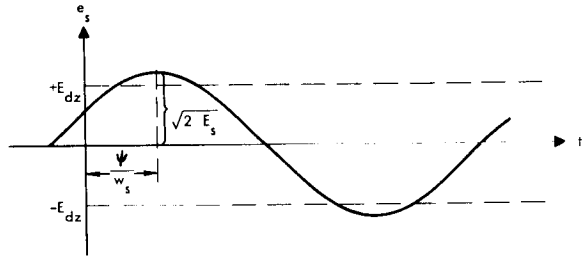

Figure 4-27. Conical Scan Output Signal for Small Error Angles

Assuming $E_L = 1$,

$$E_s = \sqrt{2}\,AE_c e^{-\nu^2\alpha^2} I_1(2\nu^2\alpha\epsilon)$$

For small values of ϵ this reduces to

$$E_s = \sqrt{2}\,E_c A e^{-\nu^2\alpha^2}\nu^2\alpha\epsilon$$

The noise mean square value at the filter output is

$$E_n^2 = \Phi B_N A^2$$

where

Φ = one-sided power spectral density of uncorrelated gaussian noise

B_N = noise bandwidth = filter bandwidth

Finally, the signal-to-noise ratio at the output of the low-pass filter is

$$\left(\frac{S}{N}\right)_f = \frac{2E_c^2}{\Phi B_N}\left(\nu^2 \alpha e^{-\nu^2\alpha^2}\epsilon\right)^2 = 2\left(\frac{S}{N}\right)_c \left(\nu^2 \alpha e^{-\nu^2\alpha^2}\right)^2 \epsilon^2$$

where $(S/N)_c$ is the carrier signal-to-noise power ratio obtained with maximum antenna gain.

To obtain a set of signal-to-noise-ratio curves with the antenna beamwidth as a variable parameter, paraboloidal antennas were assumed. The gain in terms of antenna beamwidth is given by

$$G = 2\pi\left(\frac{70}{BW}\right)^2$$

where BW is the half-power beamwidth in degrees. This expression is plotted in Figure 4-28. The signal power at Jupiter was assumed to be -142 dbm. Therefore, the received power is given by

$$P_R(\text{dbm}) = G(\text{db}) - 142$$

In the calculations that follow an attenuation of 3 db was introduced to take into account incidental losses due to interferences produced by surrounding bodies, attenuation in lines, and departure from the ideal conditions assumed in the analysis. The receiver noise power spectral density and the filter bandwidth were assumed to be -164 dbm/Hz and 1 Hz, respectively. Thus the noise mean square power is -164 dbm. With these values the signal-to-noise ratio was computed for fixed values of the pointing error with the beamwidth as a variable parameter. The resulting curves are shown in Figure 4-29. These curves will be used later to derive criteria for the selection of antenna beamwidth, signal processing schemes, and deadzone amplitudes. Before discussing these subjects, a brief review of the dynamics of the process of fine attitude control will be made in the following section.

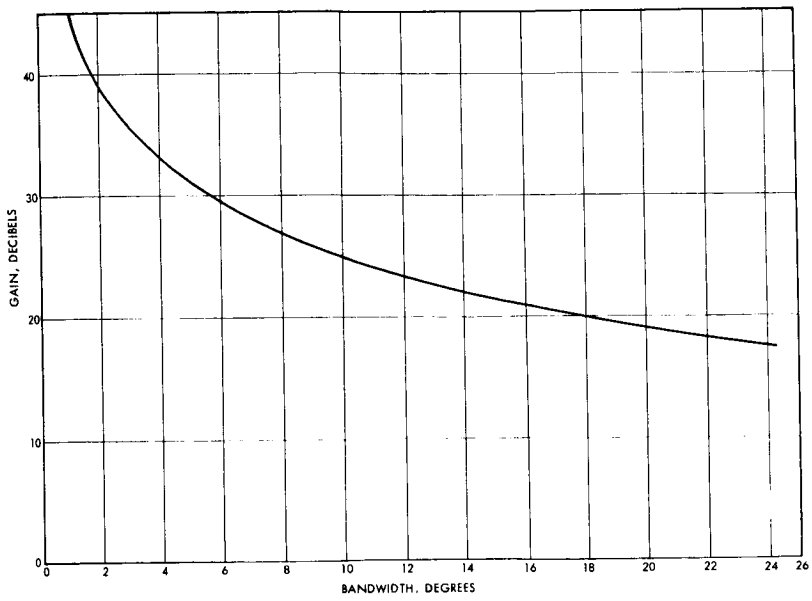

Figure 4-28. Antenna Gain Versus Beam Width

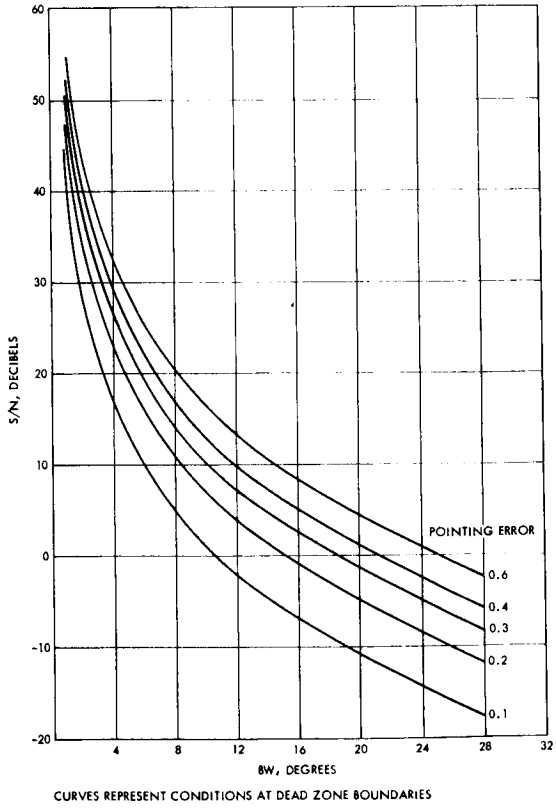

Figure 4-29. Signal-to-Ratio as the Input to the Attitude Control System Versus Beam Width

Summarizing, the attitude control subsystem will receive a signal from the communications subsystem that is a measure of the pointing error. For small values of this error the signal is almost sinusoidal, and its amplitude is proportional to the error amplitude. The maximum occurs when the beam and target axes are closest and in the same plane with the spin axis. The estimation problem consists in determining this maximum and the time at which it occurs. This is equivalent to the problem of determining the amplitude and phase of a sinusoidal signal in the presence of band-limiting gaussian noise. The peak amplitude will be compared to a deadzone. If in excess, control pulses will be commanded, dependent upon the estimated phase of the error. As long as the peak value of the conical-scan signal remains inside the deadzone, the control system will not respond. The phase measurement problem is discussed in Section 4. 4. 3 and criteria for the selection of the deadzone will be given in Section 4. 4. 4.

4. 4. 2 A Simplified Model of the Attitude Control Process

The spin axis of the spacecraft is precessed by means of a mass expulsion system which produces a discrete rotation $\Delta\theta$ of the angular momentum vector by firing a sequence of two-thrust impulses. Timing and geometry of these impulses are such that the residual wobble is negligible. This incremental precession can be accomplished only once every spin cycle. The process is illustrated schematically in Figure 4-30, where H_n represents the initial angular momentum vector, which is assumed to coincide with the spin axis. H represents the desired orientation for the spin axis, and the initial pointing error is ϵ_n. Rotation of the spin axis should take place on the plane π_n determined by H_n and H, which forms an angle ψ_n with respect to the reference plane ρ.

The signal obtained from the conical scan system would be as shown in Figure 4-27. For the purposes of the present discussion assume there is no delay between the occurrence of the first trigger pulse and the corresponding thrust pulse. Then, this trigger pulse could be generated when the conical scan signal reaches its maximum value. If there were no errors in the determination of the proper time for firing, the resulting rotation of the spin axis would be on π_n, and the final pointing error would be $\epsilon_n - \Delta\theta$.

Thermal noise will introduce errors in the process of determining the right time for firing. If the spin rate remains constant during the process, this timing error will be equivalent to an angular error $\Delta\psi_n$,

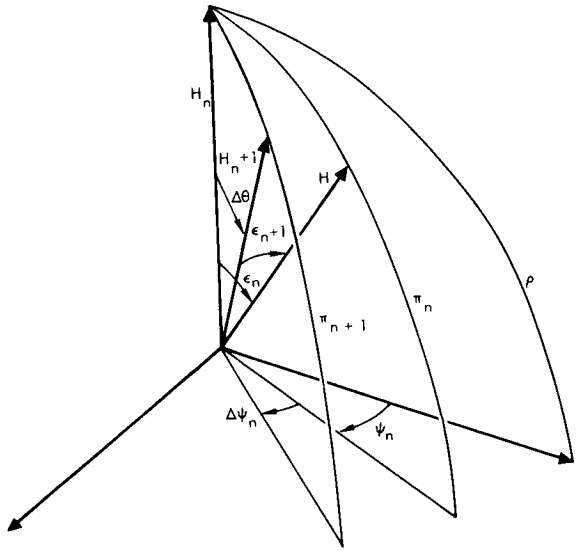

Figure 4-30. Discrete Attitude Control Process

and precession will be on the plane π_{n+1}. The resulting position of the spin axis will be H_{n+1}, and the pointing error will be ϵ_{n+1}.

For small angles, the problem can be formulated as shown in Figure 4-31. The following relationships are obtained:

$$\epsilon_{n+1}^2 = \epsilon_n^2 + \Delta\theta^2 - 2\Delta\theta\,\epsilon_n \cos\Delta\psi_n$$

$$\psi_{n+1} = \tan^{-1}\frac{\epsilon_n \sin\psi_n - \Delta\theta \sin(\psi_n + \Delta\psi_n)}{\epsilon_n \cos\psi_n - \Delta\theta \cos(\psi_n + \Delta\psi_n)}$$

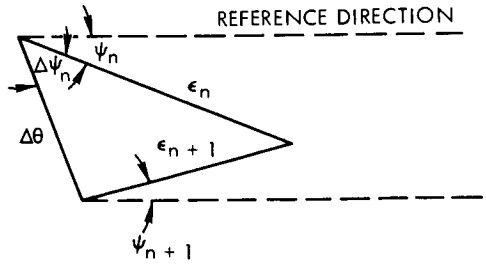

Figure 4-31. Small Angle Approximation

These recurrence relations describe a nonstationary semirandom walk process that starts with known values of ϵ_n and ψ_n and ends when the error signal becomes less than the threshold of the selected deadzone. Inside the deadzone there will be a finite probability due to the noise that the process starts again. The equivalent phase angle error $\Delta\psi_n$ is a nonstationary random variable whose probability distribution is a function of ϵ_n and the method used for estimating ψ_n. Figure 4-32 gives an example of a semirandom walk terminating inside the deadzone with a small probability of recurrence.

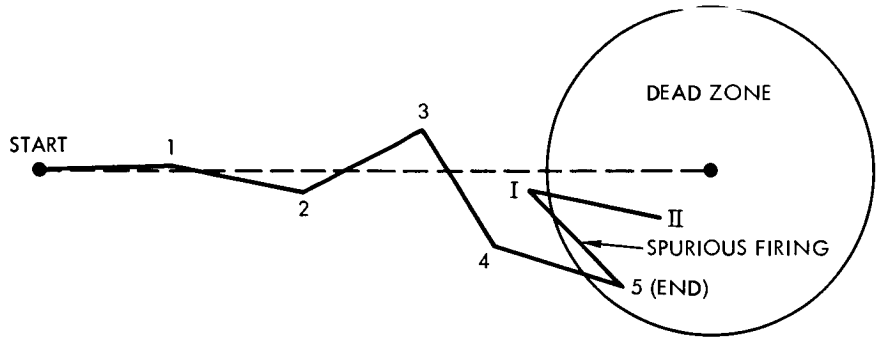

Figure 4-32. Example of Random Walk with Dead Zone Limiting

4.4.3 The Phase Measurement Problem

The problem of phase measurement will be considered first in the case of a narrowband random process.

The output signal from the conical scan system is

$$e(t) = e_s(t) + n(t)$$

where

$$e_s(t) = \sqrt{2}\, E_s \sin \omega_s t$$

and n(t) is gaussian noise with a small noise bandwidth as compared to the signal frequency. With this assumption, the noise random process can be expanded as follows:

$$n(t) = X(t) \sin \omega_s t + Y(t) \cos \omega_s t$$

where X(t) and Y(t) are independent random processes such that

$$\overline{n^2(t)} = \frac{1}{2}\overline{X^2(t)} + \frac{1}{2}\overline{Y^2(t)} = \overline{X^2(t)} = \overline{Y^2(t)}$$

The instantaneous phase measurement error will be given by

$$\tan \Delta\psi = \frac{Y(t)}{X(t) + \sqrt{2}\, E_s}$$

which for sufficiently large signal-to-noise ratios reduces to

$$\Delta\psi \cong \frac{Y(t)}{\sqrt{2}\, E_s}$$

The mean square value of this error is

$$\overline{(\Delta\psi)^2} = \frac{1}{2\left(\frac{S}{N}\right)}$$

where S/N is the signal-to-noise ratio at the input of the signal processing unit. This equation represents the effects of thermal noise only, regardless of the method used for measuring phase. Additional errors will be produced by the electronic systems, antennas, etc.

When the noise bandwidth is equal to or greater than the signal frequency, the analysis has to be made in particular for each signal processing scheme. The simplest approach consists of a zero-crossing detector and the associated electronics for measurement of phase with respect to an arbitrary reference and the generation of adequate triggering pulses. A fairly large signal-to-noise ratio is assumed so that noise effects can be analyzed in terms of the resulting shift of the zero-crossing points. The slope of a pure sinusoidal signal at its zero crossing points is

$$\dot{e}_s(o) = \sqrt{2}\, E_s\, \omega_s$$

In the neighborhood of a zero crossing the noise can be assumed to be constant. The composite signal at this point will be approximately sinusoidal and the zero crossing will be displaced a small interval Δt. For large signal-to-noise ratios the slope can be assumed invariant and the following expression will be approximately valid

$$\frac{n(o)}{\Delta t} = \sqrt{2}\, E_s\, \omega_s$$

where n(o) is the noise amplitude at the zero crossing. The corresponding angular error is $\Delta\psi = \omega_s \Delta t$, and finally

$$\overline{\Delta\psi^2} = \frac{\overline{n^2(o)}}{2E_s^2} = \frac{1}{2\left(\frac{S}{N}\right)}$$

which is identical to the previous expression for $\overline{\Delta\psi}^2$. This result proves that the angular errors are independent of the noise autocorrelation time for large signal-to-noise ratios.

The RMS value of the phase measurement error as a function of input signal-to-noise ratio is plotted in Figure 4-33.

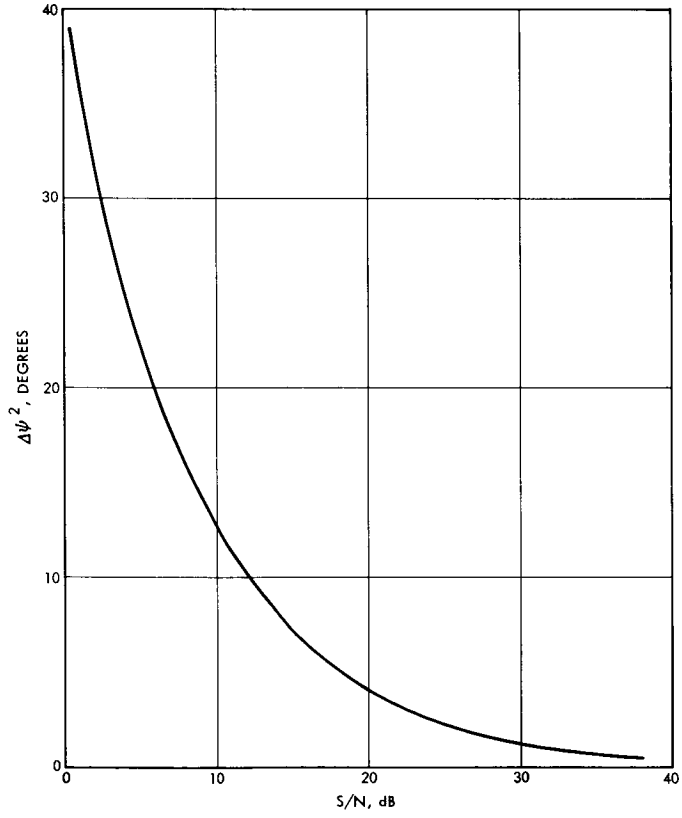

Figure 4-33. Phase Angle Error as a Function of Input Signal-to-Noise Ratio

4. 4. 4 The Amplitude Measurement Problem

Implementation of a deadzone requires measuring the peak value of the conical-scan error signal. This operation can be done easily by means of a level detector, but, due to the presence of noise, spurious

firings will occur with a frequency that is dependent on the signal-to-noise ratio. An approximate solution can be obtained by considering the case of narrowband gaussian noise when the signal-to-noise ratios are high. The output signal e(t) will be a quasisinusoidal signal of amplitude $\sqrt{2}$ E. Its RMS value is then

$$E = E_s \left(1 + \frac{N}{S}\right)^{1/2}$$

For small values of N/S

$$E \cong E_s \left(1 + \frac{N}{2S}\right)$$

and the RMS value of the differential is

$$\Delta E = \frac{N}{2S} E_s$$

For 99.7 percent probability of remaining inside the deadzone, the deadzone amplitude must be

$$E_{dz} = \sqrt{2}\, E_s \left(1 + \frac{3}{2\sqrt{2}} \frac{N}{S}\right)$$

Therefore, for a signal-to-noise ratio of 10 db, the deadzone amplitude must be approximately 10 percent greater than the value required in the absence of noise.

The case in which the noise bandwidth is the same order of magnitude of the signal frequency will not be considered here because, for the purposes of the present preliminary analysis, it is sufficient to extend to this case the conclusions derived for the narrowband process, which will define an upper bound for the required deadzone amplitude.

4.4.5 Signal Processing Requirements

The pointing accuracy requirements for the conical-scan system in the Advanced Planetary Probe are established by the needs of the communications subsystem. Errors are originated by thermal noise, mechanical misalignments, and boresight offset. In this section, signal processing requirements will be estimated for an RMS error of 0.2 degree due to thermal noise only.

The following assumptions are made:

- Main paraboloidal antenna beamwidth = 2 degrees
- Helix antenna beamwidth = 25 degrees
- Signal-to-noise ratios at the input to the ACS as per Figure 4-29

Two alternatives are considered:

- Utilization of the helix antenna for both acquisition and fine pointing
- Use of the main paraboloidal antenna for fine pointing and the helix antenna for acquisition with a deadzone of 1.2 degrees

For the first alternative, the signal-to-noise ratio at the input to the signal processing unit would be -9.3 db. A minimum of +10 db is required to maintain the phase angle error due to noise below 13 degrees, and the deadzone amplitude below 0.22 degree. Therefore, the signal processing system should be able to improve the signal-to-noise ratio by 19.3 db. A significant reduction of the noise bandwidth can be obtained by means of a phase-locked loop in place of the 1-Hz filter. The required bandwidth would be

$$10^{-1.93} \cong 0.012 \text{ Hz}$$

The second alternative results in the following signal-to-noise ratios:

Paraboloid: +35 db (0.2-degree error)

Helix: +6 db (1.2-degree error)

Therefore, with the paraboloid, the RMS angular jitter in ψ due to noise would be less than 1 degree (see Figure 4-33), but the penalty is a 3-db loss in downlink gain. A signal-to-noise ratio of +10 db could be satisfactory for closed-loop operation and, therefore, a reduction of the squint angle could be made to maximize the downlink antenna gain. A decrease of 25 db in the paraboloid's signal-to-noise ratio corresponds to a reduction of the term

$$\alpha\, e^{-\nu^2 \alpha^2}$$

by a factor of about 17.8. For α = BW/2 and BW = 2 degrees:

$$\alpha\, e^{-\nu^2\alpha^2} = \frac{1}{57.3}\, e^{-0.373} = 1.2 \times 10^{-2}$$

The desired value of α is obtained by solving the following transcendental equation:

$$\alpha\, e^{-1225\,\alpha^2} = 6.74 \times 10^{-4}$$

which gives

$$\alpha = 6.74 \times 10^{-4} \text{ rad} = 0.04 \text{ deg}$$

This result shows the significance of mechanical misalignments or bore-sighting errors on system performance.

The variation of signal to noise ratio and loss in downlink gain is shown in Figure 4-34. A squint angle of 0.1 degree gives a

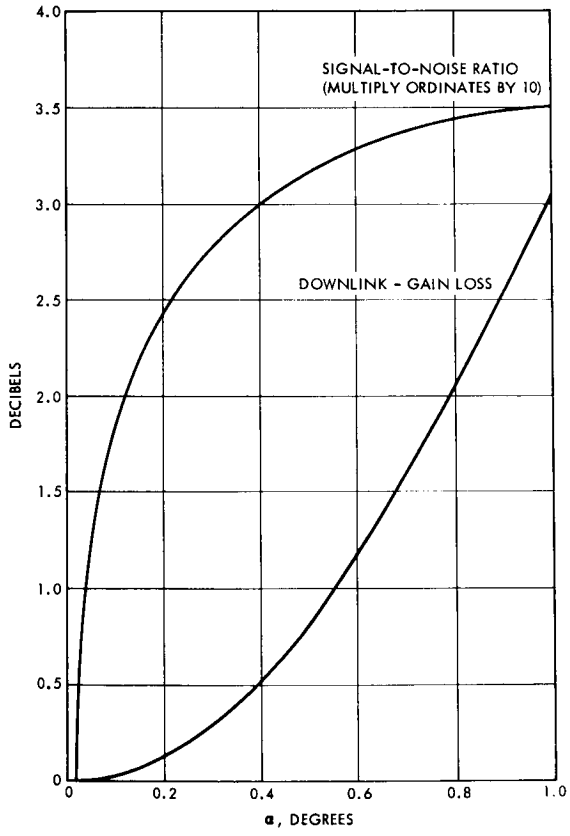

Figure 4-34. Signal-to-Noise Ratio and Downlink-Gain Loss as a Function of the Squint Angle

signal-to-noise ratio of 18.5 db, which would result in a phase error of less than 5 degrees and entails a downlink loss of less than 0.05 db. However, the achievable accuracy with which the beam can be aligned to this squint angle is probably on the order of ±0.1 degree, considering mechanical alignments, balancing, disk deployment repeatability, temperature effects, etc. Thus a squint angle of 0.1 ± 0.1 degree could lead to a variation of signal-to-noise ratio from zero to 24 db, a totally unacceptable state of affairs. On the other hand, if the squint angle corresponded to the -3 db point, an error of 0.1 degree would lead to a change of only 0.02 db in signal to noise ratio, and corresponding deadzone size, and is clearly acceptable. An error of 0.25 degree, however, would lead to a change of 1.5 db, which is only marginally acceptable.

Thus it is clear that a significant downlink loss must be accepted when using the high-gain antenna for fine tracking. Since fine tracking need be performed only about once per week near Jupiter, continuous degradation can be avoided by having a two-position feed, one position for fine tracking and the other for undegraded downlink performance. (The separation between the two positions is too small to allow the use of two separate feeds.)

Summarizing, expressions and curves have been obtained to evaluate the effects of receiver thermal noise on the performance of the conical-scan attitude control system for the Advanced Planetary Probe. The analysis has shown that the utilization of the main paraboloidal antenna for precise pointing control results in minimum signal processing requirements but entails a significant scan loss. This leads to the concept of a two position feed, an offset position for fine tracking and an on-axis position for undegraded downlink transmission.

4.4.6 Mechanization of a Two-Position Feed

This section describes a flexure method of mechanizing a two-position feed for the high-gain antenna. The two positions are: 1) on-axis and 2) one inch off axis. To minimize the power requirements the device should stay in either position without the continual application of power. Power should be used only to displace the device from one position to the other. In the case of failure of the actuating mechanism,

it is desirable to have the feed off-axis and accept some degradation of antenna performance.

In the proposed concept the metal coaxial cable leading to the feed is mounted on a flexure configuration as shown in Figure 4-35. Two stable states are obtained by making the horizontal flexure elements larger than the supporting brackets. As shown in Figure 4-36, a short section of the coaxial cable will be twisted when the feed is at any of the two end positions. A mounting bracket is provided to limit the length of cable under torsion to about 10 inches. The torques produced by the flexure assembly when the feed is at the extreme positions must be greater than the reaction torques developed by the coaxial cable.

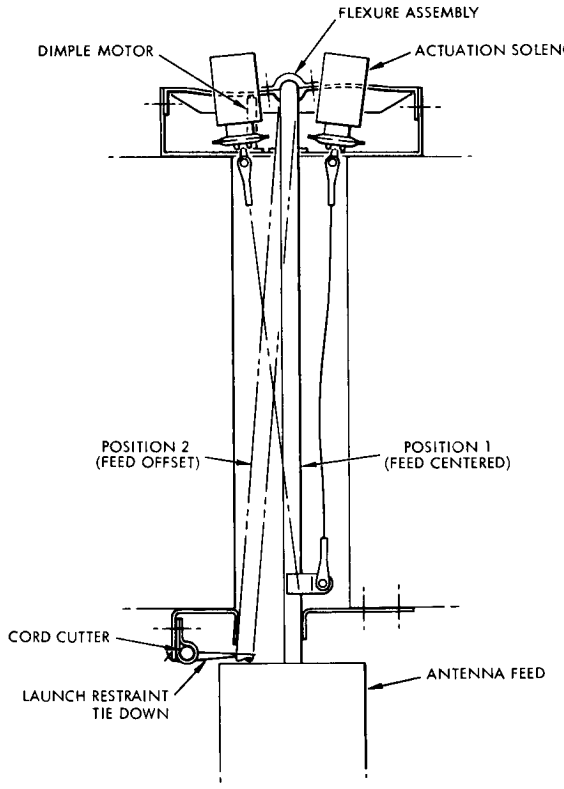

Figure 4-35. Feed Displacement Mechanism

Transitions from one position to the other are caused by an actuation system consisting of two solenoids. To decrease the stroke, the solenoids are mounted as shown in Figure 4-35. A short stroke has the advantage of permitting flexure mounting of the plunger and sealing of the

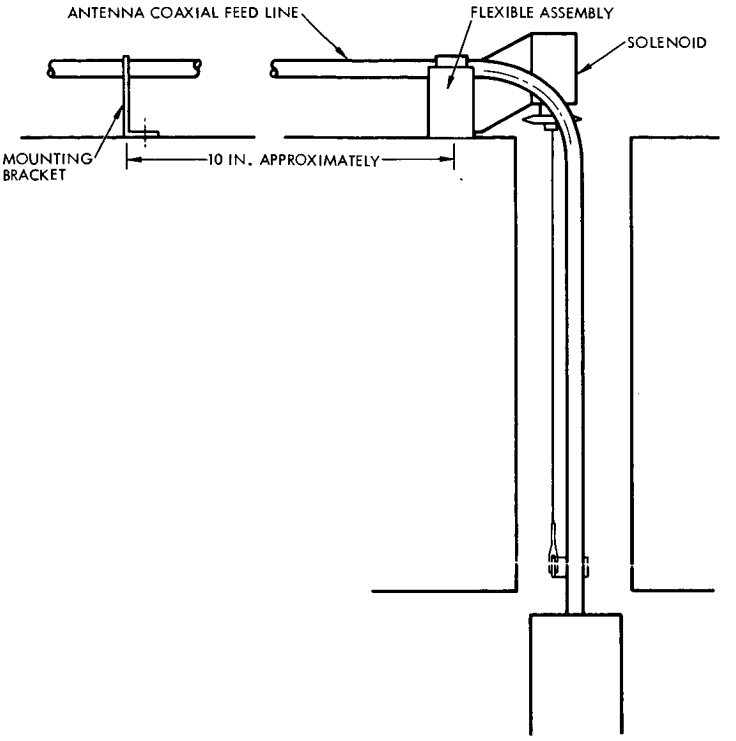

Figure 4-36. Side View of the Feed Displacement Mechanism

unit, which is desirable for the space environment. The actuation requirements can be satisfied by two 0.45-pound solenoids. At 18 volts and 1.95 amperes, a solenoid with a 10 percent duty rating and maximum on-time capability of 40 seconds has a useful work capability of 0.63 inch-pound, compared to an estimated theoretical requirement of 0.28 inch-pound. This additional capacity provides margin in the form of additional force or stroke or allowance for higher operating temperatures.

In case of failure of the solenoid system the feed would be displaced to the off-center position by means of the explosively operated dimple motor shown in Figure 4-37. During boost, the device would be tied off-center to withstand the vibration environment. An explosive cord cutter should be provided to set the feed free when needed for operation.

4.5 SPIN RATE SELECTION

As discussed in Section 2.1, an appropriate spin rate for thrust vector control of the TE-364-3 appears to be 60 rpm. Remaining problems are the final spin rate and intermediate spin rates during various deployment phases.

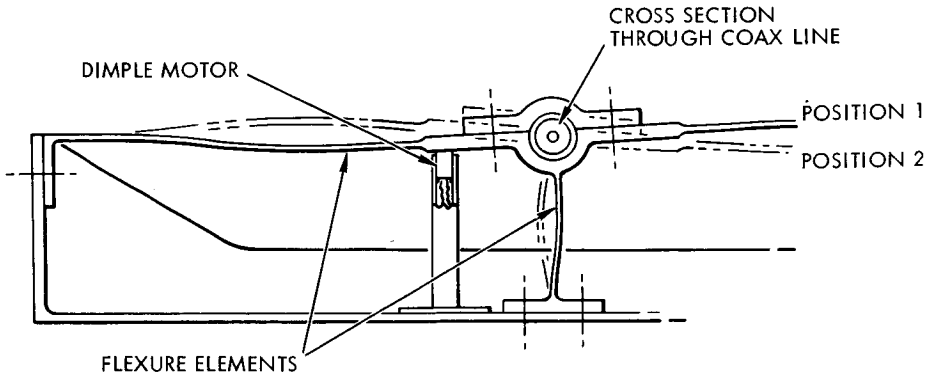

Figure 4-37. Flexure Assembly and Dimple Motor

The final spin rate is a compromise. Low spin rate is desired to:

- Reduce image smear for the TV system, doubling spin rate doubles optics aperture area for a given resolution since exposure time must be halved for a given amount of smear.
- Reduce attitude control gas requirements for reorientation and earth tracking.

High spin rate is desired to:

- Reduce drift rate arising from disturbance torques such as light pressure or meteorite impact.
- Reduce the despin accuracy necessary to achieve a given accuracy in the final spin rate.
- Reduce the percentage change in final spin rate resulting from unknown spin torques such as might arise from light pressure and spacecraft asymmetries. (Spin torques were found to be significant on Mariner in spite of the nominal symmetry.)

A final spin rate of 5 rpm was selected. Figure 4-38 shows earth-line rate and tracking rate required to compensate for light pressure torques. Figure 4-39 gives the vector sum of these rates versus time, and Figure 4-40 is a polar plot of the rates. These figures are based on data developed in Section 7. 4. Referring particularly to Figure 4-40, it is seen that light pressure torque effects dominate only for a brief period around 50 days from launch. This indicates that 5 rpm is a reasonable spin rate as far as DSIF utilization for attitude updating is concerned.

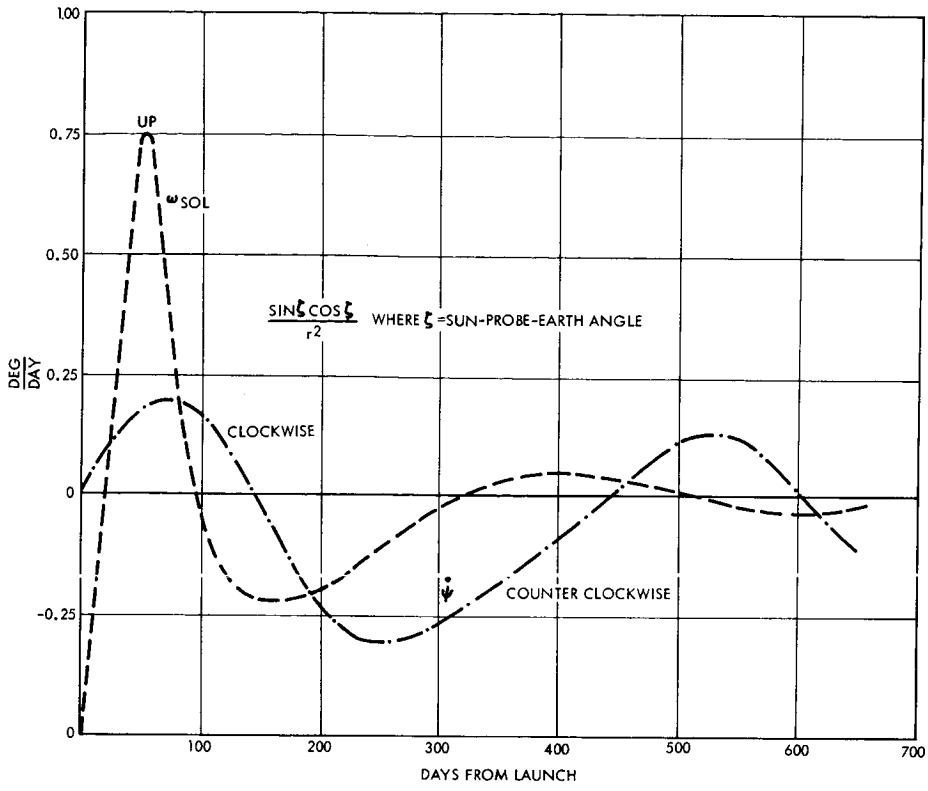

Figure 4-38. Earth Line Angular Rate and Tracking Rate Required to Compensate for Light Pressure Drift

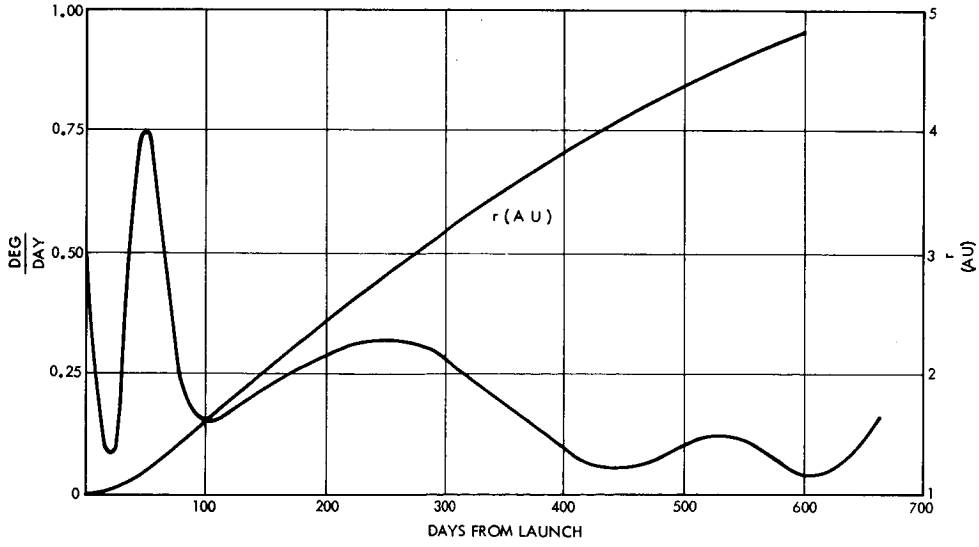

Figure 4-39. Magnitude of Required Tracking Rate Due to Both Earth Line Motion and Light Pressure Drift Rate

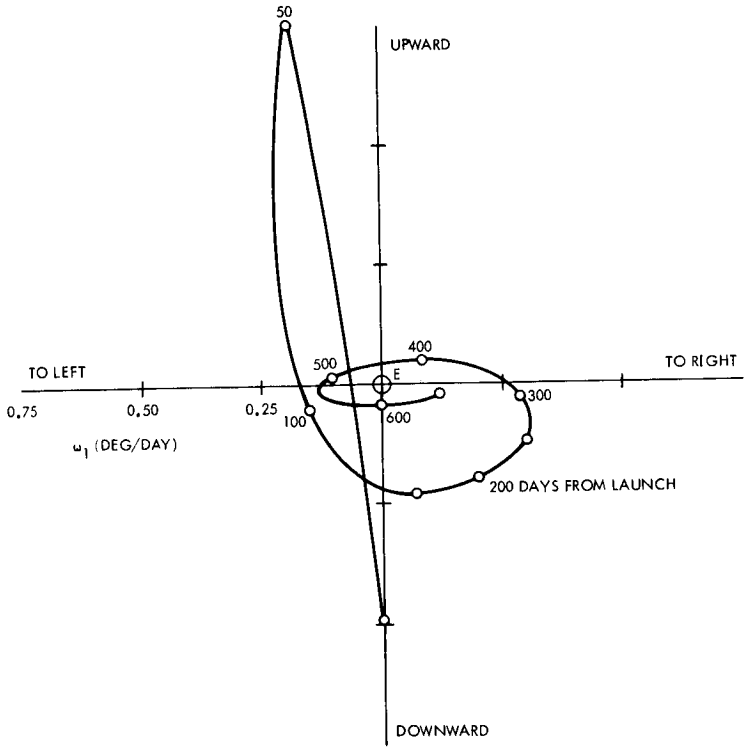

Figure 4-40. Polar Plot of Required Tracking Rate

The pointing error within which the conical scan will acquire is about 1 degree for the high-gain antenna and 10 degrees for the medium-gain antennas. Since the medium-gain antenna can always be used to start the acquisition process, the required interval between DSIF use for attitude updating can be as short as two weeks (near 50 days from launch) and extend to over six weeks later. On the other hand, if it is desired to keep within the angular acquisition range of high-gain antenna to minimize acquisition time, the updating periods vary from 1.3 days to about 20 days. Increasing the spin rate could increase these times for the period 30 to 60 days before launch, when light pressure effects dominate. However, increasing the spin rate does not seem warranted.

Section 6.1 in Volume I discusses roll rate requirements placed upon the spacecraft by the scientific instruments. The TV system places the dominant upper limit on roll rate, and it is shown that only with a TV tube of the sensitivity of a SEC vidicon can the TV experiment provide good quality data at spin rates as high as 5 rpm. A 500 line, 4-degree field of view system with 1 millisecond exposure time, however, is reasonable with the SEC vidicon, equalling the best earth-based resolution at about 100 Jupiter radii and giving a resolution (line pair spacing) of about 10 at one Jupiter radii. If the spin rate were quartered, this resolution could be about doubled; however, the stated performance seems reasonable for an early mission.

No model has yet been generated showing how a highly roll symmetric spacecraft such as we are discussing can have light pressure coupling into roll rate. Certainly the effect should be orders of magnitude less than that associated with the drift torques caused by a 16-foot earth-pointing antenna whose aperture is over 2 feet ahead of the center of gravity. Since the latter effect has a cumulative effect of the order of the momentum associated with 5 rpm, spin rate changes should be small.

The implementation of the attitude control conical scan system and science data gathering is such that a precise final spin rate is not required. As indicated in Sections 7.1 and 8.3, a two-step despin is desirable for deployment reasons. Since spin rate can be measured on the ground, the two-step procedure in which the first step is the larger, should allow an accuracy of 2 to 3 percent in the control of the final spin rate when that rate is 5 rpm. Actually, because of inertial changes during deployment, the first step removes 50 percent of the momentum and the second step, 50 percent of the remainder, leaving the momentum at 5 rpm about 1/4 of that at 60 rpm.

4.6 DATA HANDLING

The data requirements can be divided into three phases: cruise, encounter, and post encounter. Table 4-6 broadly summarizes the requirements during each of the phases. To minimize ground station

Table 4-6. Data Requirements

Data Source	Pre-Encounter Cruise Data Rates (bits/sec)		Encounter	Post-Encounter Cruise
	Nominal	High Resolution	Nominal	Nominal
Solar cosmic ray	24	48	--	24
Solar plasma	24	168	--	24
Magnetometer	24	72	72	24
Micrometeoroid	14	14	14	14
Radio propagation	8	24	(72*)	8
Galactic cosmic ray	8	16	8	8
Trapped radiation	--	--	40	--
Auroral	--	--	32	--
Infrared radiometer	--	--	100	--
TV	--	--	427**	stored data (as required)
Spacecraft engineering	8	--	8	8
Total	110	342	700	110

*During occultation only
**Not during occultation

requirements and to optimize bit rate as a function of range, 6 bit rates have been selected: 1400, 700, 512, 256, 128, and 8.

4.6.1 Design Considerations

There are three basic considerations in the design of the data handling system: system flexibility, ground station availability, and system reliability.

The primary requirement of the data handling system is to satisfy the experiment objectives, which calls for the provision of high resolution data as well as steady-state low resolution data. Because the key time in the mission is the encounter phase at Jupiter, at which time 700 bits/sec can be transmitted, high resolution data cannot be achieved in real time for every experiment. The TV system takes a sample of 1.5×10^6 bits in a millisecond and therefore some data storage is required. The SEC vidicon tube proposed provides short term storage itself. However, to gather a large number of pictures at a close range requires additional storage and subsequent readout of that stored data. Based on the considerations regarding the TV system discussed in Section 6.1 in Volume I, an appropriate photographic sequence has been developed in which one picture is taken every 10 minutes during the last five hours of encounter. This establishes a nominal data storage requirement on the order of 4.5×10^7 bits. In addition, about another 5×10^6 bits of storage will be required during the earth's occultation phase. Therefore, to achieve system flexibility our design approach is to exploit the data storage capability of the vidicon by providing a direct readout of the tube. This is used when pictures are taken infrequently and is done line by line using a small buffer core storage for each line. The buffer storage is then read out in real time. This real time mode is supplemented by providing a tape recorder for rapid picture taking.

Ground station availability is important not only in terms of cost and complexity, but, most important, in terms of time sharing the ground stations with other spacecraft. This problem of time sharing is accentuated by the fact that spacecraft acquisition time will probably be substantial at long communication ranges. Although we have assumed that ground stations will observe the encounter phase continuously, i.e., approximately 10 days, it is obvious that as little on-time as possible should be required during cruise phases. This time can be minimized by allowing little data to be transmitted or by using a stored mode coupled with a high transmitter bit rate. Because tape storage is required during the encounter phase, the tape storage mode is a

requirement during the cruise modes, thus reducing ground station time to about 8 percent of the data sample time.

For the long lifetime required of this mission, reliability is of great importance, and the introduction of tape recorders into the data handling system results in a reduced estimate of reliability. Therefore, two tape recorders have been included for redundancy. However, the principal technique for enhancing system reliability is to provide as high a real-time bit rate capability as overall system considerations allow. Thus, the system presented here gives 700 bits/sec during the encounter. This real-time mode assures that more than 100 pictures of Jupiter can be transmitted back to earth even if both tape recorders fail. Although only one or two pictures are of highest resolution, a successful mission will be accomplished and all other scientific objectives achieved. Further system reliability is achieved through the use of flexible bit rates which provide data transmission even in the event of degrading system performance. Because of the high priority placed upon this real-time mode, all other components of the data handling unit are also redundant.

4.6.2 Selected Approach

During the pre-encounter cruise, a bit rate of 1400 bits/sec is possible until about 4.3 AU. This bit rate minimizes ground station on-time requirements. Assuming a nominal data accumulation rate of 110 bits/sec and a tape storage capability of 1.2×10^8 bits, the tape recorder will be filled about once every 12 days, allowing some time for simultaneous read-in and read-out, and assuming some storage of high resolution data on the order of 342 bits/sec, as shown in the Table 4-6. For data readout, the ground stations will be required approximately one day out of every 12. After the spacecraft has exceeded a range of 4.3 AU, the bit rate will drop to 700 bits/sec, and ground stations will be required on the order of one day out of every six. It is obvious that the nominal bit rates given here can

be substantially reduced; if they are comparable with those of Pioneer 6 or Mariner 4 the ground requirements are reduced by a factor of 10. It is equally obvious that the data requirements can be made higher, requiring more ground station time.

During the encounter phase about 274 bits/sec are required, exclusive of TV. With a bit rate capability of 700 bits/sec at encounter, 427 bits/sec is constantly available for transmission of TV data. The TV experiment should begin at about 100 Jupiter radii, i.e., about seven days before closest approach. At such distances, a large number of pictures are not of great value. It is proposed that one picture be taken and then read out and then another picture taken and read out, etc. With a bit rate capability of 427 bits/sec a picture could be taken every hour. When the spacecraft is closer, this mode of operation will no longer be desirable. Since each picture contains 1.5×10^6 bits and since our tape storage capability is 1.2×10^8, it is possible to store 80 pictures. However, about 5×10^6 bits of storage of other scientific data will be required during earth occultation. Thus, about 75 pictures may be stored. One picture can then be taken every 5 minutes for 6 hours prior to passing by the sunlit portion of Jupiter. In the event of a tape recorder failure, one picture can be taken every 10 minutes. After earth occultation, the stored data can then be transmitted back to earth at 700 bits/sec. This data rate can be time-shared between real time and stored data to insure that no significant data is lost. It is assumed that the DSIF stations will monitor the full encounter phase for a minimum of 10 days.

During the post-encounter cruise, the bit rate will be changed as a function of range, and the experiment sampling will also be changed. The nominal data rates shown in the table can then be modified to be compatible with reduced mission capabilities. In the event that the data storage system is still operating, ground station availability requirements will be substantially reduced.

4.7 DATA INDEXING

As discussed in Section 2.5, a minimum roll reference system for purposes of indexing science data can be obtained by time-referencing the general science data to the plasma probe data. In general, the plasma flux (solar wind) will be peaked in the ecliptic plane. A minimum reoriented attitude reference is simply to rely on the open loop precession accuracy as discussed in Section 4.3.

The attitude control sun sensors provide a pulse once each revolution, provided that the sun is more than 10 degrees from the earth line. As this system stands, it operates out to about 2 AU, where the voltage output drops below a suitable level for direct drive of the subsequent electronics. Operation to 6 AU can be obtained through use of chopper stabilized amplifiers. Operation when the earth-probe-sun angle is less than 10 degrees (always true near Jupiter and beyond) would demand an additional narrow angle sun sensor. Typical weight and power requirements are 1 pound and 1/4 watt for a suitable unit. Such a unit could operate within a fraction of a degree of the sun. During Jupiter encounter, the planet sensor associated with the television experiment provides a roll reference signal which could be used.

The most flexible and accurate way of determining both the spin axis direction and the roll position of a spinning spacecraft is to employ a star field scanner. The use of such a scanner is particularly attractive for midcourse corrections, where it will allow precise inertial pointing of the spacecraft prior to making the correction. The following subsections discuss the possibilities of such a device. Requirements are about 5 pounds and 5 watts.

4.7.1 Sensor

The basic components of the star field scanner are shown in Figure 4-41, along with some component design data. The telescope is mounted normal to the spin axis of the spacecraft, such that the rotation of the craft provides the required scan of the star field. The relative positions of the stars in this field can be derived through processing of the time sequence of pulses resulting from successive passages of stars across

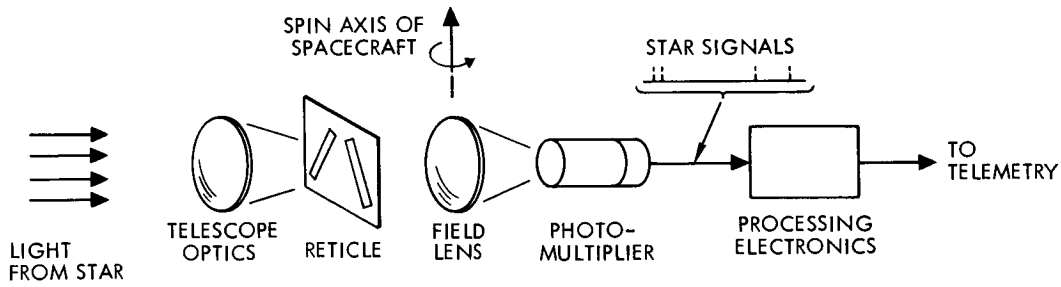

COMPONENT DESIGN DATA

- DIAMETER OF OPTICS: D = 5.1 CM
- FOCAL LENGTH OF OPTICS: f.l. = 10.2 CM
- TRANSMISSION EFFICIENCY OF OPTICS: $e_o = 0.5$
- OPTICAL DISTORTION: 0.1% OF FIELD OF VIEW
- SPECTRAL SENSITIVITY OF PHOTOCATHODE: S20
- LUMINOUS SENSITIVITY OF PHOTOCATHODE: S = 240 μA/lumen (FOR STAR OF SPECTRAL CLASS A0)
- ANODE DARK CURRENT: $i_D = 1 \times 10^{-8}$ AMPS
- CURRENT MULTIPLICATION: $\mu = 10^6$
- ANGULAR SUBTENSE OF VERTICAL SLIT: $L \times W = 30^o \times 0.005^o$
- AVERAGE STELLAR BACKGROUND DENSITY: $\rho = 200$ STARS PER DEGREE ^{2} OF MAGNITUDE $m_e = 10$
- VISUAL MAGNITUDE OF DIMMEST STAR TO BE DETECTED $m_s = 1.7$
- SPIN RATE: $\omega = 30$ DEG/SEC

Figure 4-41. Simplified Block Diagram for Star Field Scanner

the slit reticle. Performance calculations, below, indicate that an accuracy on the order of 0.05 degree is easily attained. Further improvement in accuracy could be obtained through tighter manufacturing tolerances and computer calibration of error sources, but the performance was considered adequate for this application.

Signal due to 1.7 magnitude star

$$i_s = 2.65 \times 10^{-10} (2.51)^{-m_s} e_o S \frac{\pi D^2}{4} \mu$$

$$i_s = 13.8 \times 10^{-8} \text{ amps}$$

Signal due to background stars

$$i_B = 200 \times 2.65 \times 10^{-10} (2.51)^{-m_s} e_o S \left(\frac{\pi D^2}{4}\right) \mu(2LW)$$

$$= 1.41 \times 10^{-8} \text{ amps}$$

Signal-to-noise ratio at photomultiplier output

$$\frac{S}{N} = \frac{i_s \sqrt{W}}{\sqrt{(i_s + i_D + i_B)\, ew\mu}} = 27:1$$

Standard deviation of angle estimate, due to noise

$$\sigma(e) \approx \frac{W}{S/N} = 0.002 \text{ degree}$$

Error in angle estimate due to optical distortion

$$\theta_e = 0.1\% \times L = 0.03 \text{ degree}$$

4.7.2 Coordinate Definitions

Let (x_1, x_2, x_3) be a right-handed, orthogonal set of inertial axes with origin at the spacecraft center of mass, and such that $\overline{x}_3$ points down along the nominal spin axis, and $\overline{x}_1$ is such that some particular star lies in the $x_1 - z_1$ plane. In a similar fashion, a body-fixed coordinate set (y_1, y_2, y_3), is defined forming principal axes for the spacecraft and such that $\overline{y}_3 = \overline{x}_3$ when there is no attitude pointing error, and y_1 is the

projection of star sensor axis on the horizontal plane. In general, the spacecraft attitude can be defined by relating the two coordinate sets by first a pitch rotation, θ_1, about x_2, then a roll rotation, θ_2, about the axis to which $\overline{x}_1$ transforms under θ_1, and finally a yaw rotation, θ_3, about the y_3 axis. θ_1 and θ_2 represent the components of the spin axis attitude error, whereas θ_3 defines the spacecraft spin angle. Thus, in general

$$\overline{y}_1 = \sum_{j=1}^{3} b_{ij}\, \overline{x}_j \qquad (i = 1,\ 2,\ 3)$$

where

$$b_{11} = \cos\theta_3 \cos\theta_1 + \sin\theta_3 \sin\theta_1 \sin\theta_2$$

$$b_{12} = \sin\theta_3 \cos\theta_2$$

$$b_{13} = -\cos\theta_3 \sin\theta_1 + \sin\theta_3 \sin\theta_2 \cos\theta_1$$

$$b_{21} = -\sin\theta_3 \cos\theta_1 + \cos\theta_3 \sin\theta_1 \sin\theta_2$$

$$b_{22} = \cos\theta_2 \cos\theta_3$$

$$b_{23} = \sin\theta_1 \sin\theta_3 + \cos\theta_3 \sin\theta_2 \cos\theta_1$$

$$b_{31} = \sin\theta_1 \cos\theta_2$$

$$b_{32} = -\sin\theta_2$$

$$b_{33} = \cos\theta_2 \cos\theta_1$$

The star sensor consists basically of two slits (with their associated optics) as illustrated in Figure 4-42. The optical axis for each slit is assumed to lie nominally in a plane normal to $\overline{y}_3$ such that those stars lying within the field of view of the sensor appear within one (or both) slits as the spacecraft undergoes one entire spin rotation. The time at which the star has traversed half the slit width of slit No. 1 is denoted by t_1. t_2 is similarly defined relative to slit No. 2. The difference between t_1 and t_2 is a measure of the spacecraft attitude.

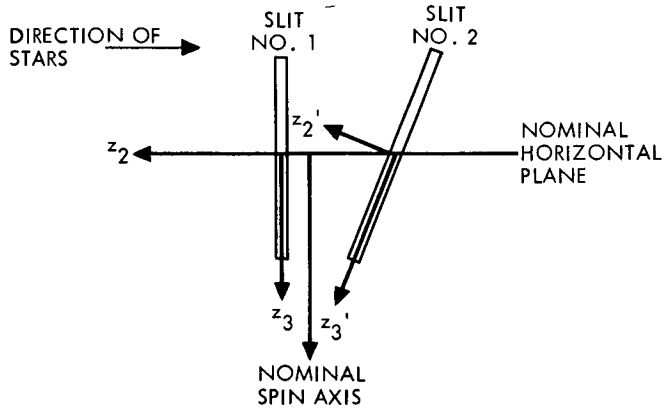

Figure 4-42. Schematic of the Star Sensor

The first slit is defined by the coordinates (z_1, z_2, z_3), as illustrated in Figure 4-42, where $\overline{z}_1$ is the optical axis and $\overline{z}_3$ is normal to the slit edge. Since, in general, a misalignment exists between (z_1, z_2, z_3) and (y_1, y_2, y_3), a minimum of three ordered rotations is necessary in order to relate these axes. Taking these ordered rotations as a_1, a_2, and a_3 in the same sense as the θ rotations were previously taken, it follows that

$$\overline{z}_i = \sum_{j=1}^{3} c_{ij}\, \overline{y}_j \qquad (i = 1,\ 2,\ 3)$$

where the c_{ij} are identical to the b_{ij} in the expression for $\overline{y}_i$, replacing θ_i by a_i for $i = 1,\ 2,\ 3$.

In a similar fashion, slit No. 2 is identified by the coordinate axes (z'_1, z'_2, z'_3) where

$$\overline{z}'_i = \sum_{j=1}^{3} e_{ij}\, \overline{z}_j \qquad (i = 1,\ 2,\ 3)$$

where two rotations, first γ_1 about z_3, then γ_2 about z'_1 relate the axes such that

$$e_{11} = \cos \gamma_1 \qquad e_{12} = \sin \gamma_1 \qquad e_{13} = 0$$

$$e_{21} = \sin \gamma_1 \cos \gamma_2 \qquad e_{22} = \cos \gamma_1 \cos \gamma_2 \qquad e_{23} = \sin \gamma_2$$

$$e_{31} = \sin \gamma_1 \sin \gamma_2 \qquad e_{32} = -\sin \gamma_2 \cos \gamma_1 \qquad e_{33} = \cos \gamma$$

4.7.3 The Basic Relations

The location of a given star is precisely defined by its unit vector, $\bar{u}$. This vector can be described in inertial coordinates by

$$\bar{u} = \sum_{i=1}^{3} a_i(t)\bar{x}_i$$

where t represents time. This star will lie half way within slit No. 1 provided

$$\bar{u} \cdot \bar{z}_2 = 0$$

Hence

$$\left[\sum_{i=1}^{3} a_i(t_1)\, \bar{x}_i\right] \cdot \left\{\sum_{j=1}^{3} c_{2j} \sum_{k=1}^{3} b_{jk}(t_1)\, \bar{x}_k\right\} = 0$$

or

$$f_1 = \sum_{k=1}^{3} a_k(t_1) \left[\sum_{j=1}^{3} c_{2j}\, b_{jk}(t_1)\right] = 0$$

Using a similar approach for slit No. 2

$$f_2 = \sum_{i=1}^{3} a_i(t_2) \left\{\sum_{j=1}^{3} e_{2j} \left[\sum_{k=1}^{3} c_{jk}\, b_{ki}(t_2)\right]\right\} = 0$$

Replacing the b_{ij} and c_{ij} by their expressions in terms of θ_i and a_i respectively (i = 1, 2, 3), the two previous equations can functionally be represented as

$$g_1 \left[\theta_1, \theta_2, \theta_3(t_1), a_1, a_2, a_3\right] = 0$$

$$g_2 \left[\theta_1, \theta_2, \theta_3(t_2), a_1, a_2, a_3\right] = 0$$

Since the spin rate Ω can be assumed constant (but, perhaps, unknown), the following equation can be added

$$\theta_3(t_2) = \theta_3(t_1) + \Omega(t_2 - t_1)$$

The last three equations represent three equations in the five unknowns θ_1, θ_2, $\theta_3(t_1)$, $\theta_3(t_2)$ and Ω. Thus the sighting of one star by a V-slit sensor is not adequate to determine the spacecraft attitude.

If, however, a second star is now observed, say at slit times t_3 and t_4, four additional equations become available, namely

$$g_1 \left[\theta_1, \theta_2, \theta_3(t_3), a'_1, a'_2, a'_3\right] = 0$$

$$g_2 \left[\theta_1, \theta_2, \theta_3(t_4), a'_1, a'_2, a'_3\right] = 0$$

$$\theta_3(t_3) = \theta_3(t_1) + \Omega(t_3 - t_1)$$

$$\theta_3(t_4) = \theta_3(t_1) + \Omega(t_4 - t_1)$$

Since the star locations and slit times are assumed known, there now appear seven equations matched by seven unknowns, the original five plus $\theta_3(t_3)$ and $\theta_3(t_4)$. Thus, except in singular star location cases, the spin axis attitude, the spin angles and the spin rotation rate can be determined by two star sightings of the V-slit sensor.

4.7.4 The Star Identification Problem

It was demonstrated in Section 4.7.2 that spacecraft attitude determination is a fairly trivial matter, provided the observed stars are

properly identified. This identification, however, is certain only when the spacecraft attitude and spin rate are precisely known, for then there exists a unique sequence of sensor slit times among the several stars which the spacecraft is known to observe. This makes it a relatively simple matter to order the stars observed chronologically in time since it is virtually impossible that two different star orderings would possess the same sequence of times. Thus the time, t_1, that a certain reference star was observed can be taken as a base and the times, t_2, t_3 . . . t_n that the second order through n^{th} stars were observed by sensor slit No. 1 can be simply determined relative to t_1.

When the attitude of the spacecraft is not exactly known but can only be bounded, the star identification problem is somewhat more complicated. For now, if the reference star is observed at time t_1, the second star will be observed in some time interval $t_2 \pm \tau_2/2$ instead of precisely at time t_2. Similarly, the n^{th} star will appear somewhere in the time interval $t_n \pm \tau_2/2$. Therefore, there now exists a finite probability that these n - 1 time values could actually appear within these defined time intervals even if the reference star were incorrectly identified. This represents the probability of falsely ordering the stars or fasely determining the spacecraft attitude.

The probability of false ordering is strongly dependent upon the expected time differences $t_2 - t_1 \ldots t_n - t_1$ and these values depend, of course, upon the expected spacecraft position and attitude in inertial space. Thus, with each attitude is associated a probability of falsely ordering its observable stars.

To obtain a simple but less exact probability expression which is independent of the nominal spacecraft attitude, it is assumed that the stars with brightness above the sensor threshold are randomly distributed on the celestial sphere. The expected observed star density (in stars per second) is then a function of this threshold and the sensor field of view, and will be denoted by the symbol λ.

The basic problem is now the following. Assuming that the reference star was incorrectly determined, what is the probability that the second star will be observed in the time interval $t_2 \pm \tau_2/2$, the third in

the time interval $t_3 \pm \tau_3/2 \ldots$ etc., assuming the τ_i to be very small? This is a typical Poisson process in which the probability of observing k stars in time t is given by

$$p(k, \lambda t) = \frac{(\lambda t)^k}{k!} e^{-\lambda t}$$

For very small values of t, the probability of observing one star is virtually λt. In our problem, we observe no stars in the interval $\left[t_1, t_2 - \tau_2/2\right]$. The corresponding probability is

$$p\left[0, \lambda\left(t_2 - \frac{\tau_2}{2} - t_1\right)\right] \approx p\left(0, \lambda (t_2 - t_1)\right) = e^{-\lambda(t_2 - t_1)}$$

One star is observed in the interval $t_2 \pm \tau_2/2$ with corresponding probability $\lambda\tau_2$. No stars are observed in $[t_2 + \tau_2/2, t_3 - \tau_3/2]$ with probability $p[0, \lambda(t_3 - t_2)]$ and so on. The probability of false ordering is merely the product of all these probabilities and is given by

$$P_n = \left[\lambda^{n-1} e^{-\lambda(t_n - t_1)}\right] \prod_{i=2}^{n} \tau_i$$

Rather than establish the various moments of P (which is a complicated process) it suffices to substitute reasonable values of τ_i into this last equation. These values are based upon the estimated attitude uncertainty and will be evaluated shortly. In particular, a value of n equal to three will be considered for both high and low values of λ. That is, the probability of false ordering as a function of the star density will be obtained when the ordering decision is based merely upon the telemetered timing information associated with three stars.

4.7.5 Timing Uncertainties

It will be assumed here that the V-slit star sensor has one vertical slit, that is

$$\left.\begin{aligned} c_{ij} &= 0 \qquad i \neq j \\ c_{ii} &= 1 \qquad i = 1, 2, 3 \end{aligned}\right\}$$

and that this slit alone is utilized for star identification. Thus for the i^{th} star, the expression for f_1 reduces in this case to

$$\sum_{k=1}^{3} a_{ik}(t)\, b_{2k}(t) = 0$$

where t is the transmitted time value. It can be assumed in this study that the spacecraft spin axis lies close to its nominal inertial axis, permitting small angle approximations to be made for θ_1 and θ_2. Thus the above becomes, for the i^{th} star

$$-a_{i1} \sin \theta_3 (t_i) + a_{i2} \cos \theta_3 (t_i)$$

$$+ a_{i3} \left[\theta_1 \sin \theta_3 (t_1) + \theta_2 \cos \theta_3 (t_i)\right] = 0$$

and the expression for $\theta_3 (t_i)$ becomes

$$\theta_3(t_i) = \theta_3(t_1) + \Omega(t_i - t_1)$$

Ignoring second order effects and then substituting in the nominal values

$$\left.\begin{aligned} a_{i1} &= \cos \theta_3 (t_i) \\ a_{i2} &= \sin \theta_3 (t_i) \end{aligned}\right\}$$

results in

$$\delta\theta_3(t_i) = a_{i3} \left[\left(\sin \Omega(t_i - t_1)\right) \delta\theta_1 + \left(\cos \Omega(t_i - t_1)\right) \delta\theta_2\right]$$

and, in particular,

$$\delta\theta_3(t_1) = a_{13}\delta\theta_2$$

A variation is now taken (where $\delta t_1 = 0$ since the reference star is assumed to be observed precisely at time t_1) and the last two equations substituted into the result. This yields

$$\delta t_i = \frac{1}{\Omega} \left\{\left[a_{i3} \sin \Omega(t_i - t_1)\right] \delta\theta_1 \right.$$

$$\left. + \left[a_{i3} \cos \Omega(t_i - t_1) - a_{13}\right] \delta\theta_2 - (t_i - t_1)\, \delta\Omega \right\}$$

for the possible time variation occurring for the i^{th} star due to uncertainties in θ_1, θ_2 and the spin rate Ω.

Letting E denote the expected value operator and noting that $\delta\theta_1$, $\delta\theta_2$, and $\delta\Omega$ are uncorrelated with each other, that a_{i3} is uncorrelated to $t_i - t_1$, a_{13}, $\delta\theta_1$, and $\delta\theta_2$, and that $(t_i - t_1)$ bears no correlation to $\delta\Omega$, it follows that, by the definition of nominal inertial axes,

$$E(\delta t_i) = 0$$

and

$$E(\delta t_i^2) = \frac{1}{\Omega^2}\left[E(A_{i1}^2)\,E(\delta\theta_1^2) + E(A_{i2}^2)\,E(\delta\theta_2^2) + E\left[(t_i - t_1)^2\right]E(\delta\Omega^2)\right]$$

where

$$\left.\begin{aligned} E(A_{i1}^2) &= E(a_{i3}^2)\,E\left[\sin^2\Omega(t_i - t_1)\right] \\ E(A_{i2}^2) &= E(a_{i3}^2)\,E\left[\cos^2\Omega(t_i\,t_1)\right] + E(a_{13}^2) \end{aligned}\right\}$$

In the above, a_{i3} is essentially the sine of the elevation angle of the i^{th} star relative to a plane normal to the spin axis. This angle is assumed uniformly distributed and, provided the sensor field of view is not too large, a_{i3} can be essentially assumed to have this distribution also. If γ represents the sensor field-of-view half angle, it then follows that

$$E(a_{i3}^2) = E(a_{13}^2) = \frac{\sin^2\gamma}{3}$$

To compute $E\left[\sin^2\Omega(t_i - t_1)\right]$, it is recognized that the probability that the i^{th} star will be observed within the time interval $t_i - t_1$ and $t_i - t_1 + dt$ is given by

$$p\,(i-2,\ t_i - t_1)\,\lambda dt = \lambda\,\frac{\left[\lambda(t_i - t_1)\right]^{i-2}}{(i-2)!}\,e^{-\lambda(t_i - t_1)}\,dt$$

so that

$$E\left[\sin^2 \Omega(t_i - t_1)\right]$$

$$= \frac{\lambda^{i-1}}{(i-2)!} \int_{t_1}^{\infty} \left[\sin^2 \Omega(t - t_1)\right] (t - t_1)^{i-2} e^{-\lambda(t - t_1)} dt$$

Specifically

$$\left.\begin{aligned} E\left[\sin^2 \Omega(t_2 - t_1)\right] &= \frac{1}{2} - \frac{\lambda^2}{2(\lambda^2 + \Omega^2)} \\ E\left[\sin^2 \Omega(t_3 - t_1)\right] &= \frac{1}{2} - \frac{\lambda^2(\lambda^2 - \Omega^2)}{2\left[(\lambda^2 - \Omega^2)^2 + 4\Omega^2\lambda^2\right]} \end{aligned}\right\}$$

In a similar way

$$\left.\begin{aligned} E\left[\cos^2 \Omega(t_2 - t_1)\right] &= \frac{1}{2} + \frac{\lambda^2}{2(\lambda^2 + \Omega^2)} \\ E\left[\cos^2 \Omega(t_3 - t_1)\right] &= \frac{1}{2} + \frac{\lambda^2(\lambda^2 - \Omega^2)}{2\left[(\lambda^2 - \Omega^2)^2 + 4\Omega^2\lambda^2\right]} \end{aligned}\right\}$$

These relationships indicate that $E\left[\sin^2 \Omega(t_i\, t_1)\right] \approx 1/2$ for low values of λ and zero for high values. Similarly, $E\left[\cos^2 \Omega(t_i t_1)\right]$ ranges between 1/2 for low λ values to 1 for large values.

Finally, $E\left[(t_i - t_1)^2\right]$ must be evaluated. This is clearly given by

$$E\left[(t_i - t_1)^2\right] = \frac{\lambda^{i-1}}{(i-2)!} \int_{t_1}^{\infty} (t - t_1)^2 (t - t_1)^{i-2} e^{-\lambda(t - t_1)} dt$$

with the specific value

$$E\left[(t_2 - t_1)^2\right] = \frac{2}{\lambda^2}$$

Assuming now that

$$E(\delta\theta_1^2) = E(\delta\theta_2^2) = E(\delta\theta^2)$$

it follows that for both large and small λ the previous relations yield

$$E(\delta t_i^2) = \frac{1}{\Omega^2}\left\{\left(\frac{2}{3}\sin^2\gamma\right) E(\delta\theta^2) + \frac{k_i}{\lambda^2} E(\delta\Omega^2)\right\}$$

where $k_2 = 2$ and $k_3 = 6$.

The square root of this equation represents the standard deviation of δt_i, namely (in this case), the roughly 67 percent likelihood that δt_i will lie between plus and minus $\left[E(\delta t_i^2)\right]^{1/2}$. Thus a reasonable assumption for τ_i in the expression for P_n at the end of Section 4.7.4 is its 1σ value, namely

$$\tau_i = 2\left[E(\delta t_i^2)\right]^{1/2}$$

P_n evaluated for $n = 3$ now reduces to

$$P_3 = 4\lambda^2 e^{-2}\left[E(\delta t_2^2)\, E(\delta t_3^2)\right]^{1/2}$$

where

$$E(t_3 - t_1) = \frac{2}{\lambda}$$

has been substituted for $t_3 - t_1$. As an example, assume the following values

$$\Omega = \frac{\pi}{6} \text{ rad/sec}$$

$$\gamma = 15 \text{ deg}$$

$$\sqrt{E(\delta\theta^2)} = 0.1 \text{ rad}$$

$$\frac{\sqrt{E(\delta\Omega^2)}}{\Omega} = 0.0001$$

$$\lambda = 0.25$$

that is, on the average one star is observed every 4 seconds. In this case the probability of false ordering is

$$P_3 \Big| = 0.746 \times 10^{-4}$$

$$\lambda = 0.25$$

which is negligible. In fact, even if the star density is 10 times as high, the telemetering of the timing information associated with only three stars still yields less than a 1 percent chance of false identification. Thus, star timing information associated with three stars appears to be an adequate method of identification.

This discussion has been concerned only with the probability of false identification. It has not been demonstrative in that it has presented no algorithm for properly identifying the stars. Actually, such an algorithm should be rather easy to implement. If there were no spin axis pointing error, the star timing pulses would be known a priori as a function $f(\theta_3)$ as in Figure 4-43(A), where the pulses are given a finite width consistent with the uncertainty in δt_i. Figure 4-43(B) (assuming ideal Ω) represents the star sensor output based upon $t_2 - t_1$ and $t_3 - t_1$, and an unknown value of yaw angle β, since the star at β has not been identified. This is a function also of θ_3, but with β as a parameter, and will be denoted by $g(\beta, \theta_3)$. The product

$$F(\beta) = \prod_{i=1}^{3} g\Big(\beta,\ \beta + \Omega(t_i - t_1)\Big)\, f\Big(\beta + \Omega(t_i - t_1)\Big)$$

is now found and evaluated for $\beta = \theta_{3i}$ $(i = 1, 2, 3)$ in Figure 4-43(A). Only one of these evaluations will not be zero, and thus the value of β can be related to the star causing the first timing pulse. This, then, permits identification of all the stars.

4.7.6 Computer Determination of Visible Stars

A TRW digital program, based upon a Yale University Observatory catalog of 9110 stars, was utilized to determine the number of observable stars per scan as a function of spacecraft attitude for an assumed star sensor design. The number of observable stars per scan was determined at approximately 15 degree intervals in both orbit position and

inclination. Assuming a scanner with a ±15 degree field of view and a threshold set to ignore stars dimmer than 1.71 in optical magnitude (which leaves only 35 stars total), between three and 18 stars can be observed depending upon the attitude of the spacecraft. The actual star distribution is illustrated by Table 4-7, which demonstrates how many of the 103 considered attitudes correspond to the observation of a given number of stars. At least three stars are seen in every case, and the observation of more than 11 stars is rare. In view of the previous comments regarding the possibility of falsely ordering the stars, it can be concluded that the above-described star sensor parameters adequately meet the needs of this system.

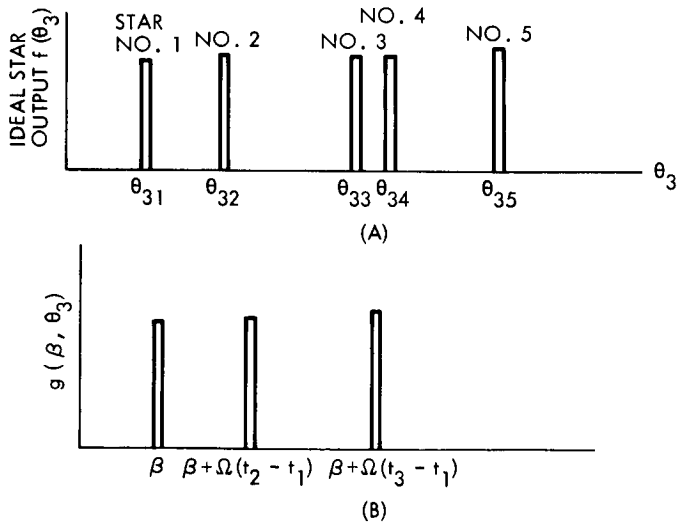

Figure 4-43. Correlating the Sensor Output to Known Star Locations

Table 4-7. Distribution of Observable Stars

No. of Observable Stars	No. of Attitude Cases
3	2
4	9
5	19
6	17
7	13
8	13
9	11
10	6
11	5
12	2
13	0
14	3
15	1
16	0
17	0
18	2
Total number of cases	103

4.8 COMMAND AND SEQUENCING

4.8.1 Requirements

The mission can be divided into three major phases from the viewpoint of spacecraft command and sequencing: 1) the launch sequence, 2) orientation and midcourse maneuvers, and 3) the planet encounter.

The spacecraft command and sequencing subsystem assumes control after Centaur separation. The series of events following this separation can be obtained from the output of a clock-driven counter. Alternately, some of these events can be controlled by direct ground commands.

The second phase of the mission covers spacecraft initial orientation and the midcourse maneuvers. These require ground command since the command content is the result of trajectory observations. The Jupiter flyby mission has been planned on the basis of one midcourse maneuver. These commands can be quantitative or discretes.

The third or encounter phase of the mission requires a sequence of commands since changes in the experiments sampled and in the sample rate will be desirable. Data will be transmitted in real time and stored during the flyby. Since the overall sequence of events will be known, it could be controlled by a sequencer. However, the total length of the sequence (approximately two weeks) and the fine granularity of some of the time relationships make ground control appear the better alternative except during the hours of closest approach. The general functions of command and control required for the Jupiter mission are broken down into three groups as discussed below. Each of the functions can be performed in a separate subsystem or unit of a subsystem.

One group of functions includes input command decoding to check the received command. This command check can be by parity check, bit count, address check, or a combination of these methods. Also, from this preliminary decoding the command destination, storage unit, or real-time decoding can be determined. These operations would be performed on both discrete and quantitative commands.

A second group of functions includes the output command decoding and generation of discrete and/or quantitative real-time commands to the correct subsystems. The number of quantitative real-time commands for the Jupiter mission is so small (three) that they may be routed by the input command decoding.

A third function is the storing and retrieving, in the correct sequence, of discrete and quantitative commands. This function may also cover the generation of repetitive commands, such as commanding a general science calibration procedure once each day or half-day.

Spacecraft-generated commands, including some repetitive commands, commands between spacecraft subsystems, and commands internal to a subsystem, are not considered as a function of the command and sequencing subsystem.

4.8.2 Design Approaches

Two approaches can be taken to the command and sequencing subsystem, as illustrated in Figures 4-44 and 4-45.

The simpler approach, Figure 4-44, uses largely ground command to control the spacecraft functions. Where stored commands are required, a sequencer unit may be used to generate time-related commands from storage. Also, repetitive functions may be generated by timers to reduce uplink communications.

A stable frequency source is required for stepping the sequencer and timers. This clock source may be generated in the command and sequencing subsystems or taken from some other stable spacecraft source. The timers are digital storage registers (timer register) where either preset values or quantitative ground commands may be stored. A countdown register is compared to the timer register at each clock pulse. When the two registers are equala discrete output is triggered. The countdown register is cleared to all zeroes and the process repeated or inhibited until an enable pulse is generated to restart the cycle.

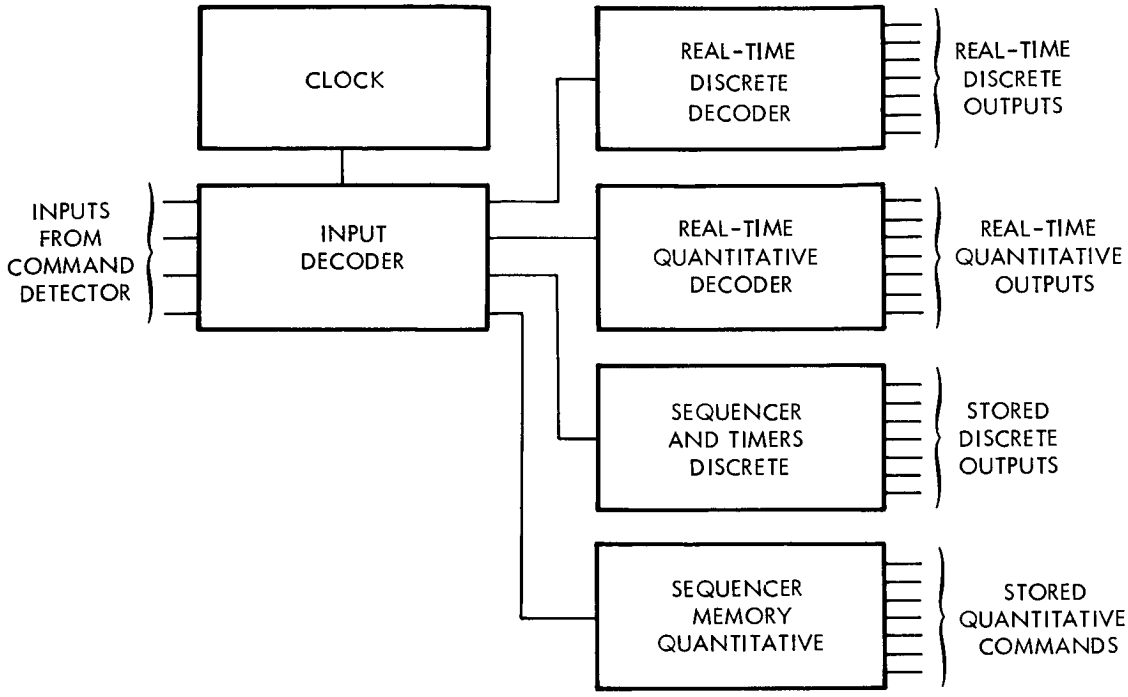

Figure 4-44. Ground Command System

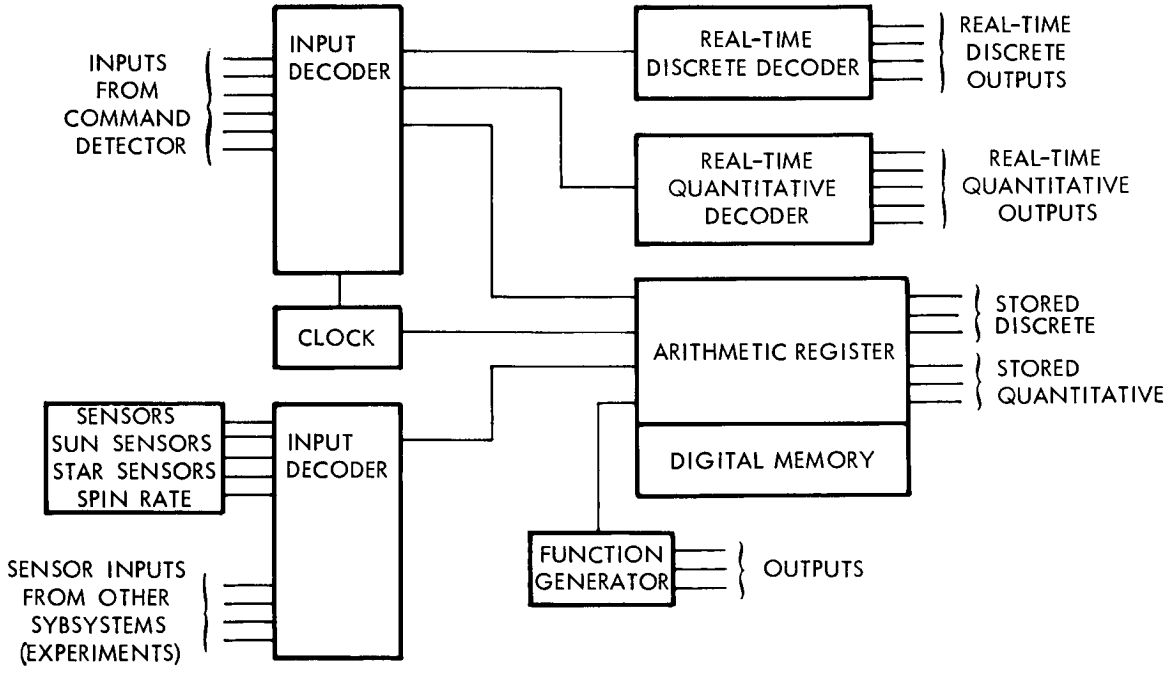

Figure 4-45. Autonomous System

The sequencer operation may be of two types: 1) a series of timers where each timer enables the next, or 2) a bank of memory storage with each memory word containing a command and a time. Every bit of each time tag of the storage is compared with a counter. A comparison triggers the readout of the command stored with the equal time tag. The stored data and time tag system is more flexible and is more efficient in terms of implementation where a large number of commands are required. Both types of sequencers may be mechanized to accept and store updated commands through the uplink communications.

The more complex approach to command and sequencing is an autonomous command system, Figure 4-45. This system would command spacecraft functions through processed information (spacecraft orientation, midcourse maneuvers, orbit injection maneuvers, etc.) with little or no reference to ground controls. Such a command system would require various processing capabilities, such as stored programs for maneuvers and instrument sensing to determine spin rate, acceleration, and position with regard to the earth, the sun, and Jupiter. Fault-sensing checkout programs and fault correction might also be a part of the processing capabilities. Implementing this system would require a special-purpose processing unit with arithmetic registers, data storage, and a stable long-term clock.

4.8.3 Comparison of Design Approaches

The ground control system costs less in weight and power and, since construction is simple and little electronics is required, it is more reliable. Such a system, of course, depends on the reliability of the uplink communications which is, in any event, an in-line item. However, there are problems with the long transmission delay times for communications to 6 AU (96 minutes) which make some sequencing necessary. Techniques such as on-board fault-condition sensing and correction can be better done as a part of the individual subsystem failure logic. Switching between redundant systems can be done from command. Sophisticated fault detection and correction would be a function of analyzing engineering telemetry on the ground and programming corrective commands through the uplink. Commands would be allotted for such subsystem switching to correct faults diagnosed on the ground. This type

of fault correction would necessarily cause interruptions of the regular mission objectives until corrective commands are received on the uplink.

The autonomous control system has the advantage of being less dependent on the command link and could reduce the DSIF contact required for long missions. While periodic updating of stored commands would be required for precise maneuvers, large portions of the mission could be completed without ground control. Urgent fault corrections, too complex for simple subsystem solutions, could be remedied by using a stored program for spacecraft checkout. Thus, little or no interruption in the mission would occur. The checkout and corrective capabilities of any such system must be somewhat limited since the best corrective procedure cannot always be preplanned. Autonomous control is at a disadvantage when weight and power are considered and where redundancy would double the penalty. Moreover, ground command overrides must be provided as a backup for any system.

4.8.4 Final Selection

The ground control system concept was selected for further study and application to this mission. The use of sequencers and timers extends the capabilities of the time commands to allow stored commands. The number and frequency of spacecraft trajectory and orientation maneuvers are few enough that they do not require extended or continuous uplink communications with ground control modes. The simplicity of this organization allows for complete redundancy without a large weight and power penalty.

4.9 THERMAL CONTROL

The thermal control subsystem must maintain temperatures of operating equipment within acceptable ranges, which are conservatively estimated as 40 to 85 °F for all electronic components and 40 to 100 °F for the propulsion system. In addition, the subsystem must keep structural and mechanical components from experiencing thermal stress resulting either from excessively high or low temperatures or from sharp temperature gradients. The subsystem must provide the required temperature control during all phases of the mission.

Each of the thermal control techniques analyzed is discussed here briefly. A detailed description of the recommended approach is given in Section 8.8.

4.9.1 Main Equipment Compartment

Four approaches to thermal control were investigated for control of the main compartment.

- Passive
- Passive utilizing RTG waste heat
- Active louver
- Thermal switches

The passive system was found to be marginal and subsequently eliminated because past experience has shown that actual heat leaks are too unpredictable. RTG waste heat usage, although attractive from a thermal standpoint, imposes penalties in a systems tradeoff where spin stability is considerably enhanced by deploying the RTG units outward from the spin axis and where electronics and experiments shielding requirements are decreased by the physical separation.

A system that uses louvers can provide the desired control, as seen in Figure 4-46. However, louvers are fragile, vulnerable to micrometeoroid damage, and would require protection from the midcourse engine exhaust plume. Thermal switches, although requiring more weight than a louver system, are reliable and simple, particularly when no duty cycling is required, and they provide a significantly greater heat leak margin.

The required radiator surface area for the four thermal control systems is presented in Figure 4-47. It can be seen that the two passive systems, as well as the louvered system, need less than three square feet of radiator surface. Since this area represents a small part of the available radiator area, there may be component positioning difficulties not encountered with the thermal switch system. However, with proper coordination of the various subsystems, an acceptable component placement arrangement can certainly be found. This same type of exercise has been successfully completed for the Vela, VASP, and Pioneer spacecraft components.

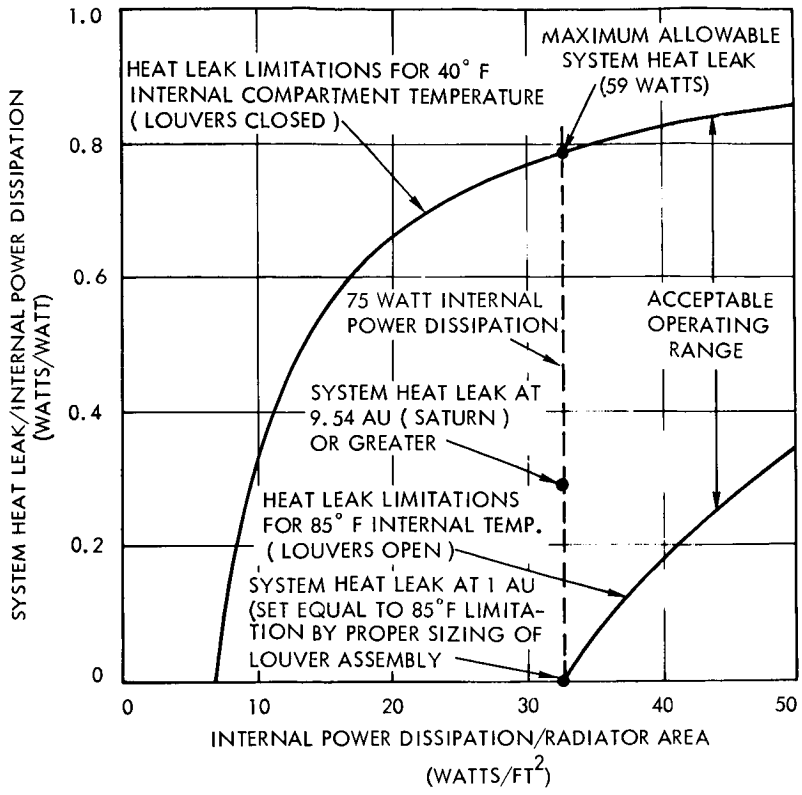

Figure 4-46. Thermal Control System Characteristics with Louvers

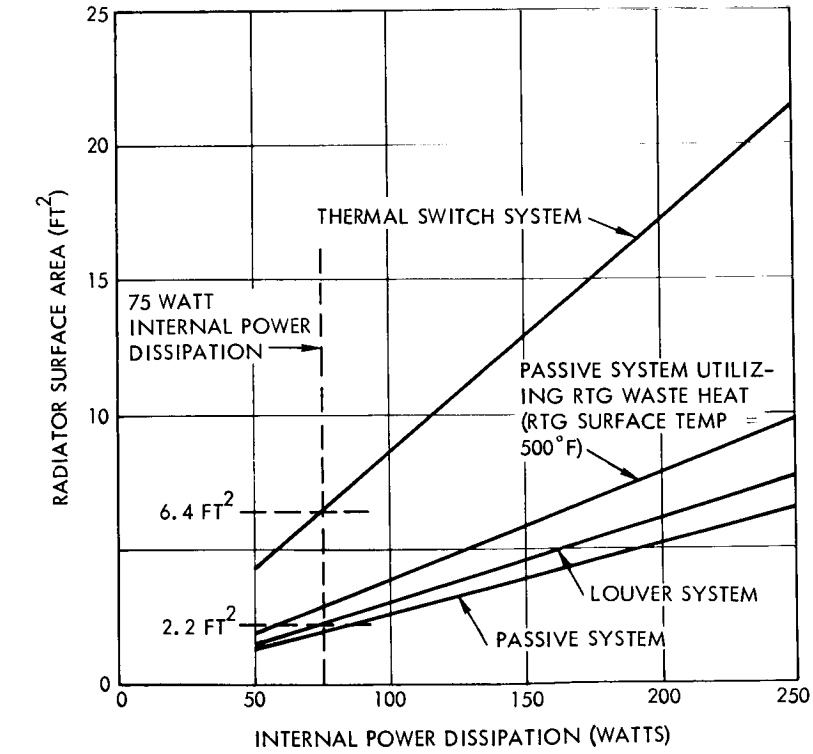

Figure 4-47. Radiation Surface Area Requirements

In a thermal switch system, the component mounting arrangement is not critical. There is, however, a weight increase since an additional radiator panel is provided. Since this augments meteoroid protection, however, it is reasonably absorbed in the meteoroid protection weight allocation.

The thermal switch and louver systems can tolerate a larger heat leak than the passive system. A comparison of the tolerable heat leaks for all systems is shown in Figure 4-48. None of the indicated systems has allowable heat leaks below the estimated minimum value of 22.4 watts for the anticipated 75 watt (RTG power minus external heater blanket power minus RF transmitted power) internal power dissipation. Keeping the heat leak to the calculated value of 22.4 watts represents a significant development problem although it is possible that the requirement can be relaxed by reducing the stringency of the heat leak requirements, in particular the requirement for low thermal conductance connectors. Hence, only the louver and thermal switch systems appear to be acceptable for the spinning spacecraft configuration.

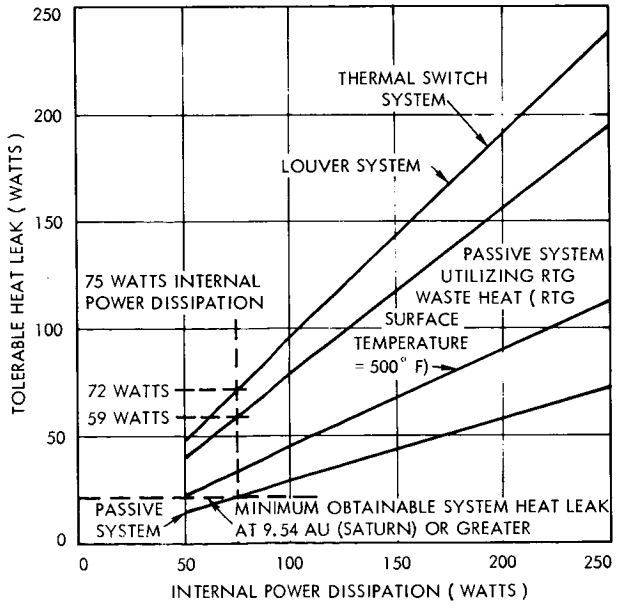

NOTE: RADIATOR HEAT DISSIPATION IS NOT CONSIDERED TO BE A HEAT LEAK.

Figure 4-48. Tolerable System Heat Leak

4.9.2 Antenna

Three alternate antenna coating concepts were studied:

- Painted black on both sides
- Painted black on front and left bare on back
- Painted white on front and left bare on back

The requirement for coating the antenna stems from the need to lower the 1 AU antenna temperature from 265°F to a value more compatible structural requirements. An all-black antenna is subject to localized RTG heating, and the white dish allows equipment mounted above the antenna plane to be exposed to stray, reflected sunlight. Therefore, the black front surface and bare rear surface are selected. This concept also reduces trajectory uncertainties arising from the effects of light pressure.

4.9.3 Experiments

To minimize the spacecraft power requirements, it is proposed that the experiment sensors be separated from their associated electronic packages and designed to operate unheated at extremely low temperatures. The electronic packages will be located in the compartment and therefore with a temperature range of 40 to 85 °F.

Operation of the sensors at low temperatures requires that power be provided in an amplification stage. Low temperature preamplifiers are in wide use. Specific studies for each experiment will, of course, be necessary. For comparison, if the electronics were located with the experiments, the curves of Figure 4-49 apply, showing the heater power demands of the magnetometer sensor, solar plasma probe and electronics, and solar cosmic ray sensor and electronics. Using a lower limit of -30 °F, the calculated heater power demand for the insulated experiments is presented below.

- Magnetometer sensor = 0.5 watt
- Solar plasma probe and electronics = 0.8 watt (with experiment operating)
  = 2.3 watts (with experiment not operating)

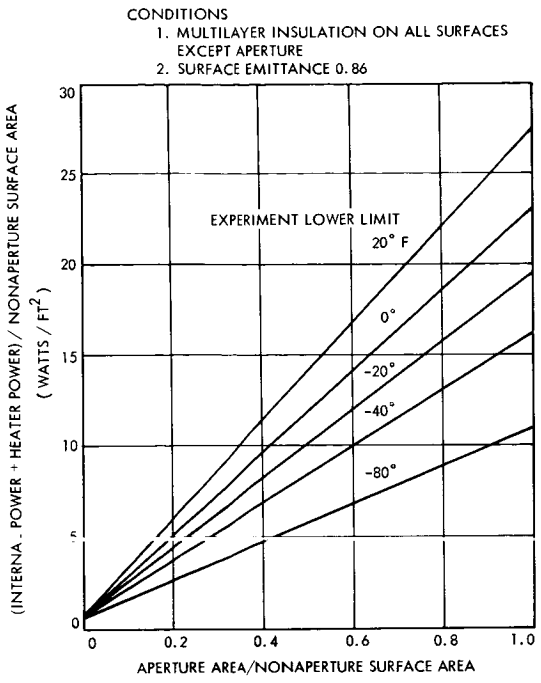

Figure 4-49. Experiment Power Requirements

- Solar cosmic ray sensor and electronics
  - = 1.2 watts (with experiment operating)
  - = 3.2 watts (with experiment not operating)
- Total experiment power
  - = 2.5 watts (with experiment operating)
  - = 6.0 watts (with experiment not operating)

Therefore, a 2.5-watt heater power would be required if the external experiments are operated with a -30 °F minimum temperature limit. It is not expected that low temperature preamplifier power requirements will be more than milliamps. Moreover, a heater power failure to the experiment does not affect system reliability.

4.9.4 Hydrazine Engine and Lines

A thermostatically controlled heater is the simplest and most reliable variable power dissipative device for the engine and line temperature control. A radioisotope heater system was also evaluated. However, since the heater demand must be variable to maintain temperatures within the acceptable 40 to 100 °F hydrazine storage range, a radioisotope heater

which dissipates heat at a constant rate would require additional complexity.

4.9.5 Reliability

The recommended thermal subsystem is primarily passive except for the slight expansion of the thermal switch bellows, and should have a high reliability. Active elements such as the electronic heaters have been flown on the OGO spacecraft. Of the 22 heaters utilized on OGO there appears to be only one heater failure. This represents a 95.5 percent success rate. For the Advanced Planetary Probe this rate should be even higher since the heater cycle rate will be greatly reduced .

The thermal switch requires a bellows displacement which subjects the materials to fatigue. The bellows is filled with a fluid which could be expelled in space if any type of fracture exists in the bellows wall. Therefore, it will be necessary to perform vibration and cyclic life tests of the bellows to insure system integrity. Preliminary laboratory tests, however, along with bellows manufacturer data, indicate that the current switch design should be reliable for long-life missions.

4.9.6 Problem Areas

Specific surface thermal properties are required to maintain acceptable spacecraft temperatures. The desired properties are normally obtained with chemical films, paints, and deposited coatings. In each instance, the surface covering is quite thin, usually about 3 mils. For the proposed missions this coating thickness may be degraded by cosmic dust erosion. The extent to which the various surface coatings will be eroded by the cosmic dust is not adequately known. Therefore, it will be necessary to study this problem in more detail, both in defining the expected cosmic dust density and in determining the rate of coating erosion.

The control of the spacecraft heat leaks will require a significant effort during the design, development, and integration phases. By providing the proper control during these activities, a satisfactory heat leak should be attained. It is also likely that even lower heat leaks may result from new concepts and techniques, particularly those incorporating new low conductance materials, such as ceramics, which will be developed prior to the 1970 to 1980 target date.

4.10 MICROMETEOROID PROTECTION

A major requirement for the spacecraft is to integrate meteoroid protection into the design. For any spacecraft configuration studied, meteoroid protection analysis establishes the probability of penetrations which will cause mission failure, $P_{(o)}$, as a function of meteoroid protection weight. Therefore, using this data, in conjunction with the other subsystem reliabilities, also derived as a function of weight, allows overall spacecraft system optimization.

The meteoroid environment, which includes the flux, the particle velocities (both magnitude and direction), and the particle densities together with the uncertainties in these parameters, is discussed in Section 2.3. In the analysis, the following ground rules are used:

a) The flux models used would be the upper bounds on the models of Section 2.3. (See Table 4-8.)

b) A mean particle density of 0.44 gm/cm^3 is used.

c) The mean relative velocity between the particle and the spacecraft is slightly greater than the average relative velocity over the region being considered except for the particles of flux E. For this latter flux, which is for particles in posigrade and close to circular orbits, the relative velocities are deterministic, see Figure 4-50. The mean relative velocities used are given in Table 4-8.

d) Particles associated with flux levels other than E are considered to impact the spacecraft from any direction. The direction of impact of particles of flux E is known as is their velocity.

e) Flux levels D and E are alternative, not additive flux levels. The trajectories of the particles associated with flux E are known and will impact the aft face of the spacecraft normal to this face. Consequently, only this face of the spacecraft is designed to flux E, but only if this flux and its associated relative velocity require greater protection than that required using flux D with its associated relative velocity.

Table 4-8. Summary of Meteoroid Environment Used

Mean meteoroid density = 0.44 gm/cm^3

Region	Equations for Flux Models	V, Mean Relative Velocity km/sec
1) Near earth	A and B	22
2) In the ecliptic plane		
a) 1 to 2 AU	A and C	36
b) 2 to 4 AU	D and E	With equations D, F and G, V = 25
(asteroid region)	D for sides and top of a vehicle E for base of vehicle	With equation E, V = 13
c) 4 to 5.2 AU	A and C	20
3) Out of ecliptic plane		
1 to 5 AU	A and C	1 to 2 AU, V = 36 2 to 4 AU, V = 25 4 to 5.2 AU, V = 20

NOTES: Equations A thru G describing the flux are as follows.

A	$M > 10^{-5}$,	$\log N = -1.34 \log M - 14.18$
B	10^{-10} gm $< M < 10^{-6}$ gm,	$\log N = -1.7 \log M - 16.87$
C	$M < 10^{-6}$ gm,	$\log N = -0.65 \log M - 10.44$
D	$M > 10^{-5}$ gm,	$\log N = -1.34 \log M - 12.18$
E	$M < 10^{-6}$ gm,	$\log N = -0.65 \log M - 8.44$
F		$\log N = -0.77 \log M - 10$

where

M is the particle mass, grams
N is the number of particles of mass M or greater/meter^2-sec.
Flux E is applied only to the base of the vehicle and then only if this is a more severe requirement than given by flux D.

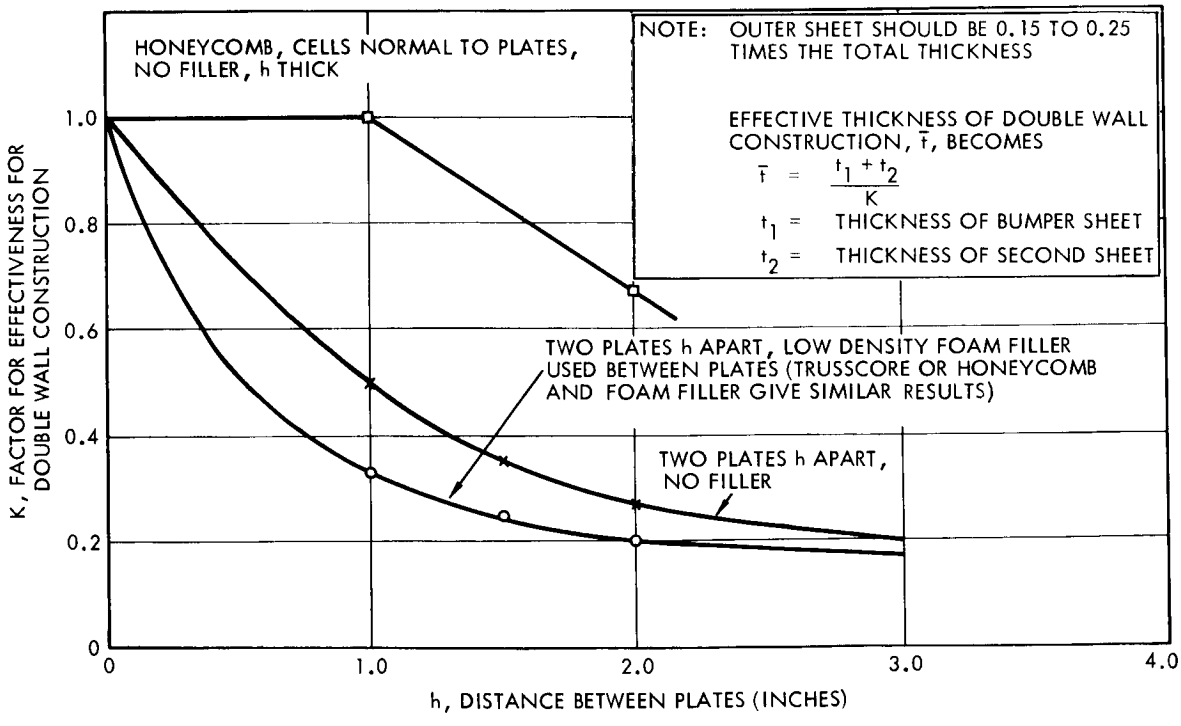

Figure 4-50. Effectiveness of Double Wall Construction

4.10.1 Penetration Equations

Present test facilities lack both the velocity capability and the means for accelerating particles with the low densities representative of meteoroid particles. Various investigators, however, have postulated penetration equations. These equations are used to determine the penetration depth, p, into semi-infinite targets. The relationship between such a penetration depth and the single sheet thickness, t, just sufficiently thick to prevent penetration, has been determined experimentally with the resulting values for the ratio t/p varying from 1.25 to 2.25. A typical variation in the equation for p for V = 22 km/sec and $\rho = 0.44 gm/cm^3$ is a factor of 3.

In the Voyager studies by TRW, three penetration equations were compared. Of these, the Summers and Charters equation gave the greatest penetration depth for a given impact velocity. Impact tests in multiple wall structures have demonstrated that such structures, with or without filler materials between the walls, provide more penetration resistance against perforation than a single sheet, of the same material, for a given weight per unit area.

No theoretical or empirical equations have been derived for the penetration of double wall structures. However, the Voyager studies gave factors to cover the increased effectiveness of double wall construction over single wall. These factors are for use in conjunction with the Summers and Charters penetration equation. The curves of Figure 4-50 show the relationship between the effectiveness factor, K, and the pertinent parameters of wall-spacing and filler material. Partially because of the additional computational flexibility available from being able to consider double wall construction, and partially because this basic equation is the most conservative, the Summers and Charters penetration equation is the one used in the analysis.

With t = 1.5 p, the Summers and Charters equation can be written in the form

$$M = \frac{t^3 \rho_t^2}{4.25^3 \rho_p} \frac{(C_t)^2}{V^2}$$

where

M = meteoroid mass, gm
ρt = target density, gm/cm^3
ρp = meteoroid density, gm/cm^3
V = impact velocity, km/sec
C_t = speed of sound in target, km/sec
t = single sheet thickness, cm

to cover double wall construction. The effective thickness $\bar{t}$ is given by

$$\bar{t} = \frac{t_1 + t_2}{K}$$

if t_1 is between $0.15\ (t_1 + t_2)$ to $0.25\ (t_1 + t_2)$

or

$$\bar{t} = \frac{1.25\ t_2}{K}$$

or

$t_1 + t_2$, whichever is greater, for $t_1 > 0.25\ (t_1 + t_2)$

where

t_1 is the thickness first sheet impacted, i.e., the bumper

t_2 is the thickness of the second sheet or inner wall

4.10.2 Penetration Rate

Using the Summers and Charters penetration equation in conjunction with the upper bound on the meteoroid flux, the velocities of Table 4-8, and a mean meteoroid density of $0.44\ gm/cm^3$, the penetration rates were computed. In Figure 4-51, the number of penetrations per square meter versus the total equivalent thickness of aluminum is given for the mission phases 1 to 2 AU, 2 to 4 AU (asteroid region), and 4 to 5.2 AU. This data is applicable to a mission close to the ecliptic plane.

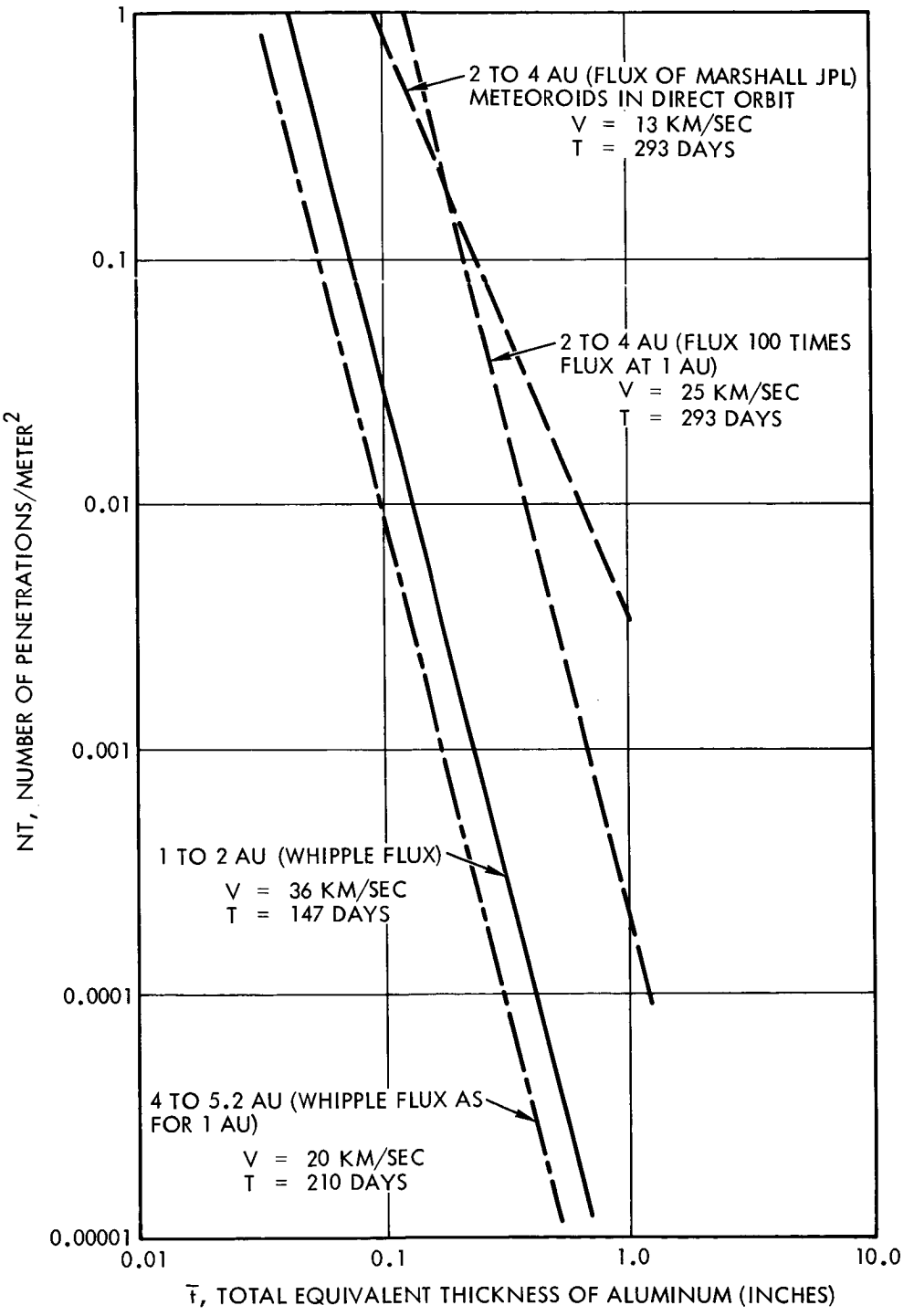

Figure 4-51. Perforation Rates of Aluminum Structures

4.10.3 Protection

It was realized early in the studies that meteoroid protection requirements would lead to additional weight in the spacecraft above that provided as basic structure. Consequently, to minimize this weight addition, at the earliest point in the spacecraft design, the equipment compartment was designed to minimize the compartment surface area. In one instance, for example, early configurations had been designed with the main compartment a toroid surrounding the injection stage. This toroid was 80 inches outside diameter, 46 inches inside diameter, and some 25 inches high, whereas the final configuration is a hexagon 42 inches across and 16 inches deep. The reduction in surface area, neglecting the inner surface of the toroid, was from 8.81 to 2.4 square meters. This meant, for example, that if these spacecraft had the same external construction and meteoroid protection system per unit area, and if this gave a probability of zero penetrations of 0.9 with the toroidal shape, the hexagonal shape would have $P_o = 0.973$.

In arriving at a type of construction to be used for the compartment in the structural design, double wall (or sandwich type) construction was used throughout. This ground rule was implemented to provide the minimum weight. On this basis alone the bottom and top panels would have been of sandwich construction, but the side panels would have been of sandwich construction only if equipment needed to be mounted to them. A weight addition of 7.1 pounds was required to meet this ground rule, but the net result, including protection against meteoroids, is a saving in weight.

All three double wall surfaces have a core or filler material. This was partially a structural requirement to make each area of double-walled construction a single structural element but served as well to provide the additional meteoroid protection associated with a suitable filler material. In selecting the filler material, low density is a major requirement since conventional aluminum honeycomb with the channels normal to the facing sheets is inefficient for meteoroid protection, polyurethane foam, density 1.2 lb/ft^3, was selected. For the aft panel, which is the thermal balance surface of the spacecraft, the use of foam is incompatible with the thermal control requirements. Rather than using a foam-filled

conventional aluminum core, the trussgrid aluminum core is used. Douglas tests indicate that this type of core is equivalent to foam as a filler in a meteoroid protection system. The lowest density version of this core, 2.3 lb/ft^3, was selected. The weight associated with any modification to this baseline design was included as meteoroid protection system weight which, as mentioned before, is 7.1 pounds above a minimum structural design. The baseline structure was as follows.

- Bottom panel, 1.25 inch honeycomb panel, facings 0.015 inch aluminum alloy, with a 2.3 lb/ft^3 trussgrid aluminum core
- Side panels, 1 inch sandwich construction, 0.01-inch facings on a 1.2 lb/ft^3 foam core
- Top panel, 2 inch honeycomb, 0.01-inch facings on a 1.2 lb/ft^3 foam core

A certain amount of meteoroid protection is inherent in the spacecraft design other than the external walls of the compartment. All the equipment was assumed to have 0.03-inch aluminum container; the propellant tank can be penetrated to 25 percent of its thickness, which is 0.005 inch of titanium, and the cabling has a cover material. The 0.005 inch of titanium, or 25 percent of the tank wall, is equivalent to 0.0067 inch of aluminum, based on Charters and Summers equation, and the cable covering has an equivalent thickness of 0.0006 inch of aluminum.

The side panels of the vehicle are shielded by the antenna. This shielding is taken as an additional thickness inherent in the design applicable to that percentage of the side panels shielded by the antenna. This additional thickness is the sum thickness of the facing sheets of the honeycomb construction used for the petals, 0.006 inch of aluminum.

The bottom panel is covered by a radiator surface, which is a 0.01 inch aluminum sheet.

In conducting the analysis, the three surfaces were considered independently; the $P_{(o)}$ versus meteoroid protection weight is computed for each. The equipment layout was examined to determine for each surface what type of equipment would be hit if the surface is penetrated. In the case of the equipment and cabling, these are affected by the component redundancies. For all electronics and the cabling, the area

associated with these was reduced by a factor of 65 percent to account for this redundancy. Then, the effective thickness of the elements penetrated was determined with the baseline structure. The double wall factor was used only at the compartment surface, i.e., the effect of the spacing between the compartment side and the equipment boxes, if any, was neglected as was the distance between the antenna and the area it shields. For example, for a component that is penetrated by a particle that came through a side panel on a total effective thickness of aluminum of

$$t = 0.006 \text{ (antenna)} + 0.03 \text{ (equipment box)} + \frac{1.25\ \ 0.015}{K} \text{ (for baseline design)}$$

$$t_1 = 0.01$$

$$t_2 = 0.02$$

where

K = 0.33 for 1 inch spacing between facings

then T = 0.093 inch

For this same surface, and considering that an equipment factor of 0.65 for redundancy is applicable, the shielded area of the side panel 0.875 meter^2, and the probability of hitting such a component is taken as 0.35 for penetration through a side panel. Hence, the reference area is 0.2 meter^2.

Table 4-9 gives the reference areas for the main equipment compartment and the inherent thickness. This thickness does not include the panel penetrated.

$P_{(o)}$ was computed for each surface with the reference areas of the table and the total thickness of the baseline design. Then the structure was modified by the addition of meteoroid protection in steps, and the $P_{(o)}$ was computed each time. Table 4-10 covers the change in structure for each step.

This table also gives the meteoroid protection weight increments, ΔW, and the associated $P_{(o)}$ for each of the steps for all three surfaces. $P_{(o)}$ versus ΔW were plotted for each surface. Then an increment procedure of obtaining log $P_o / \Delta W$ was used to determine the best weight addition procedure to maximize $P_{(o)}$ for all three sides versus total weight increment for the main equipment compartment. Results are given by Figure 4-52.

Table 4-9. Reference Areas and Thicknesses

Bottom Panel: Area 0.894 meter^2

Item	Probability of Hitting Item	Redundancy Factor	Resulting Reference Area (m^2)	Inherent Thickness (in.)
Propellant Tanks	0.05	1.0	0.045	0.0167
Equipment	0.85	0.65	0.49	0.04
Cabling	0.05	0.65	0.029	0.0016
Nothing	0.05			

Side Panels: Area, shielded = 0.875 meter^2, unshielded = 0.555 meter^2

Item	Probability of Hitting Item	Redundancy Factor	Shielded		Unshielded	
			Resulting Reference Area (m^2)	Inherent Thickness (in.)	Resulting Reference Area (m^2)	Inherent Thickness (in.)
Propellant Tanks	0.25	1.0	0.219	0.0127	0.139	0.0067
Equipment	0.35	0.65	0.2	0.036	0.127	0.03
Cabling	0.10	0.65	0.057	0.0066	0.036	0.0006
Nothing	0.3					

Top Panel: Area over tank = 0.363 meter^2, remaining area = 0.716 meter^2, total area = 1.078 meter^2

Item	Related Area (m^2)	Probability of Hitting	Redundancy Factor	Resulting Reference Area (m^2)	Inherent Thickness (in.)
Propellant Tanks	0.362	1	1.0	0.362	0.0067
Equipment	0.716	0.8	0.65	0.373	0.03
Cabling	0.716	0.1	0.65	0.047	0.0006
Nothing	0.716	0.1			

Table 4-10. Steps Taken to Provide Meteoroid Protection, Weight Increments and $P_{(o)}$'s

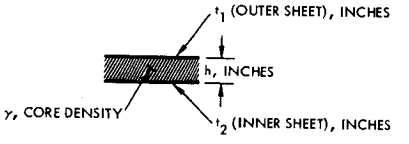

Compartment Side	Panel Data Baseline h	t_1	t_2	γ	Step 1 h	t_2	Step 2 t_2	Step 3 t_1	t_2	Step 4 t_1	t_2
Top panel	2	0.01	0.01	1.2	-	0.025	0.04	0.015	0.065		
Side Panels	1	0.01	0.015	1.2	2	-	0.03	-	0.04		
Bottom panel	1.25	0.015	0.015	2.3	2	-	0.035	-	0.06	0.020	0.095

Weight increments * associated with above steps and the corresponding $P_{(o)}$ for each are:

Compartment Side	Baseline $P_{(o)}$	Step 1 Δw	$P_{(o)}$	Step 2 Δw	$P_{(o)}$	Step 3 Δw	$P_{(o)}$	Step 4 Δw	$P_{(o)}$
Top panel	0.0043	2.5	0.808	5	0.963	11.66	0.996		
Side panels	0.0019	1.54	0.255	4.89	0.905	7.09	0.965		
Bottom panel	0.272	1.39	0.636	4.17	0.947	7.62	0.982	13.19	0.993

* These increments are from baseline, i.e., Δw at step 3 includes the weight increment of steps 1 and 2.

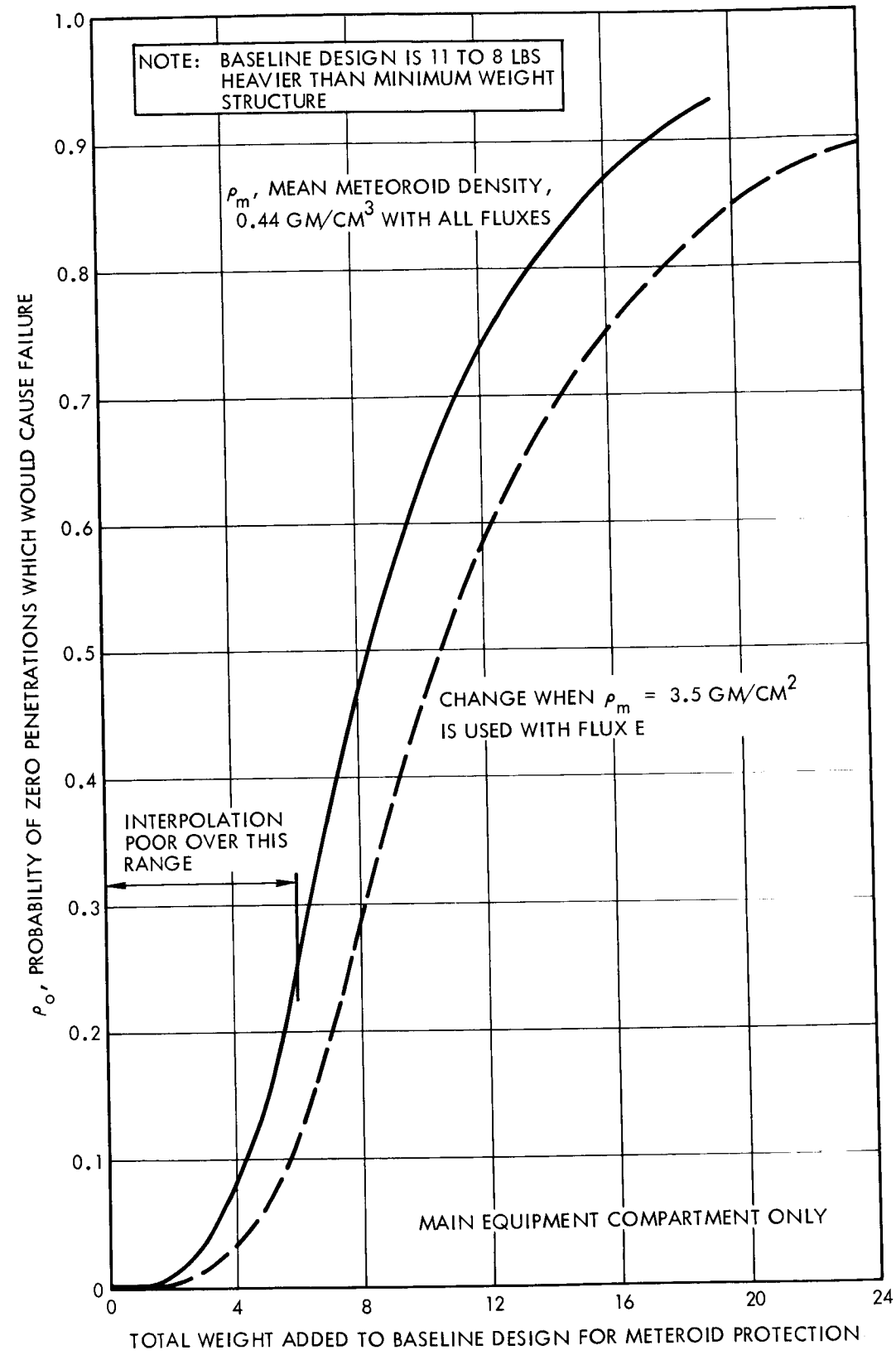

Figure 4-52. Probability of Zero Penetration Versus Meteoroid Protection Weight

If the mass of the particle that can penetrate the antenna dish is known, then the flux rate can be used to determine the quantity of particles that do or do not penetrate this surface. Such data is of interest in computing the velocity errors and disturbance torques on the spacecraft since meteoroids which penetrate transfer much less momentum than had they been stopped. Only the antenna is of concern since it represents the major portion of the spacecraft surface area.

The flux in the asteroid region is of primary concern, because of the substantial increase in the meteoroid flux over other regions. The mass of the smallest meteoroid that can penetrate and which is associated with this flux is of prime interest. In computing the spacecraft velocity error, only particles with a predominant velocity direction are of concern. The meteoroid flux, obtained by extrapolating asteroid observations, flux E of Figure 4-50, is assumed to be particles in asteroid type orbits, i.e., direct and close to circular. Consequently, the magnitude and direction of the velocity relative to the spacecraft is known. The relative velocity is 13 km/sec, and the direction is such that, in general, the aft face of the spacecraft is struck. A mean meteoroid density of 0.44 gm/cm^3 is used. The antenna dish is aluminum honeycomb, with 0.003 inch facings on a 3/8 inch core. Based on Figure 4-51, this panel has an equivalent thickness equal to the sum of the face sheet thickness, i.e., 0.006 inch.

Using the Charters and Summers penetration equation, the particle mass which will penetrate one face sheet is 1.48×10^{-8} gram, and the size that will penetrate both is 1.18×10^{-7} gram. Had a larger mean density been used for the meteoroids associated with flux E, due to the source being assumed as asteroidal, particles of even smaller mass would penetrate. This shows that using low density is conservative. The penetrating particles yield a low momentum multiplication factor due to ejecta.

4.10.4 Effect of Increased Meteoroid Density

The mean density of asteroids has been estimated at 3.5 gm/cm^3. Although this applies to the asteroids of relatively high mass and investigators postulate decreasing density with mass, the 3.5 gm/cm^3 was considered an upper bound on the mean density associated with

particles of asteroidal origin. With this upper bound, which is applicable only to the Marshall flux (flux E of Table 4-8) and is used for design of the bottom panel only, the computations were revised. The resulting probability of zero penetration $P_{(o)}$ for the main equipment section versus added meteoroid protection weight is also plotted on Figure 4-52 for comparison with the previous result, which was based on a mean meteoroid density of 0.44 gm/cm^2 with all meteoroid fluxes. This second curve is the one used for calculating meteoroid protection weight.

4.11 LOCATION OF RTG

The efficient integration of an RTG power supply with the Advanced Planetary Probe requires a thorough understanding of the interactions between the RTG and the spacecraft payload and subsystems. The constraints imposed by the spacecraft on the RTG must be considered in designing the RTG and, conversely, the constraints imposed by the RTG must be considered in the spacecraft design.

The major interactions between an RTG and the spacecraft are:

- Mechanical factors such as supporting structure, allowable geometrical envelope, and moments of inertia
- Thermal interactions such as using the RTG waste heat for environmental control
- Radiation and magnetic field interactions with the scientific payload and other subsystems
- Operational considerations such as power level and lifetime.

A description of some of the interactions and their effect on the design of the RTG and the interfacing spacecraft subsystems is presented below.

4.11.1 Mechanical Interactions

Since an RTG represents a relatively concentrated mass, adequate structural support must be provided to incorporate the device onto or within the spacecraft structure. The method of attachment may also be affected by envelope constraints existing within the booster fairing. For example, if booms are used to locate the RTG away from the main

spacecraft components during operation, the optimum length of the boom, derived from thermal and radiation interaction considerations, may be incompatible with the envelope existing within the fairing. The dynamic loads to which the RTG is subjected during boost and injection can affect the type of insulation that may be used in the RTG. The effectiveness of powdered insulation materials or foils can be severely degraded by excessive vibration or shock loads. For the spin-stabilized spacecraft, described in this section, moment of inertia considerations dictate that either a single RTG be placed on the spin-axis near the c.g. or, alternatively, a number of smaller RTG's be symmetrically distributed around the spacecraft. A single RTG will weigh less than numerous smaller units with a combined power output equal to the single RTG, but the additional weight associated with radiation shielding and thermal considerations may result in a heavier total system weight for the single generator design.

4.11.2 Thermal Interactions

The RTG produces significant quantities of heat since the nominal conversion efficiency of a typical RTG is only on the order of 5 percent. The waste heat may be used to assist in thermal control of the spacecraft if additional heat is required. From the point of view of designing the RTG, total isolation from the spacecraft is desirable. This results in a minimum radiator weight, larger temperature difference between hot and cold shoes, and thus higher RTG efficiency. However, the optimum RTG does not necessarily result in the best overall spacecraft configuration. The RTG may also be located external to the spacecraft and heat may be added to the spacecraft, if required, by radiation and/or conduction. Conversely, the RTG can be located inside the spacecraft with the excess heat not required for thermal control being rejected to space. If an active control system is required to adjust the quantity of heat rejected as the mission progresses, this can affect the overall spacecraft weight and possibly its reliability. Thermal interactions also affect the number of RTG's to be used. For example, if a single RTG is placed on the spin axis of the spacecraft, it represents a single concentrated source of heat while three RTG's on booms can distribute the entire heat flux over essentially the total spacecraft area. (See Section 8.8 for further discussion of thermal control subsystem.)

4.11.3 Operation Interactions

The mission lifetime dictates the type of isotope which may be used in the RTG. The power level is determined from the requirements of the other subsystems after extensive tradeoff studies have been made to minimize the total system weight. A decrease in power level may result from an increase in antenna size or a decrease in bit rate for a given antenna size. The effect of bit rate on the data handling system must then be considered. The combination that results in minimum weight and maximum reliability for the spacecraft/RTG system determines the power level. The use of an RTG power supply may dictate special handling requirements on the launch pad. The RTG may have to be cooled during integration with the spacecraft. Additional instrumentation may be required for checkout of the RTG prior to launch and to monitor its performance in flight.

4.11.4 Radiation and Magnetic Interactions

An RTG produces nuclear radiation and magnetic fields which may interact with one or more of the other spacecraft subsystems. Scientific instruments which measure planetary and interplanetary radiation and magnetic fields may be perturbed by the RTG fields. An investigation of each instrument is necessary to determine the possible RTG interference and to determine if it is necessary that the instrument be separated or shielded from the RTG. The limitations on spacecraft magnetic and nuclear radiation environment imposed by the science payload was discussed in Section 2.5.

In addition, all electronic components on board the spacecraft may be adversely affected by extended exposure to an RTG radiation field. The cumulative effects of ionizations and displacements in electronic components may eventually cause damage sufficient to prevent the components from operating satisfactorily. Experimental results compiled by the Radiation Effects Information Center at Battelle Memorial Institute indicate that the threshold of integrated damage for electronic circuits, systems, and equipment in general is about 10^{10} neutrons/cm^2 of displacement (neutron) radiation and about 10^4 rad of ionizing (gamma) radiation.

Two approaches can be taken to reduce possible damage: 1) the radiation field at the electronic systems can be reduced, either by

positioning the RTG further from the electronics or by installing a radiation shield to attenuate the radiation between the RTG and the electronics, and 2) the damage threshold of the electronics can be effectively increased. By redesigning circuits to eliminate certain components, or by simply replacing certain components with similar ones which are more radiation resistant, the damage threshold level may be raised as much as two orders of magnitude. It is probable that appropriate circuit design to increase the damage threshold will entail less weight penalty than either isolation or shielding.

4.11.5 Alternate Configurations

For the spin-stabilized spacecraft discussed in this volume, the critical constraints affecting the location and design of the RTG are:

- Spacecraft mass properties and moment of inertia considerations
- Nuclear radiation and magnetic field interactions with the spacecraft
- Thermal control considerations

Although a detailed tradeoff analysis of the many variables and interactions has not been completed, a number of alternate RTG configurations and locations were considered. Either a single RTG located on the spin axis near the c.g. or three smaller units placed symmetrically around the spacecraft spin axis are required to satisfy the spacecraft moment-of-inertia requirements. In either case, the final spacecraft roll moment of inertia must exceed the pitch or yaw inertias if passive nutation damping is used.

The heat rejection surface or radiator represents a considerable fraction of the total weight of an RTG. Attaching RTG's of a thin flat plate configuration to the underside of the antenna in order to utilize the antenna surface as a radiator could result in a significant weight savings for the RTG. (See Figure 4-53, Alternate A.) However, the antenna is a light honeycomb structure which would have to be thickened considerably to maintain structural rigidity and accommodate the RTG. In addition, the thermal stresses could cause warping of the antenna surface with a resultant decrease in the efficiency of the communication subsystem. A flat plate configuration with a radiating surface on one side and insulated on the other side could be attached to the spacecraft compartment (see Figure 4-53, Alternate B). This configuration would eliminate booms

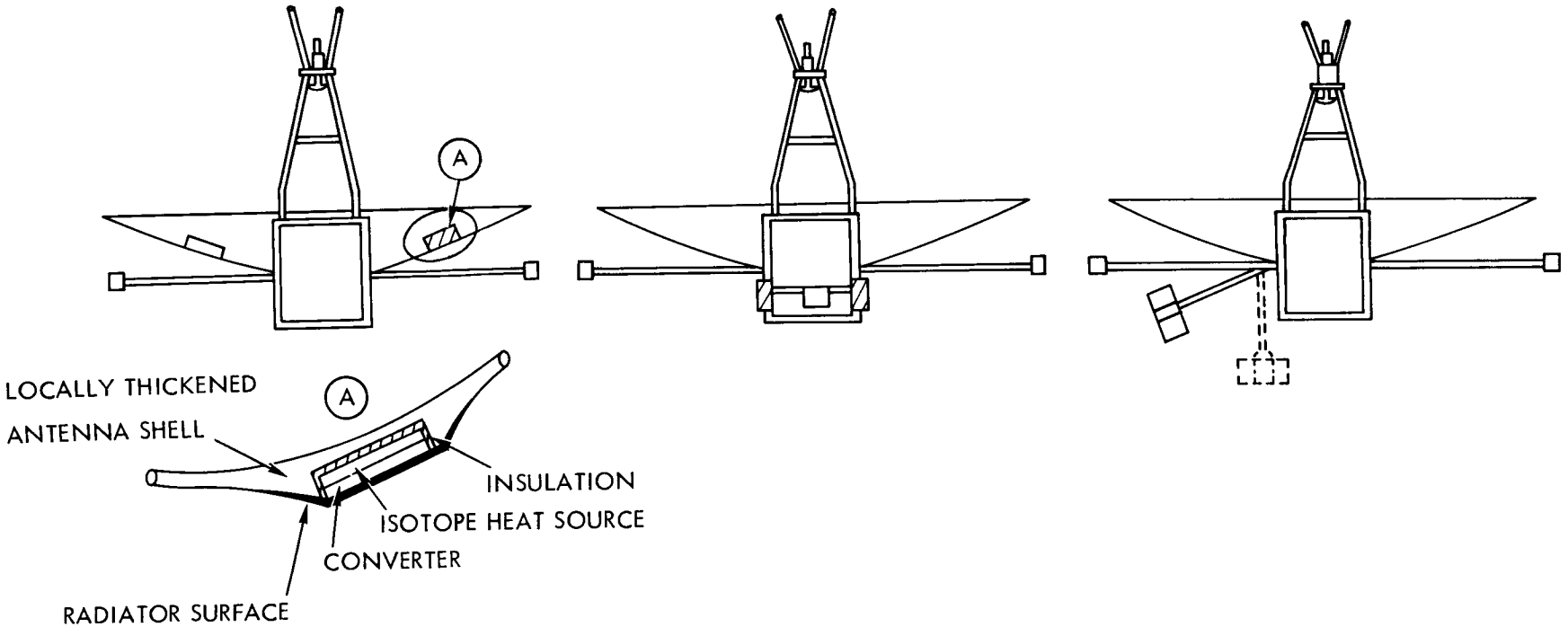

Figure 4-53. RTG Locations

for external location of the RTG's. However, the close proximity of the RTG to the spacecraft could result in nuclear radiation interactions with the electronics and the scientific instruments.

Heat pipes might also be used to transfer heat from a centrally located isotope source to three converters located symmetrically on the spacecraft compartment or body mounted to the antenna structure. The heat rejection surfaces would be located on the converter, and the isotope source would be located over the spacecraft compartment within the antenna. Since the heat source must be heavily insulated to maintain the required internal temperatures, the thermal interaction of the source with the spacecraft would be minimal. The use of heat pipes would minimize the thermal gradients in the thermoelectric converters, concentrate the heat flux, and provide a power flattening capability, all of which will improve the converter performance and efficiency. Some of the heat from the source could also be utilized for thermal control. However, nuclear interactions with the spacecraft and science payload as well as current development status preclude their immediate use on the 50-pound science payload class Jupiter probe.

The RTG can be symmetrically located around the spacecraft on booms (see Figure 4-53, Alternate C) and this will provide a favorable inertia ratio. If total thermal isolation of the RTG's from the spacecraft is desired and louvers are used for thermal control, the view factor from the RTG must be limited in order to minimize the louver surface area. Conversely, the view factor can be adjusted to permit nominal heat input to the compartment. For passive thermal control of the compartment the use of a small fraction of the RTG waste heat results in a significant reduction of the system sensitivity to heat leaks. The final position of the RTG's must insure that heating of the antenna or other components external to the compartment is not too severe.

4.11.6 Conclusions

Considering the many interface requirements, and alternative configurations, it was concluded that three RTG's mounted on booms symmetrically spaced around the spacecraft appeared to best satisfy the

total spacecraft requirements. The RTG's are right circular cylinders with a finned surface for heat rejection. This configuration satisfies the moment of inertia and mass property considerations to obtain a dynamically stable spinning spacecraft. Placement of the RTG's at a distance of about seven feet from the spacecraft spin axis results in reasonable nuclear radiation shielding requirements and is compatible with the envelope within the fairing. The thermal control subsystem does not require waste heat rejected by the RTG.

Radiation levels at various equipment locations for the selected design are given in Section 8.2. Requirements imposed by the science payload were presented in Section 2.5.

4.12 LOCATION OF SCIENCE SENSORS

Science sensor locations on the spacecraft are shown schematically in Figure 4-54 to 4-63.

The magnetometer is mounted on a 12-foot deployable boom providing the necessary isolation for measuring interplanetary magnetic fields down to 0.1 gamma. The solar cosmic ray counter is also mounted on a deployable boom on the opposite side of the spacecraft, and the sensor scans with the field of view 60 degrees pointed in the general direction of the sun and earth. The galactic cosmic ray sensor is mounted at the back of the spacecraft to shield it from solar cosmic rays. It has a field of view of 60 degrees.

The plasma probe is mounted in the feed assembly array; its field of view of 160 by 20 degrees provides a good scan mode in the ecliptic during each spin cycle.

The micrometeoroid detector is on the dark side of the spacecraft since particles in the asteroid belt will generally impact this area. The infrared radiometer is also mounted on the dark side of the spacecraft but at right angles to the spin axis so that with its 2 degree field of view it can scan the illuminated portion of Jupiter during the flyby.

The TV system with a 4 degree field of view is also mounted at the base of the spacecraft so that it can scan the planet during the approach once each spin cycle. It has a mirror which can be turned through

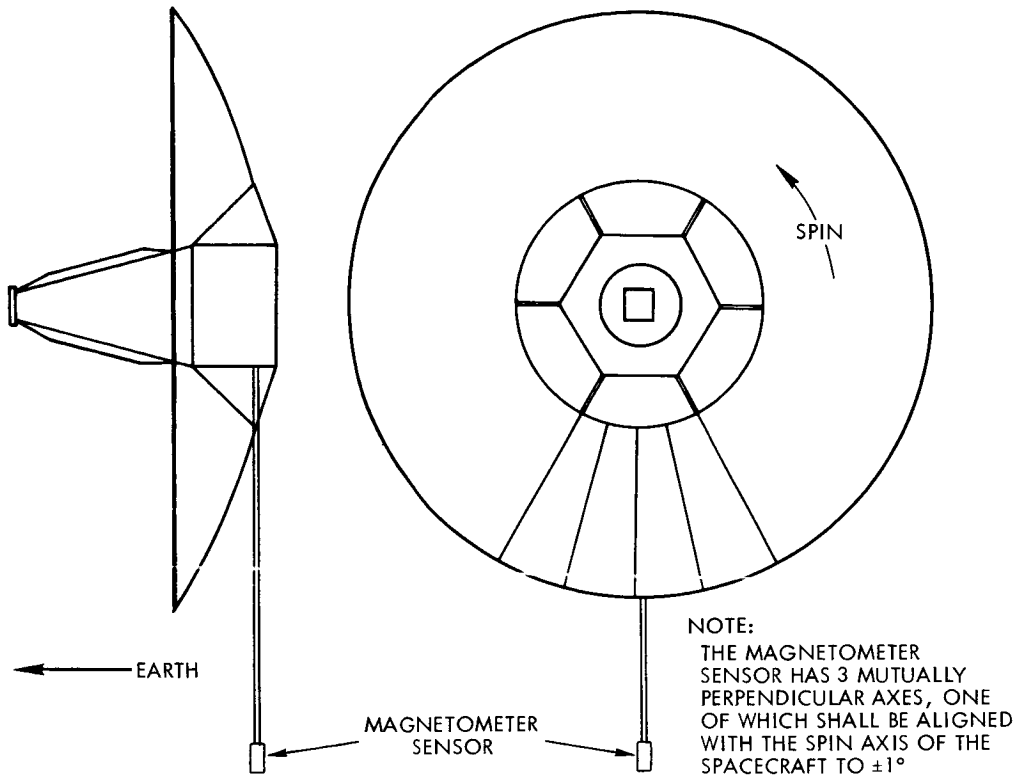

Figure 4-54. Magnetometer

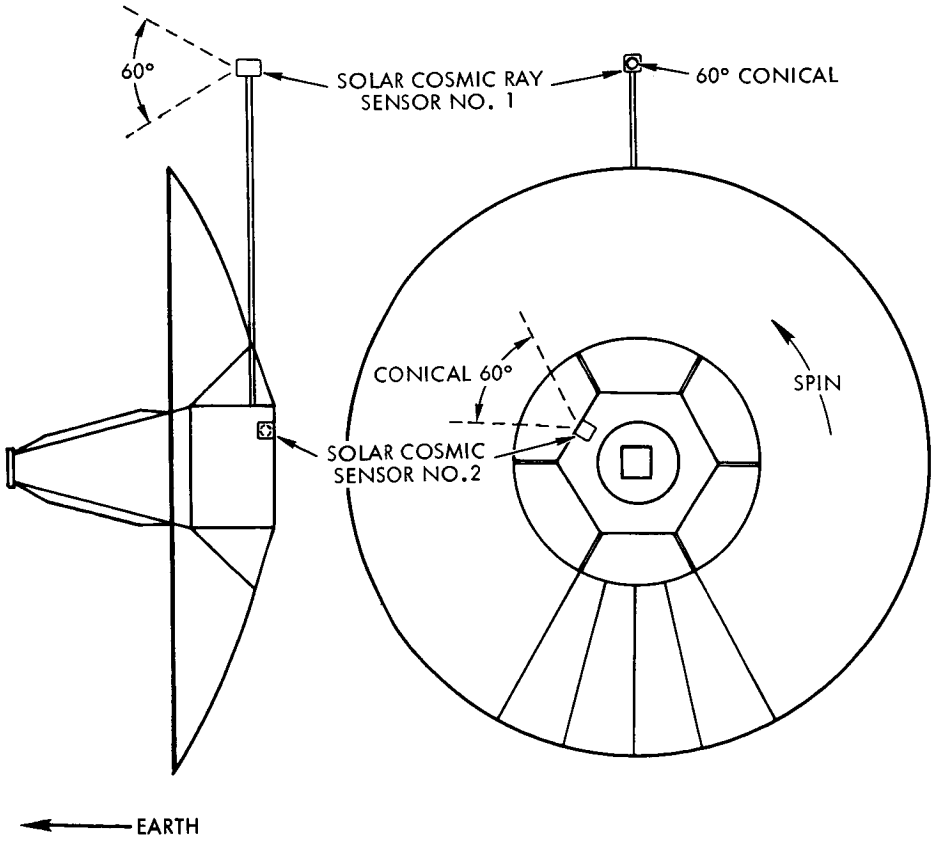

Figure 4-55. Solar Cosmic Ray

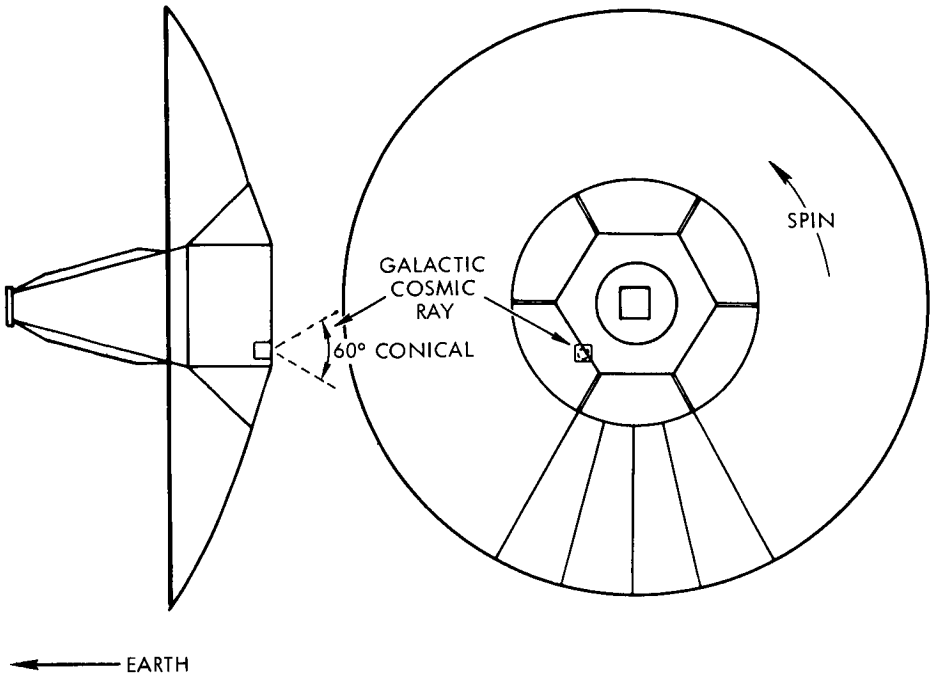

Figure 4-56. Galactic Cosmic Ray

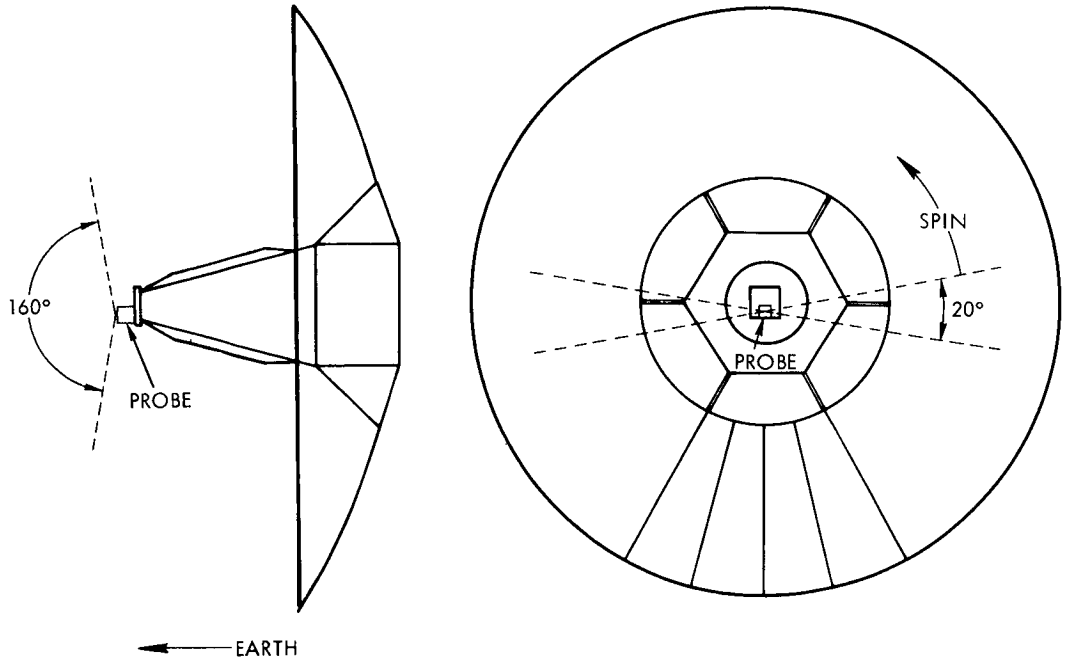

Figure 4-57. Plasma Probe

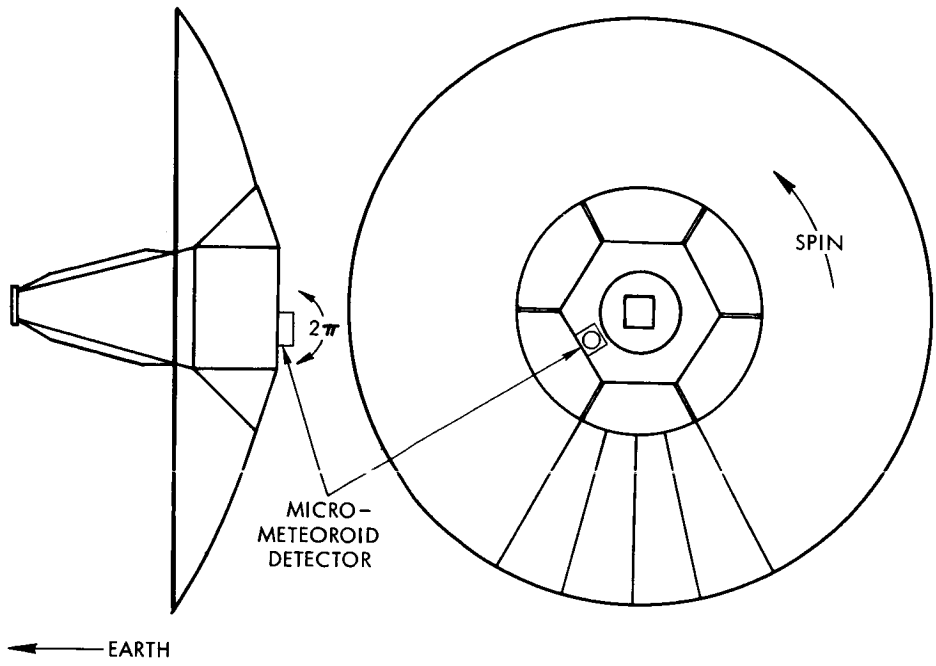

Figure 4-58. Micrometeoroid Detector

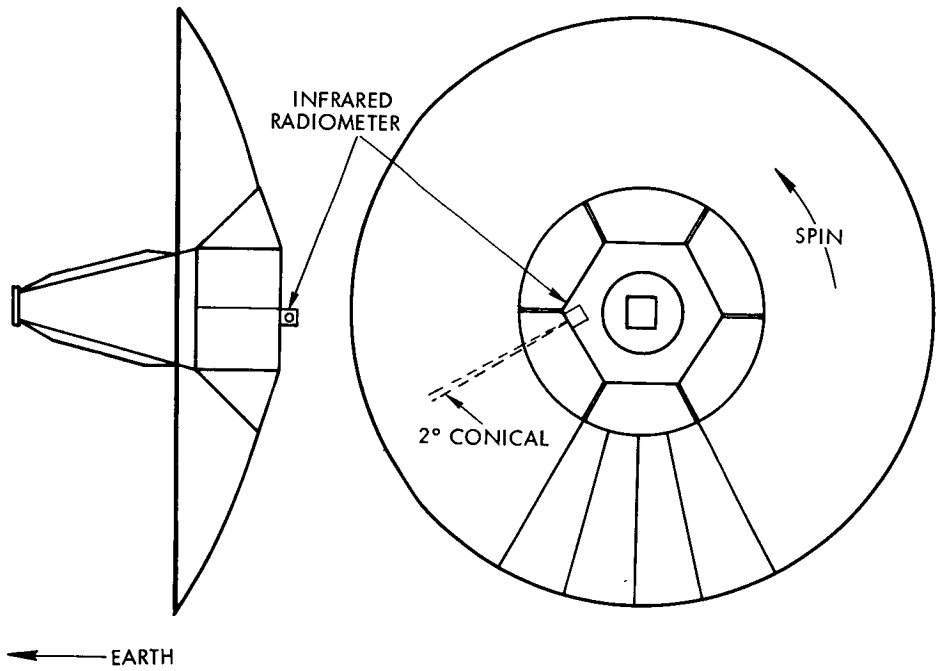

Figure 4-59. Infrared Radiometer

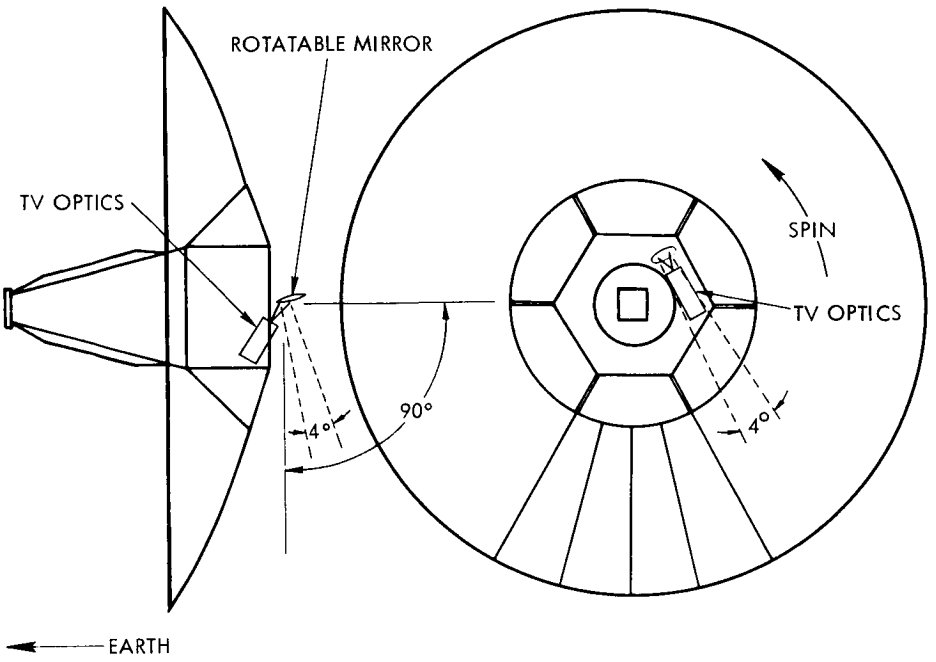

Figure 4-60. Television

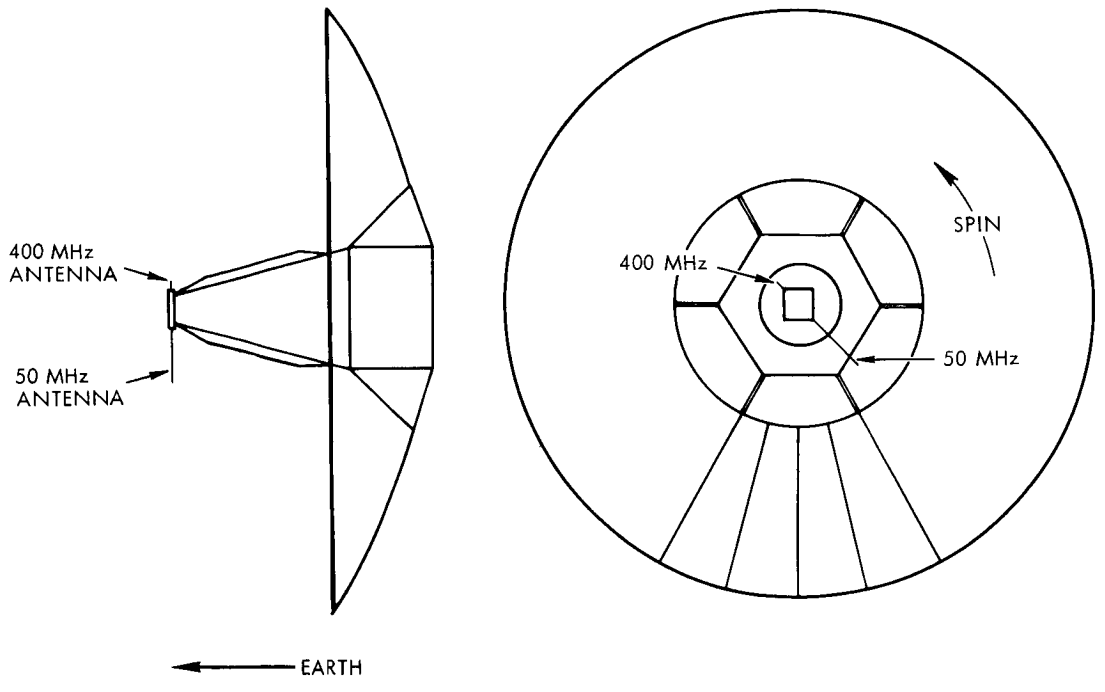

Figure 4-61. Radio Propagation

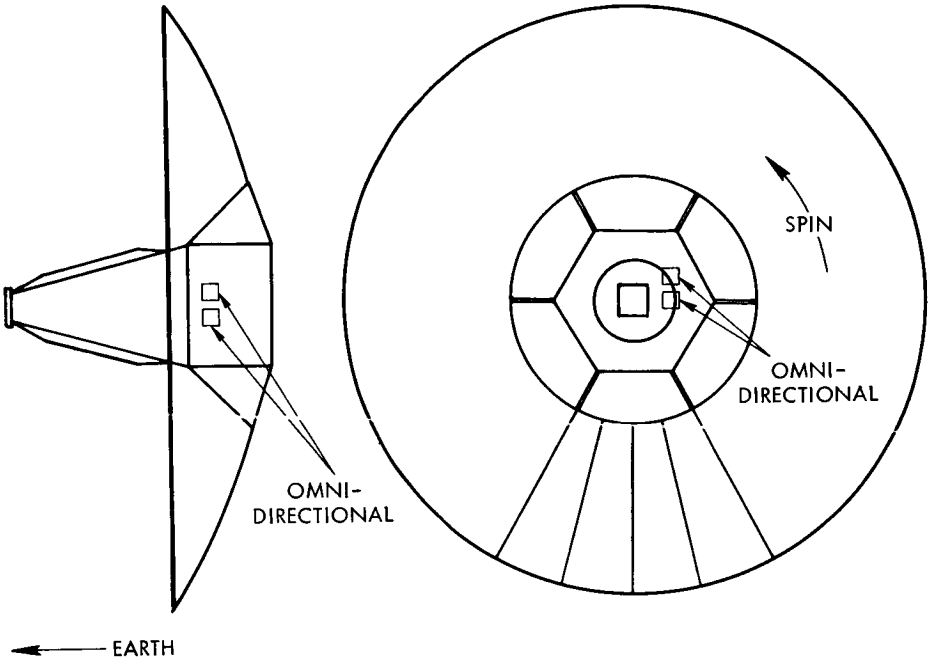

Figure 4-62. Trapped Radiation

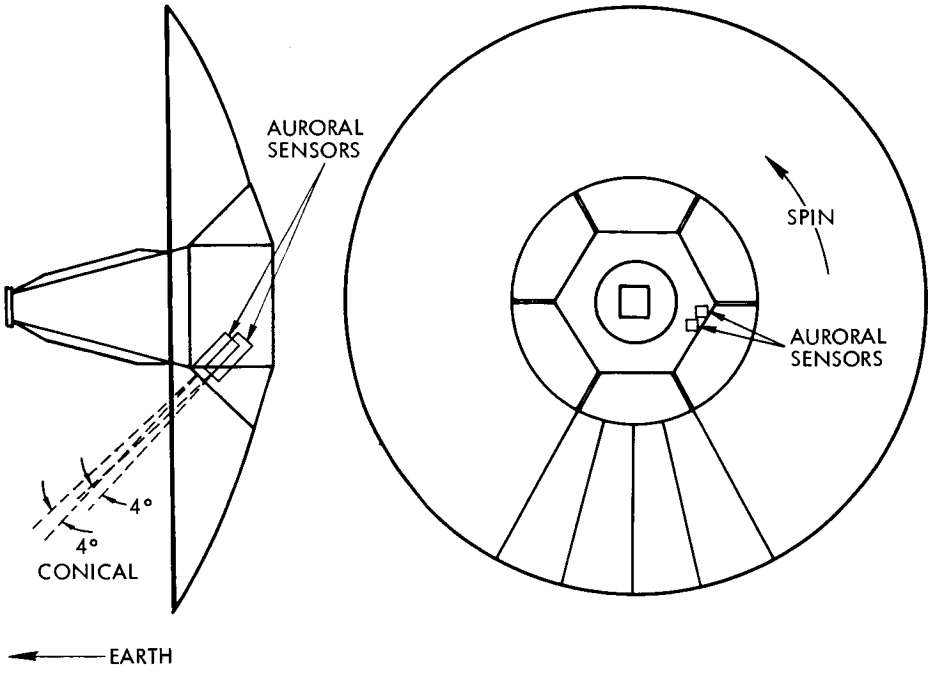

Figure 4-63. Auroral

90 degrees to permit pictures to be taken from 100 Jupiter radii through flyby.

The dual frequency radio propagation experiment has two whip antennas mounted to the feed assembly. These antennas always look toward the earth, thus assuring constant illumination by the ground transmitter.

The trapped radiation detectors are omnidirectional and are mounted in the spacecraft compartment. They present no special requirements.

The auroral sensors are mounted so that they make a conical scan in the general direction of the earth. During the flyby of Jupiter they scan the dark side of the planet once each spin cycle.

4.13 OTHER DESIGN CONSIDERATIONS

The system design considerations not discussed elsewhere in this section are presented here in the form of guidelines which the design team has employed in the development of the selected configuration for the Jupiter flyby mission. These objectives and requirements are satisfied by the selected configuration and are consistent with the following constraints:

- RTG power supply
- Fifty-pound science payload
- Spin-stabilization
- A large deployable parabolic communications antenna
- Reasonable modularity

The configuration alternatives considered during the design are also discussed to illustrate some of the salient features of the selected system and the extent to which the guidelines have influenced the basic design.

4.13.1 Design Guidelines

Early in the study a set of guidelines were adopted for the design of a baseline spacecraft. These are listed here according to the areas of design affected.

Structural and Mechanical System

a) Make maximum use of the structure for multiple purposes, i.e., equipment mounting panels for thermal radiation plates and for micrometeoroid protection.

b) Employ structural shapes and materials that yield maximum strength-to-weight ratios.

c) Minimize the number and size of joints and the surface area of all components.

d) Select design concepts to ensure uniform levels of loading for the entire structure.

e) Do not compromise the structure for the nonflight loading conditions of ground handling and transportion.

f) Minimize the number of deployable appendages.

g) Select stiffness characteristics of major assemblies so as to avoid deleterious coupling with launch vehicle resonant frequencies.

Propulsion System

a) Locate the expendables and thrusters on or symmetrically about the spin axis.

b) Modularize the propulsion system so that it can be bench-tested prior to installation.

c) Orient the thrusters to minimize spacecraft assembly contamination and heating by the exhaust plume.

d) Minimize thrust levels to limit inertia loads.

e) Use spherical tankage and select pressure levels that minimize propulsion system weight.

f) For economy, use existing thrusters where possible and minimize the numbers of different types used.

g) Use high density and high I_{sp} propellants to minimize weight.

Thermal Control System

a) Shield the thermal radiating areas of the equipment compartment from the sun for maximum thermal efficiency.

b) To enhance thermal control, insulate all equipment compartment exterior nonradiating surfaces and provide long, nonconductive structural paths for all externally mounted components.

c) Minimize the equipment compartment external surface area and external connections to minimize heat leaks.

d) Reduce the number of equipment mounting compartments and maximize the conductance and radiant energy interchange between internally mounted components, including tankage, to increase the thermal efficiency and maintain acceptable temperature limits.

e) To minimize hot and cold spots in the equipment compartment, distribute the heat producing components uniformly over the equipment mounting panel.

f) Design the spacecraft to be symmetrical with respect to the sun and control the thermal radiation characteristics of the external surfaces to minimize solar torque imbalance.

Attitude Control System

a) To minimize balance weight and attitude errors, develop a symmetrical equipment arrangement so that the geometrical spin axis, principal axis, and thrust axis are coincident.

b) Equalize line lengths between valves and nozzles to balance line losses.

c) Locate sun sensors so as to provide adequate fields of view.

d) Locate the spinup and despin nozzles in the plane of the c. g. to minimize cross coupling and maximize their distance from the spin axis to reduce propellant requirements.

e) Minimize the mass moments of inertia to reduce propellant requirements.

f) For increased efficiency, locate nozzles to minimize thruster exhaust impingement on the spacecraft.

Electrical Power System

a) Use RTG units for the primary power source.

b) Isolate the RTG's from the spacecraft to minimize radiation interference with the scientific experiments.

c) Locate three RTG's on long radial booms in the plane of the spacecraft c. g. to provide a stable spacecraft configuration, a ratio of spin axis moment of inertia to transverse axis moment of inertia equal to or greater than 1.1.

d) Protect the spacecraft from the RTG high thermal output.

Telemetry and Communications System

a) Use a large diameter deployable parabolic antenna for high gain communications.

b) Provide antennas for low gain communications which together have a 4π steradian field of view.

Science Payload Support System

a) Provide the experiment sensor with the orientation and fields of view required.

b) Insofar as possible use nonmagnetic materials in the spacecraft to minimize permanent, induced, or transient fields.

c) Provide the scientific equipment with the structural support, thermal environment, micrometeoroid protection, shock, and vibration isolation, and the protection from exhaust contamination that is required.

d) Eliminate direct or reflected sunlight on sensor apertures as appropriate.

e) Locate the magnetometer experiment sensor on a deployable boom.

Packaging

a) Include provisions for accessibility and flexibility in the arrangement of science assemblies to accommodate changes, additions or deletions in the scientific payload.

b) To reduce cabling weight, locate associated components together.

c) Provide easy access to equipment for maintainance and checkout.

d) For increased reliability, minimize the connections to deployed or articulated items.

e) To reduce the fairing size and make more weight available to the flight spacecraft, maximize equipment packaging density.

4.13.2 Alternate Configurations

This section describes the major alternate configurations considered for the spin-stabilized Jupiter flyby mission. Some of the more salient features which either conform with, or take exception to, the design adopted for the selected configuration are noted.

4.13.2.1 First Alternate Configuration

The configuration of Figure 4-64 represents a geometry that allows the spacecraft to be stowed within the minimum length "B" fairing. An unextended fairing was desired to maximize the weight available for the spacecraft.

Similar to those of the selected configuration are the relative positions occupied by the interstage, the TE-364 solid injection motor, the high gain antenna, and other assemblies. However, no aft pointing midcourse correction engine is provided. The RTG's are closer to the spacecraft which necessitates additional insulation. Unlike the selected configuration, only one separation joint is completely external to the flight spacecraft. However, this does not necessarily preclude the capability for jettisoning the empty TE-364 motor case.

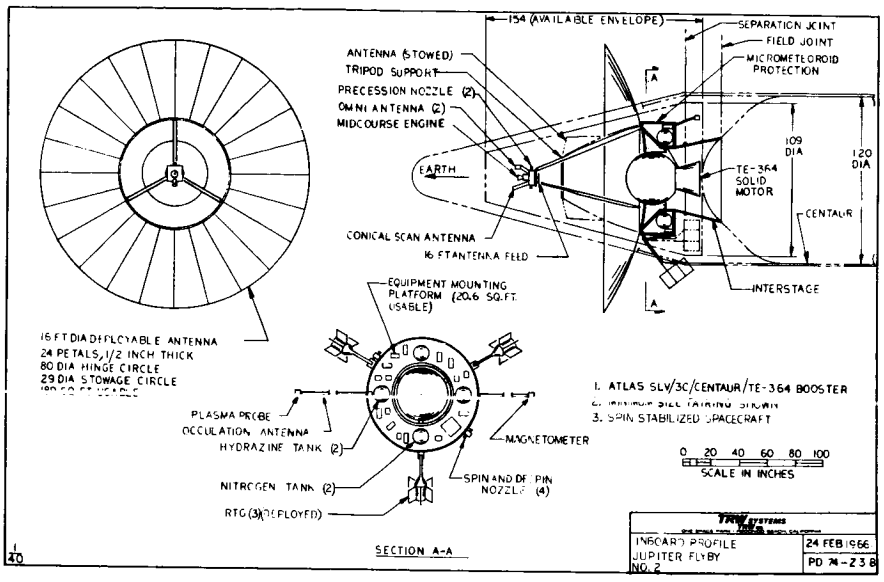

Figure 4-64. Inboard Profile — Jupiter Flyby No. 2

It was found that to retain the 16-foot diameter antenna, the appropriate size with the 10-watt transmitter, and the desired bit rate at encounter, the equipment compartment must be located at the outer periphery of the configuration if the fairing were not lengthened. As a result, the equipment compartment shown is larger than that which is actually desired and considerable weight is expended in compartment structure and micrometeoroid protection.

Subdividing the single compartment into two or three separate compartments distributed around the periphery was considered, but this also results in too much weight assigned to structural material and micrometeoroid protection and unduly complicates the thermal control system.

4.13.2.2 Second Alternate Configuration

Figure 4-65 depicts a spacecraft configuration that also stows within the minimum length "B" fairing and incorporates an on-centerline compact main equipment compartment similar to that of the selected configuration.

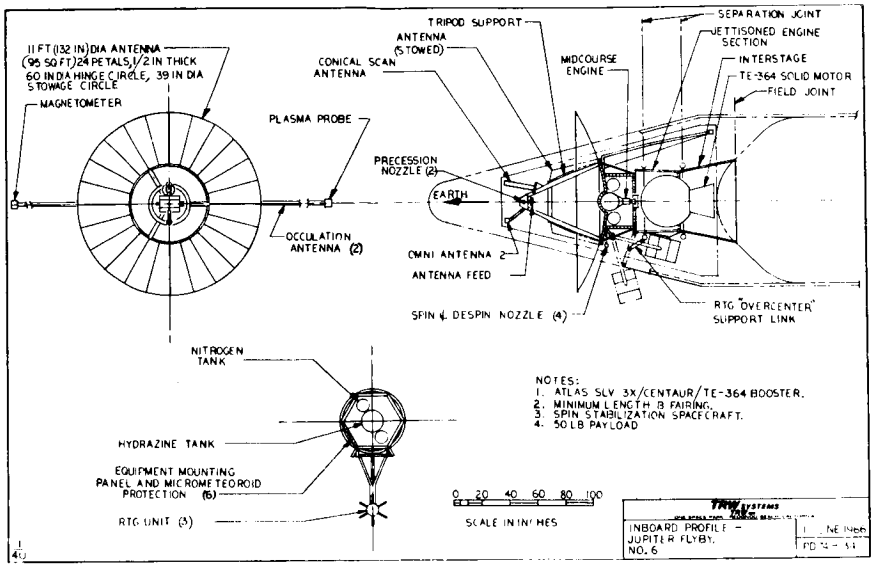

Figure 4-65. Inboard Profile – Jupiter Flyby No. 6

The interstage structure, the injection motor adapter assembly, the RTG installation, and the forward equipment platform arrangement, although pictured somewhat differently from those shown in the selected configuration, are essentially the same as those of the elected configuration.

As illustrated, the price paid to place this configuration into an unlengthened "B" fairing is a reduction in the size of the high gain antenna. The effective area of the high gain antenna is reduced by over 50 percent.

4.13.2.3 Other Alternate Configurations

Other spin-stabilized spacecraft configurations tailored for Jupiter flyby missions have been generated. The effects of different boosters, different propulsion systems, and various sizes of deployable high gain antennas (including cassegrains) as well as many arrangements of the miscellaneous spacecraft components have been examined to arrive at the currently overall optimum layout represented by the selected configuration.

In the course of configuration development, consideration has been given to modular spacecraft design to accommodate spacecraft growth for planetary orbiting and planetary capsule entry missions. For

example, a spacecraft configuration designed for a planetary flyby mission and using an Atlas SLV 3C/Centaur/TE-364 booster is shown in Figure 4-64.

By using a higher performance booster such as the Titan IIICx/Centaur, and by replacing the TE-364 injection motor with deboost propellant tankage, the flyby configuration can be changed into one having planetary orbiting capabilities. One example of such a configuration is shown in Figure 4-66.

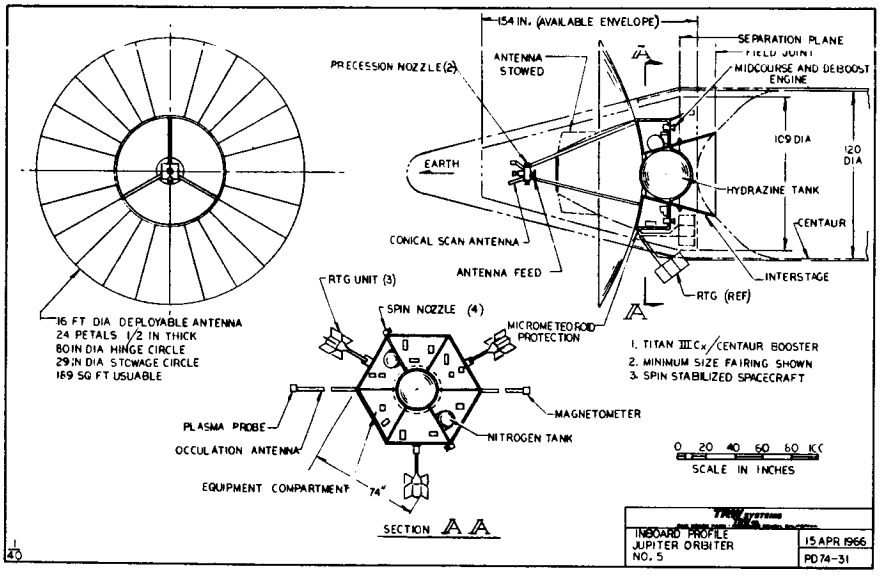

Figure 4-66. Inboard Profile – Jupiter Flyby No. 5

5. PROBLEM AREAS

A paramount consideration in the design of the 50-pound payload, spin-stabilized probe has been to minimize the potential problem areas. However, it is clear that the lifetime required for this mission presents a basic problem in reliability which can be solved only by careful procurement, development, testing, and extensive use of redundancy. In addition to this key problem, problem areas exist regarding the RTG's, the deployable antenna, thermal control, and the earth pointing techniques.

The problem with the radioisotope thermal generators centers on the availability of the fuel, Pu 238. Since these areas are the responsibility of the AEC, TRW Systems is not in a position to evaluate the problems completely. However, discussions with the AEC as well as results of a number of in-house studies indicate there are no state-of-the-art problems involved. Rather it is a matter of currently limited Pu 238 production and cost and schedule problems in increasing this production. See Section 8. 2.

The second key problem is the design and development of a deployable antenna suitable for this mission. Because deploying structures in space is a complex problem, TRW Systems has proposed the use of an already designed and ground tested deployable structure developed as a solar collector for the Air Force. The Sunflower device built was 32 feet in diameter, was tested for a Centaur launch environment in a stowed position, and tested in the deployed condition up to 5 g's. (See Section 4. 1.) The Sunflower collector was designed to stricter tolerances than are required for this antenna application, and this fact, coupled with the successful ground test, gives us confidence that there is no basic problem in the design and development, only the standard spacecraft engineering problems.

A third potential problem area is controlling the heat leaks of the spacecraft. Our past experience with spacecraft as well as extensive thermal studies have convinced us that again there is no fundamental problem, that successful achievement of the control of heat leaks is only a matter of thorough thermal design coupled with an extensive thermal test program. See Section 4. 9.

Another potential problem area lies in the data processing technique to be used with the conical scan earth-pointing system. Conical scan techniques have been used successfully for many years, but not at scan rates as low as proposed here. Our studies to date have shown that a number of techniques exist which can satisfy the mission requirement, but that each has its own problems. The technique proposed here, using a body-mounted conical scan helix up to 2 AU from earth and a flexurally offsetable feed on the high gain antenna from 2 AU out, appears at this time to be the most effective approach. (This approach and alternates are discussed in Section 4. 4.) While careful study and test is necessary to make a final selection among the alternatives, giving particular attention to reliability and failure mode analysis, there appears to be no inherent difficulties in solving the problem.

An additional problem, analyzed in Section 2. 4, is the effect of the radiation around Jupiter on the spacecraft and experiment equipment. Our analyses indicate that with proper component selection, spacecraft equipment can be expected to survive on a flyby mission. However, much study and test is necessary to verify this assumption.

6. COMPARISON WITH MARINER AND PIONEER

As specified in the statement of work, the spacecraft in this study have been compared to Pioneer 6 and Mariner 4. The spin-stabilized configuration described in this volume has a great deal in common with the spin-stabilized Pioneer 6, but much less with Mariner 4. Table 6-1 presents a weight comparison of the three spacecraft, although necessarily the subsystem comparison is somewhat arbitrary. For example, science data automation is in the command sequencer on the Advanced Planetary Probe, which also serves as the central computer and sequencer.

6.1 PIONEER 6

The 50-pound payload of the Advanced Planetary Probe has one basic difference from the Pioneer 6 spacecraft, i.e., the spin axis of the Advanced Planetary Probe lies in the plane of the ecliptic while the spin axis of Pioneer 6 is perpendicular to the ecliptic. The differences between Pioneer 6 and the Advanced Planetary Probe arise principally from this difference.

The communication link is very similar. The TWT's have approximately the same power level and the driver units are similar. The receivers are related although somewhat improved in noise figure for the Advanced Planetary Probe. The command decoder is also very similar, but a sequencer for propulsion maneuvers and for experiment operation during the terminal maneuver at Jupiter has been added. The antennas are completely different since the APP can point a high gain antenna precisely toward the earth.

The data subsystem is also similar to that of Pioneer 6 with a flexible data rate and a flexible format capability; however, tape recorders have been added to minimize ground station communication requirements and to store data during the encounter. The orientation subsystem, although based to some extent on the Pioneer 6 subsystem, requires processing the signal from the earth rather than processing the signal from the spacecraft on earth. The pneumatics and the sun sensor techniques are essentially identical to Pioneer 6. The power subsystem requires radioisotope thermoelectric generators, and is quite different from Pioneer 6; however,

Table 6-1. Weight Comparison, in Pounds

	Mariner 4	Pioneer 6	50-lb Payload Advanced Planetary Probe
Antennas	9.43	2.01	73.8
Central sequencer and computer	11.38	-	-
Command	10.12	10.72	14.6 (includes on-board sequencing)
Data encoder	22.43	8.81	11.0
Guidance and control	63.29	6.89	28.2
Power	70.95	5.08	11.3
Pyrotechnics	12.21	-	5.0
Radio	34.4	16.87	18.3
Propulsion	47.55	-	44.3*
Solar panels or RTG's	79.02 (700 watts at 1 AU)	16.89 (81 watts at 1 AU)	77.6 (100 watts)
Structure	78.44	17.36	70.1**
Cabling	45.69	9.87	18.0
Tape recorder (storage)	16.89	1.69	15.9
Temperature control	15.35	6.80	9.5
Science payload	40.78	35.09	50.0
Science data automation	11.78	-	-
Planetary scan platform	6.85	-	-
Total	574.74	138.35	450.2***

* Includes third stage spinup and spacecraft despin

** Includes 33.1 pounds micrometeoroid and radiation protection

*** Does not include 42.2 pounds contingency and balance

the fact that no batteries are carried makes the power concept similar to that of Pioneer. The thermal subsystem insofar as it is an insulated box, is similar to Pioneer 6, but the addition of thermal switches as well as heater units for equipment mounted external to the boxes, is quite different from the Pioneer 6 louver system.

The electrical distribution equipment is quite similar to that of Pioneer since the command distribution unit is essentially identical, as are the cabling approaches. A pyrotechnics control box is not used on Pioneer 6. Since there is no propulsion subsystem on Pioneer 6, there is in this regard no comparison.

6.2 MARINER 4

Because the configuration presented here is spin-stabilized, it is obviously quite different from the Mariner 4 concept. However, there are some similarities with respect to the communication system. The TWT proposed is similar to the unit carried in Mariner 4 and the receivers are related. Both the Advanced Planetary Probe and Mariner 4 carry body-mounted antennas, another common element; however, Mariner 4 takes advantage of specific trajectory characteristics to provide the high gain during planetary encounter; the Advanced Planetary Probe points toward the earth at all times. The command subsystem is considerably different in concept since most activities on the APP are carried out by ground command except for some limited sequencing for propulsion and the experiment activities at encounter. The data handling subsystem is different except that tape recorders are used on both. The power subsystem uses RTG's, not solar cells and does not require batteries for peak loads. The orientation subsystem is different from Mariner 4 since it is a torquing system. It does, however, use a nitrogen cold gas for thrust. The propulsion subsystem is, like Mariner 4, a hydrazine monopropellant system and a very similar technology is used, but the use of spin stabilization removes the requirement for jet vanes. The electrical integration techniques are not related to Mariner 4.

Because this configuration is spin stabilized, the planetary experiments are limited in their viewing time by the spacecraft spin rate and in this regard are not at all similar to Mariner 4 with its planetary scan platform.

7. SPACECRAFT SYSTEM DESIGN

This section describes the spacecraft system design which evolved from the analyses discussed in Section 4. Included herein are configuration drawings, a system block diagram, flight sequence with a weight and power estimate, and system performance characteristics including trajectory accuracy, accommodation of science objectives, reliability, and compatibility of the spacecraft with the launch vehicle. The concept described here demonstrates feasibility only, but enough study has been performed on which to base reasonable cost and schedule estimates.

7.1 SPACECRAFT CONFIGURATION

The artist's perspective drawing in Figure 1-1 shows the spin-stabilized spacecraft selected for a Jupiter flyby mission. This spacecraft, which has a 50-pound scientific payload, is boosted by an Atlas SLV 3C/ Centaur with a TE-364-3 solid motor for orbit injection. The in-board profile engineering drawing of Figure 7-1 shows the third stage and spacecraft mounted to the Centaur stage of the booster. The spacecraft is housed within a "B" fairing (see Section 2.1) which has been extended 16 inches in length.

The system block diagram is shown in Figure 7-2. The emphasis has been on system simplicity and minimum interface between the spacecraft components and experiments. For safety the pyrotechnic controls are completely separated, as is the associated cabling. All redundant components in separate boxes are shown; however, the redundancy in the input decoders and sequencer is not at the box level but at the component level, and is not shown. The command subsystem (see Section 8.6) is shown here separately. For rapid checkout, technique of spacecraft checkout has been adopted. Electromagnetic interface problems have been considered. The spacecraft structure will be used for electric grounding except for the power subsystem. One clock will be responsible for all sync functions. The cabling requirements shown here schematically are compatible with the spacecraft configuration and will be designed to minimize electromagnetic interference with the experiments. Because there is a constant, unvarying power source, all constant power loads are permanently attached to the bus, minimizing switches and converters.

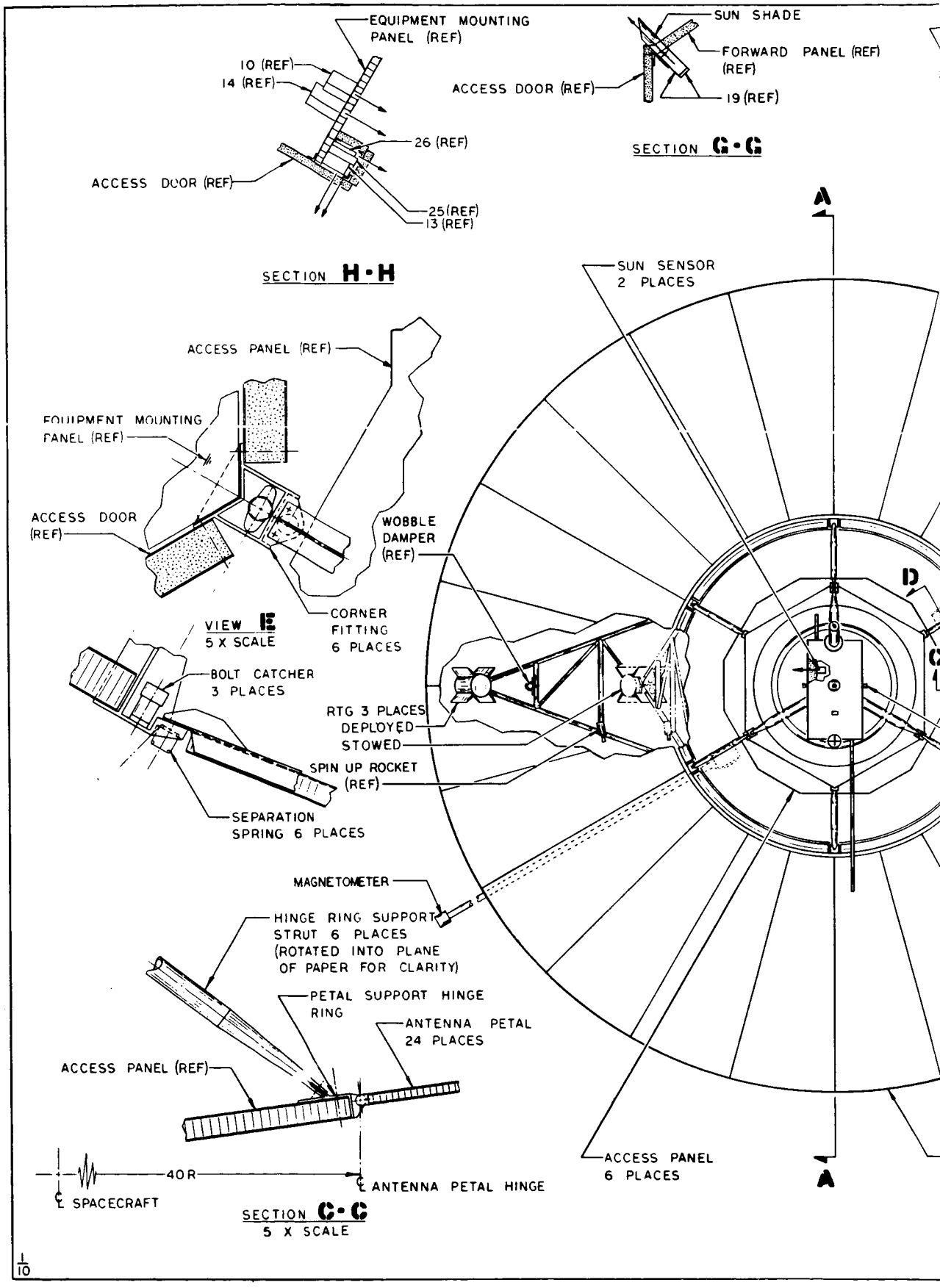
EQUIPMENT MOUNTING PANEL (REF)
10 (REF)
14 (REF)
26 (REF)
ACCESS DOOR (REF)
25 (REF)
13 (REF)
SECTION H-H
SUN SHADE
FORWARD PANEL (REF) (REF)
ACCESS DOOR (REF)
19 (REF)
SECTION G-G
A
SUN SENSOR 2 PLACES
ACCESS PANEL (REF)
EQUIPMENT MOUNTING PANEL (REF)
ACCESS DOOR (REF)
WOBBLE DAMPER (REF)
CORNER FITTING 6 PLACES
VIEW E 5 X SCALE
BOLT CATCHER 3 PLACES
RTG 3 PLACES
DEPLOYED
STOWED
SPIN UP ROCKET (REF)
SEPARATION SPRING 6 PLACES
D
MAGNETOMETER
HINGE RING SUPPORT STRUT 6 PLACES (ROTATED INTO PLANE OF PAPER FOR CLARITY)
PETAL SUPPORT HINGE RING
ANTENNA PETAL 24 PLACES
ACCESS PANEL (REF)
40R
℄ SPACECRAFT
℄ ANTENNA PETAL HINGE
SECTION C-C 5 X SCALE
ACCESS PANEL 6 PLACES
A
1/10

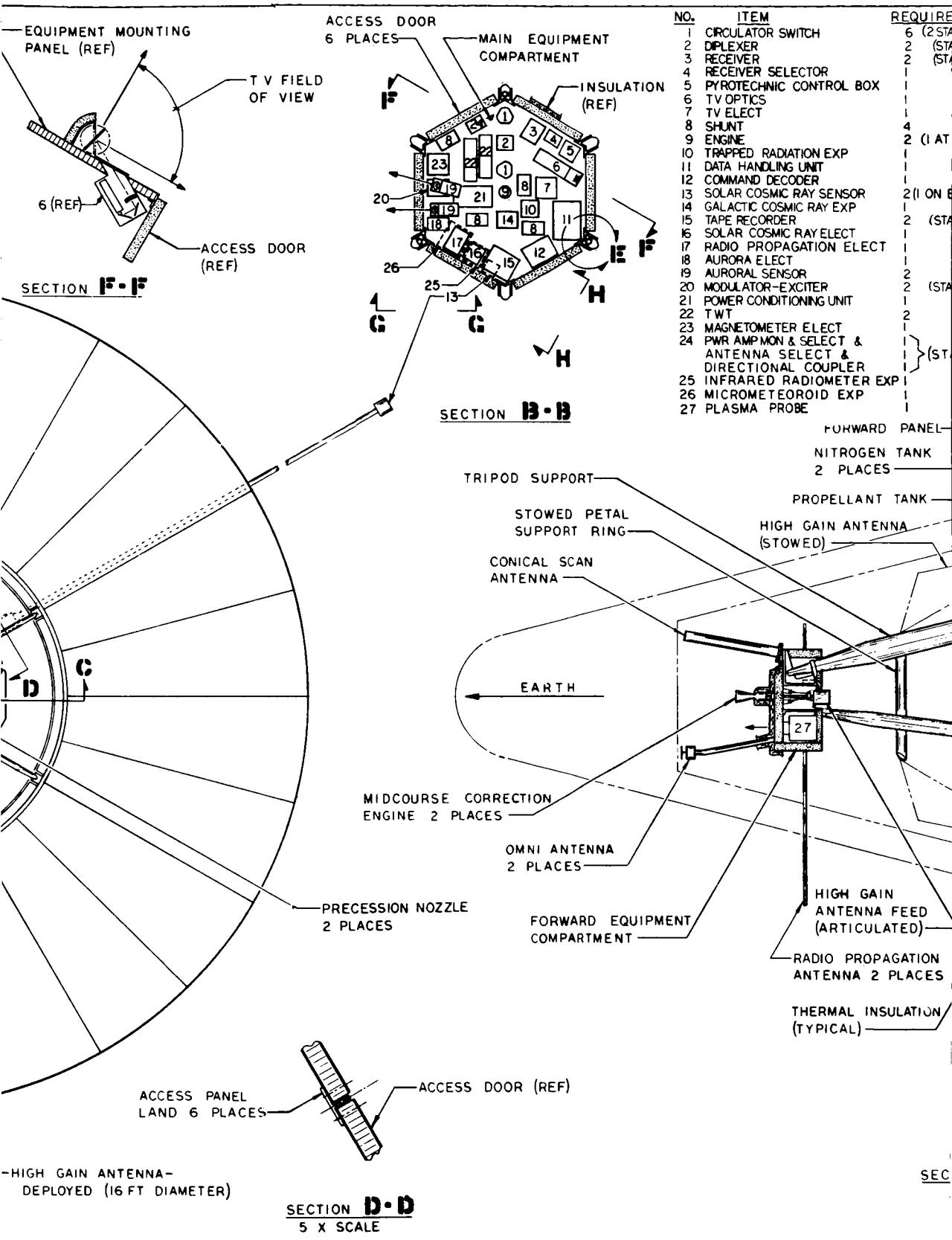
EQUIPMENT MOUNTING PANEL (REF)
T V FIELD OF VIEW
6 (REF)
ACCESS DOOR (REF)
SECTION F-F
ACCESS DOOR 6 PLACES
MAIN EQUIPMENT COMPARTMENT
INSULATION (REF)
20
26
25
13
SECTION B-B
NO. ITEM REQUIRE
1 CIRCULATOR SWITCH 6 (2 STA
2 DIPLEXER 2 (STA
3 RECEIVER 2 (STA
4 RECEIVER SELECTOR 1
5 PYROTECHNIC CONTROL BOX 1
6 TV OPTICS 1
7 TV ELECT 1
8 SHUNT 4
9 ENGINE 2 (1 AT
10 TRAPPED RADIATION EXP 1
11 DATA HANDLING UNIT 1
12 COMMAND DECODER 1
13 SOLAR COSMIC RAY SENSOR 2 (1 ON E
14 GALACTIC COSMIC RAY EXP 1
15 TAPE RECORDER 2 (STA
16 SOLAR COSMIC RAY ELECT 1
17 RADIO PROPAGATION ELECT 1
18 AURORA ELECT 1
19 AURORAL SENSOR 2
20 MODULATOR-EXCITER 2 (STA
21 POWER CONDITIONING UNIT 1
22 TWT 2
23 MAGNETOMETER ELECT 1
24 PWR AMP MON & SELECT & ANTENNA SELECT & DIRECTIONAL COUPLER 1 (ST
25 INFRARED RADIOMETER EXP 1
26 MICROMETEOROID EXP 1
27 PLASMA PROBE 1
FORWARD PANEL
NITROGEN TANK 2 PLACES
TRIPOD SUPPORT
PROPELLANT TANK
STOWED PETAL SUPPORT RING
HIGH GAIN ANTENNA (STOWED)
CONICAL SCAN ANTENNA
EARTH
MIDCOURSE CORRECTION ENGINE 2 PLACES
OMNI ANTENNA 2 PLACES
PRECESSION NOZZLE 2 PLACES
FORWARD EQUIPMENT COMPARTMENT
HIGH GAIN ANTENNA FEED (ARTICULATED)
RADIO PROPAGATION ANTENNA 2 PLACES
THERMAL INSULATION (TYPICAL)
ACCESS PANEL LAND 6 PLACES
ACCESS DOOR (REF)
-HIGH GAIN ANTENNA- DEPLOYED (16 FT DIAMETER)
SECTION D-D
5 X SCALE
SEC

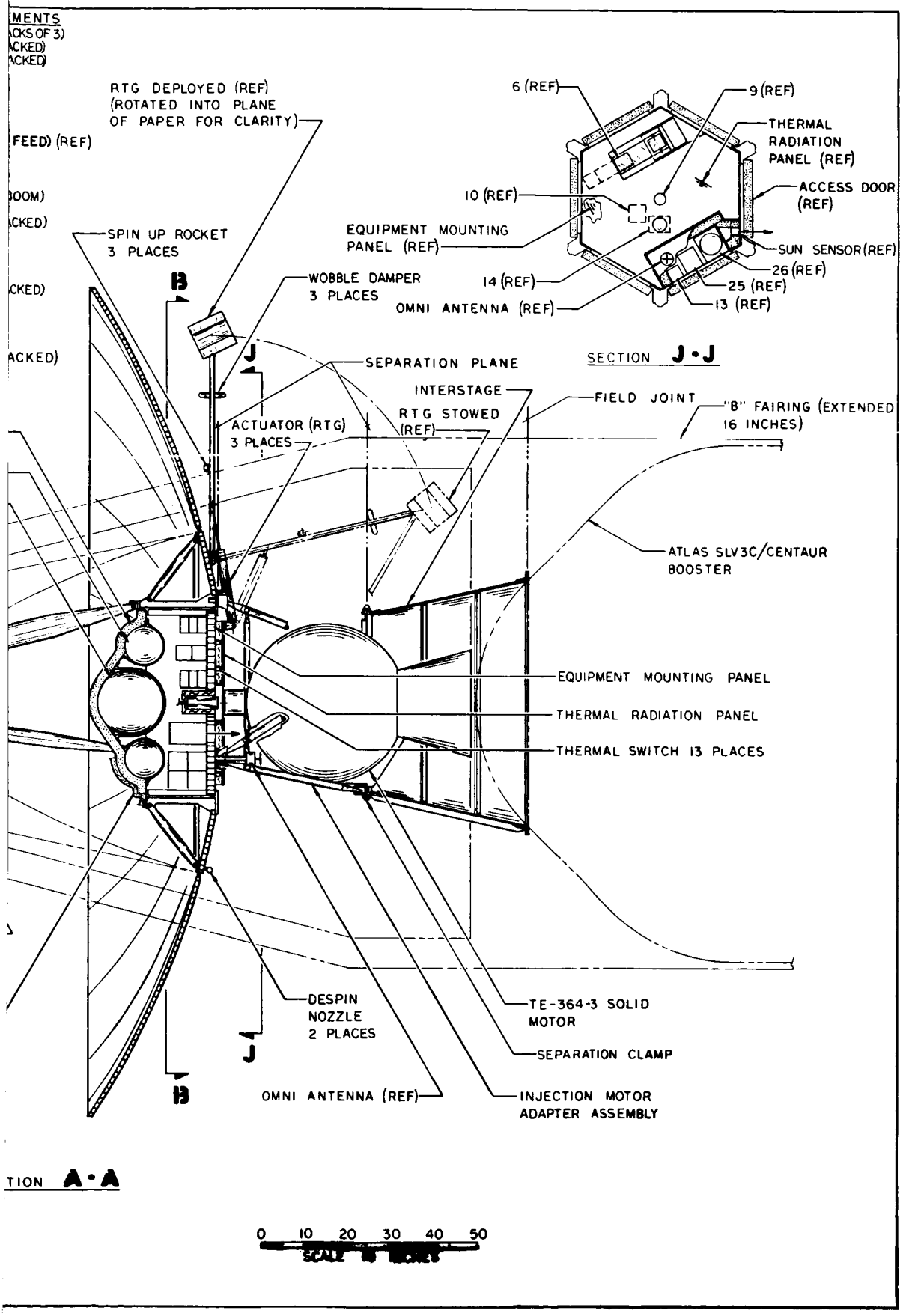

Figure 7-1. Advanced Planetary Probe-Inboard Profile

~~255~~ 25C

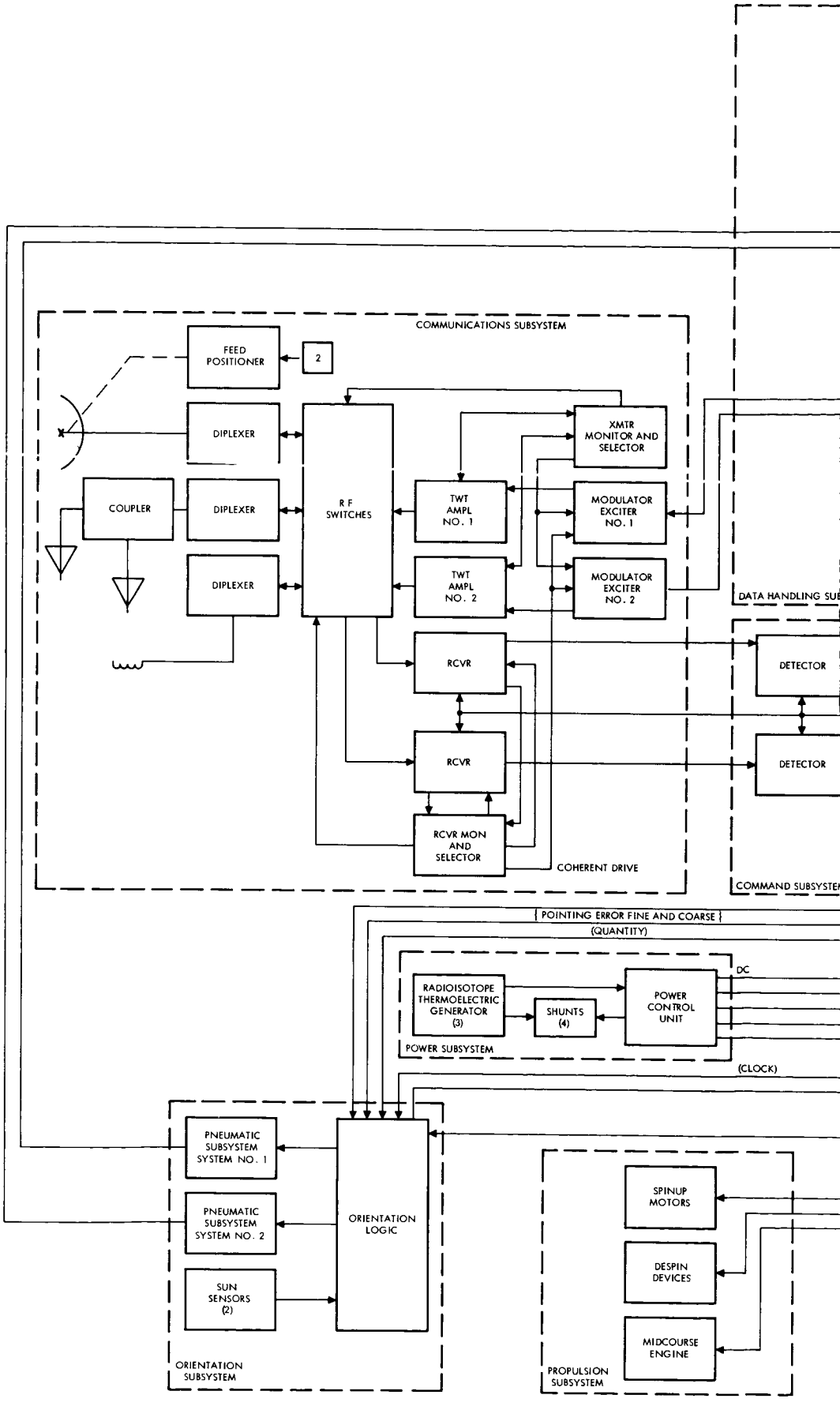
COMMUNICATIONS SUBSYSTEM
FEED POSITIONER
2
DIPLEXER
COUPLER
DIPLEXER
DIPLEXER
R F SWITCHES
XMTR MONITOR AND SELECTOR
TWT AMPL NO. 1
TWT AMPL NO. 2
MODULATOR EXCITER NO. 1
MODULATOR EXCITER NO. 2
RCVR
RCVR
RCVR MON AND SELECTOR
COHERENT DRIVE
DATA HANDLING SUB
DETECTOR
DETECTOR
COMMAND SUBSYSTEM
POINTING ERROR FINE AND COARSE
(QUANTITY)
DC
RADIOISOTOPE THERMOELECTRIC GENERATOR (3)
SHUNTS (4)
POWER CONTROL UNIT
POWER SUBSYSTEM
(CLOCK)
PNEUMATIC SUBSYSTEM SYSTEM NO. 1
PNEUMATIC SUBSYSTEM SYSTEM NO. 2
SUN SENSORS (2)
ORIENTATION LOGIC
ORIENTATION SUBSYSTEM
SPINUP MOTORS
DESPIN DEVICES
MIDCOURSE ENGINE
PROPULSION SUBSYSTEM

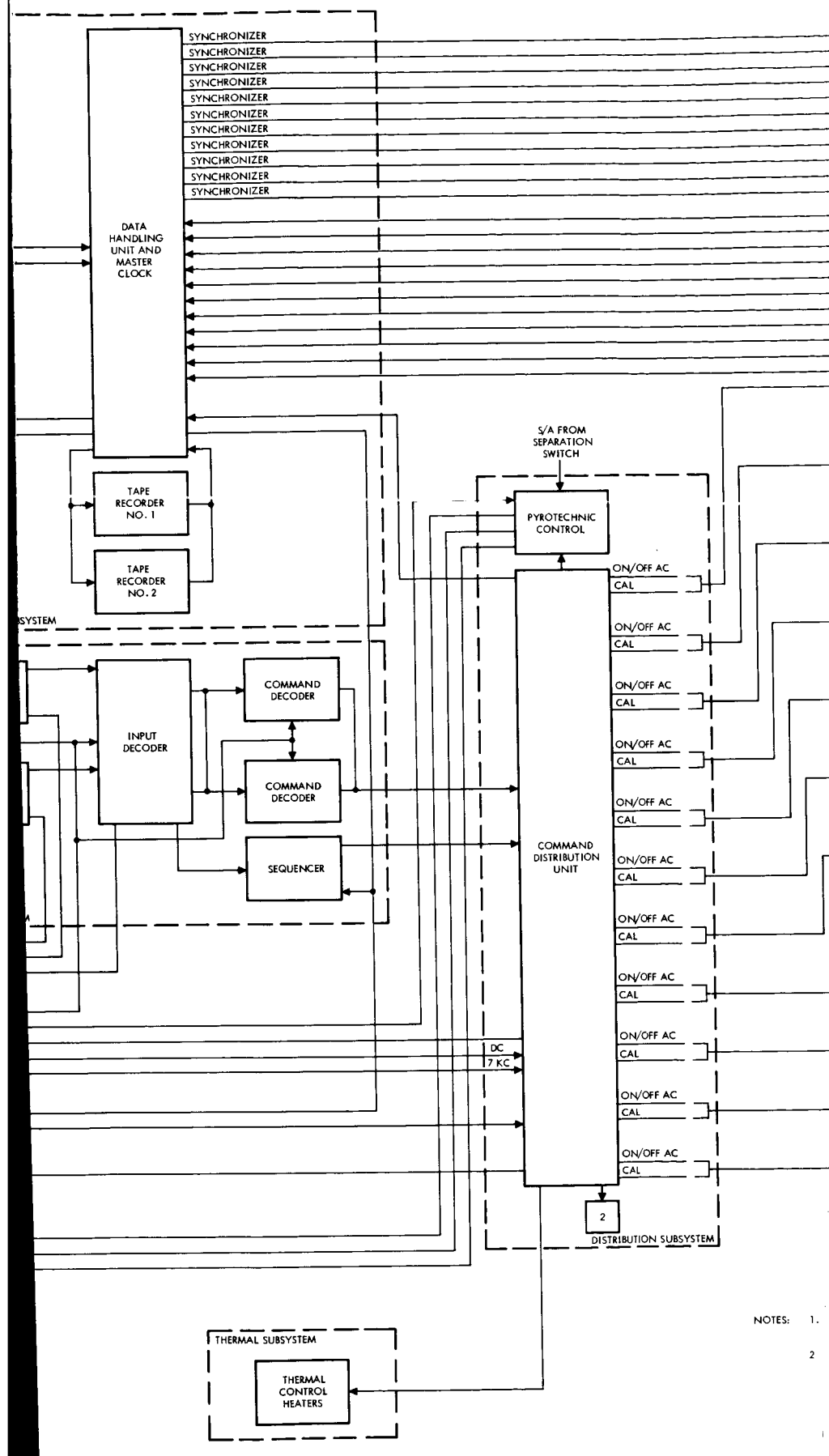
SYNCHRONIZER
SYNCHRONIZER
SYNCHRONIZER
SYNCHRONIZER
SYNCHRONIZER
SYNCHRONIZER
SYNCHRONIZER
SYNCHRONIZER
SYNCHRONIZER
SYNCHRONIZER
DATA HANDLING UNIT AND MASTER CLOCK
TAPE RECORDER NO. 1
TAPE RECORDER NO. 2
S/A FROM SEPARATION SWITCH
PYROTECHNIC CONTROL
ON/OFF AC
CAL
ON/OFF AC
CAL
ON/OFF AC
CAL
ON/OFF AC
CAL
ON/OFF AC
CAL
ON/OFF AC
CAL
ON/OFF AC
CAL
ON/OFF AC
CAL
ON/OFF AC
CAL
INPUT DECODER
COMMAND DECODER
COMMAND DECODER
SEQUENCER
COMMAND DISTRIBUTION UNIT
DC
7 KC
2
DISTRIBUTION SUBSYSTEM
THERMAL SUBSYSTEM
THERMAL CONTROL HEATERS

NOTES: 1.

2

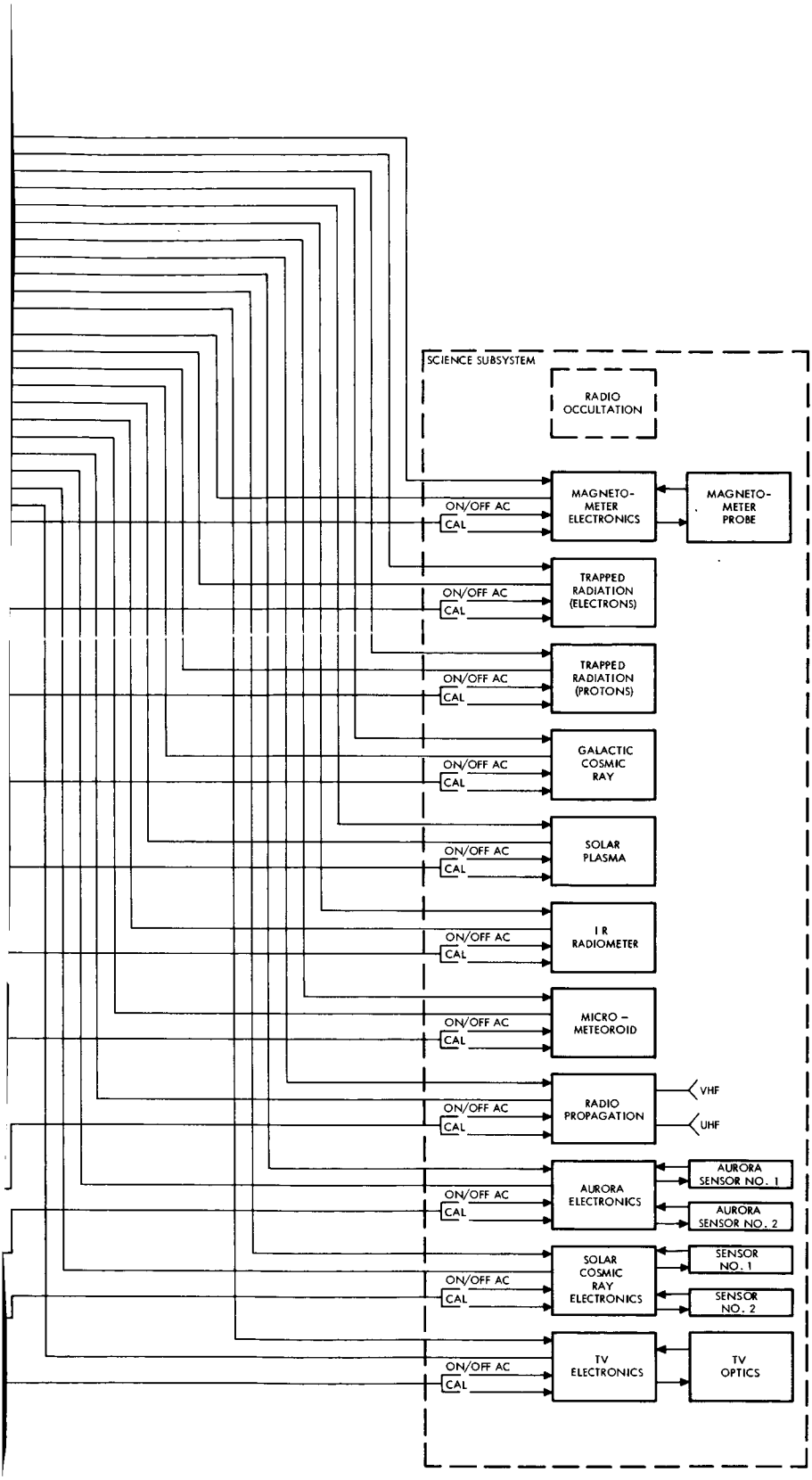

HOUSEKEEPING TLM LINES TO DHU NOT SHOWN.

COMMAND LINES FROM CDU TO FOLLOWING SELECTORS NOT SHOWN:

(a) RECEIVE SELECTOR
(b) TRANSMITTER SELECTOR
(c) FEED POSITIONER
(d) TAPE RECORDER

Figure 7-2. Advanced Planetary Probe Block Diagram

The data handling unit provides experiment signal conditioning and pulse coding of the experiment data when required.

The spacecraft mechanical configuration can be divided into the following five major assemblies: 1) a spacecraft/launch vehicle interstage, 2) an injection motor adapter assembly, 3) the main equipment compartment, 4) a large deployable Sunflower-type antenna, and 5) antenna feed and forward equipment support platform.

7.1.1 Spacecraft/Launch Vehicle Interstage

Details of the assembled spacecraft/launch vehicle interstage and the injection motor adapter assembly are shown in the engineering drawing of Figure 7-3. The interstage is a 37-1/4 inch long truncated cone, the end of which mates with the Centaur stage at a 58-1/2 inch diameter bolt circle. This bolted connection serves as the field joint between the booster and the spacecraft. The interstage is of semimonocoque construction fabricated with a mag-lithium sheet metal skin, aluminum sheet metal stringers and longerons, and magnesium ring members. The forward end of the interstage mates with the injection motor adapter assembly with the aid of a 42-inch diameter V-band clamp assembly which serves as the spacecraft/launch vehicle separation joint. A signal activates the clamping ring's redundant explosive bolts disengaging the V-band clamping shoes and the subsequent separation of the spacecraft from the booster. The signal and associated wiring are supplied by the launch vehicle.

Spring-loaded lanyards retain the released V-band clamping shoe together with the severed bolts with the interstage. Bracketry is provided on the interstage structure to ensure that the released shoes do not contact any of the flight spacecraft components. Three matched springs (2-1/2 inches in diameter) provide the impulse required to obtain a separation relative velocity of 2 ft/sec. When the separation springs physically disengage the injection motor adapter assembly from the Centaur, a switch is activated which initiates the solid propellant spinup motors mounted on the RTG booms.

This spin maneuver, necessary for thrust alignment of the TE-364, has been designed to minimize tipoff error.

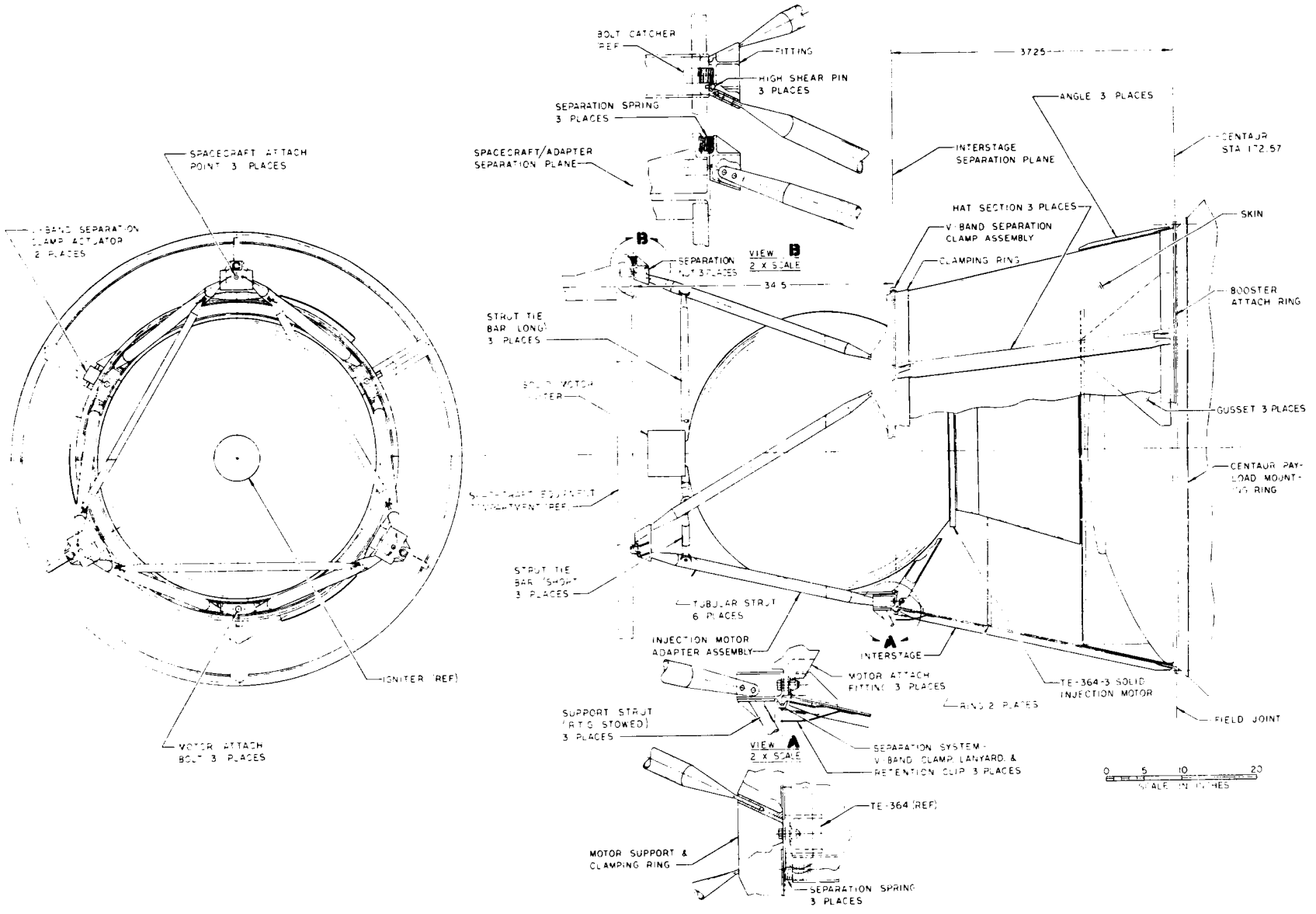

Figure 7-3. APP-Interstage and Injection Motor Adapter Assembly

7.1.2 Injection Motor Adapter Assembly

The structural portion of the adapter assembly is 34-1/2 inches long. It is an assembly of tubular struts, fittings, and a machined ring which supports the TE-364 solid injection motor. The adapter assembly interconnects the flight spacecraft with the spacecraft/launch vehicle interstage.

The aft end of the adapter assembly terminates in a channel-shaped, machined magnesium ring for the forward portion of the V-band clamp assembly noted earlier. It also provides for the structural support and tiedown of the three equally spaced attachment lugs of the TE-364 injection motor. The machined ring also contains integral "bathtub" fittings which provide the clevis attachment points for the aft ends of the main struts. The struts provide the structural load path to the spacecraft equipment compartment attachment points. As shown in Figure 7-1, the six tapered tubular struts interconnect three points (located in the injection motor attachment areas) of the machined ring with three alternate corner fittings of the equipment compartment.

The tubular struts are lightweight, efficient structural column members (having constant circular center section with tapered and coined ends) formed by a metal gathering process. As shown, the main tubular struts bolt into clevised bathtub fittings which are attached to the aft alternate corners of the spacecraft equipment compartment.

The attachment to the equipment compartment is made with the aid of three bolts and separation nut assemblies so that, on command the injection motor adapter assembly together with the spent solid injection motor may be jettisoned from the flight spacecraft immediately after RTG deployment. The retained separation nut and associated wiring are located on the aft side of the separation joint and are retained by the adapter assembly.

At separation, each bolt is driven forward into a captive bolt catcher and is retained with the flight spacecraft. The separation bolts are provided with oversized holes so that they take tension loads only.

Shear pins are mounted on the clevised fittings adjacent to the bolts and engage holes in the flight spacecraft structure to accommodate the shear loads. The compression loads are taken by the contacting surfaces of the fittings on both sides of the separation joint. The separation relative velocity of 2 ft/sec is obtained from the impulse of three 1-inch diameter matched springs.

Small diameter tubular tie bars interconnect the upper ends of the adapter assembly main struts to help stabilize them during the separation process.

The injection motor adapter assembly has fittings which tie down and stabilize the stowed RTG units prior to deployment. The forward ends of the fittings are attached to the lower machined ring of the adapter assembly so that they do not interfere with the spacecraft/launch vehicle staging operation.

The lower ends of the RTG tiedown members are provided with clevis fittings which are bolted to the fins of the main RTG support structures. Each clevis fitting is provided with a captive bolt catcher on one lug of the clevis and with a captive separation nut on the second lug. On signal, the separation nuts disengage the bolts and force them into the bolt catchers. The RTG units are then free to deploy to their normal operating positions. In this manner, all separation hardware is retained with that portion of the structure to be jettisoned.

As is apparent from the drawing, the structural concept used and the clearances maintained provide ready access to the forward end of the TE-364-3 solid injection motor for manual arming of the igniter immediately prior to launch.

7.1.3 Equipment Compartment

The main equipment compartment houses the major portion of experimental payload and the electronic equipment of the spacecraft and provides the basic support structure for mounting the RTG units, the large deployable high gain antenna, all the equipment mounted forward in the area of the high gain antenna feed, and the miscellaneous items noted

below. As shown in Figure 7-1, the equipment compartment is hexagonal and is 38 inches across its inside flats, with an average internal height of approximately 14 inches. All surfaces of the compartment are fabricated from 2-inch thick sandwich panels with aluminum face sheets and foamed cores. The compartment side and forward panel cores have been foamed to provide micrometeoroid protection as well as structural capability and rigidity.

The internal aft surface of the compartment is the mounting base for the major portion of the spacecraft's electronic and heat-producing components and utilizes a trusscore grid to provide good structural capability and micrometeoroid protection to the internally mounted equipment.

Thermal switches are mounted to the exterior surface of the aft panel and conduct the excessive internal heat of the compartment to a thermal radiating panel mounted 1-inch aft of the compartment.

The sandwich panels are interconnected by six machined fiberglass fittings located at the corners of the hexagonal equipment compartment and by magnesium angles mounted along the internal forward and aft edges of the hexagon's flats.

The six fiberglass corner fittings are fabricated with integral bathtub fittings and clevises to provide structural support for all the spacecraft components which are mounted to, but which are external of, the main equipment compartment.

To minimize thermal transfer both to and from the main equipment compartment, a long thermal path (3 inches minimum) is provided by these fittings between the metallic components of the equipment compartment and the exterior of the compartment.

The forward panel and the six side panels are attached to the angles and corner fittings by threaded fasteners to provide removable doors for access to the compartment interior. The side doors provide the shear path for the inertia loads.

All external surfaces of the equipment compartment except for thermal radiation panels are thermally insulated from the spatial environment with super insulation. Insulation is also provided in the cavity

between the radiation panel and the aft honeycomb equipment platform, except at the thermal switches. The heat-producing internal components of the compartment are uniformly distributed over the mounting surface, and the single compartment provides maximum thermal cross-coupling between all components including the propellant and gaseous nitrogen tankage.

The drawing of Figure 7-1 shows the layout of the experiment and other electronic components of the spacecraft. As noted earlier, the majority of this equipment is mounted to the equipment mounting panel of the spacecraft. In addition, two auroral sensors are mounted to the equipment compartment forward panel while one sun sensor, the TV camera system primary mirror with its protective covering, and the infrared radiometer and micrometeoroid experiments are located on the aft surface of the equipment mounting panel to satisfy their particular viewing requirements. Figure 7-1 indicates the look angles and fields of view provided for the experiment sensors.

The forward foamed panel of the equipment compartment is used to stow the on-centerline hydrazine propellant tank and the two symmetrically located gaseous nitrogen tanks of the attitude control system.

The aft pointing omni-antenna is supported by a fiberglass tube to obtain a highly thermal resistant structural path. The omni-antenna radiation field is provided a wide "field of view," as it is normally used after the injector motor and the adapter assembly has been jettisoned.

The on-centerline aft pointing midcourse correction engine is mounted to the equipment mounting platform, but is insulated from it. The engine bell protrudes through to the aft side of the platform where structure and insulation are provided to protect all spacecraft components mounted to the aft surface from direct impingement and possible heating and contamination by the engine exhaust.

7.1.4 High-Gain Antenna

The 16-foot diameter parabolic reflector of the high-gain antenna is structurally supported by the equipment compartment. The portion of the high-gain antenna reflector which extends from the equipment compartment to the 80-inch diameter point is fabricated from six 1-inch thick

aluminum honeycomb sandwich panels. Its inner corners are supported directly by the fiberglass corner fittings of the main equipment compartment, its outer edge is supported by a ring which also mounts the hinge fittings which support the 24 deployable petals which comprise the deployable portion of the high-gain antenna. The ring is supported by struts which attach to the forward ends of the fiberglass corner fittings as illustrated in Figure 7-1.

The six panels are removable to allow access to the equipment compartment when the deployable petals are attached.

In their stowed position, the petals rest against a 29-inch diameter ring which is mounted to the tripod feed support. The petals are held in the stowed position by a nylon cord. On signal, redundant cutters mounted to the petal aft faces sever the nylon cord, and centrifugal force, backed up by torsion springs located at the hinges, deploy the petals to their operating positions. Centrifugal forces also carry the severed nylon cord away from the spacecraft.

Current information at TRW indicates that a severe launch window penalty is associated with extension of the nose fairing by even small amounts on the current Atlas/Centaur configuration, as used for Surveyor, based on launch wind shear effects. However, no information is currently available as to the sensitivity of the Atlas SLV3-X/Centaur combination indicated by JPL in the launch vehicle document by W. A. Ogram dated November 1, 1965. This document indicates a 10-foot allowable fairing extension.

As a result of this uncertainty, an effort was conservatively made to keep the required fairing extension to a minimum. The result was the decision to mount the main antenna dish from the aft end of the equipment compartment. This decision leads to the requirement for removable panels on the fixed portion of the main dish to allow access to the equipment compartment. This is an awkward solution, however, as compared to mounting the dish from the top of the equipment compartment and accepting the resulting fairing extension. A more detailed study is appropriate for this tradeoff.

7.1.5 RTG

The fixed hard points just inboard of the 80 inch diameter hinge circle support the deployment hinges of the RTG units. The hinge support points are so located that the RTG loads pass directly into the tubular struts located at the corners of the equipment compartment. Local reinforcement of the removable antenna reflector panels provide the wide-footed RTG support points with lateral load-carrying capability.

After release from their stowed position tiedown, the RTG's are forced into their operating positions by linear actuators of the cylinder and piston type. The linear actuator compression springs, working against the restriction of integral velocity damping fluid, force the RTG units into operating position where they are locked in place by snap rings also built into the linear actuators.

One "ball-in-a-curved-tube" type wobble damper is located on each RTG support boom. When the RTG's are in their stowed positions, centrifugal force effectively "cages" the balls inside the tubes. When the RTG's are deployed, the wobble dampers are activated.

Spacecraft spinup occurs immediately after separation from the launch vehicle. At this time, the RTG units are locked in their stowed position. The solid rocket spinup motors are mounted to the stowed RTG support structure. One motor is mounted to each RTG support frame, thereby achieving large moment arms about the spin axis and the location of the spin rockets on the c. g. plane.

The fixed portion of the antenna reflector also supports two diametrically opposite hydrazine thrusters used to partially despin the spacecraft after the firing of the solid injection motor.

As shown on the drawing, two De Havilland STEM-type devices are mounted to the aft side of the fixed portion of the antenna reflector. One supports the magnetometer experiment sensor and is for dynamic balancing purposes, the other supports a solar cosmic ray experiment sensor. These items are deployed radially at a slow rate of speed and bring the spacecraft spin rate to its final value.

7.1.6 Forward Support Structure

The forward support structure houses the high gain antenna feed, low and medium gain antennas, a midcourse correction engine, two of the scientific experiments, a sun sensor, and the precession nozzles.

The forward mounted equipment just noted is supported by a tripod arrangement of hollow aluminum tubular struts which are attached to three of the alternate corners of the forward end of the equipment compartment through clevised bathtub fittings which are integral with the fiberglass corner posts.

The struts have an oval cross section to present a low RF interference profile to the high-gain antenna feed, and thereby shadow a minimum amount of the antennas' reflecting surface. For minimum weight, the struts are fabricated by a metal gathering process that shapes the entire strut without welded or mechanical joints.

The antennas' petal stowage support ring mounted to the tripod is made from fiberglass and has an oval cross section to minimize RF interference. The forward ends of the tripod struts bolt into a flanged fiberglass cylinder which provides structural moment capability to the tripod members and also supports the equipment housing.

The propellant, nitrogen, and electrical lines which are passed between the main equipment compartment and the forward housing are routed through the hollow sections of the tripod struts for micrometeoroid protection. The construction of the housing is similar to that of the equipment compartment. The forward and side panels are fabricated from 2-inch thick, aluminum-faced, foamed core sandwich panels for structural strength, rigidity, and micrometeoroid protection of the internal components. As the aft facing panel is "shadowed" by, and is afforded considerable micrometeoroid protection from, the basic spacecraft and antenna, it is made from a 1-inch thick foamed aluminum sandwich.

The high gain antenna feed is mounted on-centerline just aft of the forward compartment. The feed has a flexural pivot and solenoid drivers so that it may be moved laterally 1 inch off centerline on command to generate error signals for earth tracking.

Also for earth tracking, a conical scan helical antenna 2 inches in diameter and 22 inches long is mounted forward of, and to one side of, the forward housing. The axis of the antenna is tilted 10 degrees with respect to the spacecraft centerline to accomplish the antenna lobing pattern required.

The forward-pointing, low-gain, omniantenna is located forward of the compartment to achieve a radiation field of view with minimum interference from other spacecraft components. It is body-fixed to the forward housing by a cylindrical fiberglass strut.

The forward-pointing midcourse correction engine is mounted on-centerline to the forward panel. It is thermally insulated from the forward housing. The engine is normally fired only when the spacecraft is relatively close to the sun — a few days to weeks after launch — at which time the engine and the fuel lines are heated by the sun. Heaters are provided, however, to allow the possibility of thawing out the propulsion system if a sun-line correction maneuver were desired near Jupiter encounter.

The interior of the forward housing is occupied by a sun sensor and the solar plasma experiment. The look angles and the fields of view involved are indicated on the drawing of Figure 7-1.

No active thermal control system is provided for the forward housing except heaters. All exposed surfaces are covered with super insulation wherever possible, and all physical connections with external items are made through high, thermal-resistance fiberglass.

The attitude control cold nitrogen gas precession nozzles are mounted on opposite sides of the forward compartment to provide them with large moment arms about the spacecraft c.g. The lines and nozzles are insulated and heated.

The antennas for the radio propagation experiment are also mounted to the sides of the forward equipment compartment. The 6-inch long antenna is simply stubbed out from the compartment structure. The 36-inch long antenna is spring-loaded during launch and retained in a folded position by the same nylon cord that retains the petals of the deployable antenna. Therefore, the occultation antenna will be deployed simultaneously with the high-gain antenna.

7.1.7 Power Requirements

Power requirements for the spacecraft are presented in Table 7-1. The communications requirements are based upon a 10 watt TWT with an efficiency of 37 percent and two 100 mw drives at ± 5 percent efficiency. As shown in the table, the propulsion system does not require continuous loads and uses only capacitors (see Section 8.2). The attitude control system which points the spin axis at the earth does not require solenoid loads during the brief encounter period since the angular displacement of the earth will be a minute fraction of a degree. This allows 5.7 watts for science during the encounter phase. The typical science payload selected has this power requirement, and, while there could be considerable change in requirements, approximately 14 additional watts will be available during the cruise phase and an additional 5 watts during the light side encounter phase.

7.1.8 Mass Properties

Table 7-2 is the detailed weight estimate of the spacecraft and injection stage, and Table 7-3 presents sequential data on moments of inertia and longitudinal centers of gravity. Figure 7-4 illustrates the coordinate axis system used in this study.

The weight of the spacecraft is 492.4 pounds, including a 38.2 pound contingency. For the ground rules given later the spacecraft weight is realistic.

For this spacecraft weight, the launch vehicle could be either the JPL-specified Atlas SLV-3X/Centaur or the current Atlas SLV3C/Centaur combined with a TE-364-3 solid propellant injection stage. Weight estimates were made for the injection stage and the adapter required by the Centaur, with the injection stage weighing 1594.6 pounds and the Centaur adapter 45.5 pounds.

Inertia estimates verified that the spacecraft will be stable in the cruise mode, with a longitudinal-to-transverse inertia ratio of 1.2. Prior to deployment of the antenna and RTG booms, the spacecraft will be spinning about the minimum inertia axis, which is satisfactory for the short times involved.

Table 7-1. Power Requirements

Subsystem	Input (watts)	Conversion Efficiency (%)	Cruise (watts)	Encounter (watts) Light	Dark
Communications	31.3	87	37.4	37.4	37.4
Command distribution	4.0	69	5.8	5.8	5.8
Data handling	5.0	69	7.3	7.3	7.3
Attitude control					
Electronics	4.5	69	6.5	6.5	6.5
Solenoids	5.6	99	5.7	-	-
Propulsion			Only capacitors required		
Thermal control	11.0	99	11.1	11.1	11.1
Science					
Cruise	9.0	73	12.3	-	-
Encounter (light)	9.5	73	-	13.0	-
(TV)	10.0	-	-	10.0	-
Encounter (dark)	10.1	73	-	-	13.9
Total (watts)			86.1	91.1	82.0

Table 7-2. Weight Estimate – Spin-Stabilized Spacecraft for the Basic Mission

Item		Weight, lb	
Structure and Thermal Control			79.6
Equipment platform (1)		9.7	
Side panels (6)		3.0	
Top cover (1)		2.2	
Frames and longerons		9.7	
Tank supports		1.8	
Forward compartment		4.5	
Experiment booms installation (2)	3.2		
Miscellaneous attachments		2.9	
Meteoroid protection		31.1	
Radiation protection		2.0	
Thermal control		9.5	
Thermal switches (13)	3.3		
Radiative panel	0.9		
Paint	2.2		
Insulation	3.1		
Power Supply			88.9
RTG installation		77.6	
RTG units (3)	66.0		
Boom assemblies (3)	11.6		
Power control unit		8.3	
Shunt elements (4)		3.0	
Integration			32.0
Command distribution unit (1)		7.0	
Umbilical (1)		2.0	
Pyrotechnic control box (1)		5.0	
Cabling and connectors		18.0	

Table 7-2. Weight Estimates — Spin-Stabilized Spacecraft for the Basic Mission (continued)

Item		Weight, lb	
Data Handling			34.5
Data handling unit (1)		11.0	
Tape recorder (2)		15.9	
Integrated decoder and sequencer (1)		7.6	
Communications			92.1
Receiver (2)		7.0	
Modulator/exciter (2)		3.0	
TWT (2)		2.0	
Circulator switch (6)		1.8	
Diplexer (2)		2.0	
Antenna selector (1)		0.5	
Receiver selector (1)		0.5	
Power amplifier monitor and selector (1)		1.0	
Directional coupler (1)		0.5	
Omni-antenna installation (2)		1.5	
Helical antenna installation (1)		2.8	
High-gain antenna installation (1)		69.5	
Parabolic dish	49.2		
Tripod, including support ring and release mechanism	15.8		
Antenna feed including harness	2.5		
Antenna feed displacement device	2.0		
Attitude Control			38.5
Reorientation system		28.8	
Electronics assembly (1)	3.6		
Sun sensors (2)	1.5		
Regulator relief value (2)	2.6		
Solenoid valve (2)	1.0		
High pressure transducer (2)	0.4		

Table 7-2. Weight Estimates — Spin-Stabilized Spacecraft for the Basic Mission (continued)

Item		Weight, lb	
Low pressure transducer (2)	0.6		
Fill valve (2)	0.6		
Lines and fittings	1.0		
Thrusters (2)	0.2		
Nitrogen	7.2		
Nitrogen tanks and residuals (2)	10.1		
Despin system		5.5	
Thrusters (2)	0.2		
Explosive valves (12)	3.0		
Electrical	0.8		
Lines and fittings	0.5		
N_2H_4 filter (2)	1.0		
Spinup system		4.2	
Motor installation (3)	3.6		
Electrical	0.6		
Propulsion			34.6
Nitrogen fill valve (1)		0.2	
N_2H_4 fill and drain valve (1)		0.2	
Explosive valves (8)		2.0	
N_2H_4 filter (2)		1.0	
Electrical		0.8	
Lines and fittings		0.6	
Motor (2)		3.0	
Instrumentation		0.6	
Usable propellant		22.5	
Tank, residuals and pressurization		3.7	
Dynamic Balance Weights			4.0
Scientific Payload			50.0
Contingency			38.2
Spacecraft Weight			492.4

Table 7-2. Weight Estimates — Spin-Stabilized Spacecraft for the Basic Mission (continued)

Item	Weight, lb	
Injection Stage		1594.6
TE-364-3 motor at burnout	123.0	
Impulse propellant	1440.0	
Expended inerts	14.2	
Adapter and separation	17.4	
Spacecraft at Separation from SLV-3C		2087.0
Centaur Adapter and Separation		45.5
Gross Atlas-Centaur Payload		2132.5

Table 7-3. Spacecraft Moments of Inertia and Center of Gravity

Condition	Weight (lb)	$\bar{Z}^*$ in.	Moments of Inertia (slugs ft^2)			Inertia Ratio $(\frac{I_z}{I_x})$
			I_x	I_y	I_z	
Gross SLV-3C payload	2132.5	53.3	324.2	323.0	115.9	0.36
Vehicle at TE-364-3 ignition	2086.1	54.1	306.1	305.0	109.6	0.36
Vehicle at TE-364-3 burnout	631.9	71.3	208.5	207.4	68.9	0.33
Spacecraft – RTG's deployed	492.4	88.4	127.9	136.7	143.6	1.04
Spacecraft – RTG's and antenna deployed	492.4	87.5	148.6	147.5	185.3	1.25
Spacecraft in cruise mode	492.4	87.5	177.5	147.5	214.2	1.21

*Reference station 0.0 is the Centaur/TE-364-3 adapter field joint

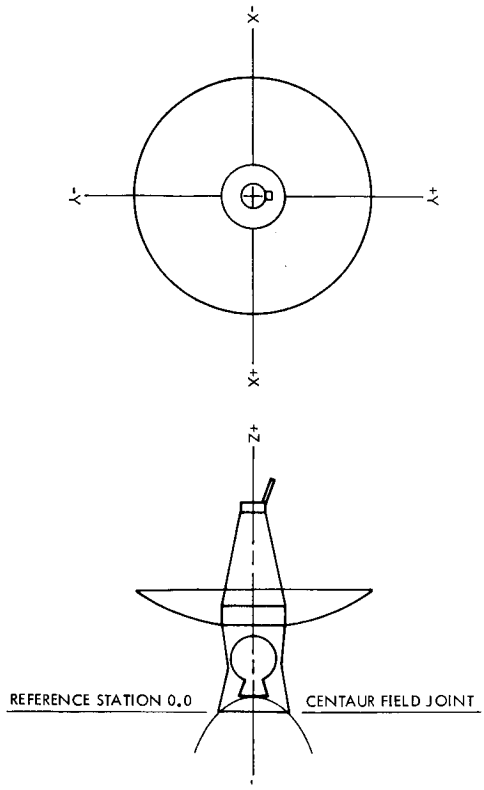

Figure 7-4. Coordinate Axis System

Centroidal moments of inertia were determined for the complete flight sequence beginning at separation from the Centaur. Table 7-3 lists the moments of inertia about the x, y, and z (roll) axes shown in Figure 7-4. Also included in Table 7-3 are longitudinal center-of-gravity positions measured from the Centaur injection stage field joint (Station 0.0).

Error analyses show that the reorientation system and earth tracking conical scan systems are sensitive to center-of-gravity position. Center-of-gravity travel must be minimized to obtain the pointing accuracies required at great distances from earth. Accuracy in predicting the center-of-gravity (as well as the moments of inertia) are therefore of prime importance. Error analyses conducted on previous spacecraft show that there will be no problems associated with obtaining accuracies in the order of:

Longitudinal c.g. position	±0.10 in.
Radial c.g. position	±0.04 in.
Moments of inertia	±2%

Equipment is available (e.g. the Miller balancing machine) which can measure to extremely high accuracies, i.e.,:

Moments of Inertia

I_x	2%
I_y	2%
I_z	1%

Center of gravity

$\bar{X}$	±0.01 in.
$\bar{Y}$	±0.01 in.
$\bar{Z}$	±0.025 in.

Products of inertia

P_{xz}	±200 lb in^2 at 6 rpm	approximately 3 minutes of arc
P_{yz}	±200 lb in^2 at 6 rpm	
P_{xy}	±200 lb in^2 at 6 rpm	

However, in the cruise mode, with all appendages deployed and subject to deflections, it seems probable that center-of-gravity fluctuation would not warrant the initial accuracies obtainable with a machine of this type.

The remainder of this section presents the basis, subsystem by subsystem, for estimating the mass properties of the spacecraft.

7.1.8.1 Structure and Thermal Control

Structural component weights are based upon preliminary stress analyses conducted during the study. The weight of the equipment platform, side panels, top cover, and forward compartment reflect the weight required to satisfy structural requirements only. For the side panels and top cover this would consist of a single sheet of 0.025 mag-lithium. The equipment platform structure weight is based on a trussgrid core, 1.25 inches thick, and two aluminum alloy face sheets, each 0.015 inch thick. The structural weight of the forward compartment was determined in a similar manner.

When the meteoroid environment was taken into account, the overall minimum weight concept appeared to be a sandwich-type panel. The weight for meteoroid protection, based upon a probability of zero penetration of 0.9, is therefore the difference in weight between the two concepts.

Therefore, taking into account the structural, thermal, and meteoroid requirements, the equipment panel consists of an 0.010-inch outer and an 0.040-inch inner aluminum face sheet separated by 2 inches of aluminum trussgrid (2.3 lb/ft^3). The weight estimate includes the inserts required for mounting the equipment. The side panels and top cover consist of a 1.2 lb/ft^3 foam core, 2 inches thick, with aluminum alloy face sheets, 0.010 inch outer and 0.045 and 0.037 inch inner, respectively.

Two De Havilland STEM devices are used for the experiment booms, each 12 feet long.

A nominal allowance has been made for radiation protection, required for the trapped radiation, solar plasma, and cosmic ray experiments.

Thermal control consists of the following:

- Cat-a-lac paint on the forward face of the parabolic dish antenna
- Thermal switches and a 0.010-inch aluminum alloy radiating plate (6 ft^2) mounted to the base of the equipment platform
- SI-4 type insulation around the two midcourse engines
- Aluminized Mylar insulation around the equipment compartments consisting of 100 layers, 0.00025 inch thick. The composite specific density is approximately 0.19 lb/ft^2.

7.1.8.2 Power Supply

The power supply system consists of the RTG installation, power control unit and four shunt elements. The three RTG units provide a total of 100 watts of raw power. Estimates of the boom assemblies include allowances for the latching mechanisms and dampers. The booms are 1.5 inch outside diameter titanium alloy, 0.025 inch wall thickness. The use of titanium was dictated by the thermal considerations involved. Total installed specific power density is 1.3 watts per pound. The power control

unit contains the redundant TWT converters, equipment converter, and the central inverter. Experiment converters are considered part of the science payload. Four shunt elements are provided to dissipate excess power in the form of heat. They are sized so that any three can handle 100 watts of power.

7.1.8.3 Integration

The integration system includes the command distribution unit, the payload umbilical, pyrotechnic control box, and the cabling harness. The command distribution unit weight estimate assumes the use of subminiature relays. The estimate for the cabling and connectors is based on an empirically derived relationship of power requirements and weight of equipment to which power must be supplied. This weight also takes into account the experiment harness.

7.1.8.4 Data Handling

The data handling system consists of the data handling unit, two tape recorders, and the integrated decoder and sequencer, which is shown in the data handling system to reflect design responsibility.

The 11-pound data handling unit includes 2.5 pounds for the core memory of the TV system, which would be eliminated if the TV experiment were not included as part of the science payload. The command decoder weight includes the timer for firing the solid propellant spinup motors.

7.1.8.5 Communications

The electronic components of the communications system are completely redundant. The largest item affecting weight is the 16-foot diameter parabolic telemetry antenna, estimated to weigh a total of 69.8 pounds. The deployable petals are made of aluminum honeycomb panels, the core 0.5-inch thick, and face sheets, each 0.003-inch thick. Including the adhesive allowance, the specific weight is 0.185 lb/ft^2. With allowances for closeouts, inserts, rim-locks, torsion bar hinges, and dampers, the overall petal specific weight is 0.22 lb/ft^2. The fixed portion of the dish is the same as the above with the exception that the core is increased to 1.0 inch. The support tubes are 1.5 inches in diameter by 0.020 inch wall aluminum

alloy. The tripod weight is based on the use of 5.5-inch outside diameter aluminum alloy tubing, with a wall thickness of 0.025 inch. The petal support ring and release mechanism is estimated to weigh 5.0 pounds.

In estimating the dish weight, considerable use was made of a report generated for NASA by Thompson Ramo Wooldridge, Inc., No. CR-46, "Sunflower Solar Collector."

7.1.8.6 Attitude Control

The attitude control system consists of the reorientation system, despin, and spinup systems. Spinup is accomplished by three solid propellant motors mounted on the RTG deployment booms at the combined spacecraft/injection stage c.g. The motors are sized to import a spinrate of 60 rpm to the vehicle. Assumptions made in the weight estimate were I_{sp} = 250 seconds and (WP/WG) = 0.35. The despin system is sized to reduce the spin rate from 60 to 5 rpm. This is accomplished with two 5-pound hydrazine thrusters. The propellant for this function is contained in the midcourse propellant tank.

The nitrogen reorientation system is sized for a total capability of 1200 degrees of reorientation over a period of 750 days. The hardware is redundant for the two completely separate systems. Gas supply is sized on the basis that either system could complete the mission after both have been used to complete an improbable second midcourse firing.

7.1.8.7 Propulsion

The monopropellant hydrazine propulsion system features a blowdown feed system. Propellant requirement and tank size is based upon the following ground rules:

Hydrazine I_{sp}	230 sec
Midcourse ΔV	100 meters/sec
Pressurization	Nitrogen
Initial tank pressure	500 psi
Final tank pressure	200 psi
Trapped and residual propellant	1 percent

Bladder allowance	1 percent
Safety factor	2.0
Tank material	Titanium with O_u = 160,000 psi
Minimum gage	0.020 inch

Based upon the above, the tank is 12.7 inches in diameter, with wall thickness 0.020 inch (dictated by the minimum gage constraint).

7.1.8.8 Dynamic Balance Weights

Because the spacecraft is to be spin stabilized both during and after the injection motor firing, the vehicle must be dynamically balanced. An allowance of 4.0 pounds has been made for this purpose.

7.1.8.9 Science Payload

The main ground rules for this configuration dictate a 50-pound science payload. In estimating the mass properties of the spacecraft, this 50 pounds was broken down into the following 10 experiments:

Magnetometer	1.5
Trapped radiation	5.0
Solar plasma	5.5
Micrometeoroid	4.0
Solar cosmic ray	3.5
Radio occultation antenna (2)	5.0
Infrared radiometer	3.0
Galactic cosmic ray	6.0
Auroral (2)	3.0
Television	13.5

7.1.8.10 Adapters

The weight estimate for the adapter to the injection stage assumes an aluminum tubular trusswork. Tube size is 1-5/8 inches by 0.025 inch wall. Included with the adapter weight is an allowance for the RTG support arms.

The Centaur adapter is a ring-stiffened, semimonocoque structure, composed of a 0.034 mag-lithium skin and aluminum rings. The stringers are magnesium alloy.

7.2 FLIGHT SEQUENCE

The flight sequence for the 50-pound payload Jupiter flyby mission is given in Table 7-4. The events in the table are largely self-explanatory; however, some additional explanation is desirable.

The first nine events are a standard launch sequence. Event 10, spacecraft and third-stage separation, occurs before spinup since analysis shows that tipoff errors are acceptable and there is a considerable weight savings over a spin table. The solid spinup rockets are fired 0.25 second after separation and the TE-364 ignited. After the 1 second spinup, the spin rate is 60 rpm. After TE-364 burnout, the spacecraft is despun to about 30 rpm and the RTG's deployed, reducing the spin rate to about 14.5 rpm. After a delay to damp out wobbles and to measure the spin rate on the ground by monitoring the spin modulation of the signal strength, the spacecraft is despun to about 7.5 rpm and the antenna deployed, reducing the spin rate to about 5.8 rpm. To avoid the possibility of arc-over during launch, the high voltage power supply is not turned on until this time, well after the spacecraft is out of the atmosphere.

The first reorientation maneuver is then performed to prevent the radiation plate at the back of the spacecraft from overheating. The radiation plate should not be exposed to the sun for more than about 3.5 hours. This reorientation maneuver will place the earth within ± 10 degrees of the spin axis. On ground command, the spacecraft communication system is switched to the medium-gain helix antenna, which will automatically point the high-gain antenna to the earth within 0.5 degree. The science payload can be turned on at any time after Event 20, high voltage power supply. The spacecraft can receive and/or transmit on the helix antenna or transmit on the high-gain antenna if desired.

The spacecraft then coasts for about 10 days during which time ground tracking determines the position and velocity of the spacecraft, and calculates the magnitude and direction of the midcourse correction.

Table 7-4. Flight Sequence

	Event	Timing	Comments
1.	Prelaunch checkout	T -	Gyro heaters on
2.	Liftoff	T + 10	
3.	Shroud separation	350,000 ft altitude	
4.	Atlas booster cutoff	T + 143 sec	
5.	Atlas sustainer cutoff and staging	T + 237 sec	
6.	Start first Centaur burn	T + 246 sec	
7.	Centaur cutoff	T + 570 sec	
8.	Centaur parking orbit	(1 to 25 min coast)	
9.	Start Centaur second burn	I + 0	
10.	Centaur cutoff	I + 110 sec	
11.	Spacecraft and third stage separation	J = I + 170 sec	Springs impart 1 deg/sec 3σ tipoff rate. Centaur backed away and tumbled.
12.	Spinup start	J + 1/4 sec	Sequencer
13.	Spinup end and TE-364 ignition	J + 1/4 sec	Sequencer
14.	TE-364 burnout	J + 41-1/4 sec	
15.	High power transmitter on	J + 1 min	
16.	Start despin	J + 2 min	Despin to 30 rpm as soon as TE-364 tailoff complete
17.	Stop despin	J + 2 min, 13.1 sec	
18.	RTG deployment	J + 2 min, 13.1 sec	Deployment uncages dampers

Table 7-4. Flight Sequence (Continued)

	Event	Timing	Comments
19.	Spacecraft-third stage separation	J + 2.5 min	
20.	Delay	Δt = 0.5 to 1 hr	To damp wobble and measure spin rate
21.	Start despin		Ground command. Despin to 7.5 rpm
22.	Stop despin		Sequencer
23.	Deploy antenna		Ground command. Spin slows to 5.8 rpm
24.	Start cone maneuver about sun line		Ground command
25.	Stope cone maneuver about sun line		Sequencer
26.	Start sun plane maneuver to point at earth		Ground command
27.	Stop sun plane maneuver to point at earth		Sequencer
28.	Switch to helix antenna for automatic earth acquisition		Ground command; back-up command search modes are provided
29.	Coast; turn on cruise science except boom-mounted sensors		Track to determine required midcourse correction
30.	Start midcourse maneuver sequence. Turn off cruise science, switch to omni antenna (receive and transmit)	T + 5 to 20 days	Ground command
31.	Orient for first midcourse maneuver		
	Start cone maneuver about sun line		Ground command
	Stop cone maneuver about sun line		Sequencer

Table 7-4. Flight Sequence (Continued)

Event	Timing	Comments
Start sun plane maneuver to desired attitude		Ground command
Stop sun plane maneuver to desired attitude		Sequencer
32. Execute midcourse correction		
Start midcourse engine burn		Ground command
Stop midcourse engine burn		Sequencer
33. Repeat earth acquisition sequence		
Back through maneuver 31		
Lock on helix antenna		
34. Coast; turn on cruise science		Track to determine if a second midcourse correction is required
35. Perform second midcourse correction if required (steps 30 through 33)		
36. Coast; turn on cruise science		Attitude updated whenever DSIF contact made (acquisition limit $\pm$12 deg)
37. Deploy booms		Spin slows to 5 rpm
38. Switch to high-gain antenna in conical scan mode	before T + 80 days	To keep maximum data rate capability
39. Switch to high gain on axis mode	beyond 4 AU	For maximum data rate between attitude updatings

Table 7-4. Flight Sequence (Continued)

Event	Timing	Comments
40. Start encounter sequence	E - 300 hr	Ground commant at 150 Jupiter radii
Trapped radiation on	E - 300 hr	
TV enable	E - 170 hr	Ground command at 150 Jupiter radii
TV gimbal angle		
TV exposure setting		
TV picture sequence		Sequencer and Jupiter prescience sensor
Solar cosmis ray off		100 Jupiter radii
Solar plasma off		100 Jupiter radii
TV switched to storage	E - 5 hr	
Infrared scanner		During flyby
Radio occultation sampling rate increased		
41. Start occultation mode		
Science switched to storage		
Auroral sensor on		
TV and infrared off		
42. Post encounter		
Regain cruise mode		
Switch to cruise science		
Transmit stored data		
Telemetry checkout		
Science sequence		Occurs early in mission to check overall operation
Engineering telemetry		May be repeated at regular intervals

The use of the high gain antenna for tracking degrades the link by 1.5 db; shifting the antenna feed between tracking and maximum data transmission positions would be by ground commands.

After about 10 days tracking, the spacecraft is commanded to switch to an omnidirectional antenna and to reorient its attitude for the first midcourse correction. After reorientation, the midcourse motor is commanded to burn a specified time controlled by an onboard clock. After the midcourse correction, the earth acquisition sequence is repeated. If the midcourse correction has placed the spacecraft on the correct trajectory no further events, except for the continuing earth-pointing changes in body attitude, will be needed until 10 days before Jupiter encounter. If the first midcourse correction has not succeeded in placing the spacecraft on the desired trajectory, a second correction can be made following the same sequence given for the first. An additional correction can be made very late in the flight along the earth-pointing line, which would allow a final vernier on the trajectory to correct any errors resulting from unknowns such as the Jupiter ephemeris, AU, solar pressure errors, etc.

At the present time it is not proposed to deploy the booms with the magnetometer and micrometeoroid sensors until after the midcourse maneuvers are complete, because these long flexible booms will introduce wobble into the orientation maneuver, resulting in larger open-loop pointing errors. The high-gain antenna is used in the conical scan mode when the medium-gain downlink degrades. Near Jupiter, and beyond, the conical scan mode is used only for attitude updating, with the bulk downlink communications being handled with the feed on-axis for maximum gain.

At about 150 radii from Jupiter, the encounter sequence is started. The auroral and trapped radiation experiments are turned on. At 100 radii, the TV system is commanded on from the earth and the TV exposure enabled. Actual exposure will use an onboard sensor to detect the leading edge of the planet. A picture-taking sequence will then begin in which a picture is taken and transmitted back once each hour. At about 5 hours from closest approach, pictures will be taken every 5 minutes and stored on tape recorders. Prior to earth occultation, all experiments will be commanded to store on a tape recorder, and after earth occultation the tape recorder will be read out. During the remainder of the flight the only commands necessary are those for change of bit rate and failure correction. Automatic earth-pointing will also be continued.

7.3 POINTING ACCURACIES

Detailed error analyses of the open-loop and the earth-pointing control modes have been presented in Sections 4.3 and 4.4, respectively. Therefore these results are only briefly summarized here. Also, spin rate changes originated by midcourse and attitude control thrust misalignments are evaluated.

7.3.1 Attitude Errors in Open-loop Precession

In the open-loop precession mode the following maneuvers can be executed:

- Precession on the plane determined by the initial spin-axis orientation and the sun.
- Coning around the spacecraft-to-sun line.

The precession error in any of the desired directions will be $\pm$ 1.44 percent of the precession increment produced by each pair of thrust pulses. The cross-axis error of transversal drift is a function of the angle ϕ between the spin axis and the sun line and is given by

$$\frac{\varepsilon_t}{\Delta\theta} = \frac{1}{2}\left(1.52 + \frac{0.6}{\sin^2\phi}\right)^{1/2}$$

This error is also given in percentage of the precession increment $\Delta\theta$. The total attitude error will be the square root of the sum of the squares of these two components. The following uncertainties in the system parameter values were assumed:

Moment arm	$\pm$0.15%
Roll moment of inertia	$\pm$1%
Pneumatic thrust	$\pm$1%
Spin frequency	$\pm$0.1%
Firing angle	0.1%
Sun sensor alignment	$\pm$0.5 deg

Sun sensor null plane position	$\epsilon_a = \frac{1.3 \sin 20^o}{\sin \phi}$ deg
Nozzle alignment	$\pm$0.5 degree
Solenoid valve opening and closing times	2 msec
Thrust rise and decay times	1 msec

The magnitude and direction components of the total precession error are plotted in Figure 7-5 as functions of the angle ϕ.

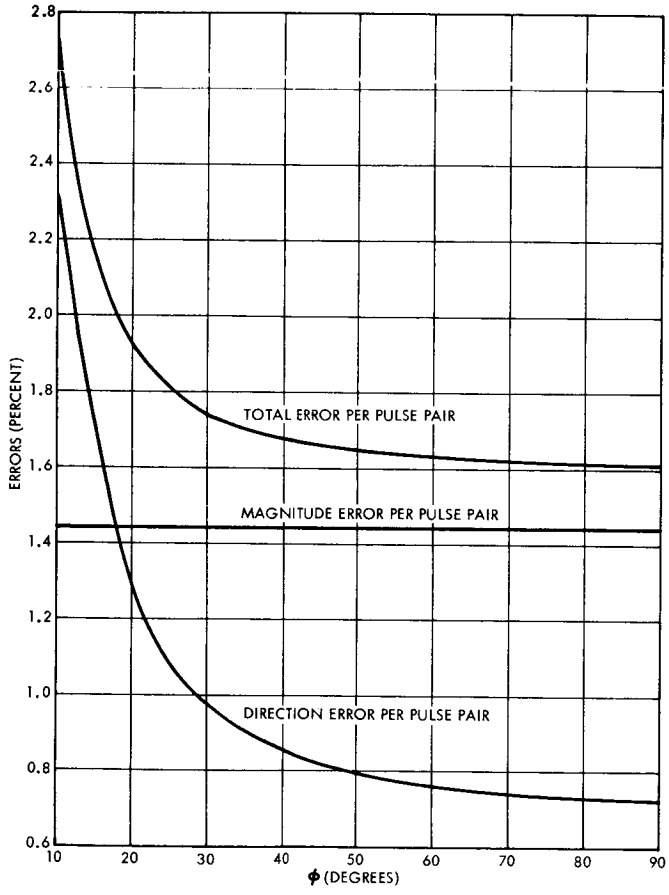

Figure 7-5. Attitude Errors in the Open-Loop Precision Mode

7.3.2 Pointing Errors in Closed-loop Earth-pointing

The earth-pointing mode consists of two types of operations: acquisition and fine pointing. Fine pointing is accomplished by means of the conical scan system operating with the main paraboloidal antenna. In the

level detector a threshold is set corresponding to a pointing error of 0.2 degree. Because of the noise, the 3σ deadzone amplitude is

$$\varepsilon_{dz} = \varepsilon_{\ell_d} \left(1 + \frac{3}{2\sqrt{2}} \frac{N}{S}\right)$$

where

ε_{ℓ_d} = angular error corresponding to the threshold set in the level detector

N/S = noise-to-signal ratio

For N/S = -21.4 db, which corresponds to an error of 0.2 degree with a worst-case squint-angle of 0.5 degree, the 3σ deadzone amplitude is

$$\varepsilon_{dz} = 0.2 \left(1 + \frac{3}{2\sqrt{2}\,1380}\right) \cong 0.2 \text{ degree}$$

In addition, the overall earth-pointing error is a result of three contributing factors:

- Mechanical misalignments
- Boresight error
- Wobble

The mechanical misalignment error is the angle between the symmetry axis of the antenna and the spin axis of the spacecraft. This error is the result of structural misalignments and thermal effects. The boresight error is the angular offset between the electrical and the symmetry axes of the antenna. Wobble or nutational motion of the spin axis about the resultant angular momentum vector produces a time-varying pointing error that will be neglected because of the following reasons:

- The two-pulse torquing system used for attitude corrections cancels most of the wobble generated by impulsive precession.
- In the steady-state, the residual wobble will be attenuated further by the damping produced by friction between antenna petals and sloshing effects in the nitrogen and hydrazine storage tanks.
- The passive wobble damper will provide additional attenuation.

As discussed in Section 3.2, mechanical misalignments of the antenna and boresight errors produce amplitude modulation of the downlink signals. If the vector sum of these errors is denoted by Σ_{mb}, the instantaneous pointing error is

$$\varepsilon = \varepsilon_{dz} + \Sigma_{mb} \cos \omega_s t$$

where ω_s is the spin angular frequency. If the 3σ value of the combined misalginment and boresight errors is 0.2 degree, the total error corresponding to worst case conditions is 0.4 degree. The RSS value is 0.282 degree and the RMS value is 0.245 degree.

Acquisition is performed by means of the helix antenna. For an actual error of 1.2 degrees the SNR is 6 db. If the level detector threshold is set to a value corresponding to 1.2 degrees error, the 3σ deadzone amplitude for any given spin cycle is 1.52 degrees. The phase angle error will be of the order of 20 degrees.

7.3.3 Spin Rate Changes

Spin rate changes can stem from two sources:

- Misalignments of the midcourse engine thrust vector.
- Misalignments of the attitude control thrust vectors.

Assuming a 50 pound midcourse thrust with an angular misalignment of 0.5 degree and an offset of 0.1 inch with respect to the spacecraft center of mass, the torque about the spin axis is

$$\tau = 50 \text{ lb} \times 8.70 \times 10^{-3} \text{ rad} \times 8.35 \times 10^{-3} \text{ ft} = 3.63 \times 10^{-3} \text{ ft-lb}$$

If the thrust duration is 200 seconds and the moment of inertia is 185 ft-lb-sec^2, the spin speed change will be

$$\Delta\omega_s = \frac{3.63 \times 10^{-3} \text{ ft-lb} \times 200 \text{ sec}}{185.3 \text{ ft-lb-sec}^2} = 3.92 \times 10^{-3} \text{ rad/sec}$$

For a nominal spin speed of 5.75 rpm the percentage change is

$$\frac{\Delta\omega}{\omega} = 100 \frac{3.92 \times 10^{-3} \text{ rad/sec}}{\frac{\pi \times 5.75}{30} \text{ rad/sec}} = 0.65 \text{ percent}$$

To estimate the effect of misalignments of the attitude control thrust vector an offset of 0.1 inch is assumed with respect to the spin axis in the plane determined by the symmetry axes of the nozzles. For a thrust of 0.174 pound the torque about the spin axis is

$$\tau = 0.174 \text{ lb} \times 8.35 \times 10^{-3} = 1.45 \times 10^{-3} \text{ ft-lb}$$

Assuming a total precession of 1000 degrees and a thrust duration of 2 seconds per degree the spin speed change will be

$$\Delta\omega_s = \frac{1.45 \times 10^{-3} \text{ ft-lb} \times 2 \times 10^3 \text{ sec}}{185.3 \text{ ft-lb-sec}^2} = 1.57 \times 10^{-2} \text{ rad}$$

For a nominal spin of 5.75 rpm the percentage change is 2.6 percent. Consequently, for these reasonable assumptions, the total percentage change in spin will be ±3.25 percent.

7.4 TRAJECTORY ACCURACY ANALYSIS

This section estimates the uncertainty of control of the interplanetary trajectory. The contributions to this uncertainty are the error execution of the midcourse trajectory correction, the uncertainty in tracking the spacecraft from injection to midcourse correction, ephemeris and astronomical unit errors, and certain identifiable but unpredictable trajectory perturbations acting after the midcourse correction. The midcourse guidance model of Section 4.2 is assumed for this analysis. It consists of a single midcourse correction about 10 days after launch, with the thrust vector directed essentially parallel to the critical plane so as to reduce $B \cdot T$ and $B \cdot R$ errors.

The root mean square and percentage contributions to the target coordinates $B \cdot T$ and $B \cdot R$ are listed in Table 7-5. The development of each error source is presented in the following sections. The percentage contribution of the total deviation in $B \cdot T$ and $B \cdot R$ are computed by assuming that the mean square error contributions are additive.

Table 7-5. Post Midcourse Trajectory Errors

Error Source	RMS B·T Error (km)	RMS B·R Error (km)	Percent of Total B·T Variance	Percent of Total B·R Variance
Injection errors	951,000	388,000	*	*
Midcourse execution errors**	8,850	10,600	93.0	99.4
Pre-midcourse tracking errors	2,050	625	5.0	0.3
Nongravitation perturbations (unpredictable portions)	1,067	217	1.4	-
Ephemeris errors	500	500	0.3	0.2
Astronomical unit conversion factor uncertainty	303	303	0.2	0.1
Total rss	9,150	10,650	100.0	100.0

Total 99% miss ellipse:

Semimajor axis = 26,300 km

Semiminor axis = 17,400 km

*Does not directly affect post midcourse target errors.

**Arbitrary pointing critical plane correction at 10 days past injection.

The largest error contribution, as might be expected, is caused by midcourse execution errors. Hence more accurate control of the trajectory, if required, could best be obtained by improving the precision of the midcourse maneuver or by increasing the number of maneuvers. Of the remaining errors, the greatest is the pre-midcourse tracking uncertainty which causes the estimated position of the spacecraft to be in error. This error is based on present state of the art tracking accuracies attainable by the DSIF. Presumably by 1972, greater accuracy can be attained. Likewise ephemeris errors and uncertainty in the AU are based on present state of the art and by 1972 may be appreciably reduced.

7.4.1 Injection Velocity Errors

The sequence of events from spacecraft separation from the Centaur through injection motor firing were studied to determine the injection velocity errors. The effects of spacecraft attitude error and wobble during injection motor firing and the uncertainty of the TE-364-3 impulse were considered. These velocity errors are used to determine the midcourse correction requirements reported in Section 4.2. The injection errors do not otherwise contribute to the post-midcourse trajectory accuracy.

The attitude errors, nutation angle, and resulting velocity errors due to the various events were calculated and it was found that a spin rate of 60 rpm was adequate to maintain attitude errors during injection motor firing to reasonable values. The Centaur attitude error using the present control system at the time of spacecraft separation was found to be the largest contributor to attitude error and the resulting velocity error. An improved accuracy will probably be available by 1972. Attitude errors, nutation angle, and resulting velocity errors are listed in Table 7-6 for typical 3σ values of thrust misalignments and tipoff rates. The effects of a change of parameters such as spin rate, spinup time, and thrust misalignments can be determined from the subsequent discussion.

The Centaur attitude error and transverse rates at the time spacecraft separation have been quoted by General Dynamics Convair, San Diego (W. Stublefield, personal communication), to be as follows for the present control system:

Attitude error:	± 1.8 deg each pitch and yaw axes
Transverse rates:	± 0.03 deg/sec each pitch and yaw axes

Table 7-6. Spacecraft Attitude Errors, Nutation Angle, and Velocity Dispersion (3σ)

Event		Attitude Error (deg)	Nutation Angle (deg)	Axial Velocity Error (m/sec)	Lateral Velocity Error (m/sec)	Comments
Centaur attitude error	(a)	2.5	-	-	135	Present control system capability
	(b)	1.0	-	-	53	Possible allowable value
	(c)	0.4	-	-	21	Modified control system capability
Delay between separation and spinup (0.25 sec)	(a)	0.25	-	-	13	Tip off rate, ω_o = 1 deg/sec
	(b)	0.18	-	-	9	Tip off rate, ω_o = 0.7 deg/sec
Spinup to 60 rpm	(a)	1.3	0.65	-	69	1-sec spinup, ω_o = 1 deg/sec
	(b)	1.7	0.55	-	90	2-sec spinup, ω_o = 1 deg/sec
	(c)	1.1	0.6	-	58	1-sec spinup, ω_o = 0.7 deg/sec
Injection motor firing	(a)	0.6	1.8	21	32	Spin rate, s = 60 rpm
	(b)	0.2	0.6	21	11	Spin rate, s = 100 rpm
RSS Totals						
1(a) + 2(a) + 3(b) + 4(a)		3.1	1.9	21	165	Worst combination
1(b) + 2(a) + 3(a) + 4(a)		1.75	1.8	21	93	Centaur error = 1 deg ω_o = 1 deg/sec
1(b) + 2(b) + 3(c) + 4(a)		1.6	1.9	21	85	Centaur error = 1 deg ω_o = 0.7 deg/sec
1(c) + 2(b) + 3(c) + 4(a)		1.33	1.9	21	70	Centaur error = 0.4 deg ω_o = 0.7 deg/sec

The present control system could be modified to reduce the attitude error to ± 0.3 degree in each axis if necessary, according to General Dynamics. An improvement such as this will be required for the Advanced Planetary Probe mission to limit the midcourse correction requirements to a reasonable value.

The separation system will induce transverse rates (tipoff rates) which can be limited to 1.0 deg/sec or less by careful alignment and matching of separation springs.

The spacecraft will be spun up by four constant-thrust solid rockets which will fire for approximately 1 second to produce a final spin rate of 60 rpm. Spinup will be initiated within 0.25 second after separation from the Centaur.

The angle of attack of the spin axis relative to its initial position is calculated from the following expression*:

$$\alpha = \gamma\pi\left(\frac{1+\lambda}{\lambda}\right)\int_0^{\sqrt{\frac{\lambda st}{\pi}}} e^{i\left(\frac{\pi}{2}\frac{1+\lambda}{\lambda}u^2\right)}\,[C(u) - iS(u)]\,du \qquad \beta$$

$$+ \omega_o\sqrt{\frac{\pi t}{(1+\lambda)s}}\left[C\left(\sqrt{\frac{(1+\lambda)st}{\pi}}\right) + iS\left(\sqrt{\frac{(1+\lambda)st}{\pi}}\right)\right]$$

where

α = angle of attack

γ = spin vector misalignment = 0.008 rad

λ = inertia parameter $(I_Z - I_X)/I_X = -0.64$

S = final spin rate = 60 rpm = 2π rad/sec

t = spinup time = 1 sec

$C(u)$, $S(u)$ = Fresnel integrals

ω_o = tipoff rate = 1.0 deg/sec

*R. S. Armstrong, "Errors Associated with Spinning-Up and Thrusting Symmetric Rigid Bodies," JPL Technical Report 32-644.

The integral has been evaluated for various inertia parameters by a TRW computer program. The Fresnel integrals are tabulated in the Handbook of Mathematical Functions, National Bureau of Standards Applied Mathematics Series 55, June 1964. The resulting angle of attack as a function of spinup time is shown in Figure 7-6.

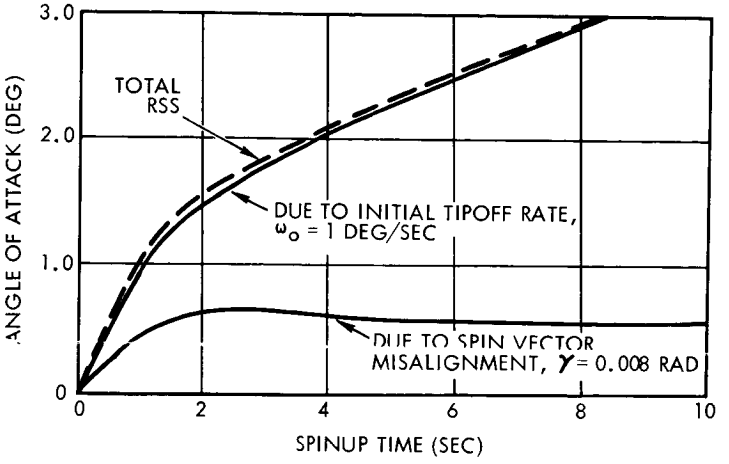

Figure 7-6. Angle of Attack Change During Spinup

The nutation (wobble) induced during spinup is calculated from the following expression.

$$\theta = \gamma \frac{\pi}{\lambda st}\left[C\left(\sqrt{\frac{\lambda st}{\pi}}\right) - iS\left(\sqrt{\frac{\lambda st}{\pi}}\right)\right] + \frac{\omega_o}{(1+\lambda)s}$$

The magnitude of the final nutation angle as a function of spinup time is shown in Figure 7-7.

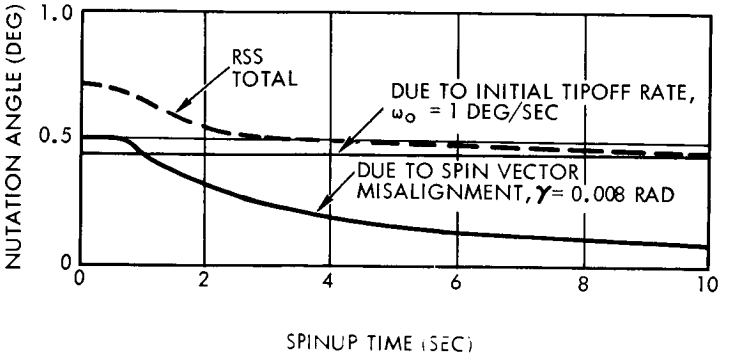

Figure 7-7. Nutation Induced During Spinup

The spacecraft average attitude shift or momentum vector position will be a combination of the angle of attack and nutation angle. The attitude shift as a function of spinup time is shown in Figure 7-8.

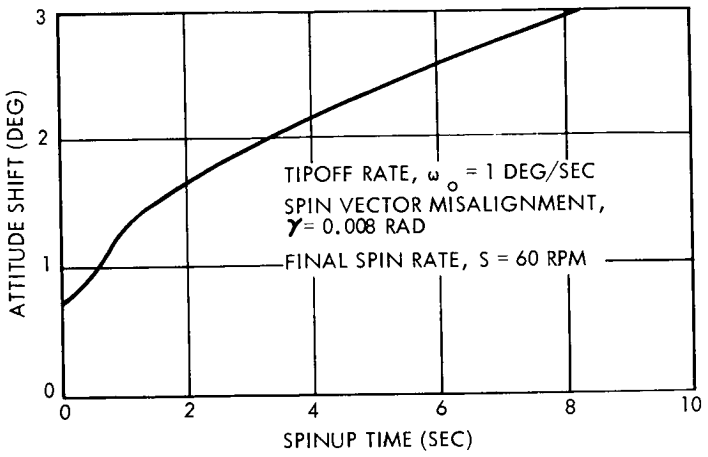

Figure 7-8. Attitude (Momentum Vector) Shift During Spinup

The misalignment of the thrust axis of the injection motor with respect to the spacecraft c. g. will induce a transverse torque on the spacecraft which will cause attitude error and nutation.

The attitude error during injection motor firing is

$$\alpha = \frac{T\epsilon}{Cs^2}(1 - \cos st)$$

where

α = attitude error (rad)

T = injection motor thrust = 8945 lb

ϵ = thrust axis misalignment = 0.004 ft

C = average spin axis moment of inertia during firing = 90 slug ft^2

S = spin rate = 2π rad/sec

t = time (sec)

For firing times much longer than the spin period, the average attitude error is

$$\alpha_{ave} = \frac{T\epsilon}{Cs^2}$$

The average attitude error as a function of spin rate is shown in Figure 7-9. The maximum nutation induced during injection motor firing is

$$\theta_{max} = \frac{2T\epsilon}{\lambda Cs^2}$$

This is plotted as a function of spin rate in Figure 7-10.

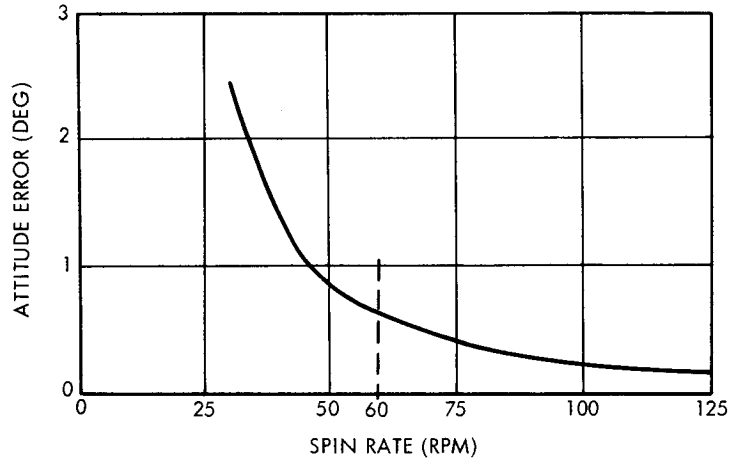

Figure 7-9. Attitude Error Induced at Injection

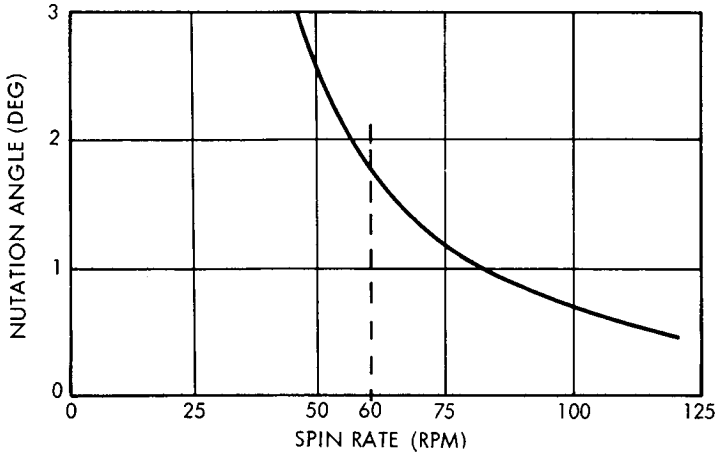

Figure 7-10. Nutation Induced During Injection

The velocity increment provided by the TE-364-3 is approximately 10,000 ft/sec or 3000 m/sec.

The uncertainty of the total impulse of the TE-364-3 is assumed to be ± 0.7 percent. This will produce a velocity uncertainty of ± 21 m/sec. This uncertainty must be combined with the Centaur velocity errors, which are not included here. The degradation of the magnitude of the velocity increment due to nutation is negligible.

The attitude errors of the Centaur and those induced during separation, spinup, and injection motor firing will produce a transverse velocity component

$$\Delta V \text{ (transverse)} = \Delta V \text{ (total)} \sin \alpha$$

For small values of attitude error, α, the transverse velocity is approximately 53 m/sec per degree of attitude error. The contributions of the various events to the total error are shown in Table 7-5.

7.4.2 Tracking Errors

This section describes the results of an analysis of pre-midcourse tracking performed to calculate the state vector uncertainties due to radar tracking. The dispersion ellipse at Jupiter was computed from these state vector uncertainties. the FORTRAN IV version of the ESPOD Program (AT85B) was used to carry out this study.

Since ESPOD does not have a capability for simulating noisy radar observations, dummy observations were simulated off line. Range-rate observations at the rate of one every 10 minutes for a period of 10 days from a single ground radar constituted the tracking configuration assumed. The mock radar was located on the equator at the Greenwich meridian and was assumed capable of observing the spacecraft continuously. The a priori standard deviation assigned to the range rate observations was 10^{-2} m/sec. Although this may depart from the design values of the mission, linear scaling applies to the resultant uncertainties. For example, if the a priori standard deviation is halved, the state vector uncertainties are halved at any given time .

The integrated trajectory used for this study is identical to the March 14, 1972, launch trajectory, Trajectory F, described in another section.

An injection a priori covariance matrix equal to that tabulated in Section 4.2 was used in the simulation. This matrix is given below, including an estimate of the position uncertainties. The units are feet squared and feet per second squared.

1	2	3	4	5	6
0.10758400 06				0	
	0.10758400 06				
		0.10758400 06			
	0		0.58296542 04	-0.47982464 04	-0.33908325 04
			-0.47982464 04	0.97054753 04	-0.22904633 04
			-0.33908325 04	-0.22904633 04	0.11319988 05

The tracking normal matrix was accumulated and inverted in double precision in earth equatorial coordinates. The normal matrix (and its inverse) are referenced to injection time. The normal and the covariance matrices in units of feet and ft/sec are given below.

Tracking Covariance Matrix

1	2	3	4	5	6
0.55978666E 05					
-0.28396648E 05	0.83668967E 05				
0.20313078E 05	-0.10648005E 05	0.83774365E 04			
-0.49836487E 02	0.44237969E 02	-0.17908070E 02	0.49963445E-01		
-0.55469450E 01	0.40367052E 02	-0.23131603E 01	0.15147935E-01	10.22569651E-01	
0.32051177E 02	-0.32254706E 02	0.12018165E 02	-0.33495578E-01	-0.14119810E-01	0.26724154E-01

Tracking Normal Matrix

1	2	3	4	5	6
0.58711940E 00					
-0.55981407E 00	0.53508633E 00				
-0.36204313E-00	0.34536415E-00	0.22405540E-00			
0.10726588E 04	-0.10240686E 04	-0.66138013E 03	0.19612143E 07		
0.69944967E 03	-0.66920002E 03	-0.43175916E 03	0.12801176E 07	0.83735375E 06	
0.49700411E 03	-0.47521200E 03	-0.30679638E 03	0.90946154E 06	0.59449866E 06	0.42238521E 06

The above tracking matrices include the a priori information. The elements of the tracking normal matrix are orders of magnitude larger than the a priori normal matrix. Hence the a priori information does not affect the results due to tracking.

The covariance matrix was propagated from injection to the B · T, B · R target coordinate system. This matix is

$$\begin{bmatrix} 4.228 & -0.4521 \\ -0.4521 & 0.3905 \end{bmatrix} \times 10^6 \quad (\text{km})^2$$

The square roots of the eigenvalues of this matrix multiplied by an appropriate factor (see Section 4.2) give the semimajor and semiminor axes of the 99 percent probability dispersion ellipse. The 99 percent semimajor and minor axes are 5110 and 1450 km, respectively. The dispersion ellipse is plotted in Figure 7-11.

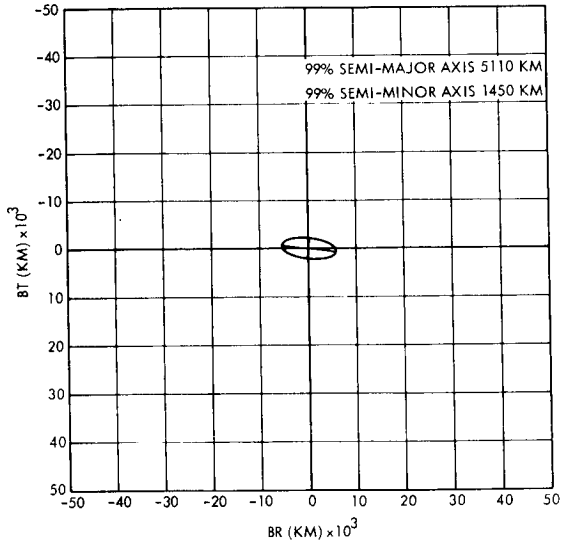

Figure 7-11. Tracking Uncertainty Ellipse Tracking from Injection to 10 Days - One Point Every 10 Minutes

7.4.3 Midcourse Correction Error

Orientation and execution errors introduced by the midcourse correction subsystem are evaluated in this section. Consideration is given to both arbitrary pointing guidance and earth pointing guidance.

7.4.3.1 Arbitrary Pointing Guidance

Thrust Vector Pointing Errors. Arbitrary pointing guidance requires that the vehicle spin axis be precessed to point in a certain direction. Detailed evaluation of the error sources and their effects on changing the spin axis an incremental amount is reported in Section 7.3. The resultant effects on the pointing direction of the spin axis for a sequence of incremental turns are evaluated here.

The spin axis may be precessed by the attitude control system in two different ways for each incremental step. The sun-spacecraft-spin axis angle (called here the spin axis cone angle β), or an angle measured in a plane orthogonal to β (called here γ) can be changed. This geometry is illustrated in Figures 7-12(a) and (b). The angle $d\alpha$ in Figure 7-12(b) is the incremental change in α, called a clock angle. The clock angle, which is like a right ascension angle, is introduced for analytical convenience.

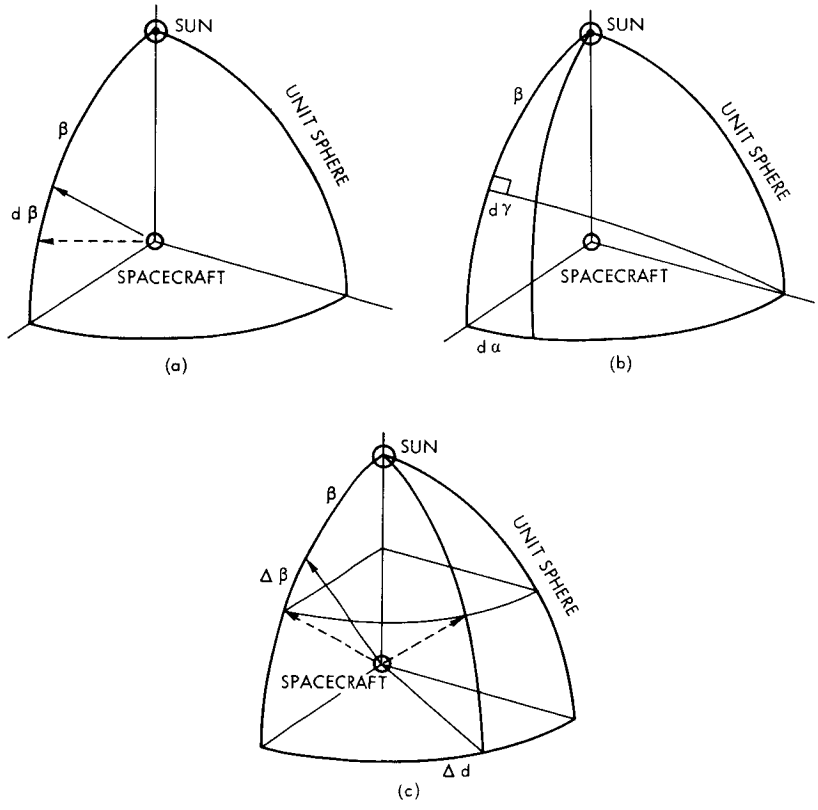

Figure 7-12. Geometry of Spacecraft Spin Axis

The spin axis may be pointed in an arbitrary direction by combining both kinds of motion. A sequence of incremental steps causes the spin axis to change its cone and clock angles. The nature of several incremental steps in cone angle $d\beta$ causes the spin axis to precess in a plane described by the initial orientation of the spin axis and the sun line. The nature of several incremental steps $d\gamma$ causes the spin axis to rotate about the sun line at a constant cone angle. An example of these motions is illustrated in Figure 7-12 (c). In this figure, the prefix Δ indicates the total desired angle change.

Two kinds of errors are introduced for each incremental step change, in-plane and out-of-plane errors. In-plane errors cause the actual change in the angle (either $d\beta$ or $d\gamma$) to be different from that desired, while out-of-plane errors cause the spin axis to precess in a slightly different direction from that desired. These incremental errors propagate to total errors of different magnitude depending upon the size of the angles precessed and the sun-spin vector geometry.

In-plane errors ϵ are estimated to be 1.44 percent (3σ) per step and out-of-plane errors $\epsilon_\perp$ are estimated per step $d\beta$ or $d\gamma$ to be

$$\epsilon_\perp = \frac{1}{2}\left[a + \frac{b}{\sin^2\beta}\right]^{1/2} \text{ percent } (3\sigma)$$

where $a = 1.52$ and $b = 0.6$. This expression is derived in Section 7.3. Thus, for the nominal step size equal to two degrees,

$$\epsilon = 0.0288 \text{ deg/step}$$

$$\epsilon_\perp = \left[1.52 + \frac{0.6}{\sin^2\beta}\right]^{1/2} \cdot 10^{-2} \text{ deg/step } (3\sigma)$$

Cone Angle Movement Errors. Consider how these errors propagate for cone angle movement. In-plane errors cause the total desired cone angle $\Delta\beta$ to be in error by

$$\Delta\beta = n\epsilon$$

where n is equal to the number of incremental step changes defined by

$$n = \frac{\Delta\beta}{d\beta}$$

Out-of-plane errors cause a clock angle component to be introduced which accrues to a value dependent upon the turn geometry. Figure 7-13 illustrates the clock angle error component $d\alpha$ introduced at each step. $d\gamma'$ represents the great circle error component introduced at each step.

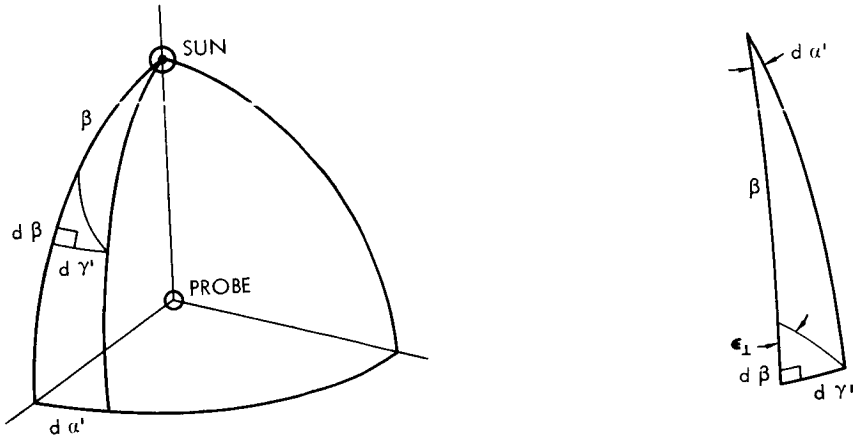

Figure 7-13. Clock Angle Geometry

Thus, from the small triangle,

$$\tan \epsilon_{\perp} \sin d\beta = \tan d\gamma'$$

$$d\gamma' \cong \epsilon_{\perp} \sin d\beta$$

From the large triangle,

$$\tan d\alpha \sin(\beta+d\beta) = \tan d\gamma'$$

$$d\gamma' \cong \sin(\beta+d\beta)\, d\alpha$$

Equating the expressions for $d\gamma'$,

$$d\alpha \cong \epsilon_{\perp} \frac{d\beta}{\sin \beta}, \quad \beta \geq 10 \text{ deg}$$

Substituting the equation for $\epsilon_\perp$ and integrating to find the total accrued clock angle error $\Delta\alpha_1$ for a large change in cone angle,

$$\Delta\alpha_1 = \int_{b_o}^{\beta_f} \left[a + \frac{b}{\sin^2 \beta} \right]^{1/2} \frac{d_\beta}{\sin \beta}$$

where the subscripts "o" and "f" denote initial and final respectively. If the substitution

$$x = \csc \beta$$

is made, it is found that

$$\Delta\alpha_1 = -\sqrt{a} \int_{\csc\beta_o}^{\csc\beta_f} \sqrt{\frac{1 + \frac{b}{a} x^2}{x^2 - 1}}\, dx$$

To obtain a closed form expression from $\Delta\alpha_1$, it will be assumed that $\epsilon_\perp$ is constant and not a function of β. This is reasonable because

$$1.29 \text{ percent} \leq \epsilon_\perp \leq 0.725 \text{ percent}$$

in the interval in which operation is restricted to occur (refer to Section 7.3). Then

$$\Delta\alpha_1 \cong \int_{\beta_o}^{\beta_f} \epsilon_\perp \frac{d\beta}{\sin\beta} = \epsilon_\perp \log \frac{\tan \frac{1}{2} \beta_f}{\tan \frac{1}{2} \beta_o}$$

Sun Line Rotation Errors. For rotation about the sun line, the errors in the incremental steps propagate differently. In-plane errors cause the clock angle error to be

$$\Delta\alpha_2 = m\epsilon$$

where m is the number of increments for sun line rotation. Because each step changes an arc of a great circle $d\gamma$, the clock angle changes according to

$$d\alpha = \frac{d\gamma}{\sin\beta}$$

Therefore the total desired excursion $\Delta\alpha$ requires m incremental steps according to

$$m = \frac{\Delta\alpha}{d\gamma} \sin\beta$$

Out-of-plane errors cause the resulting cone angle to be in error. Figure 7-14 illustrates the effect of this error. Thus

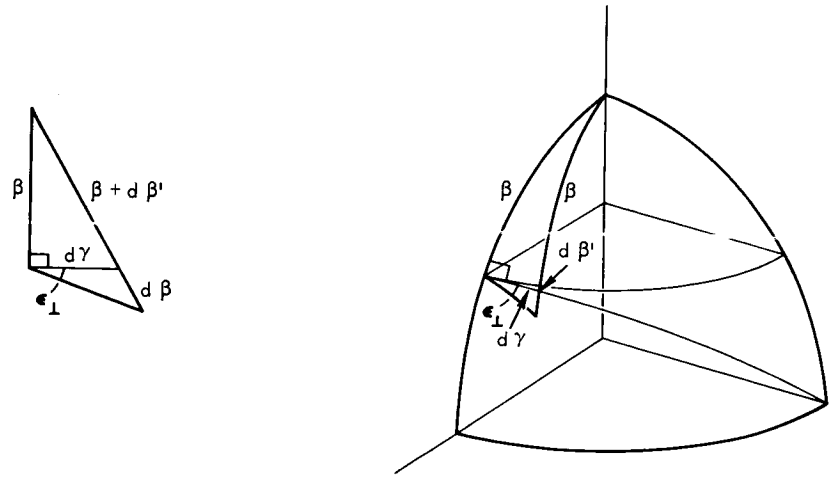

Figure 7-14. Out-of-Plane Errors for Cone Angle Movement

$$\cos(\beta + d\beta') = \cos\beta \cos d\gamma$$

where $d\beta'$ is the cone angle change caused from the fact that the spin axis precesses in a great circle during each incremental step rather than at a constant cone angle. Solving for $d\beta'$,

$$d\beta' \cong \frac{1 - \cos d\gamma}{\tan\beta} \cong \frac{(d\gamma)^2}{2\tan\beta}$$

For m steps, this causes an error

$$\Delta\beta_2 = m d\beta' = m \frac{(d\gamma)^2}{2\tan\beta}$$

The out-of-plane error effects are computed by assuming that $d\beta'$ is small for each incremental step. Then

$$\tan\epsilon_\perp \sin d\gamma = \tan d\beta$$

or

$$d\beta = \epsilon_{\perp} \sin d\gamma \cong \epsilon_{\perp} d\gamma$$

For m steps, this causes an error

$$\Delta\beta_3 = m d\beta = m \epsilon_{\perp} d\gamma$$

Total Pointing Errors. The total clock and cone angle errors from these sources are

$$\epsilon_{\alpha} = \Sigma \Delta\alpha i = \epsilon_{\perp} \log \frac{\tan \frac{1}{2} \beta_f}{\tan \frac{1}{2} \beta_o} + \epsilon \frac{\Delta\alpha}{d\gamma} \sin \beta$$

$$\epsilon_{\beta} = \Sigma \Delta\beta i = \frac{\Delta\beta}{d\beta} \epsilon + \frac{\Delta\alpha \, d\gamma \cos \beta}{2} + \Delta\alpha \, \epsilon_{\perp} \sin \beta$$

Plots of ϵ_{α} and ϵ_{β} are presented in Figures 7-15 and 7-16 for a sample precession sequence. It was assumed that the initial cone angle of the spin axis β_o is 20 degrees. The spin axis is then precessed to a cone angle equal to β followed by a clock angle change $\Delta\alpha$ equal to 90 degrees.

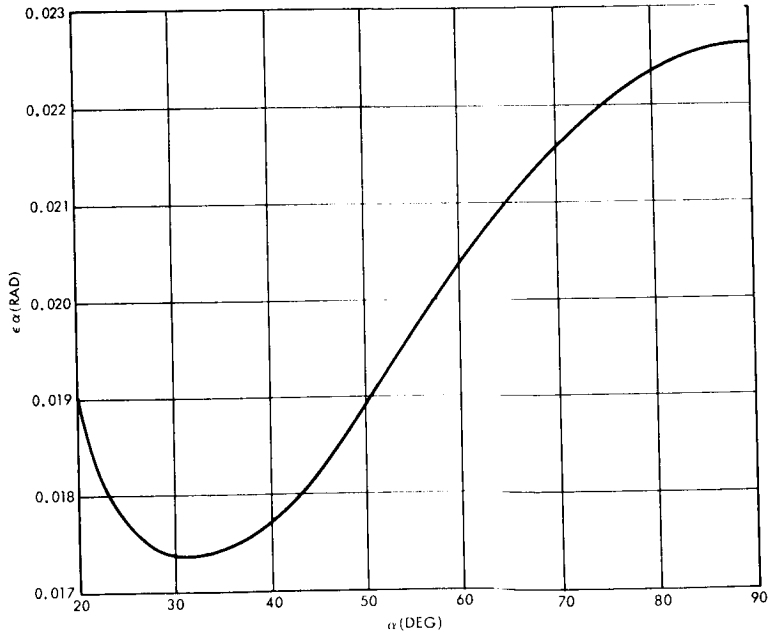

Figure 7-15. Clock Angle Errors (3σ)

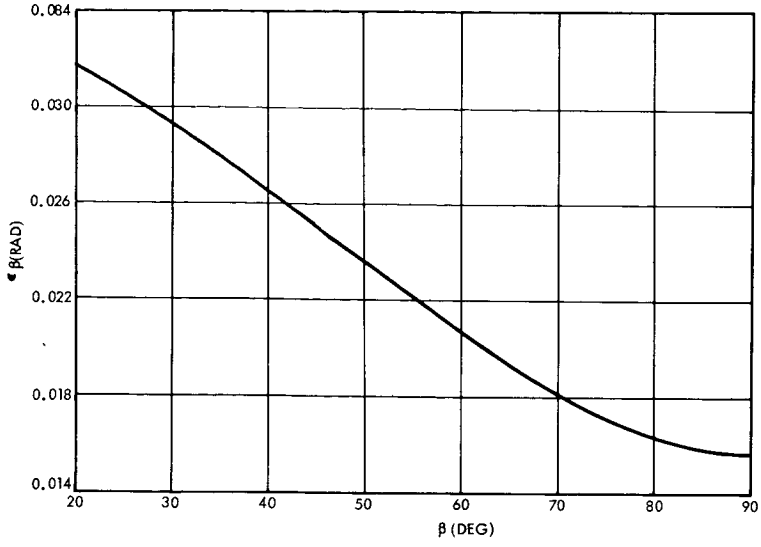

Figure 7-16. Cone Angle Error (3σ)

dβ and dα are chosen equal to 2 degrees. The additive terms in the last two equations were root sum squared so that ϵ_{α} and ϵ_{β} represent 3σ estimates for this particular turn sequence.

Thrust Magnitude Errors. The thrust magnitude errors characteristic of a timed motor burn are summarized in Appendix H. The proportional errors are a function of burn time and vary between 0.66 and 0.95 percent (1σ). A value equal to 0.75 percent is selected for this analysis. The resolution errors, which are primarily due to the motor ignition and shutdown transients, are equal to 0.0188 m/sec (1σ), if both transient errors are root-summed-squared.

Midcourse Correction Covariance Matrix. To accurately compute the effects of the pointing and velocity execution errors, a Monte Carlo simulation should be employed. In addition to a detailed treatment of the execution errors and the spin axis turn sequence, the effects on the execution errors caused from state vector errors at injection could be included.

Alternatively a second moment error analysis can be employed enabling an estimate of the execution errors to be simply computed.

Thus, the covariance matrix of execution errors Σ_e is*

$$\Sigma_e = \left(\sigma_s^2 - \sigma_p^2\right) + \left(\sigma_r^2 - \sigma_a^2\right)\Sigma_{|v|}$$

$$+ \left(\sigma_p^2 |\bar{v}|^2 + \sigma_a^2\right) I$$

where

σ_s^2 = variance of the proportional velocity error

σ_p^2 = variance of the pointing error

σ_r^2 = variance of the resolution error (nonproportional component of velocity magnitude error)

σ_a^2 = variance of the coning error (misalignment of thrust axis from spin axis)

v = midcourse correction velocity increment

$|\bar{v}|^2$ = expected value of $|v|$ squared

Σ_v = midcourse correction velocity covariance matrix

$\Sigma_{|v|}$ = normalized midcourse correction velocity covariance matrix

I = unit matrix

Because the distribution of the error sources will not generally be normal, Σ_e will not represent the covariance of a multidimensional normal distribution. However, it will be assumed that all error sources are zero mean normal so that Σ_e may be propagated to the target and compared with other error effects which are normal.

*C. R. Gates, "A Simplified Model of Midcourse Maneuver Execution Errors," JPL TR 32-504, November 15, 1963.

The previous paragraphs indicate that reasonable 1σ error estimates are

$$\sigma_s = 0.0075 \text{ (0.75 percent)}$$

$$\sigma_p = 0.0116 \text{ rad } (\tfrac{2}{3} \text{ degree})$$

$$\sigma_r = 0.0188 \times 10^{-3} \text{ km/sec}$$

The term σ_a has not been evaluated for this study; it is selected equal to zero. Section 4.2 indicates that for a critical plane midcourse correction at 10 days

$$\Sigma_v = \begin{bmatrix} 1001.6947 & -52.702607 & -98.524102 \\ & 73.535761 & 102.51410 \\ \text{symmetric} & & 143.56311 \end{bmatrix} \times 10^{-6} \text{ (km/sec)}^2$$

$$|\bar{v}|^2 = T_r \Sigma_v = 1218.79357 \times 10^{-6} \text{ (km/sec)}^2$$

in the geocentric equatorial coordinate system. Therefore for these values,

$$\Sigma_e = \begin{bmatrix} 0.085 & 0.0042 & 0.0078 \\ & 0.158 & -0.008 \\ \text{symmetric} & & 0.165 \end{bmatrix} \times 10^{-6} \text{ (km/sec)}^2$$

in this same coordinate system. Propagating this to the target coordinate plane using the matrix C (defined in Section 4.2) gives the post midcourse correction target covariance matrix

$$\Sigma_{TM} = C \Sigma_e C^T$$

which is numerically equal to

$$\Sigma_{TM} = \begin{bmatrix} 0.7845 & 0.2681 \\ 0.2681 & 1.128 \end{bmatrix} \times 10^8 \text{ km}^2$$

The square roots of the eigenvalues of this matrix multiplied by an appropriate factor which is a function of the ratio of the eigenvalues gives the 99 percent semimajor and minor axes of the post correction miss ellipse. Selection of the appropriate factor is made assuming that the errors are multidimensional normal. For non-normal distributions, the determination of such a factor is complicated. It is anticipated that this factor does not differ significantly (more than 10 to 20 percent for other continuous distributions). The semimajor axis is 24,480 km, and the semiminor axis is 17,300 km. The miss ellipse is plotted in Figure 7-17. Although it is not intended here to control the day of arrival, the time of day of arrival can be controlled to 3.6309 hours, 1σ, by the single-correction program.

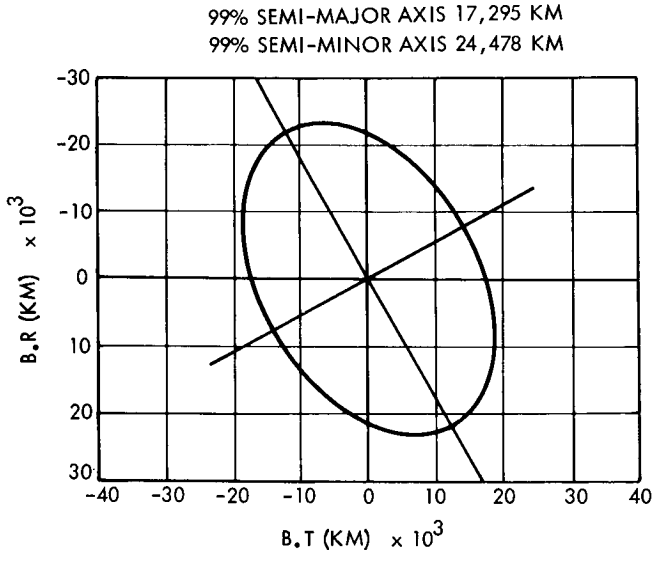

Figure 7-17. Critical Plane Correction at 10 Days, 99 Percent Post Correction Miss Ellipse

7.4.3.2 Earth-Pointing Guidance Errors

Because earth-pointing guidance does not require that the spin axis be precessed to point in an arbitrary direction prior to the midcourse correction, the pointing errors will be equal to the high-gain antenna pointing errors. The motor thrust magnitude errors are of course not

a function of how the spin axis is pointed. It will be assumed here that the spin axis is pointed along the earth line and that the motor thrust errors are equal to those tabulated in the previous section.

As for the arbitrary pointing guidance, a Monte Carlo simulation is necessary to evaluate the execution error effects in detail. Similarly, a second moment error analysis will be employed here to enable a simple estimate of the error effects to be computed.

The RMS change in the magnitude of the impact parameter B caused from an error in a correction is directed along the correction sensitivity at the time of the correction. Then

$$\Sigma_{TM} = \theta\sigma_V (\theta\sigma_V)^T = \theta\sigma_V^2\theta^T$$

where Σ_{TM} is the post-correction covariance matrix and θ is a 2 x 1 vector which projects the error in velocity to B·T and B·R miss components for a correction at a certain time. θ is evaluated from the correction sensitivities, in this instance plotted in Section 4.2. The velocity mean square error σ_V^2 is

$$\sigma_V^2 = \sigma_S^2 \, Tr \, \Sigma_V + \sigma_r^2$$

where σ_S^2 and σ_r^2 are defined in the previous section. Combining these equations gives

$$\Sigma_{TM} = \theta \left[\sigma_S^2 \, Tr \, \Sigma_V + \sigma_r^2 \right] \theta^T$$

The previous section indicates that

$\sigma_S = 0.0075$ (0.75 percent)

$\sigma_r = 0.0188 \times 10^{-3}$ km/sec

Σ_V is tabulated in Section 3.2 and

$$\theta_{10} = \begin{bmatrix} -14,800 \\ -24,900 \end{bmatrix} \text{ km per m/sec}$$

$$\theta_{100} = \begin{bmatrix} -25,100 \\ -8,900 \end{bmatrix} \text{km per m/sec}$$

as 10 and 100 days, respectively. Evaluating Σ_{TM} for corrections at 10 and 100 days,

$$\Sigma_{TM_{10}} = \begin{bmatrix} 1.7543 & 2.9238 \\ 2.9238 & 4.8731 \end{bmatrix} \times 10^8 \text{ km}^2$$

$$\Sigma_{TM_{100}} = \begin{bmatrix} 0.4225 & 0.1521 \\ 0.1521 & 0.05475 \end{bmatrix} \times 10^8 \text{ km}^2$$

The covariance matrix following the last correction is

$$\Sigma_{TM} = \Sigma_{TM_{10}} + \Sigma_{TM_{100}}$$

$$\Sigma_{TM} = \begin{bmatrix} 2.177 & 3.076 \\ 3.076 & 4.9278 \end{bmatrix} \times 10^8 \text{ km}^2$$

The square roots of the eigenvalues of this matrix multiplied by the appropriate factor are the 99 percent semimajor and minor axes of the post-correction miss ellipse. The 99 percent semimajor and minor axes are 65,850 and 10,680 km, respectively. The miss ellipse is plotted in Figure 7-18.

The largest error contributor to the corrections is the proportional velocity error. This error, unknown prior to flight, may be a predominantly systematic type. Thus it might be possible to track the spacecraft following the first correction to determine the proportional error contribution thus calibrating the motor in flight. This calibration could be used to compute a new standard firing time to eliminate proportional errors from the second correction. Figure 7-19 shows the 99 percent miss ellipse following the second correction assuming no proportional errors in the second correction. Since this calibration improves only the second firing, there is not a great improvement over Figure 7-18.

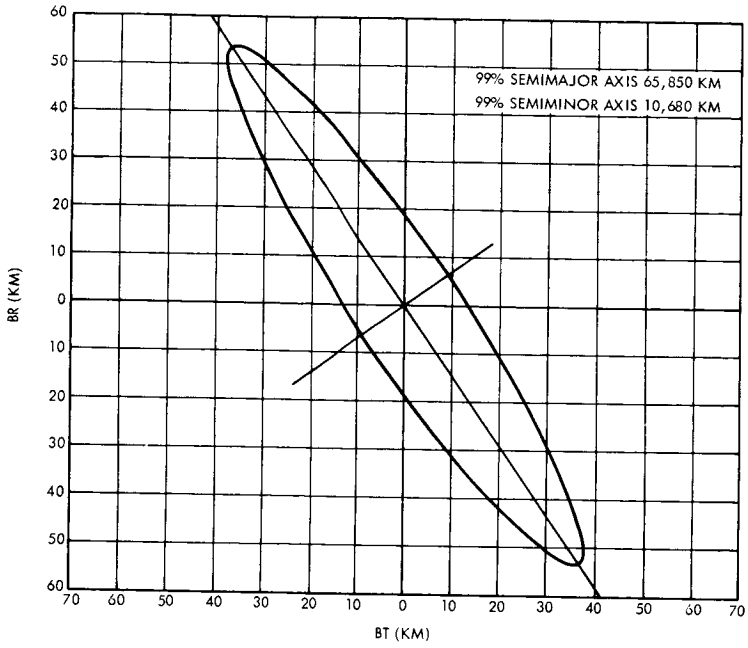

Figure 7-18. Earth-Poiting Corrections at 10 and 100 Days, 99 Percent Miss Ellipse.

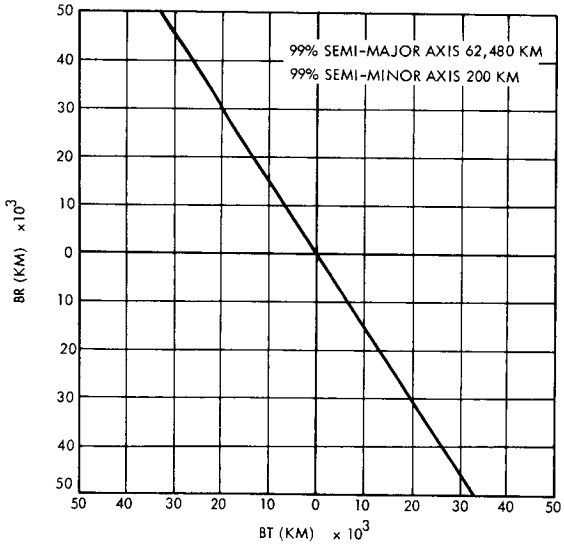

Figure 7-19. Earth-Pointing Corrections at 10 and 100 Days, 99 Percent Post Correction Miss Ellipse, Assuming no Proportional Errors from Second Correction.

Conceivably, however, this approach will further improve accuracy if the time of execution of the second maneuver as well as the firing duration are established based on tracking after the first midcourse. By this means, both components of miss arising from first maneuver execution error can be compensated.

7.4.4 Nongravitational Perturbations

This section presents estimates of various trajectory perturbations accruing from nongravitational micro-accelerations from solar radiation pressure, micrometeoroid impingement, and unbalanced attitude control forces. In cases where the exact model of the micro-acceleration effect is not well known or presents unwarranted complications for purposes of this analysis, simplified models are assumed, in some instances representing worst case effects. This is particularly true for the effects of micrometeoroid impingement, which may differ by orders of magnitude depending upon the assumptions of micrometeoroid flux present in the interplanetary space between earth and Jupiter.

The principal objective of this section is to establish typical levels of predictable trajectory perturbations due to the above sources as well as unpredictable errors which are caused by unknown variation of significant parameters in the spacecraft and in the perturbing force model. It is assumed that predictable trajectory perturbations can be compensated for at the time of injection into the interplanetary transfer trajectory or during the midcourse correction maneuver. The unpredictable part of the perturbation remains uncorrected and thus contributes to the total miss vector at Jupiter encounter. The unpredictable components will be estimated on the basis of conservative assumptions regarding the magnitude of their sources. The in-plane and out-of-plane displacements computed here correspond closely to $B \cdot T$ and $B \cdot R$ displacements respectively. The correlation coefficient between these miss components is assumed equal to 1 so that the miss covariance matrix in $B \cdot T$, $B \cdot R$ coordinate is

$$\begin{bmatrix} 1.1449 & 0.232 \\ 0.232 & 0.0461 \end{bmatrix} \times 10^6 \text{ km}^2$$

for 3σ values of the target displacements summarized in the second part of Table 7-7.

Table 7-7. Trajectory Perturbations
(distances in 10^3 km)

	Assumed Absorptivity		
Predictable Perturbations	α = 1.0	0.92	0.32
In-Plane: Aphelion Change δr_a			
Solar pressure			
Radial component	368	388	535
Transverse component	0	1.1	9.5
Unbalance compensation	10.3	10.9	15.0
Micrometeoroid pressure	0.7	0.7	0.7
In-Plane: Miss Parameter ΔB_1	124	131	180
Out-of-Plane: Miss Parameter ΔB_2			
Earth tracking torque	32.8	32.8	32.8
Total Predictable Miss ΔB_P	128	135	183
Unpredictable Perturbations (3σ uncertainties)			
In-Plane: Aphelion Change δr_a due to $\Delta\alpha$			
Solar pressure			
Radial component	---	4.8	12.3
Transverse component	---	0.28	0.70
Unbalance compensation	---	0.14	0.35
Aphelion Change δr_a due to ΔP_o			
Solar pressure			
Radial component	7.4	7.8	10.7
Transverse component	0	0.02	0.19
Unbalance compensation	0.2	0.22	0.30
Micrometeoroid presure	1.0	1.0	1.0
Combined Aphelion Change δr_a	7.5	9.23	16.35
Combined In-plane Miss ΔB_3	2.5	3.11	5.5
Out-of-Plane Miss ΔB_4			
Earth-tracking torque			
Uncertainty due to ΔI_1 (1%)	0.65	0.65	0.65
Total Unpredictable Miss ΔB_U (due to 3σ uncertainties in α, P_o, I_1)	2.6	3.2	5.6

The results typify the magnitude of in-plane and out-of-plane perturbations to be expected for trajectories comparable to the transfer trajectory assumed in this analysis. For convenient comparison, the results are summarized in Table 7-7 separated into predictable perturbations and 3σ-uncertainties corresponding to variations in absorptivity α, solar pressure constant P_o (2 percent), and moment of inertia I_1 (1 percent). These trajectory deviations are added vectorially since the individual sources of perturbation can be considered as statistically independent.

Results of this simplified analysis were confirmed in the case of solar pressure perturbation by comparison with more exact trajectory data obtained from a complete, three-dimensional digital computation for comparable launch and arrival conditions. Moreover, the results of this analysis are in exact agreement with those obtained by Flandro* for the effects of solar pressure perturbation on minimum energy trajectories to Jupiter and other planets. Thus, the results of the simplified analysis are considered sufficiently accurate for purposes of this investigation.

Miss uncertainties will vary depending on the type of nominal trajectory assumed for the mission. The history of relevant variables used in the sample trajectory applied here is shown in Figure 7-20. For longer flight times the magnitude of the deviation due to solar pressure increases. This is true, particularly if Jupiter encounter occurs in the vicinity of the aphelion of the unperturbed probe trajectory, i.e., for missions which are nearly of the minimum energy type. For example, for the area-to-mass ratio typical of the Advanced Planetary Probe (7.4×10^{-2} m^2/kg) the radial solar pressure perturbation at encounter for a minimum energy trajectory would be 270,000 km, i.e., more than twice the miss parameter deviation obtained for the sample trajectory assumed here. The effects of other sources of perturbation such as unbalanced attitude control forces and micrometeoroid pressure

*G. A. Flandro, "Effects of Non-Gravitational Perturbations on Minimum Energy Interplanetary Transfer Orbits," JPL Space Programs Summary 37-33, Vol. IV.

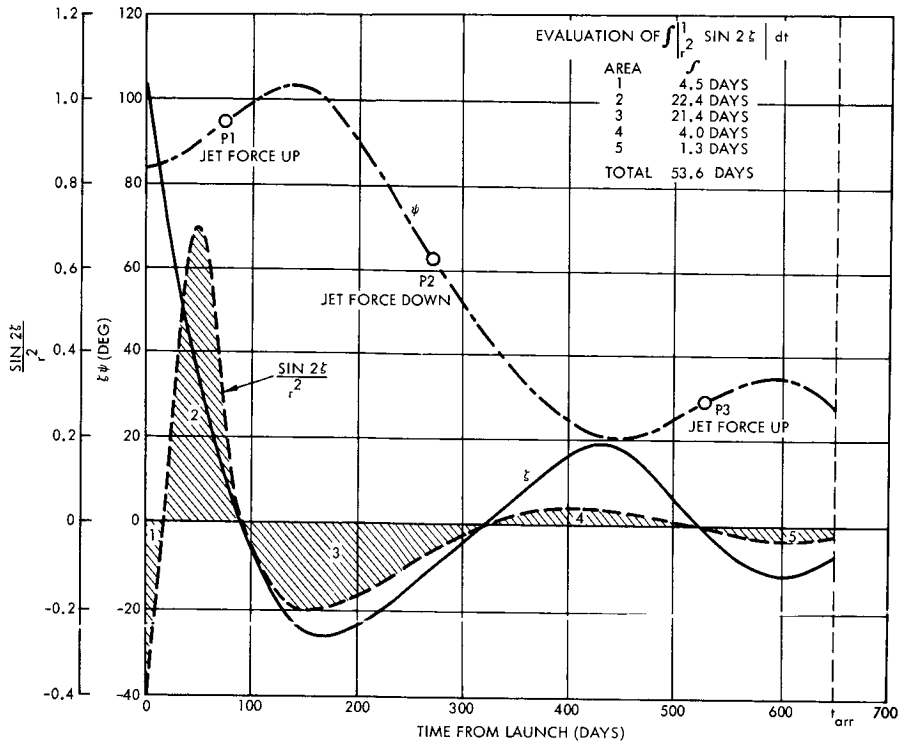

Figure 7-20. Time History of Sample Probe Trajectory: Earth-Probe-Sun Angle ζ, Earth Line Angle ψ, and Function $1/r^2 \sin 2\zeta$

would also tend to increase with increasing flight time and vice versa. However, the small values of miss uncertainty found in this study suggests that these variations would not be of a critical magnitude.

The effect of spacecraft design parameters and their uncertainty has been reflected in the combined miss parameter uncertainty (Table 7-7). The assumption of 1 percent uncertainty in moment of inertia I_1 is predicated on small uncertainties of laboratory test results of the flight model. After midcourse correction a somewhat larger uncertainty ΔI_1 may result due to temperature changes. Uncertainties of spin rate ω_1 are considered negligible at midcourse correction and will remain small since the two-pulse precession system minimizes cumulative spin rate changes resulting from attitude control operations during the remainder of the mission.

The low value of absorptivity ($\alpha = 0.32$) assumed yields perturbations up to 50 percent larger than the high absorptivity value ($\alpha = 0.92$) of a diffuse, black-painted antenna dish. The case of $\alpha = 0.32$ was assumed to provide a conservative estimate of solar

pressure effects. However, for reasons of thermal and structural design the choice of black paint is preferred, and hence the larger uncertainties of white paint characteristics, including deterioration in the ultraviolet radiation environment in space, can be avoided.

The direct solar pressure and the micrometeoroid pressure effects presented above also apply to the 3-axis stabilized spacecraft discussed in Volume 3. The unbalanced attitude control force effects pertaining to asymmetrical solar pressure and to earth tracking precession are, of course, applicable to the spin-stabilized configuration only.

Regarding the effect of micrometeoroid impingement, the resulting small contributions to miss distance are at least two orders of magnitude smaller than misses due to solar pressure, even for high values of momentum multiplication factor Q and for conservative models of the micrometeoroid flux. Since estimates of flux density vary by several orders of magnitude, the relatively minute perturbations obtained here provide confidence that even in the worst case the effects will not be significant.

7.4.4.1 Solar Radiation Pressure

The solar radiation pressure constant

$$P_o = 9.70 \times 10^{-8} \text{ lb/ft}^2$$

acting on an ideally absorbing (black-body) flat plate at a distance of 1 AU is assumed in first analysis of this effect. The flat plate of area A is used as a model of the high gain spacecraft antenna dish on which the solar pressure is acting. Since the solar pressure varies inversely with the square of solar distance, this effect can be conveniently computed by making an equivalent small change in the gravity constant of the heliocentric field. The effect of non-ideal absorption can then be derived by varying the result in terms of the absorption coefficient α, which is less than 1.0 in cases of practical interest. Two values of the absorption coefficient have been assumed:

Case 1:

$\alpha_1 = 0.92 \pm 0.02$ — High absorptivity if antenna dish is painted black

Case 2:

$$\alpha_2 = 0.32 \pm 0.05$$

Low absorptivity if frontal surface of antenna dish is painted flat white.

In either case it is assumed that the antenna dish is an ideally diffuse reflector to avoid the complexity associated with the equations of specular reflection. The solar pressure force model for this type of reflection (Figure 7-21) is given by radial and transverse components*

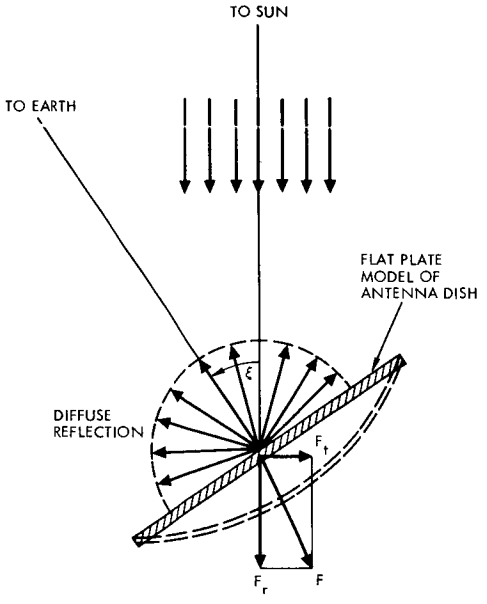

Figure 7-21. Components F_r, F_t of Solar Pressure Force

$$F_r = PA \cos\zeta \left[1 + \frac{2}{3}(1 - \alpha) \cos\zeta\right]$$

$$F_t = \frac{1}{3} PA (1 - \alpha) \sin 2\zeta$$

*J. D. Acord and J. C. Nicklas, "Theoretical and Practical Aspects of Solar Pressure Attitude Control for Interplanetary Spacecraft," JPL Report, August 1963.

where

ζ = time varying earth-probe-sun angle

α = absorptivity

$A = \pi R^2$ = antenna aperture area

$P = P_o/r^2$ varing with sun distance r (AU)

An out-of-plane component of solar pressure will not be considered since the axis of the antenna dish normally moves in the orbit plane (ecliptic) while tracking the earth during the entire mission.

The magnitude of the uncertainty in forces F_r, F_t is directly proportional to the uncertainty in α (see Appendix K), and hence Case 2 leads to an unpredictable trajectory error 2.5 times greater than Case 1. This together with the desire to minimize RTG heating effects on the 16-foot dish led to the selection of a dish painted black on the sunlight side but with a bare specular aluminum surface on the back.

7.4.4.2 Asymmetrical Attitude Control Forces

Attitude control in the spinning spacecraft configuration is exercised by uncoupled forces from the cold gas jet mounted on the antenna feed structure. The cumulative effect of prolonged expenditure of attitude control gas can be an in-plane or out-of-plane trajectory perturbation (see Appendix K). Two primary effects are investigated here:

- The effect of balancing asymmetrical solar radiation pressure acting on the tilted antenna dish when the earth-probe-sun angle is different from zero.
- Forces required for continuous tracking of earth, introducing a slow spacecraft precession around an axis perpendicular to the orbit plane.

The perturbation forces acting on the spacecraft as a result of these attitude control functions are illustrated in Figure 7-22. It is seen that forces of type (a) in that figure produce in-plane perturbations alternating in direction with sign-reversal of the earth-probe-sun angle ζ. Forces of type (b) produce an out-of-plane perturbation, the direction of which is associated with the direction in the angular rate $\dot{\psi}$ of the spacecraft-to-earth line which is distinct from the rate $\dot{\zeta}$.

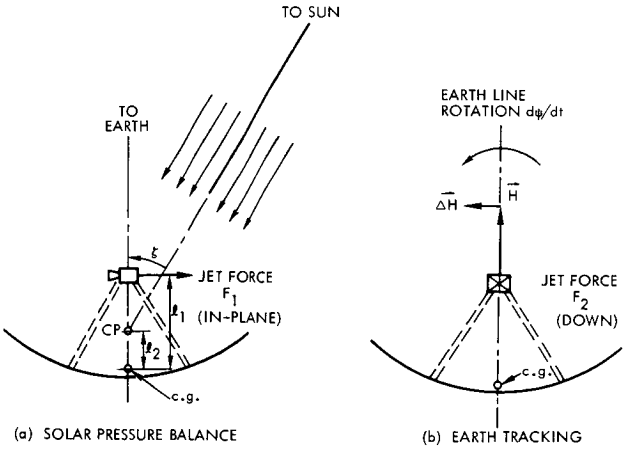

Figure 7-22. Attitude Control Functions and Resulting Perturbation Forces

7.4.4.3 Gas Leaks

The most likely source of leakage in the spacecraft occurs through the attitude control nozzle. The spin-stabilized spacecraft has the advantage of producing complete cancellation of force components perpendicular to the spin axis. There remains a small axial component due to possible impingement of gas leakage on the antenna dish. For reasonably small leakage this effect is considered negligible compared to the cumulative effects just discussed.

7.4.4.4 Micrometeoroids

Perturbations by the impingement of micrometeoroids on the large antenna dish must be taken into consideration in spite of the small and relatively uncertain magnitude of forces acting on the spacecraft as a result of this effect. In the estimate of some investigators the micrometeoroid pressure can have an effect exceeding that of solar radiation pressure.*

*R. R. Stephenson, "On the Possibility of Measurable Spacecraft Attitude and Trajectory Perturbations Due to Micrometeoroid Pressure," JPL Report 312.5-66, January 1965.

Figure 7-23 illustrates the mechanism by which the micrometeoroid stream produces a systematic perturbation force on the spacecraft. The following assumptions are made to simplify the analysis:

- Micrometeoroids which produce a systematic perturbation effect move in direct circular orbits around the sun (see also Section 4.10).
- The largest relative velocity has essentially a radial direction toward the sun and that for practical purposes an average direction not far from radial can be assumed, e.g., during the period of asteroid belt crossing.
- The relatively small magnitude of perturbations due to micrometeoroid impingement justifies omission of nonradial components of the micrometeoroid pressure.
- Two flux density models defined in Appendix K are used, one for the higher density prevailing during the passage through the asteroid belt and one for the lower density elsewhere in interplanetary space. The higher densities in the immediate vicinity of earth are not taken into consideration.

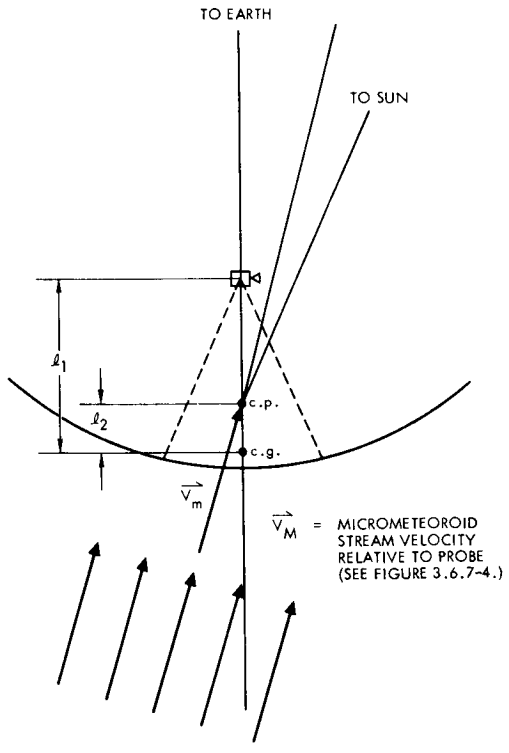

Figure 7-23. Model of Micrometeoroid Impingement

The higher densities in the immediate vicinity of earth are not taken into consideration.

The exchange of momentum caused by micrometeoroid impingement is described by

$$\Delta V = \frac{1}{M_s} Q M_m V_m \tau A'$$

where

M_s = spacecraft mass

A' = effective dish area = $A \cos (\gamma - \zeta)$

τ = time interval in which a particular flux density is assumed valid

Q = momentum multiplication factor due to ejecta

M_m = integrated effective mass of particles impinging on area of 1 m^2/sec

V_m = relative velocity of meteoroid stream averaged over time interval during which assumed flux density is valid.

The assumed momentum multiplication factor Q is subject to wide variation depending upon the amount of surface material ejected as a result of the high velocity particle impact. A very conservative value, Q = 36, is assumed by some authors to account for the large amount of material ejected by cratering of a surface of brittle material. Values of Q closer to 1 apply when cratering is minimized or when the meteoroid is large enough to penetrate the spacecraft skin. In this analysis a value of Q = 3 is assumed in view of the thin, easily penetrated antenna dish structure. To substantiate this value as a reasonable multiplication factor the mass of meteoroid particles which penetrate either one or both of the surface sheets of the antenna dish was determined for impact velocities of 13 km/sec encountered during asteroid belt crossing as follows (see Section 4.10):

Penetration of one sheet (thickness 0.003 inch) = $m_1 = 1.5 \times 10^{-8}$ gram

Penetration of both sheets = $m_2 = 1.2 \times 10^{-7}$ gram

The choice of $Q = 3$ is conservative since for particles larger than m_2 which penetrate the dish entirely, a multiplication factor $Q \leq 1$ should actually be assumed.

7.4.4.5 Other Sources

The following additional sources of small trajectory perturbations which may be encountered during the interplanetary transfer phase are not considered in this analysis: interaction of an electrically charged spacecraft of large diameter with the plasma environment; interaction of an electrically charged spacecraft with the local magnetic field; solar wind effects; high-gain antenna emission; unsymmetrical emission of thermal energy. Justification for the omission of these effects is their extremely small magnitude compared to the dominant solar radiation pressure effect. A preliminary estimate indicates, for example, that the magnetic and plasma interactions in interplanetary trajectories are at least five orders of magnitude smaller than the solar pressure effect.

7.4.5 Astrophysical Constant and Ephemeris Uncertainty

Uncertainty in the astronomical unit to kilometer conversion factor causes the computed injection conditions to place the spacecraft on a trajectory with a slight error. The velocities and distances in the solar system are accurately known in astronomical units per second and astronomical units, respectively. The launch vehicle, however, imparts a velocity to the spacecraft in "earth units," for example in kilometers per second. Thus, in order to relate the two unit systems, a conversion between astronomical units and kilometers is required.

The AU enters two-body central force trajectory equations as a scale factor, and an uncertainty causes the orbit to change size and shape. Consideration of more attracting bodies, however, introduces a time-increasing perturbation* which might be appreciable in near-Jovian space.

The effect of the AU uncertainty on the target error is estimated according to the analytic partial derivatives summarized in the JPL

*J. B. McGuire et al, "The Size of the Solar System," Scientific American, April 1961.

series of earth-Jupiter trajectory data. Because this information does not exist for the particular trajectory studied in detail in this report (1972 launch), the values of the partial derivatives were selected from the earth-Jupiter 1974 trajectory information.

The May 30, 1974, trajectory, with a flight time of 760 days, has similar injection conditions. The numerical value of the partial derivative is

$$\frac{\partial B}{\partial au} = 4.5498$$

Thus for an AU uncertainty of 66.6 km (1σ) the impact parameter B uncertainty is 303 km (1σ). It is assumed that this error is circularly distributed on the B·T, B·R plane.

Jupiter ephemeris errors were estimated as 500 km (1σ). As with AU error effects, it was assumed that this error is circularly distributed on the B·T, B·R plane.

7.5 REDUNDANCY

To achieve the lifetime required for this mission requires constant application of all reliability improvement techniques, such as stress derating, parts screening and selection, etc. However, even with all of these techniques exploited fully, redundancy is necessary (see Section 9). A computer program has been developed at TRW Systems which not only establishes reliability rapidly but can perform certain tradeoffs, including reliability versus weight optimization. The relative value of a given redundancy requires critical engineering judgement to determine the effects of various failure modes and the effects of alternate solutions to the failure problem. For example, the transmitter includes the driver, the power amplifier, and its converter; it is clear that a degradation of any one of these degrades the whole system. On the other hand, a failure of most components in the data handling system results in only partial system degradation. Thus, all elements of the transmitter have a weighting factor of unity, while the weighting factor for the data handling system can be anywhere between 0.3 to 0.8. It is the weighting factor that introduces complexity into the numerical reliability analysis.

The 50-pound payload, spin-stabilized system contains much redundancy. The entire transmitter subsystem, the receivers, the command chain, and the orientation and propulsion subsystems, for example, are completely redundant not only because of the reliability versus weight tradeoff, but because the potential design failures are also higher for those components. However, passive items, such as fixed antennas, diplexers, thermal elements, are not redundant for the same reason that the structure itself need not be redundant. The RTG's are not redundant since they are essentially passive, but a power margin is provided to allow for degraded RTG performance. The system concept is such that degraded power performance, for example, can be tolerated by reducing the loads, or by sequencing certain power functions, such as data transmission with heater power requirements or orientation maneuvers, etc. This sequencing capability is in itself a type of redundancy.

There are certain failure modes which are catastrophic and which are not amenable to prevention by means of redundancy. Typical of these is deployment of the 16-foot antenna. However, the deployment, which is the only significant failure mode of the antenna, is a one-shot operation and can be made highly reliable by an extensive test program. Another in-line mode of operation which cannot be made redundant is the fine earth-pointing mode using the mechanically tipped, high gain antenna feed. In the event of failure of that conical scan feed, a mode of operation using the helix antenna is possible, although the bit rate will on the average be lower and the real-time transmission capability reduced. Even these off-nominal modes are compatible with the system concept since a great deal of storage is provided through tape recorders, making real-time transmission unnecessary.

The high real-time bit rate capability of the spacecraft acts to some extent as a redundant mode of operation for the tape recorders. The tape storage, necessary to achieve all scientific objectives, not only permits degraded performance in the earth-pointing maneuvers, but in turn acts as a redundancy mode for the real-time transmission. Because the tape recorders have a low reliability as compared to the rest of the system, they are redundant.

The attitude control subsystem has two gas jet systems which when operating serve an additional function: reducing wobble during the orientation maneuvers. The effect of the failure of one cold gas system, however, merely increases the time to complete a given orientation maneuver and does not result in system failure. The propulsion subsystem also has two engines, each with redundant start capabilities. But, in addition, the combination of two engines simplifies the mode cruise considerably since a 180-degree reorientation is no longer required. The failure of one engine assembly merely results in the requirement for a large reorientation maneuver, and not in a system failure.

With respect to black box redundancy, the critical choice is a parallel versus standby mode. Since a standby mode requires twice the power of a parallel mode, the power tradeoff usually results in the selection of parallel redundancy. However, for items such as the receivers and the command chain we must have standby redundancy to maintain constant access to the spacecraft in the event of chain failure.

On-board failure detection and automatic switching is a desirable feature of any system, providing the technique does not create additional unreliability. A ground command mode, especially on a long term, relatively inactive mission, has an extremely reliable potential, and thus to minimize on-board complexity a ground command is used for switching. Moreover, even when automatic switching maneuvers are carried, a ground command override is provided.

In addition to black box redundancy, the more sophisticated approach of component redundancy within a black box has been examined. For example, in the data handling unit tradeoffs have been made between various types of modules, and those with low reliability have been made redundant to give them the same reliability as the highest single elements. This approach not only minimizes weight, but often results in a higher overall reliability, since cross strapping within a black box is possible.

As will be seen in Section 9, a highly reliable mission has been achieved within the weight constraint. But it is obvious that a more detailed study would further enhance the probability of mission success.

7.6 ACHIEVEMENT OF SCIENTIFIC OBJECTIVES

The 50-pound payload, spin stabilized spacecraft satisfies scientific objectives well beyond what might be called a minimum precursor Jupiter flyby mission. At the same time, it can be launched using the least expensive launch vehicle which has a Jupiter flyby mission potential, the Atlas/Centaur with a solid rocket third stage.

Since the largest portion of a planetary flyby mission is spent in interplanetary space, experiments should be selected which can make both planetary and interplanetary measurements. However, as is discussed in Section 2, it is not reasonable to select only experiments which perform both functions, since the experiments would be unable to take important planetary measurements such as images in the visible and infrared. The experiments which have been chosen, then, are a combination of both, but many perform both functions.

The experiments proposed for the interplanetary mission, that is, the solar cosmic ray, solar plasma magnetometer, micrometeoroid, radio propagation, and galactic cosmic ray, provide a broad spectrum of related experiments of the interplanetary mode. The nominal sample rate provides considerably more data than is possible on either the Pioneer 6 or Mariner 4 spacecraft. Moreover, the high resolution modes, either stored or transmitted in real time, considerably enhance capabilities of these experiments for fast event analysis.

The solar cosmic ray and solar plasma experiments are perhaps best done with a field of view scanning in the plane of the ecliptic once each spin cycle. The spacecraft configuration proposed does not allow this scan mode. However, a scan mode for both of these has been proposed which allows them to scan through the plane of the ecliptic, including the sun, during each spin cycle and thus to detect anisotrophies with a good resolution. The plasma probe, in particular, has multiple 20 x 20 degree field of view detectors, allowing mapping during the scan. It is mounted in the antenna feed assembly, and the solar cosmic ray probe is mounted on a boom.

The magnetometer boom has been sized to allow measurements to 0.1 gamma. Pioneer techniques for magnetic cleanliness will be used.

The micrometeoroid detector experiment is on the dark side of the spacecraft since the particles in circular orbits, typical of the asteroid belt, will impact there. To some extent then the data from the micrometeoroid detector will be biased. It is feasible to add a Pegasus capacitance-type experiment to the antenna structure and in this way provide a much larger cross section and reduce the effect of the spacecraft shielding.

The radio propagation experiment antennas are mounted on the feed assembly thus assuring a good constant look angle to the earth's transmitter. If it is desired to extend the capability of this experiment beyond the capability of the ground transmitters, feeds at the specified frequencies could be designed which would make use of the main antenna collector array.

The galactic cosmic ray sensor is also mounted to the base at the back of the spacecraft looking always away from the sun. This shielding assures that solar cosmic rays are not detected.

At encounter, the Jovian magnetosphere, magnetic field intensity, and trapped particle radiation will be measured using the same magnetometer, an omnidirectional trapped radiation counter, and the RF occulation. In addition, the micrometeoroid detector will operate to detect any local dust characteristics.

Three experiments provide direct measurements of the atmosphere of Jupiter. A TV system with a tippable mirror allows observation of Jupiter during approach and flyby until Jupiter passes out of the spacecraft's rear hemisphere. An infrared radiometer looks out the side of the spacecraft and maps the thermal radiation of the planet with successive scans during the flyby portion of the trajectory. An auroral sensor will scan the dark side of the planet to detect auroral phenomena. Finally, the earth occultation experiment will be performed using the high gain antenna, which, because of its gain, should provide a good measurement of atmospheric properties to some substantial depth into the atmosphere.

In general, it can be said that the spacecraft configuration satisfies the selected payload extremely well, and the experimental results from the spacecraft will serve to check current theoretical models of Jupiter and provide the preliminary results necessary for the performance of later, more sophisticated experiments. The only experiment which appears to be significantly compromised by spin stabilization is the TV, whose achievable resolution is limited by spin-induces image smear. Even in this case, however, an attractive experiment is possible and much more data could be gathered then it is possible to transmit.

7.7 LAUNCH VEHICLE

As shown in Section 4, a spacecraft of 500 pounds can carry a 50-pound payload on a flyby mission to Jupiter. All the boosters described in Section 2.1 can provide sufficient C_3 to launch such a vehicle on this mission. The simplest low cost booster, SLV3X/Centaur/TE-364-3, can carry 500 pounds to a C_3 of 100, which provides a launch window greater than 20 days for every launch to Jupiter between 1970 and 1980. The minimum flight time for this C_3 is about 550 days. The cost of this boost vehicle is estimated to be about $10 million without mission peculiars.

The next higher performance boost vehicle is the SLV3X/Centaur/HEKS, which can boost 1000 pounds to C_3 of 90, or 500 pounds to a C_3 of about 120, which would give a minimum flight time to Jupiter of about 460 days. It is estimated that this vehicle would cost $14.5 million without mission peculiars. The high energy kick stage is not yet developed.

A third possibility is to use the Titan IIICx/Centaur. This vehicle can boost up to 1800 pounds to a C_3 of 90 or carry 500 pounds to a C_3 of 110, leading to a minimum flight time to Jupiter also of about 500 days. While this vehicle appears attractive for heavier spacecraft, the addition of the TE-364 widens its capability for light spacecraft to very large values of C_3. For example, with the addition of the TE-364, this vehicle can boost up to 2500 pounds to a C_3 of 90 or carry 500 pounds to a C_3 of 182 for a minimum flight time to Jupiter of about 350 days, or Saturn in 800 days. However, a Titan IIIC is not a part of the NASA boost vehicle stable. It is estimated to cost $20.4 million.

In view of the questions regarding the high energy kick stage and the Titan IIICx, we propose that the SLV3X/Centaur/TE-364-3 booster be used. Because TRW has recently been working with Atlas boost vehicle combinations we have become aware of recent changes in the Atlas configuration. The recent division of the SLV3X vehicle into two configurations, designated 3A, to be used with the Agena, and 3C, to be used with the Centaur, has caused us to question General Dynamics, Convair Division, and Boeing, who is working on Burner II, an upper stage using the TE-364-3, as to the performance of the Atlas SLV3C/Centaur/Burner II combination. Their calculations, attached to this section, show that the SLV3C/Centaur/Burner II-3 (spin table version) has a 539-pound payload capability to C_3 of 90, thus assuring that the proposed mission can be carried out with that launch vehicle. Further, using their data and our interstage weights, a capability of about 590 pounds is available. These values were calculated for a 90 nmi parking orbit and give somewhat greater values than would be obtained with a 100 nmi parking orbit. Use of the TE-364-4, a lengthened case version of the TE-364-3, results in an additional improvement of about 50 pounds.

The principal launch vehicle-spacecraft interfaces arise out of the use of the solid propellant TE-364 stage. Longitudinal acceleration of 14 g's will occur, but this presents no serious spacecraft problem since all of the equipment proposed has been designed to this level. The vibrational environment of the TE-364 stage configuration has been measured and is considerably less than that experienced on the Delta launches.

One specific launch vehicle area requires detailed study, i.e., the wind constraints on the launch window. Present information indicates that the launch window constraints on the Surveyor vehicle (basically the same vehicle discussed here) are significant. The effects of changing to the SLV3 vehicle and the particular shroud configuration proposed must be analyzed thoroughly.

GENERAL DYNAMICS
Convair Division

ABM-66-011
Revision A
27 June 1966

Subject: Atlas SLV-3C/Centaur/Burner II (-3, -4) Performance Capability, Revision A

Summary

A performance analysis study was conducted on the Atlas SLV-3C/Centaur booster with a Boeing Burner II spin stabilized stage. This analysis utilized updated Burner II -3 and -4 weights with the Surveyor shroud to determine performance for interplanetary missions, in general, and specifically for a Jupiter probe (C_3=90 KM^2/Sec^2). Both the one burn and two burn Centaur were used in computing performance. Payload weight versus velocity capability in excess of the velocity required to attain a 90 n. mile parking orbit (Figure 1) is presented. In addition, payload capability is tabulated for a range of potential interplanetary missions.

Discussion

Ground Rules

A summary of major flight profile constraints and requirements is presented in Table 1.

TABLE 1 - Mission Parameter Summary

Parameter	Value	
	1 Burn Centaur	2 Burn Centaur
Launch Azimuth	90 degrees	90 degrees
Parking Orbit Altitude	-	90 N. Miles
Perigee Altitude	90 N. Miles	-
Parking Orbit Coast	0 Minutes	20 Minutes
Flight Performance Reserve	1% of the total vehicle velocity increment for the Atlas/Centaur. 0% for Burner II	1% of the total vehicle velocity increment for the Atlas/Centaur. 0% for Burner II

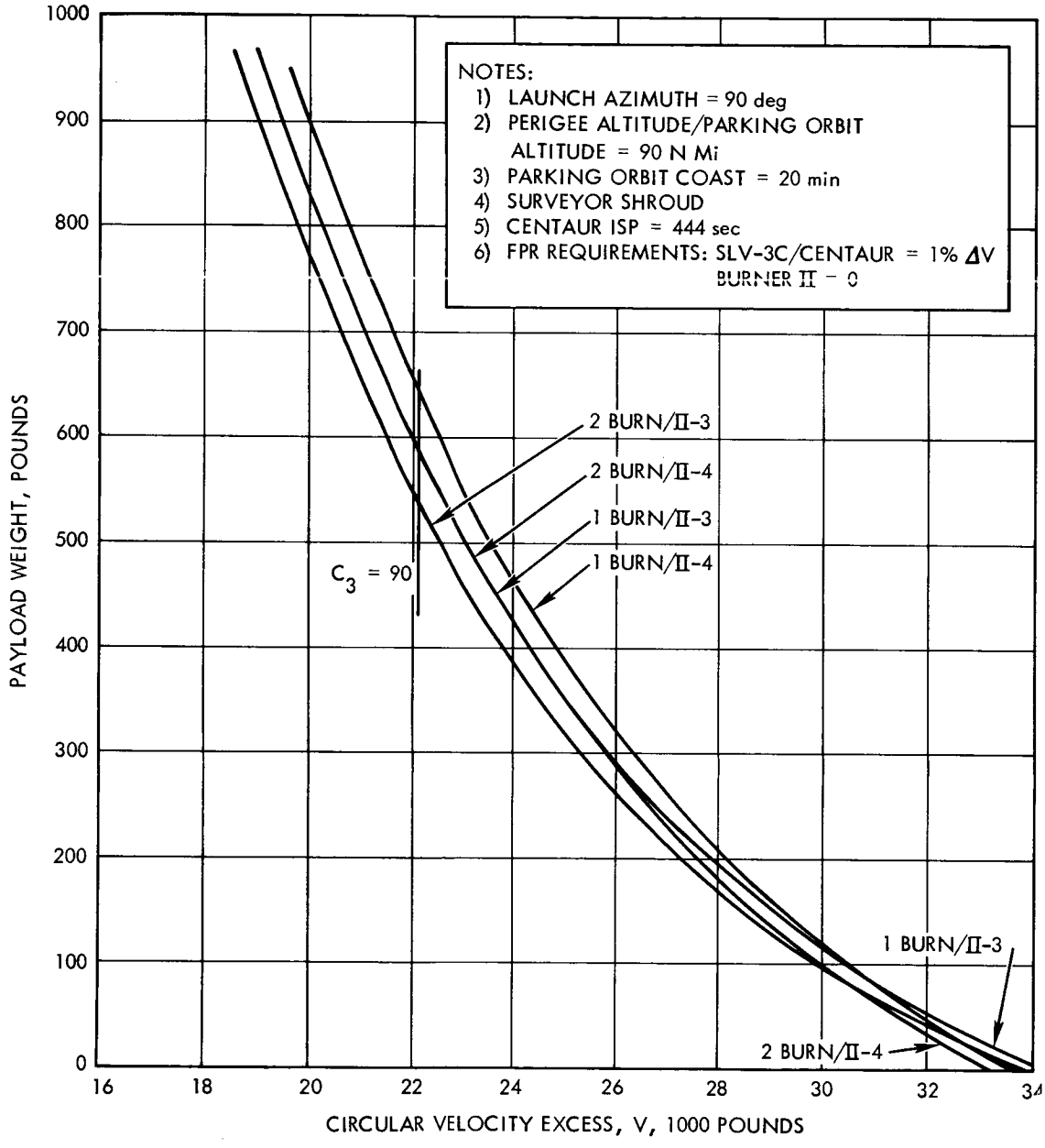

Figure 1. Atlas SLV-3C/Centaur/Burner II Payload Capability Versus Circular Velocity Excess

WEIGHT AND PROPULSION SUMMARY

The Atlas SLV-3C vehicle was used in this analysis. The Centaur stage used herein corresponds to the AC-15 two burn configuration documented in the December issue of the "Centaur Monthly Configuration, Performance and Weight Status Report."

Atlas SLV-3C and Centaur propulsion data are presented below

TABLE 2 - BOOSTER PROPULSION DATA

ATLAS SLV-3C	THRUST (LB)	ISP (SEC)
Booster Engines (2)		
Sea level	331,595	253.2
Vacuum	382,139	290.1
Sustainer and Vernier		
Sea level	58,733	213.6
Vacuum	81,564	305.5
Centaur		
Centaur Main Engines (2)	30,000	444.0

An Atlas SLV-3C/Centaur weights summary is presented below

TABLE 3 - BOOSTER WEIGHTS SUMMARY

Centaur Stage	Dual Burn Centaur Weight(lbs)	Single Burn Centaur Weight
Centaur Jettison Weight (does not include Burner II Adapter)	4,005	3,850
Main Impulse Propellant	29,911	30,040
Equipment Jettisoned in Boost Phase		
Nose Fairing	1,956	1,956
Insulation Panels	1,219	1,219

ATLAS SLV-3C	(WEIGHT (LB)
Booster Jettison Weight	7,467
Sustainer Jettison Weight	8,208
Main Impulse Propellants	268,102

Burner II weights and propulsion data are summarized in Table 4.

TABLE 4 - BURNER II WEIGHTS AND PROPULSION

Weights	Burner II -3	Burner II -4
BURNER II	1,598	2325
Propellant Wt.	1,440	2,100
Motor Inerts (expended)	14	35
Stage Inert Wt.	174	220
Centaur/Burner II Adapter	152	152
Lower	42	42
Upper	80	80
Spin Adapter Ring	30	30

Propulsion

Burner II -3

ISP = 287.2 sec.

Burner II -4

ISP = 285.2 sec.

RESULTS

Payload capability for an interplanetary mission of C_3 = 90 KM^2/Sec^2 (Jupiter mission) is 588 lbs. and 539 lbs for the 1 burn and 2 burn Centaur with Burner II -3 respectively and 640 lbs. and 588 lbs for the 1 burn and 2 burn Centaur with Burner II -4 respectively.

TABLE 5 - INTERPLANETARY PERFORMANCE SUMMARY

MODE	PERFORMANCE (LBS)							
	C_3 = 80Km^2/Sec^2 ΔV=21,000 Ft/Sec		C_3 = 90 Km^2/Sec^2 ΔV=22,150 Ft/Sec		C_3 = 100 Km^2/Sec^2 ΔV- 23250 Ft/Sec		C_3 = 120 Km^2/Sec^2 ΔV = 25,400 Ft/Sec	
	II -3	II -4	II -3	II -4	II -3	II -4	II -3	II -4
Two Burn Centaur	655	712	539	588	444	487	296	327
One Burn Centaur	712	773	588	640	487	532	327	361

Prepared by K. E. Campbell
K. E. Campbell

Approved by J. J. Andrews
J. J. Andrews
Design Specialist
Aeroballistics

CC: F. Rosacker
D. Mancuso (3)
K. Campbell
F. B. Anthony/File

8. SUBSYSTEM DESIGNS

This section describes each of the conceptual designs for the subsystems making up the spin-stabilized, 50-pound payload spacecraft. In general, the requirements of each subsystem are first identified and then the selected subsystem approach is described and analyzed. Included also are descriptions of possible problem areas, subsystem reliability, and a subsystem performance summary. Alternate designs are discussed both in the description of the selected design and in Volume 3. Although this is not a preliminary design study and these subsystems have not been optimized, the depth of the analyses does demonstrate feasibility, and permits a relatively accurate estimate of subsystem costs.

8.1 STRUCTURE AND MECHANISMS

This subsection discusses the structural design of the spacecraft and its adapter. A general discussion of the structural requirements and their implications is covered first, followed by a description of each of the major structural components of the spacecraft and its adapters, both spacecraft/TE-364 and TE-364/Centaur.

8.1.1 Design Requirements

The critical sustained limit acceleration levels used for the spacecraft design is covered in Section 2.1. The structure is designed to withstand limit loads without detrimental yielding and ultimate loads, defined as limit loads times an ultimate factor of safety of 1.25 without failure.

Section 2.1 also gives the vibration test levels recommended for preliminary design or feasibility studies of payloads used with Centaur. The normal frequency response range for the structural responses with a spacecraft configuration as selected is 20 to 30 Hz for the overall structure, 40 to 80 Hz for the individual structural elements of the spacecraft. With these frequency ranges, the random vibration test levels will result in much lower loads for the structure than experienced in the vibration testing of spacecraft for launch on the Atlas/Agena vehicles. However, the sinusoidal test levels are extremely high for payloads of 2000 pounds, similar to the spacecraft with the TE-364 combination and

the test levels normally associated with components. Consequently, the structural design was conducted with a less severe environment. The environment selected was used for the Vela 5 spacecraft launched by the Atlas/Agena. In the critical frequency range, the qualification vibration level is a 1.5-g rms sinusoidal excitation combined with a 0.015 g^2/Hz random excitation. The structural analysis summary reflects this latter environment. However, having designed the structure, some components subsequently increased in stiffness and strength because of meteoroid protection, and the consequences of the Centaur sinusoidal tests were reviewed. The conclusion reached was that all structures would be structurally adequate but the RTG booms, the tiedown strut, and the antenna feed truss structure would have lower margins of safety.

The Centaur specification recommends a first cantilever frequency for the spacecraft of 20 Hz or higher. Estimates of this cantilever frequency, considering the spacecraft and TE-364 motor combination mounted on the adapter to the Centaur with a rigid support at the base of this adapter, gave 20 to 25 Hz. This would then appear acceptable.

8.1.2 Centaur/Spacecraft Interstage with TE-364 Solid

The interstage structure is designed as a conventional skin-stringer-ring construction. The three main axial stringers are at the attachment points for the TE-364 motor at the top of this structure. All the loading on the interstage is applied at these points. The selection of three stringers was based on the fact the TE-364 motor constitutes some 75 percent of the weight on the adapter and, consequently, the major load on this structure is applied at these points. The skin was considered ineffective under the axial loads. However, a large gusset is used at the base of each stringer to spread the load over a larger section of the Centaur adapter ring. The critical load for these stringers was the Atlas burnout condition with limit load factors of 5.85 g axially and 1.0 g laterally. This lateral load factor is conservative. These stringers are designed as AZ31B-H24 magnesium alloy hat sections to give the required ultimate axial load capacity.

The skin of this adapter is fabricated from LA-141 mag-lithium alloy. The critical design condition is the shear due to the limit lateral

load of 1.5 g. The design condition is that the skin panels do not buckle in shear under ultimate side loads, i.e., 1.875 g. The skin thickness was computed for 0, 1, and 2 intermediate rings. The adapter weight decreased with the increasing number of rings. A design with two intermediate rings was selected since the required skin thickness, 0.034 inch, was considered sufficiently small. The intermediate rings are magnesium angle sections. This is the design shown in Figure 7-3, and used for the weight determination for this structure. However, an alternative design was considered. Realizing the large part of the weight in this structure is in skin, skin thickness using Lockalloy (a beryllium-aluminum alloy) was computed. With this material, a 0.019-inch thick skin is adequate and approximately 1.3 pounds could be saved on this component if the additional fabrication costs are acceptable.

8.1.3 Adapter Structure TE-364/Spacecraft

The adapter between the spacecraft and the TE-364 was designed as a truss, this being the minimum weight construction when the load in the structure is applied at only three points. This critical load is at the burnout of the TE-364 motor, when the longitudinal acceleration is 13.8 g. Two designs were considered. The first is that shown in the configuration, Figure 7-3. In this, the motor is attached to the spacecraft by six struts attaching the three motor attach points to alternate corners of the equipment section on the spacecraft. The second design had an additional three struts between the same three points at the motor and the remaining corners of the box.

For the first design, these struts were adequate, fabricated from 6061-T6 aluminum alloy with a cross section 1.825-inch in diameter and a 0.025-inch wall thickness. The 0.025 inch was considered a minimum thickness.

With the second design, the strut loads were reduced 22 percent for three struts and 34 percent for the remaining six, compared to the first design. However, the tube cross section diameter would only be reduced to approximately 1.4 inches, and the total truss would be heavier.

The first design was selected, since it gives the minimum number of attachments (three) between this structure and the spacecraft. This

is a separation plane, and the fewer attachments will give higher reliability for separation. The second design can be accomplished with only three tension attachments requiring separation and six shear attachments only if some of the members were preloaded. However, such preloading would be hard to duplicate from spacecraft to spacecraft, and it would be difficult to ensure this preload would not cause unacceptable tipoff errors at separation.

8.1.4 Antenna Feed Truss Structure

The loading for the antenna feed truss in the launch configuration is due to two sources: 1) the equipment compartment at its apex, and 2) a portion of the mass of the folded antenna petals supported by the truss. The critical design condition will be the vibration testing of the spacecraft. The primary structural requirement will be to ensure frequencies for the truss or any of the single strut elements, making the truss frequency sufficiently high to avoid coupling with the overall spacecraft response frequencies and to ensure that displacements during vibration testing are small. In line with the requirement, a minimum frequency of 40 Hz was a design goal.

The main design feature of the truss is that the loading from the folded antenna elements is below the apex of the truss. The primary functional requirement is minimum blockage for the antenna. A secondary requirement is to limit the heat leak from the main equipment compartment.

Two basic designs were considered: a simple three-element truss; the ring mounting the folded antenna elements ties down these elements approximately 60 percent of the way up the truss, as shown in Figure 7-2; and a second design with additional members, three diagonals between the ring and the base of the truss.

With the first design, the critical design requirement is to provide a 40 Hz frequency for the struts with a portion of the folded antenna mass acting effectively at the position of the ring. Considering the members as circular cross section tubes, the following sizes were obtained for various materials. A minimum wall thickness of 0.025 inch was used for the metal tubing and 0.06 inch for the fiberglass

	Low Weight Materials			Low Thermal Conductivity Materials		
	Beryllium	Magnesium	Aluminum	Titanium	Steel	Fiberglass
Diameter (in.)	3.45	6.32	5.48	4.08	3.8	5.14
Wall thickness (in.)	0.025	0.025	0.025	0.025	0.085	0.06
Total strut weight (lb)	4.0	7.0	9.4	12.8	18.3	12.7

The aluminum design was selected; the thermal requirement of minimizing the heat leak is then accomplished by insulation at the strut ends. This is not the lightest solution, but the fabrication will be easiest. The forming of the end fittings as an integral part of the tube will save fitting weight, and welding will not be necessary. Fiberglass is attractive thermally, but the weight difference is too large.

To minimize the antenna blockage, the tube section has been made elliptical with the major axis in a radial line. This has a negligible effect on tube weight because the support ring for the antenna elements should prevent vibration with strut displacements in a tangential direction, but not in the radial direction. The stiffness will be increased for displacements in this radial direction by changing the cross section to elliptical.

With the second design, the critical design requirement, again, is to provide a 40-Hz frequency with the whole truss vibrating with the mass of the folded antenna at the ring position and the equipment compartment at the apex. Now the tube cross sections have only an area requirement since the struts carry primarily axial loading. The resulting tube sizing gives a reduction in cross-sectional area, but the additional tube length resulted in the same strut weight, 9.4 pounds. The axial loads were computed at a frequency of 40 Hz, and an amplification factor of 10. The response of the masses on the truss is 30 g. Then, designing the main struts as columns, an adequate load capacity was obtained by a 1.5-inch diameter by 0.06-inch wall aluminum tube. This is a substantial reduction in diameter. However, these struts cannot be made elliptical in

cross section without weight increase, and the 1.5 inches has to be compared with the minimum width of the struts of the first design. Furthermore, the diagonal tubes provide large blocking, making this design unacceptable.

8.1.5 Main Equipment Compartment

Two structural designs were considered for the main equipment compartment. One is a minimum structural weight design, the other is a baseline for a meteoroid protection system analysis. The meteoroid protection system weight was minimized by adding this to a structure initially configured with meteoroid protection in mind, i.e., the baseline configuration. Consequently, the surface of this configuration, the baseline, was based on a ground rule that these elements be of sandwich construction. This is the design summarized in the following sections. Obviously, this ground rule would affect the weight of the structure. With this in mind, the weight of a minimum structural weight configuration was estimated. This minimum structural weight design was, again, a fully enclosed compartment, the side and top panels are beaded maglithium panels, and the propulsion tank is then supported by the main equipment platform. Based on the difference in these two designs, the weight of the baseline design was shown to be 7.1 pounds greater than the so-called minimum weight structural design. In the weight breakdown, this 7.1 pounds is charged to the meteoroid protection system weight.

The majority of the spacecraft equipment is mounted on this platform, the base of the equipment compartment, since this is the thermal control surface for the spacecraft. The weight of this equipment is approximately 120 pounds.

The critical structural requirement is to provide a stiffness above the spacecraft frequencies, and to have a frequency sufficiently high to ensure small displacements of the panel during vibration testing. A design goal of 40 Hz was set. The structural design solution to such requirements is best met by an aluminum honeycomb panel. The thermal control requirements dictate the minimum face sheet thickness, in this case 0.015 inch, and a requirement for an aluminum honeycomb for the core. The structural analysis then determined the panel thickness to

achieve the necessary stiffness and from the loading determined a core density from the shear stress in the core. This loading is the predicted loads due to vibration testing of the spacecraft. The core selection for a panel with both thermal and structural requirements is usually a conventional honeycomb with the cells normal to the facings. However, such a honeycomb construction is inefficient as a meteoroid protection system. The alternatives were to consider: a foam-filled conventional honeycomb or a trussgrid aluminum honeycomb. The total core densities will be similar. The foam-filled core selections will lose all the radiation portion of the thermal conductivity through the panel, and the trussgrid will lose most of it. However, if the minimum total core densities are similar thermally, it should be preferable to use metal, and the trussgrid was selected. The resulting panel design was a 1.25-inch thick panel, with 0.015-inch facing on a 2.3 lb/ft^3 aluminum trussgrid core. The qualification vibration loading will give a predicted 23 g normal to the plane of the platform, based on an amplification factor, Q, of 8. The corresponding maximum core stress is 18 psi and the allowable is 28 psi. The maximum stress in the facings is 9700 psi compared to an allowable stress of 14,200 psi.

The meteoroid protection requirements led to a final selection of a 2-inch deep panel with an increased thickness for the inner face. This will give a higher frequency, and the panel stresses will be reduced. Consequently, this change was not analyzed.

The meteoroid protection considerations were assumed to require a double wall, or sandwich construction, for the top panel, preferably with a foam core. Such a structural element, in the thickness range of interest, i.e., up to 2 inches, has substantial strength even for loads normal to the plane of the panel. Consequently, the outer portion of this panel is used to support the propulsion tank, as shown in Figure 7-2. Again, the structural design requirement calls for a frequency above spacecraft frequencies, and for these to be sufficiently high to ensure small displacement during vibration testing of the spacecraft. A design goal for the frequency was for a minimum of 40 Hz. With a sandwich construction, the procedure used to obtain a lightweight design is to set the facing thickness at some suitable minimum, then determine the

required core thickness. Initially, the panel was considered as a circular plate with a control hole loaded along its inner edge. With a facing thickness of 0.01 inch of aluminum, 2-inch thick core gave a frequency of 41 Hz. Based on the predicted vibration loads, the average shear stress in the core is so small, 3.8 psi, that the lowest density foam core available, 1.2 lb/ft^3, is adequate. The maximum facing stress is 14,900 psi. With a continuous foam core stabilizing the faces, these should be able to carry loads that will give stresses a large percentage of the material yield strength; hence, this facing stress is acceptable.

The meteoroid analysis led to a thicker inner facing and to a conical upper panel covering the hydrazine tank. This will give an increase in frequency and a significant increase in the structural margins of safety.

No analysis was conducted on the side panels. The intention is that these panels are shear webs which close off the sides of the equipment compartment. The necessity to provide a sandwich construction for meteoroid protection led to using a 1-inch thick panel for the baseline structure. The outer facing was set at 0.01 inch of aluminum, considered minimum gauge, while the inner face was set at 0.015 inch. This inner face thickness was assumed, based on the requirement for an adequate thermal conduction path with this element, for equipment mounted on these panels. The core will stabilize the facings such that high facing stresses can be achieved, making these panels much stronger than the loads in the plane of the panel would require.

The panel thickness was subsequently increased to 2 inches for meteoroid protection purposes.

8.1.6 RTG Booms

In the final operating condition of the spacecraft, each of the three RTG's are attached to the base of the spacecraft by a V-brace frame, see Figure 7-2. In the launch configuration, the RTG's are stowed folded down. In this configuration the V-frame is not an adequate structure for the launch environment, and a third member attaches the apex of the V-frame to the base of the TE-364/spacecraft structure, forming a tripod support truss. The RTG's give a temperature of this

truss of 500°F at the RTG attachment end. The critical structural design condition for this truss is the vibration testing of the spacecraft. The structural design procedure was used to assume sizes for the struts, compute the truss stiffnesses, and determine the corresponding natural frequency for the truss structure. From this frequency, assuming an amplification factor of 10, the loads at the RTG were determined and the stresses in the members checked. This procedure was iterated until an acceptable set of tube sizes were determined. The V-brace members have stresses due to bending caused by the overhang of the RTG beyond the third member attach point. For small tube diameter, these stresses are high. The 500°F exposure temperature is close to the limit for aluminum alloys usually used for such applications. Furthermore, any increase in temperature would result in substantial strength reduction for the aluminum. This latter factor, together with the high stress levels, resulted in the selection of 6Al-4V titanium for this truss structure.

The final design has the two struts of the V-brace, the members with bending and axial load, as 1.5-inch diameter by 0.025-inch wall thickness tubes. The third member, which carries only axial load, is 0.75-inch diameter by 0.025-inch wall thickness. The minimum frequency of this truss is 68 Hz, considering that the structure to which the truss is attached is rigid. This is with vibration that gives displacements at the RTG which are in the plane of the RTG V-brace and parallel to the hinge line. This gave an estimated load at the RTG's of 33 g during qualification testing. This is the critical condition for the V-brace members. These members, considered as beam columns, have a maximum total stress of 66,400 psi, 58,300 psi due to bending and 8130 psi, direct compression. The allowable stress at 500°F is 101,000 psi.

The critical condition for the remaining small diameter tube is when vibration gives displacement of the RTG's in the stowed condition, in a radial plane with respect to the booster axis, and normal to the tube axis. The frequency is 84 Hz, giving a 35 g load at the RTG. The axial stress in the tube is 12,000 psi, which is also the allowable column stress. This indicates a small, zero, margin of safety. However, the estimated frequency is high, because the flexibility of the mounting structure was neglected, and consequently the estimated loads are high.

This condition gave a higher bending moment applied to the end of the V-struts, but with a reduced axial load which made the condition less critical than the previous case.

In the deployed condition at the maximum spin rate for the satellite of 60 rpm, the load at the RTG is down to 8.8 g. Furthermore, the members we subject to direct loads only, and consequently the stresses in the V-brace are small.

8.2 ELECTRIC POWER

8.2.1 Requirements

The function of the electrical power subsystem is to provide power to energize all electrical equipment aboard the spacecraft. The functional requirements are:

- Provide continuous electrical power during the entire mission lifetime from a primary power source using radioisotope thermoelectric generators (RTG).
- Condition the output from the primary power source to the proper forms for spacecraft use.
- Provide centralized switching and distribution of power to spacecraft loads.

The performance requirements are:

- Provide a total of 99 watts of raw DC power from three identical RTG units, for a minimum duration of two years after launch. (See Figure 8-1 for load profile.)
- Provide 9 watt-seconds of energy storage capacity for peak loads during spinup ignition.
- Distribute power to other spacecraft subsystems as shown in Table 8-1.

8.2.2 RTG Design Considerations

The major components of an RTG are: (1) an isotope heat source, (2) thermoelectric converters, and (3) a heat rejection system. In addition, an abort re-entry system may be required to assure complete containment of the fuel. The isotope that will be used for the Advanced Planetary Probe is Pu 238. The half-life of Pu 238 is 87.6 years and the degradation in the thermal output of the isotope over the two-year

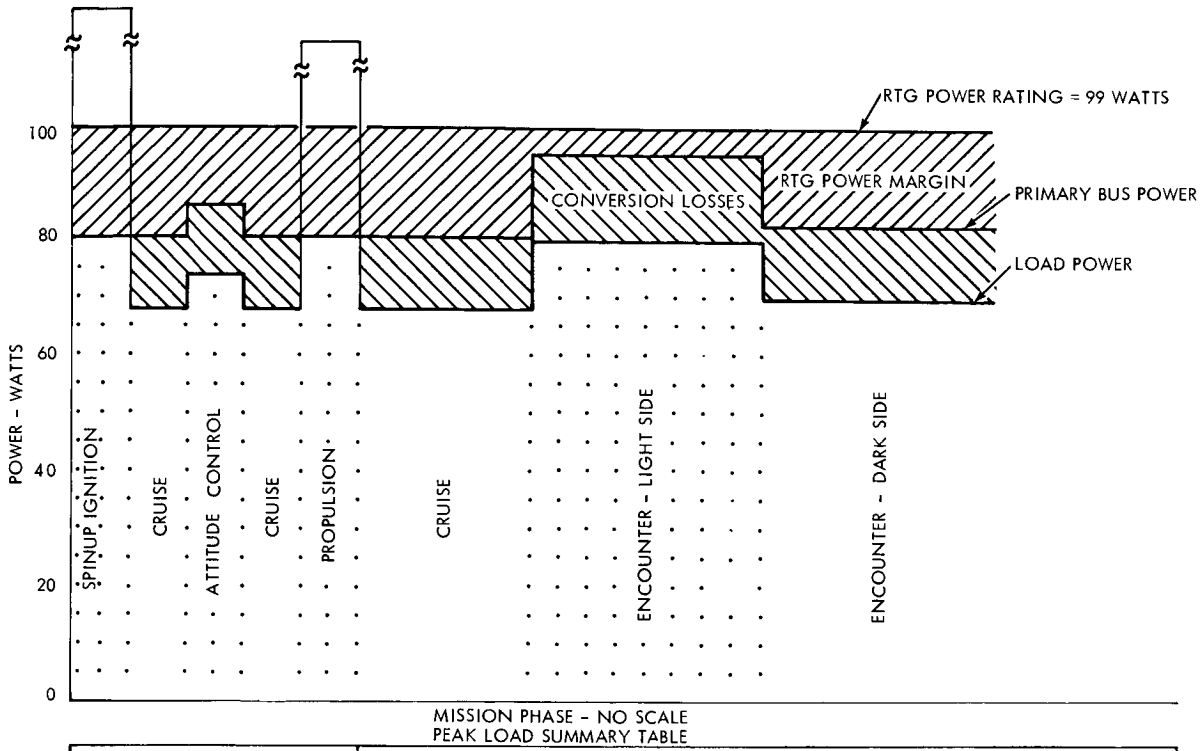

PEAK LOAD SUMMARY TABLE

MISSION PHASE	PRIMARY BUS TRANSIENTS REFERENCED TO 77.4 WATTS CRUISE POWER		
	MAGNITUDE (WATTS)	DURATION	ENERGY (WATT - HOURS)
SPINUP IGNITION	900	0.01 SECOND	0.0025
ATTITUDE CONTROL	5.6	0.4 SECOND	0.00062
PROPULSION	150	0.01 SECOND	0.00042
ENCOUNTER - LIGHT SIDE	14.3	50 HOURS	710
ENCOUNTER - DARK SIDE	1.5	50 HOURS	75

Figure 8-1. Spacecraft Power Profiles

lifetime of the mission is small. In addition, the radiation fields associated with Pu 238 are appreciably smaller than the radiation fields of other long-lived isotopes.

The isotope is encapsulated in a metallic capsule designed to insure containment of the isotope during normal operations and in the event of an accident or mission abort. Since Pu 238 is an alpha-emitting isotope, the helium gas generated by isotopic decay must also be contained, and high temperature creep of the capsule must be considered.

The converter contains the thermoelectric elements (thermocouples) in the specific configuration required to obtain the desired power and voltage levels. The elements are placed between a hot shoe, where heat is received from the isotope, and a cold shoe, from which the excess heat is transferred to a radiator and rejected to space. The isotope source

Table 8-1. RTG Power Requirements

Subsystem	Subsystem Input Power			Conversion Efficiency (percent)						RTG Power (watts)		
	Element	Mode	Input Power (watts)	Local TRF	Distribution and Protection	Central Inverter	Converter	Shunt Regulator	Overall	Cruise	Encounter Light	Encounter Dark
Communications	TWTA	All	26.7	--	--	--	88	99	87	30.7	30.7	30.7
	Ancillary	All	4.6	--	--	--	70	99	69	6.7	6.7	6.7
Command distribution	All	All	4.0	--	--	--	70	99	69	5.8	5.8	5.8
Data handling	All	All	5.0	--	--	--	70	99	69	7.3	7.3	7.3
Attitude control	Electronics	All	4.5	--	--	--	70	99	69	6.5	6.5	6.5
	Solenoids	All	5.6	--	--	--	--	99	99	5.7	*	*
	Spinup		900.0	--	--	--	--	--	--	**	**	**
Propulsion	Electronics	All	None	--	--	--	--	--	--	--	--	--
	Solenoids	All	150.0	--	--	--	--	--	--	**	**	**
Thermal control	All	All	11.0	--	--	--	--	99	99	11.1	11.1	11.1
Science	All	Cruise	12.0	85	97	88	--	99	73	12.4	--	--
	All	Encounter Light	23.5	85	97	88	--	99	73	--	26.7	--
	All	Encounter Dark	13.5	85	97	88	--	99	73	--	--	13.9
Total										86.2	94.8	82.0

*No RTG power is budgeted. Instead thermal is commanded off during ACS valve operation at encounter.

**Negligible power is required by energy storage capacitor.

may be bonded to the hot shoes to obtain conduction heat transfer, but radiative coupling is usually preferred to avoid diffusion between the capsule and the hot shoe. The temperature drop across the elements and the length-to-area ratio are key parameters in determining the converter efficiency. Typical efficiencies of the Si-Ge converter employed in this application are on the order of 5 percent.

The aerospace safety requirements, thermoelectric element considerations, and typical radiation fields from a Pu 238 fueled RTG are described below. A classified appendix (Appendix J) discusses the applicability of the Snap-19 and Snap-27 systems to the Advanced Planetary Probe, presents data on the performance of the different thermoelectric materials, and shows a preliminary conceptual design for the RTG's to be used on the Advanced Planetary Probe. In addition, calculations to determine the radiation fields are described.

8.2.2.1 Aerospace Safety

Independent of mission constraints and spacecraft-RTG interactions, the RTG must satisfy nuclear aerospace safety requirements. In fact, the use of a radioisotope requires the consideration of safety in all phases of operation, from initial encapsulation through mission completion. The key safety problem is the safe disposal of the radioisotope system in the event of any mission abort. Suitable means must be provided during each phase of the mission profile to ensure the safety of the general population as well as the personnel directly concerned with the spacecraft launch.

Safety studies performed by TRW Systems indicate that the most severe accident environment to which the system can be subjected is re-entry at or near orbital velocities. Two approaches to the problem have been conceived. The first approach requires complete burnup of the encapsulating materials subsequent to suborbital or orbital aborts with wide dispersion of an inert refractory fuel form, normally an oxide. The inert fuel forms have reasonably high melting points, and are fabricated in large sizes ($\sim$150 microns) to preclude inhalation hazards in the event of release. Preliminary calculations indicate that they probably will not melt and break up after release from the capsule when subjected

to substantial aerodynamic heating. If this can indeed be proven, then subsequent large particle fallout in a widely dispersed pattern will occur.

The second approach requires complete containment of the isotope under all mission abort conditions. This, of course, implies an intact re-entry capability and capsule survival at impact. The effect of the post impact environment on capsule integrity must then be carefully evaluated. For the longer lived isotopes, such as plutonium, it appears feasible to expect a negligible hazard when both the encapsulating material lifetime and the inert qualities of the fuel form are considered. It should be noted that all RFP's issued by the Atomic Energy Commission within the last year for radioisotope generator development have specified the use of an inert fuel form and complete intact re-entry of the encapsulating system.

In the 1970 and 1980 time period complete containment of the isotope under all mission and abort conditions will probably be required.

8.2.2.2 Thermoelectric Material

Two types of thermoelectric materials are possible candidates for use on the RTG required by the Advanced Planetary Probe, lead telluride (PbTe) and silicon germanium (Si-Ge). The PbTe thermoelectric materials have been under development longer than the Si-Ge materials. PbTe type thermoelements were used on Snap-9A and Snap-19 and will be used on Snap-27 and Snap-29. The Si-Ge type thermoelements were used on Snap-10A and were to be used for Snap-17A and Snap-25. The characteristics of both PbTe and Si-Ge thermoelements are discussed below.

Although PbTe thermoelements have superior thermoelectric conversion properties at the same ΔT when compared to Si-Ge, the thermal efficiency of the Si-Ge systems are equivalent to the PbTe system. The maximum allowable operating temperature for PbTe thermoelectrics is significantly lower than for Si-Ge elements. The Carnot efficiency attainable from the PbTe system is therefore lower than that for an Si-Ge system. The thermal efficiency of the RTG, defined as electrical power generated by the RTG divided by the heat generated by the isotope, is the product of the Carnot efficiency and the thermoelectric conversion efficiency. The lower allowable operating

temperatures for the PbTe thermoelements mean lower heat rejection temperatures with a resultant increase in radiator weight.

The magnetic field generated by an RTG is the result of current flow and the use of ferromagnetic materials. PbTe systems use iron in the shoes to which the elements are attached. Snap-19 used pure iron for the hot shoe, and the magnetic field was a factor in eliminating Snap-19 from the IMP spacecraft program. For Snap-27, which also used PbTe thermoelements, General Electric reports that significant reduction in the magnetic fields can be accomplished by careful design of circuitry and by minimizing the ferromagnetic material used. Preliminary experiments indicate that the RTG can be made as magnetically clean as the other spacecraft subsystems. Further experiments will be conducted. Si-Ge systems, on the other hand, are inherently more magnetically clean than PbTe systems since no ferromagnetic materials are used in their construction.

PbTe thermoelements must be contained within a hermetically sealed compartment with an inert atmosphere to prevent excessive degradation of the elements. Leakage of the inert gas would result in rapid degradation of performance. Si-Ge thermoelements, however, can operate in either the air or vacuum. General Atomic is developing PbTe thermoelements which operate in vacuum. However, these elements operate at very low temperatures, on the order of 650°F hot junction temperature, and therefore have very low conversion efficiencies.

The major limitation in the use of Si-Ge thermoelements has been the requirement for an isotope fuel capsule which can operate in the range of 1800 to 2000°F. For alpha-emitting isotope, such as plutonium, helium pressure buildup causes creep deformation of the capsule. At the lower capsule temperatures (1400 to 1500°F) required for PbTe systems, superalloy materials appear to be adequate. The use of refractory materials and the characteristics of higher temperature capsules is currently being actively pursued at TRW under contract with the U. S. Air Force and the Atomic Energy Commission. In the DART*

*Decomposed Ammonia Radioisotope Thruster

program, TRW Systems is developing for the Air Force a radioisotope-heated thruster, using Pu 238, for spacecraft reaction control applications. The capsules will be fabricated from a refractory alloy and will operate at temperatures on the order of 2000°F for periods of two to five years. A demonstration of this thruster containing a capsule loaded with isotope will occur in January 1967. TRW Systems is also developing for the Atomic Energy Commission refractory metal isotope capsules to contain polonium in the temperature range of 3600°F. For the proposed Advanced Planetary Probe schedule, the availability of a Pu 238 isotope capsule to operate in the range of 1800 to 2000°F should not be a limiting factor.

The degradation of the power output as a function of time for Si-Ge and PbTe thermoelements is discussed in Appendix J. Whereas two-year life tests have not been conducted on either type of thermoelectric material, the degradation of PbTe systems appears to be much worse than that of the Si-Ge systems. Further data is being obtained on both PbTe and Si-Ge as well as on new types of thermoelectric materials.

8.2.2.3 RTG Configuration for Advanced Planetary Probe

For the Advanced Planetary Probe spin-stabilized spacecraft with a 50-pound science payload, three RTG's located on booms symmetrically placed around the spacecraft will be used. The total raw power output from the three generators is 99 watts at the end of the mission. The RTG will utilize Pu 238 as the isotope and Si-Ge thermoelectrics. The configurations will have intact re-entry capability to satisfy aerospace safety requirements. A preliminary design of an RTG is described in Appendix J. The system was designed for a minimum mission lifetime of three years with a one-year shelf-life. The overall dimensions of a single generator are 5.67 inches in diameter by 8.42 inches long. The end of life power-to-weight ratio is estimated to be 1.5 watts (raw power)/lb which results in an individual RTG weight of approximately 22 pounds.

8.2.2.4 RTG Fields

The radiation field surrounding an RTG can be calculated if the fuel form and RTG configuration are known. The radiation fields for the Snap-19 and Snap-27 were calculated and compared to fields computed by the Martin Company and General Electric Company. These calculations are described in Appendix J.

Since neither Snap-19 nor Snap-27 is directly applicable for use on the Advanced Planetary Probe, the radiation fields presented in Appendix J had to be modified to describe the field characteristic of the RTG configuration employed on the Advanced Planetary Probe. The three units are located 120 degrees apart in a plane perpendicular to the spacecraft spin axis. Each unit is about 6 feet from the spin axis or about 5 feet from the main spacecraft equipment compartment. (In the final design the RTG units are almost 7 feet from the spin axis, further reducing the dose given below.)

The radiation levels in the spacecraft equipment box corresponding to this configuration are shown below:

	Gammas	Neutrons	Total
Dose rate	2.3 mrem/hr	25 mrem/hr	27 mrem/hr
Flux level	1800 γ/cm^2sec at 0.1 Mev	250 n/cm^2sec	
	200 γ/cm^2sec at 0.8 Mev		
Integrated exposure in 1 year	20 rad	0.8×10^{10} nvt	

In the configuration described above, the electronics will receive an integrated gamma exposure of about 20 rad in one year, well below the damage threshold exposure level of 10^4 rad. However, the integrated neutron exposure received by the electronics will be about $0.8 \times 10^{10} n/cm^2$ in one year. Thus, the neutron exposure in one year is seen to approach the damage threshold. For higher electrical power levels or longer mission lifetimes, the neutron dose for this system would exceed the damage threshold and some component failure might occur. Some combination of available preventative means will be necessary to ensure that component damage is avoided. For the power level and mission lifetime requirements of this Advanced Planetary Probe, it is probable that all integrated radiation damage can be avoided by careful electronics design.

The radiation flux levels which may be tolerated without compromising the scientific experiments were discussed in Section 2.5. In the case of

each of the most sensitive experiments (i.e., trapped radiation, solar plasma, and cosmic ray experiments), it was determined that a radiation field below approximately 200 (photon + neutrons)/cm^3-sec at the science instruments would be desirable. However, it was pointed out that an increase in this level of an order of magnitude would not seriously compromise the experiments and would probably be acceptable.

It can be seen from the preceding table that the neutron flux at the main spacecraft compartment is about 250 n/cm^2-sec and the photon flux is about 2000 γ/cm^2-sec comprised of 90 percent 100 kev photons and 10 percent 800 kev photons. The 100 kev photons may be virtually eliminated from the photon flux by 1 millimeter of lead foil shielding, leaving only a flux of 200 γ/cm^2-sec of 800 kev photons. Further reduction of the flux of 800 kev photons requires relatively more shielding because of the higher energy of the photons. The shielding weight penalty associated with 1 mm lead shielding is 0.0025 lb/cm^2 or 2.3 lb/ft^2. The shielding can be most efficiently used by placing it around the sensitive schience sensors. The total shield weight is estimated to be about 2 pounds.

Thus, a photon flux level of approximately 200 γ/cm^2-sec can be achieved with a small shield weight penalty. Addition of the neutron flux will raise the total particle flux to 450 $(\gamma + n)/cm^2$-sec. Although this flux level is about a factor of 2 above the maximum desirable level it is still within the acceptable level. To reduce the RTG field by this additional factor of 2 would require approximately 0.75 cm of lead and 4 cm of lithium hydride with a corresponding weight penalty of 23 lbs/ft^2. The particle flux of 450 $(\gamma + n)/cm^2$-sec achievable with 1 mm of lead shielding is considered to be a reasonable value.

Section 2.5 has specified a maximum spacecraft magnetic field at the magnetometer of about 1 gamma. The magnetic fields generated by the RTG's due to the presence of electrical currents and ferromagnetic materials can be minimized by careful design and construction of the RTG. Since the RTG design recommended for the Advanced Planetary Probe contains essentially no ferromagnetic material (due to the use of Si-Ge rather than PbTe thermoelectrics), spurious magnetic fields of

much less than 1 gamma at 10 feet should be easily achievable. The Advanced Planetary Probe magnetometer is mounted on a boom about 10 feet from the RTG's, and the spurious magnetic fields at the magnetometer from the RTG's should easily fall within the acceptable levels. This conclusion is reinforced by recent work on Snap-27, which contains much more ferromagnetic material than the proposed Advanced Planetary Probe generator design. Calculations indicate that a field of 0.1 gamma at three meters from the RTG can be achieved. An experimental program is underway to verify the analytical estimates.

8.2.3 Subsystem Design

A block diagram of the selected power subsystem configuration is shown in Figure 8-2. The RTG source is regulated by a central shunt

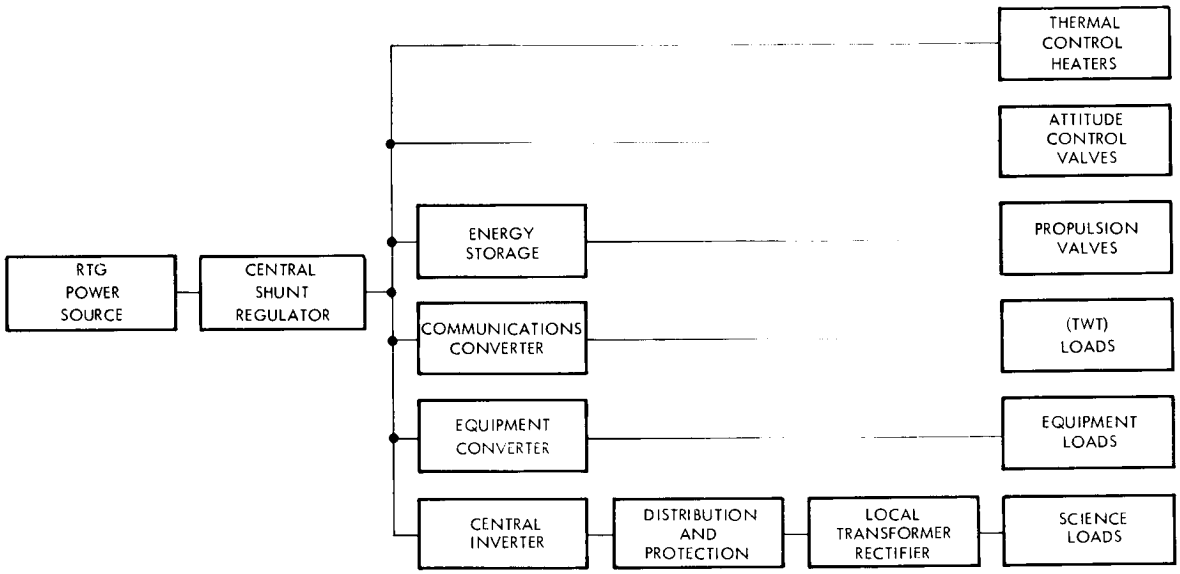

Figure 8-2. Electrical Power Subsystem Elementary Block Diagram, 50-Pound Science Payload Spin-Stabilized, Advanced Planetary Probe

to regulator to a primary bus voltage of 18 vdc, corresponding to peak end-of-life RTG output power. The primary bus is then distributed to each spacecraft load after the indicated conditioning.

The major characteristics of the selected configuration are as follows.

- Conversion of nuclear power to primary electric power by three RTG units
- Primary bus conditioning by a central dissipative shunt regulator
- Distribution of the primary bus directly to attitude control and thermal control subsystems
- Storage of secondary energy in a capacitor bank, and distribution of this energy to the propulsion subsystem and spinup ignition
- Conditioning and distribution of power to the communications and data subsystems, by parallel redundant DC-DC converters
- Preconditioning of science subsystem power by a central DC-AC inverter, and individual distribution of AC power to each science subsystem payload
- Automatic disconnect of nonessential loads in the presence of primary bus undervoltage
- Automatic and discrete disconnect of any load which draws overload current
- Provision for ground command override of automatic load disconnect

The reasoning which leads to the selection of this configuration is discussed in detail in the following sections.

8.2.3.1 RTG Power Source

Radioisotope thermoelectric generators for the Advanced Planetary Probe appear to be the best source because the extreme distance from the sun makes solar power sources impractical from size and weight considerations. Reactor-based power sources are ruled out by the relatively low power levels involved. Reactor-based systems below about 50 watts are not competitive with RTG's in terms of weight.

The need for three RTG units per spacecraft is dictated by stability requirements of the spin-stabilized design, as discussed in Section 4.11. RTG design considerations are discussed in Section 8.2 and Appendix J.

The three 33-watt RTG units are series-connected to obtain an 18-vdc input to the power conditioning equipment. Series, rather than parallel connection, is chosen to improve the efficiency of electrical conversion, which is a function of input voltage. Series connection also

eliminates the need for blocking diodes for each RTG unit which might be required if the three units were connected in parallel. The voltage drop across the diode (0.7 volt) would impose an 11 percent loss of power.

8.2.3.2 Primary Bus Conditioning

The purpose of primary bus conditioning is to provide a close regulation tolerance to the central inverter, and a semi-regulated power input to other conditioners and direct distribution lines. A nondissipative shunt regulator has the advantage of minimum shunt element power dissipation. However, its disadvantage is that the spacecraft would receive a varying thermal input as active loads change. This leads to the selection of a dissipative shunt regulator with the following advantages:

- Virtually constant thermal input to the spacecraft, except for variations in transmitted RF power and long term RTG degradation
- Convenient location of modular shunt elements for optimum spacecraft thermal profile
- Minimum power dissipation with full rated active load
- Minimum weight
- Maximum response
- Minimum electromagnetic interference

The design of primary bus conditioning is constrained by the following considerations. The RTG source must operate continuously into its rated load, as a minimum, if design Peltier cooling of its hot junctions is to be maintained. Since maximum RTG power per unit weight depends on maximum temperature difference between hot and cold junctions, hot junctions are typically operated close to rated temperature. The effect of open-circuit RTG operation is shown in Figure 8-3, where hot shoe temperature or RTG hot spot temperature is plotted against load current. Normal hot shoe temperature is 850°C, corresponding to peak RTG power output at 5.5 amperes load current and 6.0 vdc output voltage. The temperature difference between hot and cold shoes is normally 590°C, and Peltier cooling is approximately 25 percent of total cooling. When Peltier cooling is removed by open circuit operation, hot shoe temperature increases to 1018°C. This temperature is only

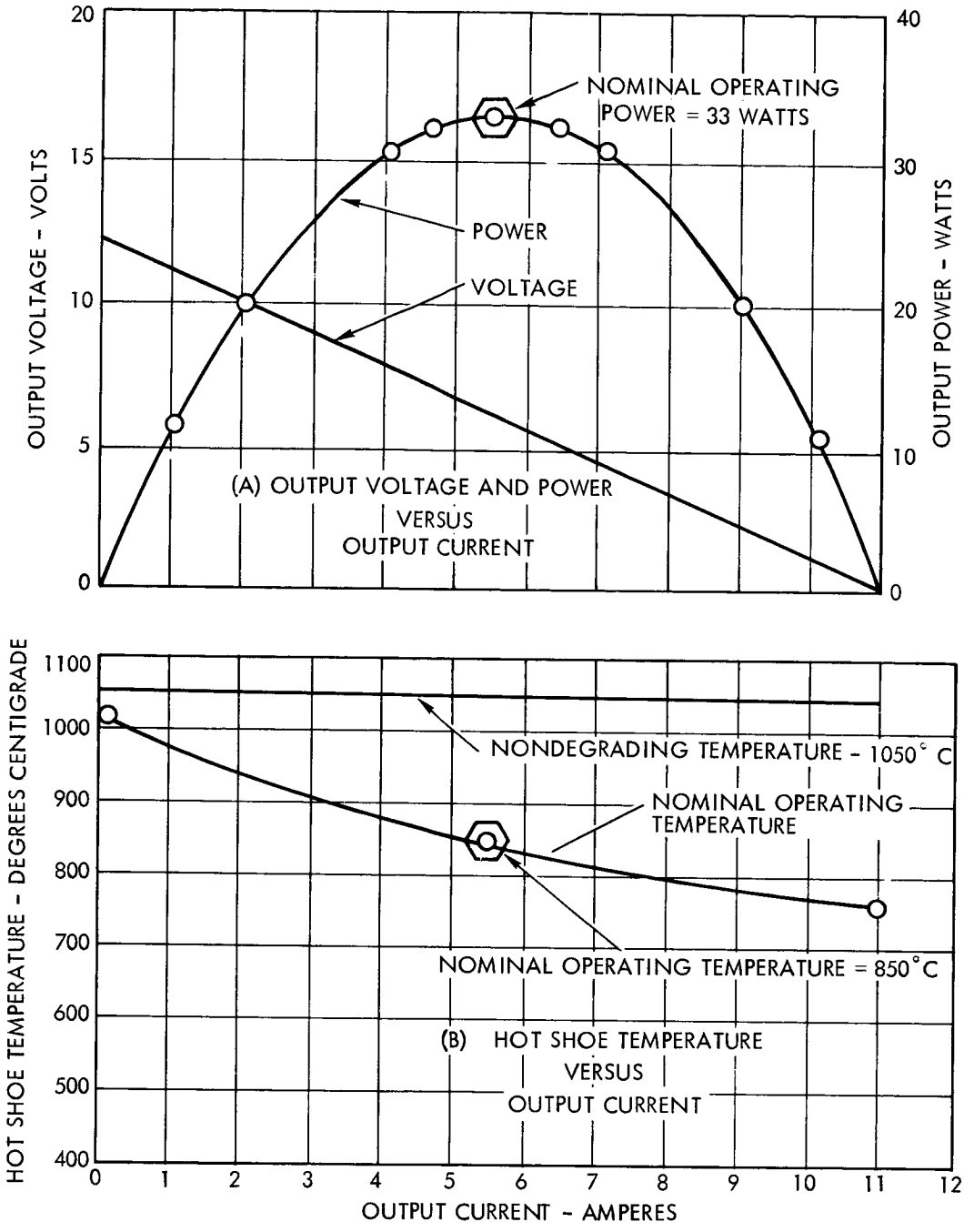

Figure 8-3. RTG Operating Characteristics

slightly below the 1050°C safe operating rating. A phenomenon not considered in this calculation is the effect of open circuit RTG operation on the heat source surface temperature, which will also increase because of the increase in hot shoe temperature. This surface temperature increase will compromise the integrity of the radioisotope container.

The RTG operating constraint leads to the selection of a shunt regulator, which maintains a constant load on the source in the presence of active load variations.

8.2.3.3 Load Power Conditioning

It is convenient to discuss load power conditioning by grouping loads according to power profile and quality considerations, since these define the selected conditioning design approach.

- Conditioning for loads requiring constant profile, moderate quality power: attitude control valves and thermal control heaters.

The attitude control valve power profile is characterized as constant during a major reorientation maneuver because maximum duty cycle is 33 percent; acceptable power quality is extremely coarse. Average heater profile is truly constant, and coarse quality is again acceptable due to closed-loop thermal control. Power is developed for short duration attitude control at encounter by command heater disconnect. Consequently, ACS valve and TCS heater power is distributed directly from the shunt regulated primary bus, at an efficiency over 99 percent and a quality far exceeding requirements.

- Conditioning for loads requiring transient profile, coarse quality power: propulsion explosive valves and spinup ignition.

Spinup ignition requires 900 watts for 0.01 second. Explosive propulsion valves require 150 watts at a maximum duty cycle of 0.04 percent. The short duration power requirements are supplied by an energy storage capacitor bank which is trickle-charged from the primary bus.

- Conditioning for housekeeping loads requiring constant profile, high quality power: communications and data electronics and attitude control electronics.

Since all housekeeping loads must operate for any measure of mission success, completely redundant conversion is necessary. In addition, the conversion redundancy must be mated with load redundancy as required by overall performance constraints. These requirements lead to the selection of integral, redundant converters in the power subsystem,

which converts the primary bus voltage to the end requirements of communications, data, and attitude control system electronics.

- Conversion for payloads requiring constant profile, high quality power: science payload.

The science payload as a whole requires a relatively constant power. Although individual load activations are uniquely determined by mission phase, the individual loads are deliberately sequenced to minimize peak science power. The range and number of science voltages is typically too high to facilitate central power conditioning. Consequently, the conventional local conditioning by each experiment is maintained for this mission. However, it is advantageous to provide power to science loads in the form most readily used by local conditioners. This approach leads to the selection of a central DC-AC inverter, which converts DC primary power into AC distribution to local transformer rectified conditioners. Advantages of this approach over local DC-DC converters are the improved efficiency and reliability of a central inverting switch and improved local conversion design flexibility. Other advantages ensue in load bus monitoring and protection.

8.2.3.4 Power Distribution and Protection

No special protection is required for direct primary bus distribution to ACS valves and heaters or for distribution of stored energy to propulsion valves, since all these loads are assumed to have open failure modes only. Should any shorted failure modes be found during detailed design, then fuses should be inserted in those lines.

Communications power is distributed from two parallel redundant communications converters, one operating and one in standby. Each converter is permanently connected to an associated traveling wave tube. In the event of input power overload on the operating converter, power is automatically transferred to the standby converted. Independent command control capability is also provided for ground transfer or complete disconnect in case of unscheduled time sharing of data storage and transmission or a need to clear frequency bands for military use.

Equipment power is distributed from an internally redundant converter directly to parallel redundant command decoders and internally

redundant data loads. All load failures are constrained to be open-circuit, so no protection is required in the power subsystem. Should this constraint be found difficult to mechanize during detailed design, protection will be inserted where required to prevent failure propagation.

Each of 10 AC distribution lines to science loads is protected by a relay contact, to implement partial mission success by the isolation of shorted mode load failures. When any distribution bus current exceeds its rating, its series relay contact is automatically and discretely opened. When primary bus voltage drops below normal tolerance, because of total overload or lack of design source power, a central voltage monitor disconnects all science loads to permit ground analysis and correction. Command reconnect override is provided for both overload- and under-voltage-initiated science disconnect.

8.2.4 Subsystem Elements

The electric power subsystem consists of three RTG's and a power conditioning unit. A preliminary RTG specification is shown in Figure 8-4. RTG design discussion is presented in Appendix J.

A preliminary PCU specification is shown in Figure 8-5. The detailed PCU design approach is shown in the functional subsystem block diagram of Figure 8-6.

Except for special purpose backup modes, subsequent reference to redundancy is omitted for convenience in presentation. Majority voting circuit redundancy is shown explicity and part-level redundancy is coded in Figure 8-5.

8.2.4.1 Shunt Regulator

The four shunt elements which constitute the shunt regulator power stage are distributed in the spacecraft equipment compartment as required by thermal control. Increased dissipation from the shunt elements compensates for reduced dissipation from disconnected loads. Each shunt element consists of two series transistors with associated drive circuits. Operation is unaffected by a shorted part failure; in the event of an open failure, increased dissipation is shared by the remaining three elements. Shunt regulator efficiency is greater than 99 percent at full load, since

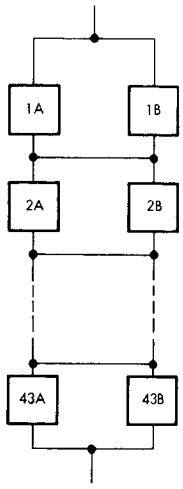

RTG BLOCK DIAGRAM SHOWING
ELECTRICAL INTERCONNECTION
OF 86 SERIES-PARALLEL
THERMOELECTRIC JUNCTIONS

PERFORMANCE CHARACTERISTICS

INPUT: 760 WATTS THERMAL, FROM PLUTONIUM 238 ISOTOPE

OUTPUT: 33 WATTS ELECTRICAL AT 6 VDC

PHYSICAL CHARACTERISTICS

THERMOELECTRIC JUNCTIONS: SILICON - GERMANIUM

WEIGHT: 22 POUNDS MAXIMUM, EXCLUDING MOUNTING STRUCTURE AND POWER CONTROL UNIT

Figure 8-4. RTG Preliminary Specification

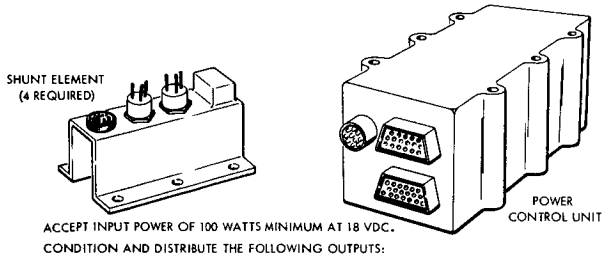

ACCEPT INPUT POWER OF 100 WATTS MINIMUM AT 18 VDC.

CONDITION AND DISTRIBUTE THE FOLLOWING OUTPUTS:

- 18 VDC + 4%, 16.6 WATTS
- 12-18 VDC, 9.0 WATT-SECONDS *
- REGULATED AC VOLTAGES TO COMMUNICATIONS LOADS 31.3 WATTS TOTAL
- REGULATED DC VOLTAGES TO OTHER HOUSEKEEPING LOADS, 13.5 WATTS TOTAL
- 50 VDC + 4% AVERAGE RECTIFIED VALVE, TO EACH OF 10 SCIENCE LOADS; 23.5 WATTS TOTAL
  - 7 KHz + O, -6%
  - SINUSOIDAL, 5% MAXIMUM DISTORTION

DISCONNECT ANY OVERLOADED SCIENCE BUS DISCRETELY AND AUTOMATICALLY. DISCONNECT ALL SCIENCE LOADS AUTOMATICALLY WHEN PRIMARY BUS VOLTAGE IS LESS THAN 17 VDC. ACCEPT COMMAND OVERRIDE OF AUTOMATIC DISCONNECT FUNCTIONS.

PROVIDE CONDITIONED OUTPUTS TO TELEMETRY FOR EVALUATION OF ELECTRIC POWER SUBSYSTEM PERFORMANCE.

SIZE AND WEIGHT

POWER CONTROL UNIT

- 5 X 9 X 5.5 INCHES HIGH.
- 8.3 POUNDS MAXIMUM

SHUNT ELEMENTS

- 3 X 5 X 2 INCHES HIGH, EACH OF 4
- 0.75 POUNDS MAXIMUM EACH OF 4
- 3 POUNDS MAXIMUM, TOTAL

*PHYSICAL CAPACITOR LOCATION IS PYROTECHNIC CONTROL UNIT.

Figure 8-5. Power Control Unit Preliminary Specification

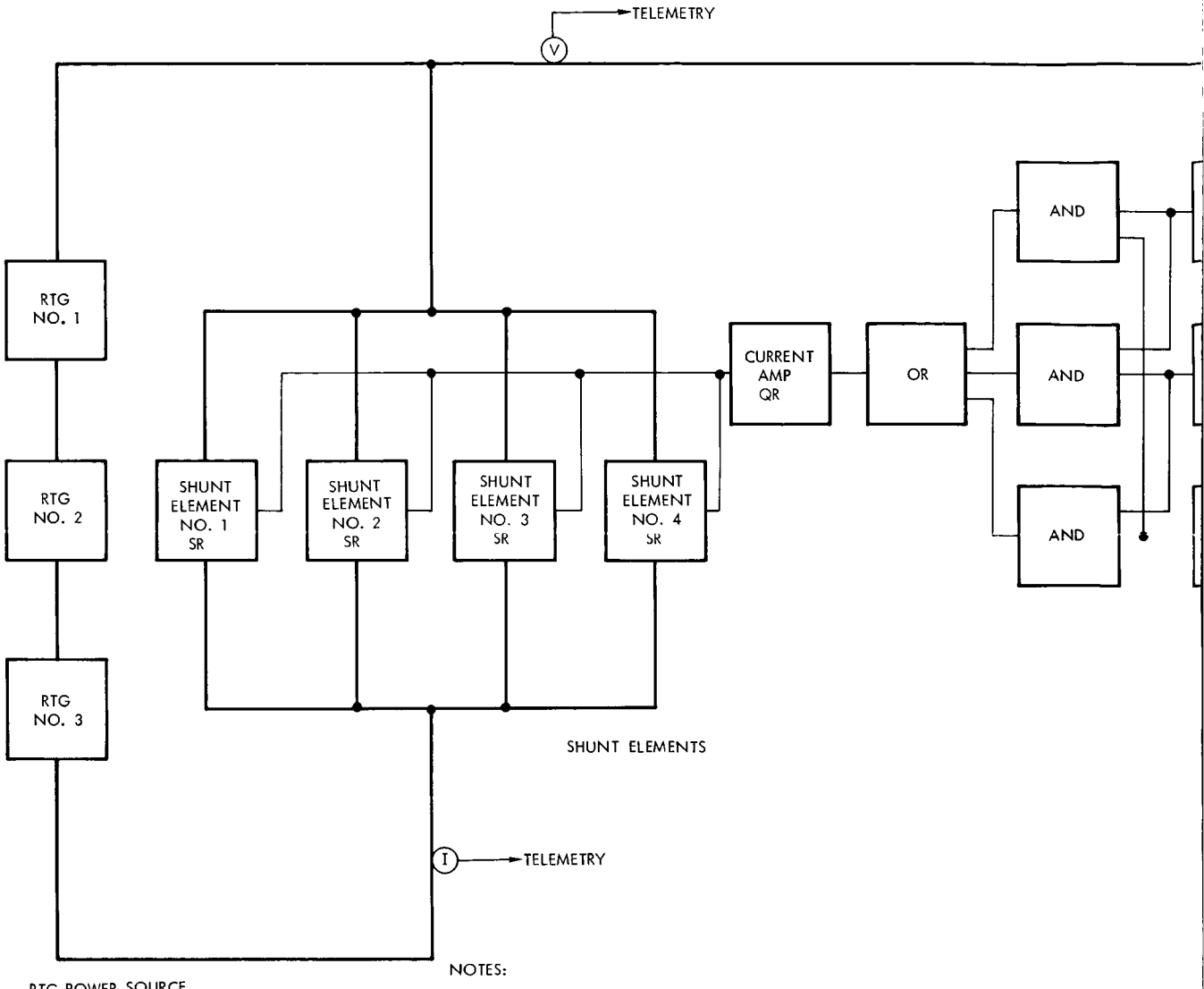

NOTES:

1. REDUNDANCY ABBREVIATIONS:
   SR: SERIES REDUNDANT
   QR: QUAD REDUNDANT
   PR: PARALLEL REDUNDANT
2. EACH CURRENT MONITORS CONTAINS INTEGRAL EXCITATION INVERTER, RESISTER - ISOLATED FROM MAIN BUS
3. INSTALLED IN PYROTECHNIC CONTROL UNIT
4. ALL INDICATED TELEMETRY OUTPUTS ARE ANALOG. STATUS OUTPUTS (NOT SHOWN) ARE PROVIDED FOR EACH RELAY
5. SCIENCE LOAD DISTRIBUTION AND PROTECTION IS PART OF CDU

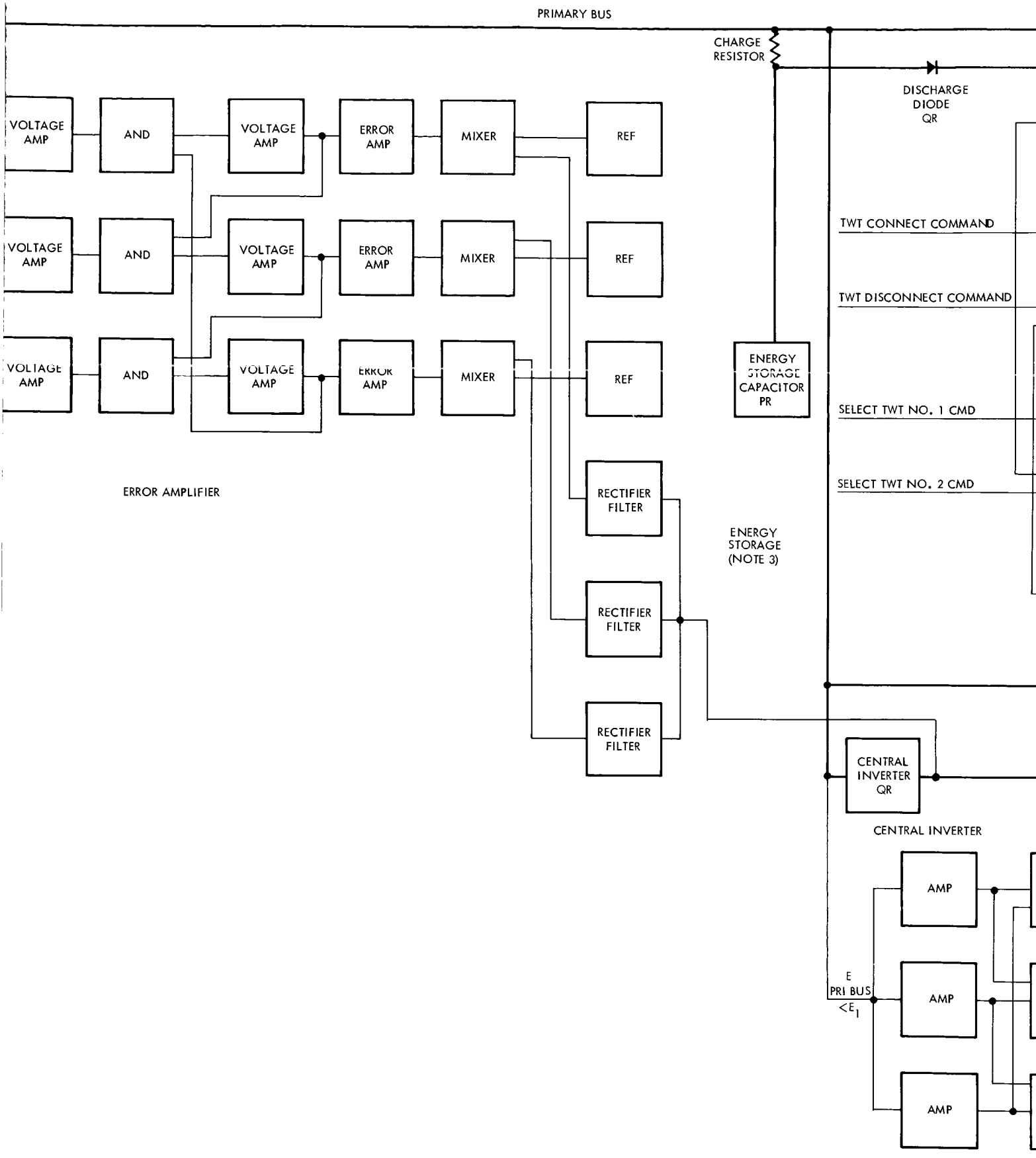
PRIMARY BUS
CHARGE RESISTOR
DISCHARGE DIODE QR
VOLTAGE AMP
AND
VOLTAGE AMP
ERROR AMP
MIXER
REF
VOLTAGE AMP
AND
VOLTAGE AMP
ERROR AMP
MIXER
REF
VOLTAGE AMP
AND
VOLTAGE AMP
ERROR AMP
MIXER
REF
ENERGY STORAGE CAPACITOR PR
TWT CONNECT COMMAND
TWT DISCONNECT COMMAND
SELECT TWT NO. 1 CMD
SELECT TWT NO. 2 CMD
ERROR AMPLIFIER
RECTIFIER FILTER
RECTIFIER FILTER
RECTIFIER FILTER
ENERGY STORAGE (NOTE 3)
CENTRAL INVERTER QR
CENTRAL INVERTER
AMP
AMP
AMP
E PRI BUS
$<E_1$

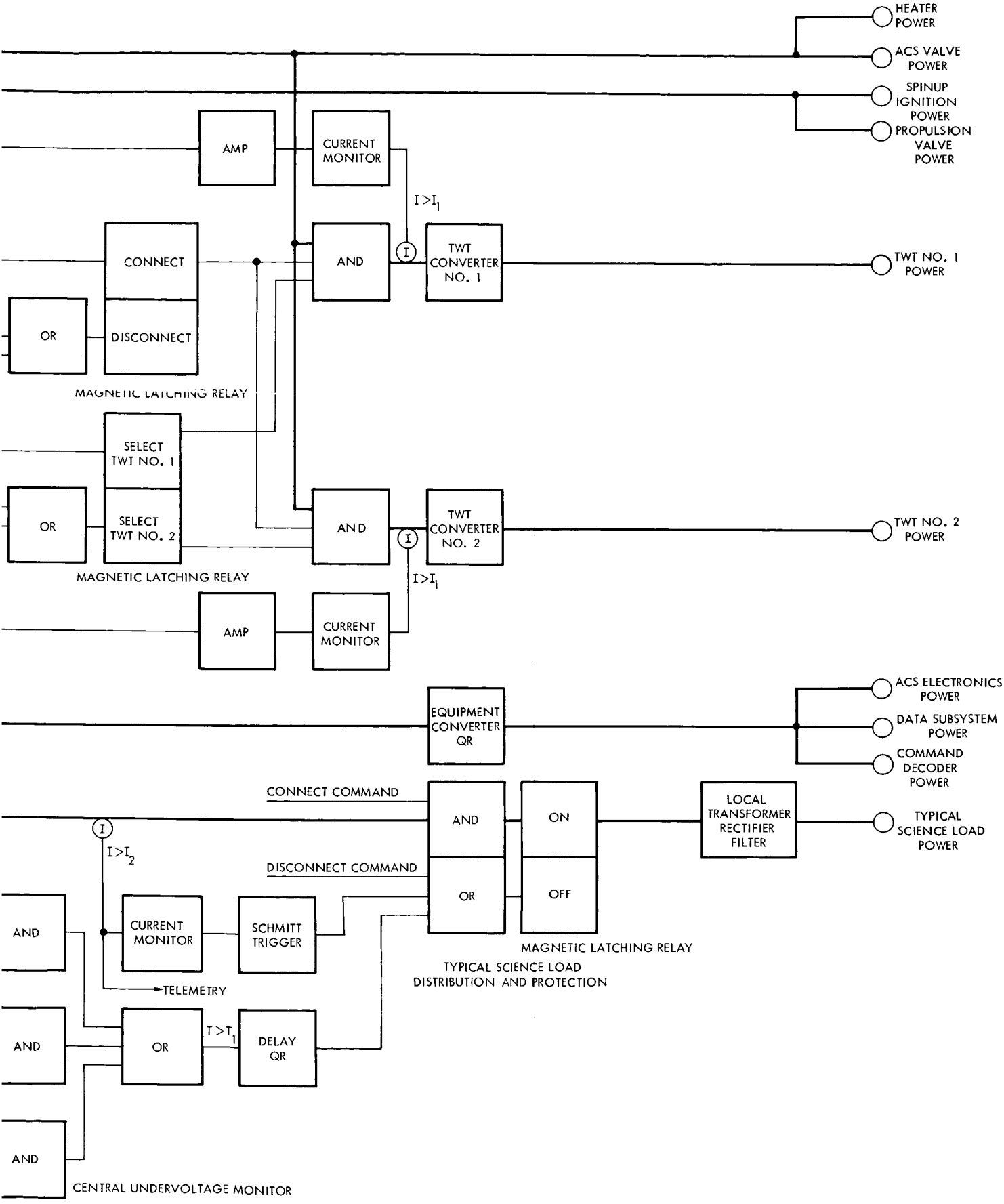

Figure 8-6. Functional Block Diagram, Electrical Power Subsystem

only error amplifier circuits dissipate power when the shunt elements are effectively opened. The error amplifier is the same as that manufactured in quantity for the Air Force Program 2029. The tolerance of the regulator is inherently ±0.6 percent including nominal, failure mode, and long term drift variations. However the sense loop is close around the inverter to eliminate the need for an inverter amplifier, giving an actual primary bus tolerance of 18 vdc ±4 percent.

8.2.4.2 Capacitors for Propulsion Valves

Capacitor energy storage is suited to the 900-watt 0.01-second power requirement of spinup ignition and to the 150-watt, 0.01-second power consumed by sequentially actuated explosive propulsion valves. Using parallel sintered tantalum capacitors, charged through separate resistors and discharged through series blocking diodes for redundancy, energy density is 0.3 pound per watt-second. Weight is 0.3 pound/watt-second x 900 watts x 0.01 second or less than 3 pounds. Energy storage capacitors are installed in the pyrotechnic control unit.

8.2.4.3 Communications Converters

Communications conversion conditions the primary bus to the several voltages required by the TWT loads. Converter efficiency of 88 percent and combined weight of 3 pounds is based on the use of integrated circuit design techniques developed at TRW. Parallel redundancy is selected because each converter is matched to an associated TWT load for maximum communications efficiency. In the event of power overload, the operating converter is automatically disconnected from the primary bus by a magnetic latching relay and the standby converter is connected. Command capability provides for independent ground-controlled connection and disconnection of each converter.

8.2.4.4 Equipment Converter

The equipment converter conditions the primary bus to the power requirements of the balance of the housekeeping loads: command and data subsystems and attitude control electronics. Efficiency is 70 percent and weight is 1.5 pounds. Because of the complexity of converter output sharing, a single internally redundant converter design is selected

instead of the parallel redundant approach used for communications. It is assumed that no shorted failure modes exist in loads which are critical to load fault clearance.

8.2.4.5 Central Inverter

The central inverter conditions the primary bus to an AC output which is distributed to all science loads. Inverter frequency is selected at 7 kHz as a compromise between a weight decrease with frequency increase versus a switching loss increase; 7 kHz is also consistent with EMI requirement estimates. The inverter is normally synchronized by the spacecraft clock, but freeruns at a lower frequency if synchronization is removed. To eliminate high frequency harmonics, inverter transistor rise-times are maintained below 2 microseconds by active filtering. A 60 degree dwell time is also introduced to remove intermediate frequency harmonics. Sinewave filtering to 3 percent maximum distortion is then performed by series and parallel tuned passive filters. Output voltage is selected at 50 vac for minimum distribution relay weight.

8.2.4.6 Science Load Distribution and Protection

The inverter output is distributed to each of 10 science loads through a series current monitor and magnetic latching relay contact. When any load current exceeds 120 percent of its rates value for a period of 1 second the relay contact is opened automatically to disconnect that load. Should primary bus undervoltage occur, whether as a result of unscheduled science load connection sequence or RTG source deterioration, reduction of the total spacecraft load is necessary to facilitate ground correction. The entire science load is selected for removal in this event because it is not required for corrective measures. Primary bus voltage less than 17 vdc for 1 second, as sensed by a voltage monitor, is then used to open all science load relays automatically. Selective ground command override is available to connect and disconnect each science load.

8.2.5 Tradeoff Studies

8.2.5.1 Energy Storage

Since the RTG power source has no inherent overload capacity, it must either be sized for peak spacecraft load requirements or supplemented with an energy storage element for peak load capacity. The spacecraft power profiles of Figure 8-1 indicate that the proposed spacecraft system is designed with minimum peak loads to provide maximum flexibility in energy storage selection. Exceptions are attitude control valves, propulsion valves, and planetary science.

Peak loads may be supplied from the following elements, arranged in order of energy density.

Silver-Zinc Primary Battery Energy Storage. Advantages are maximum energy density of approximately 20 watt-hours per pound and high storage reliability. No charge control is required and storage life is virtually unlimited. The disadvantage is a limitation to one-time moderate duration application; mission application is consequently constrained to flyby use.

Nickel-Cadmium Secondary Battery Energy Storage. The advantages of this approach are moderate energy density of over 10 watt-hours per pound, combined with repeated cycling capability. Although reliability for this mission may be justified by over two years successful application on OGO I, reliability would be very questionable for longer missions. The disadvantage is than a lack of mission duration flexibility.

Additional RTG Power Capability. Additional RTG power may be considered a special case of energy storage, where rate of energy withdrawal is severely restricted. The advantage is maximum mission flexibility. Disadvantages are the limitation on the rate of energy discharge and low energy density of 1.5 watt-hours per pound.

Capacitor Bank Energy Storage. Advantages are extreme reliability and flexibility. The disadvantage of passive energy storage is minimum energy density, 9×10^{-4} watt-hour per pound.

Consideration of peak mission loads leads to the following tradeoff selections.

Planetary Science Loads. Light side encounter loads are considered first, since energy content is highest and the energy storage element selected may also serve other peak requirements. Based on a time of 50 hours, and a power increase over cruise levels of 9 watts, the energy requirement is 450 watt-hours. Silver-zinc battery weight is 450 watt-hours x 1 pound/20 watt-hours = 22.5 pounds. RTG weight is 9 watts x 1 pound/1.5 watts = 6.0 pounds. Additional RTG power capability is selected for light side planetary science loads based on minimum weight. It may be noted that this power capability also provides for dark side planetary science and cruise attitude control valve actuation.

Attitude Control Actuation During Encounter. No energy storage is provided. Instead, thermal control heaters are commanded off as required.

Spinup Ignition. Energy requirements are 900 watts for 0.01 second, or 9×10^{2} watts x 10^{-2} second/3.6×10^{3} seconds/hours = 2.5×10^{-3} watt-hour. Weight of energy storage capacitors is 2.5×10^{-3} watt-hours x 1 pound/9.3×10^{-4} watt-hours = 2.7 pounds.

8.2.5.2 Regulation Tradeoffs

The two major methods of regulation are series and shunt designs. Series regulation has the advantage of current limiting capability. Shunt regulation has the advantage of minimum dissipation at full load; its characteristic is to impose an effective constant load on the power source.

Shunt regulation is selected for the primary bus because constant load is preferred for the RTG source and for minimum dissipation at flyby. Series regulation is selected for secondary conditioning when current limiting capability is desirable.

8.2.5.3 Conversion Tradeoffs

All loads except heaters and valves require DC voltages other than the primary bus voltage. This DC voltage conversion may be produced by separate DC-DC load converters, DC to AC to DC; or by a central DC-to-AC inverter and separate AC-to-DC load transformer-rectifiers.

The advantage of separate converters is redundancy flexibility. The advantages of a central inverter are improved efficiency of a single large unit and greatly reduced end-to-end conversion part count and weight.

Separate converters are selected for critical housekeeping loads because of their redundancy flexibility. The central inverter local transformer-rectifier approach is used for science loads in conjunction with separate fault protection.

8.3 ATTITUDE CONTROL

The Advanced Planetary Probe attitude control subsystem has the following functions:

- Control the spinup and despin maneuvers required to provide stabilization during the solid injection motor burn
- Provide capability for establishing arbitrary attitudes under earth command
- Maintain an earth-pointing attitude automatically when the DSIF uplink transmitter is turned on

As a function of mission sequences the attitude control subsystem performs these functions under the following circumstances.

a) Prelaunch and liftoff. A test mode or checkout capability must be provided to determine proper operation of electric component units prior to launch. During liftoff the attitude control system should be turned off to prevent gas expulsion.

b) Spinup. Immediately after booster separation, the spinup maneuver should be initiated automatically. A command signal will be supplied by the command subsystem. Spinup is completed in 1 second. Final spin speed is 60 rpm, the lowest rate satisfying injection accuracy requirements. With the antenna and the RTG units stowed, the spacecraft configuration is unstable because the spin axis is the axis of minimum moment of inertia.

c) Injection Motor Burn. After the desired spin rate has been obtained, the solid motor is fired to complete spacecraft injection. As a result of initial wobble and thrust axis misalignments during the motor burn, a nutational motion of the spin axis will occur and amplitude will

increase due to energy dissipation in the system. The wobble damper is disabled to reduce the rate of increase of the wobble while the spacecraft configuration is unstable.

d) Partial Despin Maneuver. Immediately after the solid motor is turned off, a partial despin maneuver is initiated to reduce the spin speed. This removes much of the angular momentum, allowing a precise subsequent despin based on ground measurements of spin speed and reduces the RTG deployment stresses. The despin is made slowly to minimize the increase in wobble. The operation will be initiated and timed by the command subsystem.

e) RTG Deployment and Wobble Damping. After the partial despin maneuver is completed, the RTG units will be deployed and the solid motor will be jettisoned. The resulting configuration will be stable with a small margin. Deployment of the RTG units enables the passive wobble damper. The resulting energy dissipation removes the wobble prior to final despin and antenna deployment.

f) Final Despin Maneuver. After the wobble has been reduced sufficiently, a second despin operation will be performed to obtain the required spin speed prior to antenna deployment. The duration of thrust will be commanded from the ground based on spin speed information obtained on the ground arising from spin modulation of the received signal strength.

g) Antenna Deployment. After the final despin maneuver is completed, the antenna will be deployed. The resulting spin speed will be slightly greater than the cruising spin speed. Final cruising spin speed will be achieved when the booms are deployed.

h) Initial Reorientation. The open-loop precession system will be enabled by ground command, and the spacecraft will be rotated to prevent its lower part from being exposed to the sun more than 3.7 hours.

i) Earth Acquisition. The spacecraft will be precessed upon command by means of the open-loop system until the spin axis is oriented within less than 12 degrees of the earth line. Earth acquisition will be completed automatically by the conical scan system.

j) Reorientations for Midcourse Velocity Corrections. Capability is provided for two midcourse reorientation maneuvers from either the fore or aft engine. The first, and probably the only corrections, will take place between 5 and 20 days after launch. The required orientations

will be achieved by open-loop precession. Midcourse attitudes will be estimated by counting the number of thrust pulses fired and computing the precession per pulse by means of calibration data and telemetered information. After the midcourse maneuvers are terminated earth reacquisitions will follow as described in Paragraph i). The open-loop precession system for the baseline configuration has been designed to operate during the early phases of the mission only because of the range limitations of the omnidirectional communication link.

k) Earth-Pointing Cruise Mode. Booms and appendages are deployed and the cruising spin speed is achieved. This mode is required to point the main communication antenna to the earth with sufficient accuracy to maintain the downlink gain within 1 db of maximum gain. Fine pointing is accomplished by using the main antenna in the track mode, in which the feed is offset by a mechanical actuator to provide conical scanning. Acquisition capability is provided by an auxiliary antenna with a larger beamwidth.

8.3.1 Requirements

Requirements are summarized below for each of the mission phases in which the attitude control subsystem is required to operate.

Initial Spinup

Spin speed = 60 rpm
Spinup time = 1 sec
Spin speed accuracy—not critical—assume ±10 percent

First Despin

Required spin speed = 30 rpm
Despin time—not critical—assume from approximately 1 to 2 minutes
Spin speed accuracy—not critical—assume ±10 percent

Second Despin

Required spin speed = 7.46 rpm
Despin time—not critical—assume same thrust level as per partial despin
Spin speed accuracy = ±5 percent

Open-loop Reorientations

On-plane precession accuracy = better than 2 percent
Cross-axis precession error = less than 2 percent

Earth-pointing Mode

Pointing error = less than 0.5 degree (3σ)

The total precession capability is at most 1200 degrees. A mission duration of 750 days is assumed.

8.3.2 Subsystem Design

The proposed baseline design for the attitude control system is represented in block diagram form in Figure 8-7. A description of the

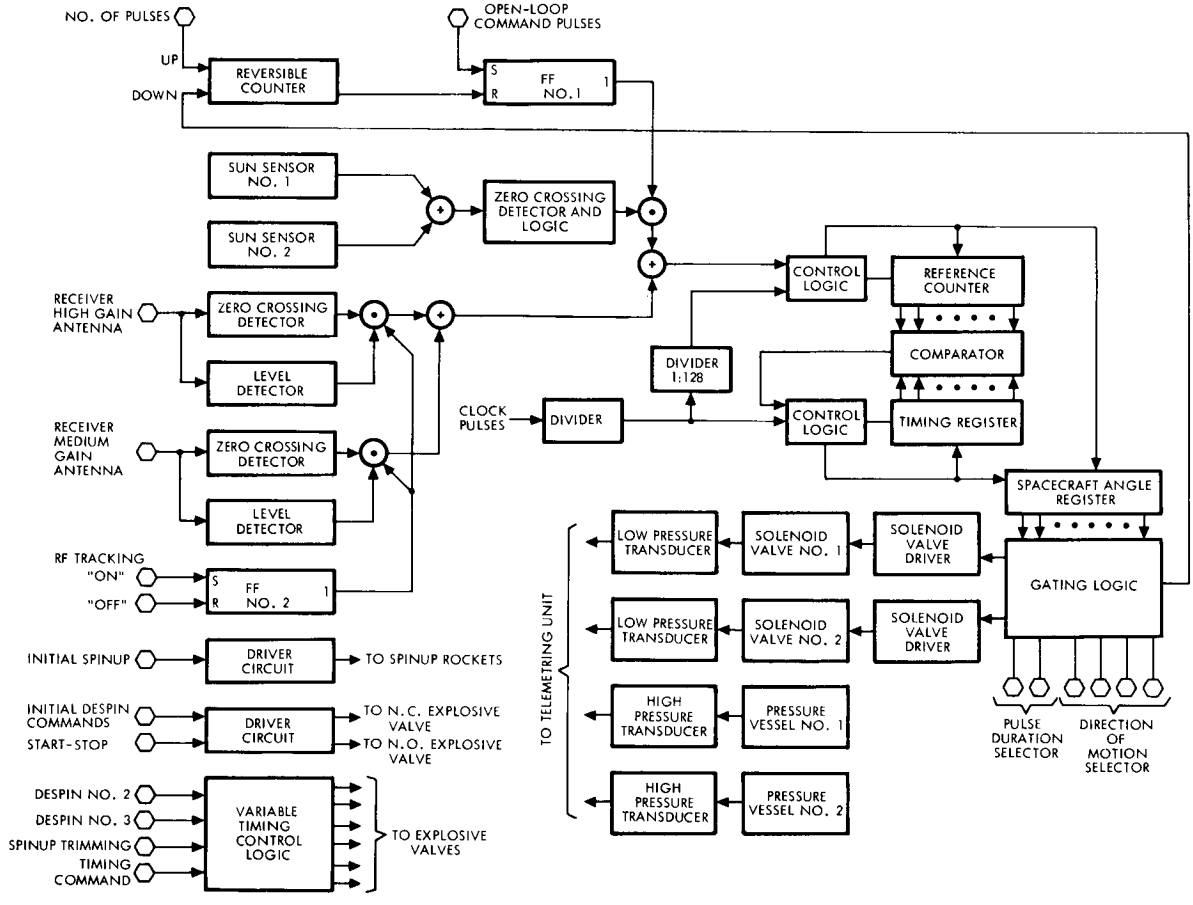

Figure 8-7. Attitude Control Subsystem

basic units that form a part of the subsystem follows in Sections 8.3.3 through 8.3.7. The sun sensors and the pneumatic assembly are described in detail in Sections 8.3.8 and 8.3.9.

The reversible counter and flip-flop No. 1 provide the capability for precessing any desired number of steps with a single execute command.

This feature is desirable when there may be orientations in which communication by means of the omnidirectional antennas is not possible. A number of pulses equal to the desired number of precession steps is loaded in the reversible counter upon command. An execute command transfers the flip-flop No. 1 to the "1" state. The associated "and" gate will let sun sensor pulses operate on the control logic unit for the reference counter. Completion of each precession step will reduce by 1 the stored count in the reversible counter. When this count becomes zero, a pulse is developed by the reversible counter and the flip flop is reset to the "zero" state. The process is thereby terminated. Flip-flop No. 2 is used to turn the RF tracking system on and off upon command. This is required to prevent undesired operation when the DSIF signal is turned off between control periods.

The attitude control subsystem provides accurate earth-pointing of the downlink communications antenna within the accuracy determined by the selected dead zone of 0.25 degree. This allows for misalignment and boresighting errors totalling 0.25 degree. The error signals for the fine-pointing and acquisition modes are obtained from communication receivers operating with the main paraboloidal and the helix antennas, respectively. An electromechanical actuator displaces the feed of the paraboloid transversally to obtain the required squint angle. The essential interface with the DSIF system involves the availability of a carrier signal for RF tracking. The required commands for attitude control are as follows.

Item Number	Description	Type
1	Open-loop, number of steps	Quantitative, 256 steps max
2	Open-loop precession execute	Discrete
3	RF tracking "On"	Discrete
4	RF tracking "Off"	Discrete
5	Pulse duration select: "Long"	Discrete
6	Pulse duration select: "Short"	Discrete
7	Direction of motion select: "To the Sun"	Discrete

Item Number	Description	Type
8	Direction of motion select: "90° Off"	Discrete
9	Direction of motion select: "180° Off"	Discrete
10	Direction of motion select: "270° Off"	Discrete
11	Initial spinup: "Start"	Discrete
12	Initial despin: "Start"	Discrete
13	Initial despin: "Stop"	Discrete
14	Spinup-despin duration	Quantitative
15	Despin No. 2 execute	Discrete
16	Despin No. 3 execute	Discrete
17	Spinup trim execute	Discrete

The following instrumentation outputs need to be telemetered.

- Low pressure transducer No. 1 — 0 to 5 VDC
- Low pressure transducer No. 2 — 0 to 5 VDC
- High pressure transducer No. 1 — 0 to 5 VDC
- High pressure transducer No. 2 — 0 to 5 VDC

8.3.3 Spinup System

For stabilization during injection motor burn, a spin rate of 60 rpm is suitable. To minimize attitude changes during spinup, the thrusting time should be of the order of 1 second. Assuming a roll moment of inertia of 109.6 slug-ft squared and a moment arm of 4 feet, the impulse is 86 lb-sec.

Selecting, for example, three 67-pound thrusters, the firing times will be 0.86 second. For this thrust level there are two alternative mechanizations, solid rockets or hydrazine monopropellant thrusters. Solid rockets are preferred for the following reasons.

- The maneuver will be performed only once
- Neither valves nor piping will be required
- Higher specific impulses can be obtained
- Solid rockets are very reliable

The use of more than two thrusters is recommended to minimize the wobble generated as a consequence of misalignments. The centers of thrust should be on the same plane with the center of mass. The initial angular momentum imparted by the spinup maneuver is approximately 690 ft-lb-sec. After solid burnout, the symmetric moment of inertia decreases to 68.9 ft-lb-sec^2. The engine firing may cause a small increase in spin speed due to vortex friction in the engine thrust.

Specific hardware details are discussed in Section 8.7. Initial spinup design parameters are as follows:

Impulse	86 lb-sec
Distance between thrusters	8 ft
Number of thrusters	3
Thrust	67 lb
Thrust duration	0.86 sec
Symmetric moments of inertia	109.6 ft-lb-sec (initial) 68.9 ft-lb-sec (final)
Final spin rate	≈60 rpm

8.3.4 Despin System

The despin maneuvers will be performed slowly to minimize the wobble buildup and reduce the size and weight of the component parts. Assuming two 1-pound thrusters separated by a distance of 8 feet, the rate of change of spin speed after solid burnout is

$$\dot{\omega} = \frac{1.0 \times 8}{68.9} = 0.116 \frac{\text{rad}}{\text{sec}^2} = 1.11 \frac{\text{rpm}}{\text{sec}}$$

If the final speed is 30 rpm (or π rad/sec), the firing times will be about 27 seconds. The corresponding impulse is approximately 54 pound-seconds. If hydrazine with a specific impulse of 230 seconds is used, the corresponding fuel weight is 0.235 pound. Design parameters for the initial despin maneuver are as follows:

Initial spin speed	≈60 rpm
Final spin speed	30 rpm

Number of thrusters	2
Thrust	1.0 lb
Distance between thrusters	8 ft
Thrust duration	27 sec
Impulse	54
Hydrazine weight	0.25 lb
Moment of inertia (roll)	68.9 ft-lb-sec^2

Hydrazine thrusters have been selected in view of the requirement for repeated operations. Cold nitrogen was not considered because of its low specific impulse. Since no more than three despin maneuvers are contemplated, one of which is for a reserve spin-speed-trim, explosive valves will be used because of their high reliability. Deployment of the RTG's increases the moment of inertia from 68.9 to 143.6 ft-lb-sec and reduces the spin rate to 14.4 rpm.

Assuming a desired spin speed of 5 rpm and a moment of inertia of 214.2 slug-ft^2, the angular momentum during cruising is

$$C\omega_s = 214.2 \times \frac{\pi}{6} = 112.2 \text{ ft-lb-sec}$$

Therefore, the spin rate prior to antenna deployment must be

$$\omega_s' = \frac{112.2}{143.6} = 0.782 \frac{\text{rad}}{\text{sec}} = 7.46 \text{ rpm}$$

The final despin maneuver will have to reduce the spin speed from 14.4 to 7.46 rpm. Assuming, again, 1-pound thrusters, the rate of change of spin speed will be

$$\dot{\omega}_s = \frac{1 \times 8}{143.6} = 5.56 \times 10^{-2} \frac{\text{rad}}{\text{sec}^2} = 0.532 \frac{\text{rpm}}{\text{sec}}$$

The firing time will be 13.1 seconds and the impulse required is 16.2 pounds-seconds. The hydrazine weight will be 0.076 pound. Hardware characteristics are given in Section 8.7. Final despin design parameters are as follows:

Initial spin speed	14.4 rpm
Final spin speed	7.46 rpm
Number of thrusters	2
Thrust	1.0 lb
Distance between thrusters	8 ft
Thrust duration	13.1 sec
Impulse	16.2 lb-sec
Hydrazine weight	0.075 lb
Moment of inertia	143.6 ft-lb-sec^2

When the paraboloidal antenna is deployed, the moment of inertia increases to 185.3 ft-lb-sec. Consequently, the spin rate becomes 5.77 rpm. After completing the guidance maneuvers, the booms will be deployed, and the moment of inertia increases to 214.2 ft-lb-sec. The cruising rate of 5 rpm will then be obtained.

Additional valving for a third despin maneuver has been added for redundancy, as shown in Figure 8-8. The desirability of this feature is still uncertain since no significant sources of environmental spin torque have been identified. Summarizing, the spin speed control system will consist of the following equipment.

- Three 67-pound solid rockets for initial spinup
- Two 1-pound hydrazine thrusters for spinup trimming with a pair of explosive valves
- Two 1-pound hydrazine thrusters for despin maneuvers with three pairs of explosive valves

The solid rockets and one pair of explosive valves for despin will be controlled directly by the command subsystem. The remaining valves will be controlled by a variable timing device of the attitude control subsystem.

8.3.5 Open-Loop Precession System

The open-loop precession system provides capabilities to perform the following maneuvers:

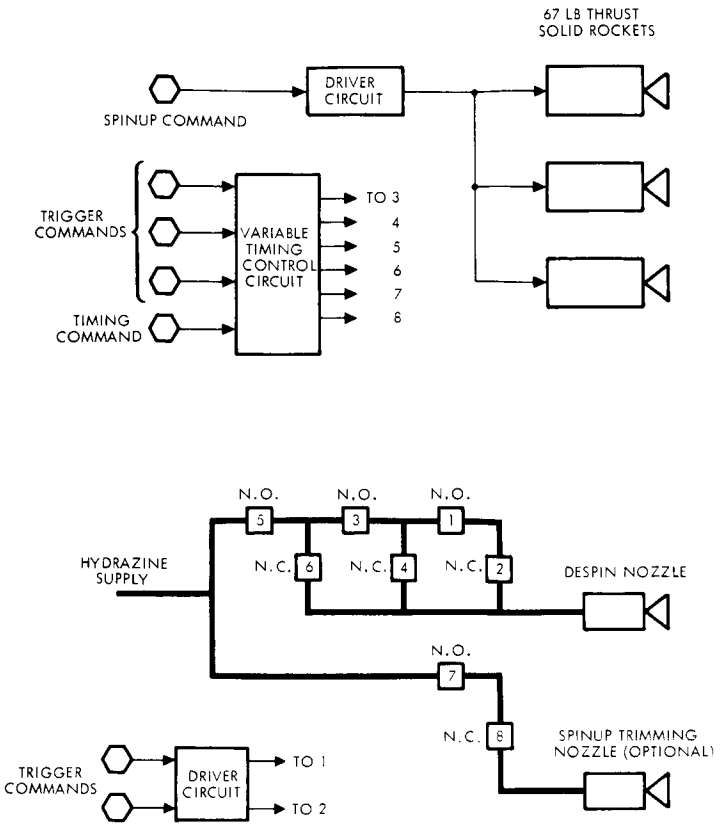

Figure 8-8. Spin Speed Control System Block Diagram

- Initial reorientation to prevent the lower part of the spacecraft from being exposed to the sun more than 3.7 hours.
- Earth acquisition to reduce the angle between the spin axis and the earth line to less than 12 degrees to enable automatic acquisition by the conical scan system.
- Orientations of the spin axis with sufficient accuracy for midcourse velocity corrections.
- Earth-pointing attitude under ground command in case of failure of the conical-scan, closed-loop system.

Precession can be made in four ways, as follows:

a) Towards the sun on the plane determined by the spin axis and the sun

b) Away from the sun on the same plane

c) Perpendicularly to the plane determined by the spin axis and the sun, resulting in a coning motion about the sun line with a constant aspect angle

d) Same as c), but in the opposite direction

Basically, the open-loop precession system consiste of two sun sensors, a digital timing unit, and two pneumatic thrusting systems.

A simplified block diagram is shown in Figure 8-9. The sun sensors supply pulses to indicate when the sun has crossed a reference

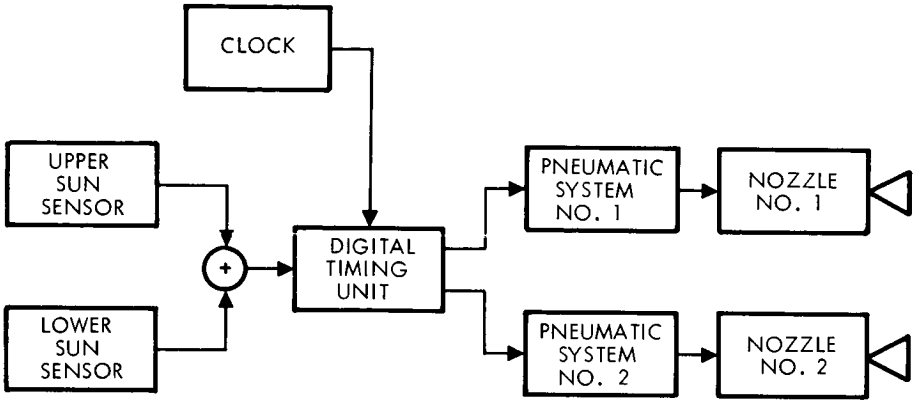

Figure 8-9. Simplified Block Diagram of the Open-Loop Precession System

plane containing the spin axis. This information is used as a reference for the timing of the thrust pulses and supplies spin rate information to the digital timing unit. Two sensors are required to obtain a field of view on the reference plane of ± 85 degrees with respect to the equatorial plane of the spacecraft. The digital timing unit controls the duration of the thrust pulses and introduces delays with respect to the sun sensor pulses in order to obtain the four precession modes listed above. In addition, the digital timing unit controls the delay between the two thrust pulses that produce each precession step. The two-pulse torquing system is used to minimize the wobble generated by impulsive torquing. This method has been discussed in Section 4. 3.

The precession process is illustrated schematically in Figure 8-10, where H_o is the initial orientation of the angular momentum vector. If a thrust impulse F_1 is developed at right angles, the angular momentum vector is precessed perpendicularly to the plane determined by F_1 and H_o. The resulting orientation is H_1. As shown in Section 4. 3, for

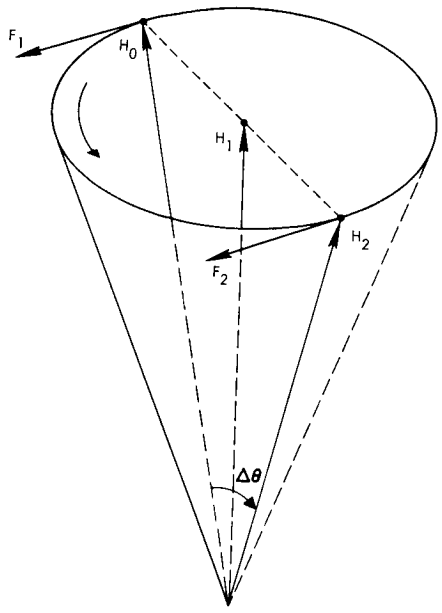

Figure 8-10. Precession by Means of a Sequence of Two Thrust Pulses

cancellation of the wobble initiated by the first impulse, the two centers of thrust must be displaced by an angle

$$\alpha = \frac{A}{C}\pi$$

where A/C is the ratio of transverse to symmetric moments of inertia. The second pulse is fired when the spin rotation has become α radians. The angular momentum is precessed to the H_2 direction and nutation originated by the first pulse is terminated. In the actual system, A/C is not known exactly, and the result will be a small residual wobble.

For open-loop precession, it is desirable to have a fairly large precession step size for the following reasons:

- Minimize the effects of timing errors and uncertainties in the rise and decay times of the thrust impulses; this is accomplished by using long pulse durations
- Provide a sufficiently fast precession rate to allow for passive damping of residual wobble between precession steps; this is required to minimize precession errors due to wobble

In addition, small step sizes are required to provide accurate reorientation and compatibility with the requirements of the closed-loop,

fine-pointing mode. A step size of 0.2 degree per pulse pair was selected for the closed-loop mode, to give a maximum precession rate of 0.0166 deg/sec with a nominal spin speed of 5 rpm. The spin speed before deployment of the booms will be

$$\omega_s' = \frac{214 \times 5}{185.3} = 5.77 \text{ rpm}$$

Consequently, the step size for a firing angle of 60 degrees will be

$$\Delta\theta = \frac{4 FL \sin \frac{\beta}{2}}{\omega_s^2 C} = 1.66 \text{ deg}$$

where

C = spin moment of inertia

L = moment arm

β = firing angle = 60 deg

The step size for a firing angle of 6 degrees will be 0.174 degree. In the calculations the thrust has been assumed 0.173 pound, which is the value that will give a step size of 0.2 degree in the cruise mode.

For a typical pressure vessel temperature of 60°F (520°R) the nitrogen specific impulse is

$$I_{sp} = 3.22\sqrt{520} = 73.4 \text{ sec}$$

The gas flow rate will be

$$\dot{W} = \frac{F}{I_{sp}} = \frac{0.173 \text{ lb}}{73.4 \text{ sec}} = 2.36 \times 10^{-3} \text{ lb sec}$$

For a spin speed of 5.77 rpm the pulse duration will be

$$t = \frac{\beta}{\omega_s} = \frac{\pi/3}{1.15\,\pi/6} = 1.735 \text{ sec}$$

The gas consumption per pulse for large precession steps is

$$W = \dot{W}t = 4.1 \times 10^{-3} \text{ lb}$$

The efficiency for a 60-degree firing angle is

$$\eta = \frac{\sin \frac{\beta}{2}}{\frac{\beta}{2}} = \frac{57.3 \sin 30^{o}}{30} = 95.5 \text{ percent}$$

The efficiency for a 6-degree firing angle is

$$\eta = \frac{57.3 \times \sin 3^{o}}{3} \cong 1$$

and for a spin speed of 5.77 rpm the pulse duration will be

$$t = \frac{\beta}{\omega_s} = \frac{\pi/30}{1.15\,\pi/6} = 0.1735 \text{ sec}$$

The angle between the centers of thrust of the two pulses must be

$$\alpha = \frac{A}{C}(180^{o}) = \frac{148 \text{ ft-lb-sec}^2}{185.3 \text{ ft-lb-sec}^2}(180^{o}) = 143.6 \text{ deg}$$

Relative locations of the sun sensor and gas jet axes are shown in Figure 8-11. The center of thrust of the 6-degree pulses must coincide

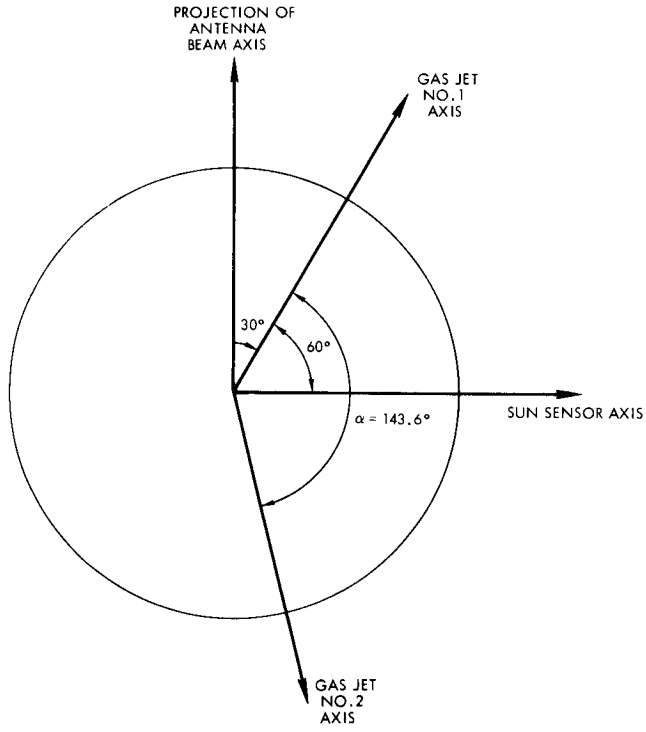

Figure 8-11. Relative Locations of Sensors and Nozzles

with that for the 60-degree pulses. This requires a delay equivalent to a rotation of 27 degrees in the initiation of the gas jet thrust pulses. This delay will be provided automatically by the digital timing unit. Timing diagrams for the four directions of precession are shown in Figures 8-12 and 8-13 for firing angles of 60 and 6 degrees, respectively. Design parameters for the open-loop precession system are summarized in Table 8-2.

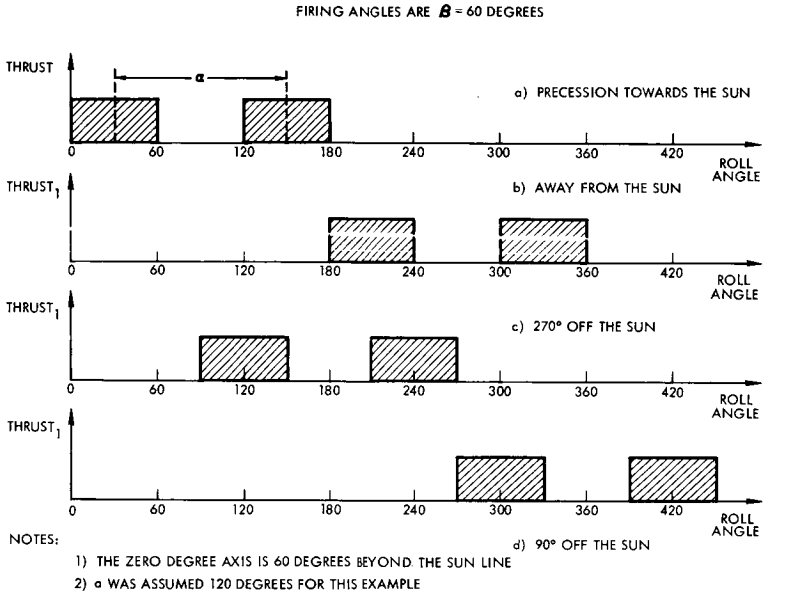

Figure 8-12. Timing Diagram for 60-Degree Pulses

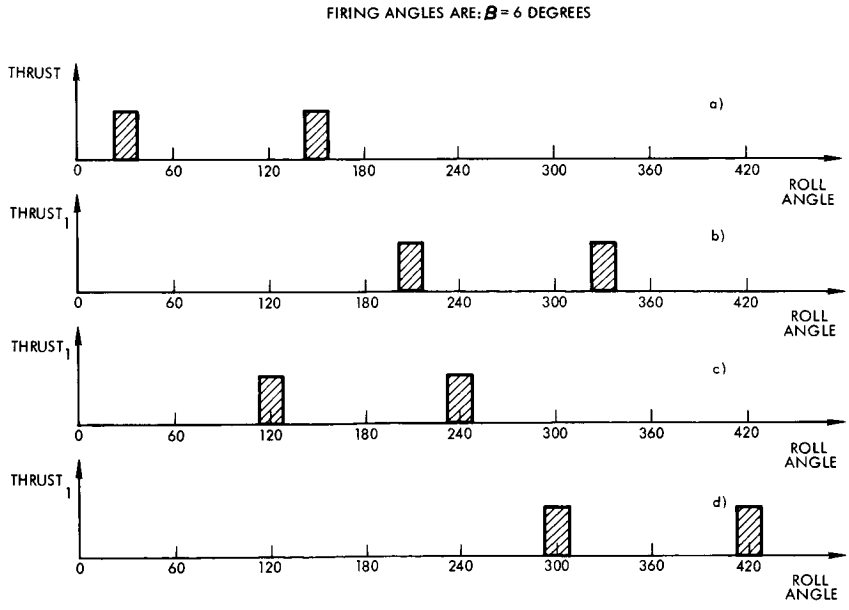

Figure 8-13. Timing Diagram for 6-Degree Pulses

Table 8-2. Design Parameters for the Open-Loop Precession System

	Firing Angles	
	60-degree	6-degree
Thrust, lb	0.173	0.173
Precession step sizes, deg	1.66	0.187
Actual spin speed, rpm	5.77	5.77
Pulse duration, sec	1.735	0.735
Moment arm, ft	5.66	5.66
Symmetric moment of inertia, ft-slug-sec	185.3	185.3
Specific impulse, sec	73.4	73.4
Gas flow rate, lb/sec	2.36×10^{-3}	2.36×10^{-3}
Gas consumption per pulse, lb	4.10×10^{-3}	4.10×10^{-4}
Gas consumption per degree, lb	4.94×10^{-3}	4.38×10^{-3}
Efficiency, %	95.5	100
Angle between centers of thrust, deg	143.6	143.6
Angle between sun sensor and gas jet No. 1 axes, deg	+60	+60
Angle between sun sensor and gas jet No. 2 axes, deg	-83.6	-83.6

8.3.6 Closed-Loop, Fine-Pointing System

The closed-loop, fine-pointing system performs the following operations:

- Maintain an earth-pointing attitude within 0.5 degree; attitude corrections may take place intermittently as required by the trajectory rates
- Acquisition within a range of about 12 degrees from the boresight axis of the main paraboloidal antenna

In either mode, precession always occurs in the direction that minimizes the angular error between the spin axis and the earth line.

The closed-loop, fine-pointing system utilizes the same equipment provided for open-loop precession except for the sun sensors. Attitude errors are sensed by means of a conical scan system, which operates on a RF signal supplied by the DSIF. A simplified block diagram of the closed-loop system is shown in Figure 8-14. Acquisition is by means of a helix antenna having a gain of 14 db and a half-power beamwidth of 25 degrees. The conical scan acquisition range is of the order of one-half the beamwidth, or approximately 12.5 degrees.

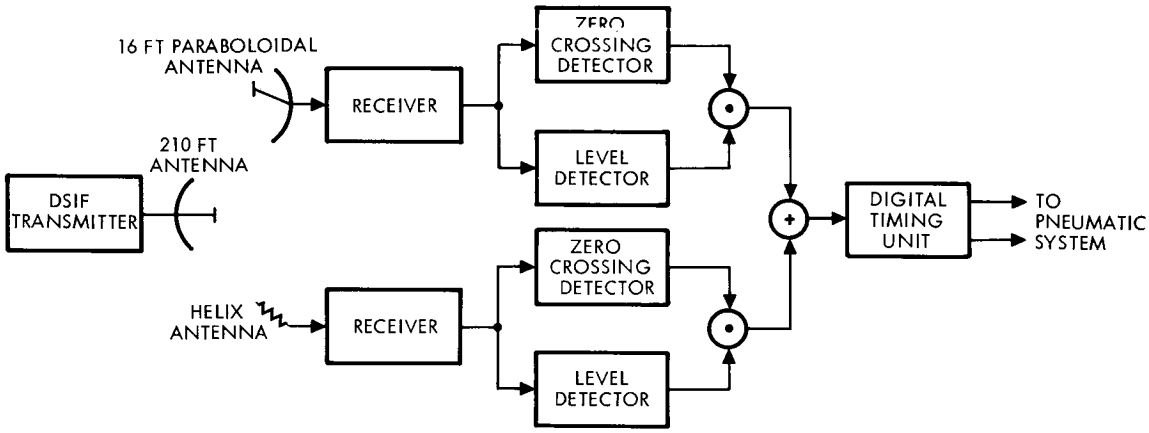

Figure 8-14. Simplified Block Diagram of the Closed-Loop, Fine-Pointing Attitude Control System

The output signal of the receiver is a sinusoidal signal whose amplitude is proportional to the amplitude of the error, and its maximum value occurs when the antenna beam axis is closest to the earth line and in the same plane with it and the spin axis. A zero-crossing detector is used to generate the trigger signals for operating the precession jets. Due to receiver thermal noise, operation with this antenna is limited to error angles greater than 1.2 degrees. For stability and to reduce gas consumption from spurious firing, a deadzone of 1.2-degree amplitude is incorporated. A level detector and a gate are used to switch the acquisition signal off when the error angle is reduced to a value inside the deadzone.

The error is further reduced by means of the fine-pointing channel which operates with the 16-foot antenna. The antenna feed is displaced about an inch from the axis of symmetry by means of an electromechanical actuator in order to obtain an adequate squint angle for the conical-scan process. A deadzone amplitude of 0.25 degree has been implemented for stability and to minimize gas consumption from spurious firing originated by noise.

A detailed analysis of the conical scan system has been presented in Section 4.4. Assuming a receiver noise power spectral density of -164 dbm/Hz, a demodulator filter bandwidth of 1 Hz and a signal power at Jupiter of -142 dbm, the signal-to-noise ratios at the input to the ACS corresponding to the deadzone boundaries will be about 6 db for the helix and 35 db for the paraboloidal antenna. The angular (phase) errors due to noise are 20 and 1 degree, respectively. The zero-crossing detector has a logic circuit to produce an output pulse on the zero crossing corresponding to a change from positive to negative polarity. The antenna beam axes must be in the same plane with the spin axis and the relative position of the antenna plane with respect to the nozzles must be as shown in Figure 8-11.

In the cruise mode, the spin moment of inertia increases to 214.2 ft-lb-sec due to the deployment of booms. Consequently, since the thrust does not change, the precession step sizes will be 0.2 and 1.91 degrees.

It will be possible to use the 1.91 degrees step site in the closed-loop pointing mode. However, the typical operation will be with the 0.2 degree step site. Design parameters for the closed-loop, fine pointing system are as follows:

Acquisition dead zone amplitude	1.2 deg
Fine-pointing, deadzone amplitude	0.25 deg
Demodulator filter bandwidth	1 Hz
Signal-to-noise ratio at the input to the acquisition signal processing unit	+6 db minimum
Signal-to-noise ratio at the input to the fine-pointing signal processing unit	+35 db ($a = \frac{BW}{2}$)

Acquisition phase angle error	20 deg maximum
Fine-pointing phase angle error	7 deg maximum
Precession step sizes	
Fine	0.20 deg
Coarse	1.91
Spin moment of inertia	214.2 ft-slug-sec

8.3.7 Digital Timing Unit

The digital timing unit has the following functions:

- Initiate the thrust pulses at the appropriate times to obtain precession in any of four possible directions
- Control the pulse durations to obtain firing angles of 60 and 6 degrees which, for the nominal spin speed of 5 rpm, will give precession step sizes of 1.9 and 0.2 degree, respectively.

A schematic diagram of the proposed digital timing unit is given in Figure 8-15. Initially, upon receipt of the first sensor pulse, the control logic associated with the reference register will let clock pulses

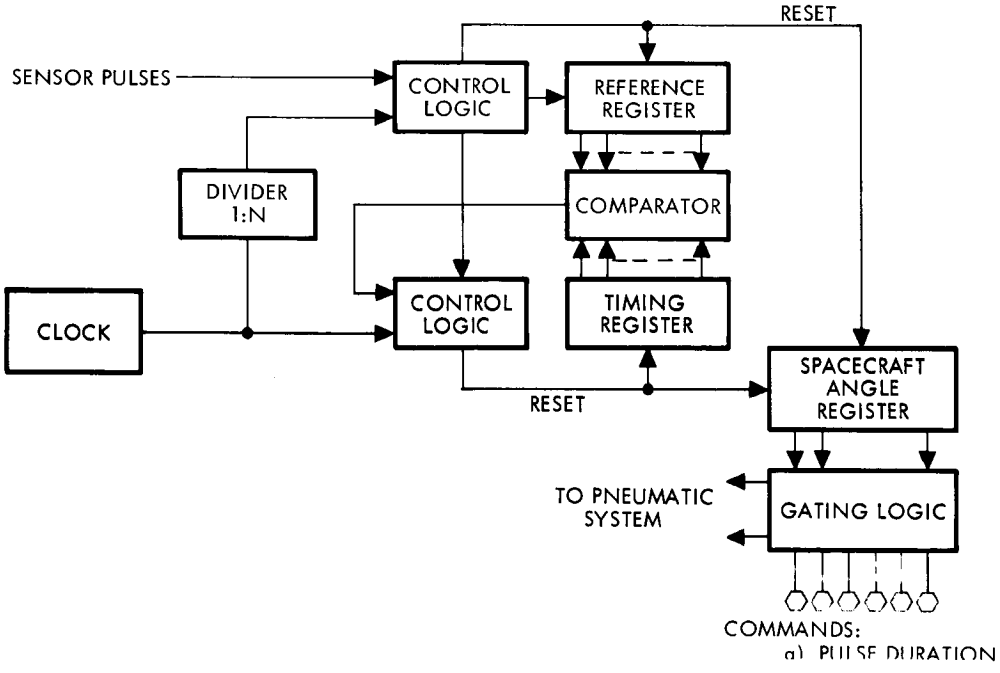

Figure 8-15. Digital Timing Unit

from the divider be counted until the next pulse stops the count. Since the pulse rate from the clock is constant, the count stored in the reference register is proportional to the spin speed. For an accuracy of 0.1 percent, at least 1000 pulses should be counted. Therefore, the register should have a word size of 11 bits to allow for variations in the spin rate. The control logic associated with the timing register will let clock pulses be counted at a rate N times faster. The comparator will generate a reset pulse every time the counts in the timing and reference registers become equal. N reset pulses will be generated per spin revolution. Therefore, if N is 128, the interval between reset pulses corresponds to a rotation of 2.81 degrees. The reset pulses are counted in the spacecraft angle register. This register is reset every time a new count is stored in the reference register. At the desired times, the gating logic turns the gas jets on and off on the basis of the instantaneous count stored in the angle register.

Assuming N = 128 and a minimum count of 1024 pulses in the reference register, the clock frequency will be on the order of 13.1 kc. This signal will be obtained by division of the command subsystem clock frequency. A tolerance of $\pm$20 percent in the spin rate has been assumed to compute this frequency. Design parameters for the digital timing unit are as follows:

Reference register size	11 bits
Timing register size	11 bits
Comparator size	11 bits
Angle register size	7 bits
Divider ratio	1:128
Accuracy	0.1%
Angular interval	2.81 deg
Clock frequency	~14 kc
Spin speed tolerance	$\pm$20%

8.3.8 Sun Sensors

The function of the sun sensors is to detect sun crossings of a plane containing the spin axis. Two sensors are used to achieve a field of view 170 degrees on this plane. The field of view of the upper sun sensor is 85 degrees above to slightly below the equatorial plane. The field of view of the lower sun sensor is from slight above to 85 degrees below its equatorial plane. Each sun sensor consists of two solar cells mounted back to back. These sensors must exhibit a well-defined null plane over a large field of view so that they cannot be tilted in one preferential direction. A well-defined null plane over a large field of view is accomplished by immersing the photosensitive surface of each solar cell with a plane convex lens. This effectively increases the field of view to slightly more than 90 degrees in all directions from the normal to the cell surface. Furthermore, the geometry of the lens, the index of refraction of the lens, and the index of refraction of the optical cement holding the lens to the cell are chosen so that the scale factor near null is enhanced by refractive shuttering. Refractive shuttering utilizes complete reflection at the lens-cement interface so that illumination of the solar cell surface is almost completely turned off when the sun is in the null plane and is almost completely turned on for small excursions of the sun away from the null plane.

The sun sensor employs silicon solar cells as detection elements. The silicon solar cell is an n-over-p junction semiconductor. A typical configuration is shown in Figure 8-16. The output characteristics of the silicon solar cells are shown in Figure 8-17 for $P_R = 140$ mw/cm^2. Basically, the device can be considered as a current source in parallel with a real diode. The current generated by this source is proportional to the radiant intensity and the effective area of the cell. For low radiant intensities, the current-voltage characteristics consist of a "constant current" and a "constant voltage" region as shown in Figure 8-18. The short-circuit current is proportional to radiant power, and the open-circuit voltage varies logarithmically with radiant intensity. Figure 8-19 shows the relative spectral response of a silicon solar cell. Figure 8-20 shows typical angle of incidence characteristics.

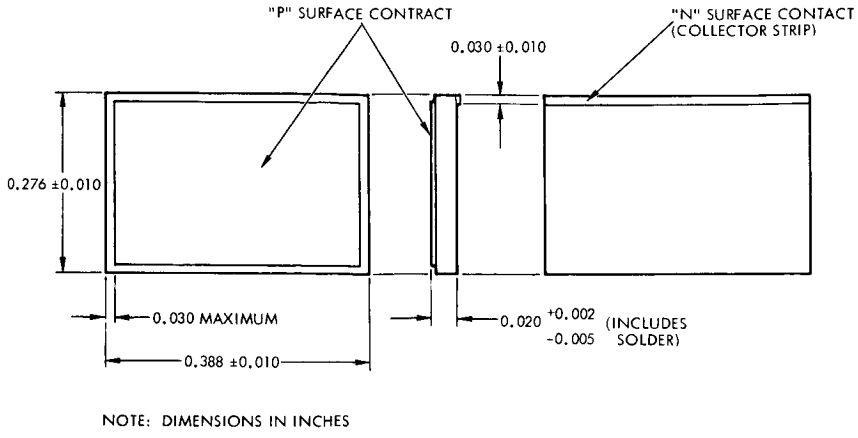

Figure 8-16. Silicon Solar Cell Configuration

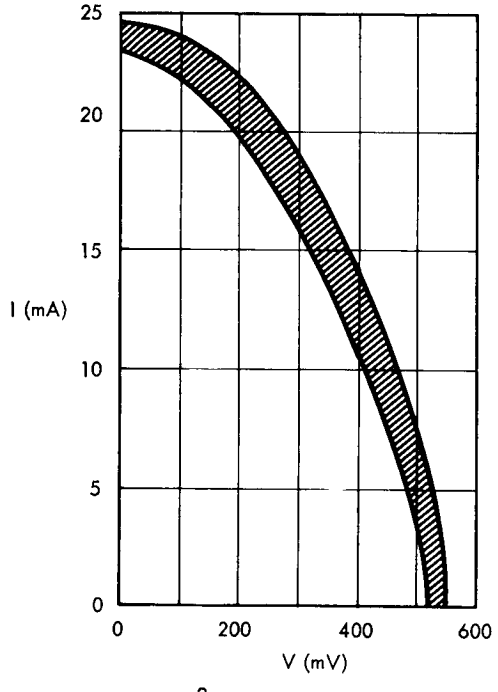

P_R = 140 mw/cm^2 (SOLAR RADIATION M = 0)
$T_{SOLAR\ CELL}$ = 28° ± 2°C
$23.4 \leq I_{SC} \leq 24.6$
$19.7 \leq \pm (200\ mv) \leq 22.2$
$10.9 < \pm (400\ mv) \leq 14.1$
$520 \leq V_{OC} \leq 550$

Figure 8-17. Solar Cell Output Characteristics

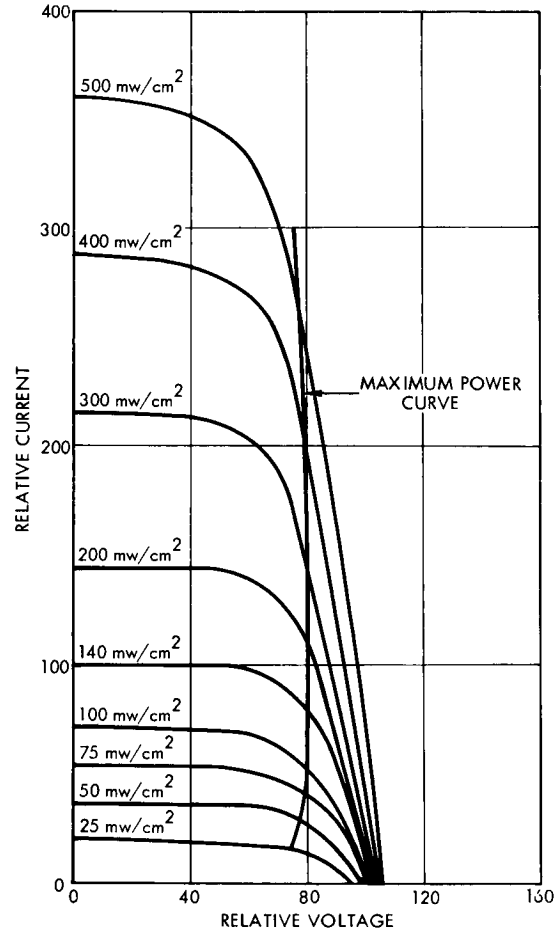

Figure 8-18. Typical Voltage-Current Characteristics Versus Radiant Intensity Normalized to I_{sc} and V_{oc} at 140 mw/cm^2

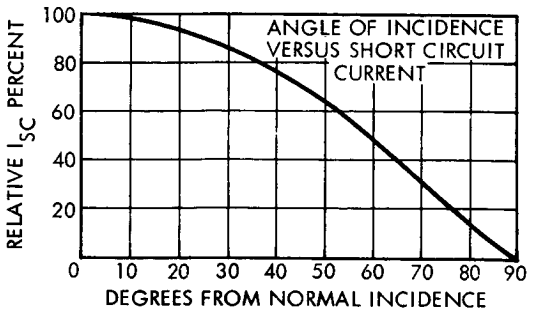

Figure 8-19. Typical Spectral Response Characteristics, Short Circuit Current Normalized to Peak Response Wavelength

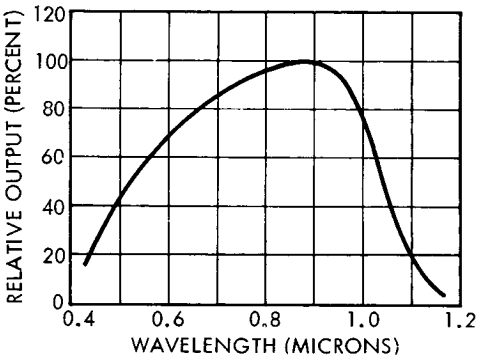

Figure 8-20. Typical Angle of Incidence Normalized at Normal Incidence

The parameter of interest is the open-circuit voltage which determines the scale factor at null. The silicon solar cells to be used in the sun sensors proposed for the Advanced Planetary Probe, manufactured by Hoffman Electronics Corporation, have the following characteristics:

Type	n-on-p, shallow diffused
Dimensions	0.398 x 0.286 in. max
Contacts	Evaporated titanium silver
Electrical output	As per Figure 8-17 at 28 $\pm 2^{\circ}$C
Grids	Gridless
Anti-reflective coating	The n-side of the solar cells will have a silicon monoxide anti-reflective coating
Material	The cells are produced from single crystal p-type silicon with nominal resistivity of 10 ohm-cm

Each sun sensor assembly consists of two silicon solar cells placed back to back with each cell surface in optical contact with plano-convex lenses. It is presently anticipated that no additional electronic parts will be required. The solar cells are connected as shown in Figure 8-21.

Adequate shading will be provided to prevent reflections on the spacecraft surfaces from interfering with the sun sensor performance. In addition, shading will be provided to limit the field of view on the null

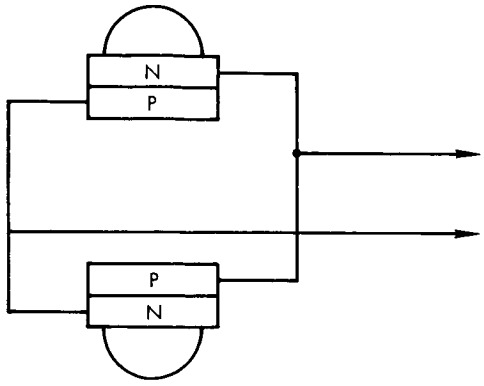

Figure 8-21. Sun Sensor Schematic

plane to 85 degrees above the equatorial plane for the upper sensor and to the same angle below the equatorial plane for the lower sensor.

Laboratory measurements on developmental units for the Vela Advanced Spacecraft have established an accuracy of 1.3 degrees in azimuth at an angle of 70 degrees from the equatorial plane. With some additional development work the area of the error region obtained in the output voltage versus roll angle characteristic could be halved, and the azimuth error would be reduced to 0.92 degree at an angle of 70 degrees from the equatorial plane. If ϕ is the angle between the spin axis and the sun line, the error in azimuth will be given approximately by

$$\epsilon_a = 0.92 \frac{\sin 20^\circ}{\sin \phi} \text{ deg}$$

The output signal of the sun sensor as a function of roll angle in the vicintiy of the null plane is shown in Figure 8-22.

The reliability of each sun sensor assembly has been taken as the reliability of the solar cells and the required interconnections. Each p-surface has a copper tab soldered at two places. The n-surfaces have a narrow copper contact with a single joint. The copper tabs are connected to two pins by means of six soldered joints. Output leads are connected to the pins by two soldered joints. The total of nonredundant soldered joints is 12. Consequently, the reliability estimate for a sun sensor assembly is as follows:

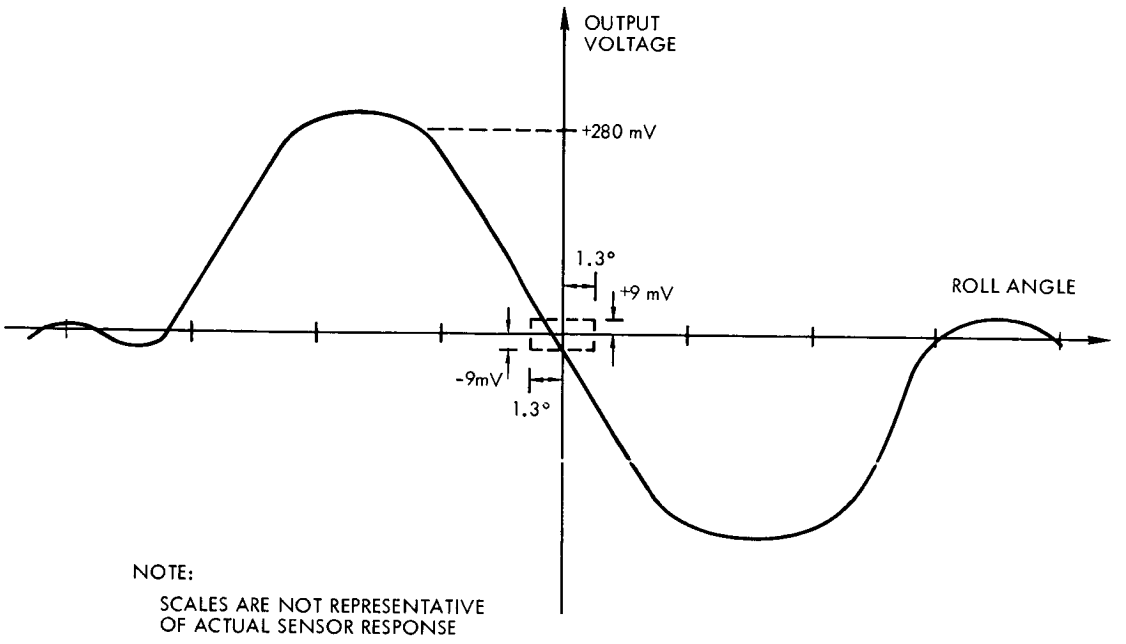

Figure 8-22. Output Signal in the Vicinity of the Null Plane

Part	Failure Rate per Part	Total Failure Rate
2 solar cells	10×10^{-9}/hr	20×10^{-9}/hr
2 solar array type interconnections	1×10^{-9}/hr	2×10^{-9}/hr
10 solder interconnections	0.5×10^{-9}/hr	5×10^{-9}/hr
Total		27×10^{-9}/hr

The reliability for 24 months is

$$R = e^{-27 \times 10^{-9} \times 17,520} = e^{0.000473} = 0.9995$$

The reliability of launch and boost is estimated to be greater than 0.9999.

8.3.9 Pneumatic Assembly

Figure 8-23 is a schematic of the proposed pneumatic assembly. For redundancy, two independent systems are used. Nitrogen is stored

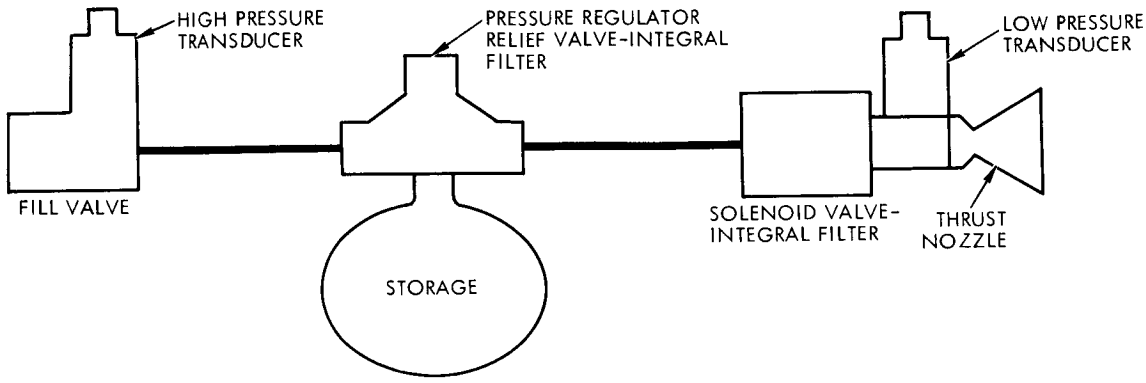

Figure 8-23. Pneumatic Assembly

in two spherical Ti-6Al-4V vessels at 4000 psi. Pressure regulators control pressure on the low pressure side of the assemblies at 50 psia, nominal, and prevent the pressure from rising above 55 psia by venting through relief valves, to prevent excessive pressure from being applied to the solenoid valves. Two solenoid valves control the flow of gas to two thrust nozzles. The pressure at these nozzles is monitored by highly accurate transducers to verify the level of thrust produced. In addition, two valves for filling purposes, two high pressure transducers for measuring the quantity of gas available, connecting tubing, and filters are provided.

Experience at TRW Systems and analysis of data from other sources has shown that leakage is the primary mode of failure for pneumatic systems. For this reason, the assembly is split into two independent sections; leakage of one section will have no effect on the other. The gas supply is sized with the assumption that no significant loss of gas will occur before the midcourse correction which takes place relatively early in the mission. However, each section contains sufficient gas to perform all of the control functions necessary during the long lifetime after the midcourse correction. Thus, if a relatively small leak causes an appreciable portion of the gas in one section to be depleted over a long period, sufficient gas will be available in the other section to complete the mission.

The pressure regulators, relief valves, and solenoid valves incorporate leakage redundancy features. In components, leakage

failures have the highest probability of occurrence at the seat. Reduction of the probability of leakage at the seat of a component will produce the most significant reduction in the probability of leakage of any of the component redundancy schemes possible. Both the Vela Advanced Satellite and the Nimbus pneumatic assemblies incorporate the features described below for the pressure regulator relief valves and the solenoid valves.

Flow enters through the filter; regulation and sealing are normally accomplished by the primary seat which consists of a tungsten carbide ball mating with the titanium housing of the unit. The secondary seat, which consists of a tungsten carbide ball mating with a delrin insert, is normally open. However, should regulated pressure rise as the result of either excessive leakage past the primary seat or normal leakage over a long period of time in the absence of gas usage, the secondary seat will close due to compression of the reference spring. The secondary seat will then perform the main sealing and regulating function.

If the secondary regulator seat becomes operative and the cavity between the seats thus becomes loaded with gas near storage pressure, the regulator will not regulate within the ± 0.5 percent required for the midcourse correction orientation maneuver. However, this difficulty will be avoided by firing sample pulses to check pressure at the regulator. A sufficient number of pulses will be fired to depressurize the cavity and restore operation on the primary regulator seat.

The relief valve also has redundant seats; one consists of a tungsten carbide ball mating with the beryllium copper piston and the other of a flat-molded silicon rubber poppet mating with a portion of the piston in a "cookie cutter" manner. Both seats open at essentially the same pressure.

Flow enters through a filter and is controlled by two seats in series. One seat is located upstream of the main moving parts and the other downstream. The first seat therefore operates in a relatively ideal, contamination-free environment. Both seats consist of molded silicon rubber poppets mating with 17-4PH steel flat surfaces. This particular seat configuration has been highly successful. Aside from

being relatively insensitive to contamination, life in excess of 1,000,000 cycles has been demonstrated.

To minimize the probability of leakage at the points of connection, the high pressure tubing will be integrally welded to both the fill valve and the pressure regulator. Flared tube fittings with soft conical seals will be used for low pressure tubing connections because of the greatly reduced probability of leakage at 50 psi, as opposed to 4000 psi, and to allow ease of installation in the spacecraft. TRW Systems is presently engaged in a company-sponsored program directed toward developing an in-house capability for automatic welding of tubing to components at the cleanliness levels required for pneumatic equipment. An automatic, orbital welder has been purchased for the program. The process is scheduled for usage on the Intelsat III hydrazine system.

Two vessels store nitrogen gas at 4000 psi normal pressure. Each vessel is a sphere constructed of Ti-6Al-4V giving a total storage capacity of 596 cubic inches. Pertinent vessel pressure specifications are as follows:

- Working pressure — 4000 psig nominal
- Proof pressure — 6000 psig minimum
- Burst pressure — 8000 psig minimum

The fill valve is a modified commercial (Robbins G250-4T) valve reworked to reduce weight and size. The valve body is constructed of 2024-T4 aluminum alloy and the bonnet and stem of 300 series stainless steel. Valve body rework consisted of removing excess material at the port ends to reduce weight. The bonnet has been rethreaded internally to accept a 112029-1 screw, which is used as part of the stem assembly. The original stem was shortened and a screw driver slot for opening and closing the valve is provided.

Storage pressure is monitored by means of the high pressure transducer. The information is telemetered to the ground station so that the amount of gas remaining is at all times known. The unit consists of a potentiometer driven by a bourdon tube. Pertinent characteristics are as follows

Scale factor	1.25 ohm/psi
Independent linearity	±1.0% full scale
Hysteresis	1.0% full scale max
Friction	1.0% full scale max
Resolution	0.3% full scale max
Total resistance	5000 ±250 ohms
Maximum pressure without calibration shift	4800 psi

Pressure at each nozzle is monitored by means of a low pressure transducer. The unit proposed is a strain gage type which has the following characteristics:

Accuracy	±0.25% full scale
Range	0-6 psia
Input voltage	25-30 VDC (unregulated)
Output voltage	0-5 VDC
Operating temperature range	0-160°F

The unit has self-contained electronics which convert the input voltage to regulated AC, amplify the bridge output, and reconvert to DC.

8.3.10 Gas Weight

The following figures give the median and maximum values of precession, in degrees through which the spin axis must be rotated, for various phases of a 1972 Jupiter flyby mission.

	Median Precession Angle (deg)	Maximum Precession Angle (deg)
Open-loop precession		
Initial orientation from the injection attitude to an attitude which will be earth pointing after several days	180	220

	Median Precession Angle (deg)	Maximum Precession Angle (deg)
First midcourse: orientation from earth-pointing to propulsion firing attitude, and reorientation to earth pointing (assumes two engines, located on the spin axis, and that the engine closest to firing direction is the one used)	160	240
Second midcourse: orientation from earth-pointing to propulsion firing attitude, and reorientation to earth pointing (assumes two engines, located on the spin axis, and that the engine closest to firing direction is the one used)	160	240
	500	700
Closed-loop earth tracking		
To maintain earth-pointing from several days after injection until Jupiter encounter (except for periods covered above); includes 124 degrees rotation of the spacecraft-earth line (counting plus and minus rotations) and the effects of solar pressure torques (equivalent to 29 degrees) and micrometeoroid pressure torques (0 to 58 degrees), recognizing that the latter two effects are at right angles to the first, and add very little increment	150 redundant 300	200 redundant 400
To maintain earth-pointing for one year after encounter; includes 45 degrees rotation of the spacecraft earth line, and the effects of solar pressure torques (4 degrees), micrometeoroid pressure torques (0 to 4 degrees), the latter two effects again being at right angles to the first	45 redundant 90	50 redundant 100
	390	500
Total	890	1200
Total precession angle for sizing gas supply		1200

Gas requirements are thus computed as follows:

W_I = 700 deg x 4.94 x 10^{-3} lb/deg = 3.46 lb

W_{II} = 2 x 250 deg x 4.38 x 10^{-3} lb/deg = 2.19

Gas leakage 5 standard cc/hr per valve (2 valves, one year past encounter) = 0.73

Total gas requirements = 6.38 lb

The weight statement in Section 7.1 conservatively lists 7.2 pounds, based on earlier estimates.

8.3.11 Lifetime Reliability

The sun sensors will be in operation up to about 20 days from launch. No redundancy has been provided because of the high reliability of the proposed devices. A preliminary reliability assessment is given in Section 8.3.8. Up to about 2 AU the open-loop precession system will provide a backup mode in case of failure of the RF angle tracking system. Extension of the operational range of the sun sensors to 5 or 6 AU will require the addition of an amplification stage to maintain the scale factor within an acceptable value.

The pneumatic system consists of the separate assemblies which can operate independently. When one of the assemblies fails, precession can be accomplished by means of the remaining one without the benefit of active wobble cancellation. Each of the tanks has been sized to contain enough gas to satisfy the precession requirements after the second midcourse maneuver.

Capability has been provided for increasing or decreasing the spin rate at any time during the mission to compensate for unforeseen changes due to leakage, misalignments in the attitude control pneumatics, or environmental disturbances. Redundancy in the digital timing unit could be implemented most economically by adding a standby unit. Further details on the reliability problem are given in Section 9.

When the spacecraft is beyond the range of the omnidirectional antennas, there is no way to command an earth acquisition in case of

complete loss of lock by the conical scan system. The probability of occurrence of this event is very small. However, it might be desirable to have provisions for an automatic reacquisition mode which would precess the spacecraft towards the sun and then about the sun line until the conical scan system locks again on the DSIF signal. This feature could be incorporated in the baseline design without much increase in complexity.

8.4 TELECOMMUNICATIONS

8.4.1 Subsystem Functions and Requirements

The functions of the telecommunication system are spacecraft tracking, telemetry, and command. In addition, for spin-stabilized spacecraft, the telecommunication system must provide earth pointing data to the attitude control system.

Tracking of the probe by the DSIF station is required in order to accurately determine the vehicle trajectory. Tracking information is obtained from the measurement of the two-way doppler frequency shift and apparent angles of arrival of the signal transmitted by the probe. It will be assumed in this study that ranging information is not necessary and is not provided. Tracking will be maintained to distances in excess of 10 AU.

The telemetry link is required to transmit spacecraft performance parameters and the experiment data. The telemetry rate that can be supported is a function of the communication range. To provide maximum bit rate, the information rate will be changed at appropriate flight times. For the telemetry link, information rates from 8 to 1400 bits/sec will be considered with the bit error probability not exceeding 5×10^{-3}. At 6 AU (Jupiter) the nominal bit rate is 700 bits/sec and at 10 AU (Saturn) the bit rate is 256 bits/sec.

The command link provides control of the spacecraft. The required data rate for the command system is low; 1 bit/sec is quite adequate. The accuracy requirement, however, is much more stringent than for the telemetry link. A bit error probability of at least 1×10^{-5}, without error detection or error correction coding, is provided. With this bit error

rate, the probability of rejecting valid command of the order of 2×10^{-3} and the probability of generating an erroneous command of about 2.5×10^{-8} is obtained. Command can be maintained over the low-gain (4 db) antennas to 10 AU and to 27 AU over the helix antenna. For this capability the 210-foot, 100-kw, DSIF transmitter is required.

For the spin-stabilized spacecraft, a modified conical scan technique is used for pointing the antenna at the earth. The RF carrier transmitted by the DSIF is tracked by the probe receiver and pointing error signals are provided to the attitude control system. This system is discussed in Section 4.4.

8.4.2 Alternate Systems

The spin-stabilized concept under study uses a 16-foot antenna with a beamwidth of 1.9 degrees, and, therefore, requires accurate earth pointing. The main functional difference between Mariner 4 (as well as Pioneer 6) and the Advanced Planetary Probe communication systems is this requirement for accurate earth pointing.

A simplified block diagram of the baseline telecommunication system is given in Figure 8-24. This system is designed for the DSN

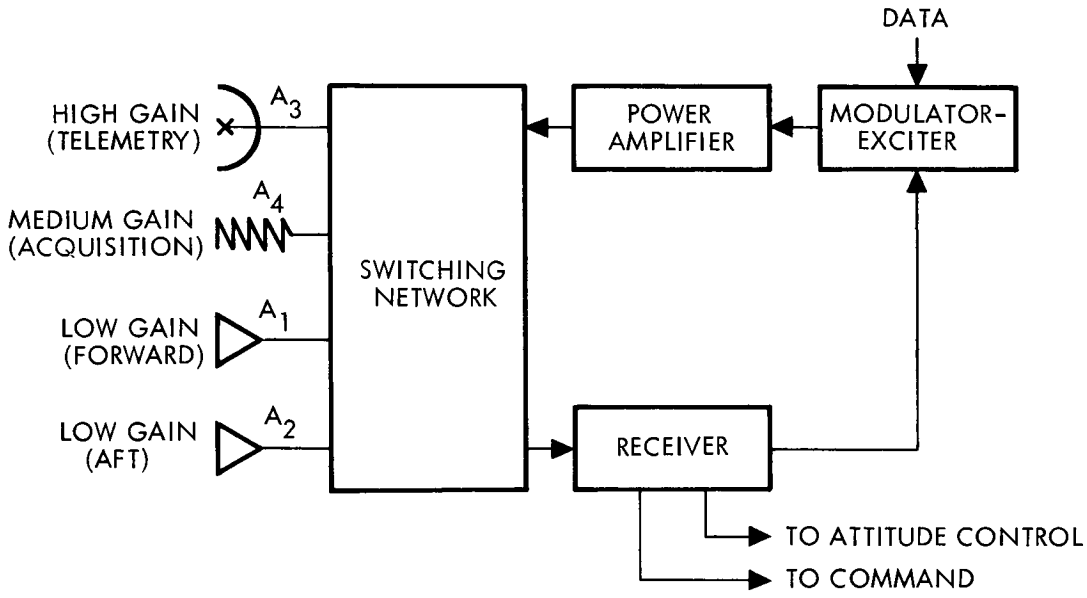

Figure 8-24. Baseline Communication System for Spin-Stabilized Spacecraft

stations. This configuration must be augmented to improve reliability. To increase probability of mission success, at least a second receiver, power amplifier, and modulator-exciter should be added. The receiver, power amplifier, and modulator-exciter requirements are similar to those of Mariner 4 and Pioneer 6.

8.4.2.1 Antennas

When the spacecraft is not pointing to earth, omnidirectional coverage for both uplink and downlink is necessary. Since no single antenna can provide full coverage, two low-gain antennas are needed. One low-gain antenna, A_1, must provide coverage for the forward hemisphere, while the second antenna, A_2, covering rear hemisphere, is needed only before reorientation and during midcourse maneuvers. Both low-gain antennas will be cupbacked turnstiles with maximum gain of 5 db at a cone angle of 90 degrees.

To support the desired bit rates a 16-foot paraboloid antenna, A_3, is used with an on-axis gain of 38.6 db and a beamwidth of 1.9 degrees, as shown in Figure 8-25. The maximum antenna positioning error allowable for a 1-db pointing loss as taken from the figure for a 16-foot antenna

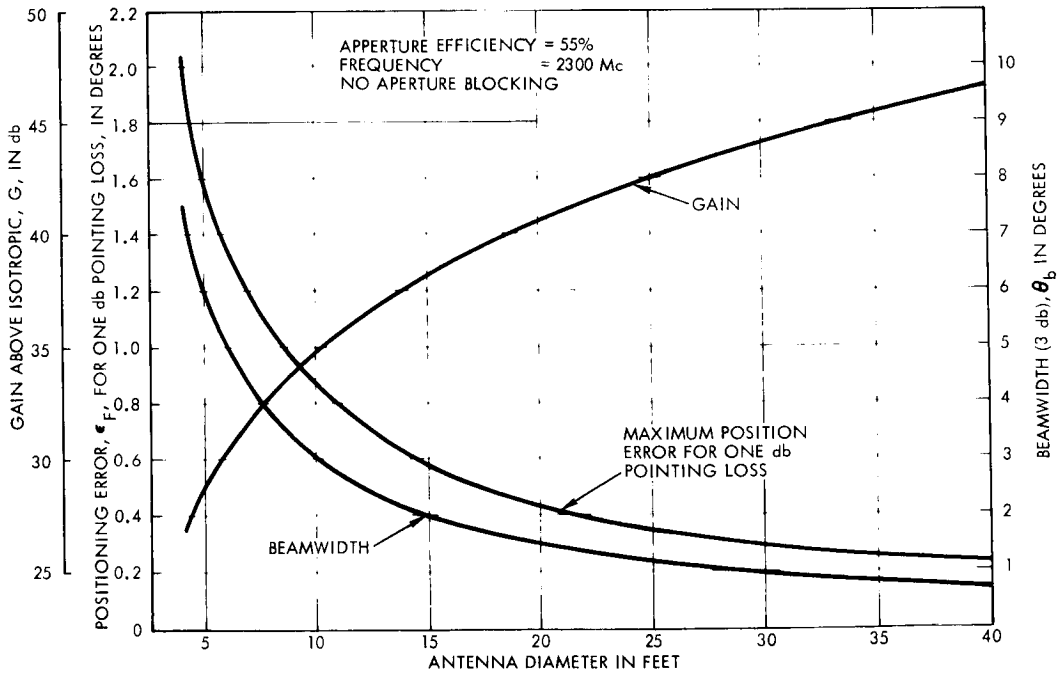

Figure 8-25. Paraboloid Antenna Performance Parameters

is 0.54 degree. It is evident that antennas of this size must be positioned very accurately. Furthermore, accurate antenna positioning should be accomplished simply. Spin-stabilized spacecraft offer such an opportunity since modified conical scan methods can be used for pointing the high-gain antenna at the earth. In this case, the RF carrier transmitted from the earth is tracked by the offset beam antennas; and pointing error signals are provided to the attitude control system.

From the results presented in Section 8.3, it appears that two tracking beams will be needed: one for acquisition and coarse tracking, another for fine tracking. The choice of the acquisition antenna is a compromise between acquisition and coarse earth-tracking requirements. It appears that antennas with beamwidths between 22 and 30 degrees would satisfy coarse tracking requirements and provide adequate acquisition coverage. Such beamwidths can be obtained with 15-inch helix antennas. The fine earth-tracking antenna characteristics are determined by the SNR required at maximum communication distance which was assumed to be 10 AU. From the expressions derived in Appendix D, it has been estimated that with reasonable signal processing techniques the fine tracking antenna beamwidth in the neighborhood of 8 degrees will be sufficient.

For acquisition a 22-inch helix with on-axis gain of 15 db and beamwidth of 25 degrees appears to be most suitable. For the fine tracking, a 4-foot parabolic antenna would be adequate. However, there is no room for a second paraboloid antenna. The use of the high gain antenna for fine tracking by addition of a second tilted feed has been examined; but, at the frequencies and antenna sizes under consideration, two feeds cannot be located at the focal point.

Another possibility is a single tilted feed for the high gain antenna. The estimated SNR needs, assuming accurate boresight axis alignment, are such that small beam offsets (less than 0.3 degree) would be adequate. It appears, however, that due to mechanical and electrical boresight axis alignment errors possible during the flight, the minimum feed offset would have to be increased to perhaps 0.5 degree. Such offsets would result in transmitting pointing losses of the order of 2 db for worst case alignment tolerances. The loss of 2 db on the downlink makes this scheme unattractive. To avoid the above problems, a movable feed for the high-gain

paraboloid dish is recommended. The simplest way to implement the telemetry and earth-tracking requirements would be with a feed having two discrete positions. When RF earth tracking is not required, the feed would be offset. Another possibility is to have a 2 degree-of-freedom positionable feed. The advantage of this mechanization is that by commands from the ground, the antenna boresight axis could be adjusted to reduce the pointing loss and defocusing to a minimum for the downlink. For tracking, the feed then would be displaced from the known on-axis position to the offset location. While the two-discrete position movable feed could be mechanized in simple manner, the hardware required to implement 2 degree-of-freedom continuous displacement (or many discrete positions) feed is less reliable. The selected two-position feed is discussed in Section 4.4.

Another earth-tracking antenna system considered was a directional array. A 40-inch diameter array assembled from 3/4-inch spiral elements would fulfill the fine positioning requirements. A subarray composed of fewer elements could be used as an acquisition antenna. This array is, however, complex and weighs 10.5 pounds; the weight of the two-position feed implementation is about a pound.

8.4.2.2 Switches

To select communication modes and improve reliability, some switching is required. Two types of switches have been considered: electromechanical and circulator. Electromechanical switches developed for the Apollo spacecraft are light (5 ounces) and require no holding power in either position. The newly developed latching circulator switches have about the same electrical characteristics, but appear to offer significantly improved reliability. The conventional circulator switches used on Mariner 4 require a holding current and need 0.2 watt operating. This type of switch, however, does not have catastrophic failure modes. In the event of loss of the holding current, the circuit becomes a transmission line with power division and increased loss due to mismatching. Therefore, complete loss of communications does not occur. The latching-type circulator switch, in case of the driver failure, remains in its previous position and does not reduce to a loss of transmission line.

8.4.2.3 Receivers

The Advanced Planetary Probe S-band receiver requirements are similar to those of Mariner 4 and several TRW space programs. The receiver must accept and process the following signals from the DSIF.

- A coherent reference for two-way doppler tracking
- Command subcarrier
- A conical scan signal to attitude control

A ranging channel, for this mission at least, is not included since ranging information is not needed during the cruise portion of the mission. Turn-around ranging cannot presently be extended to Jupiter.

Since the tracking errors and acquisition times should not limit the receiver phase-locked loop noise bandwidth, the minimum bandwidth should be consistent with design simplicity and reliability. To obtain wide dynamic range, spacecraft receivers sometimes include coherent automatic gain control (AGC). In our case AGC will also be used to coherently demodulate the conical scan signal as described in Appendix D.

Tunnel diode amplifiers may be able to provide the lowest receiver noise figure (below 4 db) as well as high gain. To insure stability, however, a four- or five-port circulator is needed. In addition, the power supply requirements are quite rigorous since the diode has to be accurately biased. Regulation of ± 0.5 percent is required. The regulated voltage is derived from a temperature-compensated Zener diode voltage regulator.

Transistors with noise figures comparable to tunnel diodes are becoming available. Unfortunately, it is not expected that the gain of these units can be made as high as that of tunnel diodes. The system noise figure for the transistor preamplifier, therefore, will be somewhat higher because of greater second-stage noise contributions.

8.4.2.4 Modulator-Exciter

The function of the modulator-exciter is to provide a phase-modulated signal to the power amplifier. The modulator-exciter for the Advanced Planetary Probe operates in either a coherent or noncoherent mode. A switch operated by the receiver AGC selects the output of the auxiliary

crystal oscillator or the coherent reference from the receiver. The signal selected by the switch is frequency-multiplied and phase-modulated by the telemetry subcarrier. The modulated carrier is then amplified to 50 milliwatts and frequency multiplied to S-band.

The modulator-exciter can be used as a low power transmitter to provide telemetry during the flight through the earth's atmosphere if desired.

8.4.2.5 Power Amplifiers

Numerous semiconductor and vacuum tube devices were considered for power amplification. The most promising devices for an output power of the order of 10 watts appear to be diode multipliers and TWT (Appendix E). Multiplier circuits utilizing the voltage-variable diodes are expected to remain the only significant solid-state RF sources for the near future. The high power signal generated by transistor stages at about 100 MHz is frequency-multiplied by silicon diodes to S-band. At present, the output is limited to 4 watts; short-term technology advances are expected to push this to 10 watts. If gallium-arsenide diode performance approaches theoretical limits, it is conceivable that 100 watts at 2 GHz may be available before 1970. Efficiency and reliability are continuously improved as a result of higher power generated by transistor drivers, thus requiring fewer stages of frequency multiplication. Conversion efficiencies of 15 to 30 percent should be readily obtainable in the near future.

TWT power amplifiers with output powers of about 10 watts have been successfully used by Mariner 4, Pioneer 6, and many other space programs. A 20-watt TWT, qualified for the Apollo program and currently in production, has minimum efficiency of 30 percent. Although tubes rated at 50 watts (40 percent tube efficiency) are available, the constraints of variable RF drive, environmental excursions, aging, and long-term power regulation are expected to yield a worst case tube efficiency of the order of 35 percent (DC/DC converter efficiency). TWT's require, however, a power supply with several stable high voltages.

8.4.3 System Comparison and Selection

The selected communication system is as shown in Figure 8-26. This system is a compromise among performance, simplicity, and reliability.

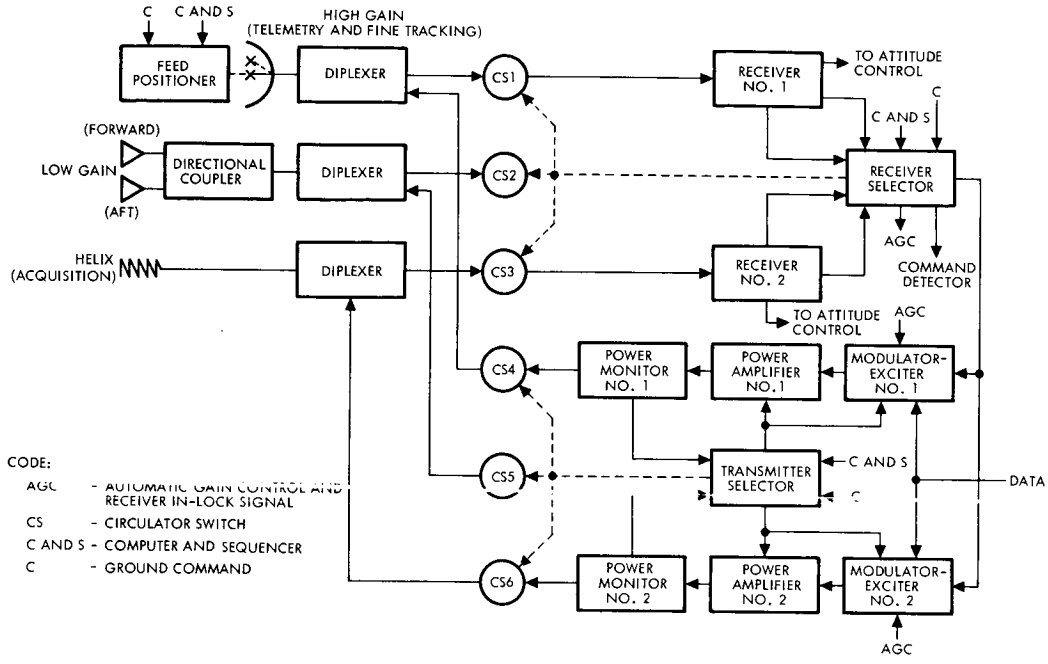

Figure 8-26. Recommended Telecommunication System for Spin-Stabilized Probe

8.4.3.1 Low-Gain Antenna

To reduce the number of switches, the two low-gain antennas have been connected through a directional coupler. To optimize the system for its nominal orientation, the forward antenna will have a 1-db insertion loss, while the aft low-gain antenna will have about 10-db insertion loss. The narrow nulls in the composite pattern caused by interference between the two antennas are not a significant problem. Both low-gain antennas will be cup-backed turnstile antennas with a maximum gain of 5 db at 90 degrees off axis.

8.4.3.2 High-Gain Antenna

The high-gain antenna is a 16-foot paraboloid with a feed having two discrete positions. Normally the feed will be located on the boresight or spin axis. When fine RF tracking is required, the feed will be mechanically positioned to the offset location by a command from the ground. A backup command from the computer and sequencer will be provided to change feed positions in case of command system failure (see also Section 4.4).

8.4.3.3 Acquisition Antenna

The acquisition or coarse tracking antenna will be a 22-inch, 22-turn, 2-inch diameter helix. The beam of this antenna will be tilted 11 degrees off axis. The on-axis gain is 15 db and the 3 db-beamwidth is 25 degrees.

8.4.3.4 Switches and Diplexers

Latchable ferrite circulator switches in conjunction with diplexers were chosen to switch transmission and reception modes. These switches are extremely reliable, have low insertion loss (0.3 db), require no holding power, and have minimum weight (5 ounces). With the recommended switching arrangement, all combinations of antennas, power amplifiers, and receivers are possible. Altogether, there are six transmission modes and five reception modes.

An alternate switching arrangement with the required antenna modes is given in Figure 8-27. Although this switching implementation is simpler

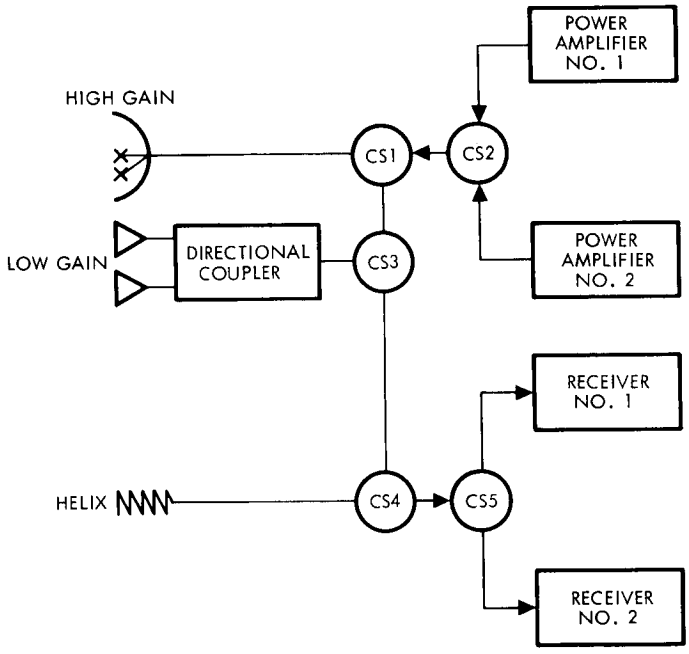

MODE	RECEIVING ANTENNA	TRANSMISSION ANTENNA
1	LOW GAIN	LOW GAIN
2	HELIX	LOW GAIN
3	HELIX	HELIX
4	HELIX	HIGH GAIN
5	HIGH GAIN	HIGH GAIN

Figure 8-27. Alternate Telecommunication System

than the former, the recommended mechanization should be more reliable. To avoid complete loss of the telemetry over the high-gain antenna, non-latchable circulator switches, requiring about 0.2 watt of holding power,

should be used in Figure 8-27. Furthermore, the transfer from acquisition antenna to fine-tracking antenna is not as elegant since both receivers cannot be used simultaneously.

Since the antennas are used for both transmission and reception, diplexers are needed. The use of different frequencies for transmission and reception facilitates design of diplexers as bandpass filters. Isolation at both transmit and receive frequencies of more than 80 db with insertion loss of about 0.3 db can be obtained. Although the antenna selection network can be designed without the use of diplexers, filters still may be required to filter power amplifier noise and to improve receiver design.

8.4.3.5 Power Amplifiers

Two redundant 10-watt TWT's with estimated nominal efficiency of 37.5 percent were selected for power amplification. Only one amplifier is operated at any time. The transmitter utilizes power monitor probes to provide on-board switching of the standby exciter and power amplifier in the event of RF power loss. Ground command backups are also provided.

8.4.3.6 Transmitter Selector

The transmitter selector provides signals to switch modulator-exciters, power amplifiers, and antennas. The normal transmitter modes are shown in Table 8-3 and the backup modes in Table 8-4. These modes are controlled by commands from the ground. Since two different antennas are always connected to two separate receivers, in case of a single antenna failure or a single receiver failure, after reorientation it will be possible to switch antennas by ground command. Power amplifiers and the modulator-exciters are controlled by the power monitor signals and commands from the ground as backup.

8.4.3.7 Modulator-Exciters

Each TWT is provided with a separate modulator-exciter. Switching of the modulator-exciter outputs between the power amplifiers is not necessary because of their high reliability compared to TWT's. Only one modulator-exciter will be turned on at any time. The modulator-exciters operate either from the coherent reference supplied by the receiver or from the auxiliary oscillator. The choice is made by the receiver AGC.

Table 8-3. Normal Transmission Modes

Normal Mode	Antenna	Circulator Switch Position CS4	CS5	CS6	Exciter and Power Amp
1	Low-gain	CCW	CW	CCW	2
2	Helix	CCW	CW	CW	2
3	High-gain	CCW	CW	CW	1

Notes: See Figure 8-26
CW = clockwise
CCW = counterclockwise

Table 8-4. Backup Transmission Modes

Backup Mode	Initial Mode	Malfunction	Antenna	Circulator Switch Position CS4	CS5	CS6	Exciter and Power Amp
4	1	Loss of power	Low-gain	CW	CCW	CCW	1
5	2	Loss of power	Helix	CW	CW	CCW	1
6	3	Loss of power	High-gain	CW	CCW	CCW	2

8.4.3.8 Receivers

Two redundant S-band receivers were selected. Each is a multiple conversion superheterodyne receiver with a phase-locked loop. The receivers lock onto and track the received signal supplying a coherent reference to the modulator-exciter, a demodulated subcarrier to the command detector, and an angle-tracking signal to the attitude control system. Each receiver will have a transistor preamplifier with a maximum system noise figure of 5.5 db. Although the tunnel diode could be built with a lower

system noise figure, the transistor preamplifier is conservatively chosen. The receiver threshold noise bandwidth of 10 Hz, rather than 20 Hz, was selected to improve communication efficiency.

8.4.3.9 Receiver Selector

Both receivers operate continuously; the output of one is selected by the preset logic in the receiver selector (subject to ground command override). In addition, the receiver selector determines receiving antenna modes. The normal and backup reception modes are listed in Tables 8-5 and 8-6, respectively. The spacecraft will be launched in Mode 1 and will remain in it until fine pointing is required. Switching to Mode 2 will be

Table 8-5. Normal Reception Modes

Mode	Mode Description	Receiver No. 3	Receiver No. 2	Circulator Switch Position		
				CS1	CS2	CS3
1	Before fine tracking	Low-gain	Helix	CCW	CW	CCW
2	When fine tracking is required	High-gain	Helix	CW	CW	CCW

Note: Underlined antenna and the corresponding receiver is chosen as the receiver selector output.

accomplished by ground command. In case of failure (no in-lock signal for preset period of time while in Mode 1), on command, Mode 3 will be selected. In case in-lock signal is not received while in Mode 2, it will be assumed that attitude control failed and, on command, receiver selector switches to Mode 1. Additional backup modes for multiple antenna-receiver, command, and attitude control failures will also be implemented in the receiver selector. This, however, requires detailed knowledge of most likely failures since it is believed that backup modes for all multiple failures are not required.

To make the switching from earth acquisition tracking to fine earth tracking (for attitude control) simpler, conical scan signals from both receivers will be supplied to attitude control system. In case one receiver

Table 8-6. Backup Reception Modes

Backup Mode	Initial Mode	Malfunction	Receiver No. 1	Receiver No. 2	Circulator Switch Position CS1	CS2	CS3
3	1	No in-lock signal; assumes receiver failure.	High-gain	Low-gain	CCW	CCW	CW
1	2	No in-lock; assumes attitude control failure.	Low-gain	Helix	CCW	CW	CCW

fails, switching from acquisition antenna to fine-tracking antenna will be accomplished by ground commands.

8.4.4 Link Performance

8.4.4.1 Modulation

The modulation method selected for both links is coherent uncoded PEM/PSK/PM. This modulation technique can be described as follows: the PCM data biphase modulates the square wave subcarrier which in turn phase modulates the RF carrier with modulation index less than $\pi/2$. This modulation method is the same as that used in Mariner 4 and Pioneer 6.

For telemetry link, the single-channel bit synchronization system was selected. This choice was based on simplicity of encoder and greater growth potential as described in Appendix F. For the command link, the two-channel PN synchronization system was chosen. Again, this choice is based on simpler spacecraft detector hardware.

Suppressed carrier techniques offering improvement in efficiency were considered for Advanced Planetary Probe communication links. The price of improved data efficiency is the inferior phase-locked loop performance and more complex receiver mechanizations. For these reasons, the suppressed carrier technique is not attractive.

Application of coding to the Advanced Planetary Probe telecommunication system was briefly investigated. For the telemetry link a 128-word biorthogonal code dictionary with potential performance improvement of 2.4 db at 5×10^{-3} error rate is most appropriate. The only disadvantage of coding appears to be the ground decoder complexity. Since a mission-dependent encoder is probably too costly, and DSIF at present does not plan to provide such decoders, coding was not selected. For command link there does not seem to be any need for coding. Choice of modulation, bit synchronization, and coding are discussed in more detail in Appendix F.

8.4.4.2 DSIF Parameters

The performance has been calculated for two DSIF station configurations. During the early portion of the mission, the standard existing 85-foot antenna, 10-kw diplexed, station configuration was assumed. Later in the mission, to support high bit rates, the 210-foot antenna (at present available at Goldstone only) will be required. According to EPD-283, 210-foot antennas will be provided for Voyager at each longitude. Furthermore, it is planned to provide one 100/400-kw transmitter at each longitude designed to operate in diplexed and low-noise temperature modes. For the Advanced Planetary Probe it was conservatively assumed that a diplexed, 210-foot, 100-kw, station configuration will be available. Note that 85-foot antenna, 400-kw transmitter is only about 3 db worse in ERP than a 210-foot antenna, 100-kw transmitter.

The receiver noise bandwidth at threshold, $2 B_{LO}$, was taken to be 12 Hz as presently implemented. There are plans, however, to provide 5 Hz and 1 Hz noise bandwidths (EPD-283). The resulting improvement in telemetry efficiency, as discussed in Appendix F, at high Advanced Planetary Probe bit rates is not significant.

8.4.4.3 System Noise Temperature

One of the parameters that determines telecommunication system performance is the system noise temperature, or noise spectral density. In turn, the noise spectral density depends on the antenna temperature. In this application, there may be occasions when the ground antennas will be pointed at Jupiter, which radiates a considerable amount of RF noise at S-band. In addition, spacecraft antennas may be pointed at the sun or

Jupiter. The increase in system spectral densities due to these sources has been computed (Appendix G). Although in some instances the degradation is large, it will occur rarely. For this reason the RF noise radiated by the sun and Jupiter should not seriously affect Advanced Planetary Probe missions.

8.4.4.4 Spacecraft-to-Earth Link

Figure 8-28 presents the telemetry link performance as a function of range for most possible modes of operation. The selected bit rates, except 8 bits/sec, are based on the engineering and science data requirements and tape recorder capacity. The 8 bits/sec rate was chosen as emergency bit rate, in case of attitude control or high-gain antenna failure.

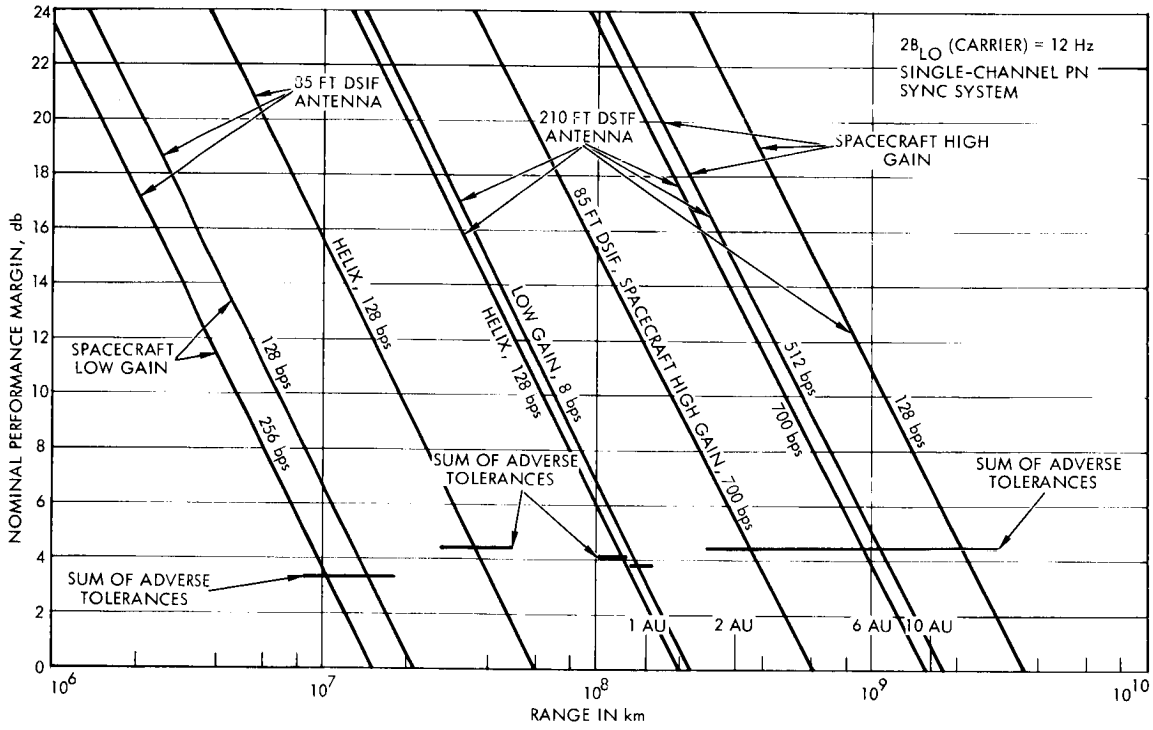

Figure 8-28. Spacecraft-to-Earth Performance Versus Range

The performance margin for each mode of operation is the nominal available signal power in a given channel (carrier, data, or sync) minus the nominal power required in that channel for threshold. For all bit rates, except 8 bits/sec, the performance margin for the data channel is given since this is the controlling channel. The sum of the adverse tolerances is found by adding all tolerances which result in SNR degradation. When

the performance margin exceeds the sum of adverse tolerances, telemetry at error rates lower than 5×10^{-3} is highly probable.

Sample telecommunications design control tables presenting performance parameters used are included in Tables 8-7 through 8-9. Table 8-9 indicates that it will be possible to transmit 700 bits/sec at the maximum Jupiter distance of 6.03 AU.

8.4.4.5 Earth-to-Spacecraft Link

Figure 8-29 shows command performance margin versus range. For the command channel, only a single bit rate (1 bit/sec) was selected. There does not appear to be a need for higher bit rates, while at lower data rates the detector mechanization becomes complicated and the total power requirements cannot be appreciably reduced. Tables 8-10 through 8-12 present most of the parameters used in calculating the results presented in Figure 8-29. As shown, reliable command capability over the low gain antenna with the 210-foot antenna and 100-kw transmitter is available all the way to 10 AU.

Spacecraft received carrier power level versus range is presented in Figure 8-30. The received carrier signal levels determine conical scan SNR (Appendix D). The conical scan SNR requirements are discussed in Section 4.4.

8.4.5 Typical Mission Profile

At launch both power amplifiers are turned off to avoid arcing while flying through the earth's atmosphere. The amplifier turn-on time will depend on the time required for the air to escape from the critical components. Since the transmitter can be turned on as late as five hours after launch, arcing should not be a problem. The minimum safe transmitter turn-on time will be determined during design and testing phases. Furthermore, special component design procedure can be followed to minimize "degassing" time.

Initially, power amplifier No. 1, switched to aft low gain antenna (transmission Mode No. 1), as indicated in Table 8-3, will be used to transmit data at 128 bits/sec to 15 million kilometers. Higher bit rates for science and to reduce ground station support requirements using the

Table 8-7. Spacecraft-to-Earth Link Performance (128 bits/sec, spacecraft low-gain, 85-foot DSIF antenna, single-channel PN sync)

Parameter	Value	Tolerance +	Tolerance -	Source
Total transmitter power	40.0 dbm	1.0	0.0	Note 1
Transmitting circuit loss	-1.7 db	0.4	0.5	
Transmitting antenna gain	+4.0 db	0.5	0.5	Note 2
Transmitting antenna pointing loss	-0.1 db	0.1	0.1	
Space loss 2295 MHz $R = 10 \times 10^6$ km	-239.7 db	0.0	0.0	
Polarization loss	-0.4 db			
Receiving antenna gain	53.0 db	1.0	-0.5	TM-33-83
Receiving antenna pointing loss	0.0 db	0.0	0.0	MC-4-310A
Receiving circuit loss	-0.2 db	0.1	0.1	TM-33-83
Net circuit loss	-185.1 db	2.1	1.7	
Total received power	-145.1 dbm	3.1	1.7	
Receiver noise spectral density (N/B) T system = 55 ± 5°K	$-181.2 \frac{\text{dbm}}{\text{Hz}}$	0.9	0.7	TM-33-83
Carrier modulation loss $Q_D = 1.25 \pm 5\%$	-10.0 db	1.4	1.8	
Received carrier power	-155.1 dbm	4.5	3.5	
Carrier APC noise BW ($2 B_{LO} = 12$ Hz)	10.8 db·Hz	0.5	0.0	TM-33-83
Carrier Performance Tracking (one-way)				
Threshold SNR in $2 B_{LO}$	0.0 db	0.0	0.0	MC-4-310A
Threshold carrier power	-170.4 dbm	1.4	0.7	
Performance margin	15.3 db	5.9	4.2	

Note 1: Adverse tolerances are listed as negative tolerances.
2: Forward low-gain antenna with 1 db directional coupler loss.

Table 8-7. Spacecraft-to-Earth Link Performance (continued)

Parameter	Value	Tolerance +	Tolerance -	Source
Carrier Performance Tracking (two-way)				
Threshold SNR in 2 B_{LO}	2.0 db	1.0	1.0	MC-4-310A
Threshold carrier power	-168.4 dbm	2.4	1.7	
Performance margin	13.3 db	6.9	5.2	
Carrier Performance				
Threshold SNR in 2 B_{LO}	6.0 db	0.5	1.0	MC-4-310A
Threshold carrier power	-164.4 dbm	1.9	1.7	
Performance margin	9.3 db	6.4	5.2	
Data Channel				
Modulation loss	-0.4 db	0.2	0.2	
Received data subcarrier power	-145.5 dbm	3.3	1.9	
Bit rate (1/T)	21.1 db·bps	0.0	0.0	
Required ST/N/B	8.5 $\frac{\text{db·bps}}{\text{Hz}}$	0.7	0.7	
Threshold subcarrier power	-151.6 dbm	1.6	1.4	
Performance margin	6.1 db	4.9	3.3	

Table 8-8. Spacecraft-to-Earth Link Performance (128 bits/sec, spacecraft helix, 85-foot DSIF antenna, single-channel PN sync)

Parameter	Value	Tolerance +	Tolerance -	Source
Total transmitter power	40.0 dbm	1.0	0.0	
Transmitting circuit loss	-1.2 db	0.3	0.3	
Transmitting antenna gain	14.5 db	0.7	0.7	
Transmitting antenna pointing loss	-2.4 db	2.4	1.0	
Space loss 2295 MHz, $R = 20 \times 10^6$ km	-245.7 db	0.0	0.0	
Polarization loss	-0.2 db	0.0	0.0	
Receiving antenna gain	53.0 db	1.0	0.5	TM-33-83
Receiving antenna pointing loss	0.0 db	0.0	0.0	MC-4-310A
Receiving circuit loss	-0.2 db	0.1	0.1	TM-33-83
Net circuit loss	-182.2 db	4.5	2.6	
Total received power	-142.2 dbm	5.5	2.6	
Receiver noise spectral density (N/B) T System = 55 ± 5°K	$-181.2 \frac{\text{dbm}}{\text{Hz}}$	0.9	0.7	
Carrier modulation loss $Q_D = 1.25 \pm 5\%$	-10.0 db	1.4	1.8	
Received carrier power	-152.2 dbm	6.9	4.4	
Carrier APC noise BW ($2B_{LO} = 12$ Hz)	10.8 db·Hz	0.5	0.0	TM-33-83
Carrier Performance Tracking (one-way)				
Threshold SNR in $2B_{LO}$	0.0 db	0.0	0.0	MC-4-310A
Threshold carrier power	-170.4 dbm	1.4	0.7	
Performance margin	18.2 db	8.3	5.1	

Table 8-8. Spacecraft-to-Earth Link Performance (continued)

Parameter	Value	Tolerance +	Tolerance -	Source
Carrier Performance Tracking (two-way)				
Threshold SNR in 2 B_{LO}	2.0 db	1.0	1.0	MC-4-310A
Threshold carrier power	-168.4 dbm	2.4	1.7	
Performance margin	16.2 db	9.3	6.1	
Carrier Performance				
Threshold SNR in 2 B_{LO}	6.0 db	0.5	1.0	MC-4-310A
Threshold carrier power	-164.4 dbm	1.9	1.7	
Performance margin	12.2 db	8.8	6.1	
Data Channel				
Modulation loss	-0.4 db	0.2	0.2	
Received data subcarrier power	-142.6 dbm	5.7	2.8	
Bit rate (1/T) 138 bits/sec	21.1 db · bps	0.0	0.0	
Required ST/N/B $P_e^b = 5 \times 10^{-3}$	8.5 $\frac{\text{db} \cdot \text{bps}}{\text{Hz}}$	0.7	0.7	
Threshold subcarrier power	-151.6 dbm	1.6	1.4	
Performance margin	9.0 db	7.3	4.2	

Table 8-9. Spacecraft-to-Earth Link Performance (700-bits/sec, spacecraft high gain, 210-foot DSIF antenna, single-channel PN sync)

Parameter	Value	Tolerance +	Tolerance -	Source
Total transmitter power	40.0 dbm	1.0	0.0	
Transmitting circuit loss	-1.2 db	0.3	0.3	
Transmitting antenna gain	38.1 db	0.5	1.0	
Transmitting antenna pointing loss	-1.0	1.0	1.0	
Space loss 2295 MHz R = 6 AU	-278.8 db	0.0	0.0	
Polarization loss	-0.1 db			
Receiving antenna gain	61.7 db	1.0	0.5	EPD-283
Receiving antenna pointing loss	-0.5 db			EPD-283
Receiving circuit loss	-0.2 db	0.1	0.1	EPD-283
Net circuit loss	-182.0 db	2.9	2.9	
Total received power	-142.0 dbm	3.9	2.9	
Receiver noise spectral density (N/B) T system = 30 ±5°K	-183.8 $\frac{\text{dbm}}{\text{Hz}}$	0.8	0.7	
Carrier modulation loss Q = 1.25 rad ±5%	-10.0 db	1.4	1.8	
Received carrier power	-152.0 dbm	5.3	4.7	
Carrier APC noise BW ($2 B_{LO}$ = 12 cps)	10.8 db·Hz	0.5	0.0	
Carrier Performance Tracking (one-way)				
Threshold SNR in $2 B_{LO}$	0.0 db	0.0	0.0	MC-4-310A
Threshold carrier power	-173.0 dbm	0.8	0.7	
Performance margin	21.0 db	6.1	5.4	

Table 8-9. Spacecraft-to-Earth Line Performance (continued)

Parameter	Value	Tolerance +	Tolerance -	Source
Carrier Performance Tracking (two-way)				
Threshold SNR in 2 B_{LO}	2.0 db	1.0	1.0	MC-4-310A
Threshold carrier power	-171.0 dbm	1.8	1.7	
Performance margin	19.0 db	7.1	6.4	
Carrier Performance				
Threshold SNR in 2 B_{LO}	6.0 db	0.5	1.0	MC-4-310A
Threshold carrier power	-167.0 dbm	1.3	1.7	
Performance margin	15.0 db	6.6	6.4	
Data Channel				
Modulation loss	-0.4 db	0.2	0.2	
Received data subcarrier power	-142.4 dbm	4.1	3.1	
Bit rate (1/T) 512 bits/sec	28.6 db · Hz	0.0	0.0	
Required ST/N/B: $P_e^b = 5 \times 10^{-3}$	8.5 $\frac{\text{db} \cdot \text{bps}}{\text{Hz}}$	0.7	0.7	
Threshold subcarrier power	-146.7 dbm	1.5	1.4	
Performance margin	4.3 db	5.6	4.5	

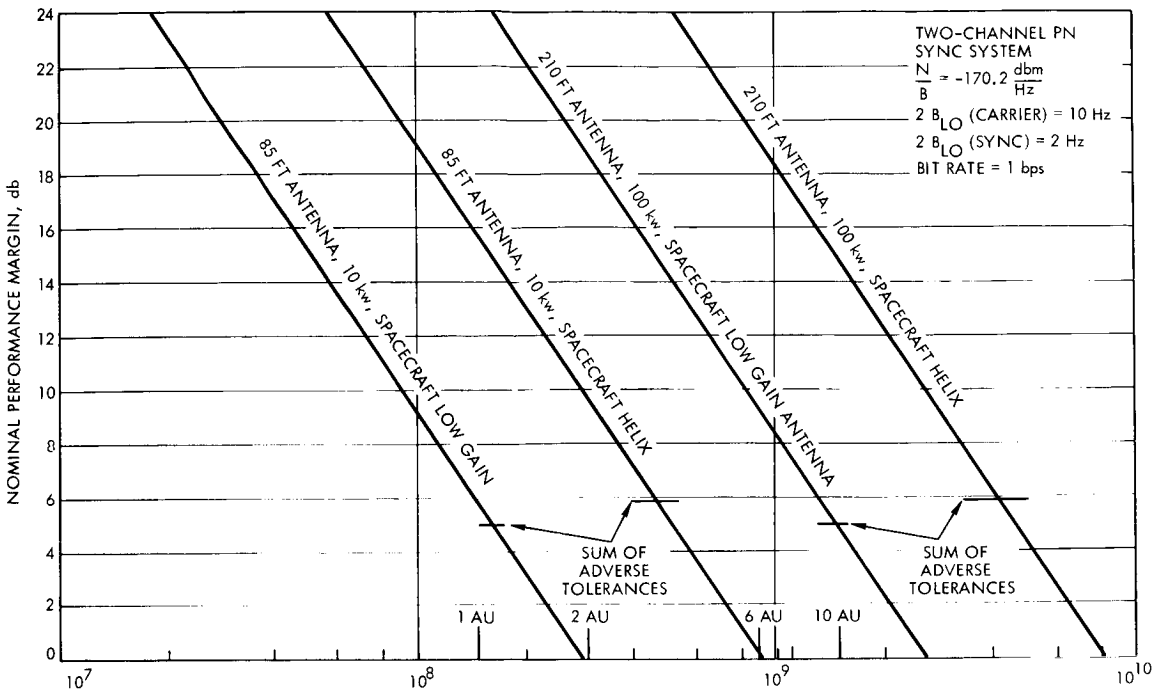

Figure 8-29. Command Channel Performance Versus Range

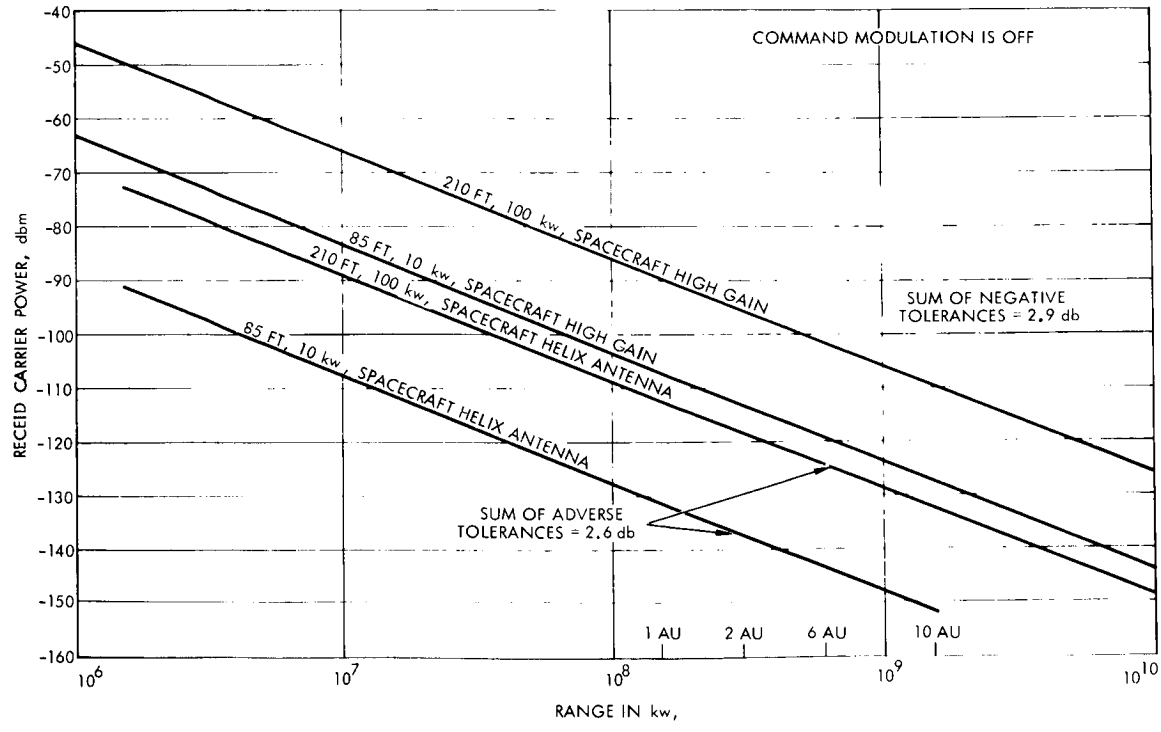

Figure 8-30. Spacecraft Received Carrier Power Versus Range

Table 8-10. Earch-to-Spacecraft Link Performance (85-foot DSIF antenna, 10 kilowatts, spacecraft low gain antenna (forward), two-channel PN sync system)

Parameter	Value	Tolerance +	Tolerance -	Source
Total transmitter power	70.0 dbm	0.5	0.0	MC-4-310A
Transmitting circuit loss	-0.4 db	0.1	0.1	MC-4-310A
Transmitting antenna gain	51.0 db	1.0	0.5	EPD-283
Transmitting antenna pointing loss	0.0 db	0.0	0.0	MC-4-310A
Space loss 2115 MIIz $R = 100 \times 10^6$ km	-259.0 db	0.0	0.0	
Polarization loss	-0.7 db			
Receiving antenna gain	3.2 db	0.5	0.5	
Receiving antenna pointing loss	-0.1 db	0.4	0.5	
Receiving circuit loss	-1.7 db	0.4	0.5	
Net circuit loss	-207.7 db	2.1	1.7	
Total received power	-137.7 dbm	2.6	1.7	
Receiver noise spectral density (N/B) T system = 870°K maximum	$-170.2 \frac{\text{dbm}}{\text{Hz}}$	1.0	1.0	
Carrier modulation loss $Q_D = 0.96 \pm 5\%$ $Q_S = 0.82 \pm 5\%$	-5.4 db	0.3	0.3	
Received carrier power	-143.1 dbm	2.9	2.0	
Carrier APC noise BW ($2 B_{LO}$ = 10 cps ± 10%)	10.0 db · Hz	0.5	0.4	
Carrier Performance Tracking (one-way)				
Threshold SNR in $2 B_{LO}$	0.0	0.0	0.0	MC-4-310A
Threshold carrier power	-160.2 dbm	1.5	1.4	
Performance margin	17.1 db	4.4	3.4	

Table 8-10. Earth-to-Spacecraft Line Performance (continued)

Parameter	Value	Tolerance +	Tolerance -	Source
Carrier Performance Tracking (two-way)				
Threshold SNR in 2 B_{LO}	3.8 db	0.0	0.0	MC-4-310A
Threshold carrier power	-156.4 dbm	1.5	1.4	
Performance margin	13.3 db	4.4	3.4	
Carrier Performance				
Threshold SNR in 2 B_{LO}	8.0 db	1.0	1.0	MC-403A
Threshold carrier power	-152.2 dbm			
Performance margin	9.1 db	5.4	4.4	
Data Channel				
Modulation loss	-7.7 db	0.6	0.6	
Received data subcarrier power	-145.4 dbm	3.2	2.3	
Bit rate (1/T) 1 bit/sec	0.0 db · Hz	0.0	0.0	
Required ST/N/B $P_e^b = 1 \times 10^{-5}$	15.7 $\frac{\text{db} \cdot \text{bps}}{\text{Hz}}$	1.0	1.0	
Threshold subcarrier power	-154.5 dbm	2.0	2.0	
Performance margin	9.1 db	5.2	4.3	
Sync Channel				
Modulation loss	-4.8 db	0.5	0.5	
Receiver sync subcarrier power	-142.5 db	3.1	2.2	
Sync APC noise BW (2 B_{LO} = 2 Hz)	3.0 db · Hz	0.8	0.8	
Threshold SNR in 2 B_{LO}	15.7 db	1.0	1.0	
Threshold subcarrier power	-151.5 dbm	2.8	2.8	
Performance margin	9.0 db	5.9	5.0	

Table 8-11. Earth-to-Spacecraft Link Performance (85-foot, 10-kilowatts, spacecraft helix, two-channel PN sync)

Parameter	Value	Tolerance +	Tolerance -	Source
Total transmitter power	70.0 dbm	0.5	0.0	
Transmitting circuit loss	-0.4	0.1	0.1	
Transmitting antenna gain	51.0 db	1.0	0.5	
Transmitting antenna pointing loss	0.0 db	0.0	0.0	
Space loss 2115 MHz R = 400 x 10^6 km	-271.0 db	0.0	0.0	
Polarization loss	-0.7 db			
Receiving antenna gain	15.0 db	0.7	0.7	
Receiving antenna pointing loss	-2.4 db	2.4	1.0	
Receiving circuit loss	-1.2 db	0.3	0.3	
Net circuit loss	-209.7 db		2.6	
Total received power	-139.7 dbm	5.0	2.6	
Receiver noise spectral density (N/B) T system = 870°K maximum	-170.2 $\frac{\text{dbm}}{\text{Hz}}$			
Carrier modulation loss $Q_D = 0.96 \pm 5\%$ $Q_S = 0.82 \pm 5\%$	-5.4 db	0.3	0.3	
Received carrier power	-145.1 dbm	5.3	2.9	
Carrier APC noise BW ($2B_{LO}$ = 10 Hz ±10%)	10.0 db · Hz	0.5	0.4	
Carrier Performance Tracking (one way)				
Threshold SNR in 2 B_{LO}	0.0 db	0.0	0.0	MC-4-310A
Threshold carrier power	-160.2 dbm	1.5	1.0	
Performance margin	15.1 dbm	6.8	3.9	

Table 8-11. Earth-to-Spacecraft Link Performance (continued)

Parameter	Value	Tolerance +	Tolerance -	Source
Carrier Performance Tracking (two-way)				
Threshold SNR in $2B_{LO}$	3.8 db	0.0	0.0	MC-4-310A
Threshold carrier power	-156.4 dbm	1.5	1.0	
Performance margin	11.3	6.8	3.9	
Carrier Performance				
Threshold SNR in $2B_{LO}$	8.0	1.0	1.0	MC-4-310A
Threshold carrier power	-152.2 dbm	2.5	2.0	
Performance margin	7.1 db	7.8	4.9	
Data Channel				
Modulation loss	-7.7 db	0.6	0.6	
Received data subcarrier loss	-147.4 dbm	5.6	3.2	
Bit rate (1/T) 1 bit/sec	0.0 db · bps	0.0	0.0	
Required ST/N/B $P_e^b = 1 \times 10^{-5}$	15.7 $\frac{db \cdot bps}{Hz}$	1.0	1.0	
Threshold subcarrier power	-154.5 dbm	2.0	2.0	
Performance margin	7.1 db	7.6	5.2	
Sync Channel				
Modulation loss	-4.8 db	0.5	0.5	
Receiver sync subcarrier power	-144.5 dbm	5.5	3.1	
Sync APC noise BW ($2B_{LO}$ = 2 Hz)	3.0 db · Hz	0.8	0.8	
Threshold SNR in $2B_{LO}$	15.7 db	1.0	1.0	
Threshold subcarrier power	-151.5 dbm	2.8	2.8	
Performance margin	7.0 db	8.3	5.9	

Table 8-12. Earth-to-Spacecraft Link Performance (210-foot antenna, 100-kilowatts, spacecraft helix, two-channel PN sync)

Parameter	Value	Tolerance +	Tolerance -	Source
Total transmitter power	80.0 dbm	-	-	EPD-283
Transmitting circuit loss	-0.4 db	0.1	0.1	EPD-283
Transmitting antenna gain	60.6 db	1.0	0.5	EPD-283
Transmitting antenna pointing loss	-0.5 db	-	-	EPD-823
Space loss 2115 MHz R = 10 AU	-282.5 db	0.0	0.0	
Polarization loss	-0.7 db	-	-	
Receiving antenna gain	15.0 db	0.7	0.7	
Receiving antenna pointing loss	-2.4 db	2.4	1.0	
Receiving circuit loss	-1.2 db	0.3	0.3	
Net circuit loss	-212.1 db	4.5	2.6	
Total received power	-132.1 dbm	4.5	2.6	
Receiver noise spectral density (N/B) T system = 870°K maximum)	-170.2 $\frac{\text{dbm}}{\text{Hz}}$	1.0	1.0	
Carrier modulation loss $Q_D = 0.96 \pm 5\%$ $Q_S = 0.82 \pm 5\%$	-5.4 db	0.3	0.3	
Received carrier power	-137.5 dbm	4.8	2.9	
Carrier APC noise BW ($2 B_{LO} = 10$ Hz) $\pm 10\%$)	10.0 db · Hz	0.5	0.4	
Carrier Performance Tracking (one-way)				
Threshold SNR in $2 B_{LO}$	0.0 db	0.0	0.0	MC-4-310A
Threshold carrier power	-160.2 db	1.5	1.4	
Performance margin	22.7 db	6.3	4.0	

Table 8-12. Earth-to-Spacecraft Link Performance (continued)

Parameter	Value	Tolerance +	Tolerance -	Source
Carrier Performance Tracking (two-way)				
Threshold SNR in 2 B_{LO}	3.8 db	0.0	0.0	MC-4-310A
Threshold carrier power	-156.4 dbm	1.5	1.4	
Performance margin	18.9 db	6.3	4.3	
Carrier Performance				
Threshold SNR in 2 B_{LO}	8.0 db	1.0	1.0	MC-4-310A
Threshold carrier power	-152.2 db	2.5	2.4	
Performance margin	14.7 db	7.3	5.3	
Data Channel				
Modulation loss	-7.7	0.6	0.6	
Received data subcarrier power	-139.8 dbm	5.1	3.2	
Bit rate (1/T)	0.0 db · bps	0.0	0.0	
Required ST/N/B $P_e^b = 1 \times 10^{-5}$	15.7 $\frac{db \cdot bps}{Hz}$	1.0	1.0	
Threshold subcarrier power	-154.5 dbm	2.0	2.0	
Performance margin	14.7 db	7.1	5.2	
Sync Channel				
Modulation loss	-4.8 db	0.5	0.5	
Receiver sync subcarrier power	-136.7 dbm	5.0	3.1	
Sync APC noise BW ($2 B_{LO}$ = 2 Hz)	3.0 db · Hz	0.8	0.8	
Threshold SNR in 2 B_{LO}	15.7 db	1.0	1.0	
Threshold subcarrier power	-151.5 dbm	2.8	2.8	
Performance margin	14.6 db	7.8	5.9	

on-board tape recorders) will require Mode 2 (helix antenna). The helix antenna will be able to support 1400 bits/sec initially, 700 bits/sec to about 15 million kilometers, and 128 bits/sec telemetry rate to about 35 million kilometers or 50 days from launch. Bit rates will be switched to 700 bits/sec at the time of interplanetary science turn-on. The 210-foot DSN antenna will be required to support 700 bits/sec after 150 days. When Jupiter is at 6 AU at encounter, the bit rate may have to be reduced to 512 bits/sec if Jupiter noise is significant. Telemetry at 256 bits/sec can be supported all the way to 10 AU (Saturn) distances.

At launch, the low gain antenna will be switched to receiver No. 1 and helix will be switched to receiver No. 2. (See Table 8-5.) Both receivers are operated continuously; however, receiver selector using built-in logic will select command subcarrier and coherent reference from receiver No. 1 initially. The RF tracking signals from both receivers will be supplied directly to attitude control system at all times. Reception Mode 1 will be adequate until fine earth tracking over the high gain antenna is needed. It is estimated that this will occur at 1 AU. At this time, ground command will be sent to switch to reception mode No. 2: receiver No. 2 connected to helix and receiver No. 1 to high gain antenna. Reception mode No. 2 will be retained to the end of mission. The 210-foot antenna and 100-kilowatts transmitter are not required with the high gain antenna.

8.5 DATA HANDLING SUBSYSTEM

8.5.1 Data Handling Requirements

The data handling subsystem performs the following functions:

- Samples and encodes 135 engineering inputs, 10 science data inputs, and TV data into a time-multiplexed PCM signal for real-time transmission or for storage.
- Converts analog inputs into 6-bit digital data for the TV experiment and for the 115 engineering analog inputs.
- Supplies timing signals to those experiments, TV, and subsystems which require synchronization with data handling or timing.

- Operates at 6 bit rates (1400, 700, 512, 256, 128, and 8 bits/sec) and in 5 sampling formats.

The five possible telemetry formats are used for cruise science both before and after planetary encounter, early encounter science, encounter science, television, and all-engineering. Except in the television format, engineering data is included as subcommutated data; the all-engineering format transmits this normally subcommutated telemetry as a main format during, for example, spacecraft maneuvers and diagnostic operations.

In the cruise science format, the following data is handled:

Experiment	Bits/Sec
Solar cosmic rays	32
Galactic cosmic rays	5
Magnetometer	24
Solar plasma	24
Micrometeoroids	14
Radio occultation	6
Total	105

In addition, the format sync and parity bits are included along with the engineering subcommutated data, science subcommutated data, and the subcommutation identification words. The engineering data incorporates 125 engineering measurements in a 128-word format. In the science subcommutation are six science inputs and 10 additional engineering inputs.

The early encounter format is the same as the cruise format except that the experiment data carried is as follows:

Experiment	Bits/Sec
Solar cosmic rays	32
Galactic cosmic rays	5
Magnetometer	24
Trapped radiation	24
Solar plasma	24
Micrometeoroids	14
Radio occultation	6
Auroral	30
Total	159

In the encounter format the experiment data is shifted to the following:

Experiment	Bits/Sec
Galactic cosmic rays	5
Magnetometer	24
Trapped radiation	24
Micrometeoroids	14
IR radiometer	28
Radio occultation	72
Auroral	30
Total	197

Usual considerations in the design of a single format include such factors as frame synchronization, frame and word sizes, etc. Additionally, it is desirable to provide a common design for all formats, since they will be used in different combinations to provide five data transmission modes.

Since the frame size is related to a multiple number of words, it is practical to consider word size prior to the choice of frame size. The following states the approximate accuracy (in bits) required from various data sources

- Science 7 to 8 bits
- Video 6 bits
- Engineering 6 to 7 bits

Using a 7-bit word appears compatible with using a 63-bit PN code to derive word synchronization. Choice of frame size should be primarily based on efficiency, i. e., it should be reasonably long so that fixed words such as group synchronization and format (or mode) identification result in a low percentage of the total bit rate capacity. A 64-word frame will be assumed for the science format and 128 words for the engineering format.

The various formats and bit rates are used in several modes of operation which are related to the mission phase and spacecraft operation. The format and mode relationships are shown in Table 8-13.

8. 5. 2 Design Approach

The design concept proposed is based on the system discussed in Section 4. 6. This concept (high rate transmission from stored data) is organized to maximize the data return and minimize ground station utilization time. Figure 8-31 illustrates the data handling subsystem. As shown, it consists of a PCM encoder and redundant tape recorder storage. Figure 8-32 illustrates the transmitted data profile, and Figure 8-33 the data sampling profile.

All input data is processed and formatted in the PCM encoder for either real-time transmission or storage. The storage is used as a buffer for the following functions:

- To match high rate TV data to real-time transmission.
- To store science data during the occultation period.
- To accumulate cruise data for compression into high data transmission periods when commanded by the uplink communications.

Each TV frame is approximately 1.5×10^6 digital data bits. This data is fitted into the telemetry formats at 256 bits/sec or about one picture every 100 minutes of transmission. To obtain a series of TV pictures taken 12 minutes apart, the digitized TV will be put into storage at about 2048 bits/sec.

An occultation period of up to six hours will occur during the encounter. Digital storage for 5.5×10^6 bits will be required to preserve all the science during this interval.

Table 8-13. Format and Operation Modes

Mission Phase	Formats	Sampling Rates (bits/sec)	Transmission Rates (bits/sec)
1 Postlaunch 2 Reorientation 3 First midcourse 4 Second midcourse 5 Fault detection and checkout	Engineering subcom operated as a main communication	128 nominal (8 backup)	1400 or 700 from storage 128 real-time 8 real-time backup
Transmission 100% Engineering			
6 Pre-encounter cruise	Cruise science main format Science subcom Engineering subcom	128 (8 backup)	1400 or 700 from storage 512 from storage 128 real-time 8 real-time backup
Transmission 95% Science, 5% Engineering			
7 Encounter Phase			
a) Early science	First encounter format		256
b) Main science plus TV	Second encounter format plus TV format		512
c) Main science	Second encounter format	256	512
d) Real-time Main science Storage	Second encounter format	128 (8 backup)	No transmission during occultation; all data stored
e) Post-occultation science real-time	Second encounter format plus stored data transmission		512
Transmission 97% Science, 3% Engineering	All modes contain engineering and science subcom		During all phases except d), real-time transmission at the lower bit rates 256, 128, and 8 bits/sec wo would be available as backup for reduced sampling transmission
8 Post-encounter cruise	Cruise science main format engineering subcom No. 1	Sampling rate reduced as distance from earth increases 128 to 8	Transmission rate decreases as distance from earth increases 512, 256, 128, and 8 from storage or in real-time
Transmission 95% Science, 5% Engineering			

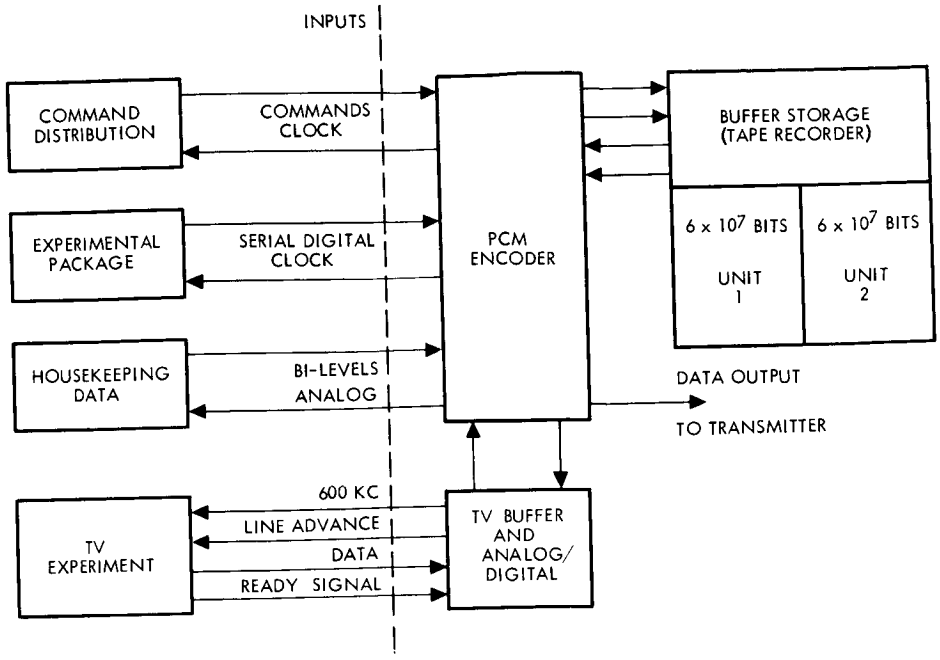

Figure 8-31. Data Handling Subsystem

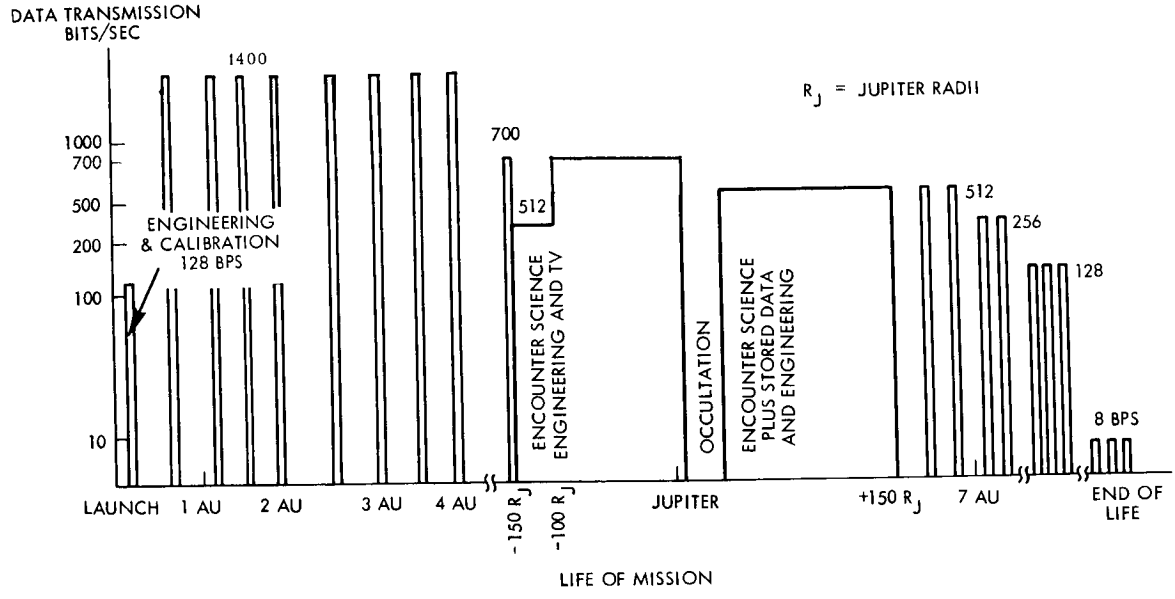

Figure 8-32. Data Transmission Profile

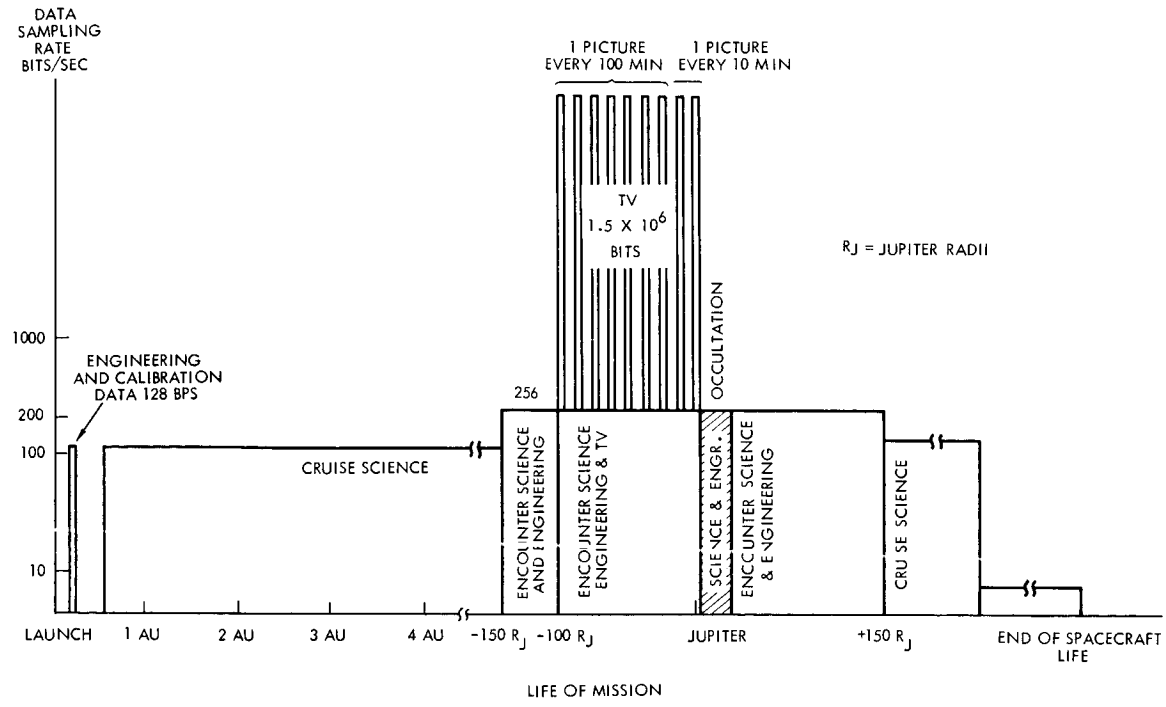

Figure 8-33. Data Sampling Profile

The use of storage during the cruise phase of the mission is an important part of the organization required to maintain continuous experimental sampling. Sampled data would be continuously recorded at 128 bits/sec and, by later transmitting at 700 bits/sec, a 5.46 to 1 compression is obtained. Monitoring time by the DSIF net is reduced to one hour for each 5.46 hours of recording. Depending on the availability of the DSIF net, available storage capacity would allow for up to 10 days of recording if both of the data storage units are utilized. Ten days of recording represents 44 hours of transmitting time.

Figure 8-34 is a more detailed block diagram of the data handling subsystem. This figure does not show equipment redundancies other than for data storage. The data handling subsystem is broken down into the following eight operational units: 1) clock and programmer, 2) digital and analog multiplexers, 3) analog to digital converters, 4) combiner, 5) format synchronization and identification generator, 6) parity generator, 7) data storage, and 8) pseudo-noise generator and binary adder.

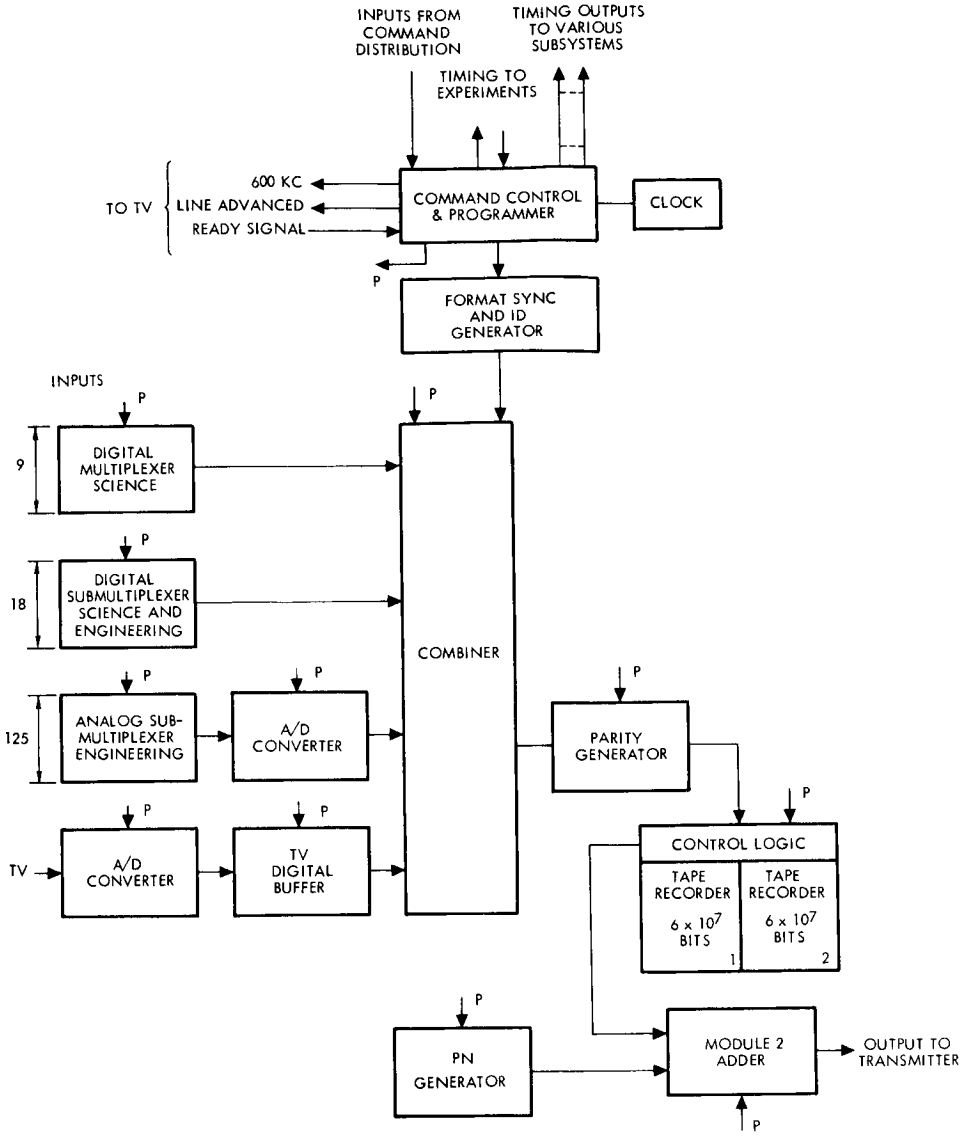

Figure 8-34. Block Diagram of Data Handling Subsystem

8.5.2.1 Clock and Programmer

In the clock and programmer unit, Figure 8-35, a crystal oscillator furnishes a stable pulse train for clocking purposes. This pulse train is counted down in the programmer. Basic timing for all units in the data handling and for other subsystems (power converters, command decoder, experiments) is taken from the programmer countdown chain. Commands from the command decoder subsystem act on the data handling through the command control logic. This programmer logic circuitry forms the control and sequencing center for the data handling. Format changes and bit rate selection are functions of this logic.

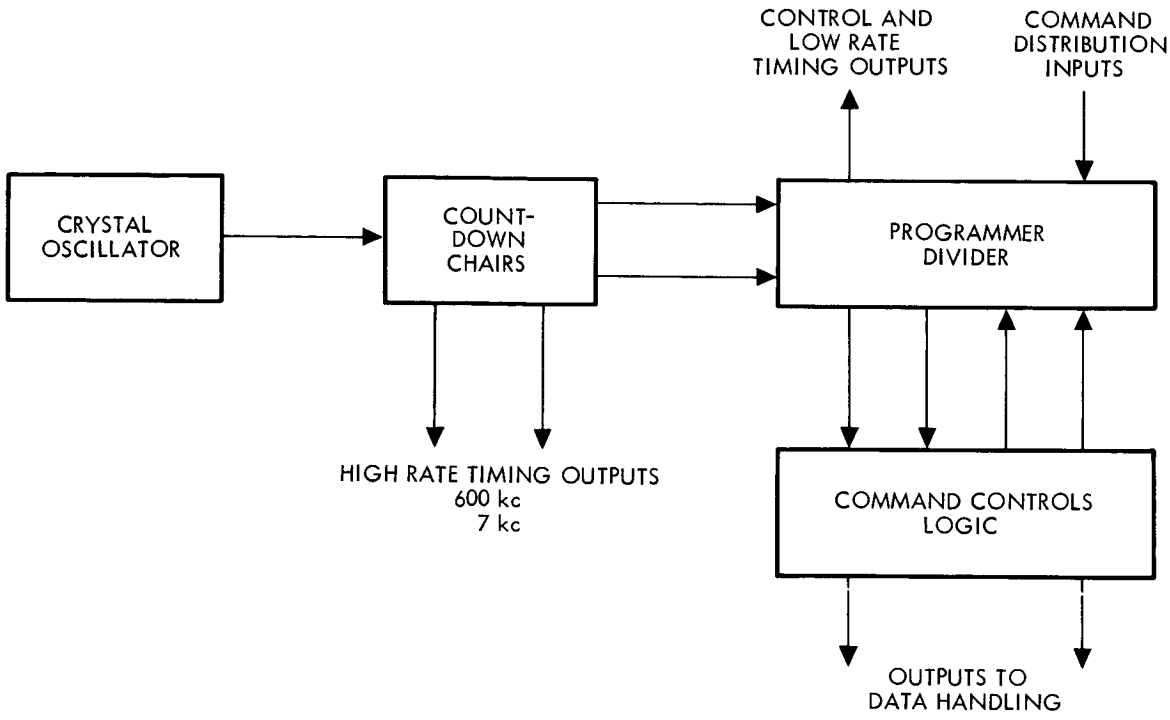

Figure 8-35. Clock and Programmer

8. 5. 2. 2 Digital and Analog Multiplexers

The digital and analog multiplexers are gating matrices. Within these matrices a gate connecting an input to the A/D (analog) or combiner (digital) is selected by a digital word from the programmer countdown chain. Each time that count is repeated the gate opens. By the prewired selection of gating signals a gate may be held open for a single bit time or several bit times. Combined with these gating terms are enable terms used to change the format of gate selection.

8. 5. 2. 3 Converters

The data handling unit requires separate analog to digital converters (Figure 8-36) to convert the engineering analog data and the vidicon experiment analog input. During the period when TV data is stored, simultaneous operation of both A/D converters would be required. Time sharing of a single converter would require buffer storage for several words of engineering data and could create a restrictive timing condition. Therefore, two A/D's are proposed to increase flexibility. Both inputs will be converted to 6 bit digital words, but at different digital rates. The analog-to-digital converter used for converting engineering data will operate at a

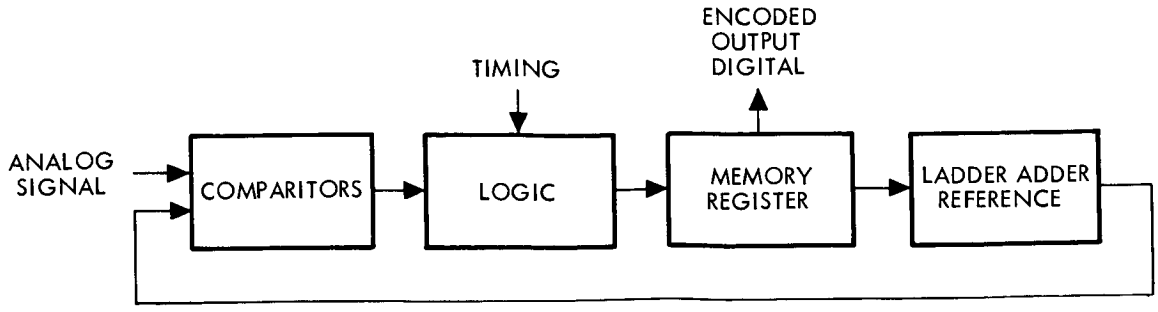

Figure 8-36. Low Rate A/D Converter

maximum rate of 512 bits/sec. The TV signal A-to-D converter will operate at a 600-kc digital rate.

The converter consists of a comparator, digital logic, memory register, and a ladder adder reference. An analog voltage is compared to a trial voltage preset in the ladder adder. At successive bit times, the A/D logic forces the trial voltages from the ladder adder to change in such a direction as to eventually approximate the input sample. Encoded binary data, triggered by each comparison, is stored in the converter memory, for serial readout to the combiner or, in the case of TV, into buffer storage.

For the TV A/D converter a modified half-split sampling technique is used to obtain the fast conversion rate required (6×10^5 bits/sec). To half-split the sample, the signal range to be converted (0 to 5 volts in this case) is split for each comparison. The first comparison determine if the sample falls in the lower half, the second comparison determines if the sample is within the upper or lower quarter of the lower half, and so on until the desired accuracy of approximation is obtained. The modified half-split sampling proposed for the TV A/D provides four subranges for each comparison, rather than two. Two ladder adders and three comparators, with attendant logic, are required for this mechanization, Figure 8-37.

The output of this A/D goes to a core storage unit which acts as a buffer between the high rate input and the slower data rate of the data handling. High rate TV sampling proceeds one TV line at a time with pauses between each line while the buffer is emptied into the telemetry stream (256 bits/sec) or into tape storage ($\approx$2048 bits/sec).

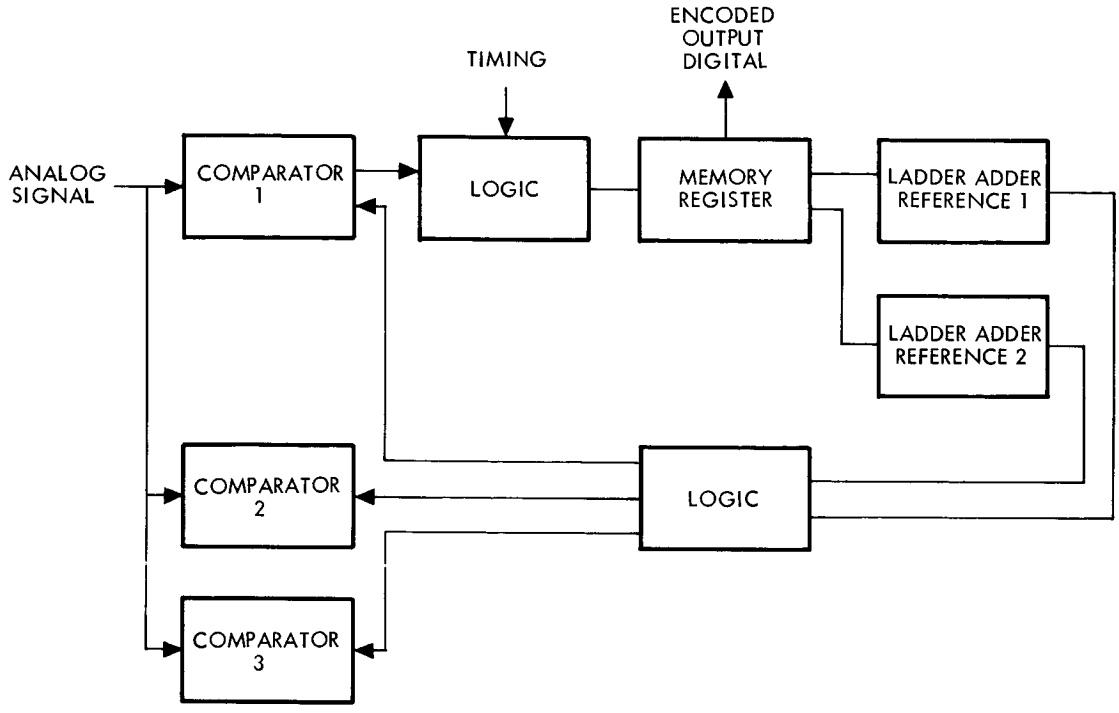

Figure 8-37. Television A/D Converter Block Diagram

8. 5. 2. 4 Combiner Unit

The combiner unit is a logic function which integrates the various digital inputs into a telemetry format with synchronizing and identifying data from the sync and ID generator.

8. 5. 2. 5 Format Synchronization and Identification Generator

The format synchronization generator furnishes digital sync and ID words to the combiner. Inputs and timing from the programmer are used to develop these words.

8. 5. 2. 6 Parity Generator

The data output from the combiner passes through a parity generator where odd parity bits are added. These bits are not added to TV data.

8. 5. 2. 7 Data Storage Units

Data storage for this subsystem is in the form of two 6×10^7 bit tape recorders. Simultaneous operation of the two recorders, to record on one while reading from the other, is proposed as a method of obtaining all data during the mission cruise phase. Logic circuitry is included to

control the selection of tape recorders and the mode of operation (read, store, or bypass for real-time transmission).

8.5.2.8 Pseudo-Noise Synchronization Generator

A single channel pseudo-noise (PN) bit synchronization technique has been selected for the telecommunications downlink. A PN word generator, clocked by the programmer, is part of the data handling subsystem. This system is taken from JPL development work and the TRW Voyager study reports.

The telemetry data and PN sync are summed in a binary adder which produces a binary composite waveform as the data handling output.

8.5.3 Reliability

The basic approach to reliability in the data handling subsystem has been to use components and techniques which have been proven reliable and to use simple, straightforward mechanization wherever possible. This approach has been further improved upon by making redundant critical portions of the subsystem (i.e., PCM encoder and tape recorders). In the event of a failure, power is switched, by ground command, to the alternate subunit. Further mission safeguards are available in alternate modes of operation such as use of one tape recorder only, switching to real-time monitoring, or reduced sampling and transmission rate modes.

8.5.4 Problem Areas

The data handling subsystem design is based principally on known techniques and components. Further improvements in the areas of integrated circuits would contribute to reductions in weight, power, and volume.

The characteristics specified for the digital tape records used in data handling are currently available in state-of-the-art recorders (high capacity, variable speeds, and low weight and power). The variable speed capabilities will require further improvement and proof of reliability. Alternately, a second small core buffer could be implemented to improve tape recorder data rate matching.

8.6 COMMAND DECODING AND DISTRIBUTION

8.6.1 Command Requirements

A list of the direct commands required for the Jupiter flight is given in Table 8-14. Up to 133 discrete commands are indicated to define the size of the output decoding and the command distribution unit.

For the most part, sequencing of spacecraft operations will be performed by ground command. The times at which discretes are to be issued are generally not tied to the occurrence of specific events. Therefore, long delays in the signal transmission time create no problem, and only a few short sequences are needed on board. These sequences are given in Table 8-15.

For on-board sequencing, 0.1-second and 1-minute granularity are needed. Consequently, two timers are needed. Approximately 20 storage locations are required to provide commands off of these timers. For the ΔV correction, a burn time of up to 400 seconds is possible. A 1-second resolution is also desirable. Thus, a 9-bit time word is necessary for one timer. For the 1-minute granularity timer, a range of several hours may be needed. It is reasonable, therefore, to allow a range of greater than eight hours and use the same number of time bits as in the 1-second timer.

8.6.2 Design

Only a few alternative designs satisfy the command requirements and are at the same time reliable, of light weight, and low power. Certain aspects of these alternatives were covered in Section 4.8.

For decoding discrete ground commands, a decoder with the capability for decoding 133 commands is needed. Since ground computation is used for midcourse maneuver, only sequencing and timing operations are involved. At most, a general purpose programmer is required (i.e., a sequencer with a random access memory). In such a system any given storage location may be used (at different times) for different functions. A command in this system must carry a tag which identifies the current function of the storage location. Thus storage requirements must include the worst case maximum tag length on each memory location along with each command.

Table 8-14. Commands

	Discrete	Quantitative
Guidance and Control System		
ACS electronics on	1	
Step size select (fine - coarse)	2	
Number of pulses		1
Maneuver select	4	
Start spinup	2	
Stop spinup	1	
Start despin	4	
Stop despin	2	
Spin speed trimmer position		1
Number of pulses for spin		1
Radio frequency tracking (on - off)	2	
Execute maneuver	1	
Propulsion System		
Explosive valve (start - stop)	8	
Data Handling and Telemetry		
Data format select (on - off)	10	
Data rate select (on - off)	10	
Recorder (read - write)	4	
Redundancy switching	4	
Science		
Experiment (on - off)	20	
Calibration, acquisition, shutter actuation	12	
Initiate calibration timer	1	
Power		
Magnetic latch relay (on - off)	20	
TWT and equipment converters (on - off)	8	
Communication		
Transmitter/antenna select	6	
Receiver mode select	2	
Receiver (on - off)	2	

Table 8-15. On-Board Sequencers

Centaur Separation (initiated by separation signal)

1. Enable G and C electronics
2. Arm pyrotechnics (backup)
3. Start vehicle spinup
4. Stop vehicle spinup
5. Ignite TE-364 (backup)
6. Separate TE-364 (backup)

TE-364 Separation (initiated by separation signal)

1. Start despin
2. Stop despin
3. Deploy high-gain antenna
4. Deploy magnetometer boom
5. Enter engineering telemetry format
6. Enter engineering data rate

Calibration (initiated by ground command)

1. Calibrate all instruments
2. Reset timer
3. Repeat calibration

Propulsion System (initiated by ground command)

1. Start midcourse burn
2. Stop midcourse burn

Science Various science sequences as required

If a special-purpose programmer is used in place of the general programmer, each memory location is wired for a specific command function. Therefore, the memory capacity is reduced by the number of tag bits. The savings in storage elements is realized at the cost of flexibility in meeting changing operational requirements. The functional diagram for the command subsystem is shown in Figure 8-38. The word format for a special-purpose programmer, derived for the commands in Tables 8-14 and 8-15 is shown in Figure 8-39.

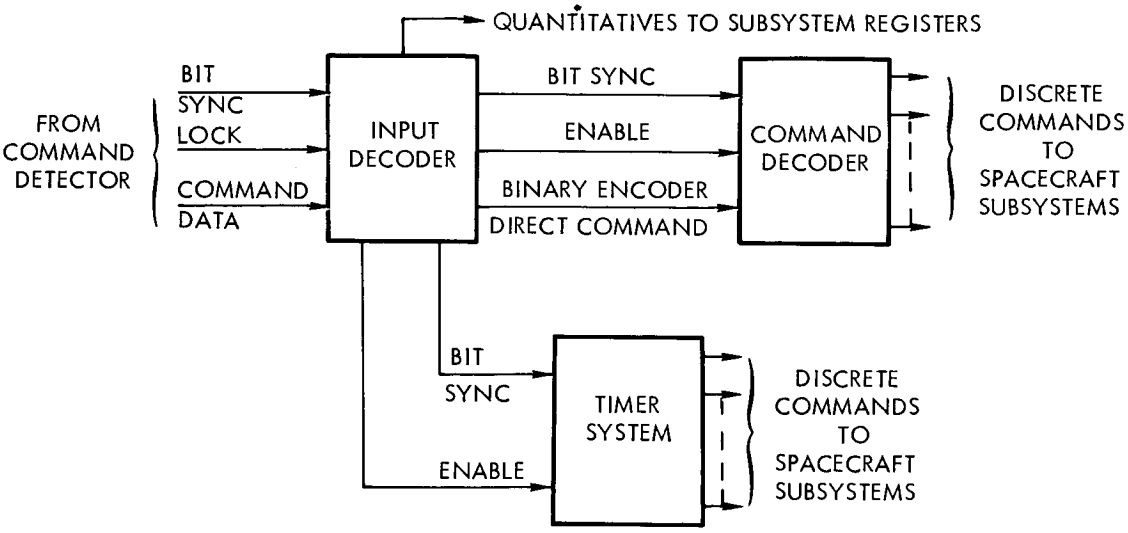

Figure 8-38. Command Distribution System Functional Diagram

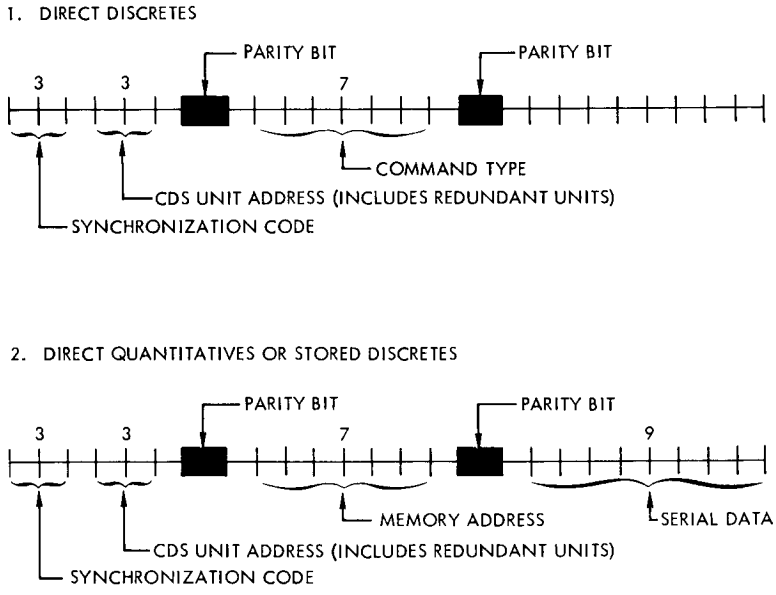

Figure 8-39. Word Formats for Special Purpose Programmer

8.6.2.1 Command Decoder

The command detector proposed for implementing the command system was taken from the JPL-developed two-channel PN synchronized system. Figure 8-40 gives the block diagram for this system. The command data rate will be 1 bit/sec through the command detector. This system was assumed as a conservative and flight-proven detector.

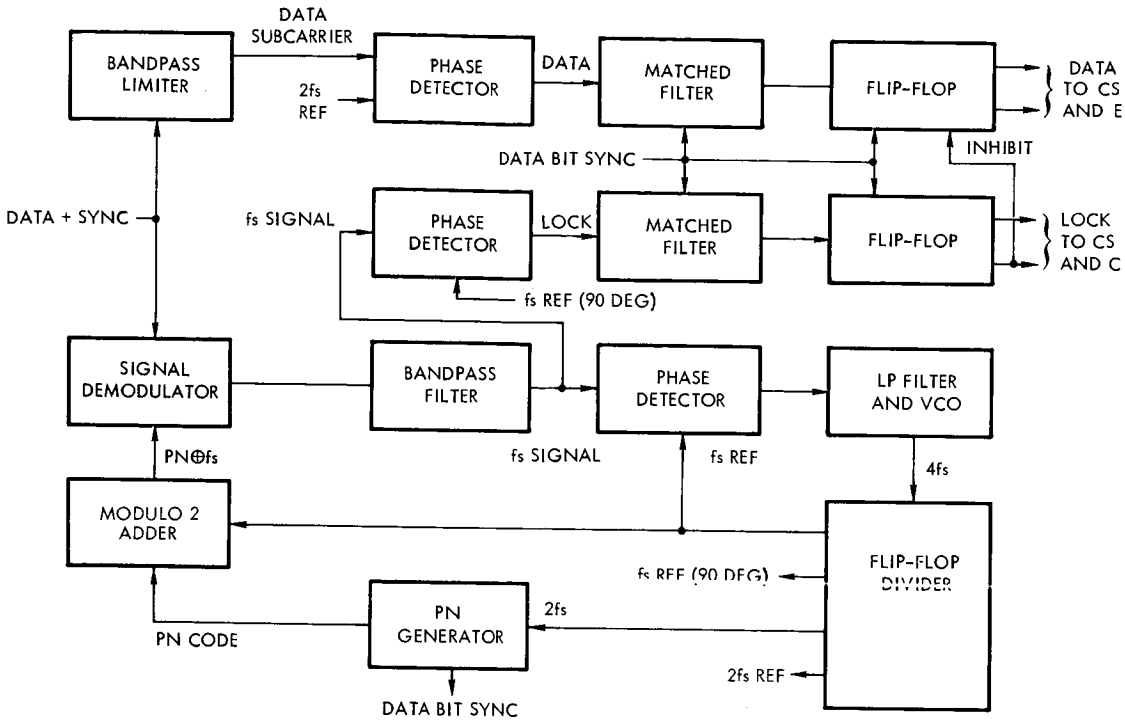

Figure 8-40. Command Detector

8.6.2.2 Input Decoder

The input decoder, Figure 8-41, receives the coded command from the command detector, performs a parity check, and enables the routing of the command data to one of seven locations. The three real-time quantitative commands go directly to external subsystem registers. Real-time discrete commands go to one of two command decoders, and timed or sequenced commands go to one of two timer systems. The command decoder and timer systems are redundant for increased reliability. The address bits in the command code determines which part of a redundant pair is used.

8.6.2.3 Command Decoder

Real-time command data goes to the selected command decoder and is set into a decoding matrix. This matrix outputs discrete commands to the spacecraft systems, Figure 8-42.

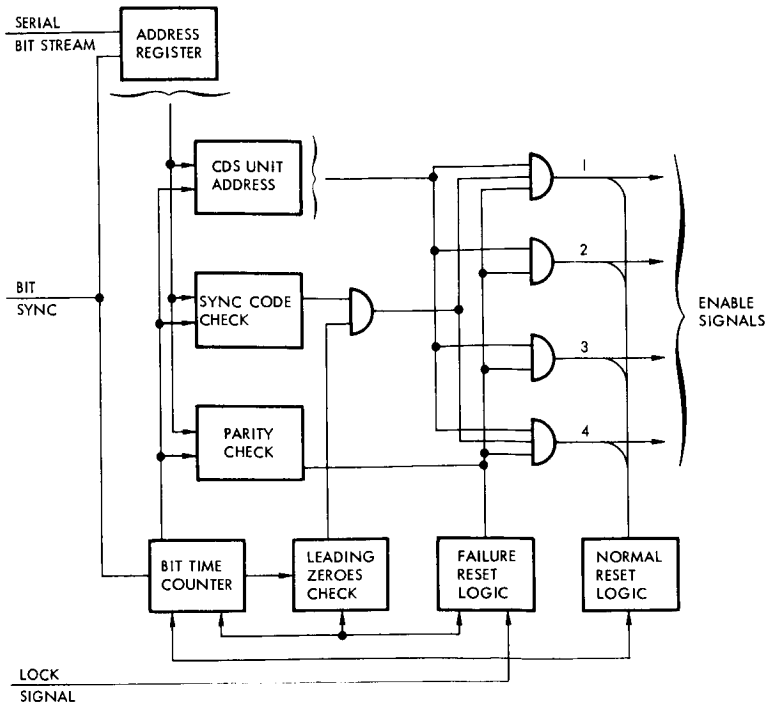

NOTE: COMMAND DECODER
1 = 1ST COMMAND DECODER
2 = 2ND COMMAND DECODER
3 = 1ST TIMER SYSTEM
4 = 2ND TIMER SYSTEM

Figure 8-41. Input Decoder

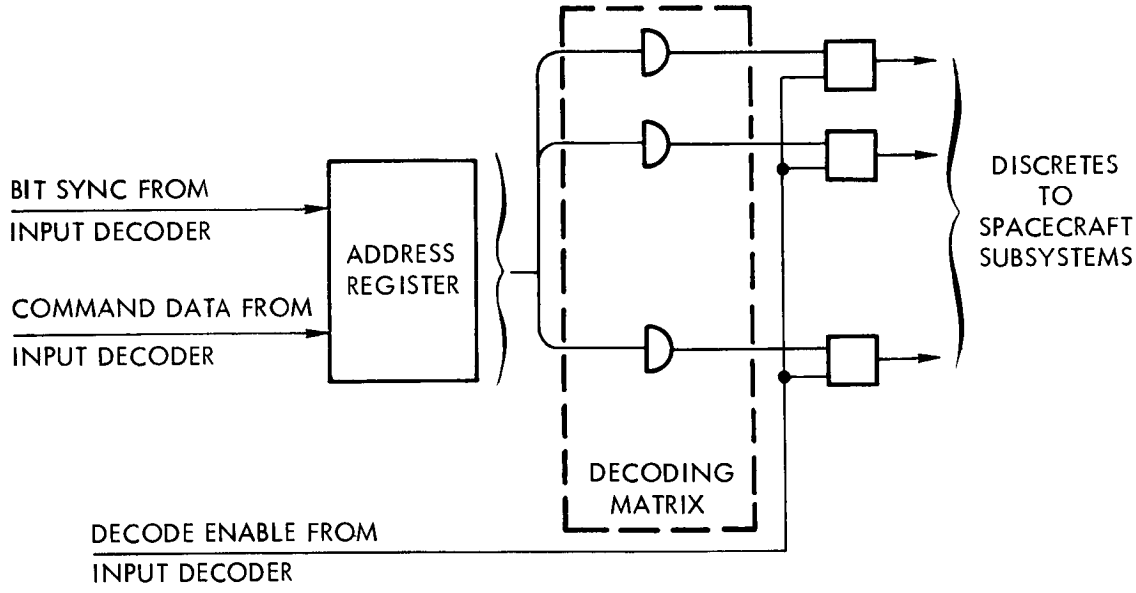

Figure 8-42. Command Decoder

8.6.2.4 Timer

The special-purpose programmer-type timer system is shown in Figure 8-43. Each timer or ΔT register contains a quantitative command which indicates a time delay between events in the sequence. The timer register contains the delay between the start of the sequence and

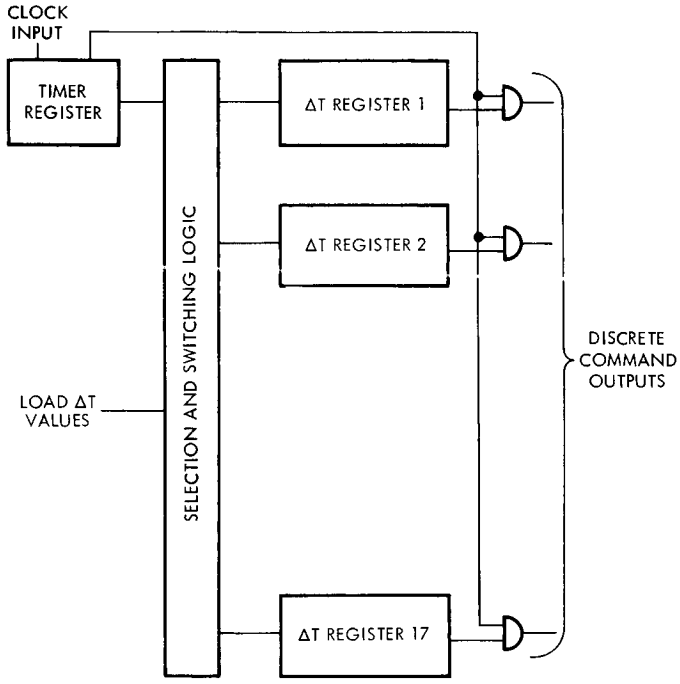

Figure 8-43. Timer System

the first command output. The command enable is accomplished by counting down the timer register to zero. At zero, three things occur: 1) a discrete command is issued, 2) the quantitative value stored in the next ΔT register is dumped into the timer register, and 3) the counting down resumes. Each ΔT register is dumped into the timer register, in turn, and at the end of each countdown the command related to that ΔT register is issued.

Several sequences may be run through the same sequencer by using discrete commands to control the output gating. Between each separate sequence the timer and ΔT registers must be reloaded with quantitative commands via the uplink. A discrete command would then be used to enable the sequencer and the correct output gating. This special purpose

programmer appears to be the simplest method of meeting all the system requirements.

8.6.2.5 Command Distribution Unit (CDU)

The CDU accepts discrete commands from the decoders or sequencers and amplifies and distributes them for use in the proper subsystem. It consists mainly of switches. The choice of switches to be used is based on considerations of reliability, weight, power consumption, etc. Three types of switches have been considered, as follows:

- Crystal-can 2 pdt relays, latching or nonlatching
- TO-5 case, 1 pdt relays
- Solid state (sample circuit shown in Figure 8-44.)

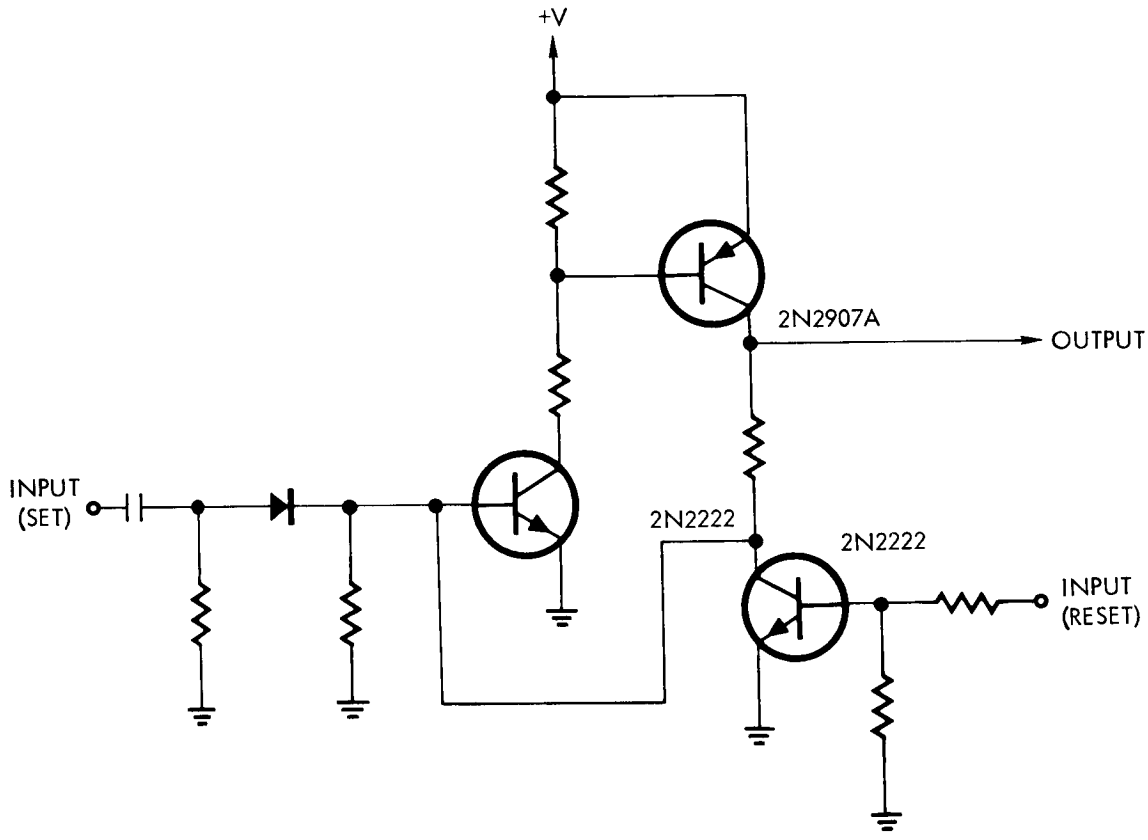

Figure 8-44. Solid State Switch (Set-Reset F-F)

A tradeoff analysis between these types brings out the following points:

- Crystal-can relays are heavier than the two other types
- For few cycles (say less than 1000) solid state switches are less reliable
- Solid state switches take power (voltage drop)
- Relays are magnetic components
- Most solid state switches have a turnoff problem with a DC supply
- Relays close two (bigger ones up to six) independent circuits
- Relays cause more interference (contact bounce, etc.)
- Relays are less susceptible to interference (spikes)
- Relays take more peak power
- Relays (latching) have "memory."

In this CDU, 130 to 160 command circuits are required. With weight and reliability as prime consideration, it is proposed to use mainly TO-5 case relays. Some highly repetitive low-level switches could be solid state (estimated at less than 5 percent) and some switching, requiring either more than 1-ampere contact load or a second set of contacts, would be crystal-can relays (estimated at 20 percent).

In general, every command uses one relay, which can be commanded from either of the two redundant decoders. Some vital circuits will use redundant relays cross-strapped from the decoders in order to further improve reliability.

The weight of the CDU can be estimated as follows:

	Ounces
10 solid state switches at 0.5 ounce	5
120 small relays at 0.15 ounce	18
30 crystal-can relays at 1 ounce	30
Enclosure	24
Mountings and wire, arc suppressors	32
Connectors	8
	117 oz ≈ 7 lb

Volume is estimated at 48 cubic inches, or about 4 x 4 x 3 inches.

The CDU receives its input in form of pulses from the command decoder (for ground commands) or from the sequencer (for on-board stored events). These pulses must be a minimum of 300 milliwatts for 2 pdt or 50 milliwatts for the smaller relays with a voltage of 18 to 28 volts and a duration of 5 milliseconds or longer.

Quantitative commands are routed directly from the decoder to the ACS register; the CDU provides only the execute command for these command sequences.

Every relay coil has two input lines from the two redundant decoder positions. At 150 command relays, this amounts to 150 or 300 connector pins. This large amount of wiring can be reduced, either by packaging the CDU and the decoders in one package or by including the decoder matrix with the CDU so that only a serial pulse train per decoder and matrix must be transferred between packages.

The outputs of the CDU are relay closures to actuators in various subsystems. The only actuators which are handled separately are the electroexplosive devices. These are fired through separate circuits (safe/arm and firing) packaged in the pyrotechnic control unit.

8.6.3 System Reliability

The design was conservatively based on proven techniques and components combined with redundancy in the command detectors, decoders, and timers. Improvements in integrated circuits and further reliability data on their reliability in space environments would affect this design by

reducing weight and power requirements. Successful integration of large low-power, semiconductor arrays for use as memories and decoder matrices could make the use of a general-purpose programmer more attractive. These developments would lead to a more flexible program design which could be extended, with little change, to the longer and more sophisticated flights.

8.7 PROPULSION

The propulsion subsystem consists of the midcourse propulsion system, a spacecraft spinup system, and a despin set of thrusters.

The spinup propulsion system is used to spin the spacecraft and third stage from 0 to 60 rpm. At Centaur separation, spin cancels out the thrust vector misalignments of the TE-364-3 injection motor. The spinup is completed in less than 1 second and is immediately followed by TE-364-3 ignition.

The despin propulsion thrusters are used to despin the spacecraft to 5 rpm, a rate which is suitable for the science payload, and yet gives adequate stability from light pressure effects, etc. Despin is accomplished in two steps, a major step before the RTG's are deployed, and a final vernier correction based on ground measurements prior to antenna deployment.

A flyby mission requires that the trajectory of the spacecraft be precisely controlled so that the time of arrival and the approach trajectory is optimized for the mission. The midcourse propulsion system satisfies this need by reducing the launch injection dispersion errors. This maneuver will be performed approximately 10 days after launch. The spacecraft will be maneuvered by the attitude control system to a precise pointing position, where the midcourse propulsion system will deliver the required corrective impulse with a capability for a backup midcourse correction.

8.7.1 Requirements

The propulsion subsystem requirements can be summarized as follows. The subsystem:

- Must have a midcourse subsystem capable of delivering a variable total impulse which can impart a maximum velocity increment of 100 meters/second to the spacecraft along the spin axis in either direction
- Must have a velocity increment with a proportional accuracy of 2 percent of the increment and nonproportional error of $\pm$0.01 meter/second
- Shall be designed for one nominal firing per thruster with a backup capability for two
- Shall be space storable for 2 years without affecting spacecraft attitude or operation
- Shall have a thrust level low enough so that the acceleration imparted to the spacecraft is less than 0.1 g
- Must be extremely reliable
- Must be capable of withstanding booster static acceleration loads
- Must withstand booster vibratory loads
- Must withstand a shock load due to shroud separation and spacecraft separation
- Must be capable of starting in a zero-g field and starting and operating in a vacuum
- Must operate satisfactorily over a temperature range of 40 to 100°F

The functional interfaces that result because of the above requirements are shown in Figure 8-45. The subsystem interfaces with:

a) Structure and mechanisms for mechanical attachment of the propellant supply and engine assembly so that it can survive the boost and launch environment

b) Data handling for storage and subsequent transfer to communications for transmission to earth of propulsion subsystem sensor outputs needed to determine subsystem operation and for performance of malfunction analysis

c) Thermal control for maintenance of propellant supply temperatures within +40 to +100°F and for providing heat to the thruster to keep the catalyst bed temperature above -40°F for engine starts

d) Pyrotechnic control for the arming, switching of signals to the required explosive valves, and for the firing and shutdown initiation power

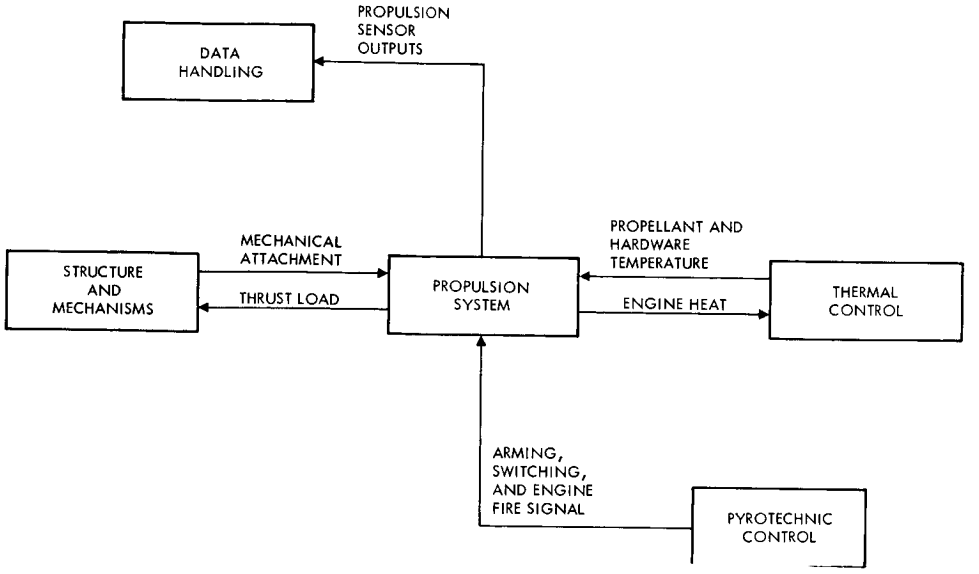

Figure 8-45. Propulsion Subsystem Functional Interfaces

8.7.2 Alternate System Implementations

The requirements to supply a variable impulse effectively precludes the use of solid propellants; therefore only liquid monopropellant and bipropellants were examined. Assuming a maximum weight of the spacecraft of 650 pounds and a maximum velocity increment of 200 meters/second, the total impulse requirement is 13,250 lb-sec. This is well below the 50,000 lb-sec total requirement where, in general, bipropellants become competitive and should be considered. The low total impulse requirement precluded consideration of a pump-fed system. Pressure fed systems were therefore selected. Monopropellants that have been used or are presently operational include hydrazine, hydrogen peroxide, ethylene oxide, and propyl nitrate. Propyl nitrate was dropped from consideration because of its shock sensitivity. Ethylene oxide and hydrogen peroxide were also eliminated because they have lower performance than hydrazine without providing any advantages. Thus, only hydrazine systems are suitable. The alternates to be considered were therefore narrowed down to either regulated or blowdown hydrazine midcourse propulsion subsystems.

Schematics of a blowdown system configuration and a regulated system containing redundant regulators are shown in Figure 8-46. The

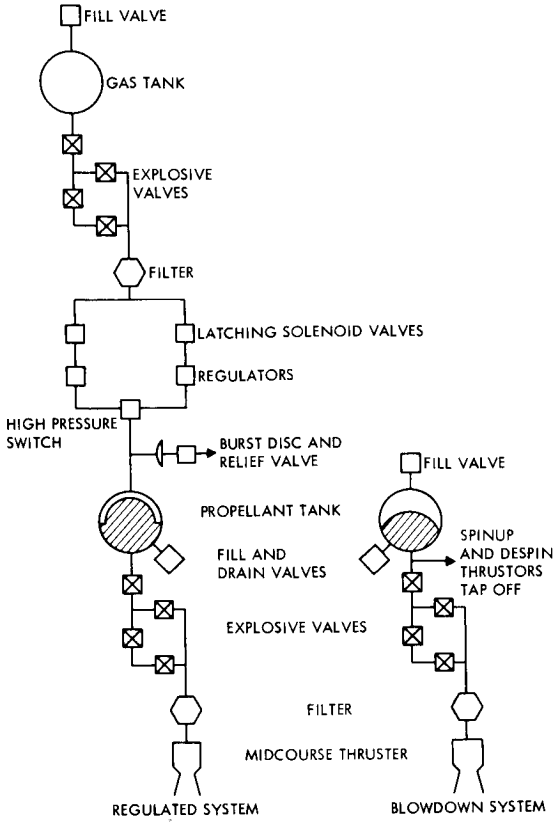

Figure 8-46. Schematics of Alternate Propulsion Subsystems

rationale behind the regulated system is to employ redundant regulators to increase their reliability and to use latching solenoid valves to cut out a failed regulator and cut in the spare one. A high pressure sensor provides the signal based on tank overpressurization. To prevent catastrophic failure, the propellant tank is fitted with a relief valve. A burst disc is incorporated upstream of the relief valve to ensure zero long-term leakage prior to relief valve operation. Explosive valves were incorporated downstream of the high pressure gas bottle to again ensure zero, long-term gas storage. Filters are used in both systems to preclude contamination of downstream components because of particles emanating from the explosive valves.

Since the exact spacecraft weight and needed velocity increment could not be determined until late in the study, propellant weights and subsequent subsystem weights were investigated parametrically over what was considered a probable range of variation. Spacecraft weights were investigated between 450 and 650 pounds for the 50-pound payload flyby

mission and to a maximum velocity increment of 200 meters/second. A plot of feed system weight versus velocity increment and spacecraft weight is shown in Figure 8-47. The curve is based on fixed-feed system

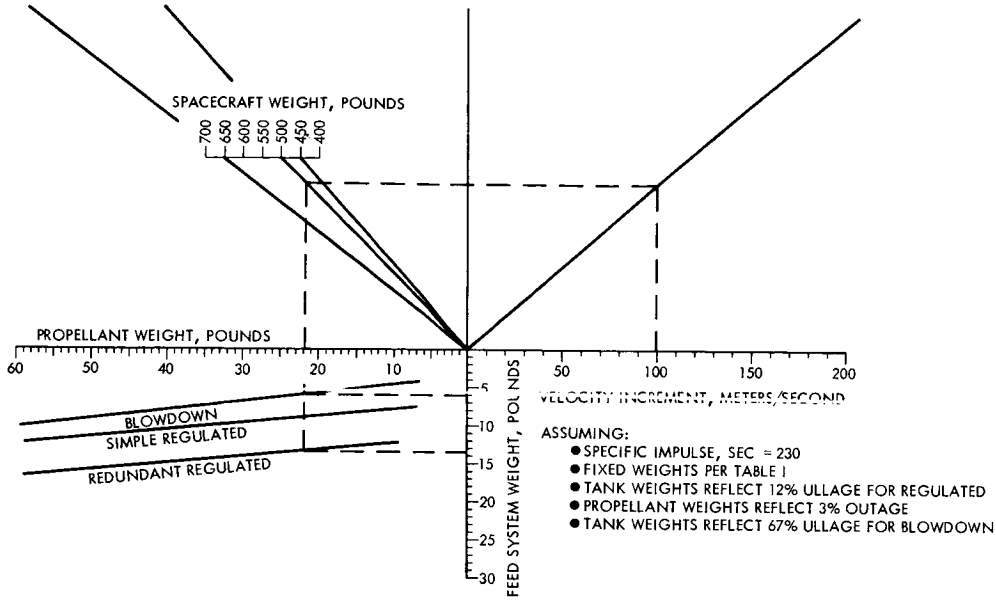

Figure 8-47. Hydrazine Feed System Weight Versus Velocity Increment and Spacecraft Weight

weights for the regulated and blowdown systems as shown in Table 8-16 which are based on using 1/4 inch components and line sizes. The variable feed system quantities are the tankage and bladder weights.

Figure 8-47 shows that the two systems have a feed system weight crossover point, but it is beyond the range of the assumed values. Assuming an initial design point of 100 meters/sec velocity increment and a spacecraft weight of 500 pounds results in feed system weight of 13.4 pounds for the regulated and 6.0 pounds for the blowdown feed systems. If the velocity increment was as high as 150 meters/sec and the spacecraft weight reached 600 pounds, the blowdown feed system weight would still be lighter by 7.0 pounds. Elimination of the redundancy in the regulated system and the resultant lowering of reliability still results in the blowdown system being lighter as shown in Figure 8-47. The accuracy of both systems is about equal. Since the blowdown system is much simpler, more reliable, and lighter, it was selected for this application.

Table 8-16. Feed System Fixed Weights for 1/4 Inch Components and Line Sizes (does not include tank or bladder)

System	Item	Quantity	Redundant Regulated (lb)	Blowdown (lb)	Quantity	Simple Regulated (lb)
Gas Pressurization	Regulators	2	2.40		1	1.20
	Lines and fittings	-	0.50			0.50
	Fill valve	1	0.15	0.15	1	0.15
	Explosive valves	4	1.00		4	1.00
	Filter	1	0.50		1	0.50
	Latching solenoids	2	1.66		0	--
	High pressure switch	1	0.50		0	--
	Burst disc and relief	1	0.75		0	--
	Pressure transducer	1	0.30	0.30	1	0.30
	Cabling	-	0.50			0.30
Propellant Feed	Temperature transducer	1	0.30	0.30	1	0.30
	Lines and fittings		0.50	0.50		0.50
	Fill and drain valve	1	0.15	0.15	1	0.15
	Explosive valves	4	1.00	1.00	4	1.00
	Filter	1	0.50	0.50	1	0.50
	Cabling	-	0.50	0.50		0.50
Total, pounds			11.21	3.40		6.90

The remaining component to be selected is the thruster. There are several factors to be considered in selecting the thrust level. On a purely weight basis, the larger the thrust level, the heavier the thruster. Figure 8-48 plots thruster weight versus thrust level over a range applicable for a spacecraft of this size for a constant chamber pressure of

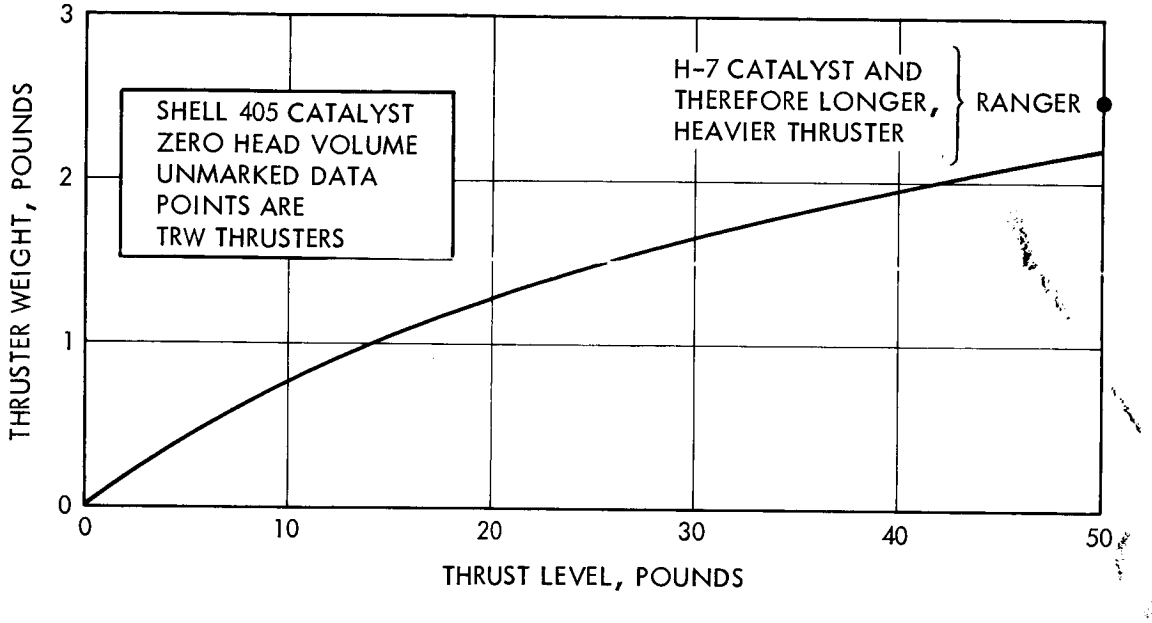

Figure 8-48. Monopropellant Hydrazine Thruster Weight Versus Thrust Level

100 psia. As can be seen, the amount of weight involved is not great and therefore is not in itself a critical factor. Thrust cannot be above a level which will impart more than 0.1 g to the spacecraft. However, with a spacecraft weighing approximately 500 pounds, a thrust level of 50 pounds produces the 0.1 g which the deployed components can tolerate. The lower limit on thrust level for a fixed amount of propellant to be burned might be engine performance or life.

Hydrazine engines are capable of almost indefinite steady-state operation. Life is generally limited by the number of pulses that can be tolerated as a function of response time. This involves degradation due to thermal shock and hydraulic mining of the catalyst bed. Since the midcourse engine will be operated in a steady-state mode, engine life is not a factor in determining selected thrust level.

The engine performance value of 230 seconds of specific impulse used for this design is a conservative one. An engine as low as a few pounds of thrust is quite capable of providing this performance, but performance falls off on engines below this level. This sets the lower limit on thrust level.

Arbitrarily 300 seconds was selected as a reasonable burn time for a hydrazine thruster. As shown in Figure 8-49, the thrust level should be about 17 pounds in order to consume 22 pounds of propellant in 250 seconds. However, with a blowdown system, the 17 pounds would be the average thrust level. The thrust requirement at initial conditions would be about 25 pounds.

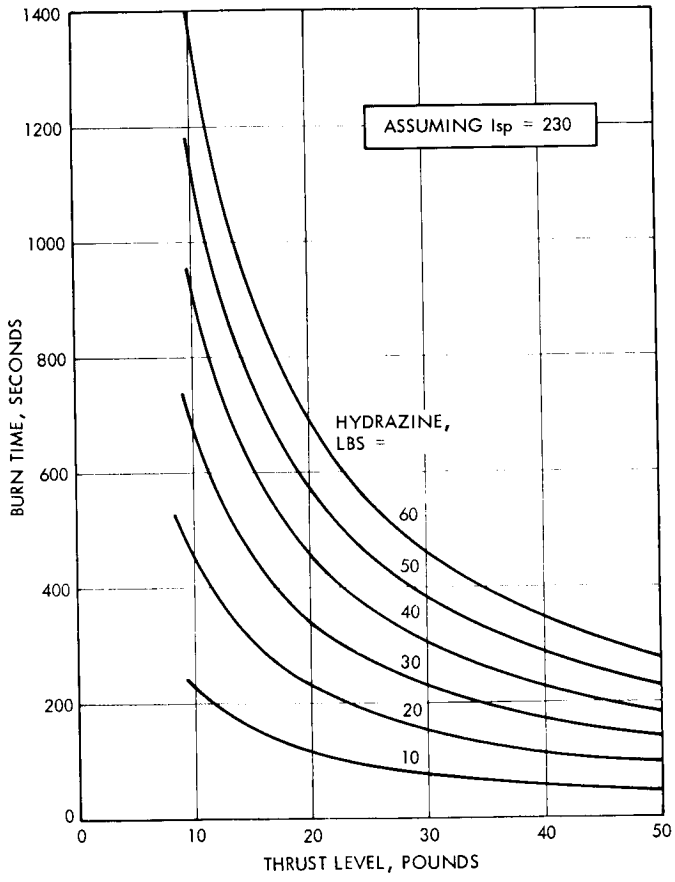

Figure 8-49. Burn Time as a Function of Thrust Level and Weight of Propellant Burned

8.7.3 Selected System

The midcourse and despin propulsion system is a blowdown system using anhydrous hydrazine for the propellant and explosive valves for initiating and terminating thrust. The system is extremely simple and uses only a few, very reliable components. The pressurant is stored on one side of the propellant tank bladder with the propellant on the other. When the downstream valve is opened, the gas forces the propellant out of the tank through the injector capillary tube into the catalyst bed where decomposition takes place and chamber pressure is created to produce thrust.

There are no regulating components and therefore no moving parts during engine operation. There are also no components held electrically open during the burn. Thrust termination is accomplished by firing another explosive valve which seals off the propellant supply reliably. A filter is provided downstream of the explosive valves to prevent clogging of the small capillary injection tubing.

The spinup motors are also part of the propulsion system. They consist of three 79-pound solid propellant thrusters.

Figure 8-50 is a preliminary specification of the midcourse propulsion subsystem. It shows the propulsion system tankage, line runs, and thrusters and their relation to the envelope of the spacecraft. It also provides information concerning the system performance, physical characteristics, and operation. Table 8-17 provides a weight breakdown of the entire system and Figure 8-51 shows the operational characteristics. The system accuracy is shown in Figure 8-52. The analysis supporting the figure is in Appendix H.

During a nominal mission operation, the midcourse correction maneuver is performed approximately 10 to 20 days after launch. The spacecraft is precessed to place the thrust vector in a position to minimize the ΔV. It is planned to supply heat to the forward thruster and lines only before firing. This is feasible because hydrazine contracts upon freezing rather than going through the more usual expansion process.

The required velocity increment to be furnished by the on-board midcourse propulsion system is transmitted through the earth-spacecraft

FUNCTION

SUPPLY MIDCOURSE VELOCITY INCREMENT FOR THE SPACECRAFT, AND SPINUP MOTORS AND DESPIN THRUSTERS REQUIRED BY ATTITUDE CONTROL

EXPLOSIVE VALVE CHARACTERISTICS

SEE FIGURE 3.7.7-13 FOR DESCRIPTION AND SPECIFICATIONS AND FIGURE 3.7.7-14 FOR DIMENSIONS

PERFORMANCE CHARACTERISTICS

	MID-COURSE	SPIN-UP	DESPIN
TOTAL IMPULSE CAPABILITY-LB-SEC	4491	200	460
THRUST, LB	25 TO 112	79	2 TO 1
MINIMUM SPECIFIC IMPULSE, SEC	230	225	230
MAXIMUM BURN TIME, SEC	258	1	230

PHYSICAL CHARACTERISTICS

	MID-COURSE	SPIN-UP	DESPIN
PROPELLANT	HYDRAZINE	ARCITE 427B	HYDRAZINE
PRESSURANT	NITROGEN	NONE	NITROGEN
NUMBER OF THRUSTERS OR MOTORS	2	3	2
PROPELLANT WEIGHT, INCLUDING ONTAGE	22.4	0.92	
PRESSURANT WEIGHT	0.73	NONE	NONE
INERT WEIGHT	11.35	1.54	5.65
TOTAL WEIGHT	34.48	2.46	6.65

PIPING SCHEMATIC

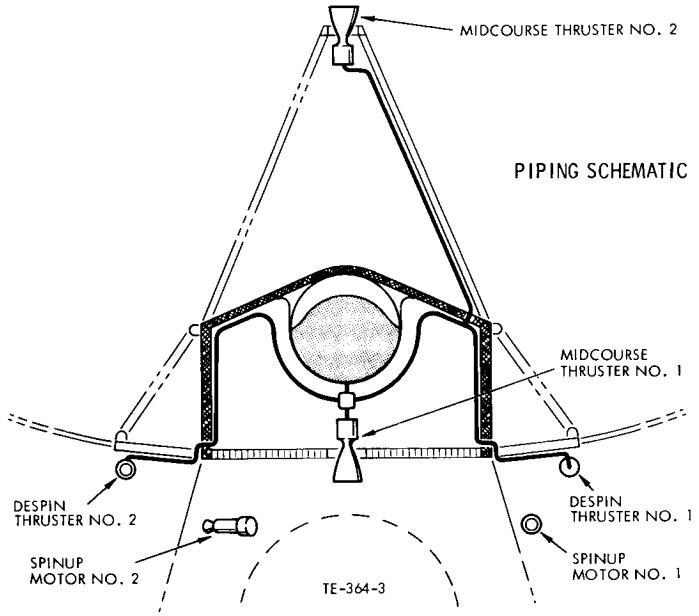

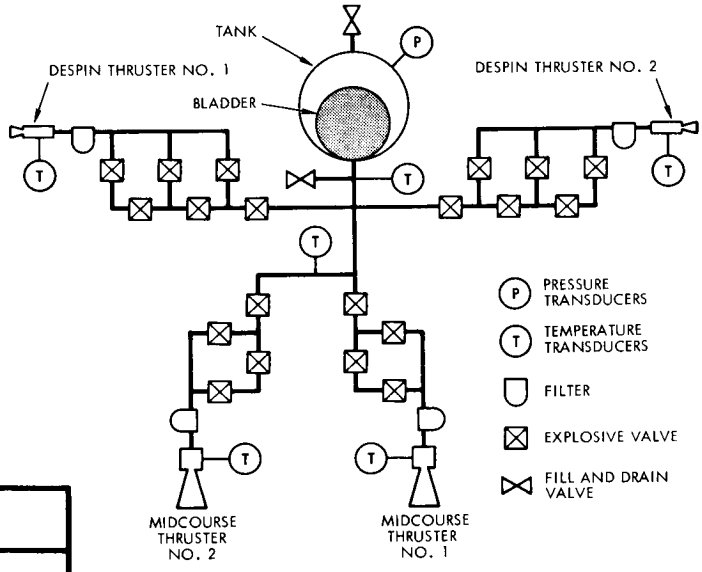

OPERATION

MIDCOURSE AND DESPIN SYSTEMS

PROPELLANT FEED BY BLOWDOWN SYSTEM. WHEN EXPLOSIVE VALVE ACTUATED, GAS PRESSURE COMPRESSES BLADDER FORCING PROPELLANT INTO THRUSTER. CATALYST BED IN THRUSTER DECOMPOSES THE HYDRAZINE GENERATING CHAMBER PRESSURE AND THRUST.

SPINUP MOTORS

SOLID MOTORS, SQUIB-ACTUATED. TENTATIVELY USED ATLANTIC RESEARCH MOTOR NO. 1KS-75

Figure 8-50. Preliminary Specification Propulsion Subsystem

Table 8-17. Propulsion System Weight Breakdown

Item	Midcourse		Despin		Spinup	
	Qty.	Weight (lb)	Qty.	Weight (lb)	Qty.	Weight (lb)
Pressure transducer	1	0.3	0		0	
Temperature transducer	4	0.4	2	0.2	0	
Propellant tank	1	2.5	0		0	
Bladder	1	0.50	0		0	
Lines and fittings		0.60		0.5	0	
Explosive valves	8	2.00	12	3.00	0	
Filter	2	1.00		1.00	0	
Cabling		0.75		0.75		0.60
Gas fill and drain valve	1	0.15	0		0	
Propellant fill and drain valve	1	0.15	0		0	
Thruster	2	3.00	2	0.20	3	1.54
Total Dry Weight		11.35		5.65		2.14
Useful propellant		21.7		1.00		0.92
Outage propellant		0.7				
Pressurization gas		0.73				
Total Weight		34.48		6.65		3.06

command link and stored in the command distribution subsystem. Initiation of subsystem operation occurs after the system has been armed by command distribution, and a signal sent to electric power to provide power to the explosive normally closed squib valve. Propellant flows to the thruster, is spontaneously decomposed by the catalyst bed, and thrusting commences. When the commanded burn time is completed, the squib of the normally open valve is fired, thus terminating the engine burn. Since the spacecraft is spinning during the entire burn, thrust vector misalignment is averaged out. There is no thrust vector control incorporated into the midcourse propulsion subsystem. Zero gravity propellant feed is assured by the employment of a positive displacement bladder.

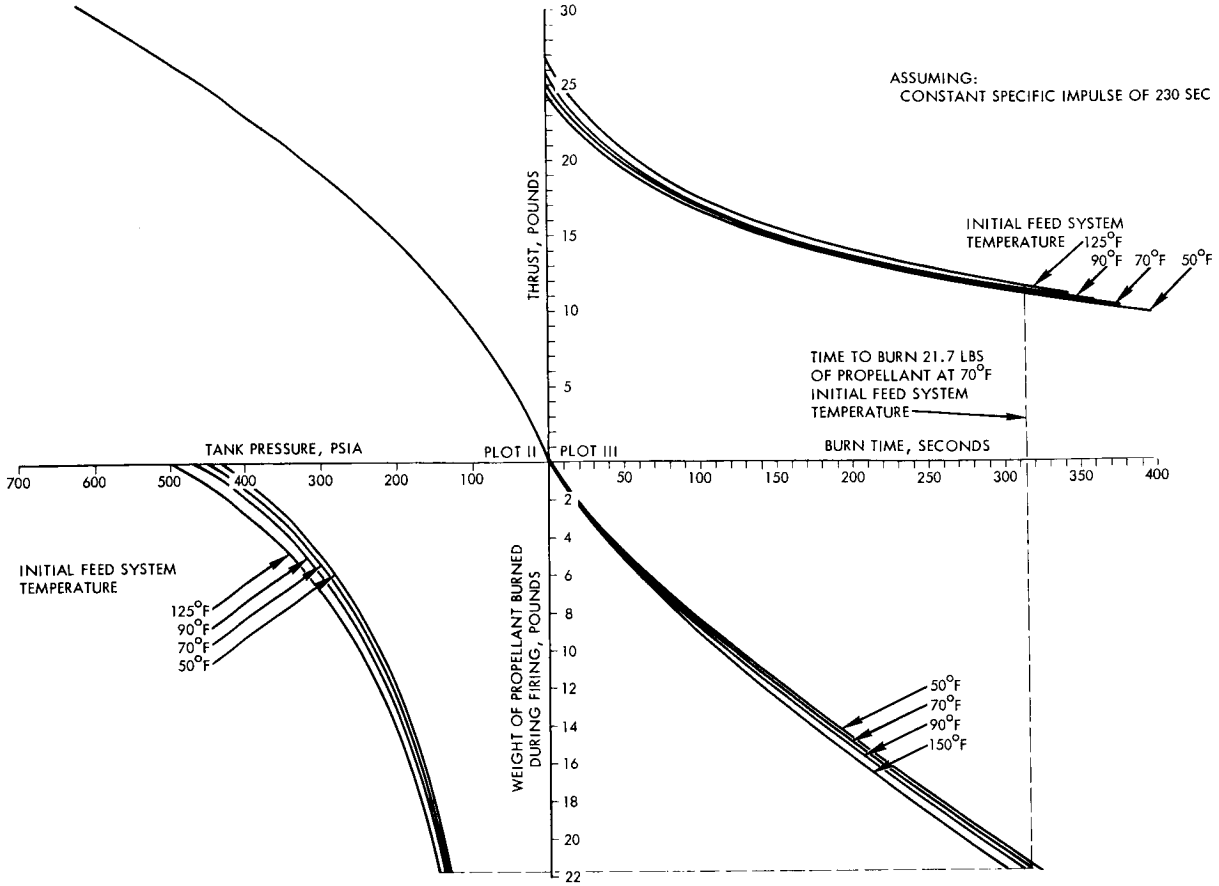

Figure 8-51. Midcourse Propulsion System Operational Characteristics

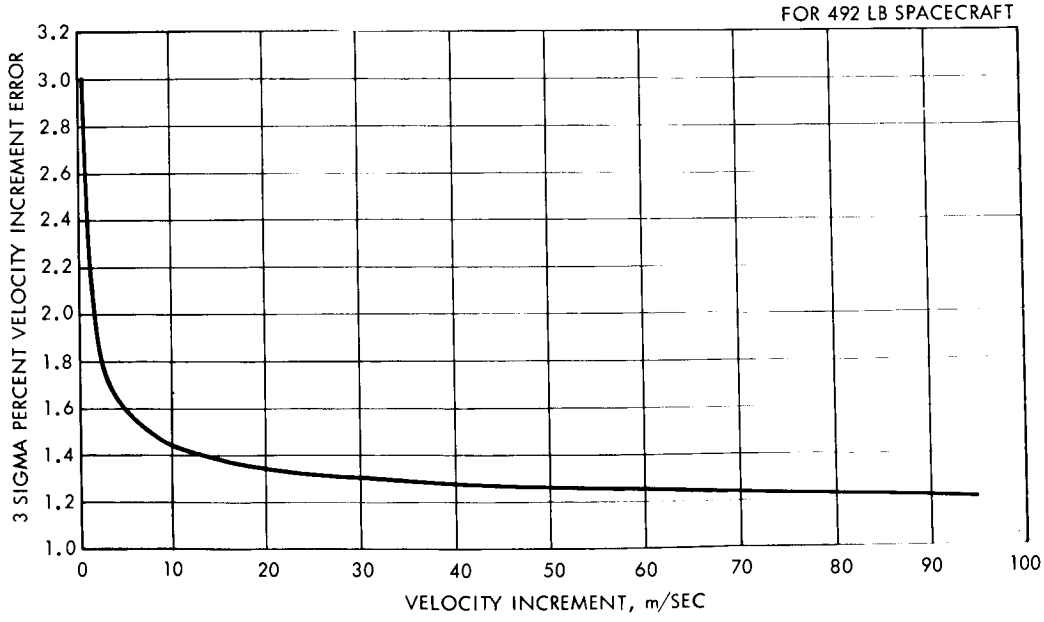

Figure 8-52. Velocity Increment Error Versus Velocity Increment

The subsystem is instrumented to determine status prior to and during operation. The outputs of the sensors are stored in data handling and are available upon command at any time. Ground calibration tests will provide data for determining burn time as a function of system temperatures and pressures. The expected execution accuracy is shown in Figure 8-52.

The dominant design criterion used for the selection of the propulsion system was high reliability for long term space flight without advancing the state of the art. Therefore, a requirement for all components was high inherent and, if possible, demonstrated reliability. Redundancy was used wherever it would clearly improve reliability. The system was designed with a set of redundant valves for one firing of either engine. The redundant valves provide for possible mechanical malfunction, or for another firing if a trajectory correction malfunction occurs.

The fuel is pressure-fed by gaseous nitrogen. Nitrogen was selected rather than lighter helium to minimize possible leakage. Liquid gas separation in zero gravity condition is assured by using a bladder to obtain positive expulsion.

The thrust variation of a blowdown system poses no particular problem since thrust decay can readily be calibrated during ground test firings.

Loss of either gas or fuel through a leaking fill, bleed, or drain valve could result in mission failure. To preclude such a failure, it was decided to use no remote disconnects for service connections. The tanks were designed with a safety factor of 2.2, which permits safe manual fueling and pressurization. The fill, bleed, drain and connections utilize valves with provisions for sealing the entire connection so that no fluid could escape from the system in the event of leakage across the inner valve seat.

One of the most crucial problems in a liquid propulsion system is the reliability of liquid flow control valves. To attain high reliability, explosively actuated valves were used in series pairs comprised of a normally open and a normally closed valve. The normally closed valve

was actuated to initiate flow, and the normally open valve was closed to stop the flow. A parallel flow circuit was provided for each engine operation. The normally closed valve incorporates a diaphragm integral with the valve body precluding leakage before use. The force produced by the explosive squib easily ruptures the diaphragm. Therefore, the reliability of the valve is essentially squib reliability. The squib type used has a demonstrated reliability of 0.999 at a 95 percent confidence level.

The normally open explosive valve utilizes the firing of a squib to force a stainless steel plug into the aluminum seat. As in the case of the normally closed valve, normally open valve reliability is essentially squib reliability.

Each component in the subsystem is provided with welded or brazed connections. The subsystem will be fully loaded and checked out prior to its mating with the spacecraft.

8.7.3.1 Thruster

The thruster is a device for decomposing the anhydrous hydrazine into its gaseous products and accelerating the gases through a nozzle and expansion cone to produce thrust. The thruster consists of an injector and a chamber which contains a Shell 405 catalyst to decompose the hydrazine. A capillary tube injector is used to provide a heat barrier between the hydrazine and the hot decomposition chamber and provide minimum dribble volume. This type of construction at TRW has resulted in smooth combustion and reliable starting in a wide range of thruster sizes and configurations. Additional heat barrier is obtained by supporting the valve and filter package off of the decomposition chamber by a small cross section, high heat resistance path support.

The catalyst is held in the chamber by stainless steel screens at both ends.

Maximum reliability is assured by the all-welded construction of the thrust chamber assembly. There are no threaded joints or bolted flanges of any kind. The cap, sleeve, and screen supports are all machined from Haynes Alloy No. 25 bar stock, while the decomposition

chamber and nozzle is spun into shape from the same material. Advantages associated with the material are low thermal conductivity, high melting point, and high creep strength at hydrazine decomposition temperatures. The capillary tube injector is a piece of drawn tubing, electron-beam welded to the filter outlet. The sleeve and cap are positioned on the filter outlet and electron-beam welded in place. The stainless steel screen assembly, previously assembled and resistance welded, is positioned with the reaction chamber and nozzle. The chamber is filled with catalyst, covered by the screen assembly, and electron-beam welded to the previously completed valve, sleeve, and cap assembly.

A preliminary specification of the thrust chamber assembly is shown in Figure 8-53. The specification contains the physical characteristics of the decomposition chamber, filter, and valves which make up the thruster unit.

Over 15 years ago it was recognized that hydrazine had the potential of becoming the principal monopropellant for use in low thrust propulsion systems and many auxiliary power generation applications. Until recently, this potential had been only partially realized because sufficiently flexible ignition techniques had not been developed. The value of the monopropellant for spacecraft midcourse corrections had been clearly demonstrated in its successful application in the Able 5*, Ranger**, and Mariner spacecraft. However, the ignition systems used in all of these applications involved the use of a hypergolic oxidizer to initiate decomposition. Such ignition systems, although completely successful to date, were suited only to a limited number of engine firing cycles. The development by NASA, approximately two years ago, of a room temperature, spontaneous decomposition catalyst has provided the basis for a simple and highly reliable ignition method for use with monopropellant hydrazine. The parametric design of monopropellant hydrazine reactors for thrusting purposes as well as gas generators has been subjected to extensive investigation, and test data is available dating back

---

*R. L. Larson, et al, "A Monopropellant Space Vehicle Propulsion System", Paper 2217-61, American Rocket Society, Oct. 1961

**D. H. Lee, "Development of the Midcourse Trajectory-Correction Propulsion System for the Ranger Spacecraft," JPL Tech. Rep. 32-335, March 15, 1963

FUNCTION
CONTROL PROPELLANT FLOW AND PRODUCE REQUIRED THRUST FOR THE MIDCOURSE MANEUVER

PHYSICAL CHARACTERISTICS OF DECOMPOSITION CHAMBER AND VALVE PACKAGE	
SIZE	
2 FT DIAMETER (NOMINAL)	
6 INCHES LONG	
WEIGHT	
DECOMPOSITION CHAMBER	1.5 LB
VALVE PACKAGE	1.0 LB
FILTER	0.5 LB
THRUST AXIS ALIGNMENT ±1/4° NOZZLE GEOMETRIC CENTER LINE TO CENTROID OF ATTACH FLANGE	

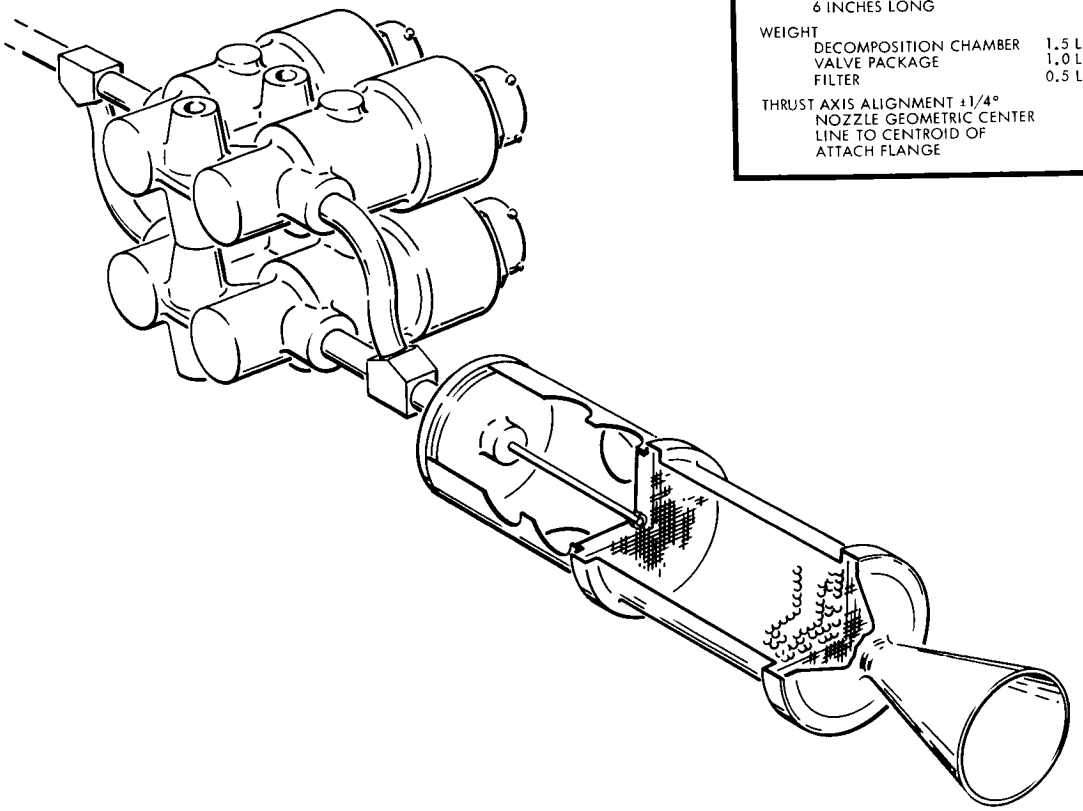

EXPLOSIVE VALVE CHARACTERISTICS
SQUIB PRESSURE SEAL GOOD TO 8000 PSI AFTER FIRING
HERMETIC SEAL LEAKAGE RATE NOT TO EXCEED 10-6 CC/SEC NTP
RECOMMENDED FIRING CURRENT - 5 AMPS APPLIED TO ONE BRIDGE WIRE
MINIMUM FIRING CURRENT - 3.5 AMPS
FUNCTIONING TIME - 4 MC
NO FIRE CURRENT - 1 AMP
POWER DRAW - 1.5 WATT-SEC FOR 0.01 SEC PER VALVE
NO FIRE - WITH STATIC DISCHARGE OF 25,000 VOLTS FROM A 500 PICOFARAD CAPACITOR APPLIED BETWEEN PIN AND CASE - WILL SURVIVE - ELECTRO-MAGNETIC FIELD OF 2 WATTS PER SQUARE METER FROM 150 KC TO 10,000 MC

DECOMPOSITION CHAMBER CHARACTERISTICS	
THRUST RANGE	25 TO 13.8 LB
PROPELLANT	ANHYDROUS HYDRAZINE
THRUST INITIATION	SPONTANEOUS PROPELLANT DECOMPOSITION UPON EXPOSURE TO CATALYST
CATALYST	SHELL 405
PROPELLANT INJECTION	CAPILLARY TUBING
NOMINAL CHAMBER PRESSURE RANGE	185 PSIA INITIAL TO 102 FINAL
VACUUM CF	1.73
NOZZLE EXPANSION RATIO	40:1
MINIMUM VACUUM SPECIFIC IMPULSE:	230 SEC
THRUST BUILDUP (VALVE SIGNAL TO 90% F)	22±1 MC
MINIMUM IMPULSE BIT	
INITIAL	0.19
FINAL	0.12

Figure 8-53. Preliminary Specification Thrust Chamber Assembly

to the early 1950's. Perhaps the most authoritative document on the design of hydrazine reactors is by A. F. Grant, Jr.* Although Grant's work was done with the nonspontaneous catalysts available at that time, his basic analysis with appropriate extension is applicable to the design of reactors utilizing any type of catalyst, including the spontaneously reacting Shell 405. Operational data available at TRW as a result of many reactor developments permits a high degree of confidence in the design of the 1- and 25-pound thrust engines.

8.7.3.2 Injection and Catalysis

Experience with catalytic monopropellant reaction chambers using H-7, HA-3, TRW 1404-21, and Shell 405 catalysts has shown that the most important factors to consider in the design of monopropellant hydrazine devices are:

- The injection technique and depth of penetration of liquid hydrazine into the catalyst bed
- The heat transfer, mass transfer, and fluid flow processes which occur within the catalyst bed

These transport processes are, of course, intimately related to the injection technique, the catalyst particle size and shape, and the catalyst bed geometry.

The sequence of processes which occur in a monopropellant-hydrazine reactor may be described as follows.

- Liquid hydrazine enters the chanber and contacts the catalyst bed.
- The incoming liquid hydrazine is heated to its vaporization point by contact with the catalyst bed and with leaving hot gases.
- The temperature of the hydrazine vapor rises to the decomposition temperature.
- The catalyst accelerates the exothermic decomposition of the hydrazine into nitrogen, hydrogen, and ammonia. From previous studies, this decomposition appears to occur in accordance with the following reaction: $2N_2H_4 = 2NH_3 + N_2 + H_2$.

* A. F. Grant, "Basic Factors Involved in the Design and Operation of Catalytic Monopropellant Hydrazine Reaction Chambers, JPL Rep. 20-77.

- The catalyst accelerates the endothermic dissociation of a portion of the ammonia formed in the above reaction into nitrogen and hydrogen by the following reaction: $2NH_3 = N_2 + 3H_2$.
- The decomposition products leave the catalyst bed and exit from the chamber through an exhaust nozzle.

It has been shown in work at JPL using H-7 and HA-3 catalysts, and more recently by the Shell Development Corporation and TRW Systems, that a certain minimum depth of catalyst bed is necessary in order to establish a stable reaction zone in a reactor. The depth of this zone is dependent upon the uniformity of the distribution of the incoming hydrazine across the inlet surface of the catalyst bed, the size of the hydrazine droplets, the activity and temperature of the catalyst bed, the surface area of catalyst particle per unit volume, the void space between catalyst particles, and the flow density ($lb/sec/in^2$) of reactor cross section. This depth is also dependent upon the concentrations of impurities such as water, and additives such as hydrazine nitrate in the hydrazine.

8.7.3.3 Injector

Penetration of liquid hydrazine into the bed is essential to obtain rapid start transients. Thus, the hydrazine is forced into contact with a relatively large catalytic surface compared to that available at or very near the top of the catalyst bed, and a proportionally accelerated decomposition is realized. Conversely, this penetration must be carefully controlled to prevent channeling, or localized flow, through the catalyst bed with subsequent rough or unstable operation of the combustor and high pressure regions which tend to crush the catalyst. Hence, an intelligent compromise is indicated.

Irrespective of the nature of a particular application or of the size and type of catalyst employed in a monopropellant hydrazine reactor, an optimum injection technique should:

- Distribute the propellant through the catalyst bed
- Subdivide the propellant into small increments so that each of the increments may be rapidly heated and vaporized on contact with the catalyst

- Prevent heat soakback so that the incoming fuel will not decompose explosively in the injector

In addition, for minimum impulse bit operation, the short and reproducible ignition delay and the rapid thrust rise and decay rates required make it necessary to employ an injection technique that will:

- Minimize dribble volume
- Minimize the volume upstream of the catalyst bed required for propellant distribution and atomization

TRW Systems has developed and is currently testing a proprietary modified capillary tube injector which repeatedly meets these criteria. This injector is designed to operate with no "head volume" or space above the catalyst bed, thus minimizing the length of the engine and alleviating mass transport delays above the catalyst bed.

8.7.3.4 Catalyst Bed

The schedule anticipated for the Advanced Planetary Probe dictates the use of a readily available catalyst. This constraint, together with the requirement for spontaneous ignition of hydrazine, limits consideration to the materials listed in Table 8-18. Shell 405 and TRW 1404-21 are, however, nearly identical. The Shell catalyst has been selected for the Advanced Planetary Probe because Shell is currently in production. TRW Systems can produce the catalyst if an alternate source becomes necessary, however.

Table 8-18. Available Hydrazine Spontaneous Catalysts

Catalyst	Support	Sizes
Shell 405	Pressed alumina	1/8 x 1/8 inch pellets 14-20 mesh aggregate 20-30 mesh aggregate
TRW 1404-21	Pressed alumina	1/8 x 1/8 inch pellets 1/16 x 1/16 inch pellets

With the advent of the Shell 405 catalyst, great latitude in the configuration of the catalyst beds for monopropellant hydrazine was

realized. Earlier hydrazine engine designs which used JPL's H-7 or HA-3 catalysts characteristically required catalyst beds with L/D ratios greater than 1. The Ranger and Mariner midcourse engines, for example, had an H-7 catalyst bed L/D of 1.3. A Ranger engine was modified by TRW Systems to use Shell 405. This 50-pound thrust engine has a catalyst bed L/D of 0.9, contains 32.5 percent less catalyst than Ranger, and exhibits smoother combustion characteristics. The design flexibility allowed by Shell 405 is due to its exceptionally high catalytic activity with hydrazine.

Empirical data on the design of spontaneous catalyst reactors is largely unplublished or proprietary, although significant work has been done at JPL, TRW, and elsewhere. A general discussion of the basic factors involved follows.

In fixed bed catalytic reactors, the rate of mass transfer of reactants from the gas stream to the catalyst pellets, and the transfer of reaction products from the pellets to the gas stream, play an important role in determining the overall rate of a catalytic decomposition. Mass transport becomes particularly important when the surface reaction rate is very fast, such as the catalytic decomposition of hydrazine.

From studies of the three-zone conceptual model for hydrazine decomposition in a fixed bed reactor proposed by Grant (op cit) and others*, it was concluded that in the initial vaporization zone in which 30 to 40 percent of the hydrazine is decomposed, the overall reaction rate is controlled by the rate of mass transfer. Using recent mass transfer correlations,** preliminary calculations at TRW have confirmed Armstrong's conclusion. Although strictly applicable to gas flow through a packed bed rather than to the two-phase flow postulated by Armstrong, the Yoshido correlation should still predict the effect of particle size and flow rate on the rate of

*W. E. Armstrong, et al, "Development of Catalysts for Monopropellant Decomposition of Hydrazine", Final Report, Contract NAS7-97, Aug. 31, 1963

**F. Yoshido, D. Ramaswami, and O. A. Hougen, J Amer. Inst. Chem. Eng., Aug. 5 and 16, 1962

mass transfer in the vaporization zone with fair accuracy. This correlation is

$$r_v \sim G^{0.59} a_v^{1.41}$$

where

r_v = overall conversion rate per unit bulk volume of catalyst

G = mass flow rate per unit of cross-sectional area

a_v = external or geometrical surface area of the catalyst pellets per unit volume of the catalyst bed

Examination of the above relationship shows that the predominate factor in determining the rate of a diffusion-controlled reaction is the external surface area of catalyst particles per unit volume of the reactor. Therefore, optimizing the catalyst bed design with respect to diffusion-controlled reactions requires minimizing catalyst particle size and maximizing the bulk density of the bed. Unfortunately, minimizing the catalyst particle size and bed porosity will also maximize the pressure drop across the bed. Hence, optimization of the bed design with respect to diffusion-limited reactions must be accomplished while limiting the catalyst bed pressure drop. A method of calculating the pressure loss associated with a flow of fluids through a catalyst bed was derived from the Fanning equation by Grant,

$$\Delta P_c = K\left(\frac{a_v^{1-f}}{F_v^{1.7}}\right)(G)^{2+f}\left(\frac{L_c}{P_c}\right)$$

where

K = experimentally determined constant

f = exponent

a_v = Geometric surface area of catalyst particles in a unit volume of catalyst bed

F_v = porosity of the catalyst bed

G = mass flow rate per unit cross-sectional area of the catalyst bed

L_c = depth of catalyst

This relationship was applied in analyzing the bed geometry for the Advanced Planetary Probe engines. The low package diameters available dictated the use of relatively high G values. It is important to note, however, that the injection technique used implies the use of a modified G value, or G', for calculating bed drop because the hydrazine is not sprayed over the surface of the bed in the classical manner.

The basic problem is reduced to one of packaging the required amount of catalyst within the space available, maintaining acceptable flow patterns from the injector through the bed, and supporting the catalyst in such a way as to protect it from crushing pressure loads and vibration.

8.7.3.5 Effect of Thrust Decay Time

Monopropellant hydrazine engines have a characteristically longer decay time than similar bipropellant engines. This is due to the reaction kinetics of the system, i.e., the extremely low decomposition rate of hydrazine at low pressures. Although it is possible to maintain very low volume between the propellant valve and the catalyst bed, this volume is emptied by "boiling" after the valve is closed. This greatly extends the tail-off trace because of the very low pressures and driving forces present as the dribble volume clears. Ten percent of the operating pressure is reached in approximately 25 milliseconds, but tangible pressure exists for over 100 milliseconds.

8.7.3.6 Steady-State Operation

Characteristically, monopropellant engines operate with a finite roughness. This is not to be compared to combustion instability in bipropellant engines because it is an entirely different phenomenon. The roughness in a hydrazine engine accrues from the slight variations, or oscillations, of the reaction zone of the catalyst bed. These oscillations are minimized in engines of long length because of the damping effect of the volume. Large volume engines are not compatible with small impulse bit operation, however.

A major objective in the design of all TRW hydrazine engines has been to maintain acceptable steady-state characteristics. Figure 8-54

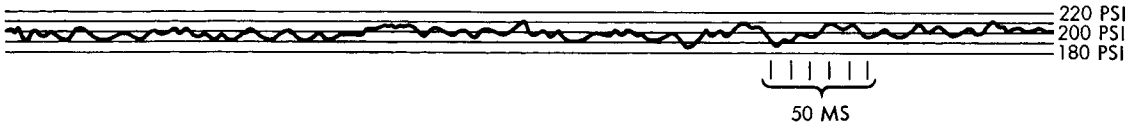

Figure 8-54. Steady State Operation

shows a portion of a steady-state trace made with a flight type 3-pound thrust engine. The pressure oscillations are random and are in the order of ±5 percent of nominal chamber pressure. There is no tendency toward "flooding" with its characteristic high amplitude, very low frequency chugging and pressure decay. This engine represents an excellent compromise in that it retains very good qualities in all modes of operation.

The nozzle expansion ratio selection is relatively unrestricted by kinetic limitations, such as the water condensation problem encountered with hydrogen peroxide. At expansion ratios greater than 40:1, however, little performance advantage is realized. Figure 8-55 shows the theoreticle relationship between thrust coefficient and expansion ratio. The

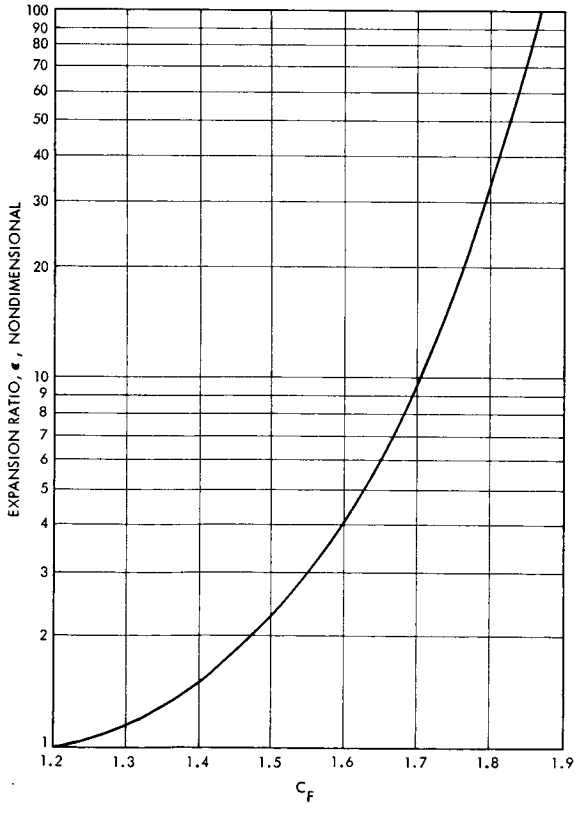

Figure 8-55. Thrust Coefficient Versus Expansion Ratio

total increase in performance, resulting from the increase of ϵ from 40 to 100, is 2.75 percent. The increase, however, results in heat shielding difficulties and additional weight which offset the potential improvement in performance.

Monopropellant hydrazine can be operated in a blowdown system without significant performance penalty. This is explained by the negligible effect on effective stay time (θ_e) of the gases in the chamber produced by the change in propellant flow. For the monopropellant hydrazine system,

$$\theta_e = \frac{\overline{P}_c L_c (1 - F_v)}{G}$$

where

$\overline{P}_c$ = chamber pressure, psia

L_c = length of the catalyst bed, in.

F_v = porosity of the catalyst bed, nondimensional

G = propellant flow per unit bed area, lb/sec-in^2

Since P_c varies almost directly with flow rate (or G, when a constant bed surface area is maintained), and bed length and porosity are not changed, θ_e remains nearly constant. Because θ_e is the major controlling factor in ammonia dissociation, characteristic velocity also remains constant. TRW test results confirm that engine throttling with monopropellant hydrazine is possible without degradation of performance, the limiting factors being injector and catalyst bed pressure drops.

8.7.3.7 Filters

Filters are used to keep possible debris generated by the explosive valves from clogging the injector capillary tube. A 100 mesh screen filter is used which would trap anything over 0.006 inch in diameter. This screen material is stainless steel AISI 347.

8.7.3.8 Explosive Valves

Commercially available, explosively actuated valves are employed to provide a positive seal. These valves operate in the following manner.

Application of power to the squib installed in the normally closed port causes it to fire and supply energy to move the normally closed ram which shears through the parent metal seal, and seats itself upon the threaded plug, thus allowing flow through the valve. For valve closure, a similar operation occurs, causing the normally open ram to deform the metal seat area, forming a positive seal. The valve body is fabricated of aluminum alloy 6061-T6, and the operating parts are stainless steel. With the exception of the external sealing serration and the ram bores, all external and internal surfaces of the valve body are anodized. A preliminary specification for the valve is shown in Figure 8-56, with dimensions given in Figure 8-57.

PRELIMINARY SPECIFICATION

EXPLOSIVE ACTUATED VALVE
1/4 Inch Restart

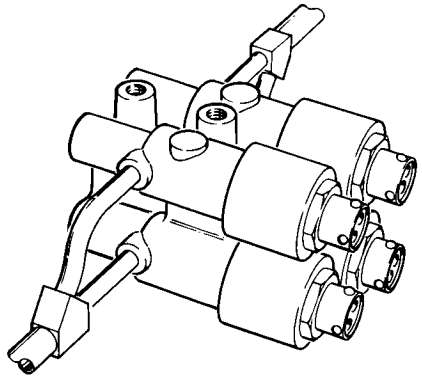

DESCRIPTION
A RESTART VALVE CAPABLE OF TWO START-STOP CYCLES. THIS VALVE CONSISTS OF TWO NORMALLY OPEN AND TWO NORMALLY CLOSED VALVES IN PARALLEL. NO SEALS ARE EXPOSED TO OPERATING FLUIDS. THE VALVE IS UNAFFECTED BY BACK PRESSURES AND NO LINE SURGE ACCOMPANIES ACTUATION OF EITHER NORMALLY OPEN OR NORMALLY CLOSED VALVES. LEAKAGE OF NORMALLY CLOSED VALVES BEFORE FIRING AND NORMALLY OPEN VALVES AFTER FIRING IS LESS THAN 1 x 10-SCCS HELIUM GAS AT 3300 PSI.

SPECIFICATIONS	PASSAGE SIZE	0.172 DIAMETER THROUGH. PRESSURE DROP IS 6.0 PSI MAXIMUM AT 0.217 LB/SEC HYDRAZINE FLOW
	WEIGHT	0.97 POUNDS INCLUDING CARTRIDGES
	MATERIAL	6061T6 ALUMINUM, TEFLON* PISTON SEALS, 303 STAINLESS STEEL VALVING
	FINISH	NONE ON ALUMINUM, PASSIVATED STAINLESS STEEL
	PRESSURE RATING	3600 PSIG OPERATING, 5400 PSIG PROOF, 8000 PSIG BURST
	CARTRIDGE	1 AMP, 1 WATT, NO FIRE, 5 AMP ALL FIRE. DUAL BRIDGE WIRE CARTRIDGE MATES WITH BENDIX PT06E-10-4S
	RELIABILITY	0.9999 AT 90 PERCENT CONFIDENCE ALL FIRE. 0.999 AT 95 PERCENT CONFIDENCE NO FIRE
	FUNCTION TIME	1 MILLISECOND MAXIMUM AT 16 AMPERES ALL FIRE FOR EACH SECTION

Figure 8-56. Preliminary Specification, Explosive Actuated Valve

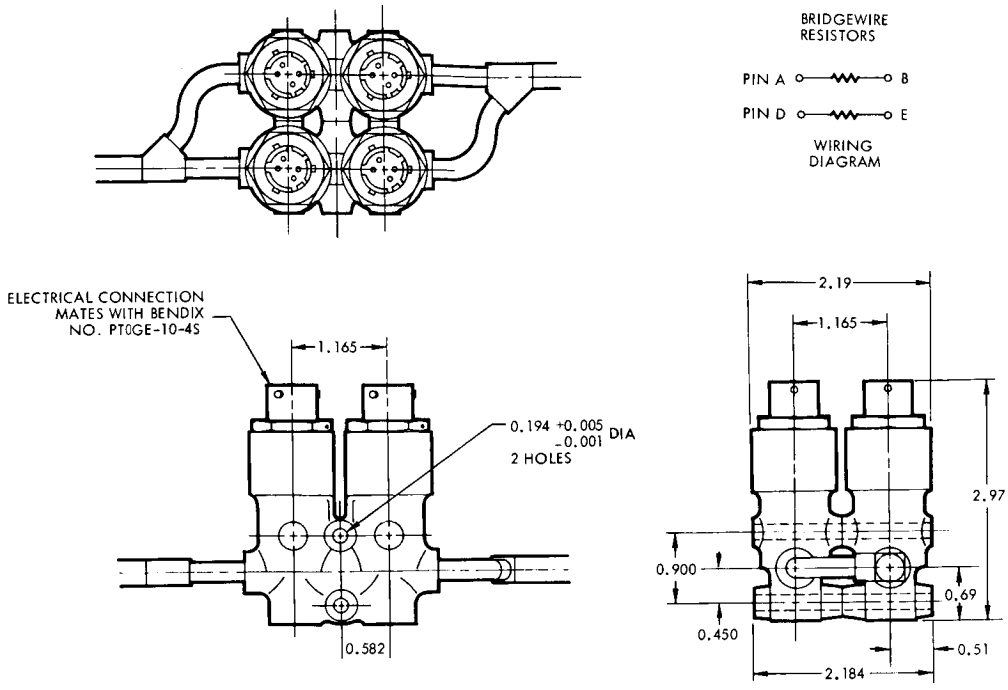

Figure 8-57. Midcourse Explosive Valve Characteristics

The squib used in the explosive valve will be nondetonating, nonventing, and nonrupturing devices. Exploding bridge wires will not be used. The devices will contain redundant bridge wires, both terminating in a connector rather than pigtails. The connectors, keyed to prevent misconnecting, will contain an environmental seal with a mating plug. Connector receptacles will be an integral part of the explosive device, with the male pins on the explosive side of the connector.

To assure electromagnetic compatibility, pyrotechnic circuits will be routed separately from all other spacecraft wiring. Continuous circumferential shielding containing no electrical discontinuities and grounded to structure at both ends will be utilized from the explosive device, either to the point at which the firing circuit leads are shorted together or to the firing power source.

The explosive devices will be installed with metal-to-metal contact resulting in a bonding impedance of less than 2.5 milliohms DC and 80 milliohms RF impedance over a frequency range of 200 kc to 20 Mc.

Power to the squibs will be blocked by normally open contacts of a safe arm circuit. A signal will be provided at spacecraft separation to arm the pyrotechnic devices.

8.7.3.9 Propellant Tank

The propellant tank is fabricated from Ti-6Al-4V titanium alloy. It has a diameter of 12.90 inches and a wall thickness of 0.027 inch and weighs 3.0 pounds including the expulsion bladder. The ullage in the tank is 67 percent to facilitate the blowdown mode of operation. The safety factor on the tank is 2.2 at a temperature of 125°F to allow for filling of the tank prior to installation in the vehicle, to eliminate propellant or gas umbilicals. The factor of safety of 2.2 is high enough to insure a no-hazard environment for personnel in the immediate vicinity.

The fill and drain valves are employed to fill gas and propellant and to insure a no-leak connection after termination of the operation. The valve is made of 6061-T6 aluminum alloy with a ceramic ball seat. The ceramic ball seats on the soft aluminum body. A cap assembly with O rings provides a redundant seal. This unit is the same design as was used on Mariner 4.

An elastomeric bladder is used to provide positive expulsion of the hydrazine in the zero-g field. The bladder is fabricated from FR 6-60-26 0.035-inch thick butyl, which showed up best on the Ranger and Mariner programs. The bladder volume is designed to be 10 percent greater than the maximum propellant volume at maximum temperature to insure against stretching if the tank is slightly overfilled.

Ribs are used on the exterior surfaces to provide a flow path for the pressurizing gas and insure uniform collapse. A perforated tube protrudes from the bottom of the tank into the bladder to prevent sealing of the outlet as the bladder collapses.

It is planned to hold the maximum temperature of the propellant and bladder to 100°F to ensure that no chemical interaction of bladder and propellant will occur. This temperature limit was verified on Mariner 4.

The lines for the liquid hydrazine system are fabricated of 6061-T6 aluminum. All fittings and connections are brazed with low melting temperature alloy to ensure permanent leak-free joints.

8.7.3.10 Comparison with Mariner

The Advanced Planetary Probe propulsion subsystem is somewhat simpler than the Mariner 4 midcourse system (Figure 8-58). The increase simplicity is attained by using a blowdown mode of operation rather than a regulated system. Selection of the blowdown system eliminates the separate pressurization tank, a set of explosive valves, and a regulator. It is also simpler in that ignition is accomplished without the separate slug start and associated components employed on Mariner 4. The elimination of the above components inherently results in a large increase in system reliability. The remainder of the propulsion system is very similar to Mariner 4. A bladder is used for positive expulsion of propellants, explosive valves are employed to obtain leak-free propellant control, and the system uses the same hydrazine monopropellant. The remaining difference is that Mariner 4 utilized H-7 catalyst, while Shell 405 is employed on the Advanced Planetary Probe decomposition chamber.

A basic difference in injection design is also apparent. The Advanced Planetary Probe thrusters uses a capillary tube injector, while the Mariner 4 configuration employs spray nozzles. (See Figure 8-59 for a direct comparison.) The different configuration also results in different concepts for spreading the hydrazine over the surface of the bed. The Mariner 4 spray nozzles spread the propellant over the top surface of the bed; a chamber volume above the catalyst is used to accomplish this. The Advanced Planetary Probe chamber has no head volume and relies on the generation of gas about an inch below the surface of the bed to spread the incoming propellant from the capillary tube injector.

A review of the above differences indicates that the best features of the Mariner 4 design have been retained, while improvements were made which hinge primarily on the new state-of-the-art Shell 405 catalyst.

8.7.3.11 Problem Areas

The proposed propulsion system is extremely simple with no moving parts or current drain required during operation. As such, potential problem areas are minor.

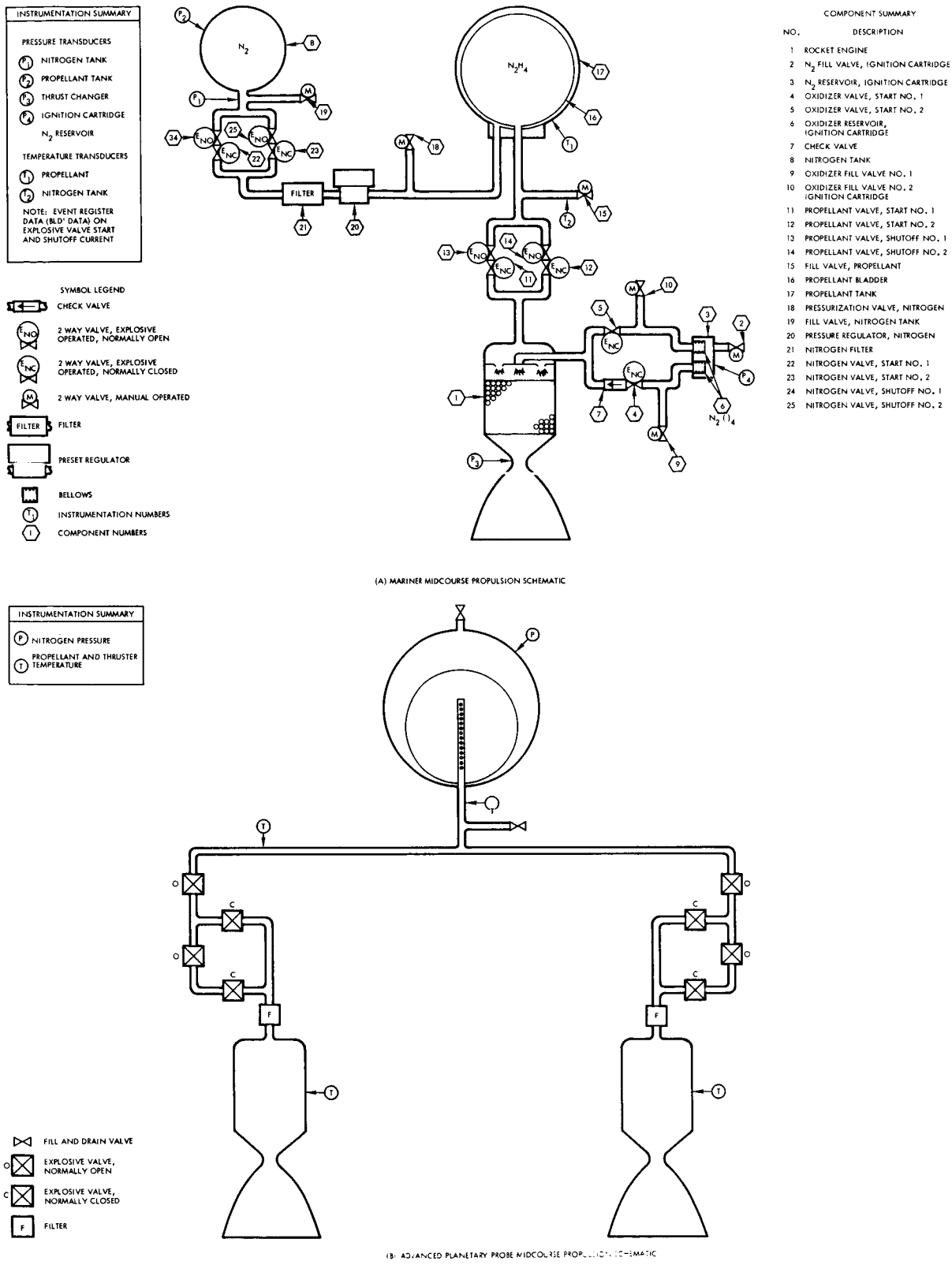

Figure 8-58. Comparison of Mariner and APP Propulsion Subsystems

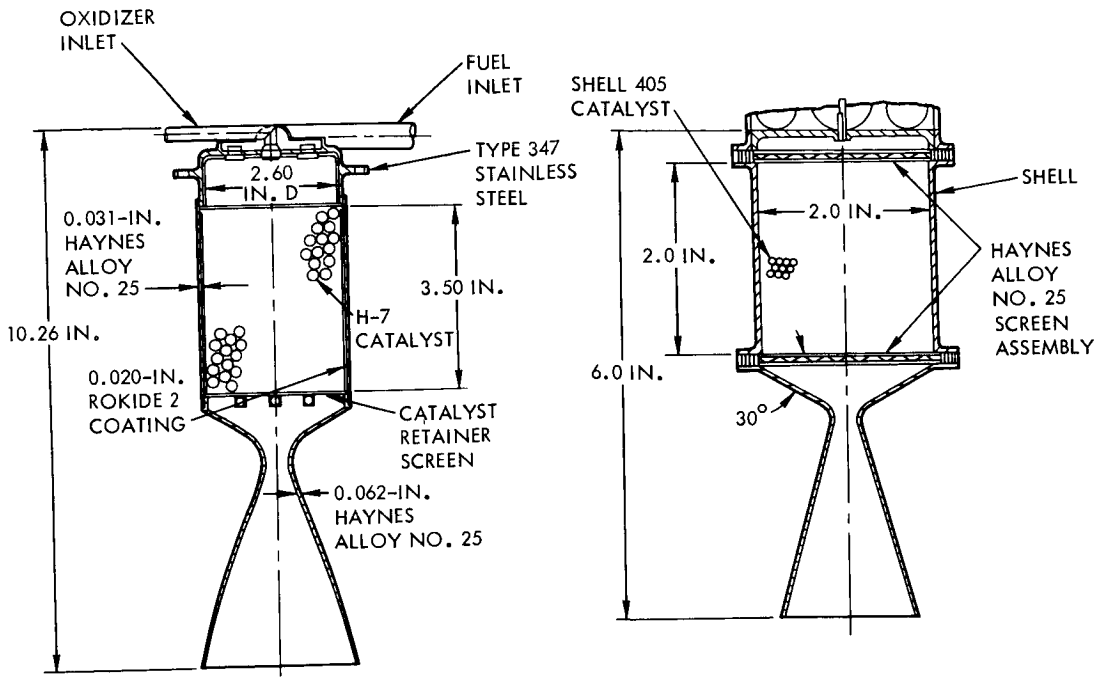

Figure 8-59. Comparison of Injection Designs

The decomposition chamber utilizing the Shell 405 catalyst presents an area which is not considered a problem, but rather something that has not yet been demonstrated in the space environment. The catalyst has been proven during ground tests and at simulated altitude, but to date no engine utilizing the catalyst has flown in space. Because of the extensive simulated altitude testing, however, TRW has a high degree of confidence in its successful space application.

Another potential problem associated with the catalyst is powdering and plugging of the capillary injector tube during the launch phase when vibration is severe. This potential problem, however, is minimized by employing a small mesh or drilled plate on the extremity of the capillary tube. Both methods have been demonstrated successfully at TRW.

Another problem is keeping the catalyst bed above $-40^{\circ}F$ on starts. Starts at temperatures below $-40^{\circ}F$ are erratic and can result in substantial pressure overshoot. A heating blanket will be employed to ensure that the catalyst bed is well above the allowable lower limit before firing.

There have also been several problem areas associated with the squib valves. Ranger, in particular, had troubles associated with valve leakage after shutdown because of inadvertent anodizing of the valve seat and ram. Ranger also had a considerable number of squib malfunctions, including ventings and rupturings. In fact, blast shields were employed to prevent damage to adjacent components. The trouble was associated with valves being sensitive to minor variations in the applied torque used on the mounting bolts, the fit of the tools used for assembly, and the quantity of thread lube employed. These items results in increases in pressure and increased the tendancy for the squib to rupture.

A possible problem area exists regarding bladder and hydrazine compatibility. Ranger and Mariner have demonstrated reasonably long storage without noticeable deterioration. However, trips to Jupiter are considerably longer and will require additional compatibility verification for the longer storage times. This is mitigated by the fact that no terminal correction maneuver is now believed to be required. As a result, bladder failure after initial midcourse correction does not influence the mission.

8.7.4 Spinup Propulsion

The spacecraft will be spun up from 0 to 60 rpm in less than one second immediately following separation from the Centaur to cancel out the thrust vector misalignment of the TE-364-3 injection motor. The TE-364-3 injection motor will be ignited immediately following completion of spinup. A nomograph of thrust required to accelerate the spacecraft to the desired rotational speed as a function of time allowed for the spinup maneuver is shown in Figure 8-60. As can be seen from the figure, with an assumed spacecraft moment of inertia of 110 slug ft^2 it will require 200 pounds of thrust to accelerate to 60 rpm in one second while at a radius of 40 inches. A 1-second firing time was used to minimize injection wobble. The total impulse required is the 1-second allowed time multiplied by the required thrust or 200 pound-seconds. These values were used for preliminary design purposes. As the spacecraft weights and moment of inertia values are refined, the effected variation of thrust required can be determined from Figure 8-60. This requirement is tailored for solid motors since it is a single burn of short duration.

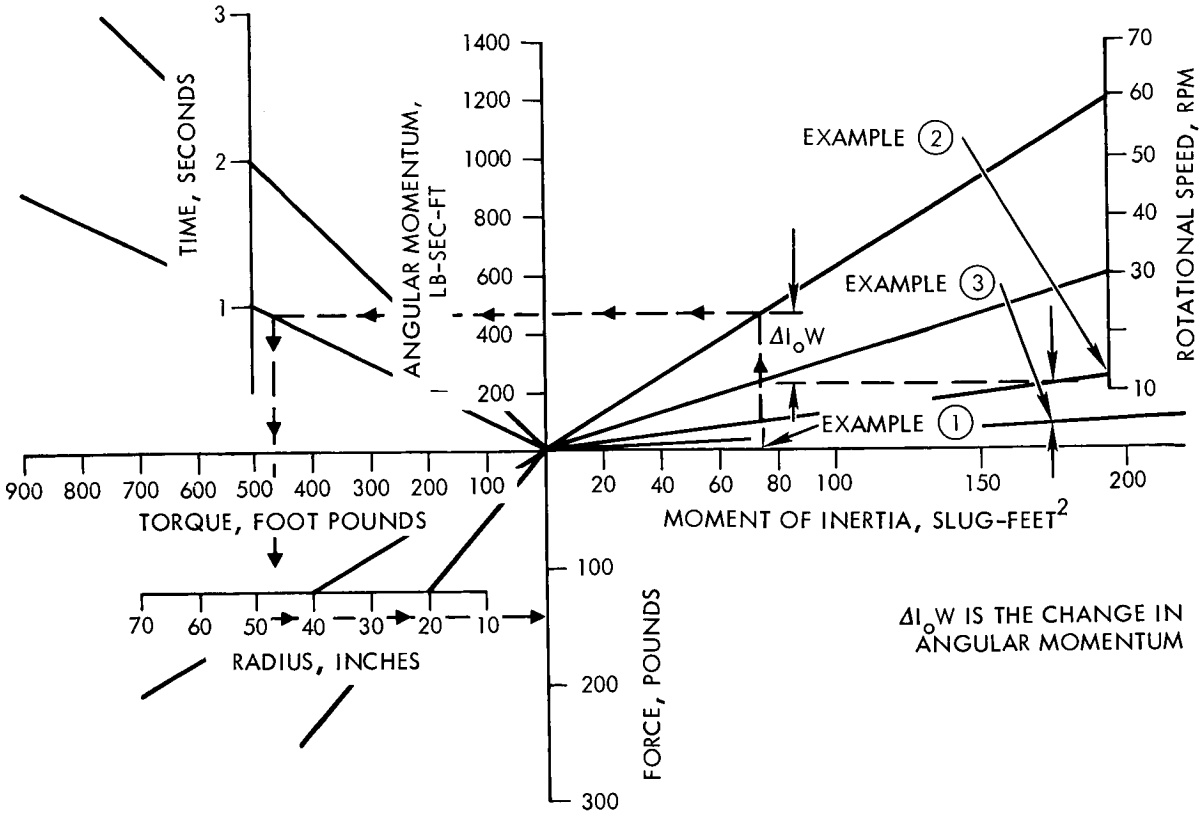

Figure 8-60. Thrust Required to Accelerate Spacecraft to Desired Rotational Speed as a Function of Time Allowed for Spinup

The design data for a typical motor which would be satisfactory for this requirement is shown in Figure 8-61. The motor performance is shown in Figure 8-62. These motors would provide 230 pound-seconds, which would be adequate for the above maneuver.

8.7.5 Despin Thrusters

The despin thrusters are required to make two firings with one backup firing possible. One firing is to decelerate the spacecraft from the spinup speed of 60 rpm down to 30 rpm where the RTG units are deployed. The despin thrusters then make the remaining firing to reduce the spacecraft rotational speed so that after antenna and boom deployment the cruise spin rate will be 5 rpm.

The despinning should occupy many revolutions to minimize wobble buildup.

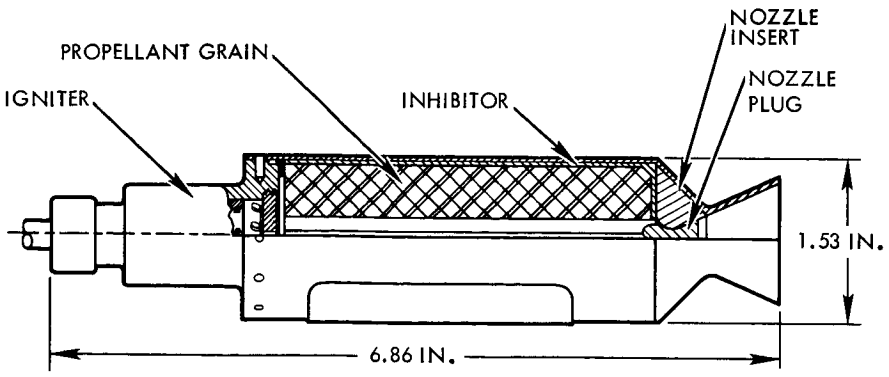

WEIGHTS

CASE ASSEMBLY	0.207 LB
INSERT	0.016 LB
IGNITER ASSEMBLY	0.266 LB
INHIBITOR	0.020 LB
TOTAL INERT	0.509 LB
PROPELLANT WEIGHT	0.305 LB
TOTAL WEIGHT	0.814 LB

OPERATING CONDITIONS

STORAGE TEMPERATURE	20°F TO 130°F
OPERATING TEMPERATURE	20°F TO 130°F
ACCELERATION LIMITS	
AXIAL	50g
LATERAL	50g
EXTERIOR FINISH	PAINT

SPECIAL FEATURES

SAME EXTERIOR CONFIGURATION AS MARC 4 SERIES
HIGH PERFORMANCE

COMPONENT DATA

CASE:	
MATERIAL	H11
FABRICATION METHOD	MACHINE
AVERAGE WALL THICKNESS	0.029 IN.
INSULATION	NONE
NOZZLE:	
EXPANSION RATIO	21.1
THROAT MATERIAL	GRAPHITE
EXIT CONE MATERIAL	H11
THROAT AREA	0.452 $IN.^2$
EXIT DIAMETER	0.96 IN.
EXPANSION CONE, HALF ANGLE	23°45'
IGNITER:	
TYPE	PYROTECHNIC
DESIGNATION NUMBER	501
SQUIB (2)	MODEL 908
BOOSTER CHARGE	75 GMS 2M PELLETS
CIRCUIT RESISTANCE	0.65-1.0 OHM
RECOMMENDED FIRING CURRENT	1.2 AMP
MAXIMUM NO-FIRE CURRENT	0.7 MAP
GRAIN:	
(SEE PROPELLANT DATA SHEET FOR PARAMETERS)	
PROPELLANT	ATCITE 373
DESIGN	SLOTTED TUBE
DIMENSIONS	1.422 IN. O.D. 0.422 IN. I.D. 3.41 IN. L
WEB THICKNESS	0.50 IN.
INHIBITOR	COTTON MESH, IMPREGNATED WITH EPOXY POLYAMIDE
RETENTION SYSTEM	CONSTRAINED WITHIN CASE
METHOD OF MANUFACTURE	EXTRUDED

Figure 8-61. MARC 36A1 1-KS-75 Engine

	74°F
TOTAL IMPULSE	76.7 LB-SEC
BURNING TIME (t_b)	1.04 SEC
AVERAGE THRUST (F_{avg})	73 LB
MAXIMUM THRUST (F_{max})	79 LB
AVERAGE PRESSURE (P_{avg})	990 PSI
MAXIMUM PRESSURE (P_{max})	1100 PSI
IGNITION DELAY (t_d)	10 MS
SPECIFIC IMPULSE (DELIVERED) (I_{sp})	252 LB-SEC/LB
THRUST COEFFICIENT (DELIVERED) (C_f)	1.694

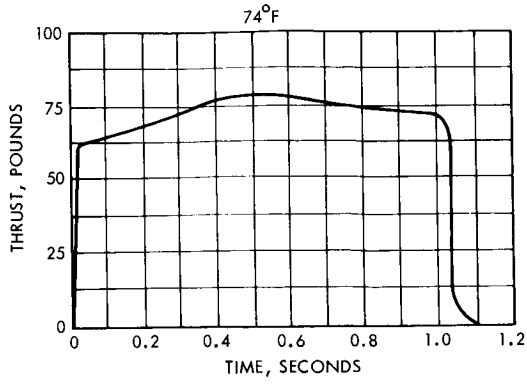

STATUS	
USER AND APPLICATION	LTV, SCOUT SPIN
DEVELOPMENT COMPLETED	1965
INITIAL PRODUCTION AS OF 1/1/65	34

Figure 8-62. Vacuum Performance of MARC 36A1 1-KS-75

For preliminary analysis, the initial spacecraft moment of inertia was the same as that assumed for determining the spinup thruster design values, i.e., 110 slug ft^2. This value was used during the despin from 60 to 30 rpm. Figure 8-60 shows that the change in angular momentum that must take place to reduce the speed to 30 rpm is 340 lb-sec-ft. Referring to Figure 8-63, if a construction line is drawn from the origin to the 100-second point on the time scale, and 340 lb-sec-ft entered as shown in example 1, a required thruster force of about 1.0 pound is needed at a radius of 40 inches. Forty inches is the preliminary design location radius for the despin thrusters. Since two thrusters are needed to obtain a pure couple, each thruster would have to be 0.5 pound in thrust. Since hydrazine is available as part of the propulsion subsystem, it would be advantageous to utilize this propellant for despin. A solid is ruled out for this application because of the probable need for variable impulse and because the despin thruster has to fire two times, and again variable impulse may be required to obtain an accurate final rotational speed. Hydrazine thrusters of 0.5 pound could be built; however, 1-pound

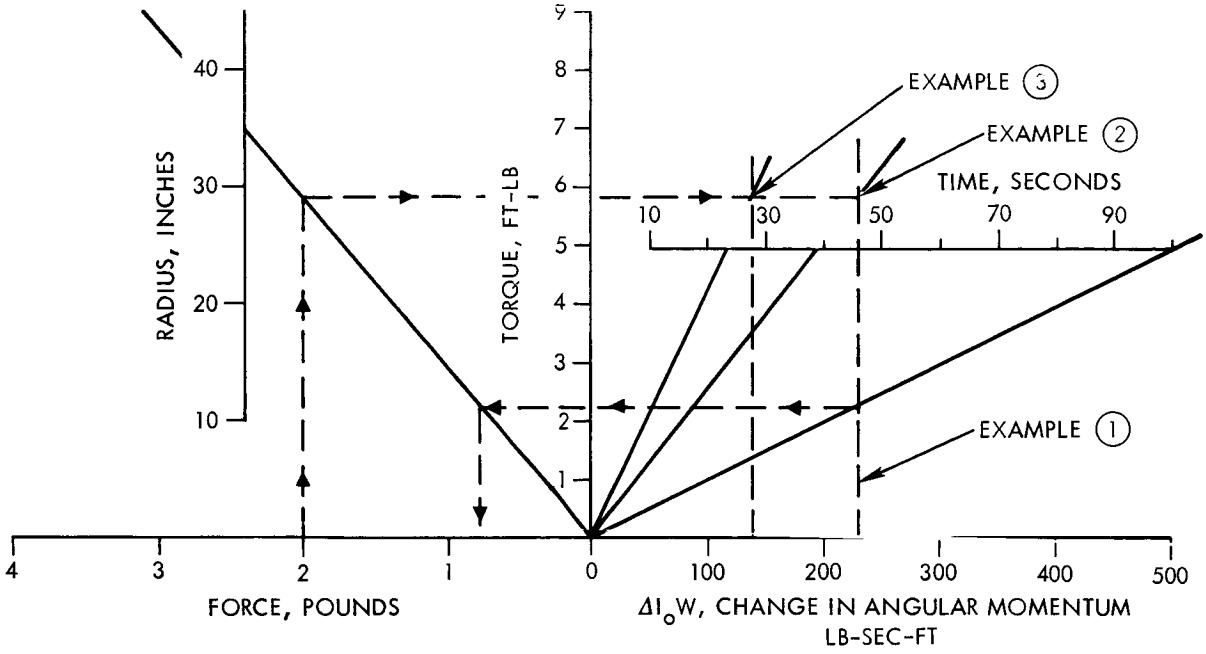

Figure 8-63. Spacecraft Change in Angular Momentum as a Function of Thrusters Radius Time of the Maneuver and Thruster Force Employed

thrusters are much more current state of the art. Using two 1-pound thrusters will result in a despin time of about 50 seconds. This value is arrived at by entering a vertical line from the 2-pound force scale and the 340 change in momentum scale. The intersection of the horizontal line, based on a turning radius of 40 inches, and the change in momentum line occur as shown in marked example 2. A line is then drawn from this intersection to the graph origin. Its intersection with the time scale provides the time of 50 seconds to accomplish the maneuver. This should be satisfactory, and therefore 1-pound hydrazine thrusters will be employed for despinning from 60 to 30 rpm.

Assuming the final inertia is 215 slug ft^2, the second firing must remove momentum equal to the difference of 110 slug ft^2 at 300 rpm and 215 slug ft^2 at 5 rpm, or a change of about 113 lb-ft-sec. Example 3 shows the change in angular momentum that must take place on about 113 lb-sec-ft. Using the same procedure used for example 2, the time required for the maneuver is about 17 seconds, as shown in example 3 of Figure 8-63.

The total impulse required to accomplish the above two despin maneuvers would be 2 pounds thrust times (50 + 17 seconds) or 134 pound-second. The propellant required for the maneuver would be 134 lb-sec/225 sec or 0.60 pound. Since the above values are based on preliminary estimates of spacecraft moment of inertia, this value should be increased to ensure enough propellant. For system sizing, the propellant quantity assumed was 1 pound.

Figure 8-64 is a preliminary specification of the 1-pound thrusters.

The valve schematic for the despin thrusters is shown in the piping schematic of Figure 8-50. There are three sets of explosive valves for each thruster; two for the needed firing, and one for backup. The explosive valves are the same as those used for the midcourse engine. The packaging will also be the same, except for the addition of the additional set, since only two sets of explosive valves are used on each midcourse thruster. Figure 8-56 gives the specifications for the valves, and Figure 8-57 shows the dimensions. These will change somewhat when the additional valve set is added.

8.8 THERMAL CONTROL

The thermal control subsystem consists of the following items.

- A 6.4 square foot radiator panel
- Thirteen thermal switches
- A high conductance honeycomb component mounting surface
- Multilayer aluminized Mylar and multilayer aluminum foil/dexiglass insulation
- Thermal coatings
- A constant internal component power dissipation
- Electric strip heaters
- Interface filler materials
- Selected structural materials
- Component placement

FUNCTION
CONTROL PROPELLANT FLOW AND PROVIDE THRUST FOR DESPIN MANEUVER

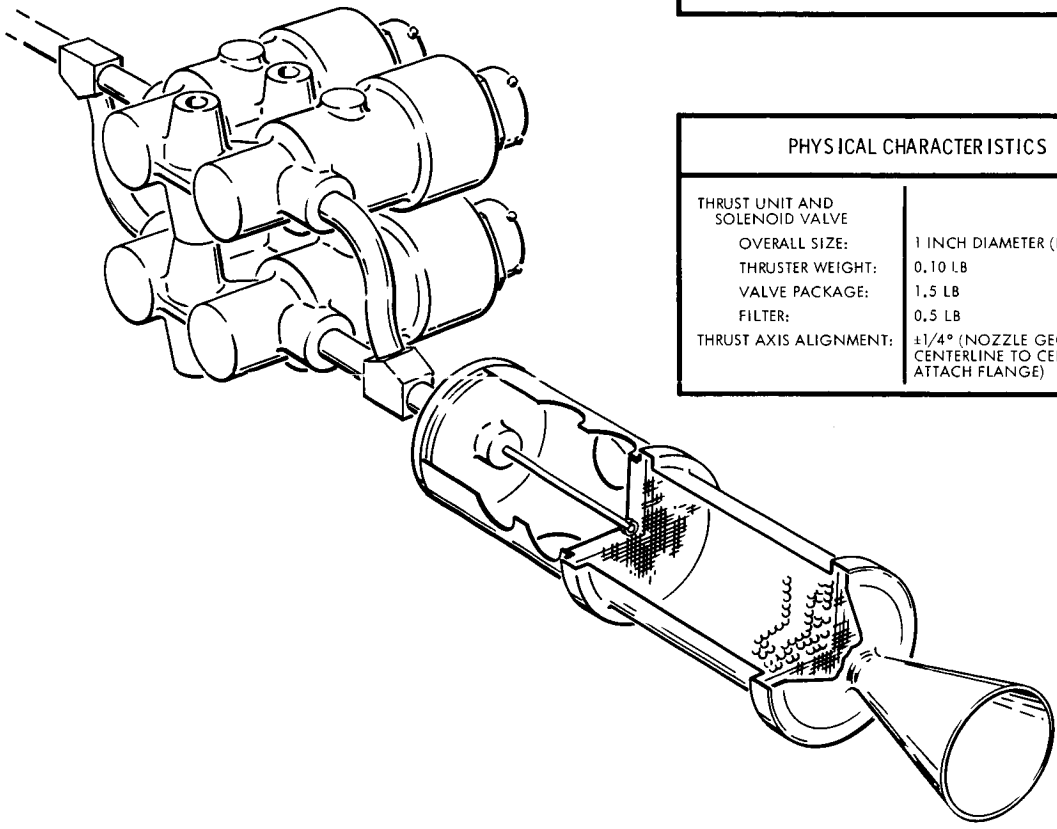

PHYSICAL CHARACTERISTICS	
THRUST UNIT AND SOLENOID VALVE	
OVERALL SIZE:	1 INCH DIAMETER (NOMINAL)
THRUSTER WEIGHT:	0.10 LB
VALVE PACKAGE:	1.5 LB
FILTER:	0.5 LB
THRUST AXIS ALIGNMENT:	±1/4° (NOZZLE GEOMETRIC CENTERLINE TO CENTROID OF ATTACH FLANGE)

EXPLOSIVE VALVE CHARACTERISTICS
SQUIB PRESSURE SEAL GOOD TO 8000 PSI AFTER FIRING
HERMETIC SEAL LEAKAGE RATE NOT TO EXCEED 10^{-6} CC/SEC NTP
RECOMMENDED FIRING CURRENT - 5 AMPS APPLIED TO ONE BRIDGE WIRE
MINIMUM FIRING CURRENT - 3.5 AMPS
FUNCTIONING TIME - 4 MC
NO FIRE CURRENT - 1 AMP
POWER DRAW - 1.5 WATT-SEC FOR 0.01 SEC PER VALVE
NO FIRE - WITH STATIC DISCHARGE OF 25,000 VOLTS FROM A 500 PICOFARAD CAPACITOR APPLIED BETWEEN PIN AND CASE - WILL SURVIVE - ELECTRO-MAGNETIC FIELD OF 2 WATTS PER SQUARE METER FROM 150 KC TO 10,000 MC

THRUST UNIT CHARACTERISTICS	
THRUST RANGE:	3.0 TO 1.9 LB
PROPELLANT:	ANHYDROUS HYDRAZINE, N_2H_4
THRUST INITIATION:	SPONTANEOUS PROPELLANT DE-COMPOSITION UPON EXPOSURE TO CATALYST IN THRUST CHAMBER
CATALYST:	SHELL 405
PROPELLANT INJECTION:	CAPILLARY INJECTION-SINGLE CENTRAL TUBE
NOMINAL CHAMBER PRESSURE RANGE:	185 PSIA INITIAL TO 102 PSIA FINAL
NOZZLE EXPANISION RATIO:	40: 1
MINIMUM VACUUM SPECIFIC IMPULSE:	
STEADY STATE:	225 SEC
THRUST BUILDUP (VALVE SIGNAL SIGNAL TO 90% F)	22± 1 MILLISECOND
MINIMUM IMPULSE BIT:	
INITIAL:	0.19 LB-SEC
FINAL:	0.12 LB-SEC

Figure 8-64. Preliminary Specification, Thrust Chamber Assembly

- Low conductance electrical connectors
- Prelaunch gaseous ground cooling.

These items will provide the required temperature control during all phases of the mission including launch, coast, orbit, midcourse correction, and transit.

All electronic components of the spacecraft will be located within a central compartment which is suitably isolated from solar heat input and radiation to space by 100-layer aluminized Mylar insulation blankets and low thermal conductivity structural attachments. The components are mounted on an all-aluminum honeycomb panel that is designed to reject internal electronic heat dissipation to space at a predetermined rate. Thermal switches in the system will provide a means of varying the established heat rejection rate to account for the increase in heat leak as the spacecraft becomes more distant from the sun. Four shunts will be used to maintain a constant internal power dissipation regardless of component duty cycling.

Experiment electronics will be located within the temperature controlled compartment. Remote external experiment sensors will be utilized except in the case of the TV experiment where the sensor protrudes through the conditioned compartment wall. The remote sensors will be designed to operate at extremely low temperatures so that heater power is not required.

External equipment such as the midcourse engines and hydrazine lines will be insulated with 30 layers of aluminized Mylar, or a combination of aluminum foil/dexiglass paper in high temperature regions (above 250°F). It will also be necessary to provide engine and line strip heaters for heat-up prior to engine use. These heaters will dissipate about five watts of heat.

A black Cat-a-lac paint (absorptivity, $\alpha = 0.92$; emissivity, $\epsilon = 0.86$) is required on the sunlit surface of the deployable antenna to achieve the proper temperature range and prevent focusing of the solar energy on the feed. The rear surface of the antenna is left bare to obtain a near-earth temperature of about 265 and -135°F at Jupiter. A black front surface

not only establishes acceptable antenna temperatures, but also reduces temperature gradients across the aluminum honeycomb antenna structure because practically all the absorbed heat is re-emitted from the same surface and little conduction takes place between the face sheets. The bare rear surface also minimizes localized RTG heat input to the back face of the antenna. The spin-stabilized configuration tends to eliminate gradients over the antenna dish by averaging the heat input to alternately irradiated and shaded points on the antenna.

8.8.1 Heat Leak

The system performance is directly related to the compartment heat leak which is described in Figure 8-65 and specified in Table 8-19. The specified maximum heat leak of 22.4 watts represents all spacecraft

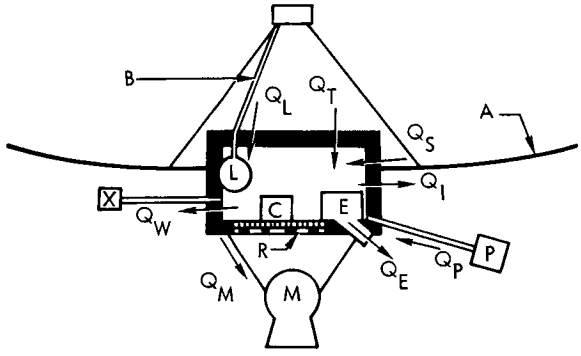

A - ANTENNA DISH
B - HYDRAZINE LINE
C - TYPICAL COMPONENT
E - INTERNAL EXPERIMENT
L - HYDRAZINE TANK
M - ROCKET MOTOR (JETTISONED EARLY IN FLIGHT)
P - RTG POWER SUPPLY
R - RADIATOR SURFACE
X - EXTERNAL EXPERIMENT

Q_E - INTERNAL EXPERIMENT
Q_I - SIDE AND BOTTOM INSULATION
Q_L - HYDRAZINE LINES*
Q_M - ROCKET MOTOR SUPPORT
Q_P - RTG POWER LEADS**
Q_S - TOP STRUCTURE*
Q_T - TOP INSULATION*
Q_W - CABLE AND WIRES

*BECOMES OUTWARD AS SPACECRAFT MOVES AWAY FROM SUN
**DIRECTION DEPENDS UPON RTG MOUNTING ARRANGEMENT
NOTE: RADIATOR HEAT DISSIPATION IS NOT CONSIDERED TO BE A HEAT LEAK.

Figure 8-65. Spacecraft Heat Leak Paths

Table 8-19. Typical 50-Pound Payload, Spin-Stabilized Spacecraft Heat Leaks (does not include controlled heat loss through radiator)

Configuration	Heat Loss at 9.54 AU or Greater (watts)	Heat Loss at 1 AU Orientation Normal (watts)	Heat Loss at 1 AU Radiator Sun-Oriented (watts)
TV window	3.5	3.5	3.5
Insulation	4.4	0.6	2.3
Antenna support 1-in. fiberglass	4.9	-0.7 (heat in)	-0.7 (heat in)
Booms and structure 3-in. fiberglass	8.6	-1.2 (heat in)	-1.2 (heat in)
Attitude control engine lines	1.0	-	-
Jettisoned engine supports	-	-	-0.7 (heat in)
Total	22.4	2.2	3.9

Assumptions:

1. TV experiment aperture is the only experiment penetration in conditioned compartment wall.
2. Compartment insulation covered with 100 layers aluminized Mylar.
3. Hydrazine line, hydrazine motor, and attachments covered with 30 layers aluminized Mylar.

heat losses except that through the radiator panel and is the minimum value that might be attained with state-of-the-art practice. To achieve this goal it will be necessary to monitor and control the detailed structural design of the spacecraft to a far greater extent than has been accomplished on other spacecraft. The need for controlling the structural design is evident from Table 8-20.

Insulation loss characteristics of Figure 8-66 were used in the analysis. These values can be expected for a well-insulated spacecraft. From this curve it was determined that each insulation blanket should be fabricated with 100 aluminized Mylar layers. Although there is not a

Table 8-20. Detailed Structural Heat Leaks

Item	Heat Loss at 9.54 AU or Greater (watts)	Heat Loss at 1 AU Radiator Sun-Oriented (watts)
Experiment Apertures		
a. Experiments No. 2, 4, 7, 8, $9_{a, b}$, 10	16.4	
*b. TV experiment only (No. 10)	3.5	3.5
Antenna Support		
*a. Fiberglass supports 1-in. long	4.9	-0.7 (heat in)
b. Stainless steel supports 2-in. long with fiberglass washers	35.3	-4.8 (heat in)
c. Stainless steel supports 1-in. long with fiberglass washers	50.6	-7.0 (heat in)
Booms, Engine and Antenna Supports		
a. Fiberglass section 6-in. long and insulated	4.3	-0.6 (heat in)
*b. Fiberglass section 3-in. long and insulated	8.6	-1.2 (heat in)
c. Fiberglass section 1-in. long and insulated	25.8	-3.5 (heat in)

*Recommended configuration

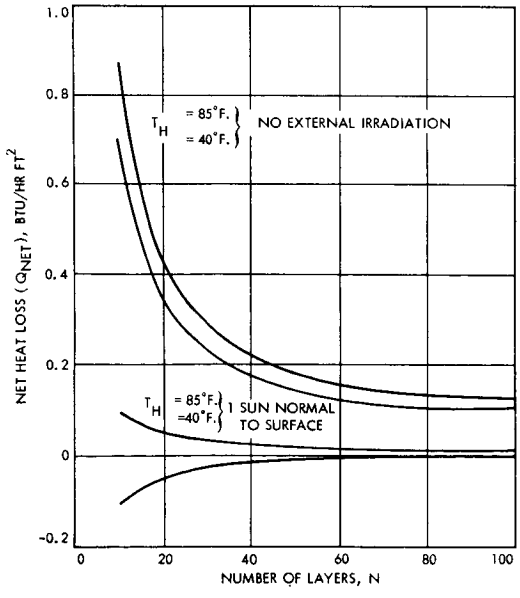

Figure 8-66. Heat Losses Through NRC-2 Insulation

great heat leak reduction between 60 and 100 layers, the heat leak effects are severe enough to warrant the small weight penalty of a 100-layer blanket. (This insulation will complicate accessibility to the compartment. However, TRW tests have indicated that insulation can be removed and replaced without drastically affecting heat leak if care is exercised during integration.) The substitution of Dimplar insulation in place of the NRC insulation may further reduce the net heat leak. This insulation is also better suited to resist handling and integration damage, but requires a greater volume and is somewhat heavier.

The 22.4-watt heat leak value considers the use of low thermal conductance connectors, such as the one shown in Figures 8-67 and 8-68. An advantage of the thermal switch systems is that they readily tolerate an additional 3 to 8 watts of heat leak due to the use of ordinary connectors.

8.8.2 Thermal Switch Radiator Panel

TRW-designed thermal switches are incorporated into the basic thermal control subsystem. The thermal switch, a prototype of which is shown in Figure 8-69, consists of a small stainless steel bellows, the exterior of which is exposed to a sealed fluid reservoir mounted on a baseplate. The baseplate is fastened to the component mounting panel whose temperature is to be controlled. Fluid expansion caused by an increase in box temperature extends the bellows which closes a low resistance thermal conduction path between the baseplate and a heat sink, in this instance the radiator panel.

A series of thermal resistance tests have been performed on the laboratory prototype TRW thermal switch. The primary purpose of the tests was to accurately determine the thermal resistance of the laboratory prototype in both the open and closed position. The model tested has an overall diameter of 3 inches, a thickness of 1-1/8 inches, and weighs approximately 4.8 ounces. Thermal resistance in the closed position was found to be approximately 6.1°C/watt. Open switch resistance was approximately 232°C/watt, giving an open-to-closed ratio of about 38. A plot of the switch resistance characteristics is presented in Figure 8-70. It is expected that this ratio will be doubled before 1970, with an open contact resistance of 576°F/watt and a closed contact resistance of 7.2°F/watt.

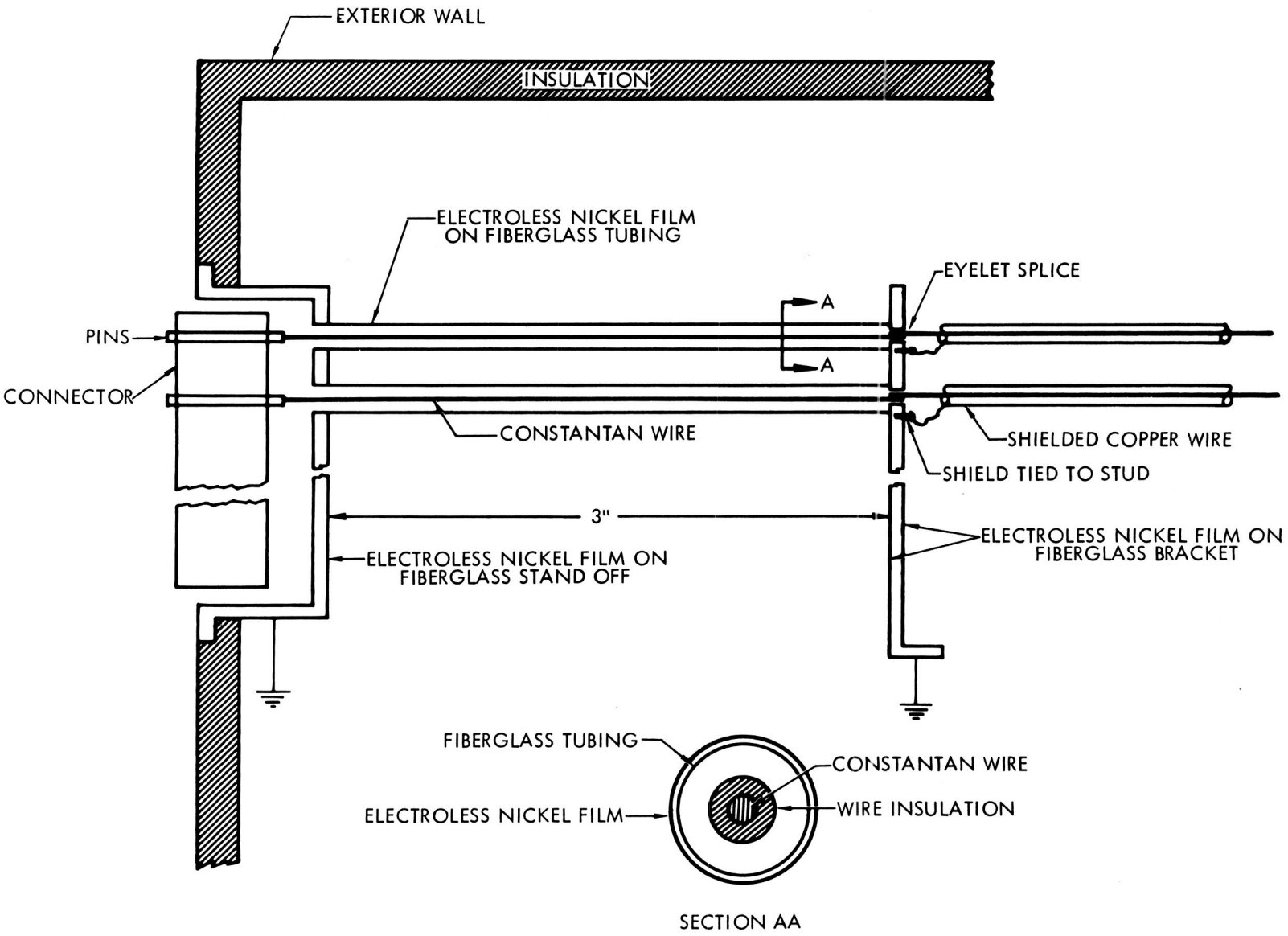

Figure 8-67. Low Thermal Conductance Electrical Connector Schematic

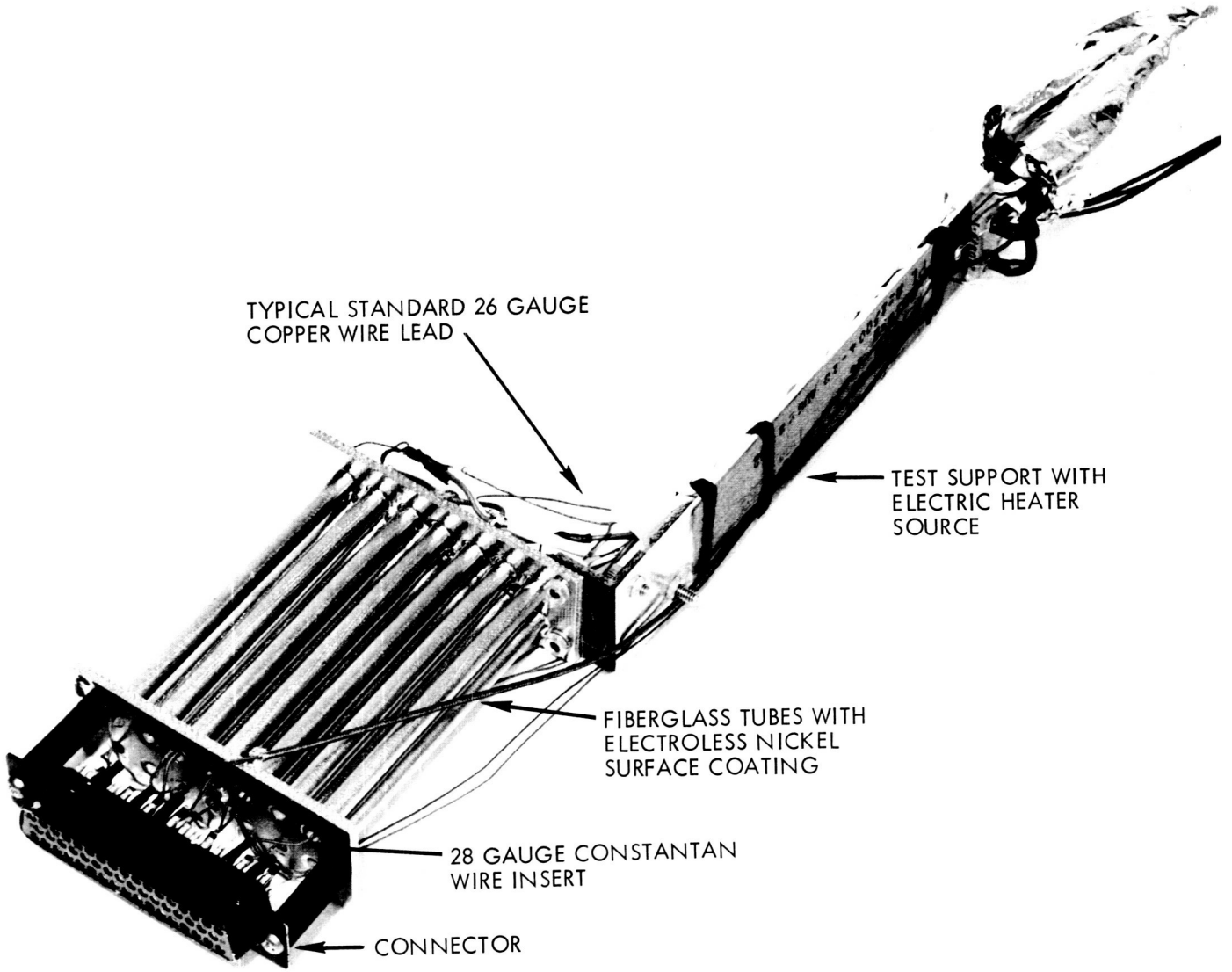

Figure 8-68. Low Thermal Conductance Electrical Connector

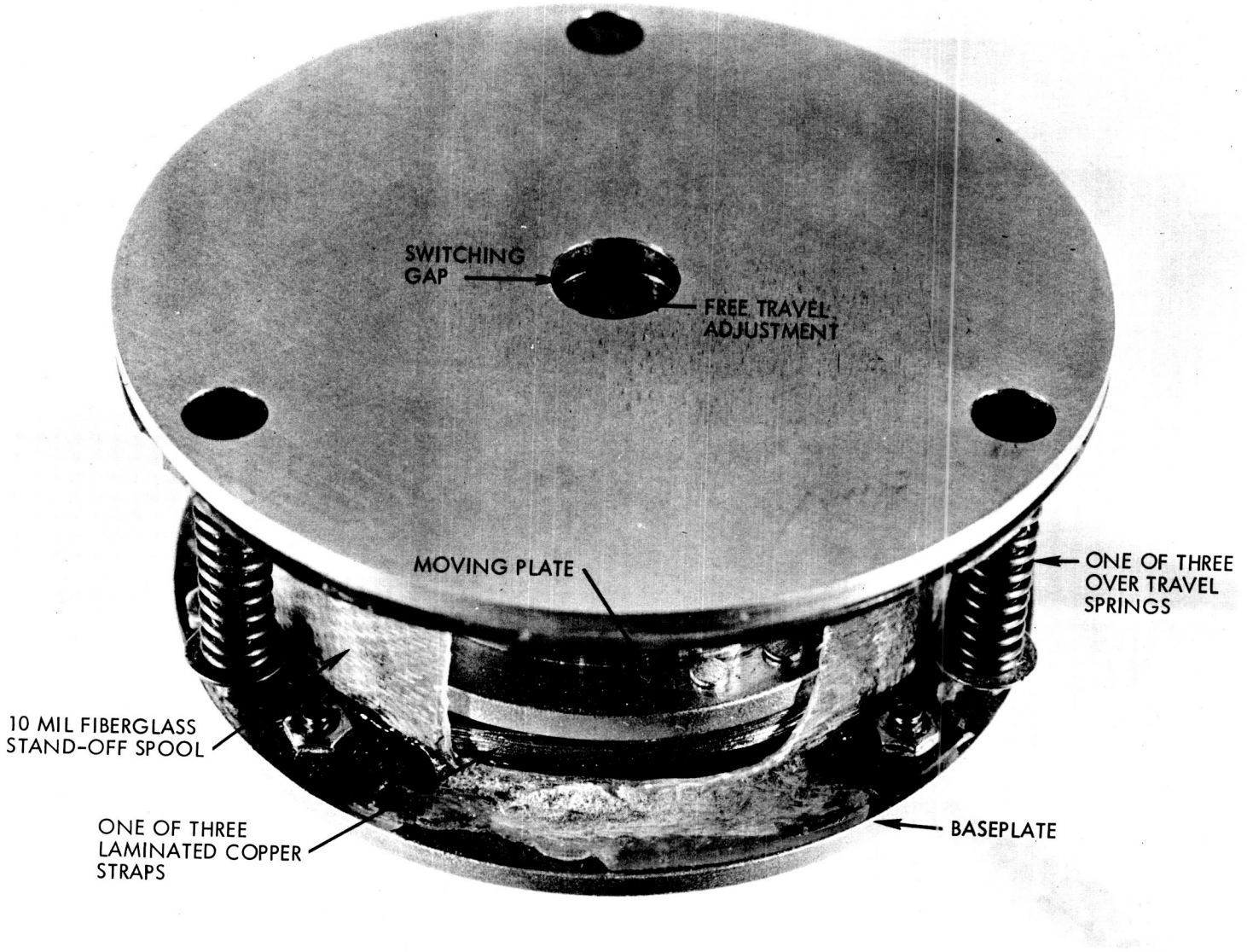

Figure 8-69. TRW Thermal Switch

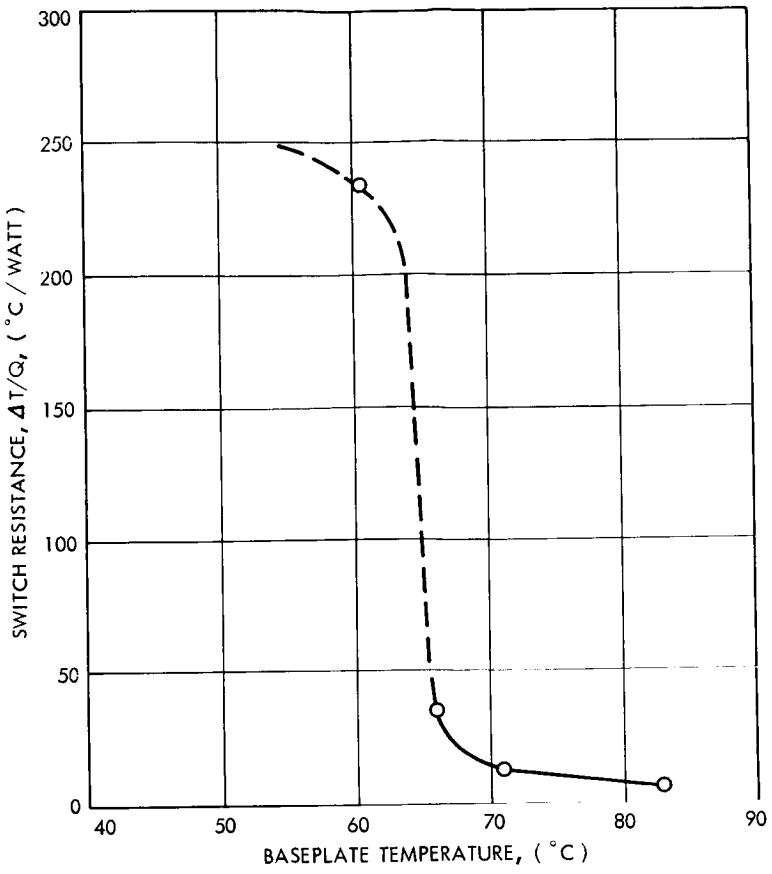

Figure 8-70. Thermal Switch Test Results with a 16-Degree Sink Temperature

It appears from Figure 8-70 that the switch acts as a proportional controller over a limited range, most likely due to changes in the contact resistance with switching pressure. In the switch tested the cold side of the joint was covered with a thickness of 4 mils of vinyl to prevent cold welding. Because of the proportional control characteristics, the switch did not tend to oscillate or cycle from open to close at any of the temperatures tested. A desirable characteristic of the switch is to control to very close temperature tolerances.

The operating point or set-point temperature can be changed simply by adjusting the free travel between the bellows and the moving plate radiator. This allows the internal experiment temperature to be maintained at a desired level during a large portion of the operating time period.

Tests were conducted within the 18-inch vacuum chamber at a pressure below 10^{-6} torr to eliminate gaseous conduction and convection. Heat was supplied to the base of the switch by a thin 3-inch diameter wire-wound electrical element and removed from the opposite side by a water-cooled plate. Heat fluxes in and out of the switch were measured by 1/16-inch thick heat meters which were built and calibrated especially for these tests. Each heat meter contains approximately 684 constantan-silver thermopile junctions, half of which are on either side of a 31-mil micarta separator. A 5-mil Mylar face sheet was bonded to each side with an adhesive silicone rubber to protect the junctions. One heat meter was placed between the source and the switch, the other between the switch and the sink. Approximately five layers of aluminized Mylar were wrapped cylindrically around the switch to reduce radiation losses from the switch perimeter.

The parametric performance of this system with the 1970 switch resistances is shown in Figure 8-71. For a conservative zero heat leak value at 1.0 AU, an 85°F component temperature, and a 75-watt internal power dissipation, the internal power dissipation/radiator area ratio is 11.7 (a radiator area of 6.4 square feet). With this radiator area the system can tolerate a 72-watt heat leak if the minimum internal temperature limit is specified to be 40°F. The initial design range of 40 to 85°F was selected based on past TRW program specifications. Of course, a greater heat leak can be allowed if a lower component temperature level is acceptable. Since the actual heat leak will probably be greater than the calculated minimum value the selection of the thermal switch concept provides a margin of safety. In fact, the heat leak can be over 3 times as great as predicted and the system will still operate satisfactorily.

During the initial phase of the mission, the radiator panel can be exposed to direct solar irradiation. Figure 8-72 indicates the temperature rise of the compartment-mounted components during this time interval. It is apparent that a white painted surface, although somewhat heavier than an anodized surface, is the only means of maintaining an acceptable internal temperature if exposure times greater than 1.2 hours are expected. Even for shorter exposure times, the white painted surface appears desirable.

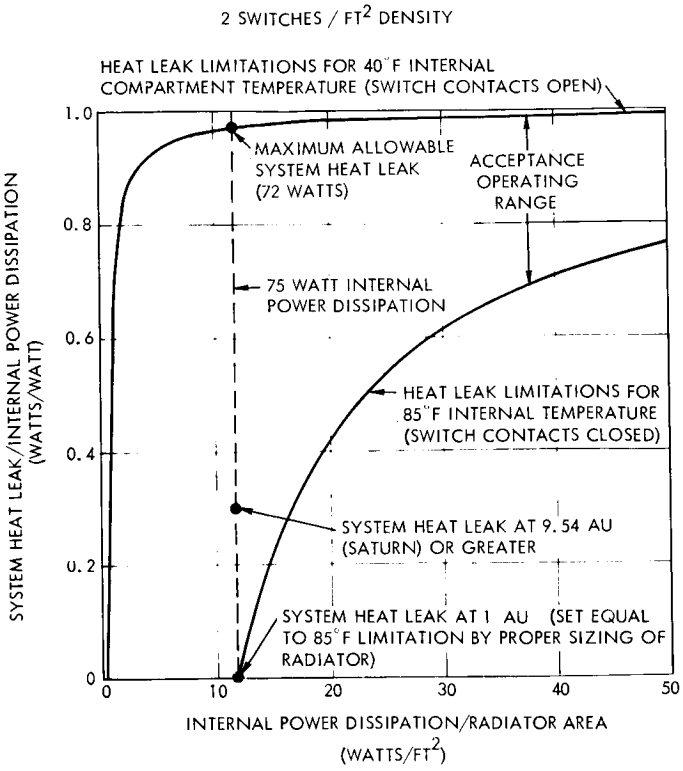

Figure 8-71. Thermal Control System Characteristics with Thermal Switches

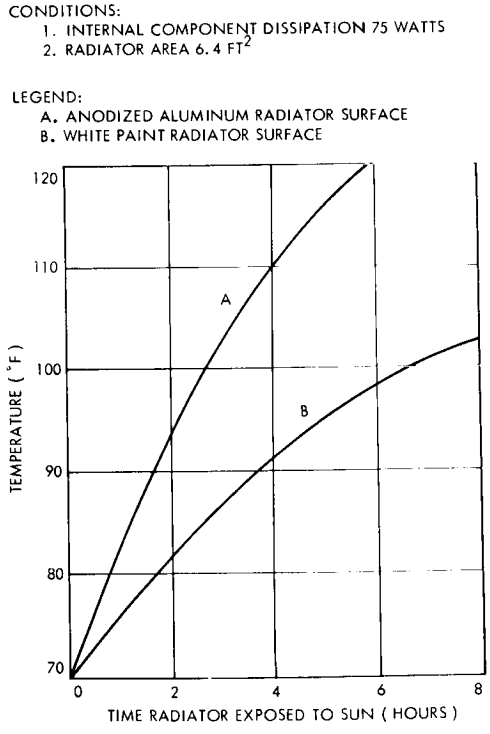

Figure 8-72. Compartment Temperature with Sun Normal to Radiator Panel

8.8.3 Cosmic Dust Erosion

The white radiator surface, as well as the black antenna surface, is subject to cosmic dust erosion. This erosion, if significant, could wear away the surface coatings and expose portions of the substrate material. However, this process should be relatively slow and will help the thermal control subsystem because the emittance of, and heat rejection from, the radiator surfaces decreases as the overall heat leak increases. The slow degradation assumption is based on temperature data from the TRW Vela spacecraft which has indicated that vacuum-deposited aluminum detector thermal contact surfaces have not appreciably deteriorated in over 2 years of exposure to the space environment. Any erosion of the antenna surface will increase the absorptance/emittance ratio and keep it from failing to such a low temperature level as the distance from the sun increases.

8.8.4 Hydrazine Engine

Figure 8-73 presents the main hydrazine engine temperature fluctuation as a function of orientation and distance from the sun. Considering that the specified acceptable hydrazine temperature range is 40 to 167°F, it is impossible to use passive techniques to control the engine temperature. For example, if an absorptance/emittance (α/ϵ) ratio of 1.0 is provided, the maximum temperature at 1.0 AU is a satisfactory 65°F, but the minimum temperature is -82°F which is well outside the acceptable range. For a 3.3 α/ϵ ratio, the minimum engine temperature is a tolerable 40°F, but the maximum temperature is too high at 235°F. Therefore, it will be necessary to use heater blankets to heat up the engine and lines before ignition. During ignition of the rear engine, the exhaust plume might impinge upon the radiator panel. However, since the panel has a high emittance, the exhaust gas is not expected to produce any significant change in the panel emittance. A change in panel absorptance is unimportant because the panel is never exposed to the sun after the engine fires. Base pressure effects should not affect the radiator panel either, since the thermal switch and panel are a rigid structural unit.

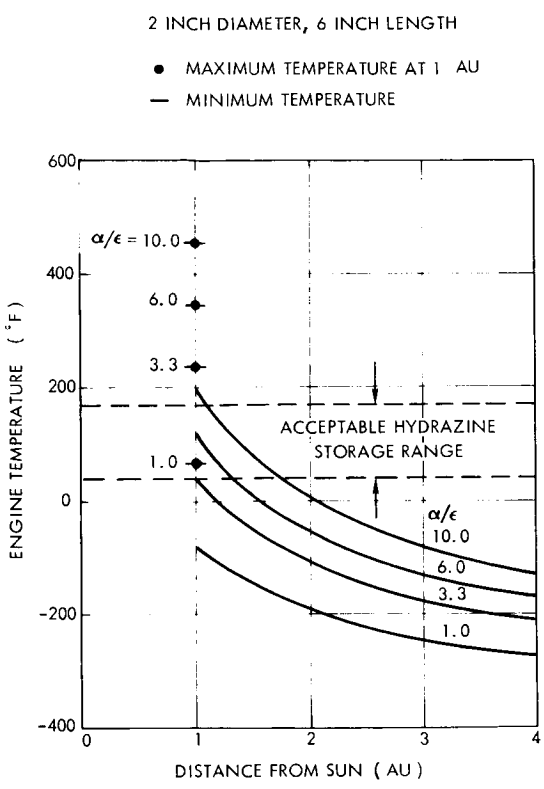

Figure 8-73. Hydrazine Engine Temperature

8.8.5 RTG Units

An acceptable on-stand RTG temperature is maintained by directing an inert gas flow over the exterior surface of the unit. The gas inlet temperature and flow rate are such that the RTG temperature is depressed to a level low enough to compensate for the boost RTG self-heating effect (prior to fairing ejection).

The design of the RTG unit is unknown at this stage of the study. Therefore, the analysis considered that the RTG properties were directly proportional to those of the Snap-27 unit being developed for the ALSEP Program. The Snap-27 characteristics are listed below.

Overall length	18 in.
Overall diameter (includes fins)	15.7 in.
Capsule diameter	5.5 in.
Weight	36.3 lb
Electrical power output	56 watts
Power dissipation (heat)	1450 watts
Surface area (including fins)	12.4 ft^2 actual (8 ft^2 used in calculations)

A factor of (P/56) was used to modify the above Snap-27 weight, power output, power dissipation, and surface area values. P represented the desired output power, or RTG power rating, in watts.

An inert gas, probably gaseous nitrogen, will be passed at a moderately high velocity over the RTG unit, or units. With the proper flow control it should be possible to obtain an average, somewhat conservative, convection heat transfer coefficient of 7 Btu/hr-ft^2-^{o}F with this system.

Figure 8-74 presents the parametric prelaunch temperature rise of the cooling gas with the selected heat transfer coefficient. As expected,

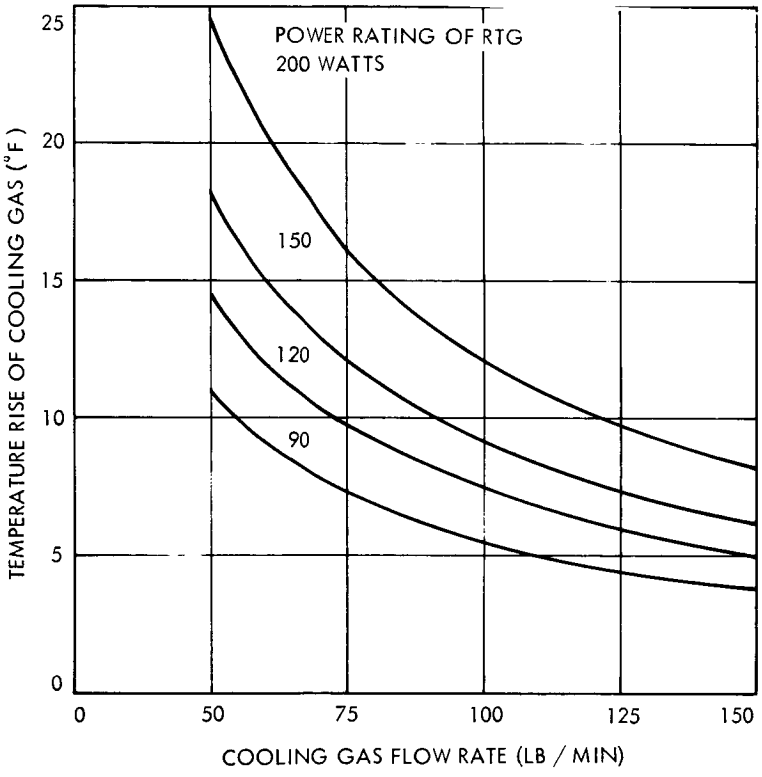

Figure 8-74. Prelaunch Cooling Gas Temperature Rise

the temperature rise increases with higher RTG power ratings and decreased flow rates. This figure indicates, however, that the rise is less than 25^{o}F with the maximum 200-watt RTG electrical output and a flow rate greater than 50 lb/min (usually available on most stands). A 25^{o}F temperature rise is acceptable for Advanced Planetary Probe on-stand thermal control if the inlet cooling air temperature is below 70^{o}F.

The RTG heats itself during boost since cooling gas is unavailable and radiation transfer to space is prevented by the fairing. The level of heating depends upon the prelaunch RTG temperature and the duration of the flight prior to fairing ejection. The effect of both of these parameters is shown in Figure 8-75. Power was not a factor in this curve because

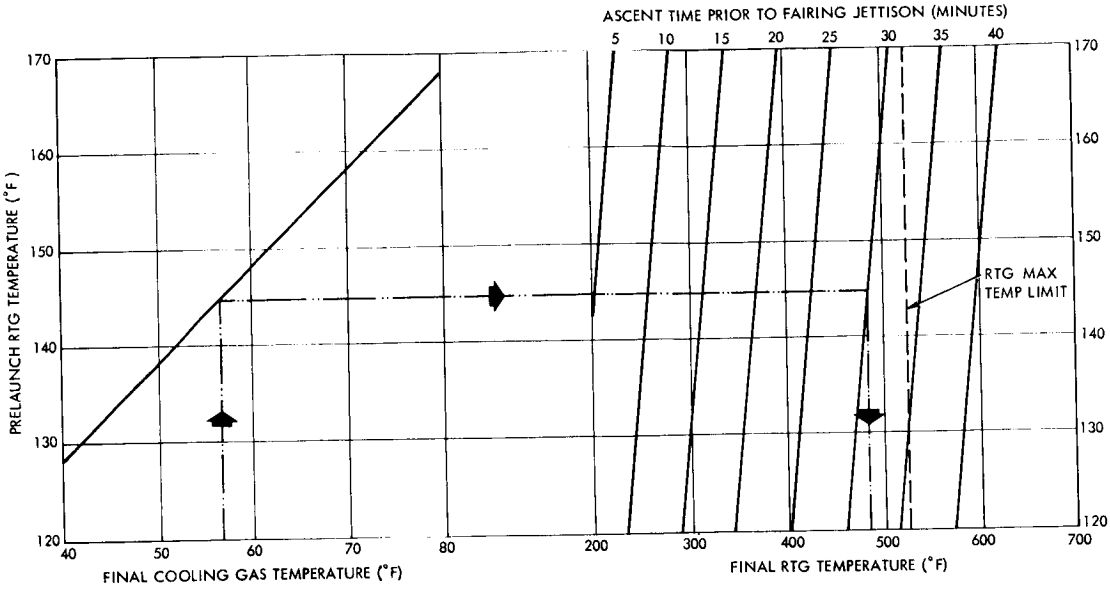

Figure 8-75. RTG Ascent Temperature Rise

the Snap-27 was proportioned to other power levels and the ratios of power dissipation (waste heat)/surface area, and the power dissipation/RTG weight remained constant. In actual practice this will not be exactly true, but should suffice in this preliminary analysis. In addition, for all boost calculations it was assumed that the cooling gas rose 25°F, again a conservative estimate. Even with this temperature rise, the fairing will not have to be jettisoned for at least 30 minutes for the assumed RTG maximum surface temperature limit of 525°F.

9. SPACECRAFT RELIABILITY

A reliability analysis for the spin-stabilized, 50-pound payload configuration was made on the basis of the parts lists for each of the subsystems. The analysis shows a reliability for 750 days of approximately 79 percent for the configuration adopted. This high value is achieved through the use of redundancy in all the critical subsystem areas.

In this analysis a k factor of 1 for the space environment has been adopted, although considerable evidence is at hand today that this value is quite conservative for the apparently benign environment of space. TRW has six Vela spacecraft operational in orbit, two of which have operated for more than three years with only a single failure in a redundant transmitter. Three OGO's are currently operational. One has been operating for more than 21 months without any failures other than those associated with the failure mode during spacecraft initial orientation. Pioneer 6 has been operating for 7 months without a single electronic failure. It did have a temporary gas leak which has since subsided and which did not affect the spacecraft performance. The Alouette top side sounder has been operating for about four years. OSO 1 has operated in a very complex mode in an orbit about the earth for more than three years. Mariners 2 and 4 both operated on complex missions for long durations. There appears no reason to expect Mariner 4 not to continue considerably longer than it has already.

The reliability analysis has been of the spacecraft only. It does not include scientific payload nor does it include any circuitry, such as TV buffer readout, associated with experiments. In addition, the tape recorders have not been included in the in-line assessment since the primary spacecraft mission objectives can be met without their use. With the addition of two redundant tape recorders, the effect is to reduce the reliability of the system from 0.79 to less than 0.5. The launch and separation sequence were not included in the assessment, since they are such a small percent of the total flight time. Redundancy at the black-box level is sequential except for the receivers and command decoding and distribution, which are standby.

9.1 RELIABILITY ASSESSMENTS

Reliability assessments were performed for the various black boxes that comprise the subsystems using black-box parts count estimates by the designers and by comparison to black boxes of equivalent complexity in other spacecraft built at TRW. These assessments were performed by a unique TRW computer program "Parka 3" (Parts Count Assessment) recently developed by the Reliability Department of TRW's Electronics Division. This allowed a relative assessment of many alternate redundant configurations. The computer program is described in Appendix I, along with the computer results.

Assessments are based on the analytical methods applied by TRW to the Voyager study.* The failure rates used are for high reliability, screened parts. They are estimates projected to 1970 and are consequently somewhat lower than those used in present spacecraft estimates. The projection is conservative, however, because it does not allow for decreasing failure rate with time. On the other hand, the bulk of the present failure rate data, from which the projection is made, does not fully account for long-term (e.g., five years) drift or wearout failure modes. It appears in general that these two considerations cancel one another.

Black-box assessment based upon parts count in each black box substantially biases the analysis since only a few individual failures result in a black-box failure. In a detailed assessment a careful study can be made to determine what parts failures result in a catastrophic failure and what lead to either a partial or negligible failure. In our assessment we have introduced a "role bias" factor, ℓ, which allows for component failure in a black box without unduly penalizing the subsystem. For example, switching functions of the command distribution unit are principally used during the first few days of operation. Moreover, only a few switching failures result in catastrophic system failure. Experiment calibration switching failures, perhaps the most frequent switching functions, will only partially degrade a given experiment.

---

*See, for example, p 153 et seq, "Phase IA Task B Final Technical Report, Voyager Spacecraft," Volume 5, 17 January 1966.

Moreover, certain switching functions such as those switching from one redundant mode to another are usually used only once during the entire flight and essentially have no failure rate associated with continuing use. These roll bias factors are given in Appendix I.

The reliability block diagram for the spacecraft is shown in Figure 9-1. The thermal control system since it is largely structural has very high reliability. The failure mode for the thermal switches is open which protects the primary portion of the flight from serious degradation. Early failure of one or two thermal switches would increase compartment temperatures only a small amount, which would not result in catastrophic failure.

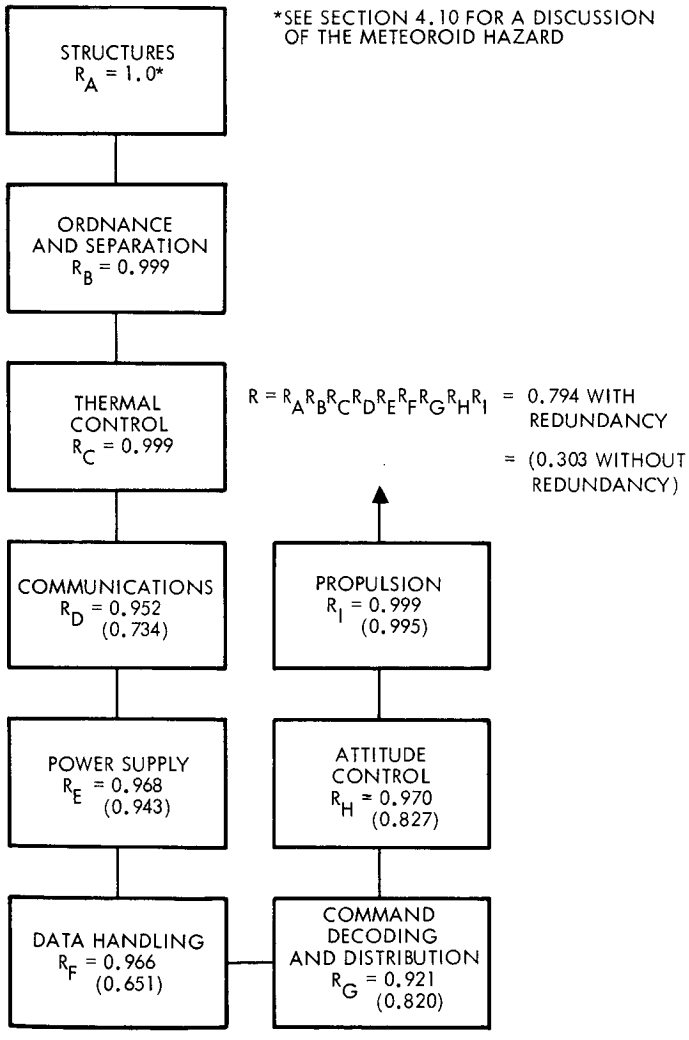

Figure 9-1. Reliability Block Diagram for 750-Day Mission, with and without Redundancy

The communication subsystem, which is almost identical to that of Pioneer 6, is based upon extensive analysis and experience. All critical items including the receivers, modulators, exciters, and power amplifiers, are redundant.

The reliability for the power subsystem shown here includes an estimate for the RTG's, and the power control unit and shunts. The projected estimate of the reliability of an RTG is very high.

The data handling here includes only the DTU which is identical to that on Pioneer 6 except for its slightly larger size. All of the critical components are redundant.

Command and distribution includes both the integrated decoder and sequencer and the command distribution unit. Both the command decoder and the command distribution unit are very similar to those on Pioneer 6 although somewhat larger.

The attitude control subsystem has redundant pneumatics and redundant electronics. On Pioneer 6 neither the pneumatics nor the electronics are redundant; however, they are not in line after the first 20 days of flight as they are on the Advanced Planetary Probe. The propulsion system and the despin system are required only during the first few days. Moreover, the reliability is high enough to make the probability of successfully completing a late midcourse correction very high if one is needed.

In the computer runs, in Appendix I, reliability values are presented for each subsystem for the mission times of 20, 50, 580, 750, 1100, and 1600 days. The 20-day period represents the time to the first orientation and velocity change maneuver, the second the time to a possible second maneuver; the 580, 750, and 1100 days are minimum, nominal, and maximum mission times to Jupiter; the 1600 days is the nominal mission time to Saturn.

9.2 RELIABILITY VERSUS WEIGHT

A study was made of the optimum system from the point of view of reliability versus weight. The total weight variables were, however,

only 26.8 pounds in a total of 492 pounds since the RTG's structure, large antenna, scientific payload, contingency, and other invariant weights consumed about 466 pounds.

Since the penalty for redundancy was only 5 percent of the gross weight, since the gross weight is well within the booster capability, and since the reliability increased from 0.303 to 0.794, there seemed no question that all the redundancy considered should be used. A more detailed study will be necessary to optimize within a specific set of constraints.

9.3 FAILURE MODE ANALYSIS

A failure mode analysis for the spacecraft system is summarized in Table 9-1. Each significant unit is identified and various failures and their possible causes described. The effect upon the system and its significance is then given and possible back-up modes identified. The major back-up mode given, of course, is redundant components, but various alternate modes of operation are possible and are described.

Table 9-1. Advanced Planetary Probe Failure Mode and Effects Analysis

Subsystem: Telecommunication

Unit	Failure Mode	Possible Causes	System Effect	Criticality	Backup Mode
Modulator exciter	No output	Catastrophic failure of any part excluding modulator parts	No payload and housekeeping data; loss of doppler tracking	Catastrophic	Redundant
	Carrier with no or garbled modulation	Catastrophic failure of any part excluding modulator parts	No payload and housekeeping	Catastrophic	Redundant
	Spurious frequency output	Failure of neutralization parts; design instabilities	Loss of data depending on severity and persistency of the instability	May be catastrophic	Redundant
Power amplifier	No output	Catastrophic failure of one or more parts	No payload and housekeeping data; loss of doppler tracking	May be catastrophic	Redundant
	Spurious output	Internal instability	Loss of data depending on severity and persistency of the instability	May be catastrophic	Redundant
Diplexer	Excessive insertion loss	Bad connectors	Power loss with resultant range decrease for both transmission and reception	May be catastrophic at extreme ranges	None
	Detuned	Cavities deformed	Power loss with resultant range decrease for both transmission and reception	May be catastrophic at extreme ranges	None
Omni-antenna A3	Mismatch to open	Bad connection	Loss of forward hemisphere coverage	Not catastrophic	None
Omni-antenna A4	Mismatch to open	Bad connection	Loss of rear hemisphere coverage	Not catastrophic	None
Receiver	No tone output and signal present conical scan output	Front end or mixer or intermediate frequency amplifier or variable controlled oscillator failure	Loss of remote control of spacecraft capability; also loss of earth pointing attitude control	Catastrophic	Redundant

Table 9-1. Advanced Planetary Probe Failure Mode and Effects Analysis (Continued)

Unit	Failure Mode	Possible Causes	System Effect	Criticality	Backup Mode
	No coherent output	Coherent output buffer amplifier	No doppler tracking data; no earth pointing control	Catastrophic	Redundant
	No audio tone output	Failed phase detector	Loss of remote control of spacecraft and of earth pointing attitude control	Catastrophic	Redundant
	No signal present output	Failed signal present detector, relay driver	Depends on control exercised by this output	May be catastrophic	Redundant
	No conical scan output	Failed conical scan buffer	Loss of earth pointing control	Not catastrophic	Sun sensor data and command reorientation can be used to retain degraded earth pointing mode
Circulator switches	Inability to switch; high insertion loss	Coil open	Inability to connect receiver to high gain antenna; loss of data at large ranges due to loss of remote control of spacecraft	Catastrophic	
Antenna selector	Inability to automatically select antenna	Internal part failure	Inability to connect receiver to high gain antenna; loss of data at large ranges due to loss of remote control of spacecraft	Catastrophic	Ground command override
High-gain antenna	Mismatch	Defective connector	Downlink range degradation; data loss at extreme range	Catastrophic at long range	Use medium-gain antenna until range excessive
Medium-gain antenna	Mismatch to open	Defective connector	Difficulty of earth acquisition by attitude control system	Not catastrophic	Ground control can compensate for this failure

Table 9-1. Advanced Planetary Probe Failure Mode and Effects Analysis (Continued)

Subsystem: Attitude Control

Unit	Failure Mode	Possible Causes	System Effect	Criticality	Backup Mode
Electronics assembly	No valve driver output	Part failure in clock divider, gating logic, zero crossing detector, valve driver	Inability to maintain earth pointing mode; if one valve, then damping effected with resultant performance degradation	Catastrophic if no output to two valves; degraded operation if one valve output fails	Dual drive allows degraded control if a failure effects one driver only
Sun sensors	No pulse output	Sensing element shaded or open	Valve impulse timing based on sun sensor timing; spacecraft unable to properly precess	Catastrophic if two sun sensors fail; degraded performance if one fails	Dual sun sensors offers a type of functional redundancy
Pneumatics	Leakage; no gas	Leakage in fittings, lines, solenoid valves, etc.	Inability to maintain earth pointing mode	Catastrophic when gas exhausted	Redundant
Despin system	Leakage	Leakage in fittings and lines	Inability to adjust spin rate	Not catastrophic	Operating procedure with spin rate knowledge can compensate
Subsystem: Power					
Equipment converter	No outputs	Part failure in oscillator or input line regulator	Complete spacecraft blackout except for TWT	Catastrophic	Redundant
	Loss of individual outputs	Part failures in rectifier, filter	Loss of capability depends on which output failed	Possibly catastrophic	Redundant
Central inverter	No output	Any part failure	Science payload deactivated	Catastrophic	Redundant
Central undervoltage monitor	Failure to provide overload protection to inverter in case of science payload short	Part failure	Secondary inverter failure resulting in loss of scientific payload	Catastropdic	Redundant
	Inadvertent line open	Change of current sensing calibration	Loss of single experiment	Not catastrophic; loss of at least two lines is defined as a failure	Redundant

Table 9-1. Advanced Planetary Probe Failure Mode and Effects Analysis (Continued)

Unit	Failure Mode	Possible Causes	System Effect	Criticality	Backup Mode
Radioisotope thermal generator	No or low output	Two adjacent thermocouples open	Power blackout of spacecraft	Catastrophic	
	Degraded power generating capacity	Open single thermocouple, increased contact resistance of thermoelectric element and hot junction electrode	Power duty cycle operation of spacecraft	Not catastrophic	Use of bypass diodes
Subsystem: Data Handling					
Digital Telemetry Unit	No output	Failed biphase modulator; failed clock; loss of power; failed combiner	No telemetered data	Catastrophic	Redundant
	Missing or scrambled data in transmitted format	Loss of or wrong timing of programmer outputs; wrong encoding due to failed A/D converter	Missing or scrambled telemetered data	Catastrophic	Redundant
	Inability to select bit rate and/or format and/or mode	Failed control logic	Depends on when failure occurs during mission; for instance at extreme ranges, inability to go to low bit rate means data loss	Conditionally catastrophic	Redundant
	Missing data channels	Failed main and subcommutator channels	Loss of data associated with channels	Not catastrophic	Redundant
	Incorrect data	Failed parity check	Infrequent incorrect data	Not catastrophic	None

Table 9-1. Advanced Planetary Probe Failure Mode and Effects Analysis (Continued)

Subsystem: Propulsion

Unit	Failure Mode	Possible Causes	System Effect	Criticality	Backup Mode
Explosive valves, hydrazine tank, line and fittings	Squib failure	Open circuit	No midcourse correction or failure to terminate midcourse correction	Conditionally catastrophic	Parallel backup midcourse firing possible (redundant explosive valves)
Hydrazine fill and drain valve, nitrogen fill valve	Leakage	Vibration	Degrade or loss of midcourse capability	Conditionally catastrophic	None
Propellant filter	Blockage	Contamination	Degrade or loss of midcourse capability	Conditionally catastrophic	Redundant
25-lb thrust engine	Burnthrough	Insulation bond separation	Degrade or loss of midcourse capability	Not catastrophic	Other ΔV thruster available

10. SCHEDULE

The schedule for the spin-stabilized Advanced Planetary Probe is summarized in Figure 10-1 and is developed in more detail in Figure 10-2. The two figures correlate by means of the shaded areas representing the main sequential and parallel phases of the program. These are the Phase B study of four months, followed by a two-month period for contractor selection, leading into a six-month Phase C definition study and a Phase D hardware program initiated one month later. Phase D includes four parallel development efforts initiated at appropriately early periods before definite requirement dates for spacecraft assembly and launch. These parallel efforts include spacecraft development, antenna development, and launch operations, all associated with the prime contract. The other major efforts are RTG development and experiment development and qualification.

The schedule is based on the following assumptions. Use of the Atlas/Centaur/TE-364 eliminates any launch vehicle lead-time problems. Proven components and techniques are employed wherever appropriate. Because the lifetime of the mission is two years or more, reliability requirements affect the design, test, and manufacturing aspects of the schedule. The hardware required for development includes the basic breadboards, unit engineering models, and an engineering model spacecraft assembled after completion of unit engineering model tests. Hardware required to demonstrate flight readiness includes structural and thermal model spacecraft, unit qualification articles, and a flight configuration spacecraft for qualification test of the complete system, including experiments and RTG. It is assumed that the experiment and RTG development and qualification efforts adhere to the same requirements as the spacecraft hardware.

The pacing sequence of the spacecraft development phase is the procurement of long lead-time material followed by manufacture, test, and assembly of qualification and flight hardware. Reliability requirements dictate the selection of certain high reliability electrical parts. Procurement of these items and other long lead-time articles is scheduled to start one month after initiation of Phase D. If this procurement action

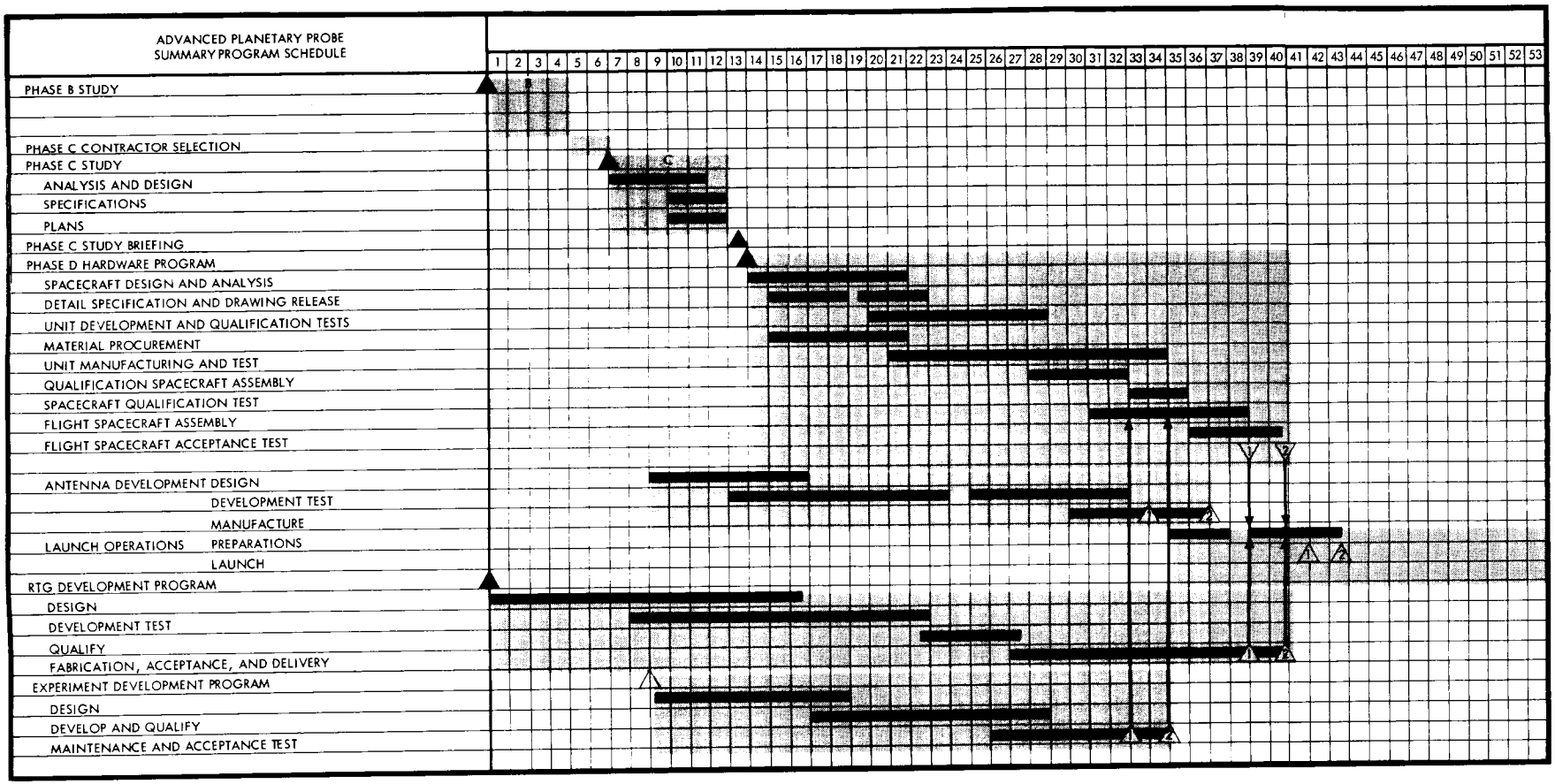

Figure 10-1. Advanced Planetary Probe Summary Program Schedule

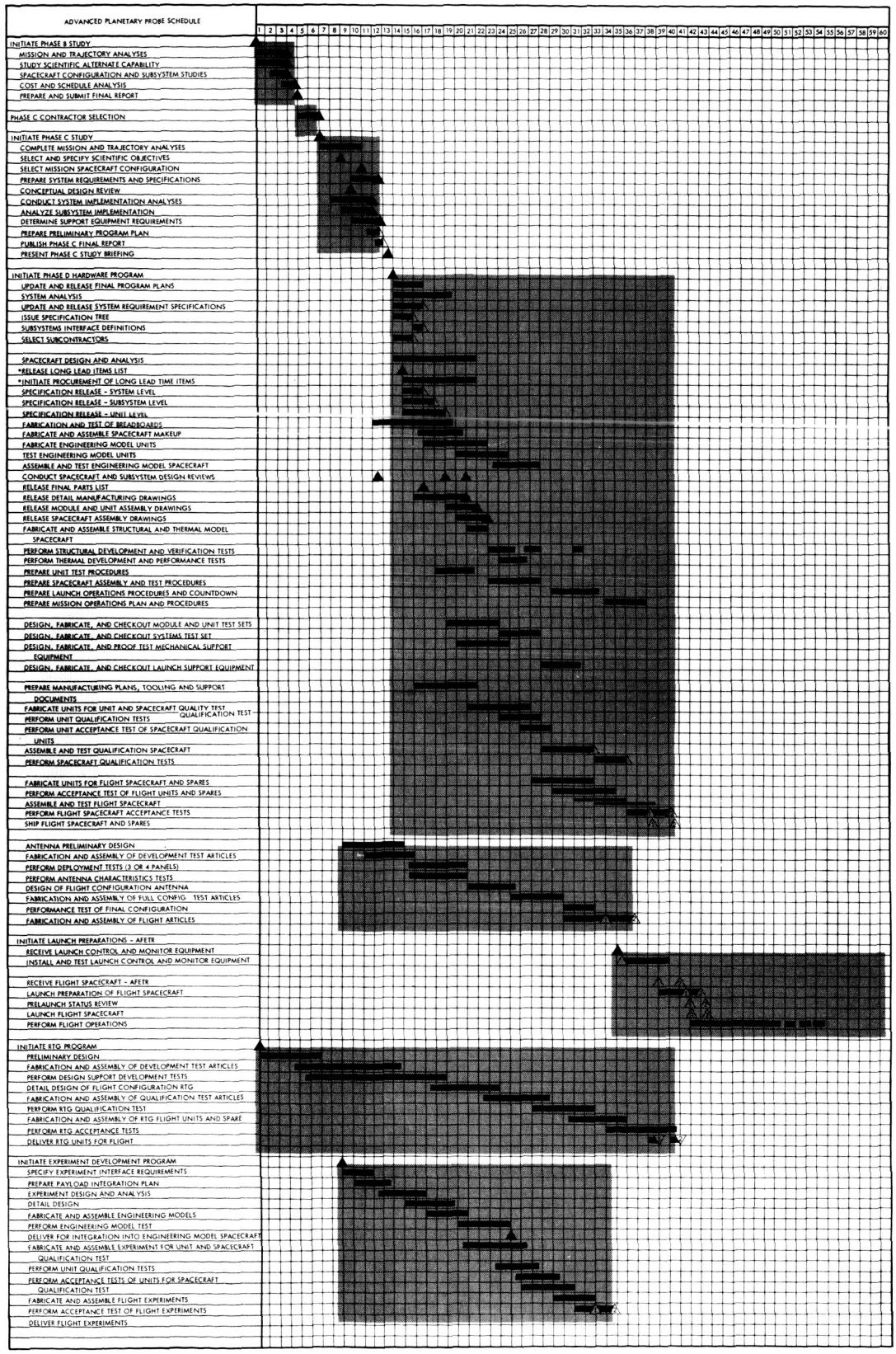

Figure 10-2. Advanced Planetary Probe Schedule

were initiated during Phase B, when design is complete enough to define these items, the launch date could be advanced by three or four months.

A critical item in this development schedule is the RTG's. Various estimates of the amount of fuel available in the future have been made, and it is the difference in the estimates of this availability that causes a fundamental problem. Therefore, the objective of minimizing the power requirements is paramount. The fuel required for each spacecraft is 2000 thermal watts, an amount which can be expected to be available for spacecraft application in the near future. We have shown the two launches requiring 4000 thermal watts, an amount which the AEC could produce by 1970 if a requirement was established. The requirements for minimum power for the mission are also critical with respect to the expected estimated cost of the fuel itself. Basically, then, we have estimated that flight qualified RTG units could be made and 4000 thermal watts of Pu-238 could be available two years after program go-ahead.

Another major development item is the deployable antenna, which we are confident can be developed and tested in 18 months. This estimate is based on our experience with the successful Sunflower solar collector performance by TRW in the early 1960's.

Since the RTG development paces the entire program, no other item has any substantial interference with the schedule. However, the use of a number of developed items can substantially reduce system costs as well as simplify development. Our experience with OGO, Pioneer 6, Vela, and other spacecraft development programs makes us confident of the schedule submitted for the Advanced Planetary Probe.

11. COST ESTIMATE

This section presents the cost estimate for the 500-pound spin-stabilized spacecraft with a 50-pound scientific payload. The schedule on which this cost estimate is based is given in Section 10. Only the portion of the program identified as Phase D has been costed, but portions of Phase D, a full design, development, test, and launch program, which might be carried out during Phase C are included.

Table 11-1 summarizes the overall cost of the program, which includes one set of qualification units, one prototype spacecraft, and two flight spacecraft. The nonrecurring cost of $21.5 million includes all of the costs associated with design and development through prototype including fabrication of all components and test equipment required. The recurring cost of $9.3 million includes all the items of cost associated with fabrication and integration for two flight spacecraft. The total estimated cost of the program is $34.4 million.

Before defining each of the areas of cost the basic ground rules of the costing work are given below:

- No experiment costs are included.
- No special experiment integration costs are included.
- The cost of the RTG units and fuel has not been included since development is carried out by the AEC and since the fuel costs are not yet known (it is estimated that the total cost of such a program might run anywhere between $5 and 15 million).
- The fundamental basis for the estimation was to use prior TRW programs such as Pioneer, OGO, Vela, etc., and to compare black boxes or subsystems on those programs with the Advanced Planetary Probe elements. This experience was used to develop ratios for number, weight, power, area, and parts quantities.
- Costs were developed for direct labor and ODC. A burdened rate of 101 percent applied to labor and a burden of 10 percent applied to ODC. The G and A rate of 10.5 percent was applied to the totals.
- Each subsystem was totaled for nonrecurring cost and for recurring cost.

Table 11-1. Cost Estimates for the 500-Pound Spin-Stabilized* Advanced Planetary Probe (in millions of dollars)

	Nonrecurring	Recurring	Total
Program management	1.6	1.0	2.6
System engineering	1.6	0.4	2.0
Program data management	0.7	---	0.7
Structure and booms	2.4	0.3	2.7
Thermal	0.8	0.1	0.9
Electrical integration equipment	0.8	0.1	0.9
Power (RTG interface and power conversion)	0.7	0.1	0.8
Data handling and command	1.6	0.5	2.1
Tape recorder	1.5	1.0	2.5
Communication	1.4	0.4	1.8
Deployable antenna	1.4	0.1	1.5
Attitude control	1.1	0.1	1.2
Midcourse and despin propulsion	1.8	0.2	2.0
Integration and test	2.8	1.6	4.4
Reliability	0.8	0.6	1.4
Quality assurance	1.8	1.7	3.5
Electronic GSE	1.9	---	1.9
Mechanical GSE	0.7	---	0.7
Launch support	---	0.5	0.5
Total	25.4	8.7	34.1

*29-month program
1 set qualification units, 1 prototype spacecraft, 2 flight spacecraft
50 pound science payload

- Cost for software portions of the program such as program management, systems engineering, reliability, and quality assurance were developed using current ratios for equivalent NASA programs.

- Costs are expressed in mid 1966 dollars; no escalation has been applied.

Each of the items in Table 11-1 are discussed briefly below.

Program management is assumed to run fairly steadily over the schedule until launch and assumes that an average program office staff of about 30 people will be needed.

The system engineering task includes a rather extensive trajectory and guidance analysis as well as analyses of mass properties and other related tasks.

Program data management costs are based upon a scale cost for data management for the Pioneer program.

The structure and booms costs are based upon a composite examination of experience on both Pioneer 6 and OGO. They include the development and test of the structural model but not the deployable antenna (costed separately) or the deployment and spin tests. A major item of the structures costs is connected with the requirements for high accuracy alignment.

Thermal costs are based upon Pioneer experience and include considerable thermal model test and heat leak analysis and test.

Electrical integration equipment includes the command distribution unit, cabling, and harnesses. Costs are based on Pioneer 6.

Power costs include two items: power control unit and RTG interfaces. It is expected that some RTG interface work will also be performed by the program office.

Data handling and command includes the cost of a digital telemetry unit and integrated decoder and sequencer but not the tape recorders. These costs are based upon both Pioneer and OGO.

The tape recorder cost is based primarily on OGO experience but scaled down somewhat to take into account the relevant development that will have preceded the APP tape recorder.

Communication costs are based directly on Pioneer since these subsystems are almost identical.

The deployable antenna cost is based upon TRW experience with the development of a Sunflower collector suitably scaled down to the desired size.

The attitude control subsystem costs are based upon Pioneer 6 but include substantial development and test of the conical scan technique, including antenna range testing.

Midcourse and despin cost propulsion are based upon Able 5 experience and Intelsat III data.

The integration and test costs are based upon the Pioneer 6 experience but suitably scaled up for the work involved with the deployable antenna and the deployable RTG's.

Both reliability and quality assurance costs are based on percent factors developed from other programs.

Electronic GSE is based having two sets of unit testers and two system testers for simultaneous work with the prototype and flight articles.

Mechanical GSE costs are based upon Pioneer 6 cost with additional costs added for boom deployment test and spin up and despin test.

The launch support costs are based upon two launches within a 30-day launch window.

As a test of the validity of the cost estimating procedure, it is interesting to compare the recurring cost of a Pioneer spacecraft with the estimated recurring cost for the Advanced Planetary Probe. The present Pioneer spacecraft weighs about 140 pounds and carries 35 pounds of experiments; the spin-stabilized Advanced Planetary Probe weighs almost 500 pounds and carries 50 pounds of experiments. The recurring cost for Pioneer is $2 million and the recurring cost for the Advanced Planetary Probe is $4.5 million. Since the gross weight of the Advanced Planetary Probe is more than a factor of 3.3 greater than Pioneer while the recurring costs are only 2.5 higher, there appears to be a significant disparity.

It must first be pointed out that the Advanced Planetary Probe costs do not include the cost of the RTG power supply so that 77.6 pounds may be subtracted from the spacecraft gross weight of 492 pounds making the weight comparison 140 versus 415. In addition, the 50 pounds of antenna dish structure as well as the 31 pounds of micrometeoroid protection need to be subtracted since these are low recurring cost items. Another item which must be subtracted from the Advanced Planetary Probe weights to make the comparison valid is propellant, which is also a very low-cost item. In addition, the third stage spinup system of 4.2 pounds must also be subtracted since this is appropriately charged to the third stage cost. The weight-cost comparison then becomes 140 to 308 pounds and $2 to $4.5 million, and, as can be seen, the difference in cost per pound although very small is higher for the as yet undeveloped Advanced Planetary Probe concept.

There is one other sitnificant item, 38 pounds for contingency. In a weight analysis it is always assumed that this contingency will be used but the particular allocation of low cost versus high cost utilization of this weight is seldom considered. Past experience at TRW Systems has generally indicated that it is in the low recurring spacecraft cost elements such as structures, cabling, and harness that this weight is consumed, and the largest percentage of this additional requirement arises out of the specific scientific payload requirements which are not appropriately chargeable to spacecraft cost. Therefore, it appears that on a rather elementry weight-cost comparison the recurring costs for the Advanced Planetary Probe are reasonable.

12. COST EFFECTIVENESS

This section evaluates the spacecraft system and its payload in terms of cost. Although the cost can be fairly well determined, the criteria for measuring the effectiveness of the design are not defined a priori. The choice of cost-effectiveness criteria depends on the interpretation of mission objectives and their priorities, and on the practical attainability of these objectives by the chosen technical approach. The analysis that follows is to a large extent qualitative and reflects subjective opinion and value judgments by the investigators.

The first item in the discussion of cost effectiveness is a review of cost elements, especially the cost of the launch vehicles considered for implementing the mission, with regard to the 500-pound class of spin-stabilized spacecraft. Alternatives of higher-cost but shorter-flight-time missions are considered in order to evaluate the gain in probability of mission success thereby attained.

Effectiveness criteria are discussed in qualitative terms with emphasis on the scientific objectives of typical first-around or precursor missions to Jupiter and the outer planets. This section also presents a quantitative analysis based on an effectiveness index in which payload weight and launch vehicle cost factors are primary variables. The result of these evaluations support the choice of a payload weight of 50 pounds for the baseline configuration of the Jupiter flyby.

12.1 COSTS

There are four basic items of cost in a scientific spacecraft program: booster, spacecraft, experiments, and flight operations. (The launch operations are charged in the cost of both the boosters and the spacecraft.)

The cost of the seven boost vehicles considered in this study, including launch operations, are estimated as follows, in millions of dollars.

Atlas/Centaur/TE-364-3	9.5
Atlas/Centaur/HEKS	14.5
Titan IIIC/Centaur	19.9
Titan IIIC/Centaur/TE-364-3	20.4
Saturn 1B/Centaur/HEKS	43.0
Saturn V	125.0
Saturn V/Centaur	130.0

Mission-peculiar equipment is not included.

The cost of spacecraft development, estimated in Section 11, will be about $35 million through the first two flight spacecraft. It is estimated that each subsequent spacecraft, not including RTG fuel, would cost on the order of $4.5 million. To this cost must be added the cost of the fuel, between $1 and $5 million. In this comparison we will use the lower figure of $1 million per spacecraft, making a total of $5.5 million. The development costs are therefore about $26 million for this 500-pound, spin-stabilized spacecraft.

Experiment costs vary substantially, of course, but for purposes of costing the program we will assume that each experiment will cost on the order of a million dollars apiece for two flight articles.

Flight operations, which include ground station time, data reduction, etc., are difficult to cost since the DSIF network is an on-going operation and has continuing costs associated with it whether it is in use or not. Data reduction costs are also difficult to measure since they are sensitive to data reduction techniques used, amount of data transmitted, etc. For purposes of this analysis we will assume that the flight operations cost $10,000 per day. The flight operations costs, of course, are then sensitive to mission time. In general the experiments change from launch year to launch year and thus continue to cost about the same for each year. On the other hand, the spacecraft should not require extensive development after the first flight.

The cost of the 500-pound spin-stabilized spacecraft flyby mission to Jupiter using the least expensive boost vehicle is listed in Table 12-1. In addition, we must of course consider the effect that shortening the

Table 12-1. Relative Costs for Jupiter Flyby Mission (millions of dollars)

	Atlas/Centaur/ TE-364	Atlas/Centaur/ HEKS	Titan IIIC/Centaur/ TE-364
Boost vehicle	9.5	14.5	20.4
Spacecraft	5.5	5.5	5.5
Experiments	10	10	10
Flight operation	7 (700 days)	5 (500 days)	3.5 (350 days)
Totals	32.0	35.0	39.4

flight time has on reliability and in turn on costs. Table 12-2 compares the cost of the spacecraft for one and two launches; these costs are then divided by the estimated reliability of the spacecraft (reliability of the boosters is assumed to be the same). In this table the term Q in the spacecraft reliability column indicates the probability of failure for various flight times, showing an approximately linear dependence in view of the low failure rate assumed here. The first term (0.05) in Q reflects the failure probability for the first 10 days, assumed to be invariant for the four launch vehicles listed.

As shown in the upper portion of Table 12-2, the resulting average cost of roughly $45 million to achieve a successful mission differs insignificantly for the two Atlas/Centaur and the Titan/Centaur launch vehicles, if only one launch is contemplated. For two and more launches the Atlas/Centaur/TE-364 shows a definite cost advantage.

For purposes of comparison only, the effect of an unrealistically low estimate of spacecraft reliability is shown in the lower part of Table 12-2. The results indicate the gains that would be achieved by

Table 12-2. Jupiter Flyby Mission Cost and Reliability for 50-lb Payload Spinner Configuration

a) HIGH RELIABILITY ESTIMATE

Launch Vehicle	Flight Time (days)	Spacecraft Reliability: First 10 days		Remainder		Q (1 spacecraft)	R (1 spacecraft)	(2 spacecraft)	Cost ($M): 1 launch	Cost ($M): 2 launches	Cost/Reliability ($M): 1 launch	Cost/Reliability ($M): 2 launches
Atlas/Centaur/ TE-364	700	0.05	+	0.25	=	0.30	0.70	0.91	32	54	46	59
Atlas/Centaur/ HEKS	500	0.05	+	0.18	=	0.23	0.77	0.95	35	60	44	63
Titan/Centaur/ TE-364	350	0.05	+	0.125	=	0.175	0.825	0.97	39.4	68.8	48	71
Saturn V/Centaur	255	0.05	+	0.091	=	0.141	0.859	0.98	142.5	275	166	281

b) LOW RELIABILITY ESTIMATE

Launch Vehicle	Flight Time (days)	First 10 days		Remainder		Q (1 spacecraft)	R (1 spacecraft)	(2 spacecraft)	1 launch	2 launches	1 launch	2 launches
Atlas/Centaur/ TE-364	700	0.05	+	0.85	=	0.90	0.10	0.19	32	54	320	284
Atlas/Centaur/ HEKS	500	0.05	+	0.757	=	0.807	0.193	0.349	35	60	182	172
Titan/Centaur/ TE-364	350	0.05	+	0.635	=	0.685	0.315	0.531	39.4	68.8	125	130
Saturn V/Centaur	255	0.05	+	0.518	=	0.568	0.432	0.678	142.5	275	329	405

Note: The assumed reliability function is $R = e^{-\lambda t}$ where t = mission time and $\lambda \cong 0.53 \times 10^{-3}$ (day^{-1}) in Case a; $\lambda \cong 3.30 \times 10^{-3}$ (day^{-1}) in Case b. $Q = 1 - R$ = probability of failure.

using excess boost capabilities to shorten flight time when the spacecraft reliability is very low. Also shown for contrast is the effect of using the Saturn V/Centaur to shorten flight time. This example clearly illustrates that excess booster capability can be used efficiently only up to a certain point. Obviously the Saturn V could better be used to carry multiple spacecraft; the flight time would not increase significantly.

A cost comparison which uses booster capability for shortened flight time is appropriate where the spacecraft weight is fixed. An alternate approach is to compare booster cost in terms of pounds of weight the booster can deliver to the vicinity of Jupiter. This comparison will be given in Section 12.3.

12.2 EFFECTIVENESS CRITERIA

There are many approaches to judging the effectiveness of a spacecraft program. It is customary to consider criteria such as pounds of of payload per dollar of launch cost, bits of information per pound, bits of information per dollar, etc. However, none of these criteria by itself has much significance independently of the objectives of the mission.

The scientific objectives of the 500-pound, spin-stabilized spacecraft are twofold. The first, to make measurements of interplanetary space out to and beyond the orbit of Jupiter, can be evaluated by itself. As such, the spacecraft mission is similar to the present Pioneer program except for probing much farther from the sun. The second, to make measurements of the planet Jupiter and its environment during flyby, although conceived as primary cannot override the interplanetary objectives since the flyby duration is only a very small percentage of the total flight time and has perhaps no more scientific value. Thus the scientific payload should be a compromise between the planetary and interplanetary objectives with as many experiments designed to combine both objectives as is practical.

Another major consideration is the character of the mission. For example, a first, or precursor flight will be looking for relatively crude scientific results since it is not possible to design sophisticated experiments without some initial data. Since the 500-pound, spin-stabilized spacecraft is a precursor, criteria such as bits of information per dollar

or pounds per dollar and even bits per pound, do not offer adequate criteria of effectiveness when it might not be possible to use a large amount of weight or a very large amount of information effectively.

In addition, the probability of mission success must also be considered since it has a bearing on the number of flights required. High reliability can be achieved by following two distinct approaches: a very simple lightweight design having few parts and these redundant, or the employment of a more sophisticated design approach leading to complex, highly redundant, heavyweight spacecraft which has onboard failure mode detection, etc. Such a spacecraft would allow a larger and greatly refined complement of science experiments. It is clear that the selection of one or the other of these design approaches cannot appear equally desirable in terms of a single cost-effectiveness criterion. Rather, several criteria must be applied to indicate which approach best meets the mission objectives.

Perhaps the most significant effectiveness criterion is to evaluate the experiments carried by determining to what extent they contribute to the objectives of the projected broad program of interplanetary and planetary exploration. Assuming that a specific deep-space interplanetary mission has been defined, one might establish a list of experiments, assign weighting factors to each, and thereby ascertain how well a spacecraft satisfies such a list. A similar list would be made for a planetary mission. Standard interplanetary experiments include magnetic fields measurements, solar wind measurements, cosmic ray measurements, micrometeoroid dust measurements, and electron density measurements, all of which the 500-pound spacecraft carries. Typical planetary experiments include magnetic fields, trapped radiation, atmospheric observations with radiometers, and television and detection of the aurora. All of these are carried on the 500-pound spacecraft. In general, an increase of payload capability does not substantially increase the interplanetary measurements but, more logically, increase the observations of the planet, since it is the planetary phenomena that offer the greater possibility of additional measurements. For example, in Table 12-3 we compare four payloads ranging from 12 to 250 pounds. As can be seen,

Table 12-3. Science Payload Classes (Jupiter)

12 Pounds (JPL Specified)	50 Pounds	100 Pounds	250 Pounds	
	Galactic cosmic ray	Galactic cosmic ray	Galactic cosmic ray	Interplanetary
	Solar cosmic ray	Solar cosmic ray	Solar cosmic ray	
	Solar plasma	Solar plasma	Solar plasma	
Magnetometer	Magnetometer (No. 1)	Magnetometer (No. 1)	Magnetometer (No. 1)	
	Micrometeoroid	Micrometeoroid	Micrometeoroid	
	Radio propagation and radio occultation	Radio propagation and radio occultation	Radio propagation and radio occultation	
	Television	Television	Television	Planetary
Trapped radiation	Trapped radiation	Trapped radiation	Trapped radiation	
	Infrared radiometer	Microwave radiometer	Microwave radiometer	
	Auroral detector	Auroral detector	Auroral detector	
		Magnetometer (No. 2)	Magnetometer (No. 2)	
		Low energy proton monitor	Low energy proton monitor	
		Visual solar occultation	Visual solar occultation	
			Topside sounder	
			Infrared radiometer	
			Visual spectrometer	
			VLF whistler	
12 pounds 9 watts	57 pounds 27 watts at encounter	108 pounds 37 watts at encounter	225 pounds 56 watts at encounter	

the experiments carried for interplanetary measurements are constant in the 50-, 100-, and 250-pound payloads. All of the increased weight capability is best devoted to the planetary experiments.

The 12-pound payload provides two interplanetary experiments which can also serve to make measurements at the planet, although the micrometeoroid experiment is not expected to give much data during the encounter. It carries only one experiment which is exclusively concerned with the planet. The overall weight of the spacecraft necessary to carry these three experiments is 287 pounds. A bit rate of 70 bits/sec is provided during planetary flyby, which is well matched to the data rate assigned to these experiments. However, the cost of this spacecraft is about 40 percent less than the cost of the 50-pound payload spacecraft, which has a gross weight of 500 pounds. The 50-pound payload is much more attractive in terms of payload composition and yield of data, with more than three times the experiments and less than twice the overall weight.

For the 100- and 250-pound payloads the increased weight has been allocated to planetary experiments and in general provides only quantitative improvements of data already incorporated by the simpler payload. In the 100-pound payload the addition of a microwave radiometer only improves findings by the infrared radiometer; the addition of a second magnetometer only increases the accuracy of the magnetic field measurements; the addition of the low energy proton monitor only enhances the trapped radiation measurements; and the visual solar occultation only enhances the radio occultation of this experiment. In the 250-pound payload such additions as the topside sounder and the visual spectrometer are also refinements of data already being gathered.

One might assert that if payload capability exists, it should be used. But to make best use of payload weight capabilities for refined measurements good initial estimates of the phenomena to be measured should be available, or mission effectiveness will be degraded. With respect to the interplanetary experiments, we are quite confident of the range of phenomena to be observed, but for the planetary experiment there is much uncertainty as to what one may be able to detect. We believe there

is a radiation belt, but this is only inferred. We do not know whether or not Jupiter has an aurora. We know that there are interesting phenomena for graphic observation (TV experiment), but we have no data to determine what resolution is desirable. Again, a matter of great concern is the detection of internal heat sources on Jupiter, but at this time a good approach for performing this experiment has not been formulated. We therefore conclude that most important in the payload composition of a precursor mission is the ability to make broad measurements which can then form the basis for later, more sophisticated experiments. Planetary orbiters designed for long-duration observations are needed to perform the second-round of planetary exploration missions beyond Jupiter. Before embarking on the orbit mission, the type of data that a relatively simply flyby mission can provide is necessary. On these grounds it appears that the 50-pound payload is the more appropriate.

A criterion of particular interest is the cost of ground facility operations during the mission, as listed earlier. Ground station availability is not merely a matter of cost; perhaps more critical is the problem of time sharing with other missions. A DSN ground station requires typically 4 hours of set-up time on a day when communication contact and lock-on is to be established with a particular spacecraft. Long communication round-trip times to a spacecraft at 5 to 6 AU will further increase the lock-on time period, unless contact and control is "handed over" from the preceding station. To the extent that the number of station-days scheduled for contact with the Advanced Planetary Probe can be made small, cost savings and reduction of the DSN operational burden can be achieved. This in turn implies that the spacecraft should have a large storage capability coupled with a moderate data sampling rate and a high data transmission rate, because a large amount of data may be stored and transmitted in relatively short bursts. It is further recalled that the spin-stabilized configuration does not require updating of its earth-pointing orientation more often than approximately once per week during most of its cruise period (see Section 4.5).

Another item which at this date appears to be significant is the cost of the fuel for the RTG's, which generally suggests that electrical power requirements should be minimized. To a large extent this minimization

has occurred on the 12- and 50-pound payloads but is less easily achieved with the 100- and 250-pound payloads because of the peak power requirement at encounter associated with greater emphasis on encounter science. It is not desirable to size the RTG's to meet these peak power requirements or to add batteries to meet them.

12.3 PRELIMINARY COST EFFECTIVENESS MODEL

This section attempts to express the effects of several key parameters of launch vehicle cost and spacecraft development cost versus payload weight in terms of a quantitative model. Such a model will serve as a criterion of cost effectiveness and will be used to exhibit in quantitative terms the advantages and penalties associated with the choice of certain payload weights. The objective is to show basic trends in the payload weight versus cost relationship which may assist the spacecraft designer in the selection of a preferred weight class.

Since the simple analytical model adopted here reflects only a few of the factors which actually must enter into the tradeoff, the results obtained will have to be interpreted carefully and checked against realistic constraints in the spacecraft and launch vehicle cost, in the utilization of the payload, etc. For example, if a range of payload weights appear favorable in terms of this cost-effectiveness criterion, it must still be ascertained whether a payload of this size is practical in precursor missions such as those projected for the Advanced Planetary Probe.

The ratio of payload weight to cost per spacecraft launch can be expressed by

$$W_1 = \frac{ax}{b + cx} \left(\frac{\text{lb payload}}{\text{dollars per launch}}\right)$$

where

x = nondimensional variable ($0 < x \leq 1$) representing payload weight

a = maximum payload weight in pounds contemplated for the missions; in this study $a = 250$ pounds

b = cost of launch vehicle and spacecraft (in dollars per launch) for negligibly small payload weight

c = cost increase over minimum cost b (dollars per launch), including spacecraft development and launch vehicle cost, for the largest payload weight contemplated for the mission

The term appearing in the denominator

$$U = b + cx \text{ (dollars per launch)}$$

is a simplified model of cost variation with payload weight, assuming that spacecraft gross weight and complexity, and hence development cost, increases approximately in proportion to the increase in scientific payload for a given mission profile. A more realistic representation of cost variation is contained in the modified cost effectiveness index discussed below.

If more than one spacecraft is to be developed and launched the cost b at x = 0 remains essentially fixed while the increment c is reduced (see Figure 12-1), reflecting the reduction in spacecraft cost which results due to nonrecurrent cost elements. The figure shows data points for the cost and weight capabilities of several launch vehicles, as

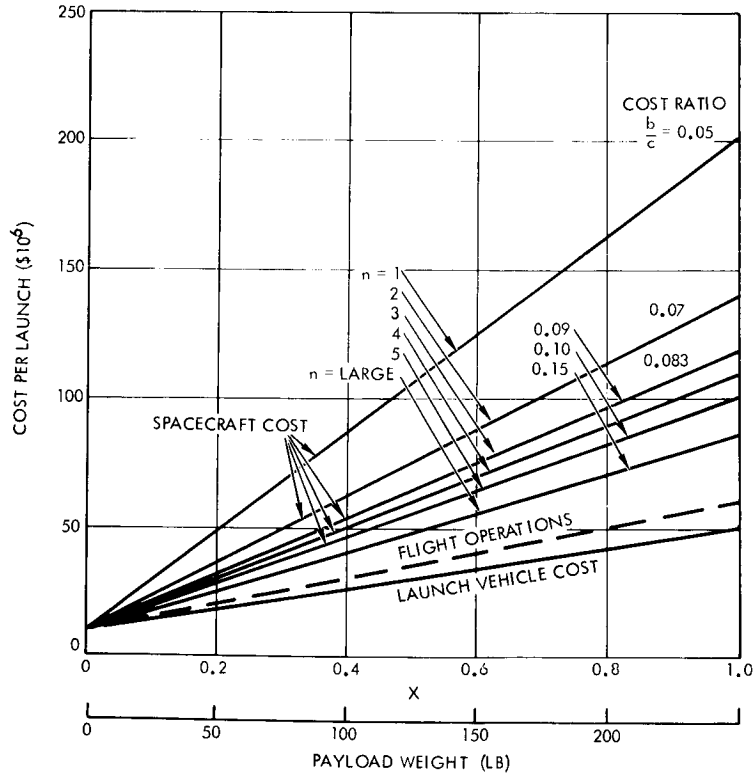

Figure 12-1. Cost Function Versus Payload Weight for Typical Mission Profile

discussed in Section 12.1. The actual discontinuous cost changes required by stepping into the regime of larger launch vehicles as x increases from 0 to 1 is not reflected in this simplified analysis.

A modified cost effectiveness index can be defined by including a penalty function

$$p(x) = \frac{1}{1 + ex}$$

with a weighting coefficient $e > 0$ which reflects in lumped form the adverse effects of several factors that would come into play as spacecraft weight and complexity is increased. These include:

- Greater development risk
- Mission reliability penalties due to increased complexity in some cases (unless more sophisticated design approach is used which would, in turn, reflect in a higher development cost)
- Increase in cost per launch over the simple linear relation
- Miscellaneous factors, such as greater burden on ground facilities; uncertainty of phenomena to be measured in a precursor mission, which limits the usefulness of increased payload complements; redundancy of payload instruments like magnetometers, occultation experiment, etc., which would be included in the larger payload complements (see Table 12-3).

The penalty coefficient e is not well defined; it expresses judgment which affects the rating of advantages versus risks involved in designing spacecraft of increasing complexity. Nevertheless, the penalty function p(x) provides the format for giving a quantitative weighting to the various adverse effects of unrestrained payload growth. The results of the analysis will show the interesting fact that the preferred region of payload weight is quite insensitive to the value assigned to e.

The modified cost effectiveness index which takes into account the penalty function p(x), and a fixed mission reliability term R_o, is defined by

$$W_2 = R_o \frac{ax}{(b + cx)(1 + ex)}$$

or

$$W_2 = R_o \frac{a}{c} \frac{x}{\left(\frac{b}{c} + x\right)(1 + ex)} \left(\frac{\text{lb payload}}{\text{dollars per launch}}\right)$$

In the discussion which follows we consider the nondimensional term

$$L = \frac{x}{\left(\frac{b}{c} + x\right)(1 + ex)} = \frac{W_2}{R_o \frac{a}{c}}$$

which contains two principal parameters, b/c and e. The significance of these parameters and of a/c is illustrated in Figure 12-2, which shows the payload-to-cost ratios W_1 and W_2 as functions of x. The diagrams indicate the following:

$\frac{a}{c}$ = Upper bound of W_1 for large x and small b/c, i.e., $W_1 \to a/c$ as $x \to \infty$.

$\frac{b}{c} = \frac{\text{max cost}}{\text{min cost}} - 1$; this parameter determines how closely W_1 or W_2 approach the asymptotic value at the maximum payload $x = 1$.

e = determines the drop in the upper bound of W_2 as a function of x as defined by the penalty function p (x). At maximum payload (x = 1) the effectiveness has the upper bound $1/(1 + e)$.

It is seen that L varies over the range $0 \leq L < 1$ as a function of x and the cost parameters. The singular point L = 1 would correspond to the condition b/c = 0 and x = 0 for any value of e. This case has no practical significance.

Figure 12-3 presents the cost effectiveness index L as a function of x with b/c as parameter for two values of e. Figure 12-4 shows a contour plot of L in the x, b/c plane, for e = 0.5. The locus of maximum L values is given by

$$x_{L_{max}} = \sqrt{\frac{b}{ce}}$$

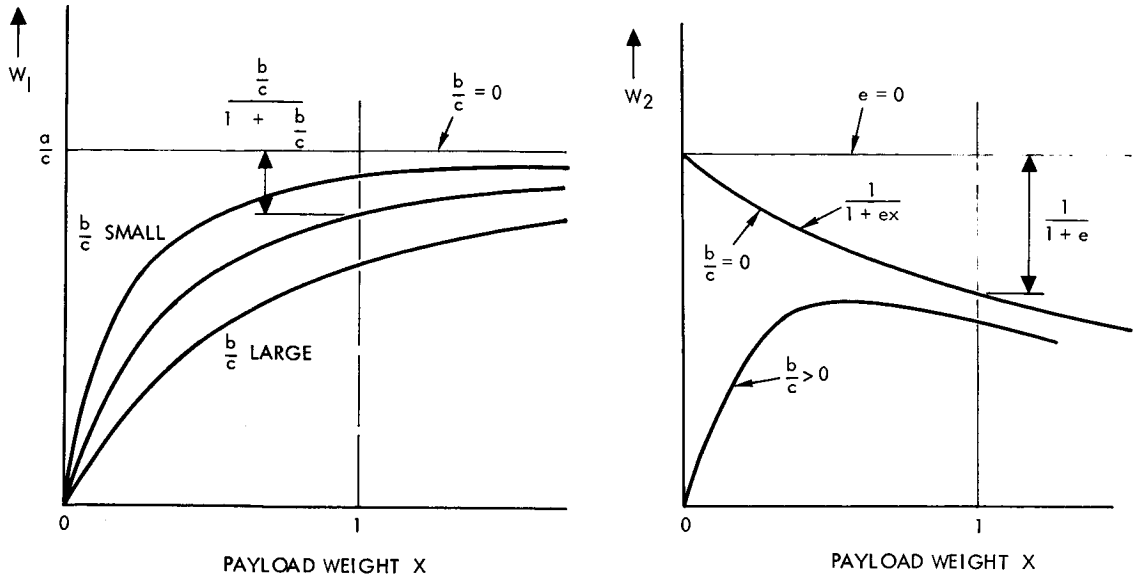

Figure 12-2. Payload Weight-to-Cost Ratios W_1 and W_2

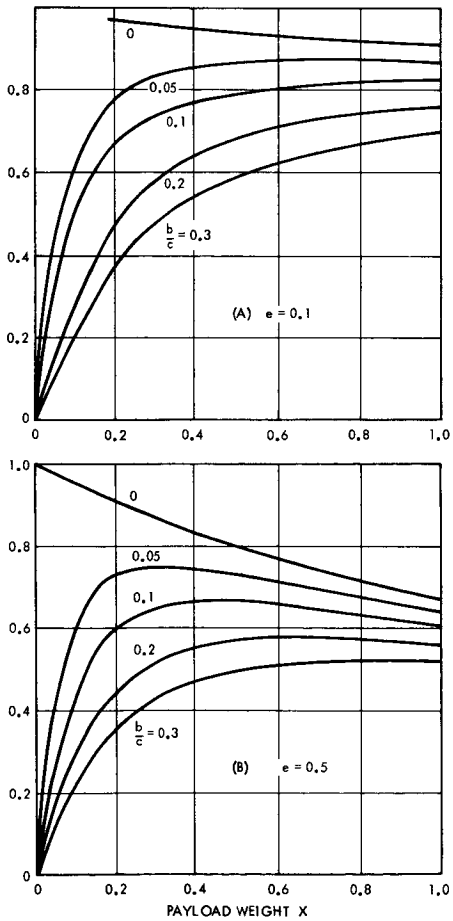

Figure 12-3. Cost-Effectiveness Index Versus Payload Weight

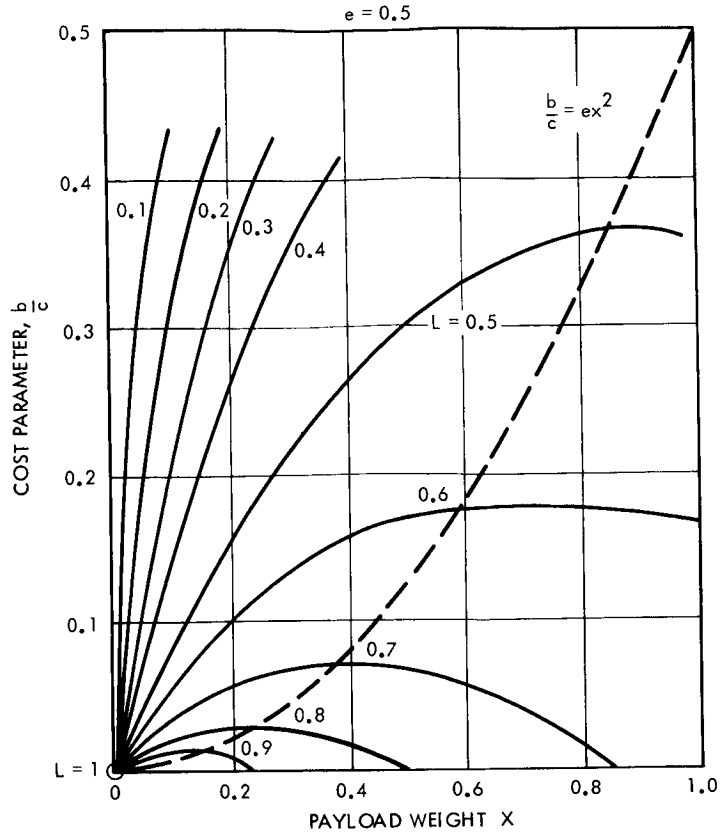

Figure 12-4. Contours of Cost Effectiveness Index

as derived from the previous expression for L. The points on this locus are points of "optimum payload weight" as defined in terms of our simplified cost effectiveness index W_2. However, the preferred choice of payload weight is probably not at the exact location of the "optimum" but at somewhat lower values of x, in a region where the rising curve L = L(x) for a given parameter b/c begins to level off, i.e., in the region of diminishing returns per dollar. This preference is dictated by the desire to achieve good cost effectiveness at a low absolute cost for the mission.

Practical launch vehicle and spacecraft development costs indicate that typical values of the parameter b/c range from 0.05 to 0.15. If more than one spacecraft is developed and launched (i.e., n > 1 in Figure 12-1) the incremental cost factor c decreases as n increases; hence b/c increases, which tends to shift the optimum in the direction of increasing payload weights. The net value of W_2 in pounds per dollar per launch increases with a/c for decreasing c although the maximum value of the index L tends to decrease slightly.

These results are in good agreement with qualitative reasoning. However, a significant quantitative result, not obvious without inspection of the L function, is the fact that a well defined preference is indicated for payloads ranging from $x = 0.2$ to $x = 0.3$. The lower values of x in this range apply to low values of the parameter b/c, for example $b/c = 0.05$ corresponding to the cost ratio of spacecraft launched by Atlas/Centaur/TE-364 and Saturn 1B/Centaur/HEKS.

It is further seen that this result is quite insensitive to the value assumed for the penalty factor e. This is illustrated in Figure 12-5, which shows L as a function of x for three values of e (0.1, 0.5, 1.0) for $b/c = 0.05$. The preferred payload weight $x \simeq 0.2$ is nearly invariant with e.

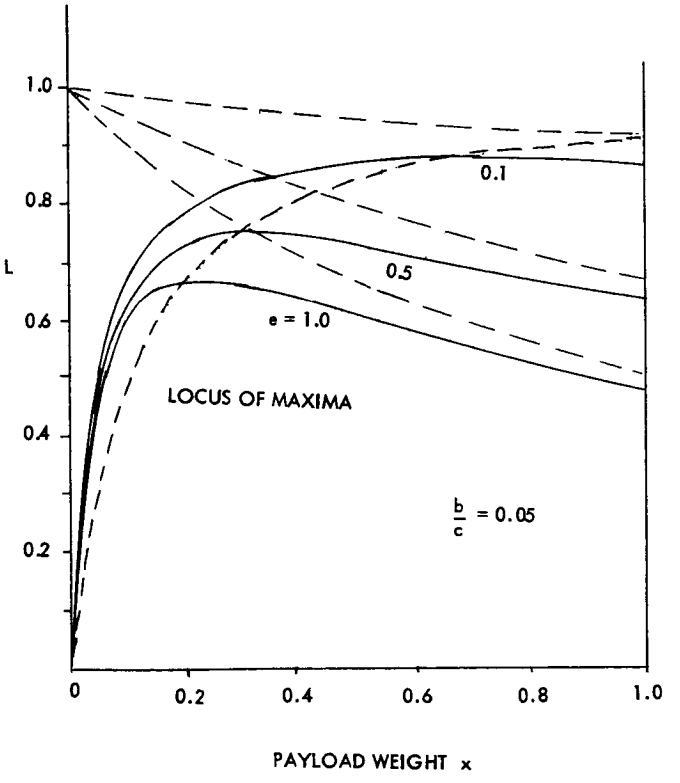

Figure 12-5. Cost-Effectiveness Index, L, for Three Values of Penalty Factor e

The foregoing analysis shows that the lower range of payload weights ($x = 0.2 \ldots 0.3$) is preferred for good cost effectiveness. With the maximum weight of payloads considered here of the order of 250 pounds, the choice would be in the range of 50 to 75 pounds. The actual choice of a payload weight of 50 pounds is consistent with these findings.

Refinement of the model is possible by including details of payload composition and by representing step changes in launch vehicle cost and performance. Mission duration should also be included in a more comprehensive model of cost effectiveness.

This analysis does not evaluate the quantitative tradeoff of the amount and value of scientific and engineering data returned per pound of payload, relative to cost of spacecraft development and mission cost. The analytical formulation of these factors would enhance the usefulness of the quantitative model.

12.4 CONCLUSIONS

The cost effectiveness analysis presented above for the 500-pound class of spin-stabilized spacecraft has shown that, particularly for precursor missions, a payload weight capability of approximately 50 pounds is desirable to provide a well-balanced complement for the interplanetary and planetary science objectives of a Jupiter flyby mission at a comparatively favorable cost. The Atlas/Centaur/TE-364 launch vehicle is used to achieve low energy trajectories with flight times on the order of 700 days. If two or more spacecraft launches are made the cost advantage of the Atlas/Centaur/TE-364 is increased.

The precursor mission has the essential role of providing broad, if not necessarily highly sophisticated or comprehensive, measurements of the interplanetary and planetary environment, which will serve to refine our knowledge of the phenomena to be measured and the range of their physical characteristics for the design of payload complements of subsequent missions. This aspect was essential in arriving at the conclusions stated above.

The precursor will also provide vital engineering data on radiation, micrometeoroid protection in deep space, etc., and on RTG interaction with the science measurements which will be needed in the development

of heavier, more sophisticated and costly spacecraft for later missions. This engineering data will be an essential part of the data return required to make a precursor mission truly cost-effective in the framework of the broader interplanetary exploration program.

The high data rate capability of 700 bits/sec at 6 AU provided by the 16-foot telemetry antenna is a key factor in achieving a cost-effective mission since the transmission of science and engineering data will not be data-rate limited anywhere during the interplanetary cruise and can be handled with suitable short term data storage even during the peak period of planetary encounter. By virtue of the high data rate available, the DSIF network will be tied up intermittently for only short periods of telemetry reception during most of the mission.